

Optical and laser-based in situ diagnostics in lab-scale and pilot-scale spray flames for nanoparticle synthesis

Von der Fakultät für Ingenieurwissenschaften,
Abteilung Maschinenbau und Verfahrenstechnik der
Universität Duisburg-Essen

zur Erlangung des akademischen Grades
eines

Doktors der Ingenieurwissenschaften
Dr.-Ing.

genehmigte Dissertation

von

Markus Michael Prenting
aus
Recklinghausen

Gutachter: Univ.-Prof. Dr. rer. nat. Christof Schulz
Univ.-Prof. Dr.-Ing. Lars Zigan

Tag der mündlichen Prüfung: 13.09.2024

DuEPublico

Duisburg-Essen Publications online

UNIVERSITÄT
DUISBURG
ESSEN

Offen im Denken

ub | universitäts
bibliothek

This dissertation is made available via DuEPublico, the institutional repository of the University of Duisburg-Essen and is also available as printed version.

DOI: 10.17185/duepublico/82469

URN: urn:nbn:de:hbz:465-20241016-103043-6

All rights reserved.

„Den Rest meines Lebens werde ich darüber nachdenken, was Licht ist!“

Albert Einstein im Jahre 1917 [1]

„Fünfzig Jahre intensiven Nachdenkens haben mich der Antwort auf die Frage
"Was ist Licht?" nicht nähergebracht.“

Albert Einstein im Jahre 1951 [1]

Abstract

The flame synthesis of metal-oxide nanoparticles is a rapidly evolving field of research. Nanoparticles feature unique properties and are hence of outstanding interest for numerous applications as, e.g., catalysis, battery technology, or gas sensing. The synthesis in spray flames enables the production of oxides of almost all metal elements based on low-cost precursors. It is possible to synthesize tailored particles with various morphologies and compositions, and thus properties, that are of high interest for industry. However, in its current status the synthesis of metal-oxide nanoparticles is largely on the research stage with production rates on the laboratory scale. Work to upscale processes is progressing, but further research is required to gain a deeper process understanding of the nanoparticle synthesis in spray flames.

This work was conducted within the frame of Priority Program SPP1980 “Nanoparticle Synthesis in Spray Flames” funded by the German Research Foundation (DFG). The aim of this project consortium is to establish a standardized spray burner (referred to as SpraySyn burner) that enables interdisciplinary collaboration across numerous laboratories on the identical spray flame with consistent operating conditions and characteristics. Efforts are aimed at facilitating the exchange of insight, experimental, and simulation data to advance process understanding of the nanoparticle synthesis in spray flames.

In this work, experimental data were generated by optical, mainly laser-based *in situ* diagnostics for two versions of the laboratory-scale SpraySyn flame and two pilot-scale spray flames. For the first version of the SpraySyn flame, chemiluminescence was measured in a spectrally resolved manner at different heights above the burner under various operating conditions (e.g., the synthesis of iron oxide and silica nanoparticles with the precursors iron nitrate nonahydrate and hexamethyldisiloxane, respectively). Droplet velocity and size distributions were measured for the second version of the SpraySyn burner by laser-Doppler and phase-Doppler anemometry, respectively. The data are provided for different operating conditions (variation of flow rates and liquid fuels) in form of two-dimensional maps spanning vertical and horizontal direction as well as flame-centerline profiles. For two pilot-scale spray flames, time-averaged gas-temperature maps were measured by multi-line laser-induced fluorescence thermometry of seeded NO to investigate the impact of gas temperature on the synthesis and the properties of iron oxide nanoparticles.

The main part of this work is on liquid-phase temperature measurements in the evaporating spray of the SpraySyn flame by two-color laser-induced fluorescence thermometry using fluorescing dyes dissolved in the fuel as temperature tracers. An extended study was performed on the suitability of various dyes for the challenging environment. Coumarin 152 turned out to be the most suitable tracer. Its applicability was demonstrated by measuring time-averaged liquid-temperature maps in the first and second version of the SpraySyn burner. Various operating conditions were investigated with ethanol as fuel.

The experimental results generated in this work were used by cooperation partners as boundary conditions for simulations and for the validation of various simulation models.

Kurzfassung

Die Flammensynthese von Metalloxid-Nanopartikeln ist gegenwärtig ein sich rasch entwickelnder Forschungsbereich. Nanopartikel weisen einzigartige Eigenschaften auf und sind daher von herausragendem Interesse für zahlreiche Anwendungen wie z. B. Katalyse, Batterietechnologie oder Gassensoren. Insbesondere die Synthese in Sprayflammen ermöglicht die Herstellung von Metalloxid-Nanopartikeln für fast alle Metallelemente auf Basis kostengünstiger Ausgangsstoffe. Es ist möglich, maßgeschneiderte Partikel mit verschiedenen Morphologien und Zusammensetzungen und daraus resultierenden Eigenschaften zu synthetisieren, die für die Industrie von großem Interesse sind. Dennoch befindet sich die Synthese von Metalloxid-Nanopartikeln noch weitgehend im Forschungsstadium mit Produktion im Labormaßstab. Arbeiten zur Hochskalierung des Prozesses machen Fortschritte, aber für Weiterentwicklungen sind weitere Forschungsarbeiten erforderlich, um ein tieferes Verständnis der Nanopartikelsynthese in Sprayflammen zu erlangen.

Diese Arbeit wurde im Rahmen des Schwerpunktprogramms SPP1980 „Nanopartikelsynthese in Sprayflammen“ der Deutschen Forschungsgemeinschaft (DFG) durchgeführt. Ziel des Projektes ist die Etablierung eines standardisierten Sprayflammenbrenners (SpraySyn-Brenner), der die interdisziplinäre Zusammenarbeit zahlreicher Forschungsgruppen an identischen Sprayflammen mit einheitlichen Eigenschaften ermöglicht. Die Bemühungen zielen darauf ab, den Austausch von Erkenntnissen, experimentellen und Simulationsdaten zu erleichtern, um ein tieferes Verständnis der Partikelsynthese in Sprayflammen zu erlangen.

In dieser Arbeit wurden experimentelle Datensätze durch optische, hauptsächlich laserbasierte In-situ-Diagnostik, für zwei Versionen der SpraySyn-Flamme und für zwei Sprayflammen im Pilotmaßstab erzeugt. Für die erste Version der SpraySyn-Flamme wurde die Chemilumineszenz in verschiedenen Höhen über dem Brenner unter verschiedenen Betriebsbedingungen spektral aufgelöst gemessen (z. B. die Synthese von Eisenoxid- oder Siliciumdioxid-Nanopartikeln mit den Ausgangsstoffen Eisennitrat-Nonahydrat oder HMDSO). Für die zweite Version des SpraySyn-Brenners wurden Tropfengeschwindigkeit und -größenverteilungen durch Laser-Doppler- und Phasen-Doppler-Anemometrie gemessen. Die Daten wurden für unterschiedliche Betriebsbedingungen (verschiedene Durchflussmengen und flüssige Brennstoffe) als zweidimensionale Verteilungen in vertikaler und horizontaler Richtung und als Flammennittellinienprofile dargestellt. Für zwei Sprayflammen im Pilotmaßstab wurden durchschnittliche zweidimensionale Gastemperaturverteilungen mit Hilfe der laserinduzierten Mehrlinien-Fluoreszenzthermometrie gemessen, um den Einfluss der Gastemperatur auf die Synthese und die Eigenschaften von Eisenoxid-Nanopartikeln zu untersuchen.

Der Hauptteil dieser Arbeit befasst sich mit Temperaturmessungen in der Flüssigphase der SpraySyn-Flammen durch Zwei-Farben-laserinduzierte-Fluoreszenzthermometrie. Für die herausfordernde Umgebung verdampfender Tröpfchen in Flammen geeignete Fluoreszenzmarker wurden vergleichend untersucht. Der Laserfarbstoff Coumarin 152 erwies sich dabei als am besten geeignet. Seine Eignung wurde durch die Messung zeitlich gemittelter Flüssigkeitemperaturverteilungen in den SpraySyn-Flammen nachgewiesen. Es wurden Flammen mit verschiedenen Betriebsbedingungen mit Ethanol als Flüssigbrennstoff untersucht.

Die in dieser Arbeit gewonnenen experimentellen Ergebnisse wurden durch Kooperationspartner als Randbedingungen für Simulationen und für die Validierung verschiedener Simulationsmodelle verwendet.

Content

1	Introduction	1
2	Fundamentals of nanoparticle synthesis in spray flames	4
2.1	Characteristics and applications	4
2.2	Pathways to nanomaterials production	5
2.3	Nanoparticle formation in spray-flame synthesis	5
2.4	State of research for tailored nanoparticle-synthesis in spray flames	8
3	Spray burners for nanoparticle synthesis.....	12
3.1	SpraySyn burner version 1	12
3.2	SpraySyn burner version 2.....	15
3.3	Berlin burner.....	16
3.4	HSW burner	17
4	Chemiluminescence in the context of nanoparticle synthesis in the SpraySyn1 flame...19	
4.1	Theoretical background.....	19
4.2	Experimental setup.....	20
4.2.1	Calibration.....	21
4.2.2	Postprocessing of camera images.....	22
4.3	Results	23
4.3.1	Liquid fuel: Ethanol.....	23
4.3.2	Liquid fuel: 65EHA35EtOH.....	25
4.3.3	Liquid fuel: HMDSO in ethanol	26
4.3.4	Liquid fuel: Iron nitrate nonahydrate in 65EHA35EtOH.....	28
4.4	Summary and discussion	31
5	Spray characterization of the SpraySyn2 burner (LDA and PDA)	33
5.1	Theoretical basics	33
5.2	Experimental setup.....	34
5.2.1	Signal postprocessing	36
5.2.2	Measurement error.....	36
5.3	Results	37
5.3.1	Liquid fuel: Ethanol.....	37
5.3.2	Liquid fuel: 65EHA35EtOH.....	45
5.3.3	Comparison of different liquid fuels	49
5.4	Summary and discussion	52
6	Multi-line NO-LIF gas-temperature imaging in pilot-scale spray flames	53
6.1	Theoretical background.....	54

6.1.1	Two-level model.....	54
6.1.2	Marker species.....	56
6.1.3	Spectral range for multi-line NO-LIF	57
6.2	Experimental setup.....	59
6.2.1	Dye laser.....	59
6.2.2	Measurement setup.....	60
6.3	Measurement procedure	63
6.3.1	Post-processing with LIFSim	65
6.3.2	Measurement error.....	65
6.3.3	Operating conditions	67
6.4	Results	69
6.4.1	Berlin burner	69
6.4.2	HSW burner	76
6.5	Summary and Discussion.....	79
7	Study on suitable tracers for two-color laser-induced fluorescence in liquids.....	82
7.1	Requirements for suitable fluorescence tracers.....	83
7.2	Experimental setup.....	84
7.2.1	Temperature-controlled measurement cell	84
7.2.2	Absorption spectrometer	85
7.2.3	Fluorescence spectrometer.....	86
7.2.4	Overview of fluorescent tracers and solvents	87
7.2.5	The β factor in the context of 2cLIF thermometry	88
7.3	Results.....	89
7.3.1	Absorption and fluorescence spectra of chosen tracers	89
7.3.2	Peak and centroid shift of fluorescence spectra	99
7.3.3	Temperature sensitivity for two-color LIF thermometry.....	100
7.3.4	Fluorescence signal re-absorption.....	106
7.3.5	Spectral influence of solvent composition.....	110
7.4	Discussion.....	112
7.5	Conclusions.....	114
8	Liquid-phase temperature imaging in the SpraySyn flames with two-color tracer LIF ..	115
8.1	Averaged liquid-phase temperature maps	115
8.1.1	Two-color LIF thermometry with coumarin 152.....	116
8.1.2	Experimental setup for 2cLIF temperature imaging	117
8.1.3	Large-eddy simulation of the SpraySyn flame	122

8.1.4	Results	124
8.2	Instantaneous 2cLIF droplet thermometry in the SpraySyn2 flame.....	131
8.2.1	Measurement principle of instantaneous 2cLIF droplet thermometry.....	131
8.2.2	Experimental setup	131
8.2.3	Measurement procedure	134
8.2.4	Measurement error of single-shot liquid-temperature maps.....	135
8.2.5	Results	138
8.3	Summary and discussion	144
8.4	Outlook and improvement suggestions for future work	146
9	Summary and conclusions	148
10	Outlook and future work.....	152
11	References	154
12	Appendix.....	182
12.1	Substances used in this work	182
12.2	HSW burner	183
12.3	Spectrally resolved chemiluminescence in the SpraySyn flame	184
12.3.1	Liquid fuel: Ethanol.....	184
12.3.2	Liquid fuel: 65EHA35EtOH.....	185
12.3.3	Liquid fuel: 1-Butanol.....	188
12.3.4	Liquid fuel: o-Xylene.....	190
12.3.5	Liquid fuel: Iron nitrate nonahydrate in ethanol.....	192
12.4	Droplet velocity and size distributions (PDA)	195
12.4.1	Ethanol.....	195
12.4.2	1-Butanol.....	203
12.4.3	o-Xylene.....	206
12.4.4	Isopropyl alcohol	209
12.4.5	Acetone.....	210
12.4.6	Deionized water	213
12.5	Multi-line NO-LIF (IUTA).....	214
12.5.1	Table of devices and components used	214
12.5.2	Details of the Berlin burner operating conditions	215
12.6	Absorption and fluorescence spectra of chosen tracers	216
12.6.1	Physical and chemical properties of relevant laser dyes.....	216
12.6.2	Analysis regarding 2cLIF thermometry	217
12.6.3	Spectral influence of the solvent ratio of EHA/ethanol	223

12.6.4	Temperature and concentration dependent spectra in various solvents	224
12.7	Application of smoothing filters to single-shot images (inst. 2cLIF)	235
12.7.1	Single-shot intensity maps.....	235
12.7.2	Single-shot ratio maps.....	236
12.7.3	Average liquid-temperature maps.....	237
12.8	SpraySyn2 flame: Radial average liquid-temperature profiles	238
	Archiving and Reuse of Research Data	240
	Own Publications.....	241
	Danksagung	243

Nomenclature

Latin symbols

Symbol	Unit	Meaning
A	/ m ²	Area
A_{21}	/ s ⁻¹	Einstein coefficient for spontaneous emission
B_{12}	/ m ³ J ⁻¹ s ⁻²	Einstein coefficient for absorption
b_{12}	/ s ⁻¹	Rate constant of stimulated absorption from energy level 1 to 2
B_{21}	/ m ³ J ⁻¹ s ⁻²	Einstein coefficient for stimulated emission
b_{21}	/ s ⁻¹	Rate constant of stimulated emission from energy level 2 to 1
B_h	/ -	Spalding number for heat transfer
B_m	/ -	Spalding number for mass transfer
c	/ m/s	Speed of light in vacuum constant
c_m	/ mol/m ³	Molar concentration
c_{mass}	/ mg/l	Mass concentration
c_p	/ -	Heat capacity at constant pressure
D	/ m	Diameter
E_g	/ cm ⁻¹	Energy of ground state
F	/ J/m ²	Laser fluence
f	/ mm	Focal length
f_1	/ -	Drag coefficient
f_B	/ -	Boltzmann fraction
f_{Hz}	/ Hz	Frequency
g	/ m/s ²	Gravitational acceleration
g_λ	/ -	Overlap between the absorption and laser line
h	/ kg m ² /s	Planck constant
H_R	/ J/mol	Reaction enthalpy
I_0	/ W/m ²	Excitation intensity
I_{ex}	/ W/m ²	Laser excitation irradiance
I_F	/ W/m ²	Fluorescence intensity
I_{LIF}	/ W/m ²	LIF signal intensity
I_{sat}	/ W/m ²	Saturation irradiance
J	/ -	Rotational quantum number
L	/ kJ/kg	Latent heat
l	/ m	Axial extent of the laser sheet
l_{abs}	/ mm	Absorption path length
m	/ kg	Mass
n	/ m ⁻³	Particle number density
N	/ m ⁻³	Molecule number density
Nu	/ -	Nusselt number
O	/ nm	Overlapping area of absorption and fluorescence spectra
P_{2i}	/ s ⁻¹	Rate constant of predissociation
Pr	/ -	Prandtl number
Q_{21}	/ s ⁻¹	Rate constant of collisional quenching from energy level 2 to 1
R^2	/ -	Coefficient of determination (statistics)
Re	/ -	Reynolds number
R_{LIF}	/ -	LIF signal intensity ratio
Sc	/ -	Schmidt number

S_D	/ W/m ²	Detection signal
Sh	/ -	Sherwood number
T	/ K	Temperature
t	/ s	Time
u	/ m/s	Droplet downstream velocity
V	/ m ³	Volume
v	/ m/s	Droplet radial velocity
W_{2i}	/ s ⁻¹	Rate constant of photoionization
x	/ mm	Position
Y	/ -	Progress variable
Z	/ -	Mixture fraction fraction

Greek symbols

Symbol	Unit	Meaning
ε	/ (mol cm) ⁻¹	Molar attenuation coefficient
η	/ -	Detection efficiency
Ω	/ -	Detection solid angle
π	/ -	Archimedes constant
τ	/ -	Transmittance of light
τ_d	/ s	Droplet relaxation time
ν_f	/ s ⁻¹	Frequency of light
ϕ_f	/ -	Fluorescence quantum yield
ε_r	/ -	Relative permittivity or dielectric constant
λ	/ m	Wavelength
β	/ K	Beta factor
ρ	/ kg/m ³	Density
σ	/ mol ⁻¹	Absorption cross-section
σ_{SD}	/ -	Standard deviation
$\tilde{\nu}$	/ cm ⁻¹	Wavenumber

Acronyms

Symbol	Meaning
2cLIF	Two-color laser-induced fluorescence
65EHA35EtOH	Mixture by volume of 65 % 2-ethylhexanoic acid and 35 % ethanol
BB	Berlin burner
BBO	Barium borate
BET	Gas adsorption analysis according to Brunauer, Emmet, and Teller
CFD	Computational fluid dynamics
CMD	Count mean diameter
CMOS	Complementary metal-oxide semiconductor
CPS	Counts per second
CS	Color scale
DCM	(2-(2-(4-(dimethylamino)phenyl)ethenyl)-6-methyl-4H-pyran-4-ylidene)-propanedinitrile
DEM	Discrete element modeling
DFG	German Research Foundation

DGL ratio	Ratio between dispersion-gas flow to liquid flow rate
EHA	2-Ethylhexanoic acid
EMPI-RF	Institute for Energy and Materials Processes – Chair of Reactive Fluids
EtOH	Ethanol
FCU	Frequency conversion unit
FFT	Fast Fourier transformation
FGM	Flamelet-generated manifold
FWHM	Full width at half maximum
HAB	Height above burner
HITRAN	High-resolution transmission molecular absorption database
HM	Half maximum
HMDSO	Hexamethyldisiloxane
HP	Half pilot flame
HSWB	HSW burner
ICAN	Interdisciplinary Center for Analytics on the Nanoscale
IUTA	Institute for Energy and Environmental Technology (Institut für Umwelt & Energie, Technik & Analytik e.V.)
LDLS	Laser-driven light source
LES	Large-eddy simulation
LIF	Laser-induced fluorescence
MDR	Morphology-dependent resonances
MFC	Mass-flow controller
MMC	Multiple mapping conditioning
Nd:YAG	Neodymium-doped yttrium aluminum garnet
NP	Nanoparticle
OC	Operating condition
PDA	Phase-Doppler anemometry
PDF	Probability density function
PFGM	Premixed flamelet-generated manifold
PMT	Photomultiplier
PsiPhi	In-house code on equidistant Cartesian grids, name from the two main variables Psi and Phi
PTP	p-Terphenyl (1,1':4'1"-terphenyl)
RANS	Reynolds-averaged Navier–Stokes
ROI	Region of interest
SEM	Scanning electron microscope
SFM	Sum-frequency mixing
SFS	Spray-flame synthesis
SpraySyn1	SpraySyn burner version 1
SpraySyn2	SpraySyn burner version 2
TEM	Transmission electron microscopy
TTIP	Titanium tetraisopropoxide
UDE	University of Duisburg-Essen
UV	Ultraviolet
XRD	X-ray diffraction

1 Introduction

Nanotechnology is currently a very active research field with the potential of revolutionary impacts in numerous areas. It offers a broad spectrum of opportunities for a variety of applications and holds prospects for innovation and breakthroughs within multiple sectors. At present, progress is made across many domains in the field of nanotechnology. One major focus is on nanoparticles and their applications due to their unique characteristics [2, 3]. Typically, particles within the diameter range of 1 to 100 nm are denoted nanoparticles [2, 4]. Particles smaller than 1 nm are commonly referred to as atomic clusters. To provide an estimation, that size range corresponds to an atom number of approximately 100 to 10^8 [5-7] (diameter of oxygen atoms: ~ 0.1 nm, diameter of metal atoms up to ~ 0.6 nm [8, 9]). The particles in this size range feature unique properties, different to those of larger particles or the bulk form of the same material. Due to their small size, nanoparticles are characterized by a large surface-to-volume ratio that cause a high reactivity, e.g., catalytical activity [10, 11]. Moreover, nanoparticles feature new material properties in various fields, such as, e.g., antibacterial properties [12], light-matter interaction [13-17], magnetism [18], optoelectronics [19], melting point [20, 21], and other physicochemical properties [22, 23] which can potentially be utilized in many new applications.

Because of these unique material characteristics and application possibilities, the synthesis of tailored nanoparticles with desired properties is a dynamic field of research. In general, nanoparticle production is classified in two pathways [23, 24]. On one hand the top-down process describes approaches where the nanoparticles are produced from bulk material, e.g., milling or laser ablation [25]. And on the other hand, the bottom-up process describes all approaches where the nanoparticles are formed by growth at the atomic level, e.g., chemical synthesis in liquids [26]. Among the bottom-up processes, flame synthesis is a promising approach for the continuous-flow production of tailored nanoparticles with high purity and various morphologies. In this field, the focus is particularly on the synthesis in spray flames [27, 28] as the liquid enables the delivery of almost all elements of the periodic table to the flame. The entire spectrum of metals becomes available for nanoparticle synthesis and a nearly endless variety of materials compositions [29-31] can be produced.

Metal-oxide nanoparticles with adjustable morphologies and compositions are of great interest because their properties make them very promising for numerous applications in many areas, as e.g., energy storage [32, 33], battery technology [34, 35], or medical technology [36]. The laboratory-scale spray-flame synthesis (SFS) of various metal-oxide nanoparticles was already successfully realized. Comprehensive overviews are given in the reviews of Li et al. [37] and Teoh et al. [38]. However, to improve the control of the nanoparticle synthesis and to extend the spectrum of producible nanoparticles more process understanding is a prerequisite. Currently, research in various fields is in progress by numerous research groups around the globe [39-46]. One further topic of high interest is the large-scale production of nanoparticles [47, 48]. Particle synthesis in spray flames is a promising approach that can be scaled from laboratory to industrial production rates. So far, progress in upscaling has mainly been achieved through empirical studies rather than through profound process understanding, so that research in this area offers great potential for further improvements. Above all, advancing *in situ* diagnostics for application in spray flames is paramount to attain deeper insight into the chemical and physical processes of nanoparticle synthesis. Overall, the scale-up of targeted

nanoparticle production remains challenging and further process knowledge is required for its systematic implementation [49].

This work was conducted as part of the DFG research program SPP1980 “Nanoparticle synthesis in spray flames” that aims at closing the aforementioned gaps of knowledge by joint research of numerous groups on a standardized spray burner for nanoparticle synthesis. This so-called SpraySyn burner (section 3.1) is a modified version of the concept introduced by Mädler et al. [28] and was designed to provide simulation-friendly boundary conditions and enable optical access from multiple directions to facilitate non-intrusive optical measurements. Specific operating conditions were defined to enable the comparability of experimental and simulation results across various research groups working on different topics. Figure 1 shows two photographs of the SpraySyn flame operated with different solvents. On the left the pure-ethanol spray flame is shown and on the right the flame during iron oxide nanoparticle synthesis. The project is targeted at the synthesis of metal-oxide nanoparticles (e.g., Fe_2O_3 , TiO_2 , or SiO_2) from precursor solutions of inorganic metal salts (e.g., iron nitrate nonahydrate), metal organic compounds (e.g., TTIP) or other organic compounds containing metalloids (e.g., HMDSO). Comprehensive simulations of the nanoparticle synthesis in spray flames are a central aim of the priority program to enable the tailored design of synthesis processes. To achieve this goal deeper process understanding based on experimental data generated from in situ diagnostics are a prerequisite. A broad spectrum of experimental data is delivered by numerous sub-projects with a variety of measurement techniques (cf. section 3.1) to enable the progression from sub-process simulation to comprehensive simulations of the holistic spray-flame synthesis.



Figure 1: Photographs of the SpraySyn1 flame operated at the standard condition. Liquid fuel, left: Ethanol, right: Solvent mixture by volume of 65 % 2-ethylhexanoic acid (EHA) and 35 % ethanol with the precursor iron nitrate nonahydrate for iron-oxide nanoparticle synthesis.

Experimental investigations of various aspects of the nanoparticle synthesis in spray flames are the basis for deeper process understanding and the development of simulation models. In collaboration with other research groups, the main aim of this work was the generation and delivery of optical measurement data for, e.g., the improvement and upscaling of burner designs, development of reaction mechanisms, and for the validation of spray-flame simulations.

The selection of optical measurement techniques resulted from several pivotal advantages, notably their non-intrusive nature, ensuring that flame chemistry and physics remain unaffected during the measurements. In contrast to most other approaches, optical techniques enable spatially resolved measurements to obtain data maps of various parameters, such as temperature [50] or species concentrations [51]. By the utilization of high-repetition-rate cameras or pulsed lasers, data with high temporal resolution can be generated, enabling the analysis of rapid events, such as droplet micro-explosion [52] or turbulent flows [53-55].

In this work, optical – mainly laser-based – measurement techniques are further developed and adapted to the application case of laboratory- or pilot-scale spray flames. Data packages were generated and provided to the SpraySyn data base [56] for collaboration across research groups. A brief overview of the contents of this thesis is given below. Chapter 2 presents fundamentals of spray-flame synthesis of nanoparticles and a brief literature review, followed in chapter 3, by a description of the four laboratory- and pilot-scale spray burners investigated in this work. In chapter 4 spectrally resolved flame chemiluminescence measurements at different heights above the SpraySyn1 burner operated with different precursor solutions are presented and the location of various species emission (e.g., OH*, CH*, SiO*, FeO*) analyzed. Chapter 5 contains a broad data set of droplet velocity and size distributions measured by laser-Doppler and phase-Doppler anemometry. The measurements were performed in the cold spray and the flame of the SpraySyn2 burner operated with various solvents (ethanol, 1-butanol, o-xylene, EHA, isopropanol) and dispersion gas flows (in the range of 4–8 slm O₂). In chapter 6, time-averaged flame-temperature maps are provided for two pilot-scale spray burners, measured by multi-line NO laser-induced fluorescence (LIF) thermometry under multiple operating conditions (variation of dispersion-gas flow rate, type of pilot flame fuel and liquid fuel). Chapter 7 presents a study on suitable tracers for two-color laser-induced fluorescence thermometry in liquids aimed at the challenging application case of evaporating sprays, in particular spray flames. In this study, 13 laser dyes were investigated focusing on their temperature sensitivity, fluorescence-signal re-absorption, and sensitivity to changes in the solvent composition. Based on this study, coumarin 152 was chosen as the most-suitable candidate to measure average liquid-phase temperature maps of the SpraySyn1 flame by two-color laser-induced fluorescence. Details of the measurement procedure and the results are presented in the first part of chapter 8. In the second part the technique is extended to single-shot measurements in the SpraySyn2 flame. In chapter 9, the central measurement results of this thesis are summarized and analyzed, while also discussing the findings and advancements for further development of the applied measurement techniques. Chapter 10 concludes the thesis by providing an outlook on potential future steps.

2 Fundamentals of nanoparticle synthesis in spray flames

This chapter introduces the fundamentals of nanoparticle synthesis in spray flames with a focus on the flame parameters affecting particle formation and consequently their properties. Some selected phenomena (e.g., droplet micro-explosions) are highlighted and discussed. In the end an outline of recent progress and active fields of research within the scope of nanoparticle synthesis in spray flames is given.

2.1 Characteristics and applications

Nanoparticles are of great interest because their small size causes unique properties that open a wide range of possible applications. Due to their small size (<100 nm), they cannot be captured by visible light (380–800 nm), and are therefore not observable by ordinary microscopes. Nanoparticles tend to agglomerate due to their mutual attraction, primarily driven by Van der Waals forces, which become particularly significant at the nanometer scale [57]. They can consist of various substances (e.g., metal oxides, metals, carbon, or polymers) and feature different morphologies (e.g., soft and hard agglomerates [58], nanowires [59], nanotubes [60], two-dimensional flakes [61] or platelets [62]). The properties are linked to their characteristics (e.g., size, morphology, materials composition). Outlined below is an overview comparing typical nanoparticle characteristics and properties with those of larger particles or bulk materials:

- Higher surface-to-volume ratio
- Higher surface energy [63, 64]
- Higher reactivity (e.g., catalytic activity [65])
- Higher photocatalytic activity [66]
- Antibacterial properties [67]
- Superparamagnetic properties (e.g., iron oxide [68])
- Altered optical properties (e.g., quantum size effects [69] or Kerr effect [70])
- Altered thermodynamic properties [71]
- Altered electronic properties (e.g., higher electrical conductivity of ceramics [72] and higher electrical resistivity of metals [73])
- Higher thermal conductivity [4]
- Lower thermal stability, melting point [74]
- Higher hardness and yield strength [4]
- Lower impact of gravity while higher impact of van der Waals forces [75]
- Higher luminescence of semiconductors [72]
- Various altered properties when dispersed in liquids [4]

The aforementioned nanoparticle characteristics and properties provide the basis for a variety of applications. Examples for existing or proposed applications include:

- Catalysis [65, 76-79]
- Materials for batteries [80, 81]
- Gas sensors [82, 83]
- Light-emitting diodes [84]
- Data storage [85, 86]
- Stabilization of emulsions [87]
- Magnetic nanofluids (ferrofluids) [88, 89]
- Drug delivery systems [90, 91]

- Food additives (e.g., SiO₂, identifier E551 [92])
- Water purification [67, 93]
- Carbon capture [94, 95]
- Photocatalysis [66, 96]
- Biomedical applications [97]
- Molecular imaging [98]
- Solid rocket propellants [99]

2.2 Pathways to nanomaterials production

Nanoparticles are formed naturally (e.g., by volcanic eruptions or interplanetary dust), through common activities such as a camp fire or can be deliberately synthesized. One pivotal concern is the production of nanoparticles in viable quantities to exploit their unique properties for various applications, as listed above. The history of nanoparticle production started in ancient times when Egyptian (about 5,000 years ago), Indians, and Chinese produced carbon-black nanoparticles in large quantities by oxygen-deficient sooting flames for the use in inks and paints [100, 101]. According to latest findings, more than 4,000 years ago in ancient Egypt lead-sulfide nanoparticles (~5 nm) were synthetically produced for hair dyeing [102]. The famous Roman Lycurgus cup from the 4th century is made of dichroic glass that reflects green light and transmits red light. This optical effect is achieved by the dispersion of colloidal gold-silver alloy nanoparticles (50–100 nm in diameter) within the glass material of the cup [103]. In the more recent past, in 1857 Michael Faraday synthesized gold nanoparticles by the reduction of gold chloride in an aqueous solution [13], and in the first half of the 20th century the large-scale production of SiO₂ and TiO₂ nanoparticles by flame synthesis was initiated by Degussa (today Evonik) [73, 104]. Nowadays, in addition to the production of SiO₂ and TiO₂ nanoparticles using gas phase synthesis, the production of other nanoparticles, such as zinc oxides, iron, and other non-oxide ceramics, is carried out using hot-wall reactors [105-107]. Alternative production techniques for nanoparticles include, ball milling [108], laser ablation [109], inert gas condensation [110], and wet-chemistry methods, e.g., the sol-gel process [111].

Among the available production processes, nanoparticle synthesis in spray flames stands out due to its major advantage that the liquid solvent enables the delivery of an almost endless variety of precursors to the flame synthesis. This approach was introduced by Sokolowski et al. [27] in 1977 for the synthesis of Al₂O₃ nanoparticles from aluminum acetylacetonate. Because the applicable precursors can contain almost all elements, access to a large variety of novel materials [49, 112] is granted. This versatile method enables the production of a wide range of nanomaterials that are not accessible by other production techniques, such as the formation of mixed oxides through the combination of precursor species [113], or hetero-aggregates via the double-flame synthesis [114-116]. Moreover, it is a continuous production process and enables the generation of tailored nanoparticles as the synthesis can be controlled by the operating condition of the flame.

2.3 Nanoparticle formation in spray-flame synthesis

In a typical setup for the spray-flame synthesis of nanoparticles, a combustible precursor solution is atomized (usually by a two-fluid nozzle) into a pilot flame that continuously stabilizes the spray flame [49]. More detailed explanations referring to the SpraySyn burner are provided in section 3.1. Alternative spray-flame and burner concepts can be found in [117-125]. In most

cases, the solvent provides heat by combustion, while the precursor decomposes in an endothermic process (e.g., metal nitrates) or provides combustion enthalpy via oxidative decomposition, such as in metalorganic precursors (e.g., TTIP). The droplets formed experience an increase in temperature and evaporate. If certain conditions are met, the phenomenon of droplet micro-explosions occurs, which is considered to be beneficial for the synthesis of homogeneous nanoparticles as they enhance the droplet evaporation [126].

In recent years, droplet micro-explosions and droplet puffing (weak droplet disruptions) have been investigated by different techniques under various conditions, such as high-speed imaging of single-droplet combustion [127, 128], single-droplet heating [129], acoustic analysis of single droplets [130], or within spray flames by high-speed, high-magnification shadowgraphy [52, 131, 132]. Moreover, theoretical investigations and modeling of droplet micro-explosions have been conducted [133-137]. According to current knowledge from the literature, the pre-conditions for droplet micro-explosion to occur are, the presence of a solvent mixture of components with different boiling points or a shell-forming component, and a high ambient gas temperature high enough to preferentially evaporate one volatile component from the droplet surface area [137]. When a solvent mixture of components with a large difference of their boiling point is present (e.g., EHA and ethanol), the volatile solvent evaporates from the surface-near area but remains at higher concentration in the center of the droplet. By superheating of the volatile component, rapid expansion causes the droplet to explode [128]. A similar effect can occur when precursors with a low vapor pressure (e.g., metal nitrates) are used that form viscous shell at the droplet surface that hinders evaporation. As a result of superheating and rapid expansion of the volatile component, explosion occur [138, 139]. The flame temperature is a crucial factor influencing droplet micro-explosions as it affects the evaporation rate resulting in a potential imbalance of heat and species transport. Antonov et al. [140] investigated the impact of the initial diameter and flame temperature on puffing events and micro explosions of rapeseed-oil/water droplets. The results show that as the initial droplet diameter increases, the duration until puffing or micro-explosion increases, while elevated flame temperatures reduce the time to these events. Rosebrock et al. [126] showed for spray-flame synthesis of ZnO, Al₂O₃, and Fe₂O₃/Fe₃O₄ that the existence of micro-explosions result in more uniform nanoparticle powders.

There are two main pathways for the nanoparticle formation in spray flames. On one hand the gas-to-particle pathway, where particles nucleate in the gas phase, while via the droplet-to-particle pathway, particles nucleate, grow, and aggregate in the liquid phase of the droplets [141]. When the precursor decomposes before vaporization, particles are formed via the droplet-to-particle pathway, whereas the gas-to-particle pathway is followed when the precursor vaporizes before decomposition [142]. Figure 2, left shows a sketch of a spray flame and on the right schematically and simplified the mechanism steps for nanoparticle synthesis via both formation pathways, illustrated through the example of metal-oxide nanoparticle formation.

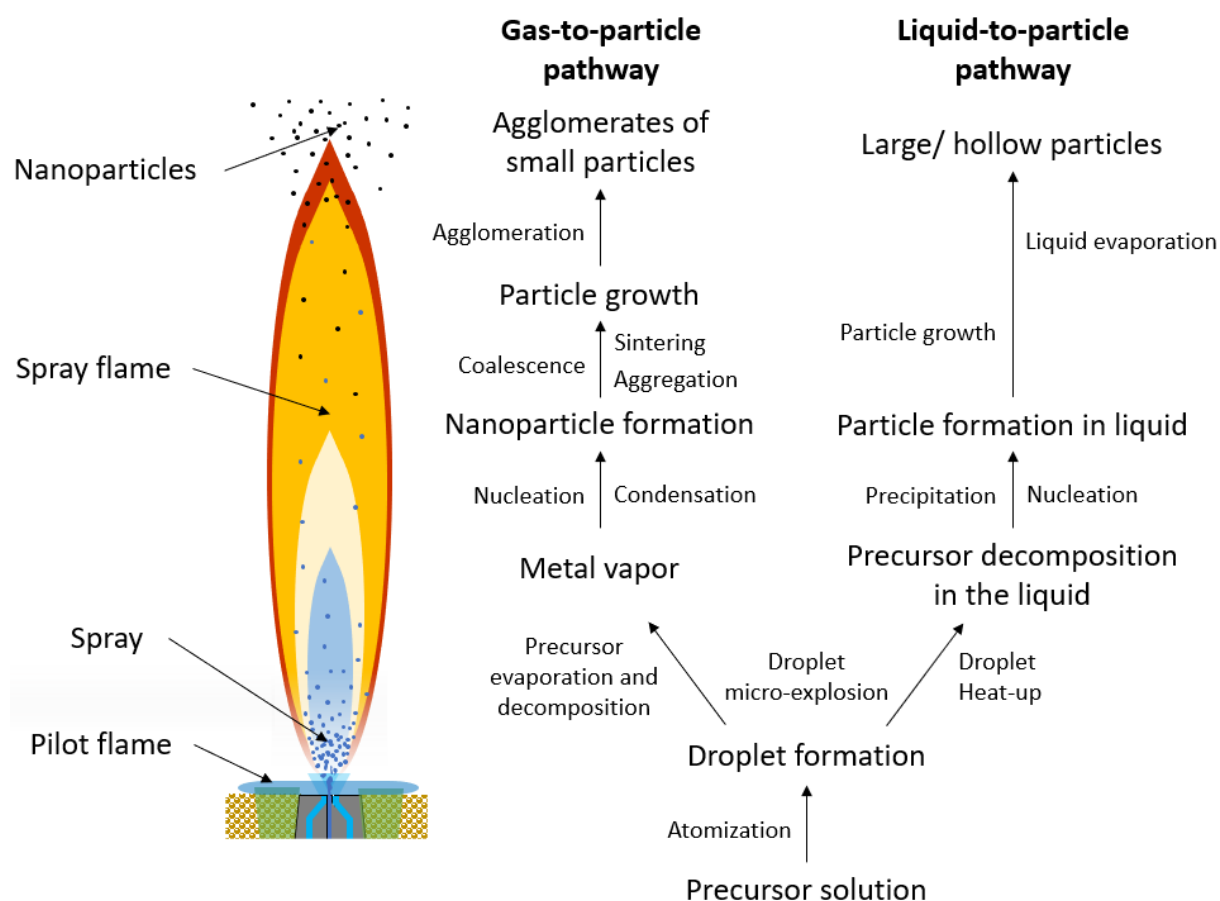


Figure 2: Schematic illustration of process steps of particle formation in spray-flames via the gas-to-particle and liquid-to-particle pathway. Adapted to the synthesis of metal-oxide nanoparticles.

Typically, the gas-to-particle formation is the desired pathway, since rather small nanoparticles with a homogenous size distribution are formed [143]. After atomization and droplet formation, the solvent combusts and the precursor (here, a metal nitrate) produces gas-phase species that due to high supersaturation lead to the nucleation of nanoparticles [141]. Subsequently, the nanoparticles grow by surface growth and coalescence, and form aggregates. As the nanoparticles enter cooler gas zones of the flame, they agglomerate and form nanoparticle clusters [58, 107].

In contrast to the gas-to-particle pathway, the usually undesired liquid-to-particle pathway forms relatively large and, in many cases hollow particles, with particle sizes often exceeding 100 nm [143-145]. Depending on various parameters (e.g., droplet size and precursor-solution properties) some droplets meet the preconditions (e.g., temperature-time history) for particle formation in the liquid phase while other parts evaporate and follow the gas-to-particle synthesis pathway. When the liquid-to-particle pathway exists in parallel to the gas-to-particle process, typically a bimodal particle-size distribution is formed [146, 147]. For the liquid-to-particle synthesis pathway the droplets experience a droplet heat-up and the precursor precipitates within the liquid. The particles grow in size within the liquid, that evaporates at some point leaving the large particle behind. Hollow particles are formed by the liquid-to-particle pathway when the particles are transported to the phase boundary combining into a solid shell. When the residual liquid evaporates without droplet disruption, hollow particles are left behind [148].

2.4 State of research for tailored nanoparticle-synthesis in spray flames

There is great interest in the targeted production of nanoparticles with desired properties to tailor them for specific applications. The properties of nanoparticles produced by spray-flame synthesis can be controlled by the operating conditions of the flame and the selection of the starting materials. In order to achieve the goal of attaining full control over the synthesis process, a comprehensive understanding of the process is imperative. There has been significant progress in this field in the recent years. From the literature, various physical and chemical factors and phenomena are already known that have an impact on the synthesis process and thus on the nanoparticle characteristics. The following section presents the current state of research by providing a concise summary of selected studies from the literature examining the influence of the most important spray-flame parameters and phenomena on the nanoparticle properties.

Abram et al. [117] investigated the impact of the gas temperature on the size of metal-oxide nanoparticles synthesized from droplets of different size. The nanoparticles synthesized from small droplets (diameter: 200 nm) at a low flame temperature of 1150 K featured particle sizes between 10 and 100 nm. When the synthesis temperature was increased to 2750 K, the nanoparticles were formed via the gas-to-particle pathway and featured sizes between 4 and 5 nm. They concluded an improved evaporation of the metal precursor into the gas phase due to the higher heat transfer. This conclusion corresponds to the reported results of Rudin and Pratsinis [149] who observed that at higher flame temperatures the droplet-to-particle pathway is suppressed and smaller numbers of large particles are formed. At the same time, their flame expanded spatially, leading to an increase in the nanoparticle high-temperature residence time. As a result, the nanoparticle size of the primary particle fraction increased due to enhanced coalescence. The observations reported in the literature are consistent with our results for pilot-scale spray flames presented in chapter 6, where we observed with increasing flame temperatures less larger iron oxide particles from the droplet-to-particle pathway and an increase in the nanoparticle size of the small particle fraction.

Heine and Pratsinis [150] reported that the flame height and flow velocity have an influence on the nanoparticle size. In higher flames and when low flow velocities are present the high-temperature residence time is longer and larger particles are formed. These conclusion were confirmed by the study of Strobel and Pratsinis [151] and are in agreement with the numerical investigations using discrete element modeling (DEM) presented by Kelesidis et al. [112]. Wei et al. [152] presented consistent results for the synthesis of TiO₂ nanoparticles in a swirl-stabilized tubular burner. They compared the size distribution of nanoparticles that experienced different temperature-time histories. The results show that the nanoparticles experiencing a short high-temperature zone residence time featured small mean particles sizes and a uniform particle size distribution (13 ± 3.2 nm) while long high-temperature zone residence times resulted in polydisperse distributions with larger particle sizes (16.9 ± 8.8 nm).

Hardt et al. [153] reported that in the spray-flame synthesis of titania nanoparticles the size distribution and crystallinity can be controlled by the reactor pressure. The mean diameter shifted from about 10 nm at 1200 mbar to about 6 nm at 250 mbar while the pressure had no influence on crystal structure and phase composition. These findings were explained by a reduced collision frequency of particle-forming species and a shorter residence time with a faster cooling of the nanoparticles.

From the literature it is known that the solvent has a large influence on the particle formation process in spray flames. Strobel and Pratsinis [145] conducted a study to investigate the effect of the solvent composition on the size of metal-oxide nanoparticles (alumina and oxides of cobalt, iron, magnesium, and zinc) generated by spray-flame synthesis. The addition of a carboxylic acid to ethanol resulted in a more homogeneous size distribution with smaller particle diameters compared to the use of pure ethanol or other solvent mixtures. They attributed the suppression of the liquid-to-particle pathway to the formation of volatile metal carboxylates within the solvent. The boiling point and the combustion enthalpy of the solvent only showed a minor influence on the particle size. The same observations were reported by Sorvali et al. [40] for the spray-flame synthesis of iron oxide nanoparticles. With an increasing volume fraction of carboxylic acids (EHA, butanoic acid, propanoic acid) in methanol the number and size of large particles decreased as the liquid-to-particle pathway was suppressed. These observations are consistent with the results presented in Refs. [146, 154, 155]. Stodt et al. [156] investigated the chemistry of iron nitrate solutions (up to 0.5 mol/kg) in alkyl alcohols at ambient conditions and reported the stability of these solutions when EHA was added.

Heine and Pratsinis [150] investigated the impact of spray atomization on the size distribution of ZrO_2 nanoparticles. The results show that larger initial droplet size distributions result in larger nanoparticles with a broader size distribution. These observations are consistent with the results of Mueller et al. [157] and Abram et al. [117]. Angel et al. [158] conducted a study on the impact of the dispersion-gas flow rate on the droplet size distribution and its impact on the size distribution of $LaMnO_3$, $LaFeO_3$, and $LaCoO_3$ nanoparticles. The main finding was the increase of the specific surface area with increasing dispersion gas flow rates, indicating a reduced formation of large particles. They concluded a shift from the liquid-to-particle to the gas-to-particle synthesis pathway, attributed to a reduction of the initial large droplet fraction.

Aromaa et al. [118] investigated for four spray-burner configurations the effect of various process parameters on the size of titania oxide nanoparticles. They reported that an increase of the gas flow rates (H_2 dispersion gas and O_2 combustion gas at a constant volume ratio), which is accompanied by a reduction in the initial droplet size, resulted in a reduction of the mean TiO_2 nanoparticle size and an increase of the number of particles produced. When employing ethanol as solvent, average nanoparticle diameters were notably smaller compared to their size when isopropanol was utilized. Moreover, with increasing precursor feed rate the production rate and the mean titanium oxide nanoparticle size increased. These findings are in agreement with the results presented by Teoh et al. [159] and by Wegner and Pratsinis [160]. Teoh et al. reported for a spray-flame synthesis of TiO_2 nanoparticles an increase of the average diameter from 11 to 21 nm when increasing the precursor (TTIP) feed rate from 3 to 5 ml/min. Wegner and Pratsinis reported for a diffusion flame, that by increasing the TTIP flow rate (1.6–26 g/h) the average TiO_2 nanoparticle diameter increased from 15 nm to 42 nm. They attributed this observation to the increase of the precursor concentration in the gas phase resulting in an accelerated particle growth.

Sorvali et al. [40] investigated the influence of the variation of H_2 and O_2 gas flow rates, and thus the equivalence ratio on the average primary size and the phase composition of iron oxide nanoparticles. The results show that the average primary particle size increases with increasing equivalence ratios. For pure alcohol solvents, the maghemite fraction increased with rising equivalence ratios while for solvent mixtures with EHA the hematite phase was entirely removed. Strobel and Pratsinis [151] performed a study on the impact of the equivalence ratio on the oxidation state of iron-oxide nanoparticles synthesized in a spray flame under controlled

atmosphere. When iron nitrate nonahydrate was used as precursor, an increase in oxygen content in the atmosphere resulted in a higher fraction of Fe_3O_4 while the fraction of Fe_2O_3 was reduced.

In contrast to other synthesis approaches the spray-flame synthesis of nanoparticles enables the production of metastable materials. Kemmler et al. [161] reported the synthesis of $\text{In}_4\text{Sn}_3\text{O}_{12}$ nanoparticles with average sizes of about 6 nm. The particles were generated by quenching the high-temperature phase and direct thermophoretic deposition on platinum electrodes for the use as formaldehyde gas sensors.

As known from studies performed within the scope of the SPP1980 project [162, 163], the stability of spray flames is a crucial phenomenon that needs to be addressed for the targeted control of nanoparticle synthesis and to increase its efficiency. Spray-flame instabilities are considered to cause inhomogeneous nanoparticle size distributions due to the presence of different local synthesis conditions. Bieber et al. [163] attributed the flame instabilities to an insufficient spray atomization by the two-fluid nozzle and were able to reduce the flame fluctuations by applying an optimized nozzle design with refined atomization. The nanoparticles produced by utilizing the new nozzle were smaller and featured a more homogeneous size distribution. Pan et al. [164] explored the use of artificial intelligence to autonomously monitor and control spray flames. They assessed the flame stability based on the brightness of the visible flame chemiluminescence (primarily CH^*), that is processed by machine learning algorithms based on principal component analysis and k-means clustering.

Scale-up of nanoparticle production in spray flames

The transfer of the spray-flame synthesis of nanoparticles from laboratory to industrial production scales is crucial in order to make the newly synthesized nanomaterials accessible for downstream processing towards system integration and finally for applications and products for the broad consumer or business-to-business market. Large-scale production is necessary for achieving commercial success due to the demand for significant quantities. In principle, from a physical and chemical perspective, nanoparticle synthesis in spray flames can be scaled up to industrial production rates, but there are still obstructive challenges and a deeper understanding of the processes is necessary to achieve this goal [49, 165]. The aim is to increase the production rates of spray-flame reactors while maintaining the nanoparticle quality. The following is a concise overview of the current state of research of nanoparticle production in spray flames, providing selected publications with nanoparticle production rates that were achieved.

Mueller et al. [166] produced SiO_2 nanoparticles from HMDSO by spray-flame synthesis at production rates of up to 1100 g/h. They investigated the impact of the production rate, precursor concentration and dispersion gas flow rate on the primary nanoparticle size, morphology and materials composition. By utilizing the same production setup, Mueller et al. [48] and Jossen et al. [167] conducted analogous studies on the upscaled spray-flame synthesis, achieving high production rates of up to 600 g/h ZrO_2 nanoparticles, and up to 350 g/h for yttria-stabilized zirconia nanoparticles ($\text{ZrO}_2/\text{Y}_2\text{O}_3$), respectively.

Heel et al. [168] reported the production of $\text{La}_{0.6}\text{Sr}_{0.4}\text{Co}_{0.2}\text{Fe}_{0.8}\text{O}_{3-\delta}$ and $\text{Ba}_{0.5}\text{Sr}_{0.5}\text{Co}_{0.8}\text{Fe}_{0.2}\text{O}_{3-\delta}$ nanopowders by spray-flame synthesis at production rates of up to 400 g/h. By adjusting the process parameters, they were able to control the nanoparticle size in the range between 20 and 100 nm (derived from a SSA of 12–48 m^2/g).

Hembram et al. [169] produced by spray-flame synthesis more than 3 kg/h ZnO nanorods from zinc nitrate dissolved in ethanol. They identified the flame temperature, cooling rate, and the zinc concentration in the vapor phase as the most important parameters affecting the formation of the nanorods.

Gröhn et al. [170] investigated the scale-up of ZrO₂ nanoparticle production through spray-flame synthesis. They were able to scale the production rate from 100 to 500 g/h while maintaining the nanoparticle properties. This was achieved by keeping the high-temperature residence time of the nanoparticles constant (consistent ratio of precursor feed rate to dispersion gas flow).

Recently, Estévez et al. [171] produced by spray-flame synthesis 100 g/h superparamagnetic iron oxide nanoparticles with a homogeneous particle size of about 12 nm. With regard to biomedical applications, they characterized the material for its superparamagnetic properties, colloidal stability, hemocompatibility and cytotoxicity.

Wegner et al. [172] reviewed in 2011 the progress made up to that point in upscaling the nanoparticle synthesis in spray flames. Moreover, they conducted an economic analysis for the large-scale production of bismuth oxide and zirconium oxide nanoparticles at production rates of 1.25 kg/h and 12.5 kg/h resulting in annual outputs of 10 and 100 t, respectively. They estimated the production costs to be less than 100 Euro/kg.

3 Spray burners for nanoparticle synthesis

In this work, two laboratory-scale burners and two pilot-scale burners were investigated in the context of the German Research Foundation (DFG) priority program SPP1980 [173]. All burners were recently developed for the spray-based nanoparticle synthesis in flames. The burners are designed to control the properties of the produced nanoparticles by adjusting the operating conditions of the flames (e.g., by the selection of precursors, flow rates or gas types).

3.1 SpraySyn burner version 1

The first version of the laboratory-scale SpraySyn burner was developed at EMPI-RF as described by Schneider et al. [49, 174, 175]. This initial version is denoted as the SpraySyn burner, or specifically as SpraySyn1 burner when necessary to emphasize the distinction from version 2, which is presented in section 3.2. The SpraySyn burner was developed as a standardized burner for the spray-flame synthesis of oxidic nanoparticles [38, 154] to ensure comparability of experimental and simulation results across research groups. It was designed with simulation-friendly boundary conditions to facilitate fluid dynamics simulations and reduce the time-consuming and expensive simulation of the flame periphery. Numerous computational studies have used the burner design for their investigations [176-183].

To ensure reproducible operation of the SpraySyn flame across various laboratories, a standardized calibration procedure was developed by Schneider et al. [174]. The optical setup for the calibration procedure is predefined and the layout of the calibration target provided. Images of the flame, recorded by a standard digital camera (e.g., Nikon D5300 with lens Nikkor AF-S 50/1.8G) are processed by a Matlab routine and compared to reference data to assess the flame shape and verify proper operation. The Matlab routine benchmarks various flame characteristics (e.g., flame length and tilt) and the color of the visible flame luminescence. For more details refer to [174]. This standardized experiment enables researchers from different laboratories to work on a spray flame with the same characteristics under identical conditions and to exchange their findings to facilitate process understanding and flame modeling. It is desired to generate a comprehensive data base [56] of experimental and simulation results which are used to support mechanistic understanding and to validate simulations. The data generated from various measurement approaches can be compared to validate the experimental results. Furthermore, experimental results can validate simulations and the results of different simulation models can be collated.

Within the scope of the SPP1980 project, a broad spectrum of experimental studies of the SpraySyn flames and the synthesis of nanoparticles using the SpraySyn burners has been conducted. A literature overview of various fields is listed below:

- Gas temperature [51, 184, 185]
- Gas velocity [186, 187]
- Spatial distribution of various gaseous species [184]
- Liquid temperature [188, 189]
- Droplet velocity and size [122, 190-193]
- Droplet explosions [52, 194]
- Nanoparticle properties [143, 195-200]
- Nanoparticle growth [201-203]
- Flame chemiluminescence [204]

- 3D field analysis via tomographic imaging [204, 205]
- Flame fluctuations [162, 163, 206]

Moreover, various specific processes and phenomena relevant for the spray-flame synthesis of nanoparticles were investigated:

- Combustion of single droplets [127, 139]
- Droplet explosions [130, 131, 135, 207, 208]
- Stability of precursor solutions [156]
- Physicochemical properties of precursor solutions [156, 209-211]
- Droplet injection by an electro spray nozzle [212, 213]

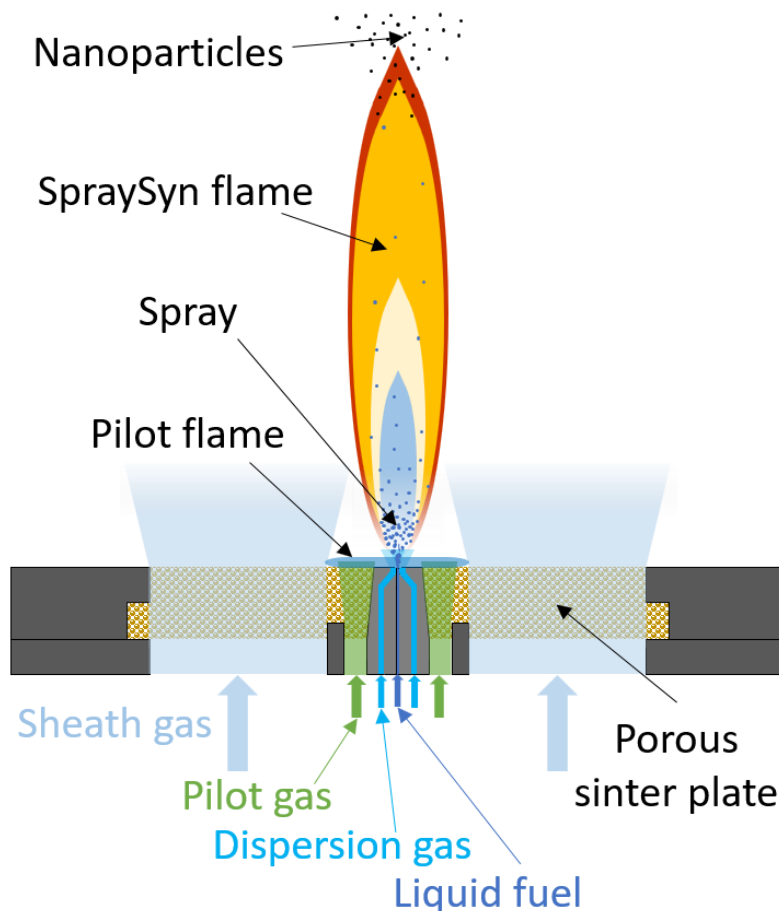


Figure 3: Schematic cross-section of SpraySyn burner (not to scale). More details about the burner design and the specific dimensions for the various burner parts are given in Ref. [174].

Figure 3 shows schematically the centerline cross-section of the SpraySyn burner. The gas flows are depicted as colored areas. Sheath gas is guided through a porous sinter plate (bronze matrix) to shield the flame synthesis from the environment and generate the simulation-friendly boundary condition of a nitrogen enclosure. The spray flame is stabilized by a premixed pilot flat flame operated by methane and oxygen. The premixed pilot gas is guided close to the nozzle through the porous sinter plate and feeds the pilot flame that is stabilized on the porous plate. The liquid precursor/fuel solution is injected through a capillary and atomized by a two-fluid nozzle with external mixing into the flame. The gas flows are generated by mass flow controllers (MFC, Bronkhorst) and the liquid flow is generated by a double syringe

pump (DSP-XL, Ayxesis GmbH). Optionally, the produced nanoparticles can be collected downstream by a filter system within the exhaust gas flow tube.

To ensure comparability and reproducibility, a standard operating condition was defined, which should be the central starting point for experimental investigations. The flow rates and gas species are given in Table 1. Other than that, the burner can be operated with different flow rates and a wide variety of gases (e.g., H_2), liquid fuels (e.g., 1-butanol or o-xylene), and precursors (e.g., iron nitrate or HMDSO). Note that the O_2 pilot-gas flow of 16 slm is crucial to prevent the porous sinter plate from overheating, which could potentially damage the plate (visible glowing of the sintered matrix must be prevented). Moreover, the lean flame with an equivalence ratio of $\phi = 0.25$ minimizes the un-desired formation of carbon deposits on produced nanoparticles. The SpraySyn burner features a Reynolds number of approximately 6300 [183]. Typically, the flame is operated at atmospheric or slightly below atmospheric pressure.

Table 1: Flow rates of the standard operating condition of the SpraySyn burner. 65EHA35EtOH: Solvent mixture by volume of 65 % 2-ethylhexanoic acid and 35 % ethanol. The volume flow unit slm is based on a reference condition at 0 °C.

Flow	Species	Flow rate
Sheath gas	Nitrogen (N_2)	120 slm
Pilot gas	Methane (CH_4)	2 slm
	Oxygen (O_2)	16 slm
Dispersion gas	Oxygen (O_2)	10 slm
Liquid fuel	Ethanol or 65EHA35EtOH	2 ml/min

Figure 4 shows a schematic drawing (not to scale) of the SpraySyn-burner two-fluid nozzle with external mixing (version 1). In the center, the capillary surrounded by the dispersion gas channel (outer diameter: 1.5 mm) can be seen and at the sides the porous sinter plate is illustrated. The inner diameter of the capillary is 0.4 mm and the outer diameter is 0.7 mm. To adjust the spray direction, the capillary can be adjusted by three micrometer screws located at the bottom of the burner. The channel design of the dispersion gas creates a parallel flow surrounding the liquid jet. The high-velocity dispersion-gas flow generates a shear zone (due to the velocity difference between the liquid and dispersion gas flow) and atomizes the liquid jet generating the spray. For the standard operating condition (Table 1) the flow velocities at the burner exit are 129.4 m/s for the dispersion gas [206], 2.5 m/s for the pilot gas (~6 m/s when reacted, at 2400 K), and 0.6 m/s for the sheath gas. A liquid flow rate of 2 ml/min results in an injection velocity of 0.265 m/s.

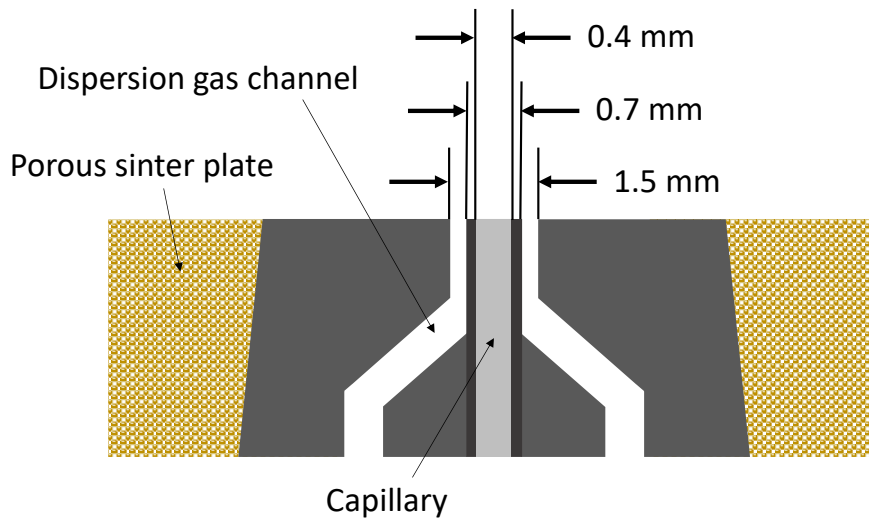


Figure 4: Schematic drawing (not to scale) of the two-fluid nozzle of the SpraySyn1 burner within the sinter bronze. The given dimensions are diameters.

3.2 SpraySyn burner version 2

The SpraySyn1 burner shows flame fluctuations under lean operating conditions in the form of frequent flame extinction and pulsation, which can be observed by high-speed imaging. Pulsation and extinction occur because the formation of the combustible fuel/air mixture from the evaporating droplets embedded in the O_2 dispersion gas is slower than the combustion of the mixture. This results in the phenomenon of alternating processes involving combustible-mixture formation and combustion. This phenomenon is connected to an inefficient flame operation (lower flame temperature, inefficient droplet evaporation) and potentially undesired particle properties because of variable temperature histories experienced by the particles. The flame instabilities are attributed to the poor efficiency of the spray atomization and thus evaporation of the first nozzle design (Figure 4).

Bieber et al. [163] performed a study on the flame fluctuations and developed a new nozzle design, where the flame stability was improved significantly. Smaller nanoparticles were produced under otherwise identical operating conditions of the burner (mean particle diameter: 3.9 vs. 5.9 nm). Different to the initial nozzle design (version 1) the flow direction of the dispersion gas was changed (angle of 45° instead of a parallel flow) to increase shear and generate more turbulence in the lower region of the flame and cause a better mixing with the pilot flame. The nozzle design was further developed by Karaminejad et al. [162] and became the new standard. In the improved design the cross-section of the dispersion gas channel decreases gradually. The investigations performed by Karaminejad et al. [162] show a better flame stability (larger flame active time) and an improved spray atomization with higher droplet velocities and smaller droplet sizes.

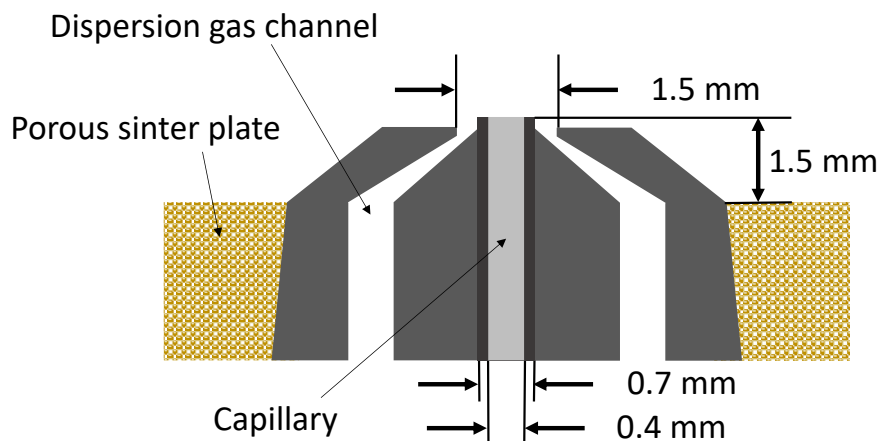


Figure 5: Schematic drawing (not to scale) of the nozzle of the SpraySyn2 burner.

In this work, the SpraySyn burner equipped with the improved nozzle (version 2) is denoted SpraySyn2 burner. Figure 5 shows a schematic drawing (not to scale) of the new nozzle design. True-to-scale drawings of both nozzle versions can be found in Ref. [200]. The standard operating condition of the SpraySyn2 burner corresponds to SpraySyn1 (Table 1) but with the O_2 dispersion gas reduced to 6 slm (from 10 slm) due to a higher flame stability when operated with a lower flow rate [162]. Despite the reduced dispersion gas flow rate, the dispersion gas exhibits a higher velocity due to the reduced diameter of the dispersion gas channel outlet. To ensure the comparable operation of the burner, an expansion of the calibration procedure (section 3.1) was implemented: A pressure of 550 mbar above atmosphere needs to be established in the dispersion gas line.

3.3 Berlin burner

One of the pilot-scale spray burners investigated in this study was developed by the Institute of Fluid Dynamics and Technical Acoustics (ISTA) from the TU Berlin to investigate the up-scaling process from laboratory to industrial production scale [123, 147, 214]. It was designed to be operated with hydrogen and precursor throughput that could lead to particle formation of several kg/day. The burner was installed in the pilot-scale particle synthesis plant of the Institute for Energy and Environmental Technology (IUTA) in Duisburg. In the subsequent sections, the burner will be denoted as Berlin burner (BB).

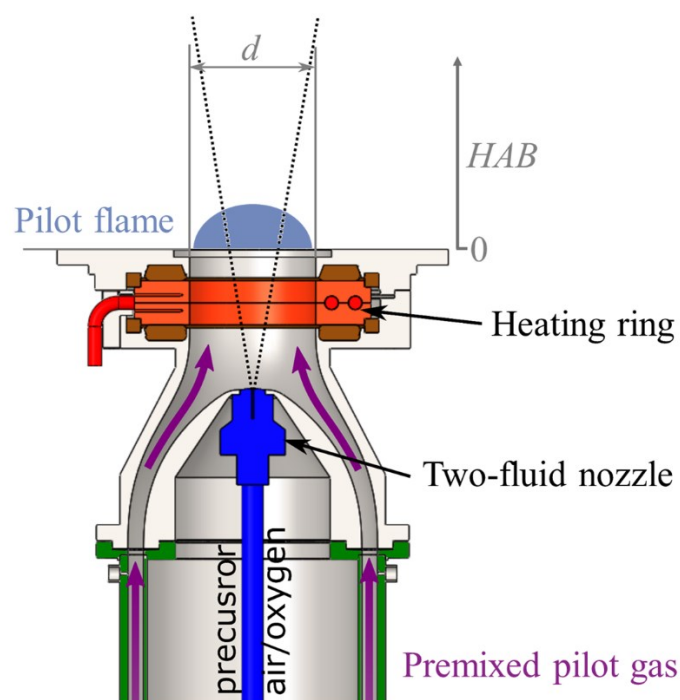


Figure 6: Schematic of the pilot-scale Berlin burner concept. The spray flame is not shown. The burner top is defined as $HAB = 0$ mm. For details of the burner design and the dimensions refer to Ref. [123]. Reprinted with permission from Ref. [147].

Figure 6 shows the cross-section of the Berlin burner. The spray nozzle (illustrated in blue) is located centrally 88 mm below the burner outlet. It is a commercial two-fluid nozzle (BETE XA SR 200, spray angle: $18\text{--}19^\circ$) that can be operated with various dispersion gases (in our case: Dried and filtered air or oxygen). The spray is oriented in the flow direction of the pilot gas, which is typically a hydrogen/air mixture. The premixed pilot gas can be electrically preheated up to $350\text{ }^\circ\text{C}$. An electrically heated ring (depicted in orange) which is capable to increase the wall temperature up to $800\text{ }^\circ\text{C}$ initiates auto-ignition of the fuel/air mixture.

The spray is formed downstream of the combustion zone and introduced into the pilot flame. The lower edge of the heated ring is located close to the burner outlet, 43 mm above the nozzle outlet. The diameter of the burner outlet, which is also the inner diameter of the heating ring, is 80 mm. The flow of the precursor solution and gases can be changed to generate different operating conditions to influence the characteristics of the produced nanoparticles. The burner can be operated with sustainable fuels only, when the H_2 pilot flame and, e.g., ethanol as liquid fuel is used. With the H_2 pilot flame and, e.g., the precursor solvent H_2O the burner can be operated carbon-free, which enables the synthesis of nanomaterials free of carbides and carbon impurities.

3.4 HSW burner

The second pilot-scale spray burner investigated in this work was developed by HSWmaterials GmbH (Kamp-Lintfort). In the subsequent sections, the burner will be accordingly denoted as HSW burner (HSWB). Figure 7 shows the nozzle section of the true-to-scale drawing of the burner. A detailed drawing is given in Figure A1. The underlying principle and design are similar to that of the SpraySyn burner (sections 3.1 and 3.2). A liquid precursor solution is dispersed by a commercial two-fluid nozzle (Schlick model 970, dispersion gas swirl angle: 26.6° ,

inner capillary diameter: 0.9 mm) and is constantly ignited by a surrounding pilot flame. Different to the SpraySyn burner the pilot gas is fed via a 0.35 mm wide circular slit (diameter: 55 mm) at an angle of 45° to the spray flame. The burner features a Reynolds number of approximately 21,500 [183]. Typically, the burner is enveloped by an air coflow that stabilizes the flame and carries the synthesized nanoparticles into the filter system.

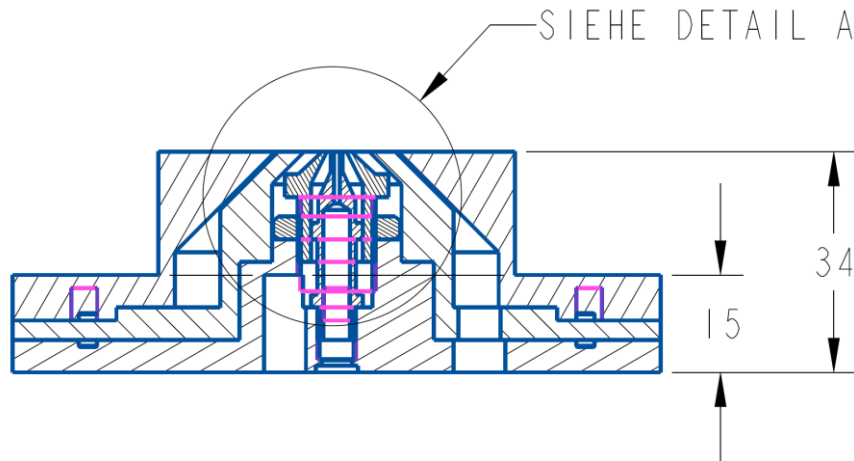


Figure 7: Excerpt from the technical drawing of the pilot-scale HSW burner. The dimensions are specified in millimeters. Printed with permission of HSWmaterials GmbH (Kamp-Lintfort) [215]. The details of image section A can be found in section 12.2 of the appendix.

In the context of the impact of the spray properties on the nanoparticle synthesis in spray flames, Alhaleeb et al. [216] conducted for the same commercial two-fluid nozzle utilized in the HSW burner (Schlick model 970), an investigation on the impact of the gap size on both the dispersion gas flow rate and the pressure drop. Moreover, simulation models are available in the literature. Dasgupta et al. [46] modeled by computational fluid dynamics (CFD) a spray-flame burner equipped with the Schlick 970 nozzle for SiO_2 nanoparticle synthesis. The primary atomization was modelled by a volume-of-fluid large-eddy simulation (LES).

4 Chemiluminescence in the context of nanoparticle synthesis in the SpraySyn1 flame

Some sections of the following chapter are reprints or else contain contents from the listed publications:

C.T. Foo, A. Unterberger, F.J.W.A. Martins, **M.M. Prenting**, C. Schulz, K. Mohri, Investigating spray flames for nanoparticle synthesis via tomographic imaging using multi-simultaneous measurements (TIMes) of emission, *Opt. Expr.* 30 (2022) 15524-15545. <https://doi.org/10.1364/OE.449269>

© 2022 Optica Publishing Group under the terms of the Optica Open Access Publishing Agreement. Reprinted with permission.

My contribution to this publication was the provision of chemiluminescence spectra of the SpraySyn1 flame for various operating conditions. I set up the experiment for spectrally resolved chemiluminescence measurements with the SpraySyn1 burner, performed the measurements and processed and analyzed the data. I supported the first author with corrections of the manuscript and was mainly responsible for the conception and writing of the section that deals with spectrally resolved chemiluminescence measurements.

In this chapter and section 12.3 of the appendix, chemiluminescence spectra measured in the SpraySyn1 flame operated with various fuels for nanoparticle synthesis are presented. The burner was operated to generate SiO₂ nanoparticles from HMDSO dissolved in ethanol and iron oxide nanoparticles from iron nitrate nonahydrate dissolved in ethanol and 65EHA35EtOH. Chemiluminescence was recorded at different heights above the burner (HAB) in the spectral range from 210 to 800 nm. Light sources with known emission spectra were utilized to record reference spectra for correcting for the wavelength-dependent detection sensitivity of the measurement setup. Measurement data set was generated to support the understanding of nanoparticle synthesis in spray flames and to provide information about the spontaneous flame luminescence background in the context of laser-based optical measurements in the SpraySyn flame.

4.1 Theoretical background

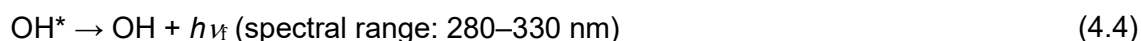
Theoretical fundamentals and specific details regarding chemiluminescence and flame luminescence are given in references [217-220]. Hence, only a brief summary is provided in this section. The term 'chemiluminescence' was introduced by Wiedemann [221] and describes the phenomenon in which electromagnetic radiation is emitted due to the relaxation of excited species generated by chemical reactions. A few nanoseconds after an electronically excited molecule has been generated by chemical reactions, it relaxes from this unstable state to a lower electronically stable state. During this process, a photon of light is emitted with a wavelength corresponding to the energy difference between the two participating electronic states. Flame chemiluminescence are light emissions and feature specific spectral characteristics in the UV and visible spectrum. In this work, the asterisk '*' marks the electronically excited state of a molecule or radical (e.g., OH*).

Formula (4.1) illustrates the formation of excited molecules by the chemical reaction between reactants A and B to form the products C and the excited molecule X* [219, 222]. As an example, in methane flames at atmospheric pressure, the chemical reaction shown in formula (4.2) is the dominant formation pathway of OH* and causes about 90 % of OH* generated [223-225]. In high-temperature environments, such as flames, excited molecules can also be created through thermal excitation by absorbing energy from their surroundings.





There are two pathways for a molecule to return from the excited state to its ground state [219, 226]. The first pathway, given in formula (4.3) is relate to the excited molecule returning to its ground state via emitting a photon, resulting in emission with specific spectral characteristics (e.g., narrow emission lines at specific wavelengths). The wavelength is determined by the energy difference between the two states (according to $E_{X^*} - E_X = h\nu$). An example of this process is given in formula (4.4), where OH^* returns to its ground state by emitting a photon in the wavelength range between 280 and 330 nm.



In the second deactivation pathway, the excited molecule returns to its ground state by non-reactive processes such as collisional quenching, as shown in formula (4.5). The excited molecule (X^*) transfers its excess energy by collision to another molecule (M) without emitting radiation. This energy is converted into kinetic energy, manifesting as heat. An example for OH is given in formula (4.6).



Chemiluminescence detection is a non-intrusive measurement method that does not disturb the flame and provides information about the local conditions at the source of light emission, such as pressure, temperature, and gas composition. In contrast to techniques based on laser excitation, where the measurement signal originates from a specific volume, the detection of flame chemiluminescence returns signal that is integrated over the line-of-sight, requiring consideration for the interpretation of the results. From chemiluminescence spectra, the existence of specific species can be inferred and conclusions can be drawn about chemical reactions involved in the flame chemistry [227]. In flame synthesis, conclusions can be drawn on precursor decomposition, and particle nucleation zones within flames can be identified through, e.g., SiO^*/Si^* chemiluminescence [228]. Moreover, the distribution of specific species and reaction zones can be identified. With respect to the flame type and flame conditions, the emission intensities of OH^* , CH^* , and CO_2^* can indicate the heat release rate, and the ratio of OH^* to CH^* can be used in specific situations as a measure for the equivalence ratio [223, 229-231].

4.2 Experimental setup

The experimental setup for recording spectrally resolved chemiluminescence in the SpraySyn flame is shown schematically in Figure 8. The SpraySyn flame is operated at ambient pressure in a housing with optical accesses. The SpraySyn burner is mounted on a height-adjustable rack to enable measurements at different height above the burner exit (HAB). Chemiluminescence light is collected by a UV-transmitting lens (B. Halle Nachfl., $f = 100 \text{ mm}$, $f/2$) and imaged on the horizontal 50- μm -wide entrance slit of the spectrometer (Princeton Instruments, Acton SP-150). An optical filter (Schott, GG420 longpass filter) was optionally placed in the light path between the lens and the spectrometer to block unwanted light and suppress second-order diffraction artifacts. The spectrometer has a focal length of 150 mm and was operated with 150 or 600 grooves/mm diffraction gratings. An intensified CCD camera (Image intensifier: LaVision, Intensified Relay Optics, CCD camera: LaVision, Imager Intense) was directly

connected via a mounting flange at the spectrometer exit port. Chemiluminescence light entering the spectrometer was collected from a $31 \times 0.475 \text{ mm}^2$ area in object space. The imaged horizontal spatial extent was determined by the distance of two illuminating points from an optical fiber placed at the burner, resulting in a nominal spatial dispersion of $61.5 \mu\text{m}/\text{pixel}$, while the vertical dimension was determined by calculations based on the optical magnification factor which resulted in a height of approximately $475 \mu\text{m}$ for the used slit width.

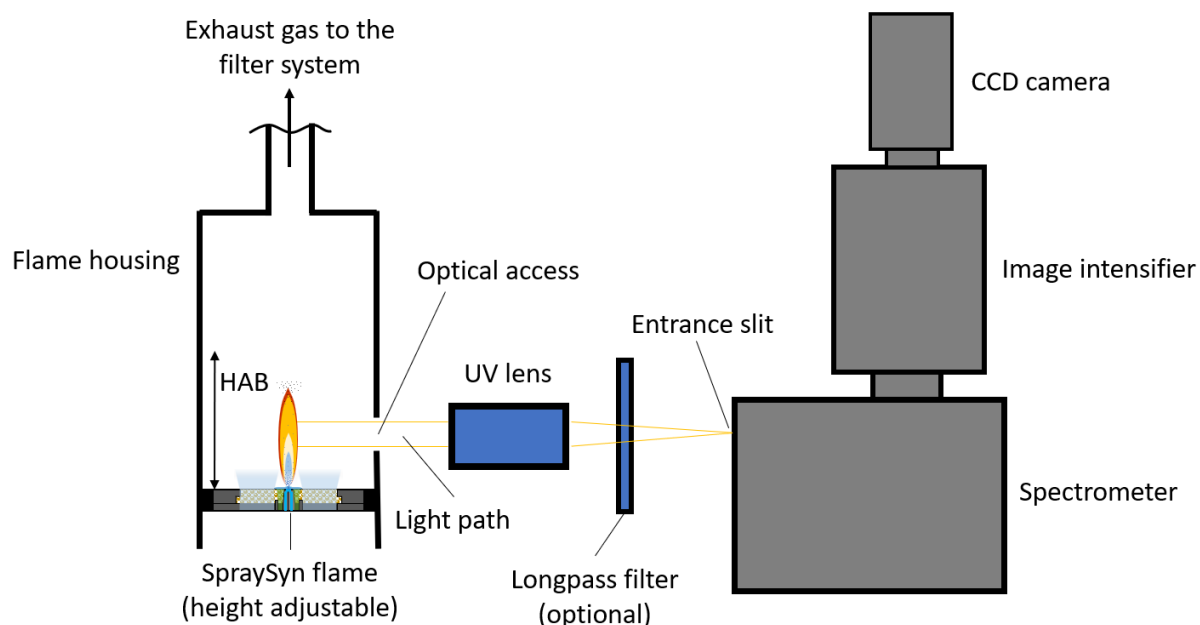


Figure 8: Schematic diagram for recording spectrally resolved chemiluminescence.

4.2.1 Calibration

The wavelength-dependent transmission efficiency and detection sensitivity of the optical setup was determined using two broadband light sources with well-known emission spectra. For the shorter wavelength range (200–500 nm), a laser-driven light source (LDLS, Energetiq Technology, EQ-99X) and for the longer wavelength range (500–800 nm) three halogen bulbs integrated in an Ulbricht sphere (LOT-Oriel Gruppe Europa, K-150WH) were utilized. The correction functions for the optical setup were determined by calculating the ratio of the known emission spectra to the measured spectra. The sharp spectral lines of a PenRay lamp (LOT-Oriel Gruppe Europa, Line-Emitter, LSP035 HG/(Ar)) were utilized to calibrate the wavelength axis.

Figure 9 shows the detected emission spectra of the LDLS and the halogen lamps (dashed lines) and the corresponding correction functions (solid lines) normalized at 500 nm. The correction functions for the LDLS, with and without using the longpass filter, are shown. A separate calibration must be performed for each diffraction grating (150 or 600 grooves/mm) and grating position.

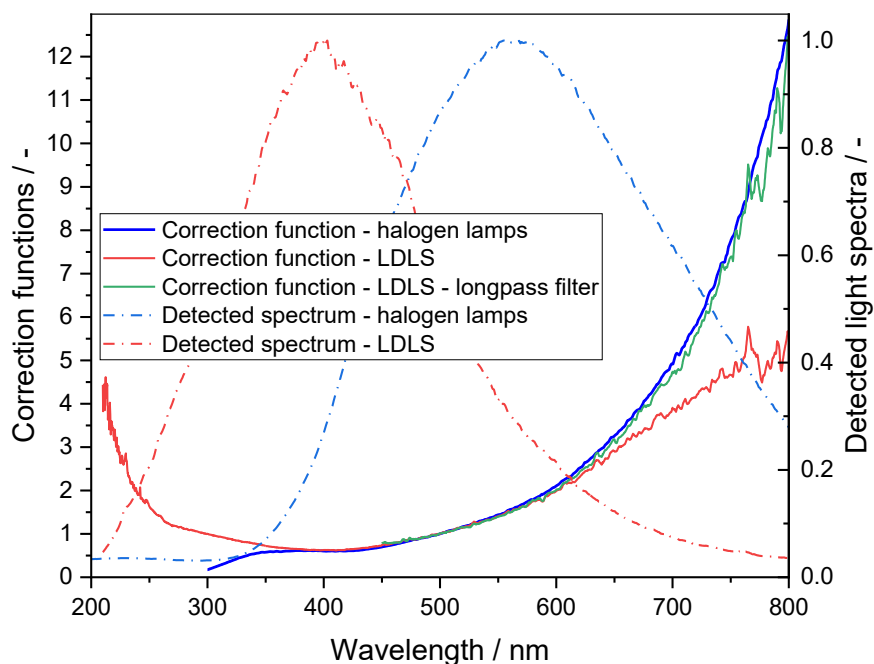


Figure 9: Detected light spectra (dashed lines) of the LDLS and the halogen lamps and the derived calibration functions (solid lines), the correction functions were normalized at 500 nm.

When determining the calibration function with the LDLS, second-order diffraction must be considered in the spectral range above approximately 500 nm, as the LDLS exhibits significant light intensity in the UV around the half wavelength of approximately 250 nm. Second-order diffraction light contributes to the detected signal (actual signal with the correct wavelength + second-order diffraction light) at twice its wavelength and thus distorts the calibration function. With increasing wavelength, the proportion of actual signal and second-order diffraction light gets continuously poorer. For the calibration with the halogen lamps integrated in an Ulbricht sphere, this effect must be considered in spectral ranges above approximately 800 nm, and thus, is not relevant for the spectral range investigated in this work. To address this issue, a longpass filter (Schott, GG420) was placed in front of the spectrometer slit to block light below 400 nm when determining the calibration function with the LDLS in the spectral range above 500 nm. Figure 9 shows both correction functions when employing the longpass filter (green line) and when not using it (red line). It can be seen that the error induced by second-order diffraction light increases with increasing wavelength. There is a very high correspondence between the two correction functions of the LDLS with longpass filter (green line) and the halogen lamps (blue line). The final calibration function for the 150 grooves/mm grating was stitched by combining the calibration function of the LDLS and Ulbricht sphere at 500 nm.

The strong decline of detection sensitivity towards the near IR range can be attributed to the IRO with a low conversion efficiency at longer wavelengths. The IRO amplifies incoming light in a wavelength range between 180 nm and the near IR. The manufacturer states a conversion efficiency of $\sim 1\%$ at 800 nm.

4.2.2 Postprocessing of camera images

Post-processing of the raw images detected by the camera mounted to the spectrometer and data analysis was done by in-house Matlab codes (Matlab R2022b [232]). One Matlab script was used to derive the wavelength axes from the recorded emission spectrum of the PenRay lamp (particular attention must be given to second-order diffraction light peaks). Another script

determined the measurement-specific correction function for the detection sensitivity of the measurement setup as described in section 4.2.1. The main script was utilized to extract chemiluminescence spectra from the raw images and subsequently postprocess them to generate graphical representations.

The main script included the option for background correction of broadband emissions to increase the visibility of single peaks and enable a targeted analysis of species emission. The background signal (e.g., CO_2^* chemiluminescence emission or blackbody radiation) was fitted and subtracted using a polynomial function of either 2nd or 4th order, depending on the profile of the background signal. Moreover, the wavelength of peaks could be selected to extract radial line-of-sight emission spectra and generate three-dimensional figures to illustrate the distribution of the respective species emissions within the flame. The radial emission spectra were smoothed by a moving average of 20 data points.

4.3 Results

In the first two sections of this chapter, chemiluminescence spectra of the SpraySyn1 flame are presented when operated with pure liquid solvents (ethanol, 65EHA35EtOH), to facilitate the distinction of peaks generated by the addition of precursors. The second part of this chapter shows the spectra of SpraySyn1 flames with nanoparticle synthesis. SiO_2 nanoparticles are synthesized from a solution of HMDSO in ethanol, while iron oxide nanoparticles are produced from iron nitrate nonahydrate dissolved in 65EHA35EtOH. Additional measurement results, such as the chemiluminescence spectra of 1-butanol, o-xylene or iron nitrate nonahydrate in pure ethanol, are provided in section 12.3 of the appendix.

4.3.1 Liquid fuel: Ethanol

Figure 10 shows emission spectra measured at various HAB in the SpraySyn flame at the standard operating condition, using ethanol as the fuel. The figure shows uncorrected (left) and background-corrected spectra (right, fourth-degree polynomial fits). The peaks are marked with the species primarily responsible for the emission.

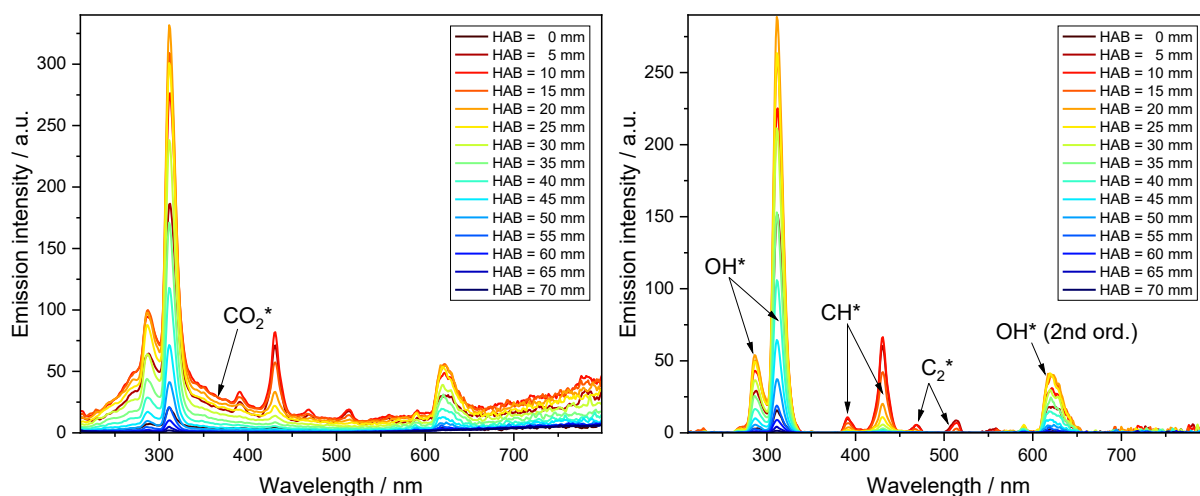


Figure 10: Emission spectra recorded in the SpraySyn flame at the standard operating condition, 2 ml/min ethanol at various HAB, detection-sensitivity corrected, 150 grooves/mm grating, left: Uncorrected spectra, right: Background corrected.

In the chemiluminescence spectra of the SpraySyn flame, several emission peaks can be identified. The most significant emissions are the OH* peaks around 287 and 310 nm [233, 234] and the broader emission from CO₂* from below 300 nm to above 600 nm [229, 235]. Further emission peaks are located at 390 and 431 nm (CH* [236, 237]), and at 470 and 515 nm (C₂* Swan bands [238, 239]). The artifact at 620 nm originates from second-order diffraction of the OH* emission at around 310 nm. This was confirmed by measurements (not shown here) with a longpass filter (Schott, GG420) placed in front of the spectrometer. To capture the entire spectrum at once, a longpass filter could not be installed in the light path, since it would block relevant emissions at shorter wavelengths. For all measurements with a higher spectral resolution (600 grooves/mm grating) in spectral ranges above 400 nm the longpass filter was used (cf. Figure A4). Measurement data with a higher spectral resolution (recorded with a 600 grooves/mm grating) and three-dimensional illustrations of these spectra are provided in section 12.3.1 of the appendix.

Figure 11 shows radial line-of-sight averaged emission intensity profiles extracted from background-corrected spectra at a chosen wavelength position. The radial profiles were smoothed with a 20-point moving average and are plotted for various HAB to form a three-dimensional illustration of chosen line-of-sight species emissions. The diagram on the left shows the emissions for OH* extracted at the peak position of 311 nm and the diagram on the right CH* emissions extracted at 431 nm. It can be seen from the diagrams that the OH* emissions are spatially more extended in both radial and vertical directions, while the CH* emissions are mainly present in the lower central part of the ethanol SpraySyn flame. The strongest CH* emissions were recorded in the flame center at approximately HAB = 10 mm.

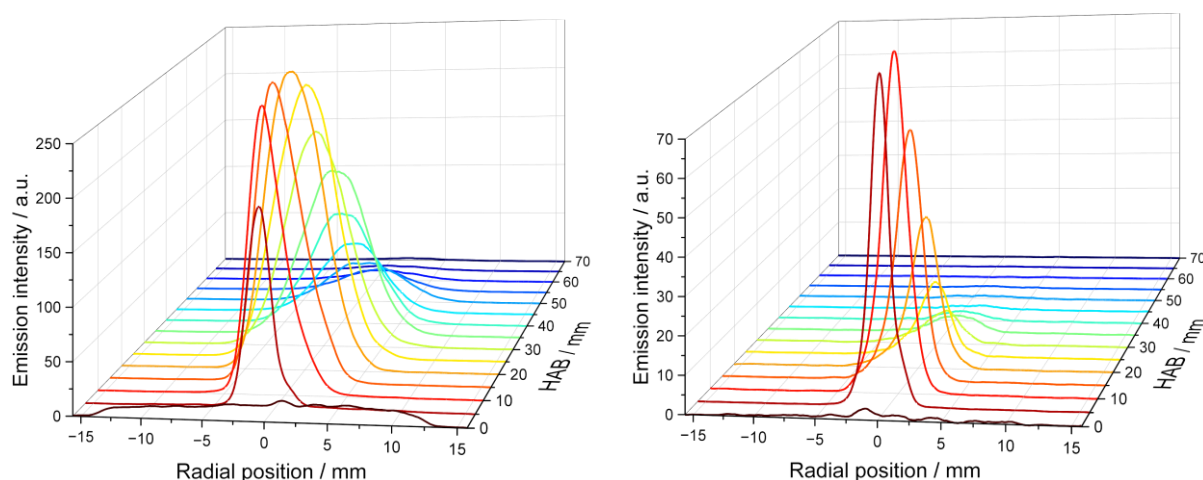


Figure 11: Emission spectra recorded in the SpraySyn flame at the standard operating condition, 2 ml/min ethanol: Smoothed radial emission spectra at chosen peak positions over HAB, left: OH* emission intensity at 311 nm, right: CH* emission intensity at 431 nm.

Figure 12 shows the emission intensity of chosen species peaks plotted over HAB. The peak profiles were extracted at the respective wavelength positions from background-corrected spectra, smoothed and normalized by their maximum value. CH* emissions are located in the lower flame regions with their maximum at approximately HAB = 10 mm. OH* emissions are distributed over a broader range with a maximum at approximately HAB = 20 mm. The profiles from different wavelengths for the same species show close agreement.

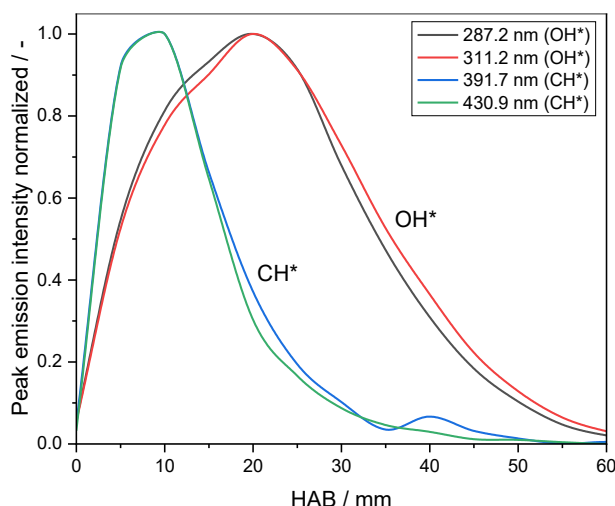


Figure 12: SpraySyn flame at the standard operating condition, 2 ml/min ethanol: Normalized emission intensity of chosen peaks over HAB extracted from background-corrected spectra (cf. Figure 10).

4.3.2 Liquid fuel: 65EHA35EtOH

Figure 13 shows the chemiluminescence spectra of the SpraySyn flame at the standard operating condition with the fuel 65EHA35EtOH. The diagrams were created by the same evaluation procedure as described for the ethanol measurements in the latter section.

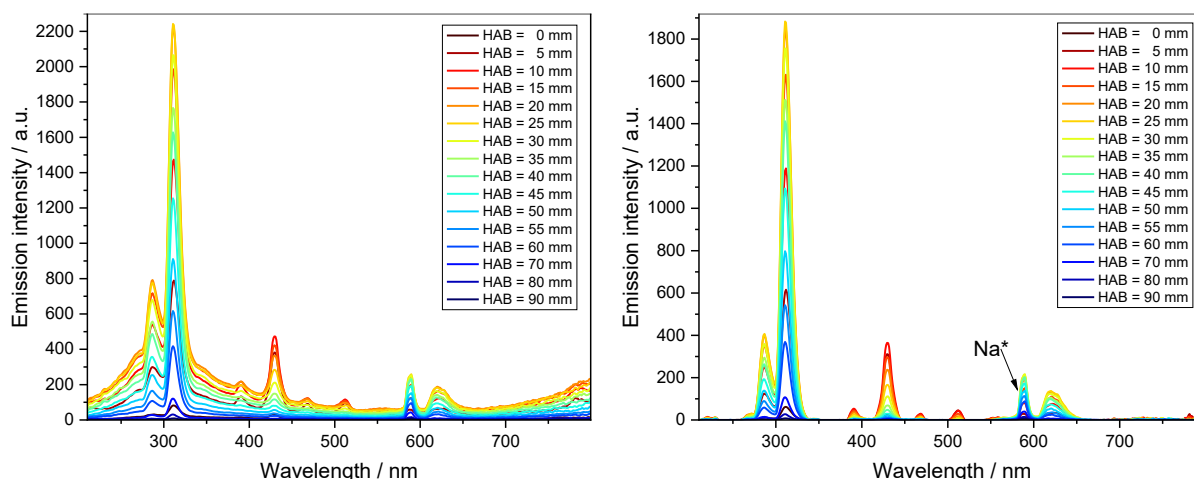


Figure 13: Emission spectra recorded in the SpraySyn flame at the standard operating condition, 2 ml/min 65EHA35EtOH: Chemiluminescence spectra at various HAB, detection-sensitivity corrected, 150 grooves/mm grating, left: Uncorrected spectra, right: Background corrected.

The chemiluminescence spectra of 65EHA35EtOH are very similar compared to those of the ethanol flame (Figure 10). Different to the ethanol flame spectra, an additional peak can be identified at 589 nm attributed to sodium [237, 240] resulting from impurities in EHA. In section 12.3.2 of the appendix, chemiluminescence spectra with higher resolution are provided for the entire spectral range from 210 to 680 nm. Additionally, three-dimensional radial line-of-sight emission profiles are presented for OH*, CH*, and Na*.

Figure 14 shows the peak-emission intensity of chosen species plotted over HAB. CH* emission occurs in lower regions of the SpraySyn flame, while OH* and Na* are spatially more extended with their maxima at larger HAB. The highest emission intensity for CH* is approximately at HAB = 10 mm, for OH* at HAB = 25 mm, and for Na at HAB = 30 mm. At

HAB = 90 mm, almost no signal can be detected, indicating the end of the visible flame at this height.

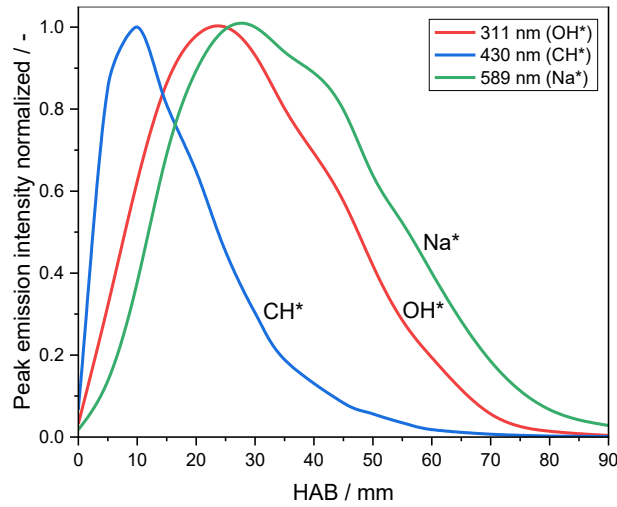


Figure 14: Emission spectra recorded in the SpraySyn flame at the standard operating condition, 2 ml/min 65EHA35EtOH: Normalized emission intensity of chosen peaks over HAB extracted from background-corrected spectra (cf. Figure 13).

4.3.3 Liquid fuel: HMDSO in ethanol

Figure 15 shows chemiluminescence spectra measured at various HAB for the SpraySyn flame operated with 0.5 mol/l HMDSO in ethanol. On the left, uncorrected spectra can be seen with background emissions from CO_2^* in the shorter wavelength range and blackbody radiation from SiO_2 nanoparticles in the longer wavelength range.

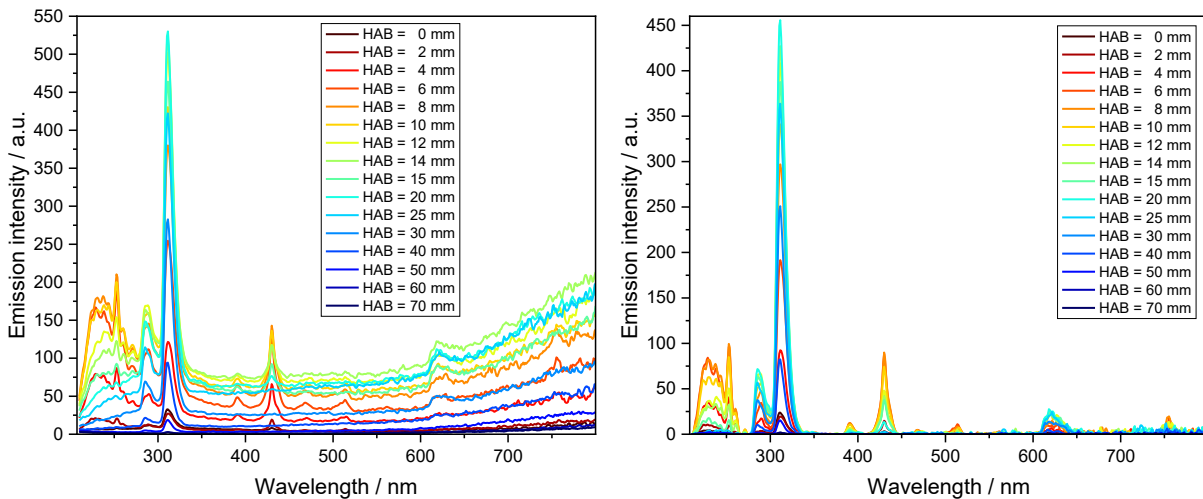


Figure 15: Emission spectra recorded in the SpraySyn flame at the standard operating condition, 5 ml/min HMDSO (0.5 mol/l) in ethanol: Chemiluminescence spectra at various HAB, detection-sensitivity corrected, 150 grooves/mm grating, left: Uncorrected spectra, right: Background corrected.

Compared to the chemiluminescence spectra of pure ethanol shown in Figure 10, emissions in the wavelength range below 300 nm are evident. No significant differences can be seen in the remaining spectral range.

Figure 16 shows the spectra of HMDSO in ethanol with a higher spectral resolution in the range between 210 and 375 nm, where the Si^* and SiO^* lines are located. Note that the flame was

operated with a liquid flow rate of 5 ml/min and a HMDSO concentration of 1 mol/l to enhance the visibility of the spectral lines.

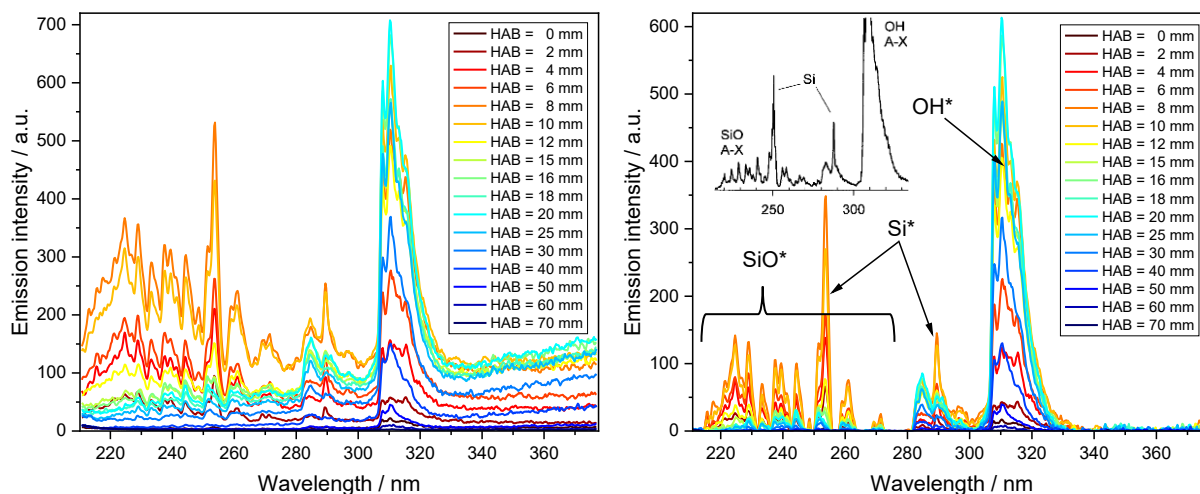


Figure 16: Emission spectra recorded in the SpraySyn flame at the standard operating condition, 5 ml/min HMDSO (1 mol/l) in ethanol: Chemiluminescence spectra at various HAB, detection-sensitivity corrected, 600 grooves/mm grating, left: Uncorrected spectra, right: Background corrected. The inset in the diagram on the right shows a reprint of the labeled spectrum of a hexamethyldisilazane flame published by Glumac et al. [241].

The Si^* and SiO^* lines were identified by comparison to the spectra published by Glumac et al. [241]. They recorded emission spectra of low pressure premixed hexamethyldisilazane flames and stated that SiO^* forms early in the flame and the emissions are chemiluminescence rather than thermal emission. The spectrum can be seen in the inset of the right diagram of Figure 16. SiO^* emissions appear as numerous small peaks within the spectral range of 215 to 275 nm. The two Si^* emission peaks at 254 and 289 nm exhibit a higher intensity than die SiO^* peaks. The Si^* peak at 289 nm overlaps with OH^* emissions. The spectral results for Si^* and SiO^* also align closely with those reported by Burkert et al. [242].

Figure 17 shows the profiles of various peak intensities over HAB and radial emission profiles of OH^* , SiO^* , and Si^* as three-dimensional illustrations. Si^* and SiO^* emissions are located in the lower central region of the SpraySyn flame where HMDSO-containing droplets are present. After the emission peak at approximately HAB = 8 mm the emission intensity decreases sharply to reach a low level at about HAB = 15 mm. No significant difference in the distribution of Si^* and SiO^* emissions across HAB are observed.

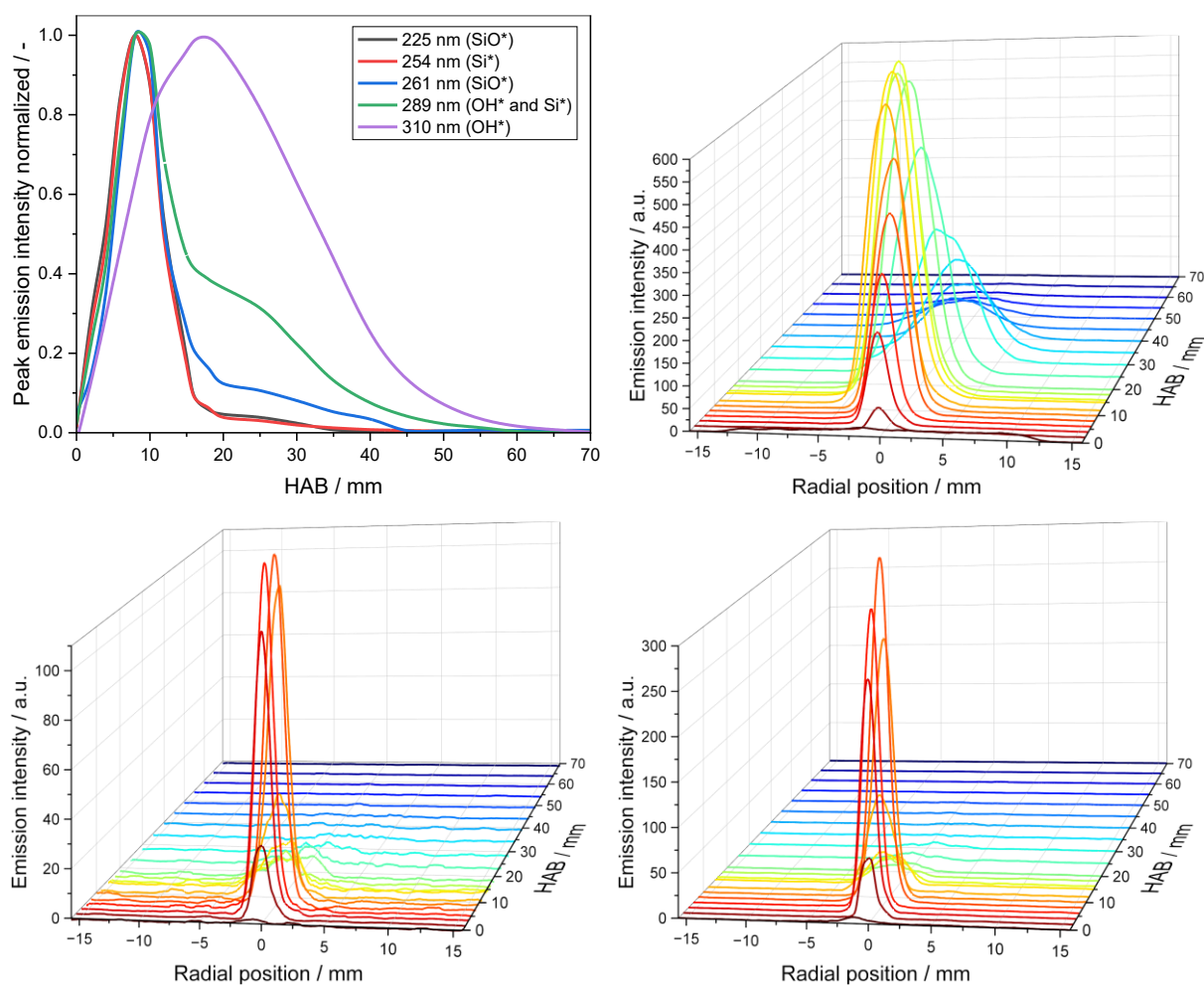


Figure 17: Emission spectra recorded in the SpraySyn flame at the standard operating condition, 5 ml/min HMDSO (1 mol/l) in ethanol: Top left: Normalized emission intensity of chosen peaks over HAB extracted from background-corrected spectra (cf. Figure 16), others: Smoothed radial emission spectra at chosen peak positions over HAB, top right: OH* emission intensity at 310 nm, lower left: SiO* emission intensity at 225 nm, lower right: Si* emission intensity at 254 nm.

4.3.4 Liquid fuel: Iron nitrate nonahydrate in 65EHA35EtOH

Figure 18 shows chemiluminescence spectra at various HAB of the SpraySyn flame operated with iron nitrate nonahydrate in 65EHA35EtOH. The spectral range from 210 to 530 nm is provided, recorded in two separate measurements by utilizing a grating with 600 grooves/mm. On the top the uncorrected spectra and on the bottom the background-corrected spectra are shown. The peaks were labeled with their attributed species.

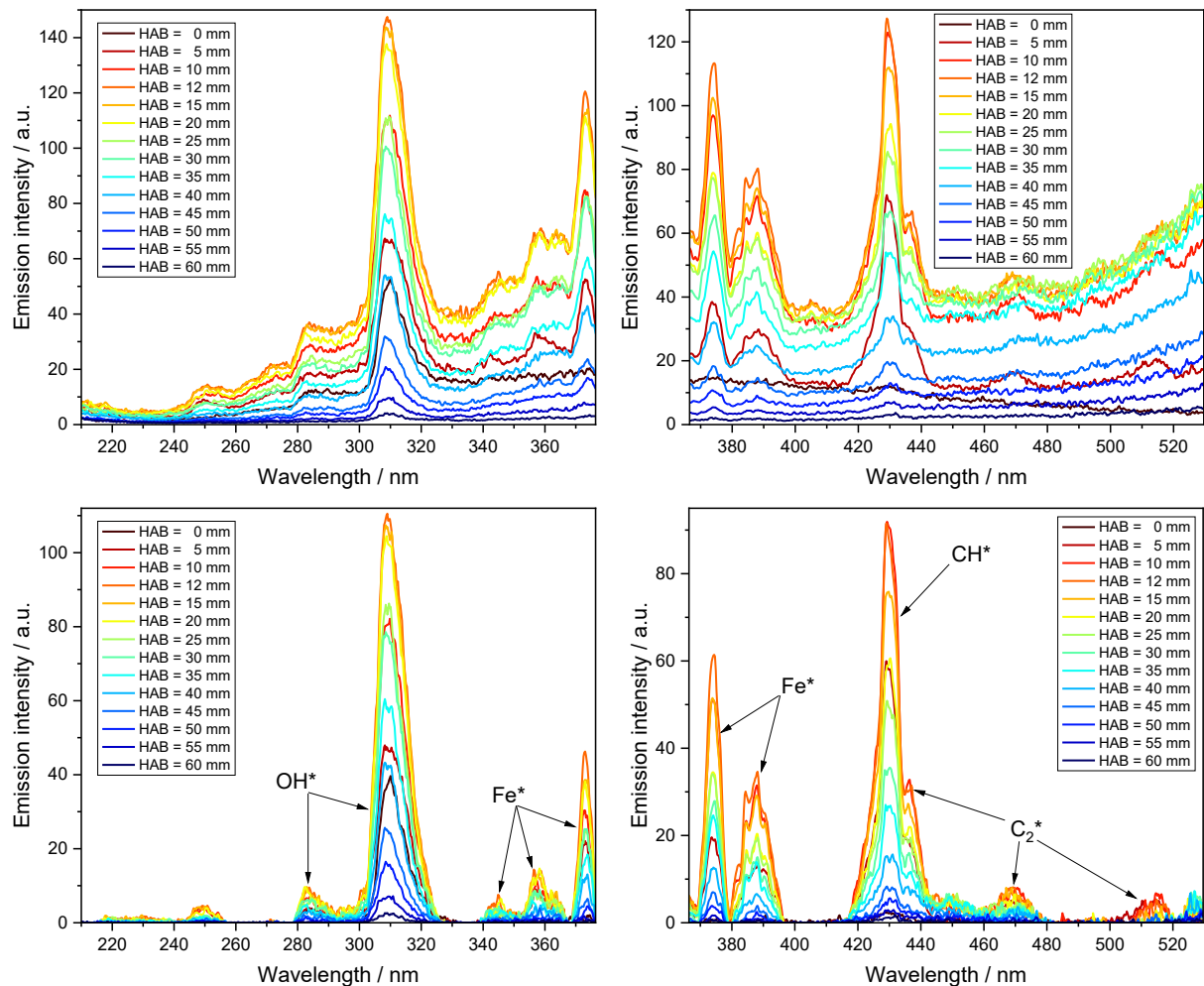


Figure 18: Emission spectra recorded in the SpraySyn flame at the standard operating condition, 2 ml/min iron nitrate nonahydrate (0.05 mol/l) in 65EHA35EtOH: Chemiluminescence spectra at various HAB, detection-sensitivity corrected, 600 grooves/mm grating, spectral region of 210 to 530 nm, bottom: Background corrected.

Several peaks in the spectral range between 340 and 400 nm can be identified that are attributed to Fe^* emission [243, 244]. Significant Fe^* peaks are located at approximately 345, 357, 373, and 386 nm. The same peak arrangement is observed for the SpraySyn flame operated with iron nitrate nonahydrate in ethanol (Figure A10). The Fe^* peaks at approximately 390 nm are superimposed by CH^* emissions (cf. Figure 13).

Figure 19 shows the chemiluminescence spectra within the spectral range from 520 to 820 nm, following the same layout as Figure 18. Additionally, an inset of measured (dotted line) and simulated (solid line) FeO^* spectra [245] was added to the top left diagram to enable an immediate comparison of the spectra.

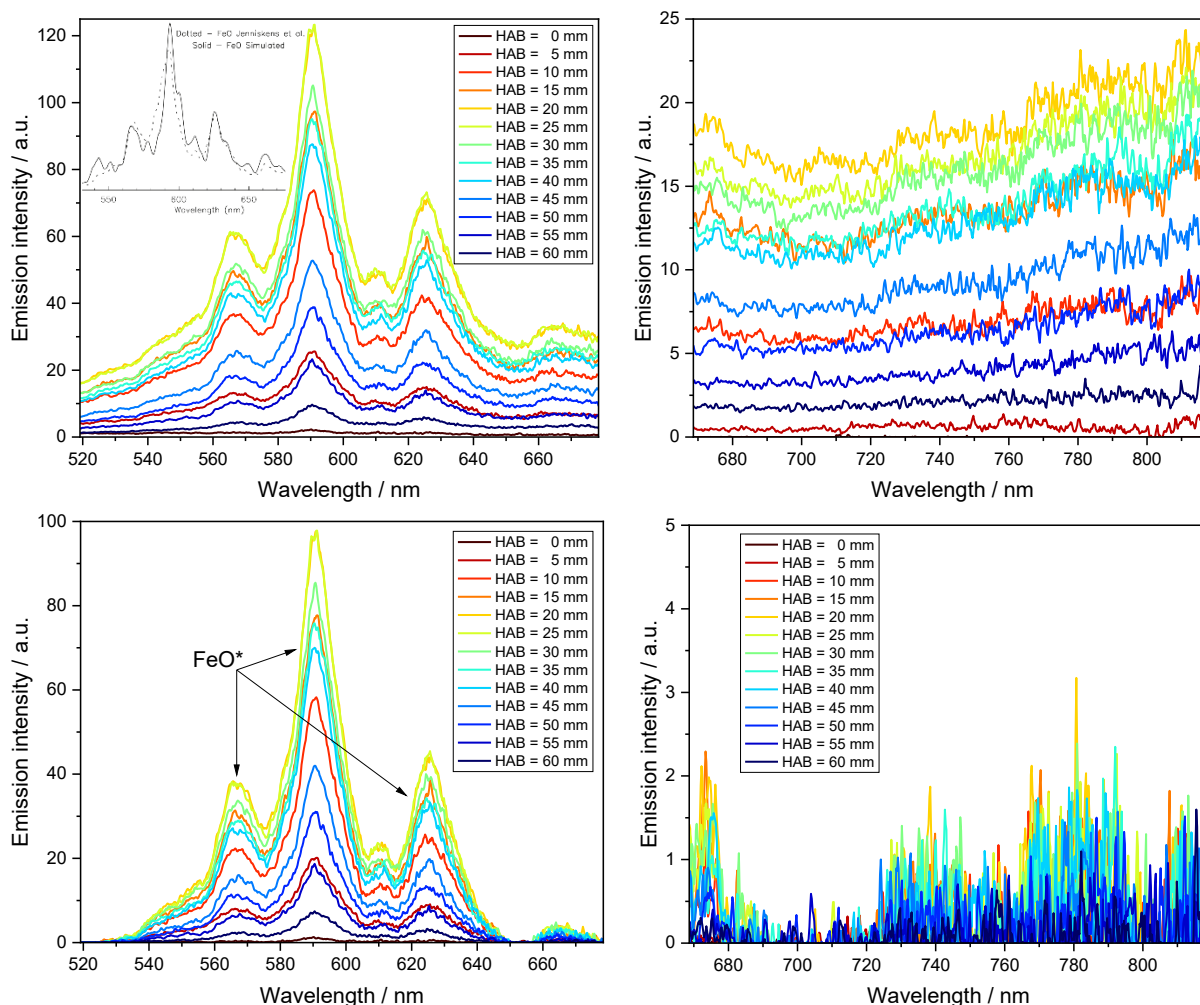


Figure 19: Emission spectra recorded in the SpraySyn flame at the standard operating condition, 2 ml/min iron nitrate nonahydrate (0.05 mol/l) in 65EHA35EtOH: Chemiluminescence spectra at various HAB, detection-sensitivity corrected, 600 grooves/mm grating, spectral region of 520 to 820 nm, bottom: Background corrected. The inset in the top left diagram shows a reprint of measured (laboratory fast flow tube spectrum, dotted line) and simulated (solid line) FeO* spectra published by Jenniskens et al. [246] and Gattinger et al. [245].

In the spectral range between 530 and 690 nm, the so-called FeO orange bands can be seen. These bands originate from FeO* emission [245, 247, 248]. Three prominent FeO* peaks were detected at 566, 591, and 626 nm. The Na* emission peaks, typically observed around 589 nm due to impurities in 65EHA35EtOH, are superimposed by the FeO* emission. In the spectral range above 690 nm, no significant emission peaks can be identified.

Figure 20 shows the normalized peak intensity of several emission peaks over HAB detected in the SpraySyn flame operated with iron nitrate nonahydrate in 65EHA35EtOH. Regarding the distribution across HAB, notable differences are evident among the different species. C₂* and CH* emission maxima are located in the lower range of the flame at approximately HAB = 6 and 11 mm, respectively. The Fe* emission peak maxima were recorded at about HAB = 13 mm. OH* and FeO* emissions are distributed over the entire flame height with their maxima at approximately HAB = 15 and 23 mm, respectively. The profiles of identical species at different wavelengths feature a close correlation. The measurement results of the SpraySyn flame operated with 0.05 mol/l iron nitrate nonahydrate in ethanol are presented in section 12.3.5 of the appendix.

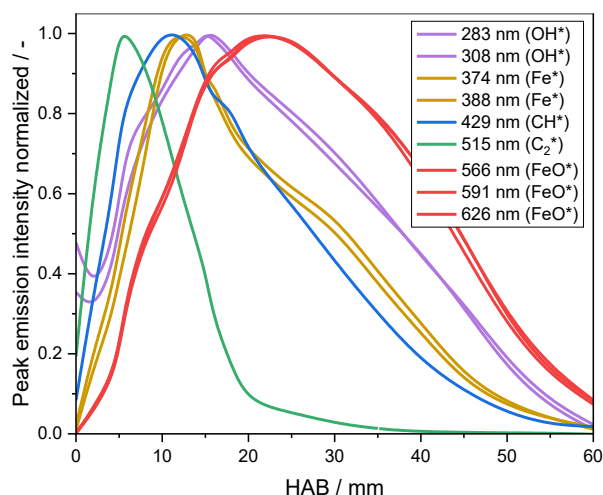


Figure 20: Emission spectra recorded in the SpraySyn flame at the standard operating condition, 2 ml/min iron nitrate nonahydrate (0.05 mol/l) in 65EHA35EtOH: Normalized emission intensity of chosen peaks over HAB extracted from background-corrected spectra (cf. Figure 18 and Figure 19).

4.4 Summary and discussion

Spectrally-resolved chemiluminescence from the SpraySyn flame was recorded at different HAB. The flame was operated with various solvents (ethanol, 65EHA35EtOH, 1-butanol, o-xylene) and with precursor solutions for SiO₂ and iron oxide nanoparticle synthesis (HMDSO in ethanol, and iron nitrate nonahydrate in ethanol and in 65EHA35EtOH, respectively). The spectra were corrected for the detection sensitivity of the measurement setup and for background radiation (e.g., blackbody radiation). Spectral emission peaks corresponding to different species were identified by comparing them to literature references. The distribution of species emissions was analyzed in both vertical and radial directions, and the results were illustrated in two- and three-dimensional diagrams.

In all flames, two significant OH* emission peaks in the UV at approximately 287 and 310 nm were observed, with the OH* peak at 310 nm being the dominant emission in flames without nanoparticle synthesis. OH* emission is characterized by a broad spatial distribution in both vertical and radial direction.

CH* features emission peaks at around 390 and 431 nm. Relative to OH*, CH* emissions reach their maxima at lower HAB and are present within a smaller area located at the lower center of the flame. The spatial distribution is similar for C₂* with peaks detected at around 470 and 515 nm. With the exception of the flame operated with o-xylene, the emission intensity is relatively low and located in the lower central range of the SpraySyn flame.

When the solvent 65EHA35EtOH was used, Na* emissions were observed at about 589 nm, across large areas of the flame, attributed to impurities in EHA since comparable measurements with pure ethanol showed no peak in this wavelength range.

When the SpraySyn flame was operated with HMDSO for SiO₂ nanoparticle synthesis, SiO* and Si* emissions were observed in the deep UV located in the lower central region of the flame. SiO* emissions manifest as numerous small peaks within the wavelength range of 215 to 275 nm, while Si* emissions result in two significant peaks at 254 and 289 nm, exhibiting higher peak intensities compared to SiO*. The SiO* and Si* emissions are characterized by a strong intensity increase within the first few millimeters downstream of the flame. The intensity maxima are attained at HAB < 10 mm for the SpraySyn flame at standard operating condition,

with emissions sharply decreasing after reaching their maxima. The spatial distribution of Si^* and SiO^* radicals is of particular interest, since they represent areas where precursor species for the formation of SiO_2 particles are present [228, 249].

Iron oxide nanoparticles were synthesized in the SpraySyn flame from iron nitrate nonahydrate dissolved in ethanol and 65EHA35EtOH. In these flames, Fe^* emission was identified in the spectral range between 340 and 400 nm and FeO^* emissions between 530 and 690 nm, often referred to as orange bands. While three spectrally broad FeO^* peaks are observed at 566, 591, and 626 nm, the Fe^* emissions feature several peaks with two prominent peaks at 373 and 386 nm. Independent of the solvent used, the emission intensity maximum of FeO^* is located at higher HAB compared to Fe^* . The emission intensity of Fe^* increases more strongly with HAB while FeO^* emission is spatially more extended and the intensity is stronger at larger HAB.

The data set provided in this work is intended to support the understanding of nanoparticle synthesis in spray flames and serve as reference data in the context of optical measurements in the SpraySyn flame. Data presented in this study were previously utilized, e.g., for the validation of tomographic flame reconstructions by Foo et al. [204] and for the identification of flame luminescence for signal analysis by Jüngst et al. [250].

5 Spray characterization of the SpraySyn2 burner (LDA and PDA)

Some sections of the following chapter are reprints or else contain contents from the listed publications:

J. Kirchmann, A. Kronenburg, **M.M. Prenting**, S. Karaminejad, T. Dreier, T. Endres, S. Patil, F. Beyrau, Characterizing the SpraySyn burners with MMC-LES, *Appl. Energ. Combust. Sci.* 15 (2023) 100182. <https://doi.org/10.1016/j.jaecs.2023.100182>

© 2023 The Authors. Published by Elsevier Ltd. Reprinted with permission.

My contribution to this publication was the provision of data sets of droplet velocity and size distributions. I set up the LDA/PDA experiment with the SpraySyn2 burner, performed the measurements and analyzed and interpreted the data. I supported the first author with corrections of the manuscript and was mainly responsible for the conception and writing of the section that deals with the LDA/PDA experiment.

In this chapter and section 12.4 of the appendix, droplet velocity and size distributions of the cold spray and spray flame generated by the SpraySyn2 burner are presented. The data is valuable as input for defining boundary conditions in simulations and for validating simulation models. Various solvents and operating conditions were investigated. The measurements were performed by laser-Doppler anemometry (LDA) and phase-Doppler anemometry (PDA).

LDA and PDA are calibration-free non-intrusive optical measurement techniques. With the LDA approach, particle or droplet velocities, and with the PDA approach, particle or droplet sizes can be measured within a small measurement volume of a moving fluid. The technique enables measurements in transparent or semi-transparent fluids with high spatial and temporal resolution (data acquisition rates of more than $f_{Hz} = 100$ kHz can be achieved). LDA and PDA measurements were successfully applied in, e.g., turbulent liquid flows [251, 252], internal combustion engines [253, 254], and spray flames [255, 256]. In this work, LDA/PDA measurements were performed with a commercial measurement system from the manufacturer Dantec Dynamics A/C.

5.1 Theoretical basics

The theoretical fundamentals and details of the established LDA and PDA measurement approaches are given in references [257-261], and therefore are only briefly summarized in this section.

For laser-Doppler anemometry, a laser beam (monochromatic and coherent) is split into two beams that are crossed within an ellipsoidal measurement volume and generate an interference pattern with dark and bright fringes. With this configuration, the droplet velocity can be measured in one spatial dimension perpendicular to the interference pattern. When three laser beams with different wavelengths (for separate signal detection) are utilized and focused from different directions into the measurement volume, all three velocity components can be measured simultaneously.

A droplet that crosses the interference pattern in the measurement volume scatters laser light and causes intensity fluctuations within the interference pattern with a specific frequency linearly proportional to the droplet velocity. The resulting shift of the frequency between the incident laser light and the scattered light is called Doppler shift and can be detected and processed to obtain the droplet velocity [259]. To perform these calculations the size dimensions of the measurement volume and the fringe pattern must be known. If both laser-beams have the same frequency, the flow direction of a droplet (either positive or negative towards the

fringe pattern) cannot be derived from the Doppler shift because of the same signal frequencies in both cases. To distinguish the laser beams and thus enable the determination of the flow direction, the frequency of one laser beam is frequency shifted (e.g., by utilizing a Bragg cell [262]). For details of the underlying calculation method of the LDA approach refer to Ref. [261]. To achieve correct measurement results it is necessary that only one droplet passes the measurement volume during data acquisition.

Phase-Doppler anemometry (PDA) is an extension of the LDA technique to enable droplet-size measurements. While LDA needs only one detector, PDA signal processing requires two detectors per laser-beam pair. When a spherical droplet crosses the fringe pattern of the measurement volume, a phase shift of the Doppler signals is caused. To determine the droplet size, the difference of the phase position of the signals with the same frequency is referenced. This difference is recorded from different view angles and processed to derive the droplet size (time delay of scattered signal due to different optical path lengths). On a logarithmic scale, the droplet size linearly depends on the phase shift [263]. Thus, the phase shift is a measure for the droplet size and the signal frequency for the droplet velocity. For further details of PDA, see Ref. [260].

5.2 Experimental setup

Droplet velocities and diameters presented in this study were measured by a commercial Phase-doppler anemometer (BSA P600 DualPDA, Dantec Dynamics, Skovlunde, Denmark). The term ‘dual PDA’ is derived from its ability to independently determine the size of a single droplet by two channels simultaneously due to its four detectors. Figure 21 shows the experimental setup of the fiber-based LDA/PDA system (optical fiber connection from the signal detector unit to the processor unit). The configuration is shown as a side view (top) and a top view (bottom).

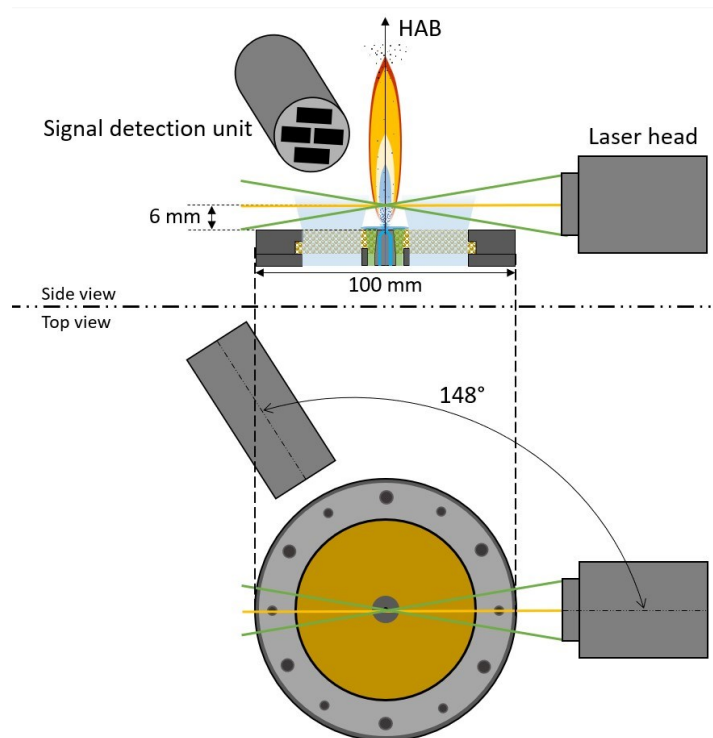


Figure 21: Schematic illustration of the experimental setup of the LDA/PDA configuration at the SpraySyn2 burner, top: Side view, bottom: Top view.

The LDA/PDA system has two laser pairs (monochrome diode lasers) with wavelengths of 532 and 561 nm incorporated in one optical head (maximum laser power: 300 mW). With this configuration, two fringe systems are generated for measuring two velocity components (axial and radial velocity). Bragg cells are used to shift the frequency of one beam of each laser-beam pair to enable the determination of the flow direction of the droplets. The signal detection unit features four detection channels to enable simultaneous measurements of the droplet diameter and two velocity components. The slit of the receiving optics can be adjusted to prevent signal overexposure of the photo multipliers (e.g., when measuring in the spray core). While the SpraySyn2 burner was fixed in its position, the optical head and the signal detection unit were mounted on a L-shaped rack and moved by a traverse system (Dantec Dynamics) in all spatial directions to scan the flow field (smallest step size: 0.01 mm). The entire LDA/PDA system was controlled, and the measurement data processed by the software BSA Flow (Version 6.50, Dantec Dynamics Group).

According to the manufacturer, droplet sizes between 1 μm to 1 mm are detectable. The measurements are however limited by the dynamic range of the detector (1:10,000) resulting in a dynamic range of the particle size of 1:100. The experimental configuration was equipped with laser-focusing optics with a focal length of 300 mm, which enables the measurement of droplet velocities between 0 and ~ 180 m/s. To enable the measurement of higher droplet velocities, a lens with a larger focal length needs to be installed in the laser head and the distance to the desired measurement position must be increased accordingly. A $f = 500$ mm lens would result in a maximum detectable droplet velocity of ~ 300 m/s. PDA measurements were performed by detecting the first-order refraction of the droplets. The angle of the receiving optics to the laser was 148° . The detection unit is equipped with an exchangeable mask to align the distance between the receiving apertures of the detection channels. The masks are designed for a specific range of droplet diameters (Mask A: Up to 46.7 μm , Mask B: Up to 61.1 μm , Mask C: Up to 131.5 μm). In this work, Mask B was used.

For the measurements presented here, the data acquisition at each measurement point was restricted to either 200,000 droplet counts or a maximum acquisition time of 10 s. The refractive index of each solvent was set in the BSA Flow software according to its chemical specifications (cf. Table A1). Typically, a uniform laser power of 30 mW was applied for both lasers. The dimension of the ellipsoidal measurement volume was defined by the intersecting laser beams to approximately $0.1 \times 0.1 \times 1$ mm³. The PDA measurements were limited to a minimum position of HAB = 6 mm because one of the laser beams (561 nm) would be blocked by the burner rim at lower positions (Figure 21, top). Note that in this work, HAB = 0 mm of the SpraySyn2 burner is defined as the top of the capillary outlet (cf. section 3.2), which is not on the same level as the position of sinter matrix (as it is the case for SpraySyn1, cf., section 3.1, or the PDA results for SpraySyn1 of Schneider et al. [122]).

For signal validation of the raw data, four validation criteria are applied by the software. The criteria can be adjusted in the software and are based on the signal-to-noise ratio, the FFT spectrum of each burst (correlation of the dominant peak and droplet frequency), and time correlation of the laser frequencies and the droplet sphericity. According to the fundamentals described above, the droplets need to be spherical for correct signal evaluation. Non-spherical droplets are rejected by the PDA validation software (comparison of the determined droplet size by both channels of the dual PDA). For the presented measurements, the limit for accepted deviations from sphericity was set to 30 %.

5.2.1 Signal postprocessing

In addition to the signal evaluation and data processing by the BSA Flow software, the measured data were further post-processed using a custom Matlab routine. Additional statistical evaluations were performed (e.g., calculation of droplet count rate, histograms, and scatter plots) and the data processed to be imported by the software OriginPro [264] in standardized format for graphical representation. For determining two-dimensional maps (flame cross-sections) of the droplet velocity, diameter and count rate, the area between the measuring points was linearly interpolated in OriginPro. Moreover, since droplets with a velocity above ~ 180 m/s cannot be detected by the LDA configuration used (as described above), the measuring points with velocity distributions that exceed this limitation were cut out from the data presented in section 5.3 (especially the case for OC with high dispersion gas flow rates, e.g., Figure 28 and Figure 29).

5.2.2 Measurement error

The measurement error of the LDA/PDA system originates from various sources and is difficult to quantify because sprays with well-defined droplet velocity and size distributions were not available for reference measurements. The manufacturer Dantec Dynamics claims a total measurement error for the PDA system of below 5 %, whereby the error for droplet sizes is expected to be higher than that for droplet velocities.

One contribution to the measurement error of the droplet size is caused by the temperature dependence of the refractive index of the liquid. In this work, various solvents were investigated in a range from room temperature to the boiling point. In his dissertation, Schneider [122] calculated for the same LDA/PDA system and the SpraySyn1 flame operated with ethanol a maximum measurement error of 4 %, based on an increase of the refractive index by 3 % from 293 to 353 K.

Grohmann [265] estimated a maximum measurement error of 6.5 % for measurements in a spray flame with a different PDA system (Artium Technologies Inc. PDI-300 MD). Moreover, the measurement accuracy might vary due to signal detection thresholds and thus results in biases for average droplet diameter and size distributions. However, quantifying these measurement biases in the SpraySyn2 flame is challenging.

The measurement error of the LDA/PDA system is given by the manufacturer as a measurement uncertainty of less than 5 %. Based on the measurement uncertainty stated by the manufacturer and the potential measurement error resulting from the temperature dependent refractive index of ethanol (4 % [122]), the systematic uncertainty regarding the measurement precision is estimated to be of the order of 9 %.

5.3 Results

In this section, the most relevant PDA/LDA results of cold sprays and spray flames generated by the SpraySyn2 burner are presented. Additional results can be found in the appendix, section 12.4. The data are presented as false-color maps of vertical and horizontal cross-sections and as profiles along the centerline and in radial direction. Error bars of the mean droplet velocity in the profile plots show the standard deviation. In the false-color maps, the black dots indicate the measurement positions (crossing laser beams). The area between the measurement positions was linearly interpolated by the software OriginPro [264]. The spatial axes of the images are true to scale. All cross-sectional images were measured at the center of the spray or flame. The top of the burner nozzle was located at the zero point ($x, y, z = 0$ mm). The data at each measurement position was acquired until either 200,000 droplet counts were detected or the time limit of 10 s was reached.

5.3.1 Liquid fuel: Ethanol

5.3.1.1 Operation: Cold spray

Figure 22 and Figure 23 depict vertical and horizontal cross-sections of the cold ethanol spray, respectively, with further details provided in the captions. The lowest mean droplet diameters of about $9\ \mu\text{m}$ are located in the flame center at approximately $\text{HAB} = 25$ mm. The mean axial droplet velocity reaches its maximum of $90\ \text{m/s}$ at $\text{HAB} = 10$ mm. High mean radial droplet velocities of up to $10\ \text{m/s}$ were observed in the lower region at $\text{HAB} = 6$ mm. The droplet count in the central range is high at all HAB within the measurement area.

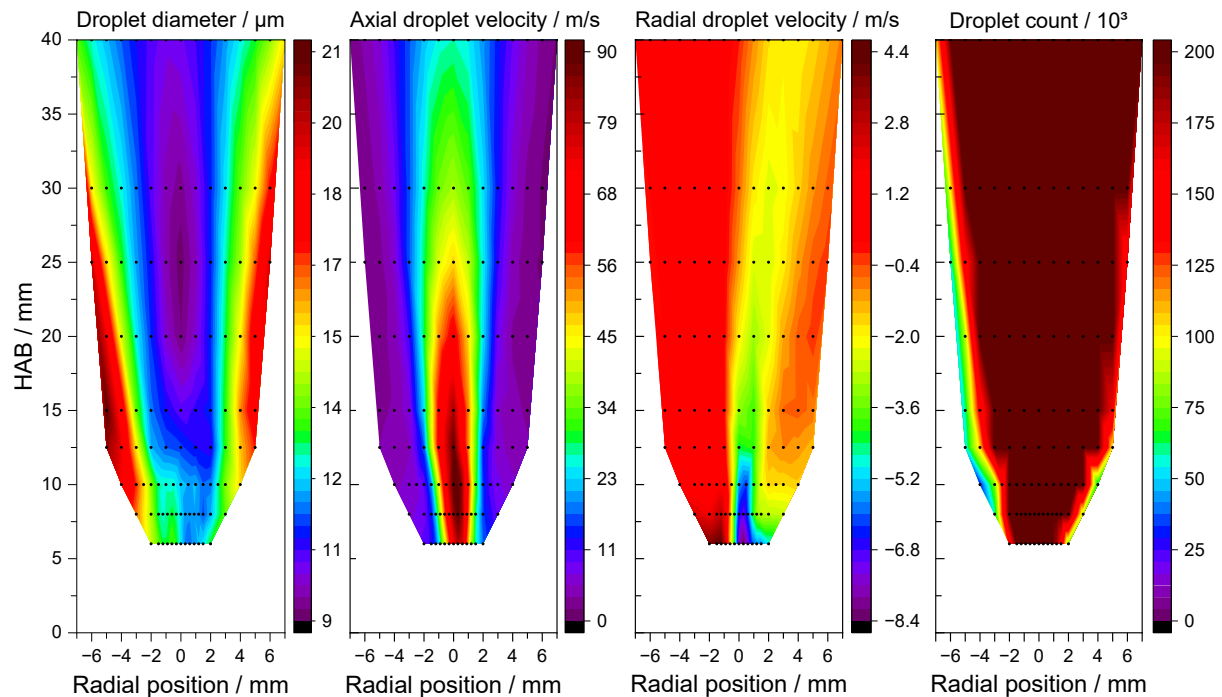


Figure 22: SpraySyn2 cold spray at the standard operating condition, 2 ml/min ethanol, 6 slm dispersion gas flow, vertical cross-sections of (from left to right): Mean droplet diameter, mean axial droplet velocity, mean radial droplet velocity, droplet counts.

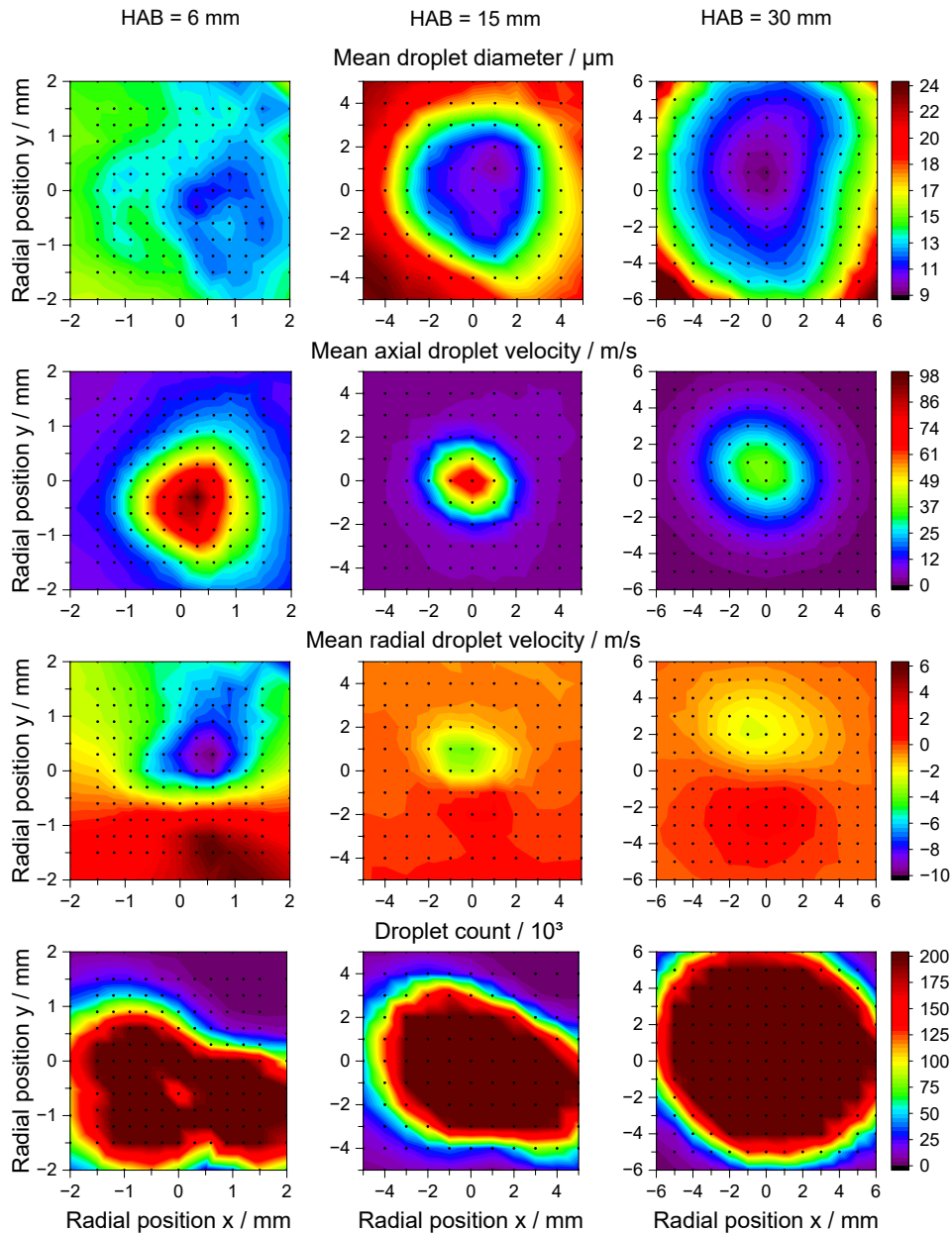


Figure 23: SpraySyn2 cold spray at the standard operating condition, 2 ml/min ethanol, 6 slm dispersion gas flow, horizontal cross-sections of (from top to bottom): Mean droplet diameter, mean axial droplet velocity, mean radial droplet velocity, droplet counts. The HAB from left to right is: 6, 15, and 30 mm. Note the differently scaled spatial axes within each row.

Vertical cross-sections with various dispersion gas flow rates

Figure 24 shows for the cold ethanol spray the effect of increasing the dispersion gas flow rate from 4 to 8 slm on the mean droplet diameter (top) and the mean axial droplet velocity (bottom). With increasing dispersion gas flows the minimum mean droplet diameter decreases from 10 μm (4 slm) to 9.1 μm (6 slm) and to 7.9 μm (8 slm), and the maximum mean axial droplet velocity increases from 69 m/s (4 slm) to 90 m/s (6 slm) and to 125 m/s (8 slm). The smallest droplet diameters and highest velocities are located in the center of the cold spray.

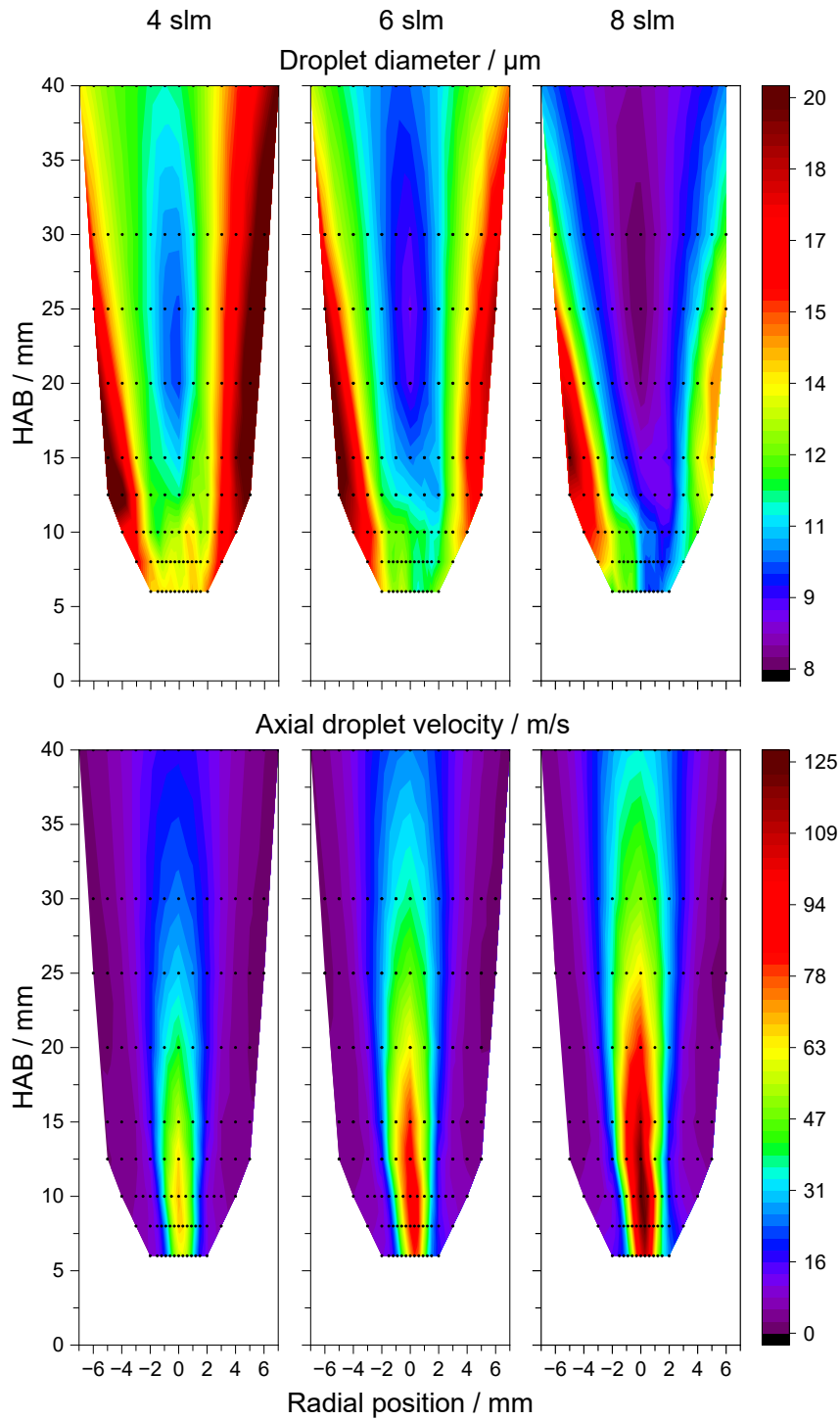


Figure 24: SpraySyn2 cold spray at the standard operating condition, 2 ml/min ethanol, various dispersion gas flows (from left to right): 4, 6, and 8 slm. Vertical cross-sections of mean droplet diameter (top) and mean axial droplet velocity (bottom).

5.3.1.2 Operation: Spray flame

Figure 25 and Figure 26 depict vertical and horizontal cross-sections of the ethanol SpraySyn2 flame, respectively, with further details provided in the captions. The smallest mean droplet diameter of $9.1 \mu\text{m}$ was measured in the flame center at $\text{HAB} = 8 \text{ mm}$. The highest mean axial droplet velocity was observed on the centerline at $\text{HAB} = 15 \text{ mm}$. Compared to the cold ethanol spray (Figure 22), the droplet count in the range above $\text{HAB} = 20 \text{ mm}$ is significantly lower indicating strong droplet evaporation within the flame.

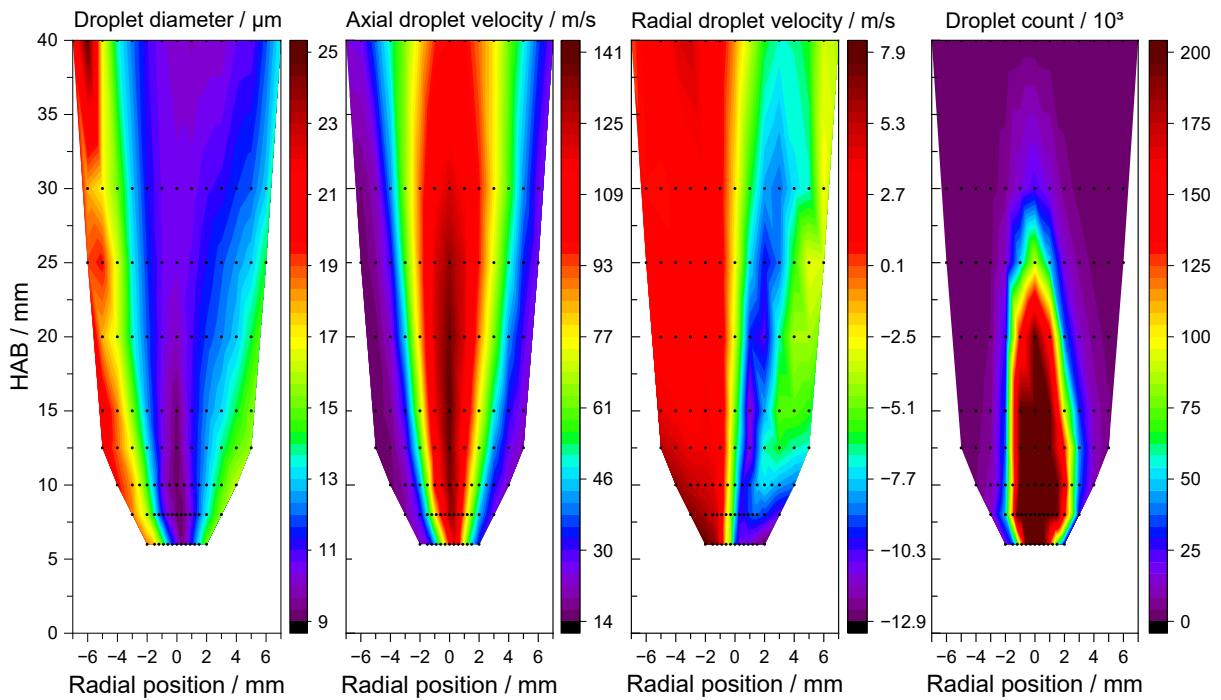


Figure 25: SpraySyn2 flame at the standard operating condition, 2 ml/min ethanol, 6 slm dispersion gas flow, vertical cross-sections of (from left to right): Mean droplet diameter, mean axial droplet velocity, mean radial droplet velocity, droplet counts.

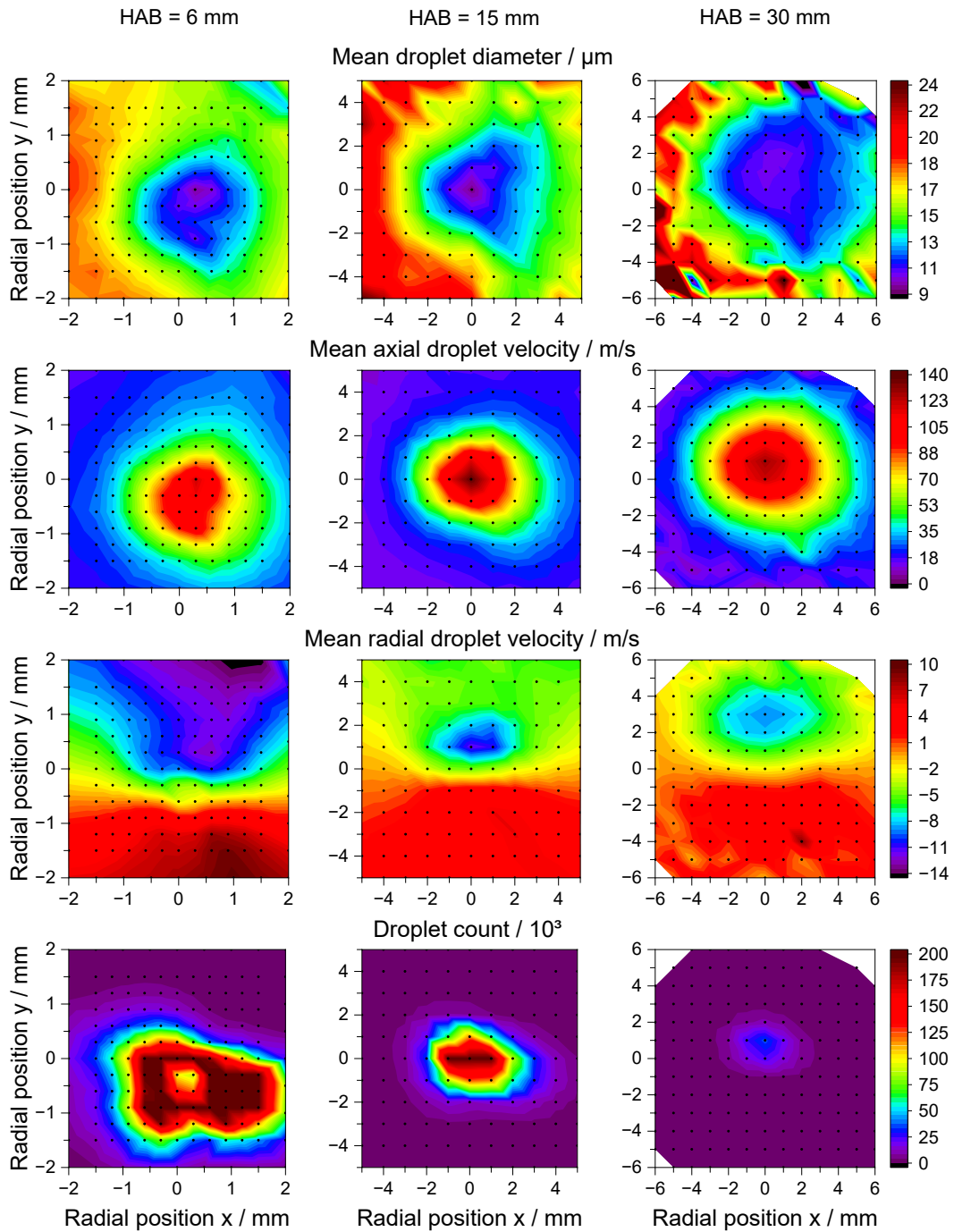


Figure 26: SpraySyn2 flame at the standard operating condition, 2 ml/min ethanol, 6 slm dispersion gas flow, horizontal cross-sections of (from top to bottom): Mean droplet diameter, mean axial droplet velocity, mean radial droplet velocity, droplet counts. The HAB from left to right is: 6, 15, and 30 mm. Note the differently scaled spatial axes within each row.

Centerline and radial profiles at various liquid flow rates

Figure 27 shows centerline and radial profiles of the mean axial droplet velocity, count rate and mean droplet diameter for the SpraySyn2 flame operated with various ethanol flow rates. On the centerline the mean axial droplet velocity decreases and the mean droplet diameter increases with increasing ethanol flow rates. This can be explained by a lower acceleration and poorer atomization due to the lower ratio of dispersion gas flow rate to liquid flow rate. At HAB = 15 mm the impact of the flow rate on the radial profiles is minor. In the upstream flow direction, the mean droplet diameter decreases up to approximately HAB = 15 mm due to secondary atomization and subsequently increases due to a faster evaporation of small droplets according to the D^2 law [266]. After about 30 mm, overall droplet evaporation results in continuously decreasing mean droplet diameters.

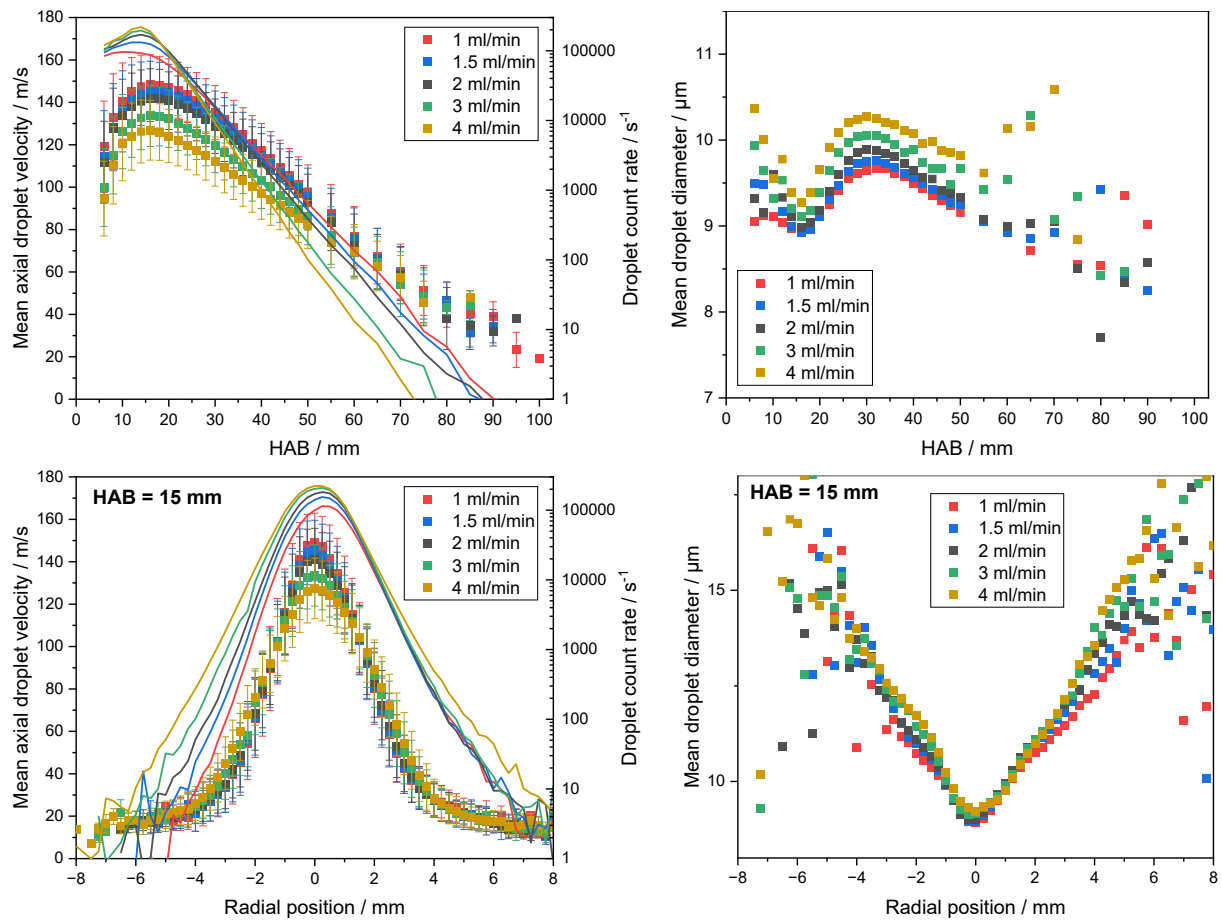


Figure 27: SpraySyn2 flames at standard operating condition, various flow rates of ethanol, 6 slm dispersion gas flow, top: Centerline profiles over HAB, bottom: Radial profiles through the flame center at HAB = 15 mm. Left: Mean axial droplet velocity (symbols) and droplet count rate (solid lines), right: Mean droplet diameter.

Centerline and radial profiles at various dispersion gas flow rates

Figure 28 shows centerline and radial profiles of the mean axial droplet velocity, count rate and mean droplet diameter for the ethanol SpraySyn2 flame operated with various dispersion gas flow rates (4 to 8 slm). On the centerline and radial profile at HAB = 15 mm, with increasing dispersion gas flow rates the mean axial droplet velocity increases, while the mean droplet diameter decreases. This can be explained by higher droplet acceleration and enhanced spray atomization due to a higher ratio of dispersion gas flow rate to liquid flow rate. For the operating conditions with dispersion gas flow rates of 7 and 8 slm, in the vicinity of a HAB = 15 mm, the droplet velocity partially surpassed the detection limit of the LDA system. The corresponding data points were cut out.

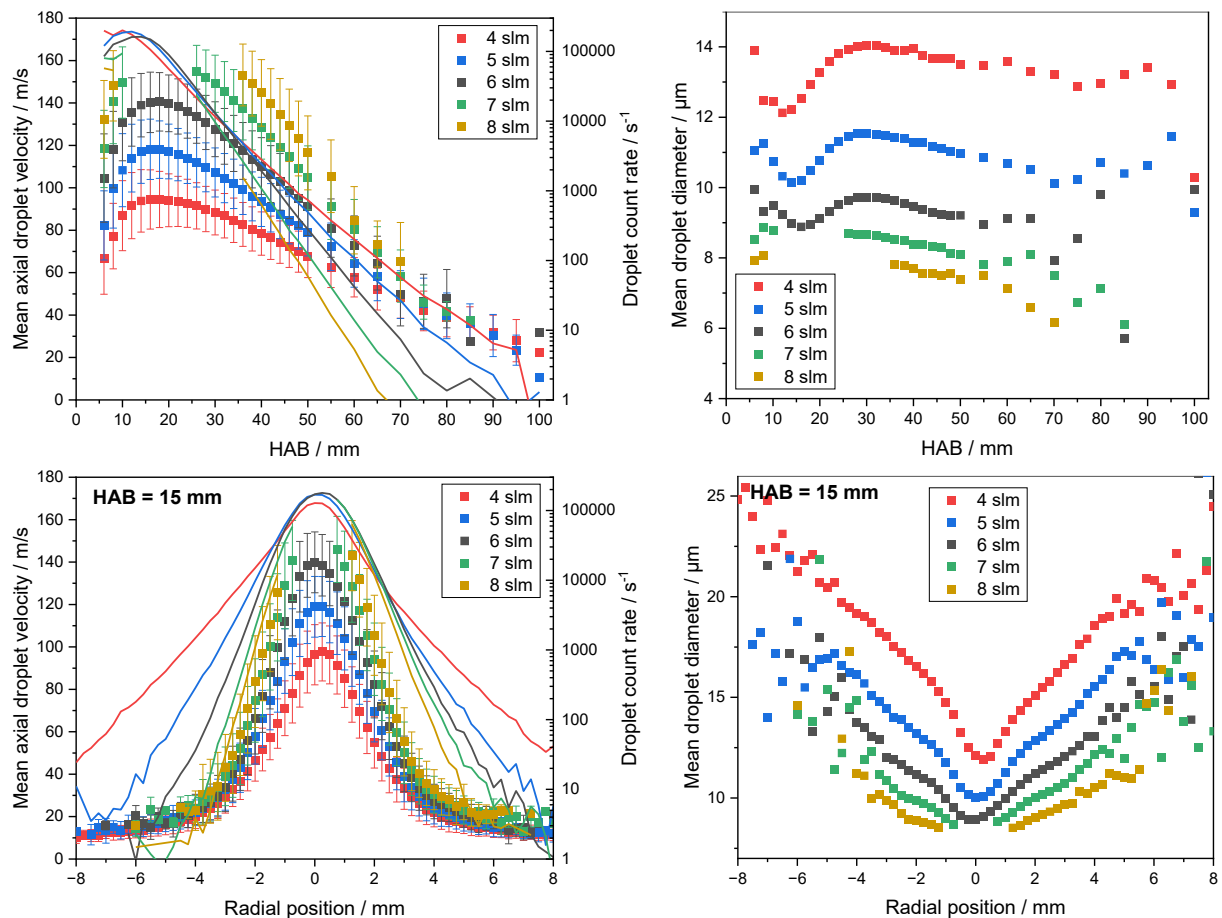


Figure 28: SpraySyn2 flames at standard operating condition, various dispersion gas flow rates, 2 ml/min ethanol, top: Centerline profiles over HAB, bottom: Radial profiles through the flame center at HAB = 15 mm. Left: Mean axial droplet velocity (symbols) and droplet count rate (solid lines), right: Mean droplet diameter.

Vertical cross-sections with various dispersion gas flow rates

Figure 29 shows for the ethanol SpraySyn2 flame the effect of increasing the dispersion gas flow from 4 to 8 slm on the mean droplet diameter (top) and the mean axial droplet velocity (bottom). With increasing dispersion gas flow the minimum mean droplet diameter decreases from 10.7 μm (4 slm) to 9.1 μm (6 slm) to 7 μm (8 slm) and the maximum mean axial droplet velocity increases from 107 m/s (4 slm) to 140 m/s (6 slm) to >150 m/s (8 slm). In the diagrams on the right, certain data points were cut out because the axial droplet velocity partially exceeds the detection limit of the LDA system in the center of the flame when operated with 8 slm dispersion gas flow.

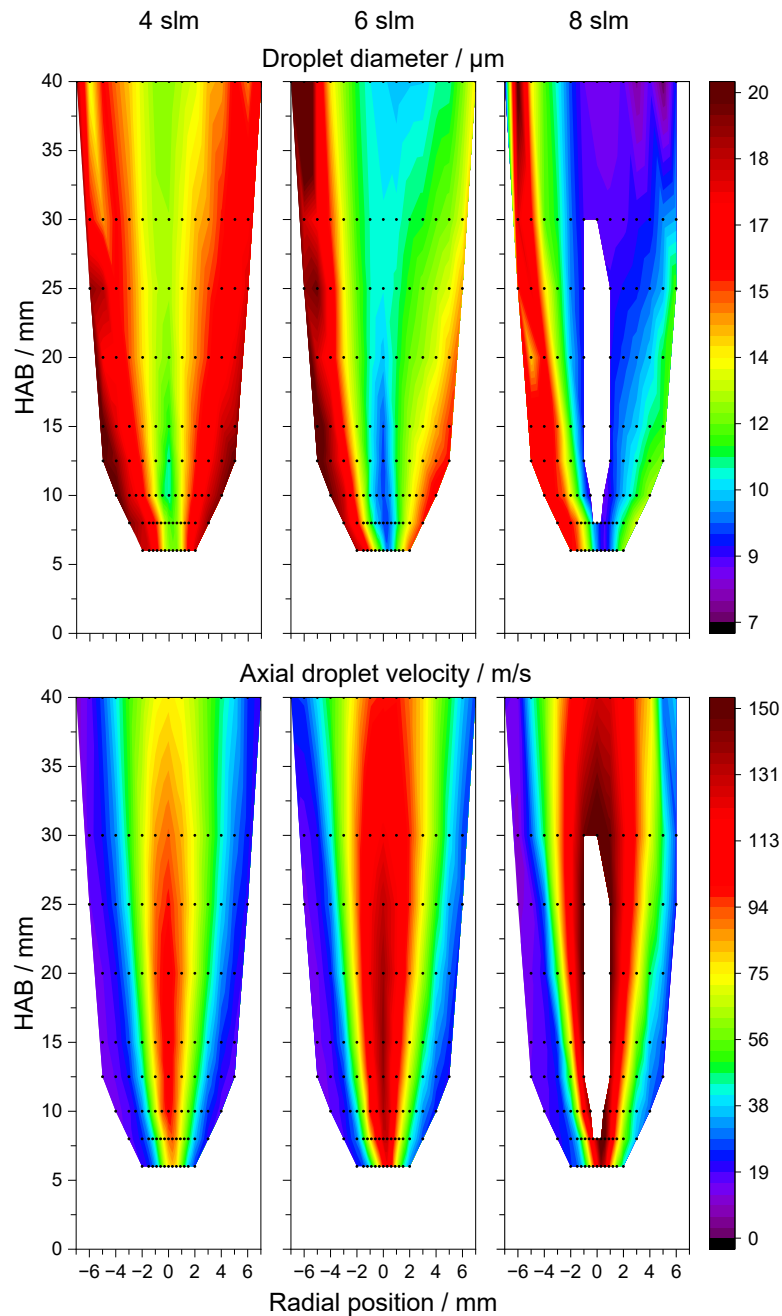


Figure 29: SpraySyn2 flame at the standard operating condition, 2 ml/min ethanol, various dispersion gas flows (from left to right): 4, 6, and 8 slm. Vertical cross-sections of: Mean droplet diameter (top) and mean axial droplet velocity (bottom).

5.3.2 Liquid fuel: 65EHA35EtOH

5.3.2.1 Operation: Spray flame

Figure 30 and Figure 31 depict vertical and horizontal cross-sections of the 65EHA35EtOH SpraySyn2 flame, respectively, with further details provided in the captions. The spray flame features the smallest mean droplet diameters ($d = 10.8 \mu\text{m}$) along the centerline within the range of 10 and 15 mm HAB. The mean axial droplet velocity reaches its maximum of 129 m/s at HAB = 15 mm. The horizontal cross-sections of the droplet diameter and axial velocity reveal an elliptical shape of the SpraySyn2 flame when operated with 65EHA35EtOH. In contrast, the flame operated with ethanol featured a nearly rotationally symmetric shape (Figure 26).

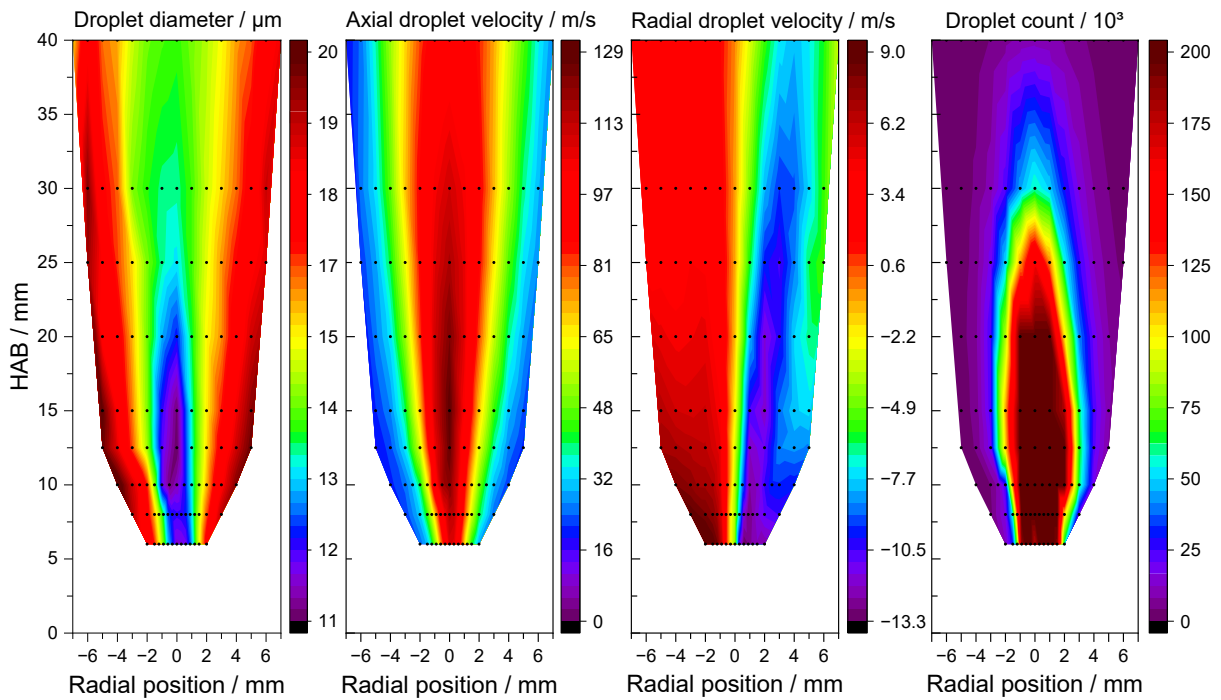


Figure 30: SpraySyn2 flame at the standard operating condition, 2 ml/min 65EHA35EtOH, 6 slm dispersion gas flow, vertical cross-sections of (from left to right): Mean droplet diameter, mean axial droplet velocity, mean radial droplet velocity, droplet counts.

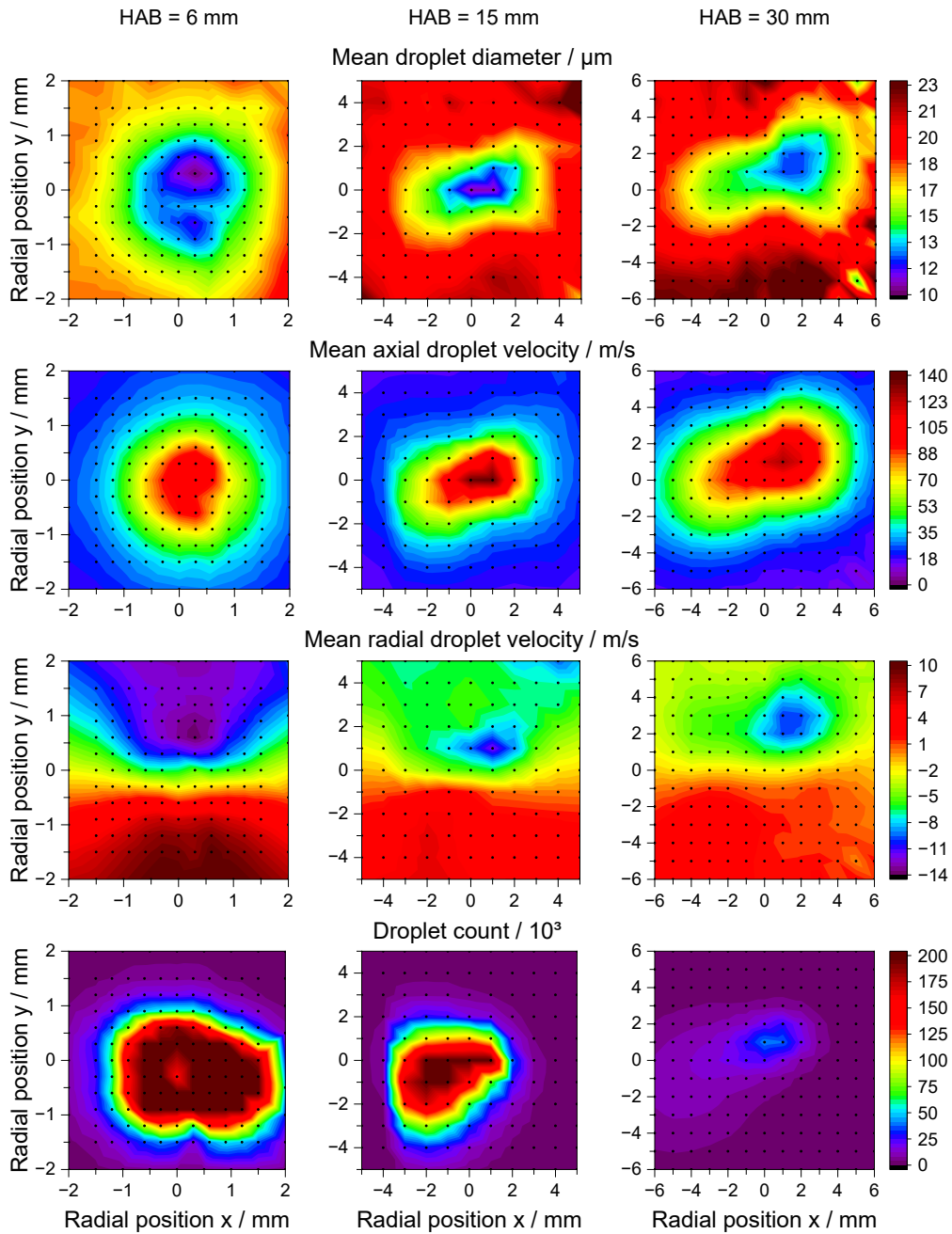


Figure 31: SpraySyn2 flame at the standard operating condition, 2 ml/min 65EHA35EtOH, 6 slm dispersion gas flow, horizontal cross-sections of (from top to bottom): Mean droplet diameter, mean axial droplet velocity, mean radial droplet velocity, droplet counts. The HAB from left to right is: 6, 15, and 30 mm. Note the differently scaled spatial axes within each row.

Centerline and radial profiles at various liquid flow rates

Figure 32 shows centerline and radial profiles of the mean axial droplet velocity, count rate and mean droplet diameter for the SpraySyn2 flame operated with various 65EHA35EtOH flow rates. From the results it can be generally concluded that an increase of the 65EHA35EtOH flow rate results in a lower mean axial droplet velocity and larger mean droplet diameters. The described impact is more pronounced on the centerline compared to radial positions more distant from the flame center. The droplet count rate indicates that a small fraction of 65EHA35EtOH droplets survive within the spray flame up to HAB = 100 mm.

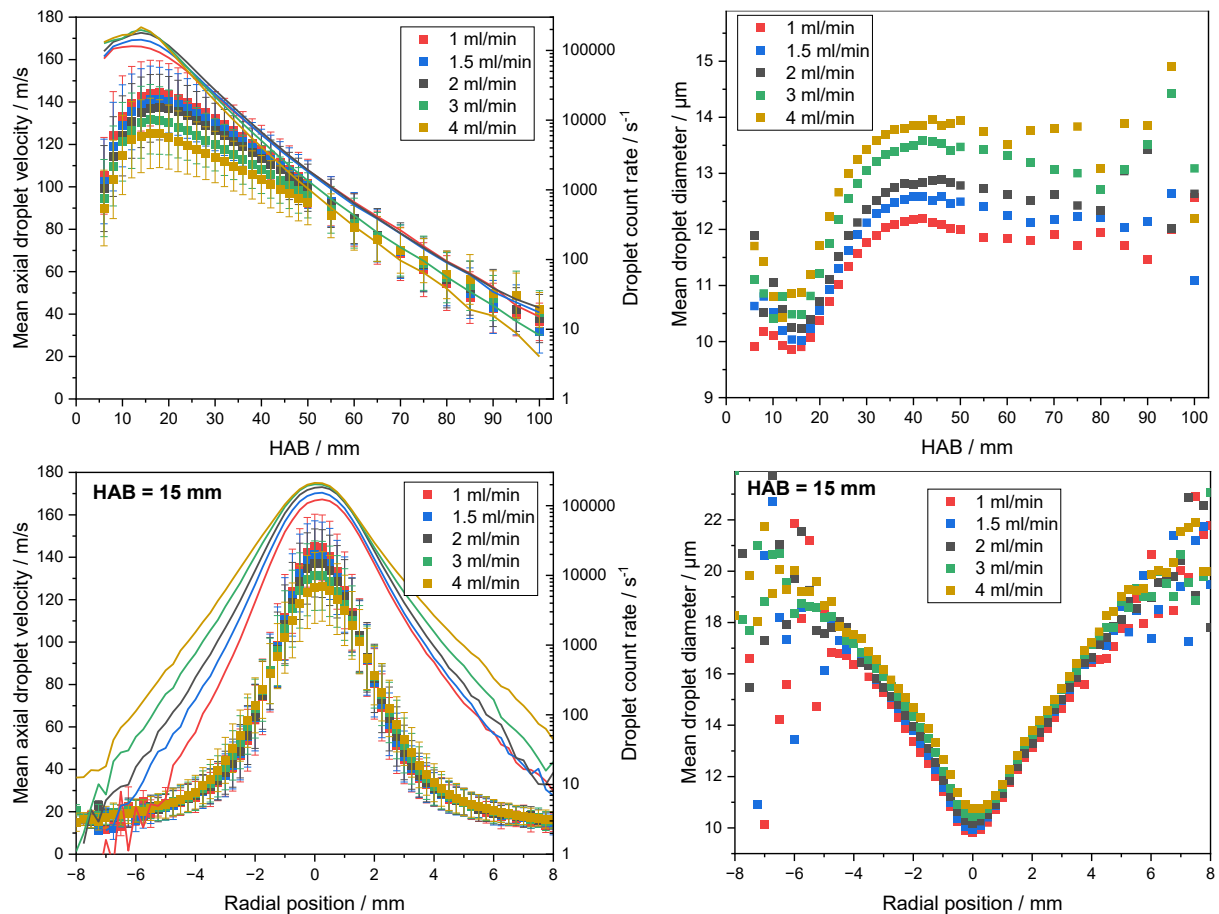


Figure 32: SpraySyn2 flames at standard operating condition, various flow rates of 65EHA35EtOH, 6 slm dispersion gas flow, top: Centerline profiles over HAB, bottom: Radial profiles through the flame center at HAB = 15 mm. Left: Mean axial droplet velocity (symbols) and droplet count rate (solid lines), right: Mean droplet diameter.

Centerline and radial profiles at various dispersion gas flow rates

Figure 33 shows centerline and radial profiles of the mean axial droplet velocity, count rate and mean droplet diameter for the 65EHA35EtOH SpraySyn2 flame operated with various dispersion gas flow rates. With increasing dispersion gas flow rates the mean droplet velocity increases and the mean droplet diameter decreases. The maximum droplet velocity and the minimum droplet diameter are reached at approximately HAB = 15 mm. In contrast to the variation of the liquid flow rate, the dispersion gas flow rate has a significant impact on the radial profiles.

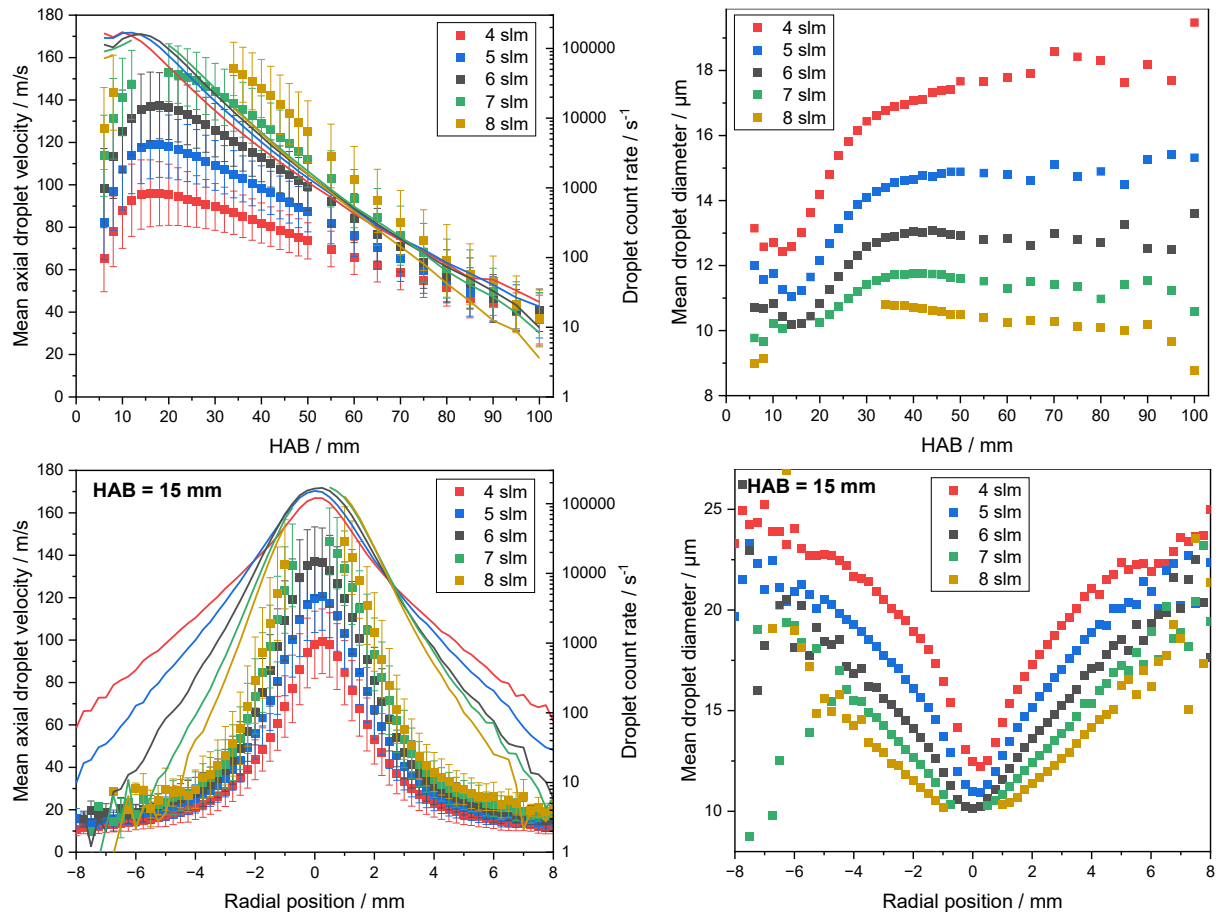


Figure 33: SpraySyn2 flames at standard operating condition, various dispersion gas flow rates, 2 ml/min 65EHA35EtOH, top: Centerline profiles over HAB, bottom: Radial profiles through the flame center at HAB = 15 mm. Left: Mean axial droplet velocity (symbols) and droplet count rate (solid lines), right: Mean droplet diameter.

5.3.3 Comparison of different liquid fuels

5.3.3.1 Mean droplet diameter

Figure 34 and Figure 35 show a comparison of the mean droplet diameter for the SpraySyn2 flame when operated with different solvents, with additional details on the cross-sections and profiles provided in the figure captions. The operation of the SpraySyn2 flame with different solvents results in significantly varying mean droplet diameters across the entire measuring range. It is generally observed that the mean droplet diameter decreases within the first approximately 15 mm along the flame center line, then increases within the distance up to a HAB of 30 to 40 mm, before slightly and continuously decreasing again. The horizontal profiles feature a minimum in the flame center, and as distance from the flame center increases, the mean droplet diameter continuously rises.

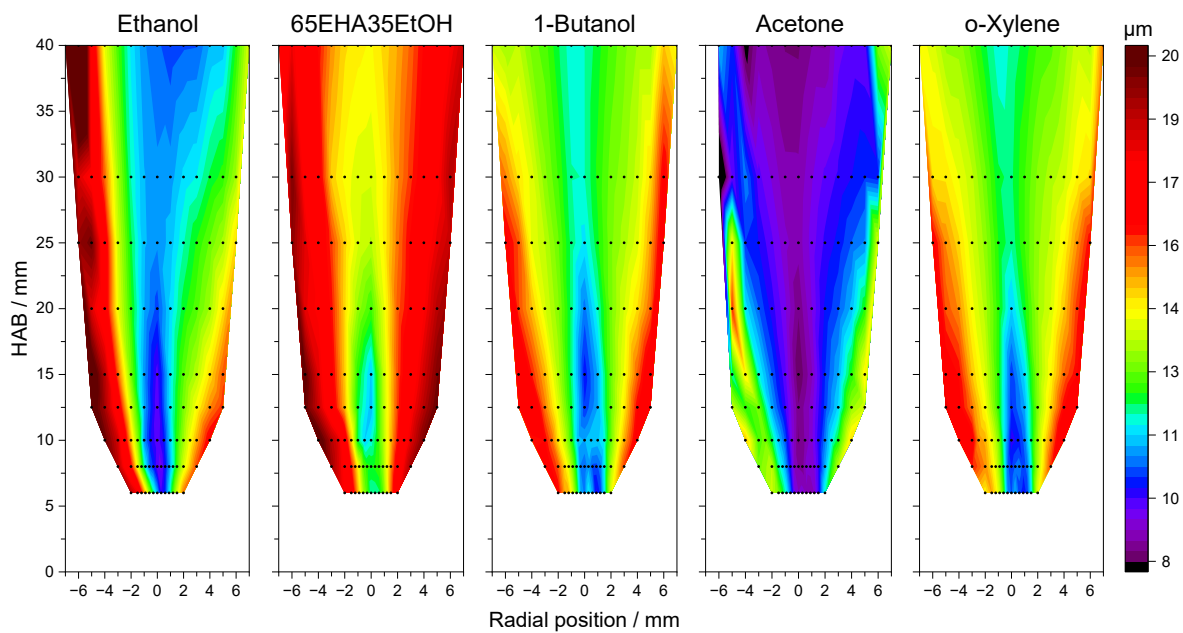


Figure 34: Vertical cross-sections of the mean droplet diameter of SpraySyn2 flames at the standard operating condition, uniform color scale. Dispersion gas flow: 6 slm, liquid flow rate: 2 ml/min, various solvents (from left to right): Ethanol, 65EHA35EtOH, 1-butanol, acetone, o-xylene.

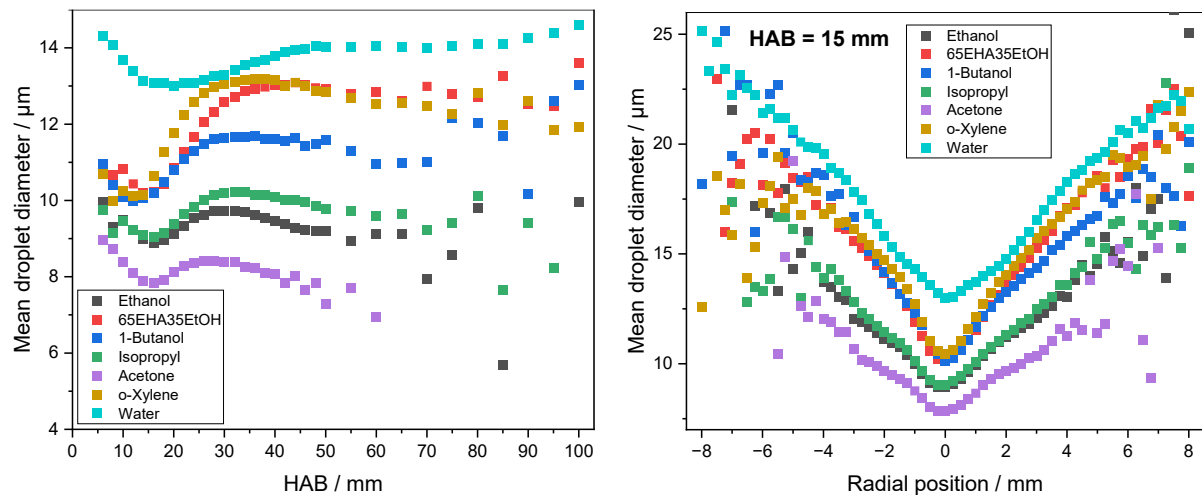


Figure 35: Mean droplet diameters of SpraySyn2 flames at standard operating condition, various solvents, 2 ml/min liquid flow rate, 6 slm dispersion gas flow, left: Centerline profiles over HAB, right: Radial profiles through the flame center at HAB = 15 mm.

5.3.3.2 Mean axial droplet velocity

Figure 36 and Figure 37 show a comparison of the mean axial droplet velocity for the SpraySyn2 flame when operated with different solvents, with additional details on the cross-sections and profiles provided in the figure captions. The impact of the solvent on the mean axial droplet velocity is low. However, a significant deviation is observed for deionized water, with a lower velocity compared to the other solvents. This observation could be explained by the higher density of deionized water, resulting in a slower acceleration. For all solvents, the maximum mean axial droplet velocity is reached between 15 and 20 mm downstream of the nozzle outlet.

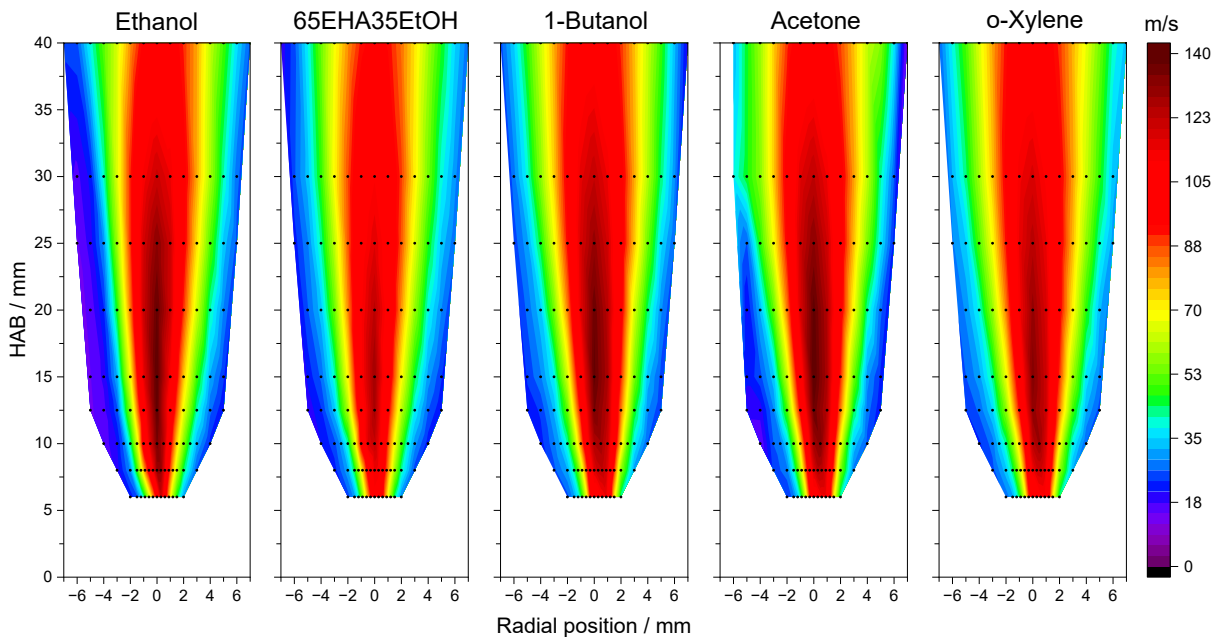


Figure 36: Vertical cross-sections of the mean axial droplet velocity of SpraySyn2 flames at the standard operating condition, uniform color scale. Dispersion gas flow: 6 slm, liquid flow rate: 2 ml/min, various solvents (from left to right): Ethanol, 65EHA35EtOH, 1-butanol, acetone, o-xylene.

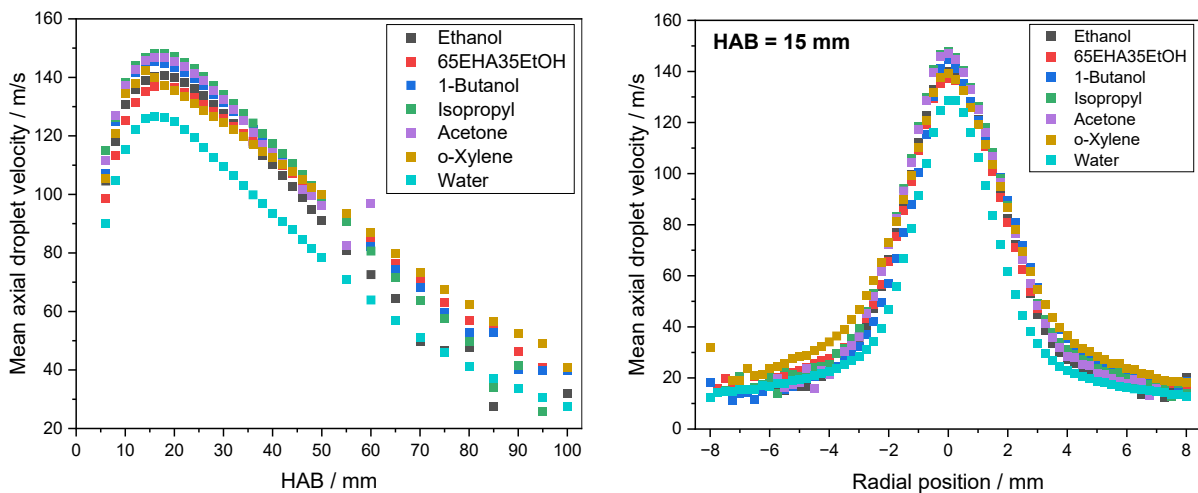


Figure 37: Mean axial droplet velocity of SpraySyn2 flames at standard operating condition, various solvents, 2 ml/min liquid flow rate, 6 slm dispersion gas flow, left: Centerline profiles over HAB, right: Radial profiles through the flame center at HAB = 15 mm.

5.3.3.3 Droplet count

Figure 38 and Figure 39 show a comparison of the droplet counts for the SpraySyn2 flame when operated with different solvents, with additional details on the cross-sections and profiles provided in the figure captions. The droplet count rates of deionized water and acetone stand out from the data set. Acetone features a sharp decrease in count rate with increasing HAB, while water exhibits the smallest decline. The high droplet count rate of deionized water across the entire measuring range in the spray flame can be attributed to its high enthalpy of vaporization [267]. In contrast, acetone is characterized by a low boiling point (Table A1) and a low enthalpy of vaporization [268]. More relevant in the context of nanoparticle synthesis, the droplet count rate along the centerline of the SpraySyn2 flame is higher when operated with 65EHA35EtOH, indicating slower droplet evaporation for this solvent compared to ethanol.

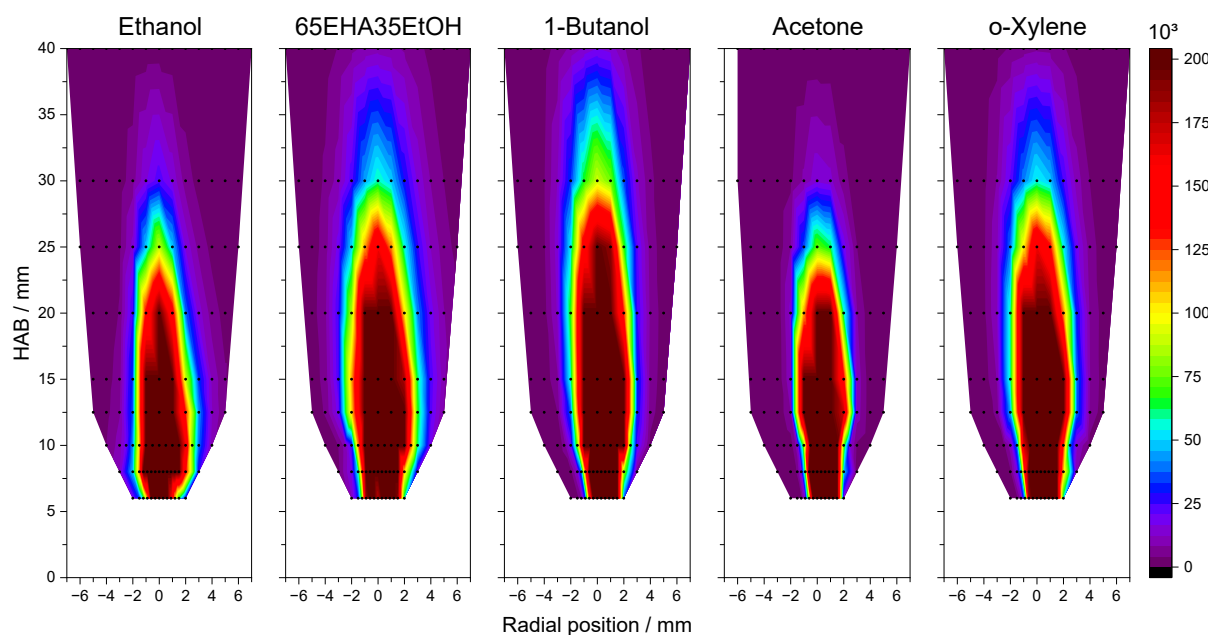


Figure 38: Vertical cross-sections of droplet count of SpraySyn2 flames at the standard operating condition, uniform color scale. Dispersion gas flow: 6 slm, liquid flow rate: 2 ml/min, various solvents (from left to right): Ethanol, 65EHA35EtOH, 1-butanol, acetone, o-xylene.

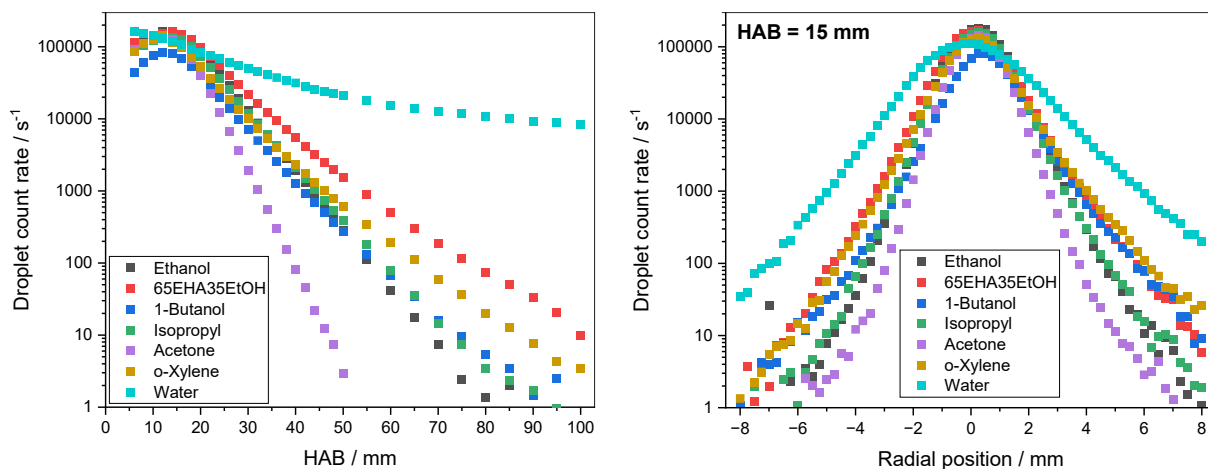


Figure 39: Droplet count rate of SpraySyn2 flames at standard operating condition, various solvents, 2 ml/min liquid flow rate, 6 slm dispersion gas flow, left: Centerline profiles over HAB, right: Radial profiles through the flame center at HAB = 15 mm.

5.4 Summary and discussion

In this chapter (and appendix, section 12.4), a data set of droplet velocity and size distributions of numerous SpraySyn2 flames and cold sprays is presented. Various operating conditions and solvents were investigated and the results are illustrated as vertical and horizontal cross-sections and profiles, respectively. Due to geometric constraints of the SpraySyn2 burner, the minimum measuring height was 6 mm above the burner nozzle. Additionally, due to optical limitations of the LDA/PDA-system, droplet velocities could only be measured up to ~180 m/s (section 5.2).

The results show that the utilized solvent, the dispersion gas flow, and the liquid flow rate have an impact on the droplet size and velocity across the entire measuring range of the SpraySyn2 flame and cold spray. The mean axial droplet velocity increases with higher dispersion-gas flow rates and decreases with rising liquid flow rates when the dispersion-gas flow rate remains constant. This can be explained by an increase in the dispersion gas velocity due to the higher volume flow that results in a stronger acceleration of the droplets. Additionally, the higher ratio of dispersion gas flow rate to liquid flow rate enhances droplet dispersion and atomization.

For the operating conditions investigated in this study, the highest mean axial droplet velocities and lowest mean droplet diameters are observed in the flame center in the range around $HAB = 15$ mm. The mean droplet diameters decrease within the first approximately 15 mm HAB , then increase to reach the maximum at about $HAB = 30$ mm, before decreasing again. This can be explained by secondary atomization within the first 15 mm, followed by a regime where small droplets evaporate faster due to the D^2 law [266] leaving larger droplet behind, and finally, a regime of generally decreasing droplet diameters due to evaporation.

For the SpraySyn2 flame, the droplet count rate decreases exponentially with rising HAB and also with increasing distance from the flame centerline. The smallest decrease was observed for deionized water, while the most significant decrease was noted for acetone. It was observed that droplets of solvents with a high boiling point and enthalpy of vaporization survive up to $HAB = 100$ mm within the SpraySyn2 flame (e.g., water, 65EHA35EtOH or o-xylene). Schneider [122] reported similar results for the SpraySyn1 burner using the identical measurement setup. For future work, particularly when operating the SpraySyn2 burner with dispersion-gas flow rates higher than the standard 6 slm, it is recommended to equip the LDA/PDA setup with laser-focusing optics featuring a higher focal length and to realign the distance between the optics and the burner. This adjustment will enable the detection and measurement of droplets with velocities exceeding ~180 m/s (section 5.2).

The data set presented in this chapter was generated to support process understanding of the SpraySyn2 flame, as input for CFD simulations or boundary conditions, and for simulation validation. Parts of the data have already been utilized, e.g., to validate LES simulations coupled to the sparse-Lagrangian multiple mapping conditioning model of Kirchmann et al. [181] or for the determination of droplet residence times within the SpraySyn2 flame by Jüngst et al. [269]. Further work utilizing or referencing this dataset is currently ongoing.

With the same measurement setup, droplet velocity and size distributions were measured for the SpraySyn1 burner. These results are analyzed and presented in section 8.1.4.1. For additional data on droplet velocity and sizes of the SpraySyn1 or SpraySyn2 burner, refer to the various studies conducted in the scope of the DFG research program [122, 190-193].

6 Multi-line NO-LIF gas-temperature imaging in pilot-scale spray flames

Some sections of the following chapter are reprints or contain contents from the listed publications:

M.M. Prenting, M. Underberg, T. Dreier, T. Endres, S.M. Schnurre, C. Schulz, Multi-line NO-LIF gas-temperature imaging in a pilot-scale spray flame for nanoparticle synthesis. 11th European Combustion Meeting (2023), Rouen, France. <https://ecm2023.sciencesconf.org/>

© Proceedings of the European Combustion Meeting 2023. Reprinted with permission.

M. Underberg, **M.M. Prenting**, M. Sieber, S. Schimek, C.O. Paschereit, T. Hülser, T. Endres, C. Schulz, H. Wiggers, S.M. Schnurre, A hydrogen-based burner concept for pilot-scale spray-flame synthesis of nanoparticles: Investigation of flames and iron oxide product materials, *Appl. Energ. Combust. Sci.* 15 (2023) 100165. <https://doi.org/10.1016/j.jaecs.2023.100165>

© 2023 The Authors. Published by Elsevier Ltd. Reprinted with permission.

S. Klukas, M. Giglmaier, M. Underberg, S.M. Schnurre, **M.M. Prenting**, T. Endres, H. Wiggers, C. Schulz, M. Sieber, S. Schimek, C.O. Paschereit, N.A. Adams, Scale-up analysis of spray flame nanoparticle synthesis by comparison of laboratory and pilot plant-scale burners, *Appl. Energ. Combust. Sci.* 18 (2024) 100263. <https://doi.org/10.1016/j.jaecs.2024.100263>

© 2023 The Authors. Published by Elsevier Ltd. Reprinted with permission.

My contributions to these publications were the design and setup of the multi-line NO-LIF gas-temperature imaging experiment, execution of the measurements supported by Martin Underberg, and analysis and interpretation of the NO-LIF data. I supported the first authors with the conception and writing of the manuscripts and was mainly responsible for the conception and writing of the sections that deal with NO-LIF thermometry and its results. The other coauthors contributed mainly to structuring and wording. The measurements and analysis of nanoparticles produced were performed by Martin Underberg in collaboration with ICAN, University of Duisburg-Essen.

Nanoparticle synthesis in spray flames is an adaptable method to produce nanoparticles with a wide range of different properties [107, 270]. Based on the liquid precursor feed, a variety of single- and multi-element metal-oxide nanoparticles can be synthesized [37]. The pilot-scale spray-flame burners for nanoparticle synthesis which are in the focus of this chapter are described in detail in section 3.3. The pilot-scale burners were located at the Institut für Umwelt & Energie, Technik & Analytik (IUTA) in Duisburg and were designed to investigate the upscaling process from laboratory to industrial production scale. The insufficient process understanding of gas-phase nanoparticle synthesis impedes the realization of industrial production. The aim of this project was to develop a scalable process design which can be transferred to industrial applications. Pilot- and large-scale nanoparticle production has already been realized for silica, titania, and alumina [72], ZrO₂ and Al₂O₃ nanoparticles at production rates of 180 g/h [271], silica nanoparticles at 1.1 kg/h [166], SiO₂ and TiO₂ at 200 g/h [272], boron-doped silicon nanoparticles at 0.75 kg/h [273], ZnO nanoparticles at >3 kg/h [169, 274], and ZrO₂ nanoparticles at up to 0.5 kg/h [170]. The gas-phase temperature in pilot-scale flames was measured at various operating conditions to analyze their impact on particle properties, to support process understanding and to provide boundary conditions and validation data for numerical simulations. The gas temperature in spray flames for nanoparticle synthesis is one of the key factors affecting evaporation processes, precursor decomposition, the kinetics of particle formation, liquid-particle, and particle-particle interaction [275, 276]. Therefore, in this work, the gas-phase temperature of pilot-scale spray flames was measured by multi-line NO-LIF temperature imaging.

6.1 Theoretical background

Multi-line NO-LIF imaging in flames introduced by Yorozu et al. [277] and further developed by Bessler et al. [278] is a non-intrusive *in situ* measurement technique for time-averaged gas-phase temperature measurements based on the temperature dependence of nitric-oxide LIF excitation spectra. The method is suitable as a calibration-free technique for use in challenging reactive flows with high background signals. The technique was applied earlier in evaporating spray systems and spray flames [279-281] proving its applicability in the presence of droplets. Moreover, multi-line NO-LIF was applied in laminar flames [277, 282-285], high-pressure flames [286-289] and nanoparticle-synthesizing reactive flows like low pressure laminar flat flames [275, 290, 291], spray flames [122, 292], and plasmas [293, 294]. For this measurement technique, the fresh gas is seeded with ppm-amounts of NO, which then is excited in a temperature-sensitive spectral range of the A–X(0,0) rovibrational electronic absorption band by a tunable UV-laser sheet while the resulting fluorescence is detected by an intensified CCD camera. The laser wavelength is stepwise tuned across a suitable temperature-sensitive spectral range (section 6.1.3) and per laser shot one two-dimensional NO-LIF intensity map is recorded. From the recorded stack of averaged LIF-signal images, per wavelength step, excitation spectra can be constructed for each pixel. LIFSim [295, 296] can calculate simulated excitation spectra for various parameters (section 6.1.3). With temperature as the main variable parameter, simulated spectra are fitted to the recorded excitation spectra by using a Levenberg-Marquardt non-linear least-squares fit function [297, 298]. To optimize the fitting procedure the simulated line positions are adjusted to the experimental line positions [299]. Same as two-line LIF thermometry, multi-line LIF is calibration-free because the measured excitation spectra are compared to detailed simulated spectra where various physical influences on the spectra are included. The retrieved local temperatures represent pulse-averaged values for the time of the laser scan duration in the cross-section of the laser sheet and the NO-doped gas phase (fluorescence signal is generated in this planar section). The desired time-averaged gas-phase temperature map is formed by assembling the determined temperature values of each pixel.

6.1.1 Two-level model

Comprehensive explanations of the theoretical fundamentals and the derivation of LIF-signal intensities can be found in references [300, 301], thus only a concise summary is provided in this section. For multi-line NO LIF, nitric oxide molecules are excited by laser light from their electronic ground state to the excited state. The excited state is not stable, and typically after a few nanoseconds, the system returns spontaneously back to the ground state. When the molecules return from the upper state to the lower state, part of the absorbed photon energy relaxes non-radiatively, and another fraction leads to the emission of photons, which represents the fluorescence. Figure 40 shows a simplified two-level model for the transition processes between the ground state and the excited state. The definitions of the related rate constants are given in the figure caption. Because the thermal population of the ground state energy levels is temperature dependent, NO features temperature-sensitive excitation spectra. These spectra can be recorded by the detection of the fluorescence signal when the excitation is in the linear regime, because then the fluorescence is proportional to the excitation irradiance. For the multi-line NO-LIF method, from the recorded excitation spectra the temperature can be derived without the necessity for calibration. The temperature dependence of the

excitation spectra is derived from the Boltzmann distribution within the interrogated molecular energy levels of NO and is well known in the literature [277, 295, 302].

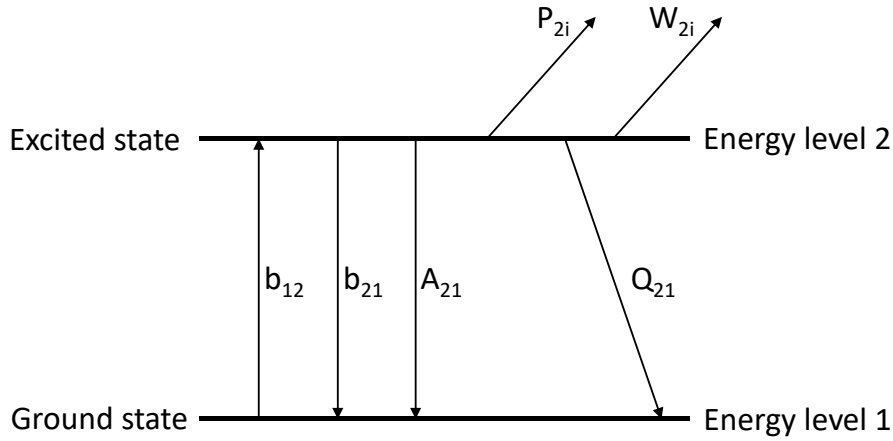


Figure 40: Two-level model with the rates of the transitions relevant for NO-LIF. Stimulated absorption: b_{12} , stimulated emission: b_{21} , spontaneous emission: A_{21} , collisional quenching: Q_{21} , predissociation: P_{2i} , photoionization: W_{2i} .

In the linear regime, the detected laser-induced fluorescence intensity, I_{LIF} , is proportional to the laser excitation intensity, I_{ex} , and can be expressed by the relationship given in equation (6.1) [303, 304]:

$$I_{\text{LIF}} \propto \text{Laser excitation intensity} \times \text{Absorption} \times \text{Fluorescence quantum yield} \times \text{Detection} \quad (6.1)$$

The recorded signal of the fluorescence depends on various influencing factors. They can be categorized in terms for absorption, emission and detection, that are given by equations (6.2), (6.3), and (6.4), respectively. The absorption can be described as follows by equation (6.2):

$$\text{Absorption} \propto B_{12} N_0 f_B g_\lambda \quad (6.2)$$

The absorption is proportional to the product of the Einstein coefficient from transition 1 to 2, B_{12} , the number density of molecules excited within the measurement volume, N_0 , the Boltzmann fraction, f_B , and the dimensionless overlap function between the absorption and laser line, g_λ . When the wavelength of the laser excitation light matches an absorption line, photons are absorbed and fluorescence generated.

The fluorescence intensity upon excitation is defined by the fluorescence quantum yield (Φ_f) and its term is given in equation (6.3) [305],

$$\Phi_f = \frac{A_{21}}{A_{21} + Q_{21} + P_{2i} + W_{2i}}, \quad (6.3)$$

where A_{21} is the Einstein coefficient for spontaneous emission and thus the rate of spontaneous emission from energy level 2 to 1, Q_{21} is the collisional quenching rate for molecules in the excited state, and P_{2i} is the molecule-dependent dissociation rate of the excited state 2. Therefore, A_{21} represents the radiative and Q_{21} and P_{2i} the nonradiative fraction of the depopulation of the excited state.

The term for the detection is defined by experimental factors. The recorded camera signal S_D can be expressed by equation (6.4) [306]:

$$S_D = I_F \frac{\Omega}{4\pi} V \tau \eta \quad (6.4)$$

The fluorescence signal from the measurement volume, I_F , is determined by the equations given above. To consider the characteristics of the camera and optical components, the detection solid angle, $\Omega/4\pi$ and the wavelength-dependent sensitivity of the detection system, η , is included in the equation. V represents the measurement volume and τ includes its wavelength-dependent transmission (fluorescence signal trapping) and the transmission of the fluorescence signal to the detector.

NO-LIF measurements are performed with laser excitation irradiance much smaller than the saturation irradiance ($I_{ex} \ll I_{sat}$). Under the assumption that the fluorescence is in the linear regime, from equations (6.2) to (6.4), equation (6.5) is obtained [299, 300]. In the linear regime the number of fluorescence photons is linear proportional to the number of excitation photons (i.e., $I_{ex} \sim I_{LIF}$). I_{LIF} represents the LIF-signal recorded by the detector (e.g., the camera) and is formed from the equations given above as follows

$$I_{LIF} = I_{ex} \frac{h\nu_f}{c} l A N_1^0 B_{12} \frac{A_{21}}{A_{21} + Q_{21}} \frac{\Omega}{4\pi} \tau \eta, \quad (6.5)$$

where h is the Planck constant, ν_f the frequency of the emitted fluorescence, and c is the speed-of-light in vacuum. The product $h\nu_f$ expresses the photon energy. The term lA represents the volume from where the fluorescence is observed (in which A is the focal area of the laser beam). The molecule number density within the measurement volume prior to excitation N_1^0 is derived according to Eckbreth [300] from equation (6.6) to (6.9):

$$\frac{dN_1}{dt} = -N_1 b_{12} + N_2 (b_{21} + A_{21} + Q_{21}) \quad (6.6)$$

$$\frac{dN_2}{dt} = N_1 b_{12} - N_2 (b_{21} + A_{21} + Q_{21} + P_{2i} + W_{2i}), \quad (6.7)$$

where N_1 and N_2 are the population densities of the lower and upper level, respectively, b_{12} and b_{21} are the rate constants for absorption and stimulated emission, respectively, P_{2i} is the predissociation rate constant and W_{2i} is the photoionization rate constant. Equation (6.8) is obtained when predissociation and photoionization are not considered and equations (6.6) and (6.7) are added.

$$\frac{d}{dt} (N_1 + N_2) = 0 \quad (6.8)$$

Equation (6.9) describes the prerequisite that the total number of NO molecules does not change.

$$N_1 + N_2 = \text{constant} = N_1^0 \quad (6.9)$$

6.1.2 Marker species

In previous work, gas-phase LIF thermometry was applied based on various target species. Besides NO, target species used for multi-line LIF thermometry include OH [51, 307-309], SiO [284, 291, 296], CH [310], and C₂ [310]. Two-line LIF thermometry was performed with NO [311-315], OH [315-323], SiO [324], O₂ [325], indium atoms [326-331], toluene [332], and iodine I₂ [333]. Single-line LIF temperature imaging was done with the target molecules NO [314, 334], I₂ [335], O₂ [336] and toluene [337]. In this study, nitric oxide (NO) was chosen as tracer species due to its many advantages for the application in flames [278, 299]. NO provides strong

LIF signal (although less than OH, for example) and therefore is well suited for imaging thermometry. NO is a naturally formed species in combustion processes where nitrogen and oxygen are present, e.g., combustion with air. Additional amounts of NO can be added to the fresh gas to increase its concentration and hence the detectable LIF signal and to also measure temperature in areas before and outside the flame. In contrast to OH or O₂ it is a stable molecule in burned and unburned gases and is largely unaffected by the flame front, thus LIF signal can be obtained from the entire flow field. This study targets gas temperatures in spray flames. The applicability of multi-line NO LIF and its stability at high temperatures was demonstrated in spray flames for temperatures up to at least 2500 K [122, 292] and in a low pressure plasma reactor up to 3000 K [293]. Typically, NO is added in trace amounts to the gas phase so that low concentrations in the range of 100–1000 ppm [278, 280, 281, 283, 291] are obtained and influences on the system under investigation (e.g., to the flame chemistry, fluid dynamics) can be neglected [278]. The use of higher NO concentrations up to 4000 ppm was also reported [293].

6.1.3 Spectral range for multi-line NO-LIF

In previous studies, depending on the targeted gas temperature, either the spectral range between 44,407–44,417 cm⁻¹ (four major peaks) [278, 279, 281, 338] or 44,407–44,423 cm⁻¹ (five major peaks) [122, 279, 291–293] in the A–X(0,0) band was used. The selected spectral range with five major peaks enables LIF thermometry in a large temperature range and based on numerical evaluations of NO-LIF excitation spectra (LIFSim) the range features the highest temperature sensitivity for temperatures between 250–2500 K [290]. With the five-peak configuration, measurements were performed for gas temperatures between 300 and 3000 K [293]. Hecht [339] reported that in the spectral range between 44,300–44,500 cm⁻¹ the selected range between 44,407–44,423 cm⁻¹ features a low LIFSim fit error of 1.3 % when a white-noise level of 5 % is introduced to a simulated spectrum of 1000 K. Errors about 2 % were calculated in other spectral ranges. The four-peak configuration features a high temperature sensitivity at room temperature and for gas temperatures above 1000 K. However, some fitting instabilities were reported for the lower temperature range between 500–1000 K due to weak spectral peaks which can get lost in the background noise [290]. The fit might return lower temperature values up to 200 K. For the interpretation of temperature regions below 1000 K these fitting instabilities need to be considered. For this work, the spectral range between 44,407–44,417 cm⁻¹ (225.19–225.14 nm) of the A–X(0,0) NO absorption band was selected according to the above-mentioned studies. The gas temperature is expected to be above 1000 K in all relevant regions of interest of the pilot-scale spray flames.

Figure 41 shows NO-LIF excitation spectra at various temperatures simulated by LIFSim [295]. The left diagram shows normalized and the right diagram absolute spectra. The simulations were done for 1 bar and a gas-phase composition of 1000 ppm NO, 79.9 % N₂ and 20 % O₂. From the normalized spectra it can be seen that the ratios of the peaks are strongly temperature dependent, which accounts for the high temperature sensitivity of this spectral range. The absolute spectra on the right show that the excitation-light absorption is small at lower temperatures. Maximum NO-LIF signal can be expected for the temperature range between 1500–2000 K. With regard to NO-LIF measurements in flames, this effect is partly compensated due to lower gas densities at higher temperatures.

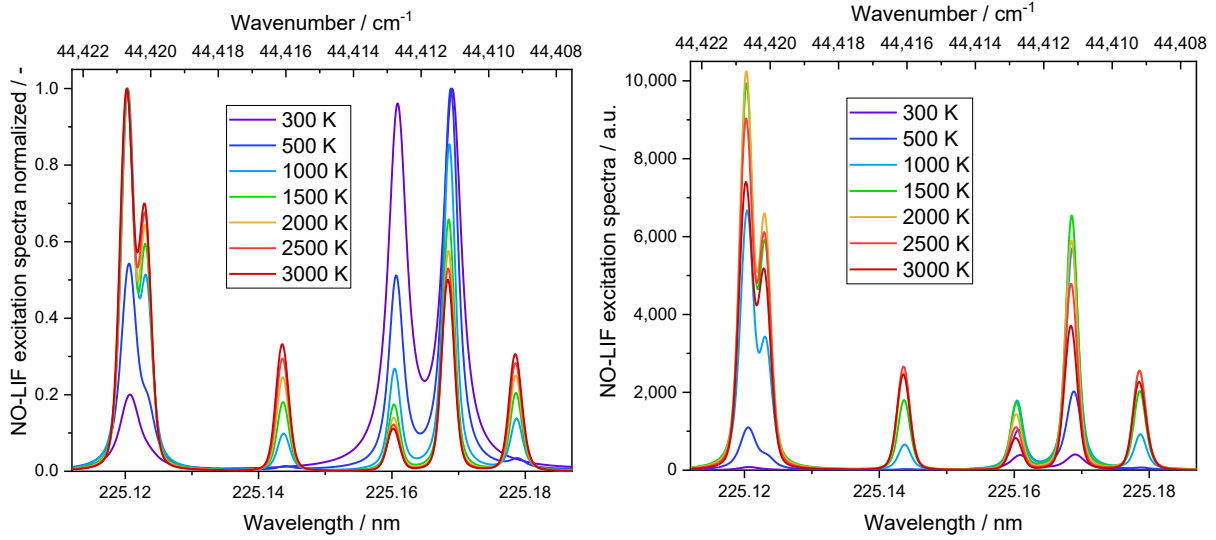


Figure 41: Simulated NO-LIF excitation spectra at various temperatures, left: Normalized intensity, right: Relative intensity.

The excitation spectra shown in the spectral range between 44,407 and 44,423 cm^{-1} (225.19–225.11 nm) consist of twelve individual absorption transitions that partly overlap. Except for the peak at 44,412.87 cm^{-1} (225.16 nm) the other four peaks result from superimposed transitions, so that these transitions appear as five peaks as shown in Figure 41. Table 2 shows the spectral positions of the twelve overlapping NO transitions with its ground-state energies and Einstein coefficients.

Table 2: 12 NO-absorption transitions A–X(0, 0) and its spectroscopic properties in the spectral range between 44,407–44,423 cm^{-1} (225.19–225.11 nm), data from LIFSim [295].

Rotational branch for NO transition	Quantum number $J_{\text{low}} / J_{\text{up}}$	Excitation wavenumber $\tilde{\nu}$ / cm^{-1}	Ground-state energy E_g / cm^{-1}	Einstein coefficient A_{21} / s^{-1}	Einstein coefficient B_{12} / $\text{m}^3\text{J}^{-1}\text{s}^{-2}$
O ₁₂	46.5 / 45.5	44409	3877.26	2.73×10^4	1.83×10^{16}
P ₁	36.5 / 35.5	44409.27	2283.36	2.13×10^5	1.42×10^{17}
R ₁	22.5 / 23.5	44411.23	882.38	1.78×10^5	1.27×10^{17}
Q ₂₁	22.5 / 22.5	44411.29	882.38	1.10×10^5	7.53×10^{16}
S ₂₁	17.5 / 18.5	44412.87	540.06	6.62×10^4	4.79×10^{16}
Q ₁₂	38.5 / 38.5	44416.07	2714.06	6.33×10^4	4.34×10^{16}
P ₂	38.5 / 37.5	44416.18	2714.06	2.19×10^5	1.46×10^{17}
R ₁₂	31.5 / 32.5	44420.13	1869.96	3.55×10^4	2.51×10^{16}
Q ₂	31.5 / 31.5	44420.22	1869.96	4.01×10^5	2.75×10^{17}
Q ₁	29.5 / 29.5	44420.72	1501.95	3.95×10^5	2.71×10^{17}
P ₂₁	29.5 / 28.5	44420.80	1501.95	4.18×10^4	2.77×10^{16}
R ₂	25.5 / 26.5	44420.86	1276.51	1.77×10^5	1.26×10^{17}

6.2 Experimental setup

6.2.1 Dye laser

For the recording of excitation spectra, a wavelength-tunable laser source is needed, which is accomplished in this work by a dye laser. Dye lasers are characterized by using fluorescence-dye solutions as lasing medium. A prism or diffraction grating is installed in the optical resonator to adjust the wavelength of the emitted laser beam. The tuning range of the emission wavelength depends on the laser dye used. A single laser dye covers a spectral range of about 30–60 nm, and due to the large variety of dyes available a spectral range from near UV (~320 nm) to near IR (~1500 nm) is accessible by dye lasers [340, 341]. Using sum-frequency mixing (e.g., in nonlinear crystals) laser-emission wavelengths down to 200 nm can be reached [342]. The gain medium is usually pumped by an external laser.

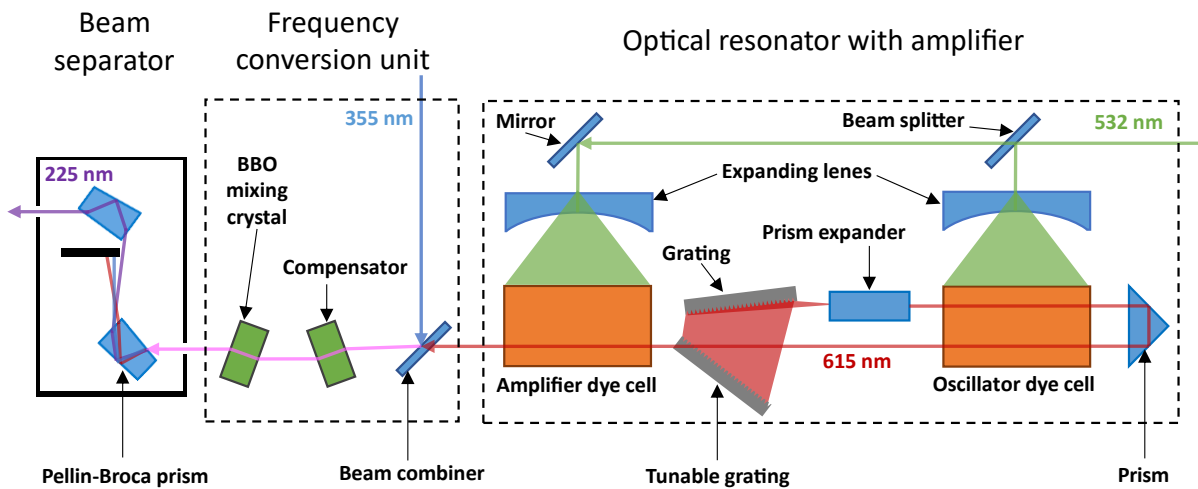


Figure 42: Scheme of the optical setup of the dye laser used in this work (Radiant Dyes NarrowScan D-R).

The dye laser used for the NO-LIF setup was the NarrowScan D-R (Radiant Dyes Laser Accessories GmbH). A scheme of the optical setup is given in Figure 42. The dye cells of the dye laser were pumped by the second harmonic of a Nd:YAG laser at 532 nm. In the resonator unit the beam was split into two and expanded via negative lenses to excite the dye solutions in the oscillator dye cell (~5 % of initial laser-beam energy) and in the amplifier cell (~70 %). The remaining 25 % of the initial laser-beam energy were reflection losses. The dye solutions (DCM in ethanol, peak fluorescence efficiency at 627 nm) were temperature controlled and circulated by pumps to prevent dye degradation. The dye concentration for the oscillator cell was 340 mg/l and for the amplifier cell 113.3 mg/l. In the oscillator cell laser light in the wavelength range between 602–660 nm was generated and amplified in the amplifier cell. A grating was mounted to the resonator to tune the laser wavelength. In the frequency conversion unit (FCU) the resulting laser beam in the wavelength range of 602–660 nm was superimposed with the third harmonic of the Nd:YAG laser (355 nm) and converted (sum-frequency mixing) by the BBO crystal (barium borate, β -BaB₂O₄, thermally not stabilized) to laser light in the wavelength range of 223–231 nm. For the NO-LIF measurements in this work a laser-beam wavelength of ~225 nm was desired (cf. section 6.1). The optical axis of the BBO crystal needed to be adjusted with respect to its cut angle and the laser beam wavelength generated in the resonator to enable sum-frequency mixing. A compensator was installed and turned by

a step motor to the negative angle of the BBO crystal to compensate for beam steering effects. The dye-laser wavelength was determined by the grating position in the resonator which was controlled by software (NarrowScan laser control, Radiant Dyes GmbH, version Rev. ATMega 3.9 2014). The step motors of the BBO crystal and the compensator needed to be driven synchronously with the resonator-grating position to maximize the conversion efficiency. BBO crystal and compensator were turned in opposite direction. A calibration curve (look-up table) was manually defined by iteratively adjusting the FCU motor position at each emission wavelength to obtain the optimized dye-laser energy output. The look-up table provided the step-motor position of the BBO crystal connected to the corresponding resonator wavelength and was referenced by the software during the NO-LIF scans. In the dye laser system used, the BBO crystal was thermally not stabilized what can cause detuning of the frequency conversion unit. After the laser beam left the frequency conversion unit it was wavelength separated from residual laser beams by two Pellin-Broca prisms. With this dye laser configuration, a laser-wavelength range between 223–231 nm can be generated. The dye-laser offset was determined as 14 cm^{-1} by the comparison of measured and simulated NO-excitation spectra. The dye laser linewidth is given by the manufacturer as $\leq 0.04\text{ cm}^{-1}$, typically 0.02 cm^{-1} HWHM. The FWHM of the laser-pulse length was measured as $\sim 20\text{ ns}$ from scattered light with an oscilloscope (Le Croy, waverunner LT342 500 MHz DSO). A consistently constant laser-pulse energy of up to 0.4 mJ per pulse was achieved reliably.

6.2.2 Measurement setup

The pilot scale spray burners investigated in this study were described in detail in sections 3.3 and 3.4. They were operated in a stainless-steel reactor housing with a diameter of 500 mm and a height of ca. 2 m. The reactor was located on the first level of the pilot plant, to enable the accessibility to the burner and its conduit system from beneath. Reactor and filter system were designed for large-scale nanoparticle production of up to 1 kg/h. It was developed and built by HSW Materials GmbH (Kamp-Lintfort, Germany). The setup was controlled via a SPS software (Siemens Simatic S7-1500) and operated by Martin Underberg from the IUTA. An air coflow in the range of 1200 kg/h surrounding the burner was guided through the reactor to quench the combustion gas and carry the nanoparticles to the filter system for product separation. The vacuum to move the exhaust gas was generated by a radial fan (Siemens AG). Typically, the pressure in the reactor chamber was approximately 20 mbar below ambient pressure. The spray flame was optically accessible via four UV-transparent quartz windows (Herasil, diameter: 160 mm).

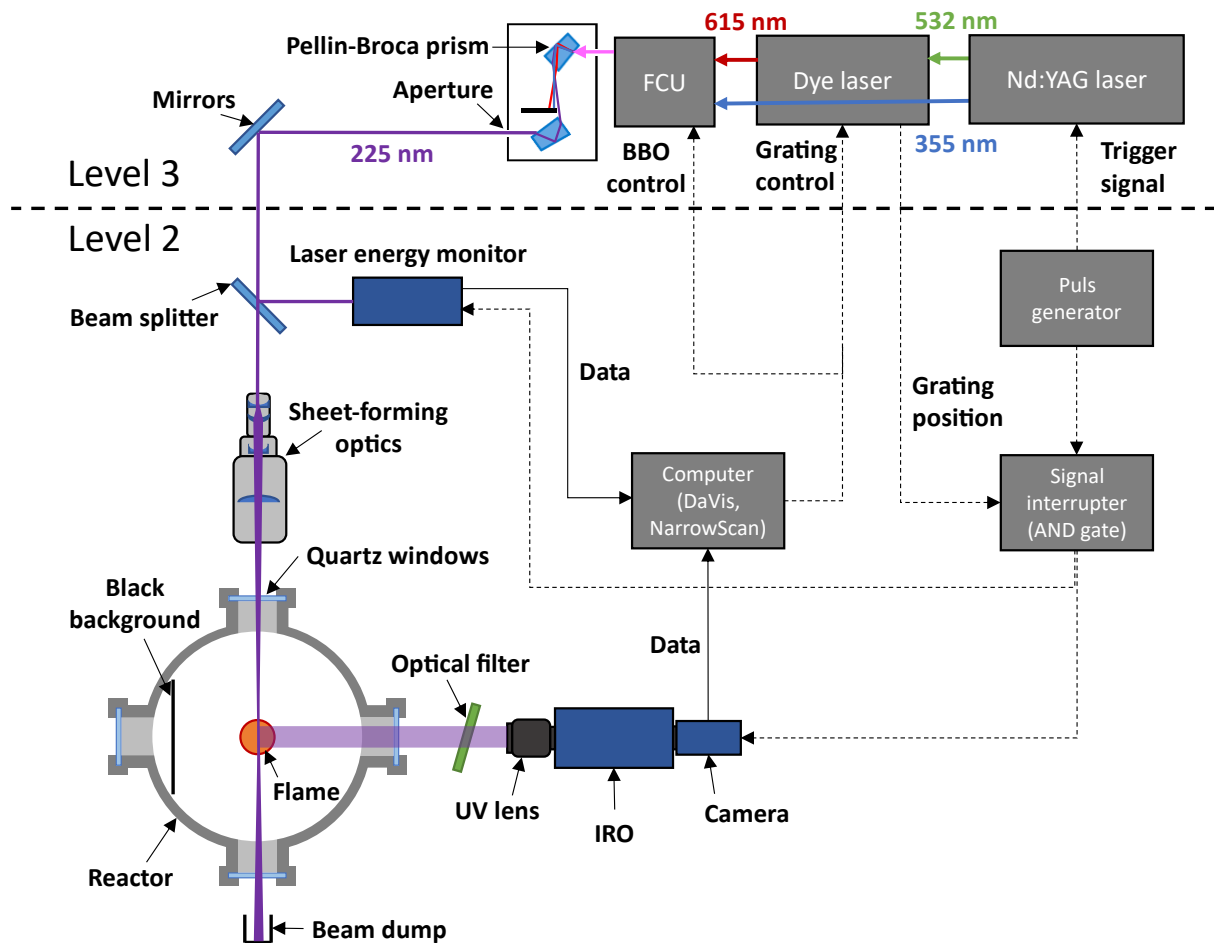


Figure 43: Multi-line NO-LIF measurement setup with simplified signal routing, the dashed arrows indicate triggering signals and solid arrows data transfer, FCU: Frequency conversion unit. A detailed list of the components used is given in the appendix 12.5.1, Table A2. The horizontal dashed line indicates the separation of the equipment across two floor levels of the reactor facility.

Figure 43 shows the experimental setup for temperature imaging in the pilot-scale spray flames with multi-line NO-LIF thermometry. Due to space limitations in the pilot plant and heat emission of the reactor, the laser system and the reactor were located on different floor levels. The horizontal dashed black line indicates where the beam transfer from floor level 3 to 2 of the synthesis facility took place. The tunable dye laser (Radiant Dyes NarrowScan D-R) was pumped with the second harmonic laser beam ($\lambda = 532$ nm, laser pulse energy: 180 mJ) of the flashlamp-pumped Nd:YAG laser (Continuum, Powerlite Precision II Scientific, Model PL8010 S/N 6800) at a repetition rate of 10 Hz. The fundamental dye-laser wavelength at ~ 615 nm was then sum-frequency mixed with the third harmonic ($\lambda = 355$ nm, laser pulse energy: 60 mJ) of the Nd:YAG laser to generate a tunable laser beam at ~ 225 nm. The resulting dye-laser UV beam was guided via three mirrors a distance of ca. 6.5 m from the second Pellin-Broca Prism to the beam splitter of the laser-energy monitor located on the lower level. The laser-energy monitor (LaVision VZ09-0530) operated at the gain level 'low' was controlled by the software Davis (LaVision, version 8.4.0) to record the energy for each laser pulse. The energy value was saved to each image for the laser-energy correction during post processing. About 90 % of the laser-beam energy was transmitted by the beam splitter and formed by sheet-forming optics (LaVision, Sheet Optics (divergent), Collimator Optics UV, VZ09-0537) into a vertical laser sheet (about 90 mm high and 1 mm thick). The laser sheet was guided through the UV-

transmissive quartz window of the reactor housing to the center of the flame. NO molecules in the flow field were excited by the crossing laser sheet and the resulting fluorescence was recorded perpendicular to it. The resulting NO-LIF intensity was several orders of magnitude lower than the laser-excitation intensity. Depending on the background signal at the operating condition of the flame, a custom-made optical longpass filter (Optics workshop, University of Duisburg-Essen) or a dielectric-reflection bandpass filter were utilized to block elastically scattered laser light. After the NO-LIF light passed the optical filter, it was collected by a UV lens (LaVision, $f = 85$ mm, $f_{\#} = 2.8$, VZ20-0620) and imaged on the screen of an intensified relay optics (LaVision, IRO, VC09-0228). The IRO was a vacuum tube with relay optics and a gateable image intensifier to amplify incoming light in a wavelength range between 180 nm and the near IR (conversion efficiency ~ 1 % at 800 nm). The collected fluorescence light was amplified and then detected by the CCD camera (LaVision Imager Intense, VC09-0231, sensor: 1376×1040 pixel). In this arrangement, the Berlin burner (cf. section 3.3) was imaged in an area of $\sim 84 \times 63$ mm² in the center of the flame right above the burner outlet. The CCD chip had a pixel size of 6.45 μm which resulted in a projected imaged region of 61×61 μm^2 per pixel. IRO and camera were controlled by Davis software (LaVision). To reduce stray light, a black background was installed inside the reactor in the camera's field of view.

The measurement setup was clocked by a pulse generator (Stanford Research Systems Inc., Four Channel Digital Delay/Pulse generator Model DG535). Flash lamp and Q-switch of the Nd:YAG laser were triggered continuously to generate a laser pulse at 10 Hz, while during a NO-LIF scan, the custom-made signal interrupter (equivalent to an AND gate) blocked the trigger signal for the camera and the laser-energy monitor when the dye laser was moving the resonator grating to the next wavelength position. When the grating was in position for the next wavelength step the camera and laser-energy monitor were triggered at 10 Hz for further image recording. Grating position and angle of the BBO crystal were controlled by the software "NarrowScan Laser control" using a previously generated look-up table. The LIF-signal images were stored directly after recording by the software DaVis on a local hard drive of the computer and the related laser-energy values detected by the laser-energy monitor were saved to the meta data of the images.

Figure 44 shows smoothed NO-LIF emission spectra simulated by LIFSim [295] at various temperatures and the filter-transmission curves of the optical filters which were used to block scattering laser light. Boundary conditions for the LIFSim simulation: Pressure: 1 bar, excitation wavelength: 225.12 nm, gas phase composition: 1000 ppm NO, 79.9 % N₂ and 20 % O₂. The transmission curve of the bandpass filter (dielectric reflection filter with 4 mirrors) was measured with the UV/VIS-absorption spectrometer described in section 7.2.2 and the transmission curve of the custom-made longpass filter was provided by the manufacturer. The transmission curve of the longpass filter is shown for an angle of 20°. When the angle is increased, the edge shifts to smaller wavelengths. An angle of 20° is ideal to block scattering light from the laser and maximize the NO-LIF transmission.

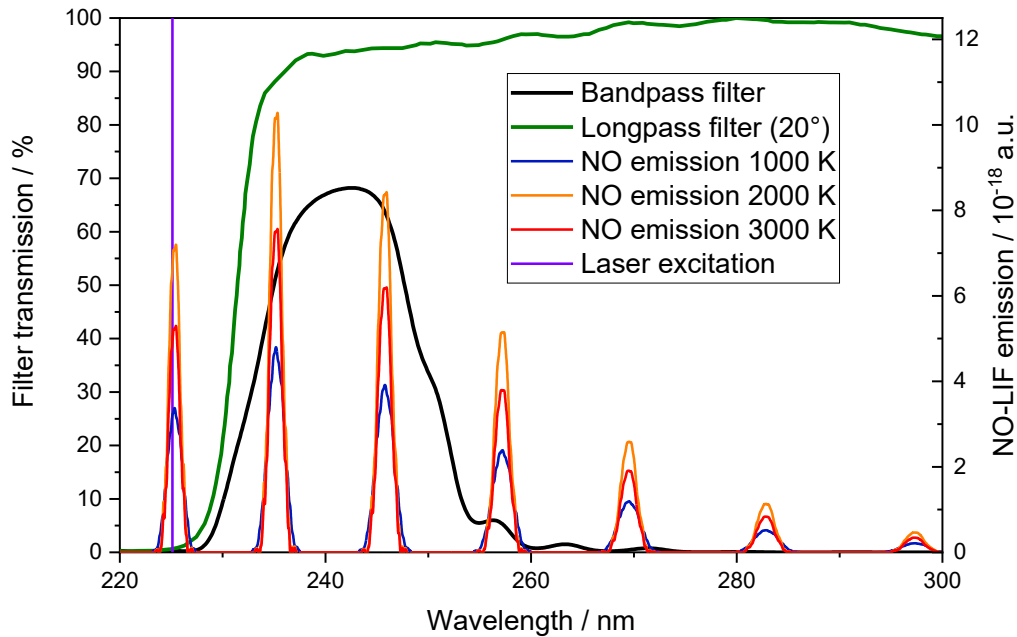


Figure 44: Simulated NO-LIF emission spectrum (LIFSim) at various temperatures, longpass-filter transmission curve (angle: 20°) and bandpass-filter transmission curve (four-mirror filter), the NO-excitation wavelength is indicated as a purple line.

The longpass filter was used when a low flame luminescence was present (e.g., hydrogen flames and the solvent ethanol). This optical filter enables a higher transmission of NO-LIF fluorescence over all bands than the bandpass filter (Figure 44). The bandpass filter was used for operating conditions with strong spontaneous flame luminosity that needed to be suppressed (e.g., when operated with 65EHA35EtOH).

6.3 Measurement procedure

Due to the high turbulence of these flames, especially when operated with hydrogen, it was necessary to record a large number of images to compensate for NO-concentration and gas-temperature fluctuations. In this turbulent environment, the averaged NO-LIF signal images per wavelength step consist of many superimposed NO-excitation spectra from different local flame conditions in time. At a fixed measurement volume, NO concentration and gas temperature are volatile and thus cause a systematic error which is discussed in section 6.3.2. This error is a result of averaging the LIF signal from varying temperatures and varying NO concentrations before deriving the temperature. Due to practical limitations, it was not possible to add NO to both pilot gas and dispersion gas. Because better mixing with the surrounding gas was expected, NO was added to the dispersion gas flow. To compensate for the resulting fluctuations in the turbulent flame and to obtain homogenous average NO-LIF signal, 160 images were recorded per wavelength position in four separate NO-LIF scans. Additionally, 4000 background images were recorded and averaged for background correction. The LIF images were background corrected and then corrected for laser pulse energy.

Due to space limitations for the optical setup at the reactor window, the laser sheet could not be expanded to cover the whole imaged area within the flame with sufficient laser energy. Within the limited space, a laser sheet with an adequate intensity distribution could not be obtained by the LaVision sheet-forming optics. Therefore, the position of the laser sheet was shifted step by step in vertical direction to cover the full imaged area. Figure 45 shows the

laser-sheet intensity profiles where the intensity centroid is located at different height above the burner. The profiles were recorded in a UV-transmissive cuvette filled with a solution of DCM in ethanol ($c_{\text{mass}} = 1.5 \text{ mg/l}$). It is evident that achieving adequate laser irradiance across the entire area of interest was not feasible with a single laser-sheet position. To compensate for this inhomogeneous laser-intensity distribution the laser sheet centroid was varied in vertical direction over four height positions to cover the full height with sufficient signal and increase the signal-to-noise ratio. The resulting overall laser-sheet intensity distribution is shown in red.

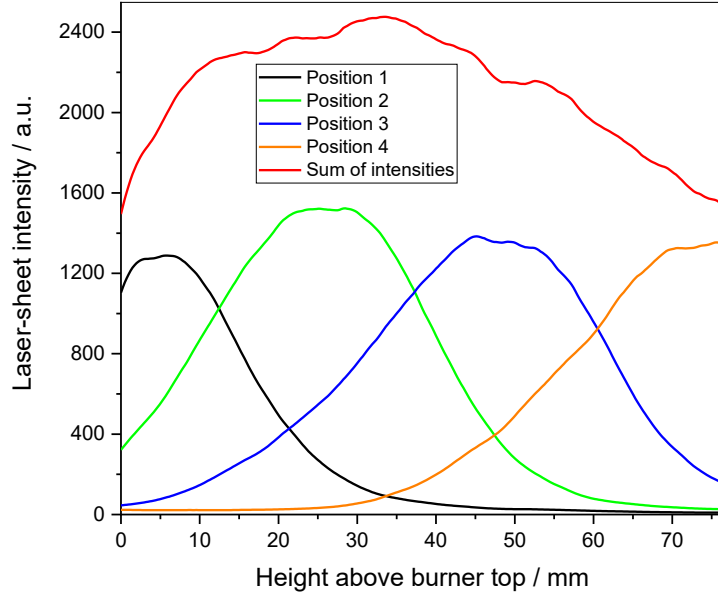


Figure 45: Averaged laser-sheet energy profiles recorded in a cuvette with 1.5 mg/l DCM in ethanol, four positions of laser-intensity centroid and the resulting sum of laser intensities.

Before measurements were performed the Nd:YAG crystals were manually adjusted to maximize the laser-energy output. The optimal angles of the BBO crystal and the related compensator were manually determined by adjusting the stepper-motor position while observing the laser-energy output with an oscilloscope. The resonator wavelength and the corresponding stepper-motor positions were saved to a look-up table which was referenced during the NO-LIF scans.

According to literature (cf. section 6.1) the NO excitation spectra were scanned in the spectral range between $44,407.5$ and $44,417.6 \text{ cm}^{-1}$ ($225.187\text{--}225.136 \text{ nm}$). With a fixed excitation-wavelength step-width of 0.05 cm^{-1} , this resulted in 203 wavelength positions. The laser was operated at 10 Hz with a laser-pulse energy in the range of 0.2–0.4 mJ (measured with a Coherent FieldMaxII-TOP Laser Power and Energy Meter, equipped with the energy head: Coherent EnergyMax 1110743, J-25MB-LE, $25\mu\text{J}\text{--}50\text{mJ}$) resulting in a maximum laser fluence of $F = \sim 1.06 \text{ mJ/cm}^2$ (at the peak of the laser-energy profiles, Figure 45). From previous work it is known that for this excitation energy the excitation of NO is in the linear regime [278, 291, 293]. Higher laser-pulse energies would have been beneficial to improve the NO-LIF results, but could not be achieved by the available dye laser system. For comparison: Bessler and Schulz [278] applied laser-pulse energies of 1–1.5 mJ in Bunsen flames and Hecht et al. [293] applied 10 mJ in a low-pressure plasma reactor. NO-LIF images were recorded at 10 Hz with an intensifier gate of 50 ns. For each operating condition, four scans were performed with different fixed laser-sheet positions equally spaced from each other (Figure 45). For post-processing, per wavelength step, 160 images from four NO-LIF scans were merged, resulting in

a total measurement time of 54 min per operating condition. Recorded images were locally stored by the software DaVis on a hard disk as .im7 files containing the related energy-monitor value for postprocessing.

6.3.1 Post-processing with LIFSim

Postprocessing was done with a preliminary version of the latest release of LIFSim 4.0 developed by El Moussawi et al. [343]. LIFSim was introduced by Bessler et al. in 2004 [295] and was continuously optimized and extended. There is also an online version of LIFSim available via Ref. [344]. The calculations of LIFSim are based on the three-level linear LIF model. The new open-source code for multi-line LIF is implemented in Matlab and can model LIF absorption, excitation and emission spectra for various molecules (e.g., NO, OH, SiO, O₂). The spectral modelling is based on experimentally-validated molecule-specific spectroscopic data [287, 296, 302], e.g., from the high-resolution transmission molecular absorption database (HITRAN) [345]. For the multi-line technique, gas temperature is determined by fitting measured excitation spectra with simulated excitation spectra, using temperature as the main fitting parameter. The spectral modeling of LIFSim considers, among others, superposition of overlapping absorption transitions, Doppler and collisional line broadening, line shifting, laser line width, collisional quenching, and spectral offsets. In the routine, the spectral baseline is subtracted, which filters the excitation spectra from, e.g., broadband radiation, and makes the approach insensitive to background signal. The newest version (made available after the study presented in this chapter was completed) also includes a 'temperature fluctuation feature' to assess flame and thus LIF signal fluctuations and its impact on the measurement error (cf. Ref. [346]).

For the determination of the gas temperature maps, the raw LIF images and background images were imported by LIFSim 4.0 and the background correction and laser-energy correction done. Next, the averaged LIF images per wavelength step were binned by a factor of three and then for each pixel the excitation spectra extracted for further processing. Fitting was done with the standard parameters for fit tolerance and boundaries. Gas-phase temperature maps obtained from LIFSim were slightly smoothed by a self-created Matlab code. The temperature value of each pixel was averaged with the eight adjacent pixels.

6.3.2 Measurement error

NO-LIF multi-line thermometry provides mean temperatures that can be affected by a bias that depends on the width of the temperature distribution at the specific measurement position during the laser scan. This is related to the fact that the measured LIF intensities do not linearly depend on temperature and the effect of this nonlinearity becomes increasingly important with increasing distribution widths. Feroughi et al. [346] performed an analysis based on numerical studies to assess the effect of temperature and NO concentration fluctuations on the derived mean temperature values. For a similar pilot-plant flame reactor, the study determined a maximum measurement error of less than ± 2 % at the core of a turbulent pilot-scale jet flame ($Re = 8300$), and up to ± 6 % in the outer regions of the flame. This study showed that multi-line NO-LIF thermometry underpredicts gas temperatures that are higher than 900 K, when temperature or NO-concentration fluctuations are present. The magnitude of this measurement error depends mainly on the local temperature distribution over time which is affected by the flame turbulence.

For the measurements with the solvent ethanol a longpass filter (Figure 44) was used to maximize the detectable NO-LIF signal and for the measurement with the solvent 65EHA35EtOH a bandpass filter was used (Figure 44) to block the strong blackbody radiation. While masking for the longpass filter was only possible based on the total background-corrected NO-LIF signal, another masking approach based on the relative standard deviation of the NO-LIF signal was feasible when using the bandpass filter, because it almost exclusively transmits NO-LIF signal. Flame regions with especially strong signal fluctuations that can lead to increased bias are analyzed and masked in Figure 58. For this analysis, the relative standard deviation of the NO-LIF signal (transition at $44,411.2 \text{ cm}^{-1}$) was calculated for each pixel and all regions of the flame. The flame regions where the standard deviation exceeds a threshold value of 0.8 are marked as uncertain and, e.g., excluded from the comparison with simulation results [183]. For a relative standard deviation of the NO-LIF signal in the same magnitude, Feroughi et al. [346] estimated a measurement error of $\pm 6 \%$ for a monomodal temperature distribution.

An increased temperature bias would occur (i) in case of the presence of areas where surrounding gas (cool and without NO) is entrained, and (ii) in case of substantial signal from thermal NO. This problem was avoided by only analyzing regions with stable LIF signal (see the above-mentioned masking strategy based on the total NO-LIF signal and the standard deviation analysis). In this region, there are no areas with zero signal. Also, on a global scale, the signal provided by thermal NO is negligible. Measurements without NO seeding showed that small amounts of evenly distributed NO are formed thermally in the flame. When the solvent mixture of EHA and ethanol (65EHA35EtOH) was used, the signal from seeded NO was five times stronger than thermally generated NO. A significant measurement error introduced by thermally formed NO is not expected since regions with strong NO-signal fluctuations were not considered.

Additional considerations for measurement errors of multi-line NO-LIF thermometry have been pointed out and analyzed in the literature. The most relevant ones are summarized below.

Yorozu et al. [277] stated in the context of laminar flames that the measurement error of multi-line NO LIF is lower than for two-line LIF. For a premixed stable butane/O₂ flame with gas temperatures between 500 and 1800 K, they calculated a measurement error of 80 K.

Bessler and Schulz [278] performed for two conditions (1 bar, 500 K and 1 bar, 2000 K) a computational study on the sensitivity and accuracy of the multi-line NO-LIF technique for various scanning ranges within a large wavenumber spectrum of $44,000\text{--}44,600 \text{ cm}^{-1}$. Based on this investigation they proposed the spectral scan range for NO-LIF thermometry used in this work, where the measurement error introduced by noise is minimized. For a Bunsen flame with a temperature of $\sim 2200 \text{ K}$, they specified the measurement accuracy to $<10 \%$. Further details of this study are given in Ref. [299].

Kronemayer et al. [279] compared the measurement error of multi-line NO-LIF in a spray flame, when increasing the number of recorded LIF shots by a factor of ten. For fixed flame and measurement conditions, the measurement precision of the gas temperature improved from 4 % to 2 %. They concluded that the signal-to-noise ratio of the measured NO excitation spectra affects the measurement error. Moreover, based on the comparison to thermocouple measurements, for a heated nitrogen flow with a maximum temperature of 350 K, the measurement error was determined to less than 1 %. More details of this study are given in Ref. [347].

An assessment of the systematic measurement error originating from averaging the NO-LIF signal of areas with temperature fluctuations was made by Düwel et al. [281]. Based on model calculations, they determined a systematic measurement error of 2 % for an evenly distributed temperature between 1200–1800 K, and 3 % for the range between 300–1500 K.

6.3.3 Operating conditions

Table 3 and Table 4 show the operating conditions (OC) of the ‘Berlin burner’ (BB, section 3.3) and the ‘HSW burner’ (HSWB, section 3.4). The Berlin burner was designed to be operated with sustainable fuels which can be easily produced by renewable energies (e.g., H₂ and ethanol). Moreover, H₂O as carbon-free precursor solvent and the addition of ammonium nitrate as additional source of oxygen and for increasing the reaction enthalpy was investigated (section 6.4.1.5). More details on volume and mass flows are given in the appendix (section 12.5.2).

In the table the NO concentration and oxygen stoichiometry is given neglecting the surrounding air coflow. Due to safety reasons in the pilot plant, a diluted gas mixture of 10 % NO in argon was added to the dispersion gas flow of the pilot-scale burners, resulting for the BB in an average NO concentration in the range of 348–596 ppm within the flow of the dispersion and pilot gas (Table 3, column 4). The NO concentration for the HSWB was significantly higher in the range between 4850–5945 ppm (Table 4, column 4). The application of a higher NO concentration was necessary because of NO loss due to the larger equivalence ratio (section 6.3.3.1) and to increase the NO-LIF signal. This became necessary because for the measurements in the HSWB flame operated with EHA the four-mirror filter was used to block blackbody radiation. For this filter, the transmissivity for NO fluorescence is significantly lower than for the longpass filter.

For the optimal operation of the two-fluid nozzle at the chosen liquid flow rate of 3 kg/h, an ideal dispersion gas flow rate of 3 kg/h was determined, based on the conversion efficiency of kinetic energy from the dispersion gas to the surface of atomized liquid [348]. The used ethanol flow rate of 3.8 l/h corresponds to a mass flow of 3 kg/h. The solvent, the pilot-flame fuel gas, the volume flow, and the type of dispersion gas were varied to study the impact of the gas temperature on the properties of the produced nanoparticles. NO-LIF thermometry was done in flames without particle synthesis, since it facilitates the measurements (e.g., signal maximization with longpass filter, prevention of window fouling, avoidance of the disturbing iron peak located within the NO-LIF spectrum [122]). The impact of the precursor concentration of 0.3 mol/l iron nitrate nonahydrate on the flame temperature is known to be not measurable [309, 349]. Additional details for the fuel gases and solvents used, such as the enthalpy of combustion, can be found in Table A1.

Identifiers for the operating conditions were created according to the following scheme:

- Pilot scale spray burners: Berlin burner (BB), HSW burner (HSWB)
- Solvent: Ethanol (E), water (W), mixture by volume of 65 % 2-ethylhexanoic acid and 35 % ethanol (MEHA), solution of ammonium nitrate in water (AN)
- Fuel gas: Hydrogen (Hy), methane (Me)
- Dispersion gas: Air (Air), oxygen (Ox), hydrogen (Hy)
- Dispersion gas mass flow in kg/h.

Table 3: Operating conditions of the pilot-scale flame (Berlin burner). Pre-heater temperature: 227 °C, heat ring temperature: 700 °C, coflow: 1200 kg/h air, tracer gas: 10 % NO in argon, calculated NO concentration in fresh pilot and dispersion gas, the stoichiometry is calculated without consideration of O₂ from the sheath gas, the volume flow unit slm is based on a reference condition at 0 °C. The dispersion gas mass flow includes, in addition to the oxidizer, 0.55 kg/h of the tracer gas mixture. More detail is given in the appendix (section 12.5.2, Table A3). The empty sections in the table correspond to the numbers provided above.

Solvent: 3.8 l/h ethanol

OC identifier	Pilot flame		Dispersion gas		NO / ppm	Equivalence ratio ϕ / -
	Fuel gas / slm	Oxidant / kg/h	Oxidant / kg/h	NO-tracer gas / slm		
BB-E-Hy-Air2	H ₂ / 108	Air / 100	Air / 2	5	355	0.46
BB-E-Hy-Air3			Air / 3		352	0.46
BB-E-Hy-Air4			Air / 4		348	0.46
BB-E-Hy-Ox2			O ₂ / 2		355	0.44
BB-E-Hy-Ox3			O ₂ / 3		352	0.43
BB-E-Hy-Ox4			O ₂ / 4		349	0.41
BB-E-Me-Air3	CH ₄ / 39.1	Air / 60	Air / 3		594	0.90
BB-E-Me-Ox3			O ₂ / 3		596	0.79

Solvent: 3 l/h water

BB-W-Hy-Hy	H ₂ / 108	Air / 100	H ₂ / 0.22		350	0.28
------------	----------------------	-----------	-----------------------	--	-----	------

Solvent: 3 l/h of 111 g/l ammonium nitrate in water

BB-AN-Hy-Hy	H ₂ / 108	Air / 100	H ₂ / 0.22		350	0.28
-------------	----------------------	-----------	-----------------------	--	-----	------

Table 4: Operating conditions (HSW burner). Coflow: 1200 kg/h air, calculated NO concentration in pilot and dispersion gas. Definitions of the columns according to the caption of Table 3. The empty sections in the table correspond to the numbers provided above.

Solvent: 3.8 l/h ethanol

OC identifier	Pilot flame		Dispersion gas		NO / ppm	Equivalence ratio ϕ / -
	Fuel gas / slm	Oxidant / slm	Oxidant / slm	NO-tracer gas / slm		
HSWB-E-Me-Ox61	CH ₄ / 7.5	O ₂ / 15	O ₂ / 56.6	5	5945	1.23
HSWB-E-Me-Ox73			O ₂ / 68.6		5203	1.05
HSWB-E-Me-Ox80			O ₂ / 75.6		4850	0.97
HSWB-E-Me-Air80			Air / 75.6		4886	2.86

Solvent: 3.8 l/h 65 % EHA – 35 % ethanol

HSWB-MEHA-Me-Ox73	CH ₄ / 7.5	O ₂ / 15	O ₂ / 68.6	5	5203	1.25
-------------------	-----------------------	---------------------	-----------------------	---	------	------

6.3.3.1 NO concentration

Low NO concentrations of several hundred up to a few thousand ppm are expected to not influence the flame chemistry of lean flames. In rich flames, however, removal of NO ('NO reburn') is expected [350]. Formation of NO₂ is not expected at flame temperatures. Schulz et al. [350-352] measured the NO-concentration reduction between the intake and the exhaust of a spark-ignition engine fueled with propane/air. They reported for the lean flame (equivalence ratio, $\phi = 0.91$) a NO reduction of 10 % when the fuel was seeded with 500 or 1000 ppm NO. For fuel-rich conditions (equivalence ratio, $\phi = 1.25$) a reduction of the NO concentration by 40 % was measured. The NO reduction was largely independent of the NO concentration seeded. It is anticipated that due to the higher oxygen excess within the BB flames investigated (for equivalence ratios see Table 3, varying in the range of $\phi = 0.28$ – 0.9) the NO-concentration reduction is lower than the aforementioned 10 %. For the HSW burner with significantly higher stoichiometry (between $\phi = 0.97$ and 2.86) higher NO concentration have been applied to compensate for NO losses and to increase the NO-LIF signal. In the present experiment, in the colorless hydrogen pilot flame of the Berlin burner, brownish flame color became visible with increasing height above burner that is not yet identified.

6.4 Results

The average gas-temperature maps of the Berlin burner and the HSW burner measured by multi-line NO-LIF thermometry are presented and analyzed in this section. The spatial diagram axes are plotted with their real spatial size ratios. If not otherwise noted, masking was done with the LIFSim 4.0 code, which masks all pixels white that feature NO-LIF signal lower than a defined threshold of 10 % of the maximum signal to prevent presentation of temperatures with exceeding uncertainty. The aim of the study is to investigate the effect of the operating conditions and the gas temperature on the nanoparticle formation within the flame and thus the nanoparticle characteristics. More details on the rationale for selecting the operating conditions and information about the produced nanoparticles can be found in Ref. [147].

6.4.1 Berlin burner

The Berlin burner (BB) is described in detail in chapter 3.3 and the definition of the operating conditions is given in Table 3. The burner top is defined as height above burner (HAB) = 0 mm (cf. Figure 6).

6.4.1.1 Pilot flames

Figure 46 shows the gas-temperature maps of the BB pilot flames operated with the fuel gas H₂ (left diagram) and the fuel gas CH₄ (right). The operating conditions correspond to BB-E-Hy-Air3 and BB-E-Me-Air3, respectively, but without ethanol injection. The dispersion gas flow of 3 kg/h air was unchanged.

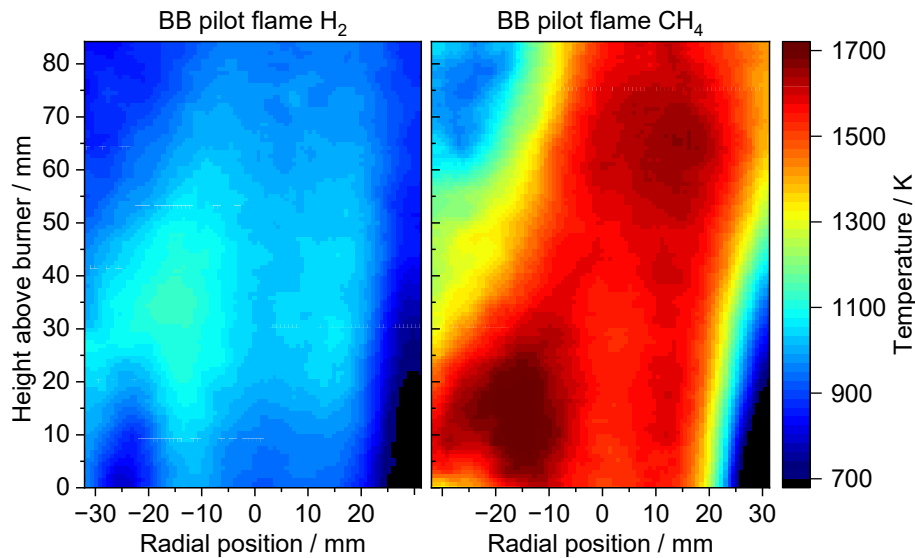


Figure 46: Gas-phase temperature maps measured in the flame of the Berlin burner, pilot flame only, uniform color scale, dispersion gas: 3 kg/h air, different pilot flame fuels, left: H₂, right: CH₄.

The gas temperature of the pilot flame operated with CH₄ is significantly higher than when operated with H₂. This was expected for the pilot flames due to the adapted volume flows and the enthalpy difference of H₂ and CH₄ combustion (Table A1). From the centerline temperature profiles shown in Figure 47 a temperature difference of 500–600 K can be seen across the entire HAB in the field of view. The vertical gas-temperature profiles were extracted at radial position of 0 mm with an extraction width of 14.9 mm (21 pixels). The results indicate that the gas temperature nearly reached its peak at the burner exit (cf. Figure 6), indicating that a significant portion of the pilot fuel gas had already undergone reaction. From the temperature maps it can be seen that the pilot flames are tilted to the right within the field of view. This is attributed to asymmetry of the sheath gas flow within the reactor housing.

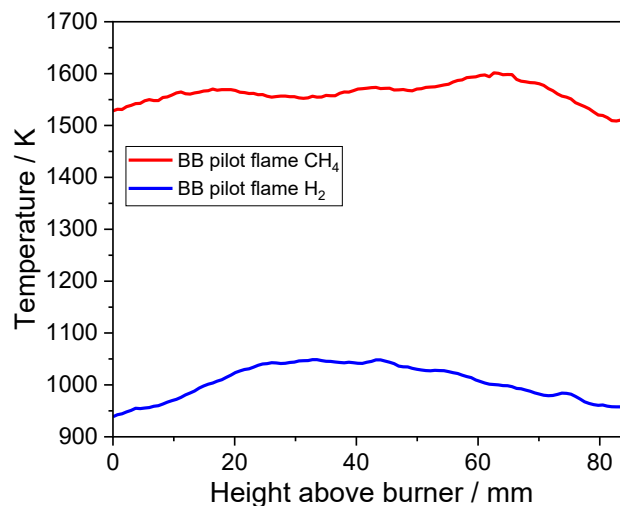


Figure 47: Centerline gas-temperature profiles of the temperature maps shown in Figure 46, extraction width: 14.9 mm, pilot flame fuel: CH₄ and H₂.

6.4.1.2 Variation of dispersion gas (air) flow rates

Figure 48 shows average gas-temperature maps of three operating conditions of the Berlin burner where the mass flow of the dispersion gas air was varied between 2 and 4 kg/h. The

identifiers of the operating conditions are given above the diagrams, respectively. The temperature maps are depicted with a uniform color scale.

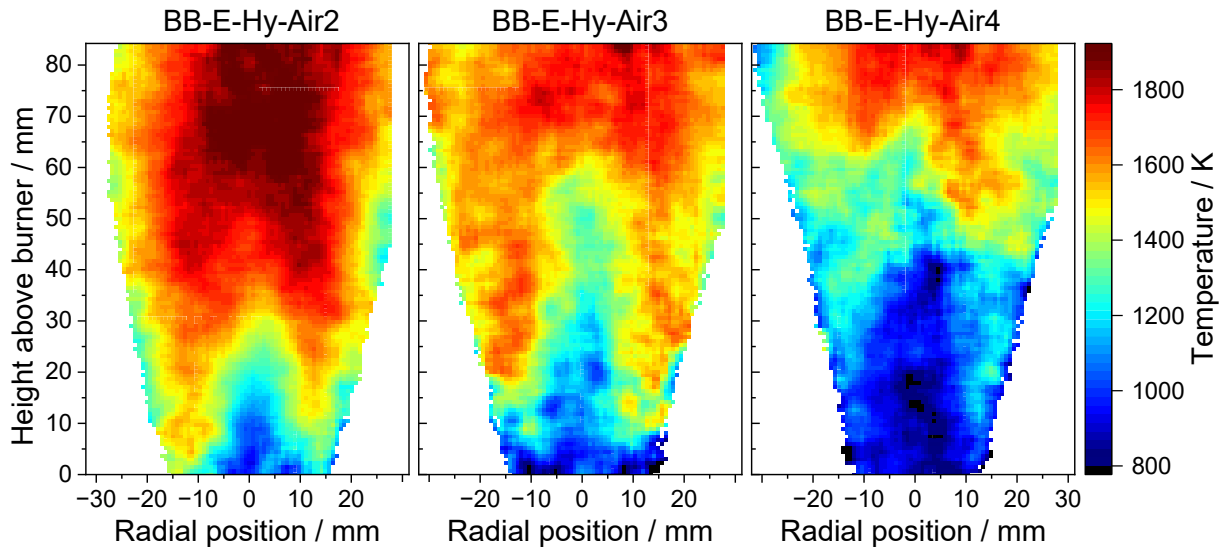


Figure 48: Gas-phase temperature maps measured in the Berlin burner. Solvent: Ethanol, pilot flame fuel: H_2 , dispersion gas: Air, variation of the dispersion gas flow, left: 2 kg/h, center: 3 kg/h, right: 4 kg/h.

With an increasing dispersion gas flow, the cold zone in the lower region of the flame extends and the hot zone moves to larger HAB. This can be explained by the rising feed of cool dispersion gas at a higher velocity and a higher fraction of inert N_2 introduced. The location of combustible mixtures (evaporated ethanol) is shifted to larger HAB. Moreover, the cold zone is generated by evaporative cooling of ethanol. At the upper end of the field of view (HAB = 80 mm), the maximum temperature for all cases is about 1800 K. Figure 49 shows the related centerline profiles of the operating conditions shown in Figure 48. The temperature gradients are largely constant across the HAB and similar for the operating conditions shown. The centerline gas-temperatures appear to converge at larger HAB.

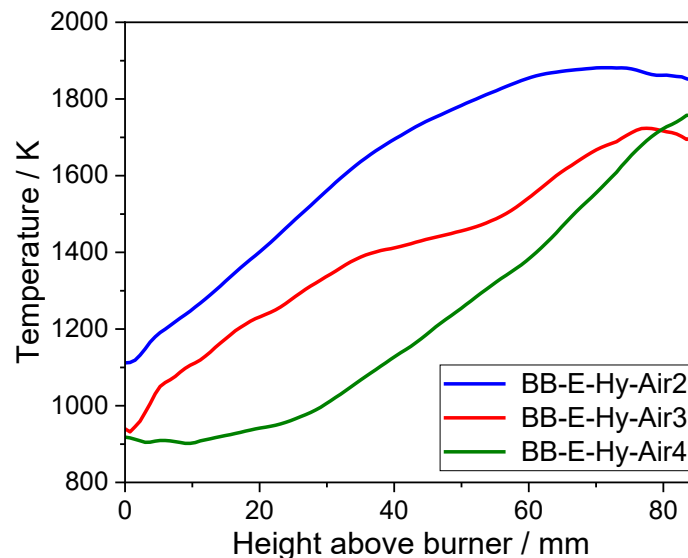


Figure 49: Centerline gas-temperature profiles of the operating conditions shown in Figure 48, extraction width: 14.9 mm, smoothed with a moving average filter with a 30-data-point range, variation of the air dispersion gas flow rate.

6.4.1.3 Variation of dispersion gas (O₂) flow rates

Figure 50 shows the operating condition where the dispersion gas O₂ is varied between 2–4 kg/h. Compared to the operating condition shown in section 6.4.1.2 the gas species of the dispersion gas was changed from air to O₂ with the other conditions being equal.

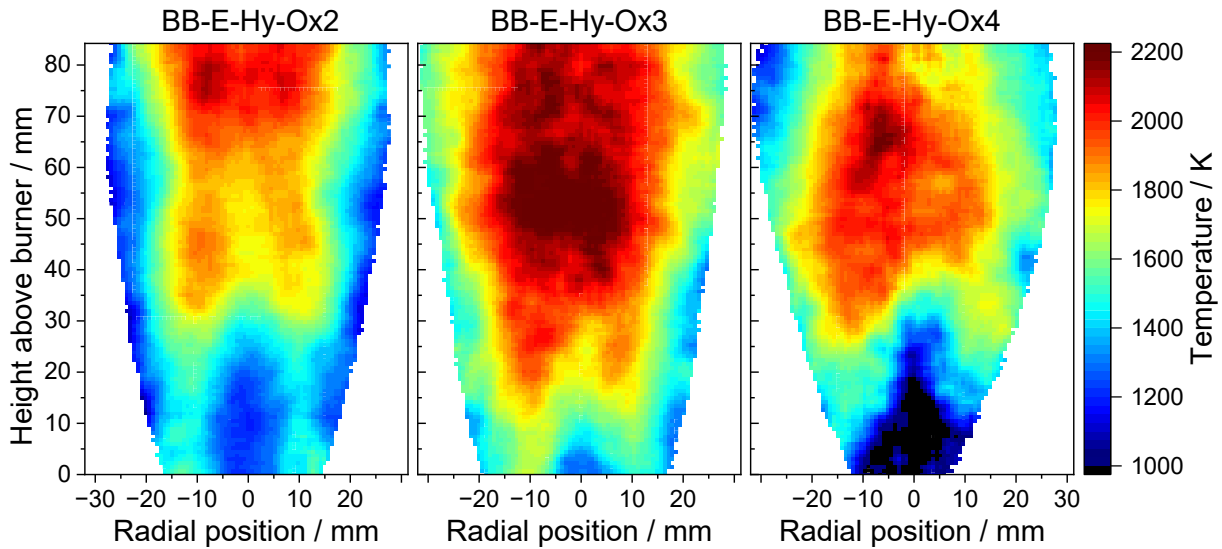


Figure 50: Gas-phase temperature maps of the Berlin burner. Solvent: Ethanol, pilot flame fuel: H₂, dispersion gas: O₂, variation of the dispersion gas flow, left: 2 kg/h, center: 3 kg/h, right: 4 kg/h.

With an increasing O₂ dispersion gas flow no clear trend can be seen for the gas temperature. The highest gas temperature of 2200 K was measured for BB-E-Hy-Ox3. Compared to the other operating conditions, the hot zone is located lower at about HAB = 50 mm. An explanation for this could be, that with a dispersion gas flow of 3 kg/h, the atomization of the ethanol spray is ideal for forming a combustible mixture within the O₂ flow (in line with the calculated conversion efficiency for the spray nozzle [93]). For BB-E-Hy-Ox2 and BB-E-Hy-Ox4 a more extended and cooler cold zone is observed. Overall, the temperature level of the operating conditions with the dispersion gas O₂ is significantly higher than with air. The maximum gas temperature difference is approximately 300 K (BB-E-Hy-Ox3 vs. BB-E-Hy-Air2). The operating conditions with the ideal spray atomization (BB-E-Hy-Ox3 vs. BB-E-Hy-Air3) exhibit a nearly constant temperature difference of 400 K (cf. Figure 53). This can be explained by the large quantity of inert N₂ (78.1 % of the dry air) introduced by the dispersion gas and a lower fraction of O₂ available for reaction. For BB-E-Hy-Ox3 a faster and more efficient burning of the spray is obvious with the hot zone located closer to the burner top. Figure 51 shows the related centerline temperature profiles. The temperature profiles of BB-E-Hy-Ox3 and BB-E-Hy-Ox4 feature a similar shape with a large temperature gradient and a maximum at about HAB = 50 and 60 mm, respectively. The shape of BB-E-Hy-Ox2 is different with a rather constant temperature gradient and a not clearly identified maximum within the field of view. The poorer atomization could cause the slower heat-up.

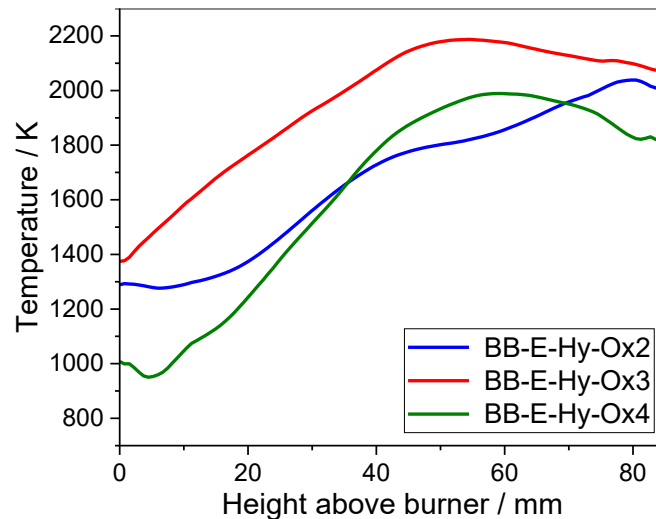


Figure 51: Centerline gas-temperature profiles of the operating conditions shown in Figure 50, extraction width: 14.9 mm, smoothed with a moving average filter with a 30-data-point range, variation of O₂ dispersion gas flow rate.

6.4.1.4 Variation of dispersion and fuel gas composition

Figure 52 shows the gas-temperature maps for four operating conditions on the left and two intensity maps of flame luminescence on the right. The operating conditions of the data shown are generated by different compositions of premixed pilot gas (H₂/air or CH₄/air) and dispersion gas (air or O₂). The ethanol injection rate for spray generation was in all cases 3.8 l/h. The temperature maps are plotted with equal color-scale limits. The flame luminescence images on the right were recorded in the same field of view and are line-of-sight averaged. They are given to facilitate the interpretation of the results by comparing the flame shapes to the temperature maps in the middle (operating condition with CH₄ as pilot flame fuel, BB-E-Me-Ox3 and BB-E-Me-Air3). The artifacts at approximately HAB = 5 mm are caused by reflections in the background. In the left column, the related operating condition with H₂ pilot flames (already shown above) are given to facilitate the direct comparison to that with CH₄ pilot flames.

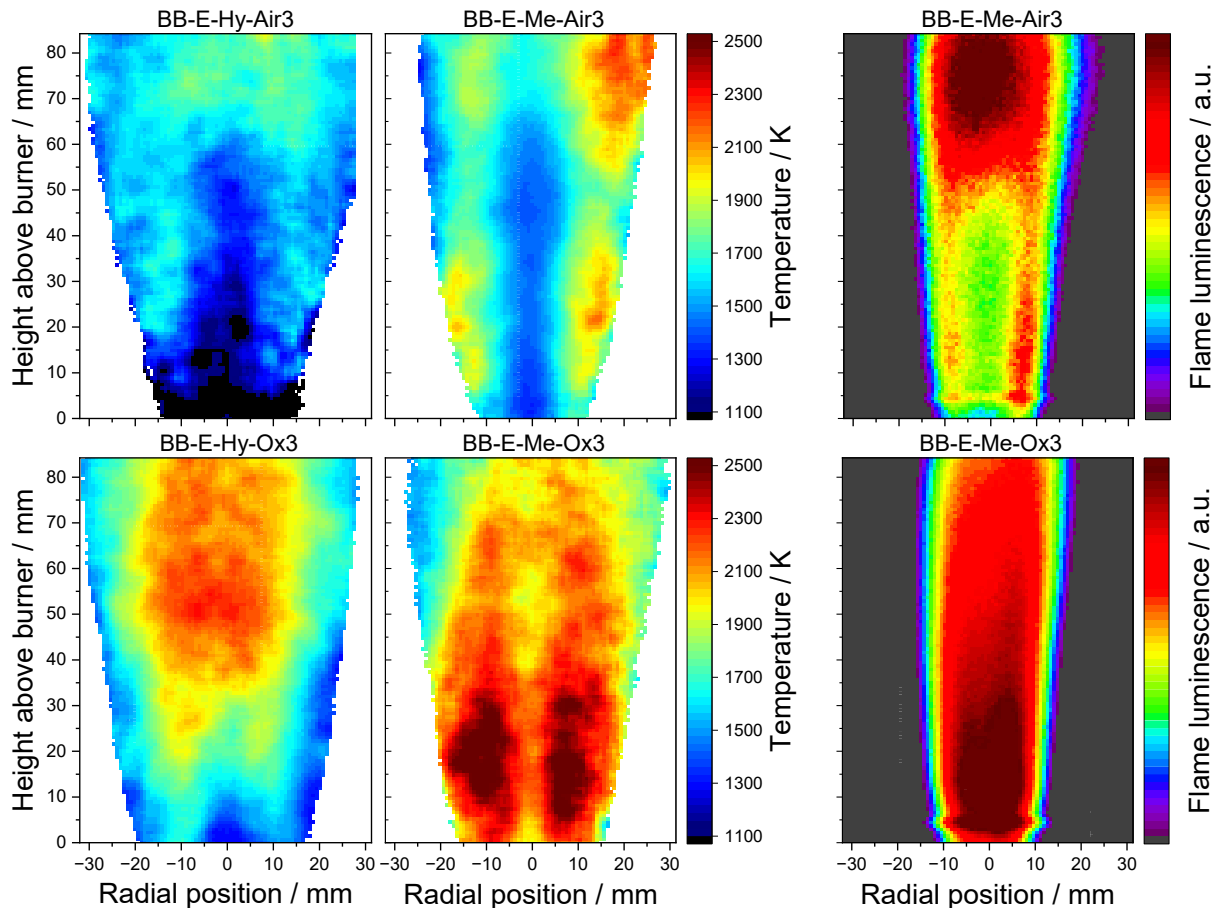


Figure 52: Gas-phase temperature maps measured in the Berlin burner. Solvent: Ethanol, fixed dispersion gas flow rate of 3 kg/h, pilot-flame fuel of left column: H_2 , center: CH_4 , right: Flame luminescence intensity maps of the operating condition shown in the middle column. Dispersion gas of upper row: Air, lower row: O_2 .

The results show that the gas temperature and its distribution across the flame strongly depends on the pilot and dispersion gas compositions and their combination. It can be generally stated that the use of CH_4 as pilot gas increases the gas temperature compared to H_2 . Compared with air, the use of O_2 as dispersion gas increases the overall gas temperature and moves the flame region with the highest gas temperature to lower HAB. BB-E-Me-Air3 features an extended cool zone in the center of the flame. The shape of the high-temperature region can be characterized as a hollow cylinder. This structure can also be identified in the line-of-sight averaged flame-luminescence image (Figure 52, top right). A similar, but less pronounced phenomenon can be seen for the CH_4 flame with O_2 as dispersion gas. These characteristics of a less reactive zone in the flame center with a lower heat release can be connected to the dispersion-gas flow, which has not yet mixed with fuel to a combustible gas mixture. This phenomenon is less distinct for H_2 as pilot gas and can be explained by a higher flame turbulence and a higher flame speed in contrast to CH_4 . At BB-E-Me- O_2 3, the hot zone is located in the lower region of the flame and can be connected to the high flame luminescence from the same flame region (Figure 52, bottom right). Here, a correlation between gas temperature and flame luminescence is evident. When O_2 is used as dispersion gas, the maximum gas temperature reaches around 2500 K, what is significantly higher than when air is used as dispersion gas, where the maximum temperature is approximately 2100 K. This difference can be partially attributed to the approximately 13 % higher enthalpy of combustion in the CH_4 pilot flame,

resulting in an overall increase in combustion enthalpy of approximately 9 %. Moreover, the rise in temperature can be linked to the 41.9 % lower volume flow rate of the pilot flame.

Figure 53 shows the corresponding centerline temperature profiles. The operating condition with CH₄ pilot flames feature a faster heat release in the lower range, whereas rather a steady temperature increase is observed for the OC with H₂ pilot flames. For BB-E-Me-Ox3 the hot zone is at about HAB = 15 mm and with increasing HAB the gas temperature decreases. When the pilot flame is operated with H₂ the temperature maximum is shifted further downstream to approximately HAB = 50 mm, with a lower maximum temperature of about 2100 K. When the spray is atomized with air, for both pilot flames, the overall temperature level is significantly reduced. Within the field of view, the gas-temperature profiles of the same pilot flame converge with increasing HAB.

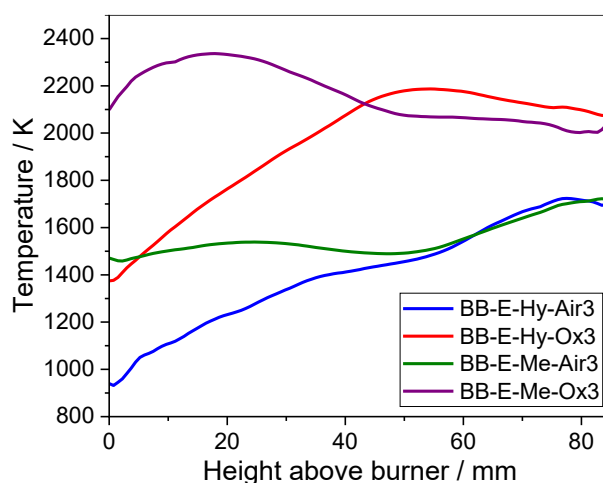


Figure 53: Centerline gas-temperature profiles of the operating conditions shown in Figure 52, extraction width: 14.9 mm, smoothed with a moving average filter with a 30-data-point range, variation of fuel gas and dispersion gas species.

6.4.1.5 Spray: H₂O and ammonium nitrate in H₂O

Figure 54 shows gas-temperature maps of the Berlin burner when operated with a H₂ pilot flame and a H₂O spray. Operation with aqueous solutions in H₂ flames is of interest because it potentially enables CO₂-free nanoparticle production in spray flames. The left temperature map shows the operating condition with a H₂ pilot flame and pure water as precursor solvent atomized by H₂ dispersion gas. For the temperature map on the right, ammonium nitrate was added at a concentration of 10 wt. % to the H₂O spray, to investigate the impact on the flame temperature. By the addition of ammonium nitrate, it was desired and expected to increase the gas temperature by supplying additional enthalpy and oxygen to the combustion process.

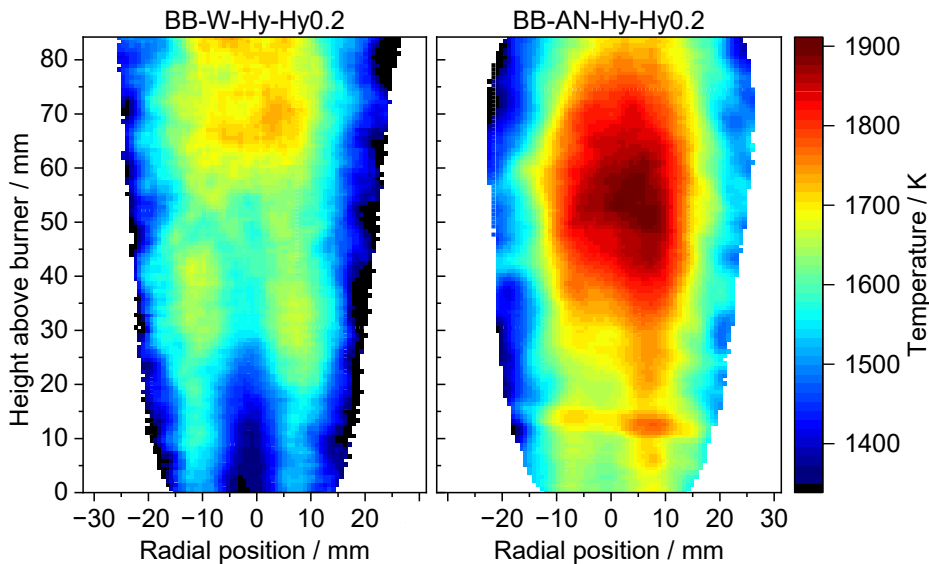


Figure 54: Gas-phase temperature maps measured in the Berlin burner. Pilot flame fuel: H_2 , dispersion gas: 0.22 kg/h H_2 , liquid flow rate: 3 l/h, variation of the solvent, left: H_2O , right: 111 g/l ammonium nitrate in H_2O .

BB-W-Hy-Hy0.2 is with a maximum flame temperature of 1700 K in the temperature range of the operating conditions with the H_2 pilot flame and air as dispersion gas. Just like for most of the other operating condition, a cold zone in the lower central flame region is observed. The H_2O spray introduces evaporative cooling without supplying additional enthalpy to the flame. The addition of 111 g/l ammonium nitrate raises the gas temperature by about 200 K and the region with the highest temperature is shifted upstream to approximately $\text{HAB} = 50$ mm (Figure 54, right). The gas temperature in the lower flame region increases more strongly by approximately 300 K. During the flame operation with ammonium nitrate, unknown deposits have built up over time on the reactor windows which blocked parts of the laser sheet and caused an inhomogeneous laser-sheet intensity distribution. For instance, the artifact at $\text{HAB} = 10$ mm in the form of a stripe of elevated temperature results from this impairment.

6.4.2 HSW burner

The HSW burner (HSWB) is described in detail in chapter 3.4 and the definition of the operating conditions is given in Table 4. The capillary exit of the burner was defined as $\text{HAB} = 0$ mm. Before assessing the results, it is crucial to note that it was not possible to adequately adjust the flame because the burner design is lacking degrees of freedom for flame alignment (e.g., for the position of the capillary). The flame was therefore never straight in vertical direction and not rotationally symmetric. Especially for the operation with air as dispersion gas the curved flame shape gets obvious (Figure 55). The same phenomenon, but much less pronounced, occurred when O_2 was used as dispersion gas. This non-ideal flame shape needs to be taken into account when assessing the following gas-temperature maps that originate from the cross-section between the straight laser sheet and curved flame. Consequently, the temperature maps do not show the ideal section through the center of the flame. Nevertheless, provided the flame shape is considered for interpretation, the measurement results offer useful information.

6.4.2.1 Dispersion gas: Air

Figure 55 shows the HSW burner flame operated with ethanol and air as dispersion gas. The gas-temperature map is given on the left and the flame luminescence image is shown on the right for the same field of view. As mentioned above the curved shape and the asymmetry of the flame can clearly be seen from the luminescence image. It corresponds to the flame shape observed by eye. Note that the field of view starts at larger HAB because strong scattering of laser light in the dense spray region impeded NO-LIF measurements. The spatial ordinate starts at HAB = 16 mm and in turn allows access to the higher flame region.

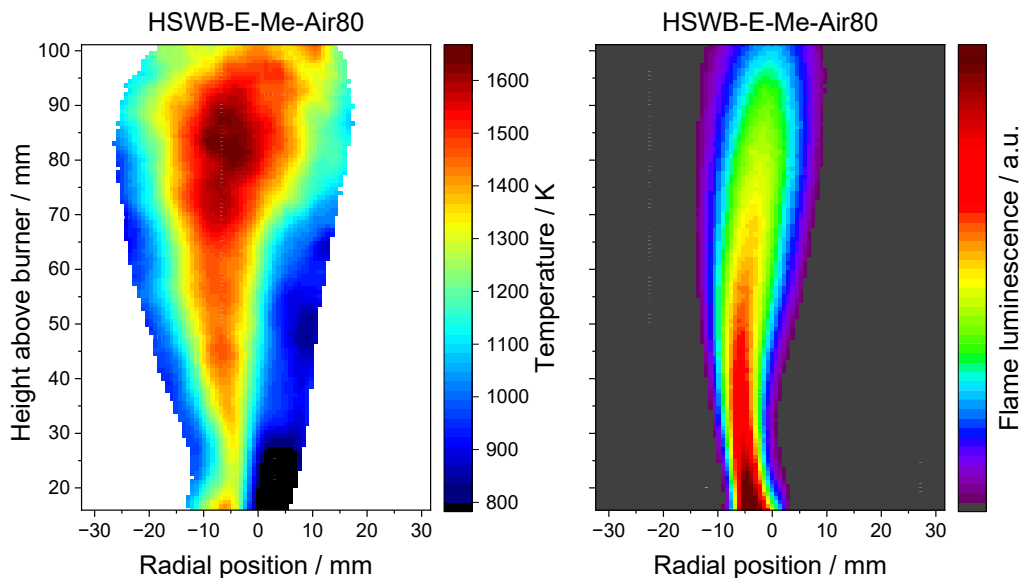


Figure 55: Temperature distribution in the HSW burner flame, spray: Ethanol, pilot gas: CH₄, dispersion gas: 80 slm air, left: Gas-phase temperature map, right: Line-of-sight averaged flame luminescence image within the same field of view as on the left.

A strong correspondence of the shape is evident between the gas-temperature map and the flame luminescence image. The maximum gas temperature in the plane of the laser sheet is about 1650 K and located at approximately HAB = 85 mm. In the lower region of the temperature map a narrow flame width can be seen. Although basically confirmed by the luminescence image, it might be that a broader part with higher gas temperature is located outside the laser-sheet plane.

6.4.2.2 Variation of dispersion gas (O₂) flow rates

Figure 56 shows the gas-temperature maps of the HSW burner when operated with ethanol and various O₂ dispersion gas flows in the range between 61 and 80 slm. The identifiers of the operating conditions are given above the diagrams. For the assessment of the results, it needs to be considered that the flame shape might slightly change with increasing dispersion gas flows. From the flame luminescence images no significant change of the flame shape can be seen (not shown here). In the lower flame region, laser-light scattering in the spray might cause some errors for the NO-LIF measurements.

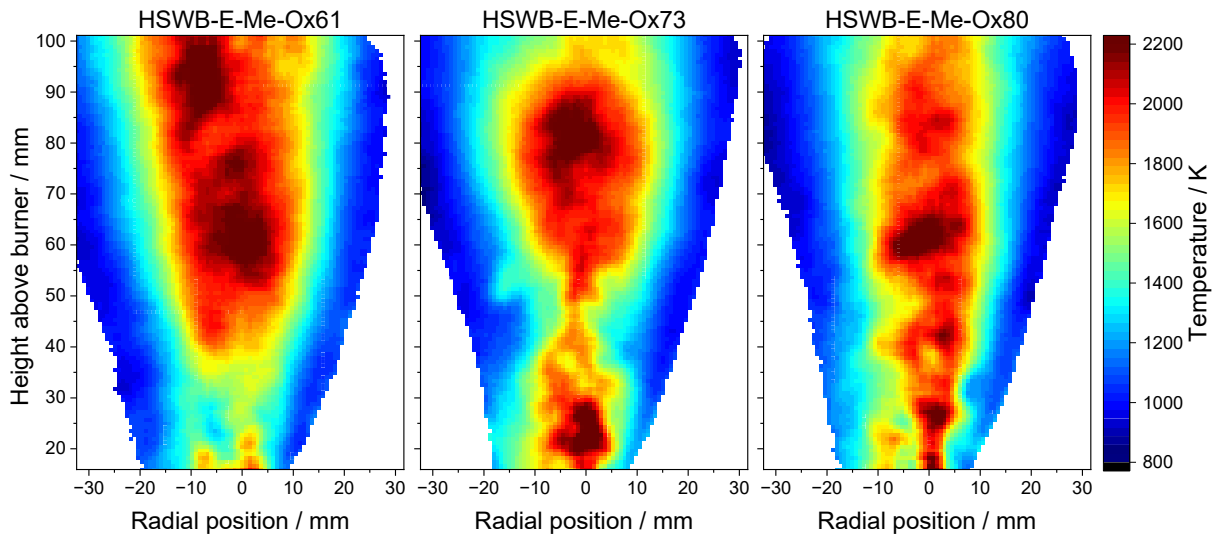


Figure 56: Gas-phase temperature map of the HSW burner flame. Spray: Ethanol, pilot gas: CH₄, dispersion gas: Various volume flows of O₂, left: 61 slm, center: 73 slm, right: 80 slm.

The temperature maps are in terms of shape and temperature level overall similar. The maximum gas temperature is for all cases approximately 2200 K. In comparison to HSWB-E-Me-Air80 (Figure 55), the flame temperature is by about 600 K significantly higher. This can be explained by a more efficient combustion of the ethanol spray within the O₂ environment. Figure 57 shows the related centerline temperature profiles of the operating conditions presented in Figure 56. Within the field of view, it can be seen that the centerline gas temperature profiles range across HAB in the same temperature corridor and feature overall the same trend.

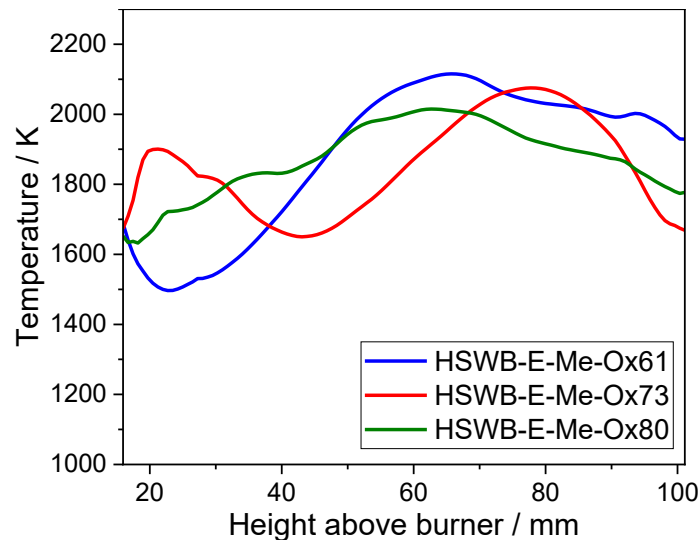


Figure 57: Centerline gas-temperature profiles for the operating conditions shown in Figure 56, extraction width: 14.9 mm, smoothed with a moving average filter with a 30-data-point range, variation of O₂ dispersion gas flow.

6.4.2.3 Liquid fuel: 65EHA35EtOH

Figure 58 shows the gas-phase temperature map of the HSW burner operated with the solvent 65EHA35EtOH atomized by 73 slm O₂ dispersion gas. The NO-LIF measurements were performed with a different optical filter than the longpass filter (transparent in the VIS) used for the operating condition shown above. The dielectric-reflection bandpass filter (Figure 44) was necessary to block the strong blackbody radiation generated by the EHA of the solvent mixture.

With this optical filter an enhanced masking approach becomes feasible. Because the filter blocks most of the background signal, primarily NO-LIF signal is detected, which allows calculating the relative standard deviation of the detected LIF signal for each pixel. With this, flame regions with a high fluctuation of the NO-LIF signal, caused by factors such as a broad temperature distribution or NO concentration fluctuations (section 6.3.2), were excluded from further analysis. High fluctuations of the NO-LIF signal indicate a large measurement error. From the study of Feroughi et al. [346] a threshold of 0.8 for the relative standard deviation of the NO-signal intensity is derived and used to mask the gas-temperature map (section 6.3.2). Due to the poor transmission at the upper edge of the dielectric reflection bandpass filter, the image area above HAB = 100 mm has been cropped. Note that the spatial ordinate axis starts at HAB = 30 mm.

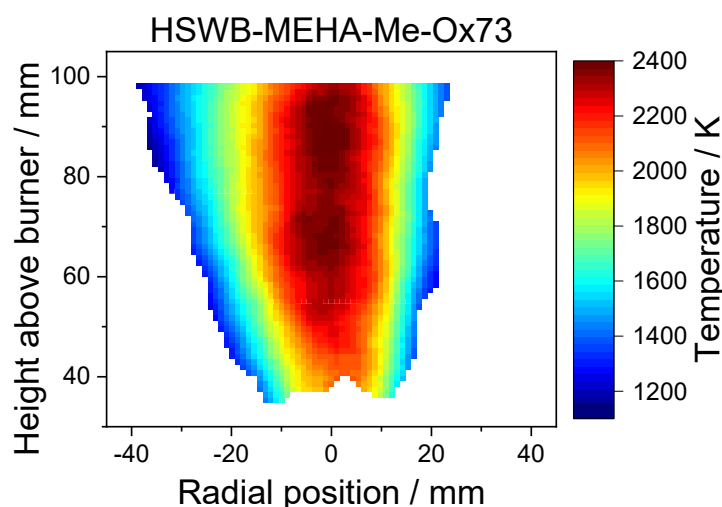


Figure 58: Gas-phase temperature map measured in the large-scale HSW spray flame, masked by a threshold of 0.8 for the relative standard deviation of the NO-LIF signal (cf. section 6.3.2), pilot gas: CH₄, dispersion gas: 73 slm O₂, solvent: 65EHA35EtOH.

For the HSWB operated with 65EHA35EtOH a maximum gas temperature of approximately 2400 K was determined. Compared to the same OC with ethanol as liquid fuel (HSWB-E-Me-Ox73) the increase in maximum flame temperature was about 200 K. The overall temperature level matches to multi-line OH-LIF results published by Karaminejad et al. [51]. In the laboratory-scale SpraySyn1 flame, higher gas temperatures were measured during operation with 65EHA35EtOH compared to pure ethanol.

6.5 Summary and Discussion

In this work, time-averaged gas-temperature maps of two pilot-scale spray burners (Berlin burner and HSW burner) were measured by multi-line NO-LIF thermometry. The burners were designed for the investigation of the upscaling process of nanoparticle production in spray flames (cf. sections 3.3 and 3.4). The measurements were executed in the pilot plant of the IUTA in collaboration with Martin Underberg. For the NO-LIF measurements the established spectral range between 44,407.5–44,417.6 cm⁻¹ (cf. section 6.1.3) was chosen to determine the gas-temperature maps using LIFSim 4.0 [343].

The gas-temperature maps were measured without iron-oxide nanoparticle synthesis to facilitate the NO-LIF measurements. This has several advantages as, e.g., the LIF signal detection could be maximized by utilizing a longpass filter without interference from particle emission,

window fouling with nanoparticles was prevented, and the disturbing Fe-LIF peak at $44,415\text{ cm}^{-1}$ was not present. The Fe-LIF signal can cause problems with spectral fitting by LIFSim 4.0 resulting in errors for the temperature determination (also when excluding the spectral range of the Fe peak). According to detailed studies of Apazeller, Karaminejad et al. [309] and Nanjaiah et al. [349] no strong impact on the flame temperature is expected from the addition of 0.3 mol/l iron nitrate nonahydrate. By using multi-line OH-LIF thermometry in a matrix burner [353] with precursor concentrations of up to 0.2 mol/l iron nitrate nonahydrate they found that this precursor additive has no measurable impact on the flame temperature. The case is different for the precursor iron pentacarbonyl where higher flame temperatures were measured and simulated [122, 354-356].

The results of the different operating conditions of the Berlin burner present a very conclusive picture overall. The gas temperature of the CH_4 pilot flame is significantly higher than the H_2 pilot flame (section 6.4.1.1). While the chosen pilot and dispersion gas species have a large impact on the gas temperature and its distribution across the flame (section 6.4.1.4), the dispersion gas flow rate has a minor influence (section 6.4.1.2 and 6.4.1.3). With an increasing dispersion gas flow, the location of the maximum gas temperature is shifted to larger HAB. A carbon-free spray flame was investigated, which is based on air as oxidizer, H_2 as pilot fuel, and H_2O as precursor solvent. When using H_2O as solvent, the gas temperature is reduced compared to ethanol, but the temperature reduction can be compensated by the addition of carbon-free ammonium nitrate (section 6.4.1.5). All gas-temperature maps of the Berlin burner show a lower-temperature zone in the lower center of the flame. This zone can be attributed to the cold spray entering the flame. The low gas temperature in this region is caused by evaporative cooling and the fact that the cold dispersion gas and liquid solvent have not yet sufficiently formed combustible mixtures.

For the interpretation of the NO-LIF measurements with the HSW burner it needs to be noted that the generated flame featured a curved shape in vertical direction (section 6.4.2). Therefore, the cross-sectional images might miss the highest-temperature zone. In the observed zone, the flame temperature is significantly higher when the HSW burner is operated with O_2 as dispersion gas than when operated with air (section 6.4.2.1 vs. 6.4.2.2). Moreover, the O_2 dispersion gas flow rate has no significant impact on the flame temperature and the overall flame shape. When the 65EHA35EtOH solvent is used, the maximum gas temperature is higher compared to ethanol (section 6.4.2.3), possibly due to the higher enthalpy of combustion (Table A1).

For the same operating conditions of the Berlin burner mentioned above, iron-oxide nanoparticles were produced from a precursor solution of 0.3 mol/l iron(III) nitrate nonahydrate in ethanol. The produced nanoparticles were characterized by various measurement techniques, as e.g., gas adsorption analysis according to Brunauer, Emmet, and Teller (BET), scanning electron microscopy (SEM), transmission electron microscopy (TEM), or X-ray diffraction analysis (XRD). For more details refer to Underberg et al. [147].

From these results [147], the impact of the gas temperature on the particle formation process and the nanoparticle properties is inferred. The specific surface area (SSA) of the produced iron-oxide nanoparticles is clearly affected by the gas-phase temperature. From the comparison between the nanoparticle properties presented in Ref. [147] and the gas-temperature maps shown in section 6.4.1, a distinct trend can be seen that the SSA increases with rising gas temperatures (i.e., the fraction of large particles decreases). This implies that elevated gas

temperatures accelerate droplet evaporation, suppress the frequently unwanted liquid-to-particle synthesis pathway (large particles), and promote the gas-to-particle synthesis pathway (small particles) [106, 149, 357]. Since the dispersion gas flow has weak influence on the gas temperature level the influence on the particle properties is small. On the other hand, the selection of the pilot and dispersion gas species has a significant impact on the flame temperature, and thus on the particle properties. The highest flame temperature and highest SSA was measured for BB-E-Me-Ox3.

Multimodal particle-size distributions with large edged and faceted, but almost spherical particles (from the liquid-to-particle pathway) were found for all operating conditions. It is observed that the count mean diameter (CMD) of the small particle fraction increases with rising gas temperature (contrary to the overall particle size trend described above). Possible explanations for this are promoted particle coalescence at higher gas temperatures or that the elevated gas temperatures intensify evaporation of iron species from the surface of coarse particles. The resulting higher iron concentration in the gas phase results in the formation of larger particles in the fraction of small iron-oxide nanoparticles [358]. Another explanation could be that higher gas temperatures promote droplet micro explosions [129, 207, 213, 359] which reduce the number of large particles [154, 255, 360]. The results of this study show that the flame temperature of pilot-scale spray flames is an important parameter influencing the nanoparticle formation in the liquid and gas phase. The results are consistent with those obtained from studies of lab-scale burners.

7 Study on suitable tracers for two-color laser-induced fluorescence in liquids

Some sections of the following chapter are reprints or else contain contents from the listed publications:

M.M. Prenting, M.I. Bin Dzulfida, T. Dreier, C. Schulz, Characterization of tracers for two-color laser-induced fluorescence liquid-phase temperature imaging in sprays, *Exp. Fluids* 61 (2020) 77.

<https://doi.org/10.1007/s00348-020-2909-9>

© Springer-Verlag GmbH Germany, part of Springer Nature 2020. Reprinted with permission.

M.M. Prenting, M. Shilikhin, T. Dreier, C. Schulz, T. Endres, Characterization of tracers for two-color laser-induced fluorescence thermometry of liquid-phase temperature in ethanol, 2-ethylhexanoic-acid/ethanol mixtures, 1-butanol, and o-xylene, *Appl. Opt.* 60 (2021) C98–C113. <https://doi.org/10.1364/AO.419684>

© 2021 Optical Society of America. Reprinted with permission.

My contributions to the publications were the design and setup of the experiment, execution of the measurements supported by students under my supervision, analysis and interpretation of the data, conception and writing of the manuscripts supported by the coauthors who especially contributed to structuring and wording.

The present study was designed to find a suitable fluorescence tracer for two-color laser-induced fluorescence (LIF) thermometry for our specific application of liquid-phase temperature measurements in spray flames. In case of quantitative measurements of the total liquid volume in a spray, the LIF intensity needs to represent the liquid volume. In this case, the tracers require similar thermo-physical properties (vapor pressure, transport properties, etc.) as the hydrocarbon [361, 362] or aqueous solvent [363] to ensure co-evaporation in the respective medium. For ratiometric measurements often used for thermometry, this requirement must not be fulfilled. Here, tracers with especially high quantum yields are often preferred because they can be applied in minute quantities without influencing the system under study [364, 365]. Variations in local volumetric tracer concentrations due to evaporation of the solvent cancels in ratiometric data analysis. Because of their high quantum yields and excellent solubility in hydrocarbons, alcohols, and water, organic dyes are often a preferred choice. In the desired temperature range, the literature provides for these dyes only a limited number of temperature-dependent fluorescence spectra [366-375]. Furthermore, available tracers in the literature feature significant disadvantages as fluorescence signal re-absorption or a low temperature-sensitivity [369, 376-378]. This motivated the study to analyze a variety of laser dyes as possible 2cLIF thermometry tracers and to investigate their potential as temperature tracer in evaporating and burning sprays.

The fluorescence spectra of dye solutions change their spectral signature with temperature. This effect is frequently used for temperature imaging in liquids and sprays based on two-color laser-induced fluorescence (2cLIF) measurements by simultaneously detecting the fluorescence intensity in two separate wavelength channels resulting in a temperature-sensitive ratio [365, 368, 379]. In this work, we recorded temperature-dependent absorption and fluorescence spectra of solutions of 13 laser dyes (most notably: Coumarin 152, coumarin 153, rhodamine B, pyrromethene 597 and DCM) dissolved in solvent systems frequently applied for spray-flame synthesis of nanomaterials. This included ethanol, a 35/65 vol.% mixture of ethanol/2-ethylhexanoic acid [145, 156], ethanol/ hexamethyldisiloxane (HMDSO) [28, 380, 381], ethanol/water, o-xylene, and 1-butanol to investigate the potential of laser dyes as temperature tracers for these solvents in evaporating and burning sprays. The dissolved tracers were excited at either 266, 355, and 532 nm (depending on the tracer) for temperatures between 296

and 393 K (depending on the solvent), and for concentrations ranging between 0.1 and 10 mg/l. Absorption and fluorescence spectra of the tracers were investigated for their temperature dependence, the magnitude of signal re-absorption, the impact of different solvents and varying two-component solvent compositions. Based on the measured fluorescence spectra the tracers were analyzed for their 2cLIF temperature sensitivity in the respective solvents and optimized choices for the selection of the two detection channels are provided. Furthermore, the impact of fluorescence signal re-absorption was measured to validate our model assumptions (cf. section 7.3.4) that were used to assess the impact of signal re-absorption on our measurements in the spray flame. Additionally, the study was extended to screen laser dyes as possible tracers for concentration measurements of two-component solvents.

7.1 Requirements for suitable fluorescence tracers

Laser dyes are widely used as fluorescence tracers for various applications [382, 383] and provide a broad range of properties which can be utilized for measurements in liquids.

Liquid-phase 2cLIF-thermometry tracers should feature a variety of properties, as listed below:

- The tracer fluorescence should exhibit a high temperature sensitivity in the respective solvent (i.e., temperature-driven change of fluorescence intensity in two color channels as different as possible to each other).
- To enable single-shot measurements the tracer should absorb radiation of most suitable and commercially available pulsed laser sources, e.g., Nd:YAG lasers with fixed wavelengths available at 266, 355, or 532 nm.
- A large Stokes shift to minimize overlap of absorption and fluorescence spectra and to thus reduce the effect of signal re-absorption. Alternatively, signal detection channels need to be located in spectral ranges without overlap with absorption.
- Strong absorption of laser light and a high fluorescence quantum yield (ϕ_f) to provide strong signal and thus provide a high signal-to-noise ratio already with small tracer concentrations that do not affect the studied medium (e.g., through modified evaporation and viscosity or through chemical processes).
- For multi-component solvents, the tracer should feature the smallest possible sensitivity to solvent-composition changes (that might occur during evaporation).
- No co-evaporation with the liquid to prevent the generation of LIF signal from the gas phase.
- Soluble in the liquid under investigation, stable over time in the solvent, and resistant to photo-dissociation.
- Additional aspects of minor importance include low price, easy availability, no toxicity, and the availability of suitable optics and filters in the respective wavelength range.

For concentration measurements of two-component solvents (e.g., ethanol fraction in ethanol/water droplets) a suitable fluorescent tracer should feature different from some aforementioned characteristics:

- The LIF signal should be preferably insensitive to temperature.
- The LIF signal should be highly sensitive to the solvent composition.

For the visualization and quantitative measurements of liquids (e.g., spray shapes or liquid thin films) a suitable fluorescence tracer should feature different from some aforementioned characteristics:

- The LIF signal should be insensitive to temperature.
- The tracer should co-evaporate with the solvent without signal contribution from the gas phase.

7.2 Experimental setup

This study is based on measured absorption and fluorescence spectra of laser dyes dissolved in solvents which are used as fuels for the SpraySyn burner. The spectra were investigated for their temperature dependence, the magnitude of signal re-absorption, the impact of different solvents and varying two-component solvent compositions. Based on the results the suitability for the respective application case was analyzed and assessed. The spectra were recorded for various tracers at various temperatures, tracer concentrations, excitation wavelengths, and dissolved in different solvents and solvent compositions. The tracer solutions were prepared in a two-step dilution process by weighing (Mettler AT201, readability: 0.01 mg) the solid powders and dissolving them in known volumes of solvent resulting in solutions with concentrations of 10 mg/l that are then further diluted to the desired concentration level. For the measurements the solution was filled into an UV-transparent optical quartz cell (Hellma cuvette 111-QS, 10 × 10 mm²) and placed in a temperature-controlled cell.

7.2.1 Temperature-controlled measurement cell

A temperature-controlled measurement cell was used to set and to maintain the desired temperature for the tracer solution under investigation. The cuvette was fixed with a mount holder and placed in the cell, which was aligned in the sample compartment of the respective analytical instrument. The cell was made from stainless steel with three UV-transmitting quartz windows (Suprasil, diameter: 10 mm). The inner walls were powder-coated in black to minimize stray light. The steel housing was surrounded by a heating wire and thermal insulation. A thermocouple was placed under the insulation to monitor the temperature. Based on the measured temperature the current through the heating wire was set by an external controller unit. Independent from that, the temperature of the tracer solution was measured by a thermocouple (type K) immersed in the solution. As can be seen in Figure 59 the cuvette can be optically accessed through the three quartz windows which are oriented 180° and 90° to each other, respectively. The arrows indicate possible light paths for absorption and fluorescence measurements.

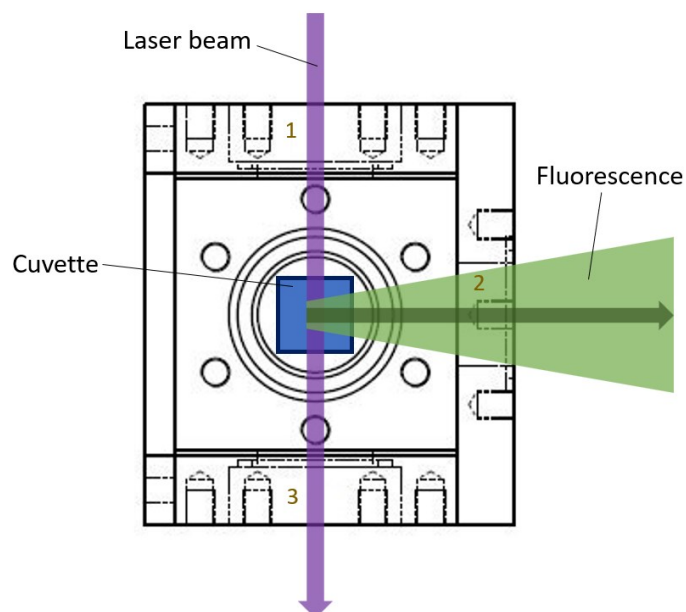


Figure 59: Top view of the temperature-controlled measurement cell, the numbers indicate the quartz windows, the cuvette is shown in blue, the arrows indicate possible light paths.

7.2.2 Absorption spectrometer

Absorption measurements were performed with a UV/VIS absorption spectrometer (Varian Inc., Mod. Cary 400) using the heatable sample cell described in section 7.2.1 and the same quartz cuvette resulting in a probe path length of 10 mm. The absorption and transmission spectra were measured with an increment of 0.5 nm between 175 and 900 nm. The measurements were corrected for the wavelength dependent intensity of the light source and detector sensitivity by the internal software (I/I_0). The absorption of the solvent and scattering effects from the cell and cuvette were corrected by subtracting pre-recorded spectra of the pure solvent in the probe containment (baseline correction).

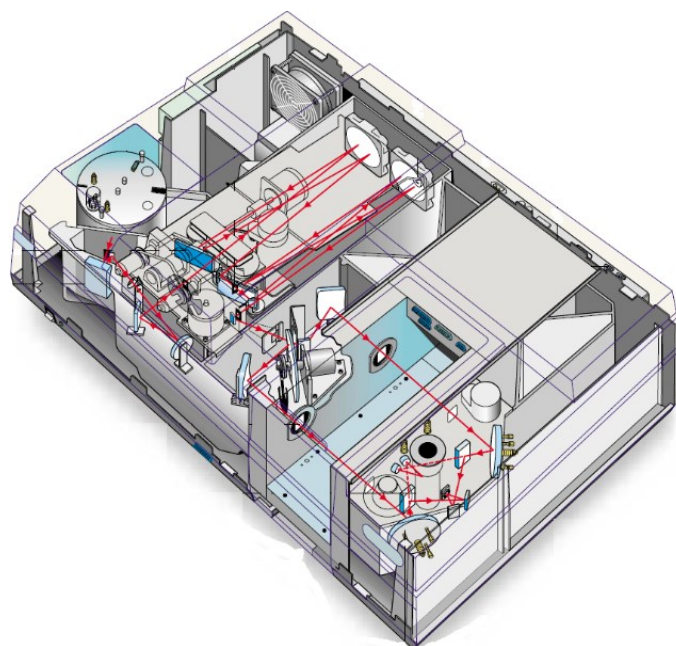


Figure 60: Sketch of the UV/VIS absorption spectrometer (Varian Inc., Mod. Cary 400), modified from [384].

7.2.3 Fluorescence spectrometer

Fluorescence measurements were performed with a spectrofluorometer (Horiba, Fluorolog-3 Model FL3-22), which uses a xenon arc lamp as light source. The basic schematic diagram is given in Figure 61. Starting from the xenon lamp the excitation light is filtered by a double-grating spectrometer followed by a width-adjustable slit to enable the selection of narrow excitation light. The excitation light is formed to a thin light sheet which is directed to the center of the sample compartment where the measurement cell (cf. section 7.2.1) is placed. The cell was designed to fit in the sample compartment of the fluorescence spectrometer with its UV-transmissive quartz windows in the beam paths of the instrument. The resulting fluorescence light can be recorded either via a detection angle of 22.5° (for highly absorbing solutions) or 90° towards the excitation light. The fluorescence light is collected, filtered the same way as described for the excitation part (Figure 61), and directed to a photomultiplier tube (PMT) detector.

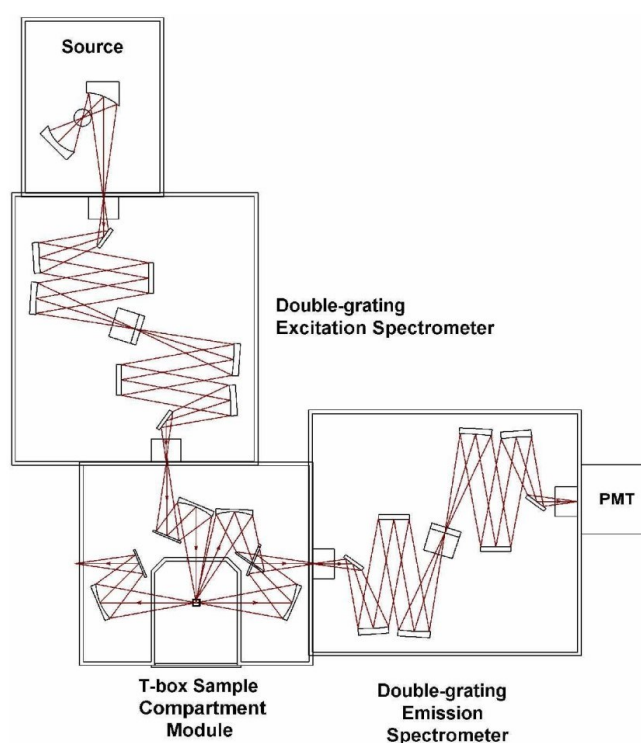


Figure 61: Schematics of the spectrofluorometer (Horiba, Fluorolog-3 Model FL3-22) [385].

Depending on their previously determined absorption spectra in the respective solvent, the tracers were excited with a bandwidth of 1 nm (FWHM) at harmonics of Nd:YAG laser wavelengths. The fluorescence spectra were recorded in a 0.5-nm increment steps with a detection bandwidth of 1 nm. The integration time was fixed to 0.1 s per wavelength increment. The slightly fluctuating excitation intensity of the xenon lamp was corrected by an integrated silicon photodiode reference detector. The wavelength-dependent detection sensitivity of the instrument was corrected by a software-integrated correction file provided and updated by the manufacturer. Furthermore, the fluorescence spectra were background corrected by prior performed fluorescence measurements of the pure solvent at all desired temperature settings, eliminating minor disturbing background artifacts. For each temperature three measurements were conducted and averaged in the evaluation process to improve the signal-to-noise ratio.

Possible tracer dissociation during the measurements could be neglected due to the low applied irradiance levels. Additionally, the dye solution was only exposed to the light beam during the actual measurements minimizing potential dye degradation by photo-dissociation. To test this assumption some dyes, after having cooled down after the measurements, were recorded again and showed no detectable impact on the spectra proving negligible photo and thermal degradation. Similar results were described recently by Koegl et al. [372], who measured the fluorescence spectra of Nile red from low to high and from high to low temperatures acquiring the same curves.

7.2.4 Overview of fluorescent tracers and solvents

Absorption and fluorescence spectra of the dissolved laser dyes were recorded in various solvents. Table 5 lists all tracers investigated in this work together with their excitation wavelengths and the concentration ranges expressed in mg/l and mol/l. The respective solvents are indicated by numbers listed in column 6 and are defined in the table caption. Further photo-physical and thermo-physical properties are provided in the appendix in Table A4.

Table 5: Tracers investigated in this study with the investigated concentration range and their molar mass. The fourth column lists the used excitation wavelengths for recording the fluorescence spectra. Solvents are given by number: Ethanol (1), 1-butanol (2), o-xylene (3), water (4), ethanol/EHA (5), ethanol/HMDSO (6).

Tracer	Molar mass / (g/mol)	Concentration / (mg/l)	Concentration / (mol/l)	Excitation wavelength / nm	Solvents
Coumarin 47	231.29	10	4.3×10^{-5}	266/355	1
Coumarin 102	255.31	10	3.9×10^{-5}	266/355	1
Coumarin 120	175.18	10	5.7×10^{-5}	266/355	1
Coumarin 152	257.21	0.1–500	3.9×10^{-7} – 1.9×10^{-3}	266/355	1, 2, 3, 5, 6
Coumarin 153	309.28	0.1–10	3.2×10^{-7} – 3.2×10^{-5}	266/355	1, 3, 5
DCM	303.37	0.1–10	3.3×10^{-7} – 3.3×10^{-5}	355/532	1, 3, 5
PTP	230.3	10	4.3×10^{-5}	266	1
Pyridine 1	378.85	10	2.6×10^{-5}	532	1
Pyromethene 567	318.22	10	3.1×10^{-5}	355/532	5
Pyromethene 597	374.32	0.1–10	2.7×10^{-7} – 2.7×10^{-5}	355/532	1, 3, 5
Rhodamine 101	591.05	6.4	1.3×10^{-5}	532	1
Rhodamine B	479.02	0.1–10	2.1×10^{-7} – 2.1×10^{-5}	355/532	1, 2, 4, 5
Stilbene 3	562.56	10	1.8×10^{-5}	355	1

Relevant chemical properties of the solvents are provided in Table 6. In the last column of Table 6, feasible excitation wavelengths are given for each solvent. The excitation wavelength is limited by light absorption of the solvent and potentially resulting fluorescence of the solvent that could interfere with the tracer fluorescence. Due to their strong absorption at 266 nm, the solvents EHA, o-xylene and HMDSO are not suitable at that laser excitation wavelength. The solvent 1-butanol partially absorbs excitation light at 266 nm and consequentially fluoresces in the spectral range between 260 and 400 nm.

Table 6: Chemical properties of relevant solvents

Solvent	Chemical structure	Molecular mass / g/mol	Boiling point / °C	Vapor pressure (20 °C) / hPa	Dielectric constant ϵ_r [386]	Excitation wavelengths / nm
1-Butanol [387]	C ₄ H ₁₀ O	74.12	117.7	6.67 [388]	17.84	266/355/532
2-EHA [389]	C ₈ H ₁₆ O ₂	144.21	228	< 0.01	2.64	355/532
Ethanol [390]	C ₂ H ₆ O	46.07	78.29	59	25.3	266/355/532
o-Xylene [391]	C ₈ H ₁₀	106.17	143	6.69	2.56	355/532
HMDSO [392]	C ₆ H ₁₈ OSi ₂	162.38	101	44	2.179	355/532
Water	H ₂ O	18.02	100	23.4	80.1	266/355/532

7.2.5 The β factor in the context of 2cLIF thermometry

The principle of two-color LIF thermometry using tracers with broadband fluorescence spectra is based on their temperature-dependent fluorescence spectra. The derivation of the relevant LIF-intensity equations is presented in the literature [365, 393, 394] and will be only briefly described here. The temperature dependence of the LIF intensity can generally be well approximated by an exponential relation $I_{\text{LIF}}(T) \sim \exp(\beta(\lambda)/T)$ [365], where $\beta(\lambda)$ is the so-called temperature-sensitivity factor. The β factor describes the extent of the variation in fluorescence intensity of the respective tracer as a function of temperature at a given wavelength. Increasing intensity (with increasing temperature) results in negative values, decreasing intensity in positive β values. Large absolute values of β (either positive or negative) are required for sensitive single-line thermometry [366, 395]. For two-line thermometry, the absolute value and its sign is meaningless (other than that it indicates either a gain or a loss in signal-to-noise ratio with increasing temperature). The relevant value here is the difference in β for the two spectral bands chosen for the ratiometric analysis. Upon laser excitation at a fixed wavelength within the absorption spectrum, the resulting signal is

$$I_{\text{LIF}} = c_m V \sigma I_0 \exp(\beta(\lambda)/T) \eta \quad (7.1)$$

with the tracer concentration c_m , the probe volume V , the absorption cross-section at the laser wavelength σ , the laser intensity I_0 , and the detection efficiency η .

As will be seen in section 7.3.1 and in the appendix 12.6, β of all investigated tracers varies with fluorescence wavelength. Therefore, temperature can be inferred from the measured fluorescence intensities by placing appropriate spectral filters with selected transmission bands and center wavelengths (illustrated in Figure 81 with the (λ_1, λ_2) pair, respectively) in front of the detectors and forming the respective signal intensity ratios [365].

$$R_{\text{LIF}}(T) = \frac{\eta_1}{\eta_2} \exp((\beta_1 - \beta_2)/T) \quad (7.2)$$

This ratio cancels several unknown quantities in Eq. (7.1). When the same ratio is formed at a known reference temperature, only parameters characteristic for the tracer fluorescence remain and provide a logarithmic intensity ratio linear in the difference of the inverse temperature values [365]:

$$\ln\left(\frac{R_{\text{LIF}}(T)}{R_{\text{LIF}}(T_0)}\right) = (\beta_1 - \beta_2) \left(\frac{1}{T} - \frac{1}{T_0}\right) \quad (7.3)$$

Therefore, the slope difference $\Delta\beta_{12} = \beta_1 - \beta_2$ of the temperature-sensitivity factors between both detection channels is a measure for the temperature sensitivity of the two-color ratio LIF

thermometry. Knowing the ratio at a given temperature T_0 , the temperature of the liquid can be derived from

$$T = \Delta\beta_{12}T_0 / \left(\ln \left(\frac{R_{\text{LIF}}(T)}{R_{\text{LIF}}(T_0)} \right) + (\beta_1 - \beta_2) \right). \quad (7.4)$$

In chapter 7.3.1, the β factor is utilized to assess the wavelength-dependent temperature sensitivity in various ranges of measured fluorescence spectra. The β factor (given in units of Kelvin) can be calculated from two fluorescence spectra recorded at different temperatures (T_1 and T_2) by

$$\beta(\lambda) = \ln \left(\frac{I_{T_1}(\lambda)}{I_{T_2}(\lambda)} \right) / \left(\frac{1}{T_1} - \frac{1}{T_2} \right), \quad (7.5)$$

where $I_{T_1}(\lambda)$ and $I_{T_2}(\lambda)$ are the fluorescence intensities at the respective wavelength.

7.3 Results

7.3.1 Absorption and fluorescence spectra of chosen tracers

In this chapter, temperature-dependent absorption and fluorescence spectra of coumarin 152, rhodamine B, and pyrromethene 597 dissolved (by volume) in a mixture of 65 % 2-ethylhexanoic acid (EHA) and 35 % ethanol (EtOH) (abbreviated as 65EHA35EtOH) are presented. For the same conditions the spectra of coumarin 153 and DCM are provided in the appendix in section 12.6.2.1 and 12.6.2.2, respectively. An investigation of the impact of changing solvent compositions during the evaporation process on the fluorescence spectra of the tracers is presented in section 7.3.5. The solvent 65EHA35EtOH is of interest in liquid-phase temperature measurements as it is used as fuel in spray-based gas-phase flame synthesis of metal-organic nanoparticles because it stabilizes the solutions and promotes droplet explosions for better droplet disintegration [154, 174]. The spectral results of chosen tracers investigated in this work dissolved in ethanol, 1-butanol and o-xylene are presented in the appendix in section 12.6.4. The absorption spectra are presented in units of a molar attenuation coefficient $\varepsilon(\lambda)$, which is derived from the Beer-Lambert law with the absorbance $A(\lambda)$, the molar concentration c and the absorption path length l_{abs} .

$$\varepsilon(\lambda) = A(\lambda) / c_m l_{\text{abs}} \quad (7.6)$$

In addition to temperature, the effect of tracer concentration and the type of solvent on the absorption and fluorescence spectra are investigated. The given values for the blue- and red-shift were calculated at the respective half maximum (HM) points of the fluorescence spectra. In the upper diagram of all figures (e.g., Figure 62) presenting the temperature dependent spectra, the absorption spectra are plotted in absolute units ($\text{l mol}^{-1}\text{cm}^{-1}$) and the fluorescence spectra are shown on an individual absolute intensity scale delivered by the spectrometer software in counts per second (CPS). The respective lower diagrams present the peak-normalized spectra, the β factors and the optimized 2cLIF detection bands as blue and red rectangles (cf. section 7.3.3). Measurements were performed for temperatures up to 393 K. For the concentration dependence of the fluorescence spectra (for a signal path length of 5 mm in the cuvette resulting from an excitation with the light sheet passing through the center of the cuvette) these were normalized at a spectral position where no overlap of absorption and fluorescence spectra exists, i.e., re-absorption of signal radiation can be neglected. From these results, the

magnitude of fluorescence signal re-absorption can be inferred, and model calculations to assess the impact of this effect on the detectable fluorescence spectra were validated (cf. section 7.3.4). Finally, the effect of the solvent on the absorption and fluorescence spectra of each tracer is shown.

With respect of tracer solubility, rhodamine B was the only tracer with a high solubility in water, coumarin 152 showed a very low solubility, and coumarin 153, DCM and pyrromethene 597 were not soluble in water. Among the other solvents only rhodamine B was not soluble in o-xylene. Furthermore, no effect of the excitation wavelengths on the fluorescence spectra was observed for all tracers.

7.3.1.1 Coumarin 152

Temperature dependence of absorption and fluorescence spectra

In Figure 62, the absorption and fluorescence spectra of 1 mg/l coumarin 152 in 65EHA35EtOH are presented for a temperature range from room temperature to 393 K. Additionally, the β factors calculated from the smoothed spectra for the temperature span 303 to 373 K are plotted in the lower diagram. Below 300 nm, the absorption spectra are cut off because EHA starts to absorb strongly. Hence, coumarin 152 in 65EHA35EtOH can only be excited at 355 nm among the possible harmonics of the Nd:YAG laser as 266 nm is strongly attenuated by the solvent and 532 nm is not absorbed by the tracer.

In comparison to other tracers, coumarin 152 exhibits a large Stokes shift and thus a small overlap of the absorption and fluorescence spectra. As depicted in the inset of Figure 62, the absolute fluorescence intensity decreases from 303 to 363 K by 17 % moderately before the intensity starts to rise strongly by 78 % from 363 to 393 K. The same behavior was described by Koegl et al. [372] for Nile red in a solvent mixture of 80 vol.% n-decane and 20 vol.% butanol. This phenomenon is also observable for the absorption spectra which we measured up to 373 K. Here, the absorption also starts to rise beyond 363 K. With 0.14 nm/K between 303 and 343 K the fluorescence spectra of coumarin 152 in 65EHA35EtOH exhibit a significant blueshift (Table 7), which becomes stronger with rising temperature. Also, the absorption spectra show a blueshift with increasing temperature – here the blueshift is with 0.09 nm/K smaller. The β factor is negative in the spectral range below 470 nm and starts to rise from -1700 K at about 430 nm to about 500 K from 550 nm on. The variation of the β factors over wavelength already indicates a high temperature sensitivity of this tracer for 2cLIF.

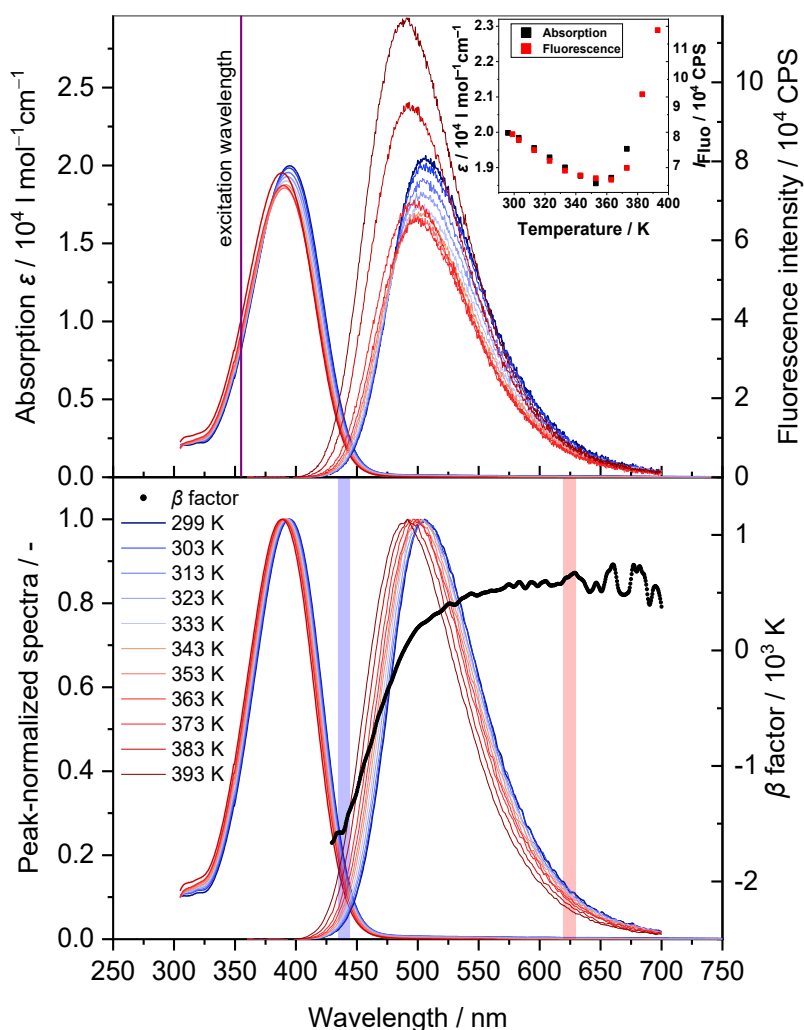


Figure 62: Temperature-dependent absorption (up to 373 K) and fluorescence spectra (up to 393 K) of 1 mg/l coumarin 152 in 65EHA35EtOH, excitation at 355 nm indicated as purple line. Top: Absolute values and inset illustrating the peak intensities vs. temperature, bottom: Peak-normalized values, optimized 10-nm wide 2cLIF detection bands (blue and red bars) and β factor for the spectra at 303 and 373 K.

Impact of concentration: Signal re-absorption

Figure 63 shows the fluorescence spectra of coumarin 152 at concentrations of 0.1, 1, and 10 mg/l dissolved in a) 65EHA35EtOH and b) *o*-xylene. The respective absorption spectra are shown to assess the impact of the spectral overlap on the fluorescence spectra. There is no change of the fluorescence spectra and hence no re-absorption measurable for coumarin 152 dissolved in 65EHA35EtOH (same with ethanol and 1-butanol – refer to appendix section 12.6.4.1). A minimal re-absorption effect is measurable in the case of coumarin 152 dissolved in *o*-xylene (difference in the spectral signature within the overlap area), apparently because of the substantially smaller Stokes shift (right panel in Figure 63). In contrast to the other solvents (cf. Figure 64), this smaller Stokes shift leads to a larger spectral overlap (the overlapping area O for the normalized spectra for 0.1 mg/l solutions $O = 3.34$ nm, which is a factor of 2.37 larger than the overlap in 65EHA35EtOH with $O = 1.41$ nm), which increases re-absorption of fluorescence light. For the concentration range (factor 100) investigated in this work and for path lengths of 5 mm it can be stated that coumarin 152 as tracer for 2cLIF in the named solvents is not measurably affected by fluorescence signal re-absorption; this is shown in some more detail in section 7.3.4 by simple model calculations using the Beer-Lambert law.

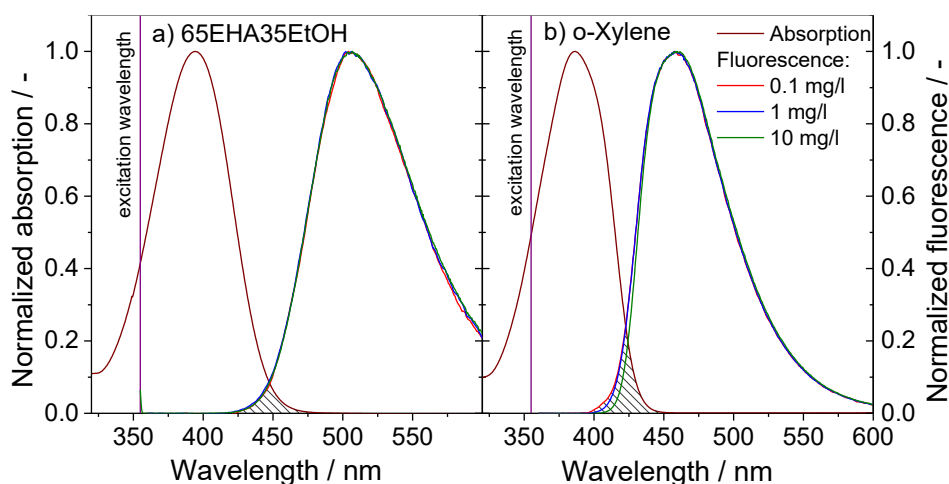


Figure 63: Peak-normalized absorption and fluorescence spectra of coumarin 152 dissolved in a) 65EHA35EtOH and b) o-xylene at various concentrations. Excitation wavelength: 355 nm indicated as purple line, temperature: 303 K. The dashed area shows the overlap O (unit: nm) between normalized absorption and emission for the 0.1 mg/l case.

Impact of various solvents

Figure 64 shows the peak-normalized absorption and fluorescence spectra of coumarin 152 dissolved in various solvents. The absorption spectra are plotted as dashed lines and the fluorescence spectra are plotted as solid lines. In all cases the excitation wavelength was 355 nm which is indicated as a purple line. As expected, the solvents have a strong influence on the spectral location and half width of all spectra, particularly the fluorescence spectra, e.g., the fluorescence spectrum in o-xylene at 303 K features its peak at 458.5 nm with a FWHM of 72.1 nm, the peak in water is at 534 nm with a FWHM of 99.6 nm. An overview of the respective values of coumarin 152 dissolved in various solvents is given in Table 7.

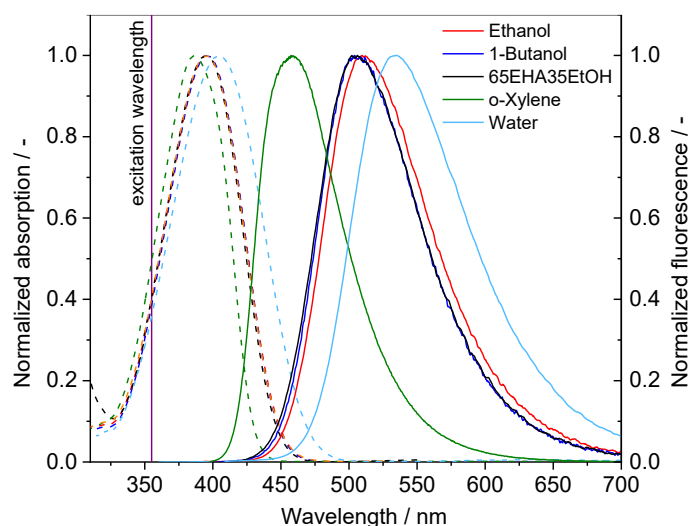


Figure 64: Peak-normalized absorption (dashed lines) and fluorescence (solid lines) spectra of 1 mg/l coumarin 152 dissolved in various solvents, concentration in water due to poor solubility not exactly known, excitation: 355 nm indicated as purple line, temperature: 303 K.

Table 7: Characterization of the fluorescence spectra of 1 mg/l coumarin 152 dissolved in various solvents, concentration in water due to poor solubility not exactly known, excitation at 355 nm. The parameters are extracted from smoothed fluorescence spectra.

	65EHA35EtOH	Ethanol	1-Butanol	o-Xylene	Water
Peak position / nm (303 K)	506	510	505	458.5	534
Peak intensity change / %/K (303 to 343 K)	-0.38	-0.59	-0.48	0.03	-0.91
FWHM / nm (303 K)	89.3	90.6	88	72.1	99.6
Blueshift at HM / nm/K (303 to 343 K)	0.14	0.15	0.16	0.12	0.18
Spectral broadening / nm/K (303 to 343 K)	0.04	0.04	0.03	0.01	0.02

The peak positions and FWHM of coumarin 152 in the solvents 65EHA35EtOH, ethanol and 1-butanol are similar, while the peak position for o-xylene and water shifts to shorter and longer wavelengths, respectively. The FWHM for o-xylene and water is narrower and broader, respectively, than in the three other mentioned solvents. Except for o-xylene, where the fluorescence intensity increases with temperature, the intensity for the other solvents decreases within the considered temperature range (cf. appendix 12.6.4.1). In water, the blueshift and the spectral broadening of coumarin 152 are the strongest, while they are the smallest in o-xylene.

7.3.1.2 Rhodamine B

Temperature dependence of absorption and fluorescence spectra

Figure 65 presents the absorption and fluorescence spectra of rhodamine B dissolved in 65EHA35EtOH. Absorption spectra were measured up to 373 K and the fluorescence spectra up to 393 K. The excitation wavelength of 532 nm is indicated as a green line. Rhodamine B exhibits a small Stokes shift and hence a large overlap of absorption and fluorescence spectra. In comparison to the coumarin tracers the overlap is substantially larger. The fluorescence intensity decreases strongly with increasing temperature and the absorption decreases moderately while the slope corresponds (see inset). From the lower plot in Figure 65, it can be observed that in the range of shorter wavelengths the fluorescence spectra show a blueshift which intensifies with temperature, while for the range of longer wavelengths a slight redshift is observable. Hence, with increasing temperature the spectra exhibit a spectral broadening which magnifies at higher temperatures. The β factors range between 0 and 1750 K with the minimum located at the short wavelength edge of the measured spectral region and the maximum at 580 nm.

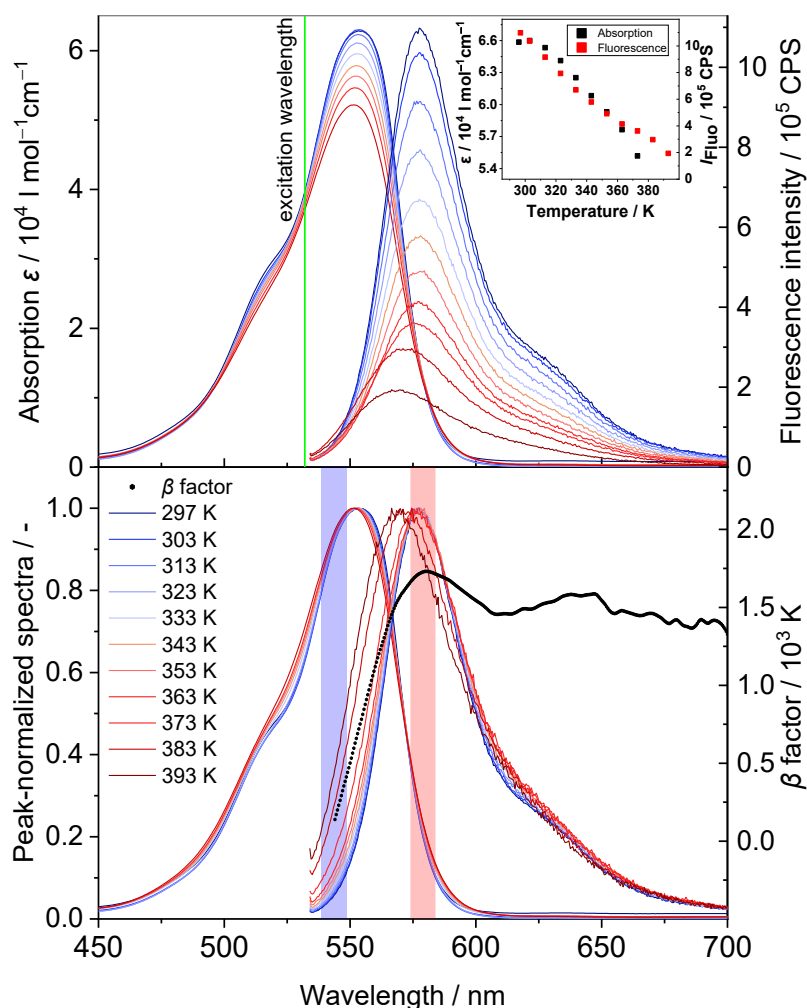


Figure 65: Temperature-dependent absorption (up to 373 K) and fluorescence spectra (up to 393 K) of 1 mg/l rhodamine B in 65EHA35EtOH, excitation at 532 nm (green line). Top: Absolute values and inset illustrating the peak intensities vs. temperature, bottom: Peak-normalized values, optimized 10-nm wide 2cLIF detection bands (blue and red bars) and β factor for the spectra at 303 and 373 K.

Impact of concentration: Signal re-absorption

The normalized absorption and fluorescence spectra of rhodamine B at different concentrations and a temperature of 303 K are presented in Figure 66. Different from the coumarin tracers, absorption and fluorescence spectra significantly overlap causing an apparent peak shift due to an increase of re-absorption (5-mm path length). Therefore, in this case, the fluorescence spectra were normalized at a wavelength with negligible overlap, i.e., at 630 nm.

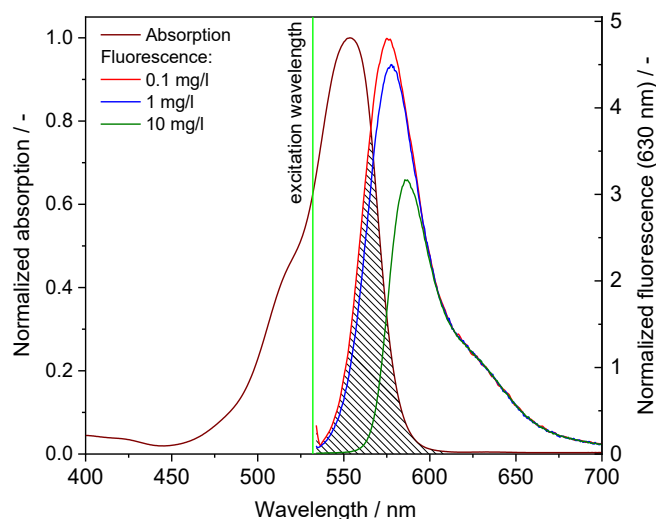


Figure 66: Peak-normalized absorption spectrum and at 630 nm normalized fluorescence spectra of rhodamine B dissolved in 65EHA35EtOH at various concentrations. Excitation wavelength: 532 nm (green line), temperature: 303 K. The dashed area shows the overlap O (unit: nm) between normalized absorption and emission for the 0.1 mg/l case.

As a result of the small Stokes shift and hence the large overlap of the absorption and fluorescence spectra, rhodamine B is strongly affected by signal re-absorption. It can be seen from the diagram that the disparities of the fluorescence spectra correspond to the spectral overlap area ($O = 16$ nm). Regions where no spectral overlap exists are not affected by variation in dye concentration. In practical applications where re-absorption comes into effect either because of strong concentration changes or sizeable fluorescence signal path length variations, the 2cLIF measurement accuracy of rhodamine B significantly declines. The effect can be illustrated by a less application-related extreme case of a concentration change from 0.1 to 10 mg/l and an assumed path length of 5 mm through tracer-doped liquid: The related spectral shift would cause a ratio change by a factor of 13.8, which corresponds to a spectral change caused by a temperature variation of ~ 850 K (at the optimized color band wavelengths presented in Table 11). A concentration change from 0.1 to 1 mg/l under the same conditions causes a ratio change by a factor of 1.27, which corresponds to a temperature difference of ~ 18 K. More relevant scenarios with model calculations of fluorescence signal re-absorption in evaporating ethanol droplets are presented in section 7.3.4.2.

Impact of various solvents

Figure 67 shows the peak-normalized absorption and fluorescence spectra of rhodamine B dissolved in various solvents at a temperature of 303 K. In comparison to the coumarin tracers, rhodamine B absorption and fluorescence spectra are less affected by the type of solvent. This can also be seen in Table 8 from the much smaller variation in peak position and FWHM than it was measured for the coumarin tracers. Additionally, in all considered solvents the fluorescence peak intensity decreases substantially with temperature. Rhodamine B exhibits the strongest and smallest blueshift when dissolved in ethanol and water, respectively. Except for 1-butanol the spectral broadening moves in the same range across the investigated solvents.

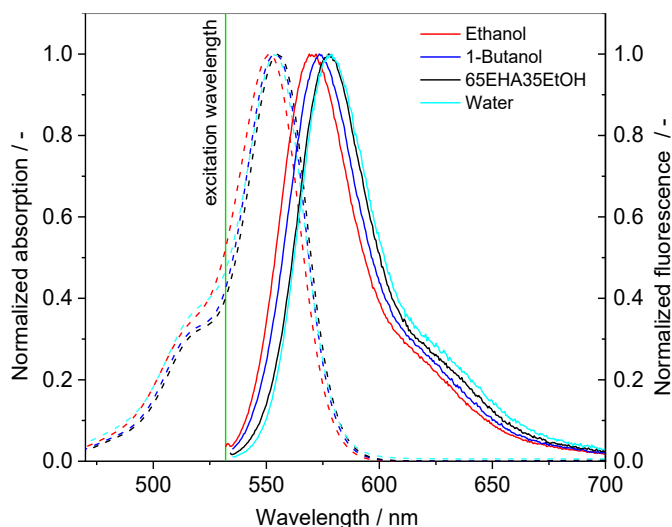


Figure 67: Peak-normalized absorption (dashed lines) and fluorescence (solid lines) spectra of 1 mg/l rhodamine B dissolved in various solvents, excitation: 532 nm (green line), temperature: 303 K.

Table 8: Characterization of the fluorescence spectra of 1 mg/l rhodamine B dissolved in various solvents, excitation at 532 nm. The parameters are extracted from smoothed fluorescence spectra.

	65EHA35EtOH	Ethanol	1-Butanol	Water
Peak position / nm (303 K)	578	569	574	578.5
Peak intensity change / %/K (303 to 343 K)	-1.1	-1.26	-1.34	-1.61
FWHM / nm (303 K)	39.9	38.2	40.7	41.0
Blueshift at HM / nm/K (303 to 343 K)	0.04	0.08	0.06	0.02
Spectral broadening / nm/K (303 to 343 K)	0.09	0.09	0.11	0.09

7.3.1.3 Pyromethene 597

Temperature dependence of absorption and fluorescence spectra

Figure 68 presents the absorption and fluorescence spectra of pyromethene 597 dissolved in 65EHA35EtOH. From the tracers investigated in this work pyromethene 597 has the strongest absorption at 532 nm. In comparison to DCM (also excitable at 532 nm, appendix 12.6.2.2) pyromethene 597 exhibits a smaller Stokes shift resulting in a larger spectral overlap. With increasing temperature, the fluorescence intensity of pyromethene 597 in 65EHA35EtOH decreases steadily. From the peak-normalized spectra it can be seen that the spectra exhibit almost no blueshift in the wavelength range left of the peak, while in the range of longer wavelengths a redshift is observable which leads to a distinct spectral broadening. The absorption spectra show no significant change with rising temperature. The peak of the absorption spectrum first decreases with temperature and then approximately stays constant (see inset in Figure 68). From the short-wavelength edge of the fluorescence spectra the β factor rises until a peak value of 2350 K at about 560 nm and decreases to 1600 K at the long-wavelength edge.

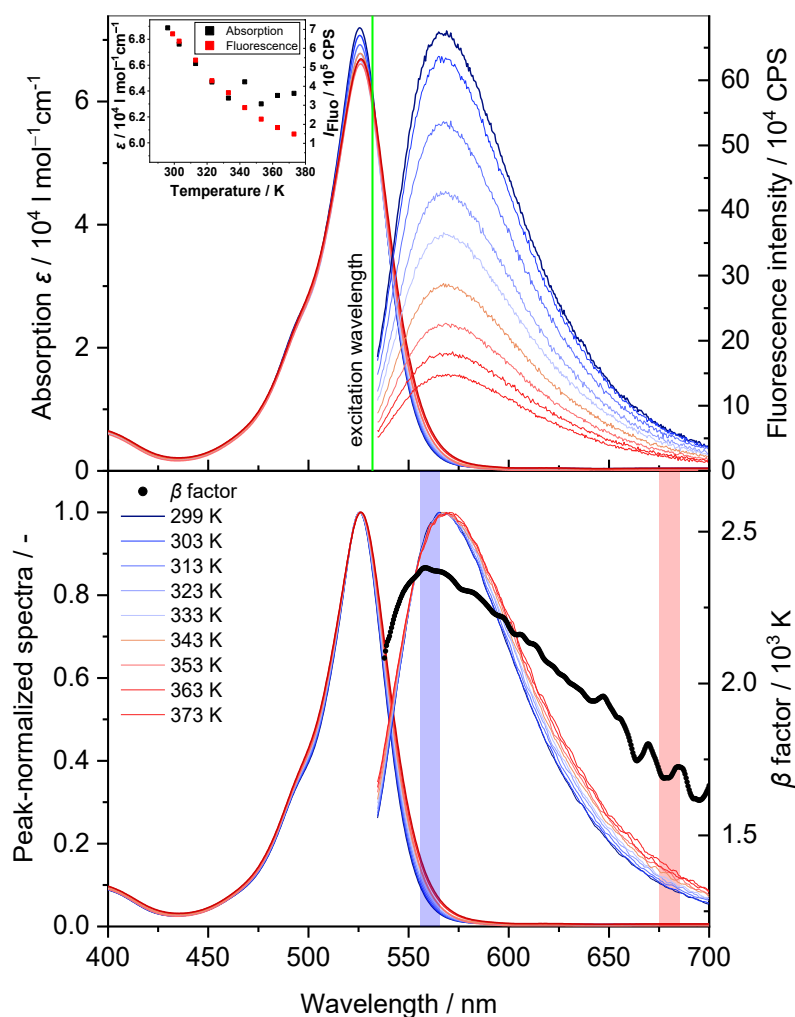


Figure 68: Temperature-dependent absorption (up to 373 K) and fluorescence spectra (up to 373 K) of 1 mg/l pyromethene 597 in 65EHA35EtOH, excitation at 532 nm (green line). Top: Absolute values and inset illustrating the peak intensities vs. temperature, bottom: Peak-normalized values, optimized 10-nm wide 2cLIF detection bands (blue and red bars) and β factor for the spectra at 303 and 373 K.

Impact of concentration: Signal re-absorption

Fluorescence spectra of pyromethene 597 at concentrations between 0.1 and 10 mg/l are presented in Figure 69. They were normalized at 600 nm, where no overlap of absorption and fluorescence spectra exists. It can be observed that due to fluorescence re-absorption especially the spectrum with 10 mg/l experiences an apparent peak shift with reduced intensity in the overlap region. Similar effects regarding signal re-absorption were measured for the other investigated solvents (appendix 12.6.4.5). Since the overlap area coincides with the excitation wavelength only the half overlap area up to the intersection of absorption and fluorescence spectrum can be calculated ($O_{\text{intersec.}} = 4.32$ nm). Since absorption and fluorescence spectra can be considered as mirror images in the overlap region an approximated estimation of the spectral overlap area is achieved by doubling the calculated value resulting in $O = 8.64$ nm.

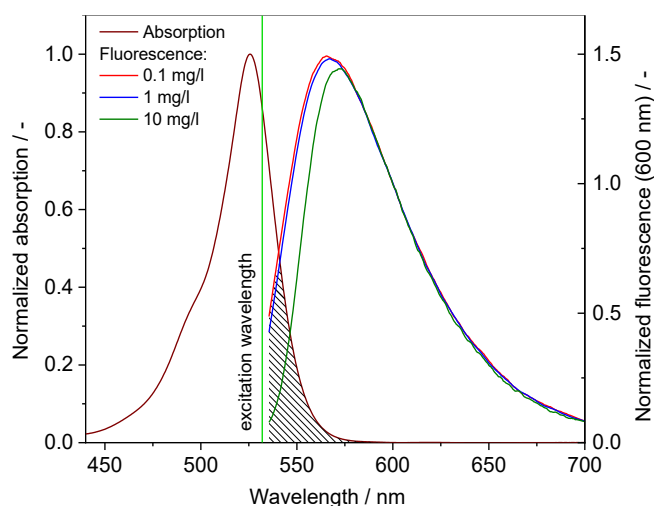


Figure 69: Peak-normalized absorption and at 600 nm normalized fluorescence spectra of pyrromethene 597 dissolved in 65EHA35EtOH at various concentrations. Excitation wavelength: 532 nm indicated as green line, temperature: 303 K. The dashed area shows the overlap O (unit: nm) between normalized absorption and emission for the 0.1 mg/l case.

Impact of various solvents

Figure 70 presents the peak-normalized absorption and fluorescence spectra of pyrromethene 597 at 303 K dissolved in various solvents with a concentration of 1 mg/l. As a unique property among the tracers investigated here, the fluorescence spectra of pyrromethene 597 do not change significantly in shape and position with the solvents investigated. The absorption spectra in ethanol and its mixture with EHA are almost indistinguishable, while the one in *o*-xylene is only slightly displaced and somewhat narrower (Table 9). While the spectral shape and position of the fluorescence spectra are nearly the same in all solvents, the peak intensity decreases for *o*-xylene somewhat less with temperature. The blueshift and the spectral broadening stay approximately constant among the investigated solvents.

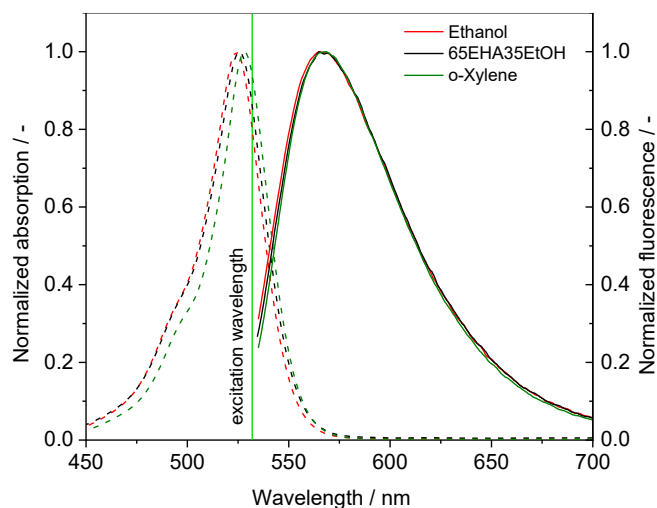


Figure 70: Peak-normalized absorption (dashed lines) and fluorescence (solid lines) spectra of 1 mg/l pyrromethene 597 dissolved in various solvents, excitation: 532 nm indicated as green line, temperature: 303 K.

Table 9: Characterization of the fluorescence spectra of 1 mg/l pyromethene 597 dissolved in various solvents, excitation at 532 nm. The parameters are extracted from smoothed fluorescence spectra.

	65EHA35EtOH	Ethanol	o-Xylene
Peak position / nm (303 K)	568	567	567.5
Peak intensity change / %/K (303 K to 343 K)	-1.38	-1.39	-1.17
FWHM / nm (303 K)	72.5	73	70.3
Blueshift at HM / nm/K (303 K to 343 K)	0.03	0.02	0.02
Spectral broadening / nm/K (303 K to 343 K)	0.14	0.14	0.13

7.3.2 Peak and centroid shift of fluorescence spectra

A useful parameter that characterizes the behavior of the fluorescence spectra of the various investigated tracers with temperature is the spectral shift of the peak or its centroid. In Figure 71 the spectral shift $\Delta\lambda_i = \lambda_i(T) - \lambda_i(T_0)$ of the positions of the fluorescence peaks and centroids (i stands for peak and centroid, respectively) is shown with respect to the reference temperature T_0 of 303 K. In diagrams a) and b) of Figure 71 these results are shown for all investigated tracers dissolved in 65EHA35EtOH and o-xylene, respectively, while in diagrams c) and d) a comparison is made for coumarin 152 and rhodamine B dissolved in various solvents. To guide the eye through the data points the centroid and peak positions were fitted with polynomials and plotted as solid and dashed lines, respectively.

For a specific tracer, the peak and centroid positions vary with temperature similarly, indicating that the shape of the spectra does not change much with temperature during a blue- or redshift (negative and positive sign, respectively). An exception is DCM in o-xylene, where the peak shifts to longer wavelengths, whereas the centroid shifts to shorter wavelengths indicating a change in the spectral shape. While coumarin 152 exhibits the strongest blueshift pyromethene 597 shows a redshift in all solvents. There is no general influence of the solvents on the shift direction or magnitude determinable. While pyromethene 597 shifts in the investigated solvents to longer wavelengths, coumarin 152 shift to shorter wavelength independent of the used solvent (Figure 71a and b). Furthermore, with a view to the lower left diagram, for coumarin 152 the solvent has only a slight influence on the trends in peak and centroid shifts, whereas this is not the case for rhodamine B (lower right graph); for instance, ethanol causes a blue- and water a redshift.

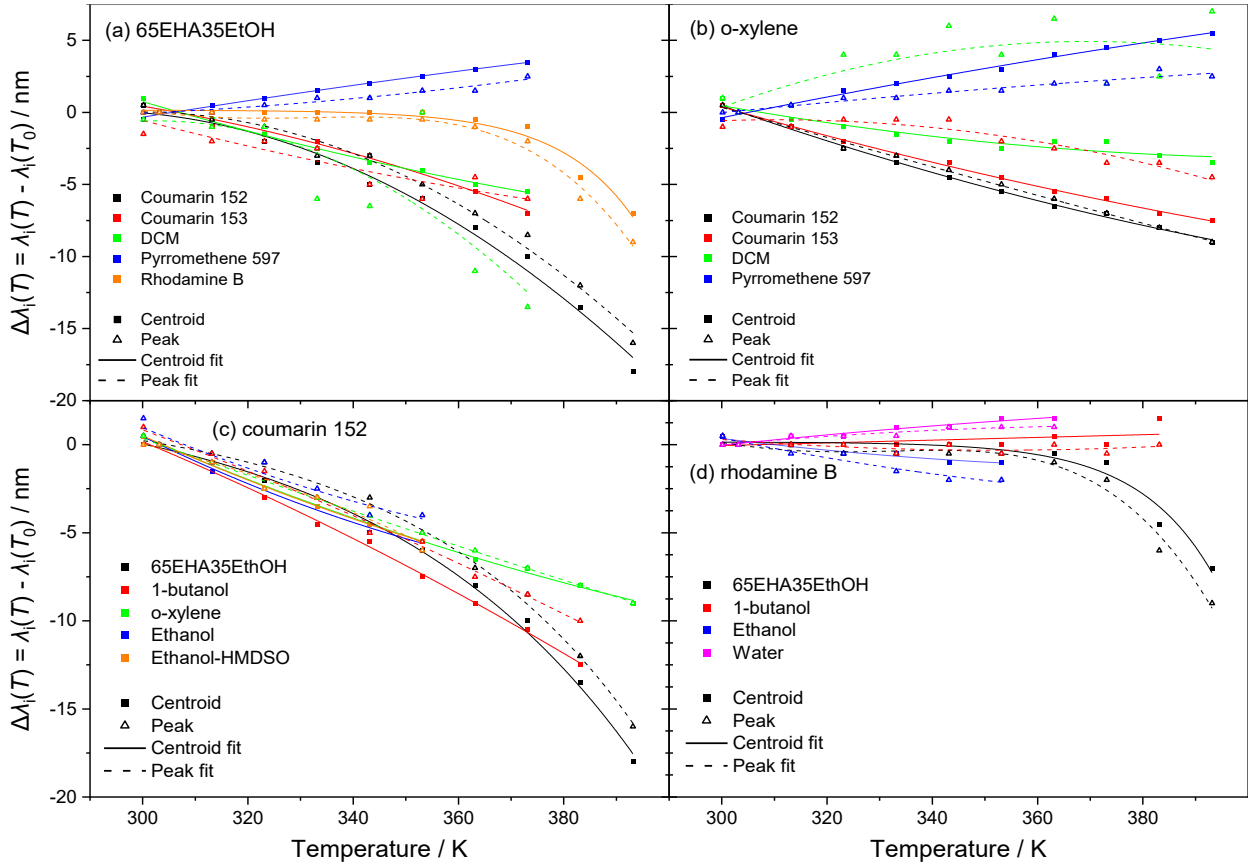


Figure 71: Shift of peak position and centroid ($\Delta\lambda_i = \lambda_i(T) - \lambda_i(T_0 = 303 \text{ K})$) of all investigated tracer fluorescence spectra (1 mg/l) dissolved in a) 65EHA35EtOH, b) o-xylene and c) coumarin 152, d) rhodamine B in various solvents: Dashed lines: Fit of peak positions, solid lines: Fit of centroid positions.

7.3.3 Temperature sensitivity for two-color LIF thermometry

Based on the measured fluorescence spectra an evaluation towards the best temperature sensitivity for liquid-phase 2cLIF thermometry was conducted. To evaluate the suitability of the tracers and to find the detection band positions with the highest temperature sensitivity, a systematic screening of all achievable spectral intensity ratios was performed by a Matlab[®] [232] software routine. After the bandwidth of the two spectral color bands was manually selected (in this investigation they were fixed to 10 and 40 nm, see Table 10–Table 12), the code calculates the color-band intensity ratios for all possible combinations of band positions (in increments of 0.5 nm) conditioned to the constraint that the integrated fluorescence intensity within each of the two color bands exceeds 10 % (an arbitrarily fixed value in the measured fluorescence spectra) of the fluorescence peak intensity (integrated within a 10-nm band). The resulting optimized color band positions provide the largest ratio change with temperature and thus the highest temperature sensitivity. In view of the fact that the ratios do not change linearly, the ratio change is given by the linear interpolated change in temperature intervals of 10 K averaged over the largest possible temperature range (e.g., for ethanol from 303 to 343 K). Accordingly, the temperature sensitivity is given as the average intensity-ratio change of the optimized color channels in percent per Kelvin.

For the tracers investigated here, the smaller the spectral band width in the detection channels and the lower the intensity constraints, the higher is the attainable temperature sensitivity. However, both trends decrease the signal-to-noise ratio and therefore the applicability needs

to be determined beforehand in the respective application to prevent data deterioration because of too weak signals, i.e., suffer temperature measurement accuracy.

The results are presented in Arrhenius-type plots as logarithmic intensity ratios normalized for the respective ratio at 303 K against the difference of inverse temperatures, where the steepness of the slope is a measure for the temperature sensitivity of the respective temperature tracer. Exponential fits of the ratios are plotted as solid lines. In this chapter results are shown for the chosen tracers dissolved in ethanol, 65EHA35EtOH and o-xylene. Overall, coumarin 152 exhibits the strongest slope of the intensity ratio, i.e., temperature sensitivity for all investigated solvents.

7.3.3.1 Fluorescent tracers dissolved in ethanol

For the solvent ethanol and assumed filter transmission bandwidths of 10 and 40 nm, the respective band positions resulting in the highest temperature sensitivity of the intensity ratio are shown in Table 10. Among the investigated tracers the coumarin dyes show generally high temperature sensitivities with coumarin 152 featuring the highest sensitivity. Besides the coumarin dyes and conditioned by their narrow fluorescence spectra, rhodamine B and DCM, excitable at 532 nm, show comparatively high temperature sensitivities for the small band width of 10 nm. While small band widths provide generally a higher temperature sensitivity as a result of a more specific selection of sensitive spectral ranges, broader band widths provide more detectable fluorescence signal and hence a better signal-to-noise ratio.

Table 10: Optimized detection band positions for two-color LIF thermometry of various tracers dissolved in ethanol. Underlying conditions of concentration, excitation wavelength, center wavelengths of the resulting best spectral band pairs are given. The resulting temperature sensitivity is given as the averaged change of the signal ratio per Kelvin in the temperature range from 303 to 343 K.

Tracer	Concentration / (mg/l)	Exc. wavelength / nm	Band width: 40 nm			Band width: 10 nm		
			Blue band / nm	Red band / nm	Ratio change / (%/K)	Blue band / nm	Red band / nm	Ratio change / (%/K)
Coumarin 47	10	355	398	514.5	1.32	403.5	508.5	1.73
Coumarin 102	10	355	417.5	553	1.45	423	552	1.9
Coumarin 120	10	355	383.5	459	1.23	389.5	451.5	1.81
Coumarin 152	1	355	447.5	634.5	1.61	451.5	632.5	1.89
Coumarin 153	10	355	471	630.5	1.53	475	632	1.84
DCM	1	532	555	665	1.06	547.5	654	1.52
p-Terphenyl	10	266	300	354	0.21	309	338	0.71
Pyridine 1	10	532	597.5	684	0.56	600	670	0.62
Pyromethene 597	1	532	563.5	681	0.56	559	679.5	0.65
Rhodamine 101	6.4	532	565.5	610	0.76	571.5	602	1.15
Rhodamine B	1	532	555	586	0.29	540	577	1.52
Stilbene 3	10	355	375	442	0.58	380.5	427.5	1.38

To illustrate in more detail the evolution of the temperature sensitivities of rhodamine B and coumarin 152 investigated here, Figure 72 presents for each tracer in the left column false-color plots of the change of the fluorescence intensity ratio, ΔR_{LIF} , in percent per Kelvin

temperature variation, against the respective center-wavelength positions for detection-channel filter bandwidths of 40 nm (coumarin 152, Figure 72a) and 10 nm (rhodamine B, Figure 72c). To simultaneously estimate the feasibility of a practical temperature measurement, the right column in Figure 72 depicts (in an exponential false-color scale) the respective fluorescence intensities recorded in the weaker detection channel of both, which in a more detailed investigation, i.e., considering intensity and detector noise contributing to the measured signal intensities, is an indication of the attainable overall measurement precision. The white circles in each plot mark the selected band positions for the sensitivity optimization of the two-color-LIF intensity ratio plots depicted in Figure 73. In this context, the dashed lines in the right column plots in Figure 72b and d mark the 10-% constraint in the detection channel intensities for the two-color intensity-ratio optimization procedure. As seen in Figure 73 the temperature sensitivity in the two-color LIF-ratio method is higher for coumarin 152 than for rhodamine B. It is also noteworthy that for rhodamine B with excitation at 532 nm the blue detection channel cannot access the region of higher sensitivity at shorter wavelengths – contrary to what was achieved by Lavieille et al. with excitation at 514 nm (detection band 1: $\lambda > 590$ nm and band 2: $\lambda_c = 530$ nm, with a bandwidth of 10 nm) [365].

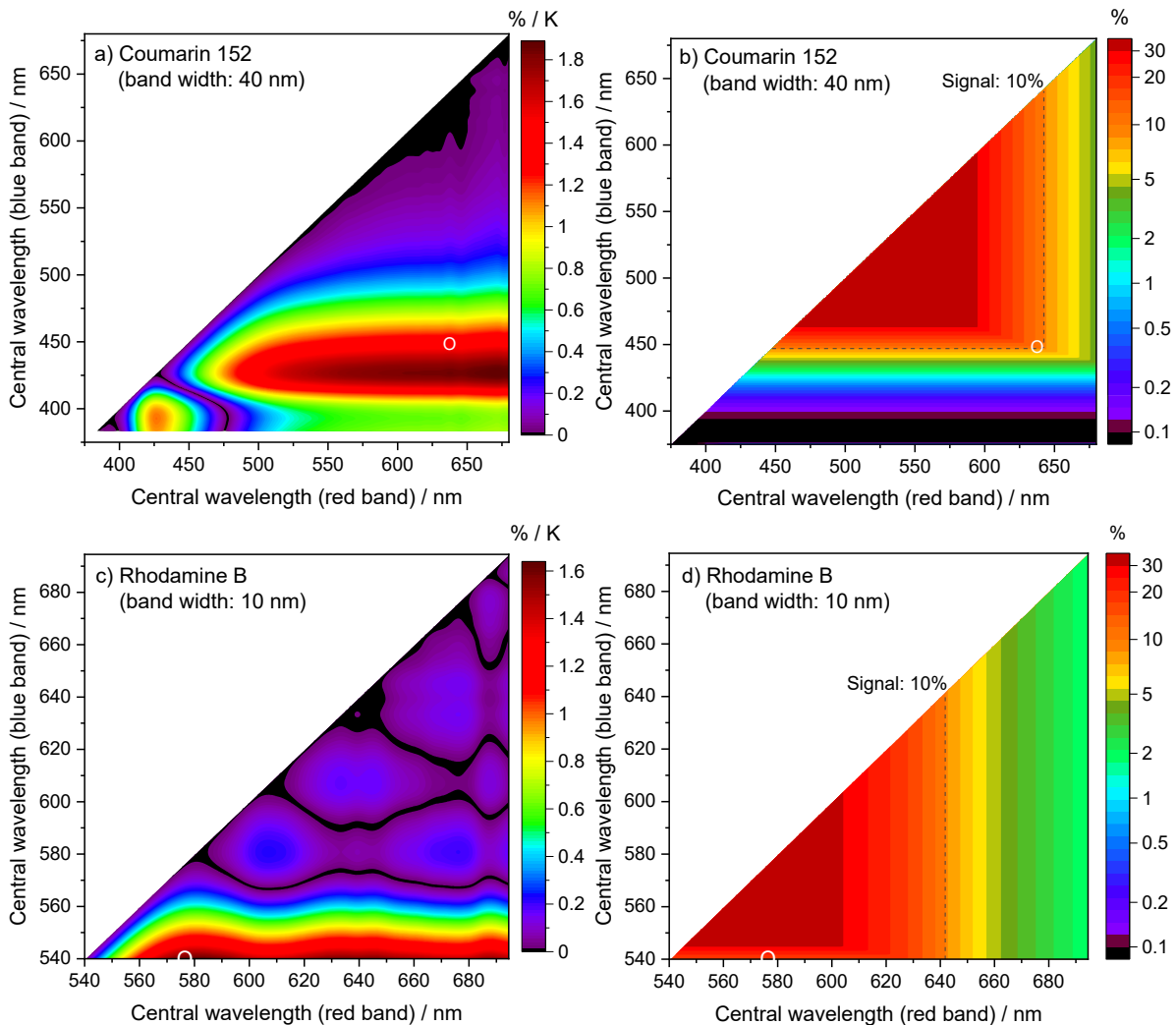


Figure 72: Left: Temperature sensitivity as ratio change in signal intensity in %/K. Right: Signal intensity as percentage of the peak signal intensity of the weaker channel, a) and b): Coumarin 152, c) and d): Rhodamine B.

The calculated highest intensity ratios (normalized at a reference temperature, $T_0 = 303$ K) for a selection of investigated tracers are presented in Figure 73 as Arrhenius-type plots. According to the normalized logarithmic ratios plotted against the difference of inverse temperatures the graphs should result in linear dependencies, whose slope is the difference of β between the selected color channels.

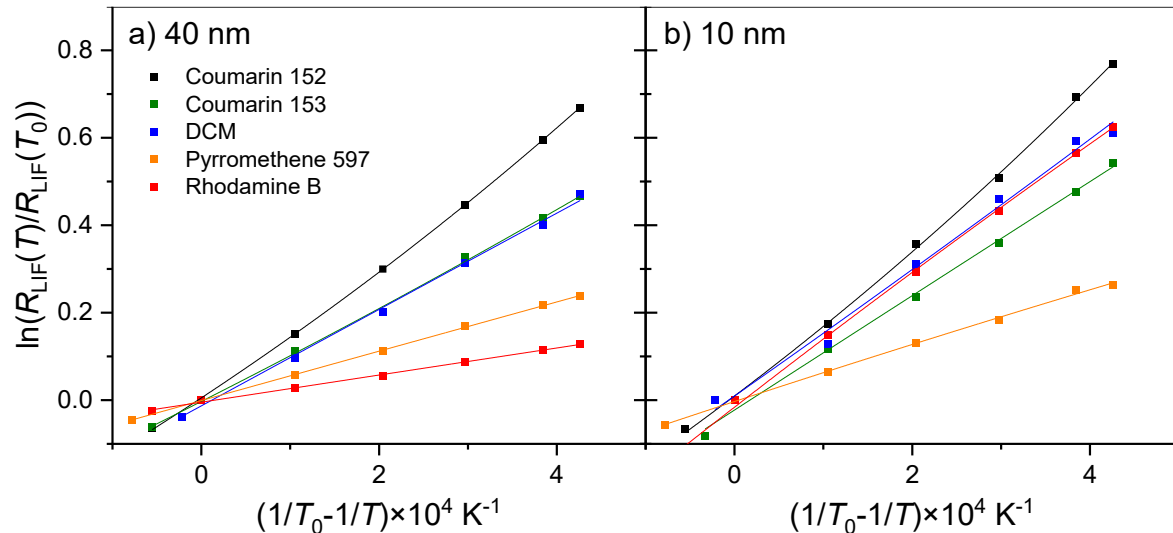


Figure 73: Calculated fluorescence intensity ratios (symbols) for selected tracers dissolved in ethanol, 1 mg/l, plotted as logarithmic ratios normalized at $T_0 = 303$ K vs. inverse temperature difference, solid line: Exponential fit of intensity ratios, assumed spectral bandwidths: a) 40 nm b) 10 nm, the chosen center wavelength positions of the “blue” and “red” filter combination are listed in Table 10; depicted temperature range: 298–348 K.

Under the above-mentioned experimental conditions and spectral detection constraints it can be derived from the diagrams for both spectral band widths that in case of excitation at Nd:YAG laser harmonics, coumarin 152 provides the strongest temperature sensitivity among the investigated tracers. Because of its narrow fluorescence spectra, rhodamine B shows a significantly higher temperature sensitivity for a spectral band width of 10 nm than for 40 nm. As known from the literature, higher temperature sensitivities are attainable for rhodamine B in case of excitation at wavelengths shorter than 532 nm because the mostly temperature independent spectral region located at 520–540 nm becomes accessible [365]. Since a pulsed Nd:YAG laser is preferable for future single-shot two-color LIF measurements, the tracer coumarin 152 and corresponding filters with a FWHM of 40 nm will be utilised in section 8.1 for temperature imaging in the SpraySyn flame. The approach to calibrate the corresponding signal-ratio-temperature function for this filter set and the measurement setup used is described in more detail in section 8.1.2.1.

7.3.3.2 Fluorescent tracers dissolved in 65EHA35EtOH

Table 11 shows the optimized spectral color-channel positions and the resulting temperature sensitivity for five tracers investigated in the solvent mixture 65EHA35EtOH. In the considered temperature range of 303 to 373 K coumarin 152 features the highest temperature sensitivity after excitation at 355 nm, while after excitation at 532 nm DCM shows the highest temperature sensitivity. There is a general range for the optimal color band positions (usually the outer region of a spectrum) which is limited to the inner spectral regions due to the pre-defined threshold color band intensity. With regard to the calculated optimized color band positions presented in Table 11 it is observed that these do not change significantly with the choice of

the pre-defined bandwidth. Among the investigated tracers and solvents there is always a trade-off between temperature sensitivity and signal-to-noise ratio.

Table 11: Optimized detection band positions for two-color LIF thermometry. Tracer concentration: 1 mg/l in 65EHA35EtOH, excitation wavelength, center wavelengths of the resulting best spectral band pairs. The resulting temperature sensitivity is given as the averaged change of the signal ratio per Kelvin in the temperature range from 303 to 373 K.

Tracer	Exc. wave-length / nm	Bandwidth: 40 nm			Bandwidth: 10 nm		
		Blue band / nm	Red band / nm	Ratio change / (%/K)	Blue band / nm	Red band / nm	Ratio change / (%/K)
Coumarin 152	355	436	612.5	1.82	439.5	624.5	2.09
Coumarin 153	355	473.5	655	0.87	479.5	663.5	1.01
DCM	532	555	653.5	0.88	540	643.5	1.61
Pyromethene 597	532	564	680	0.56	560.5	680.5	0.61
Rhodamine B	532	554	586	0.38	543.5	579	1.49

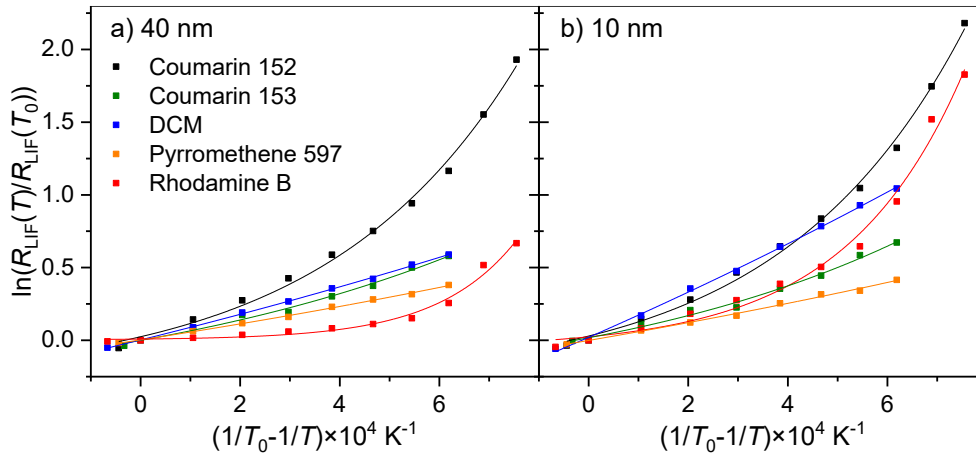


Figure 74: Calculated fluorescence intensity ratios (symbols) for various tracers dissolved in 65EHA35EtOH, 1 mg/l, plotted as logarithmic ratios normalized at $T_0 = 303$ K vs. inverse temperature difference, solid line: Exponential fit of intensity ratios, assumed spectral bandwidths: a) 40 nm b) 10 nm, the chosen center wavelength positions of the “blue” and “red” filter combination are listed in Table 11; depicted temperature range: 298–393 K.

As can be seen from Figure 74, coumarin 152 shows the highest temperature sensitivity for both color bandwidths. Because of the much narrower fluorescence spectrum, the temperature sensitivity of rhodamine B is significantly higher for bandwidths of 10 nm. In the case of smaller bandwidths, the best spectral ranges can be selected more specifically, whereas in the case of broader bandwidths the color band inevitably includes regions which are less temperature sensitive. Pyromethene 597 shows the overall lowest temperature sensitivity. Coumarin 153, DCM, and Pyromethene 597 show an almost linear behavior in the temperature range investigated here, whereas in the cases of coumarin 152 and rhodamine B clearly a strong non-linear behavior can be observed. The temperature sensitivity of the two tracers in the solvent 65EHA35EtOH increases significantly at higher temperatures, as can be seen in Figure 74 from the exponentially increasing normalized intensity ratio. Hence, in this case, temperature measurements at higher temperatures are more sensitive.

7.3.3.3 Fluorescent tracers dissolved in o-Xylene

For all tracers, the fluorescence spectra in o-xylene were measured from room temperature up to 393 K. Rhodamine B is excluded in this investigation because of its poor solubility in o-xylene. As described in the appendix 12.6.2.2 (Figure A37), DCM was excited at 355 nm due to its low absorption at 532 nm. The results are presented in Table 12.

Table 12: Optimized detection band positions for two-color LIF thermometry. Tracer concentration: 1 mg/l in o-xylene, excitation wavelength, center wavelengths of the resulting best spectral band pairs. The resulting temperature sensitivity is given as the averaged change of the signal ratio per Kelvin in the temperature range from 303 to 373 K.

Tracer	Exc. wave-length / nm	Bandwidth: 40 nm			Bandwidth: 10 nm		
		Blue band / nm	Red band / nm	Ratio change / (%/K)	Blue band / nm	Red band / nm	Ratio change / (%/K)
Coumarin 152	355	416	553	1.20	410.5	551	2.68
Coumarin 153	355	426	578.5	1.57	432	580	2.05
DCM	355	503	583.5	0.80	496	588	1.78
Pyrrromethene 597	532	565	680.5	0.55	561.5	680.5	0.59

As Figure 75 shows, coumarin 153 (for a bandwidth of 40 nm) and coumarin 152 (for a bandwidth of 10 nm) show the overall highest temperature sensitivity. It is also seen in the Arrhenius-type plots, that for o-xylene (in contrast to 65EHA35EtOH) all investigated tracers show a close to linear increase of the normalized intensity ratio with temperature, i.e., constant temperature sensitivity. The temperature sensitivity of coumarin 153 is significantly higher than in 65EHA35EtOH, and pyrrromethene 597 again shows the lowest temperature sensitivity of all tracers investigated here.

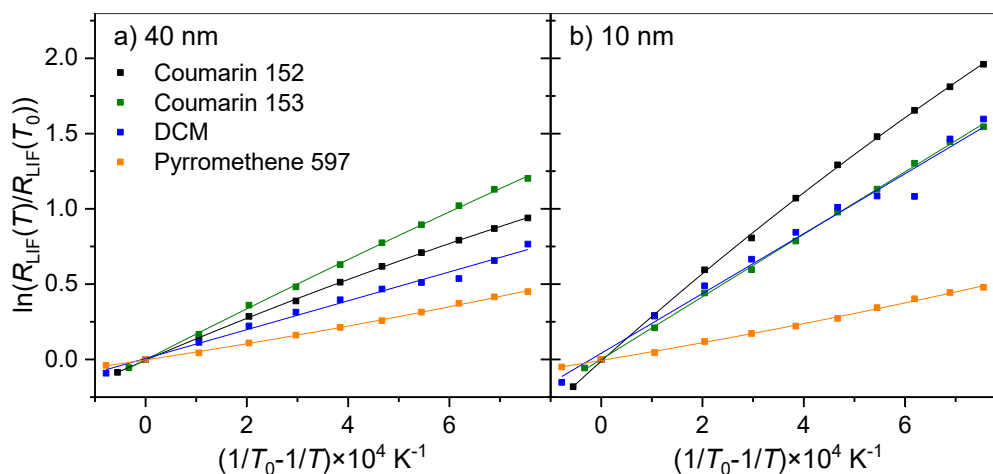


Figure 75: Calculated fluorescence intensity ratios (symbols) for various tracers dissolved in o-xylene, 1 mg/l, plotted as logarithmic ratios normalized at $T_0 = 303$ K vs. inverse temperature difference, solid line: Exponential fit of intensity ratios, assumed spectral bandwidths: a) 40 nm b) 10 nm, the chosen center wavelength positions of the “blue” and “red” filter combination are listed in Table 12; depicted temperature range: 298–393 K.

7.3.4 Fluorescence signal re-absorption

7.3.4.1 Concentration dependence of the fluorescence spectra of rhodamine B and coumarin 152 in ethanol

From section 7.3.1 (also cf. appendix 12.6.4) it is clear that the absorption and fluorescence spectra of rhodamine B overlap significantly [365, 395], whereas for coumarin 152 this is much less the case. Signal re-absorption was already described for rhodamine B by Lavieille et al. [376] who were able to correct this drawback with a three-color detection technique by forming signal ratios between LIF intensities measured in a temperature-insensitive channel and in two temperature-sensitive channels with and without suffering from fluorescence signal trapping, respectively.

To investigate the impact of re-absorption for coumarin 152 and rhodamine B, fluorescence spectra were recorded in $10 \times 10 \text{ mm}^2$ cuvettes, where the optical path length of fluorescence light through the tracer-doped liquid is about 5 mm in the standard 90° excitation/detection geometry. Additionally, fluorescence measurements were done under the same conditions using thin-layer cuvettes in a front-illuminating geometry (a 22.5° angle between excitation and detection light paths) providing path lengths of 50 and 100 μm depending on the thickness of the cuvette. This latter variation of path lengths is similar to the spray measurements described in chapter 8 with small and sparse droplets in the measurement volume.

The fluorescence spectra for the two measurement configurations are presented in Figure 76 for concentrations starting at 0.5 mg/l (coumarin 152) and 0.1 mg/l (rhodamine B), spanning a factor of 100. All spectra were measured at 303 K and are plotted for the 5 mm absorption path-length and the thin layer cuvettes with solid and dashed lines, respectively. The spectra are normalized at a wavelength where no overlap exists with the absorption spectra (i.e., 600 and 630 nm for coumarin 152 and rhodamine B, respectively). For comparison, the respective absorption spectra in the spectral overlap region of interest are plotted on a separate y-axis. The spectra illustrate the effect of fluorescence re-absorption in the spectral regions where significant overlap with the absorption spectrum exists. Due to its large Stokes shift, the spectrum of coumarin 152 is largely unaffected, while for rhodamine B there is an apparent spectral shift and attenuation of the peak, depending on the concentration and/or re-absorption path length through the sample.

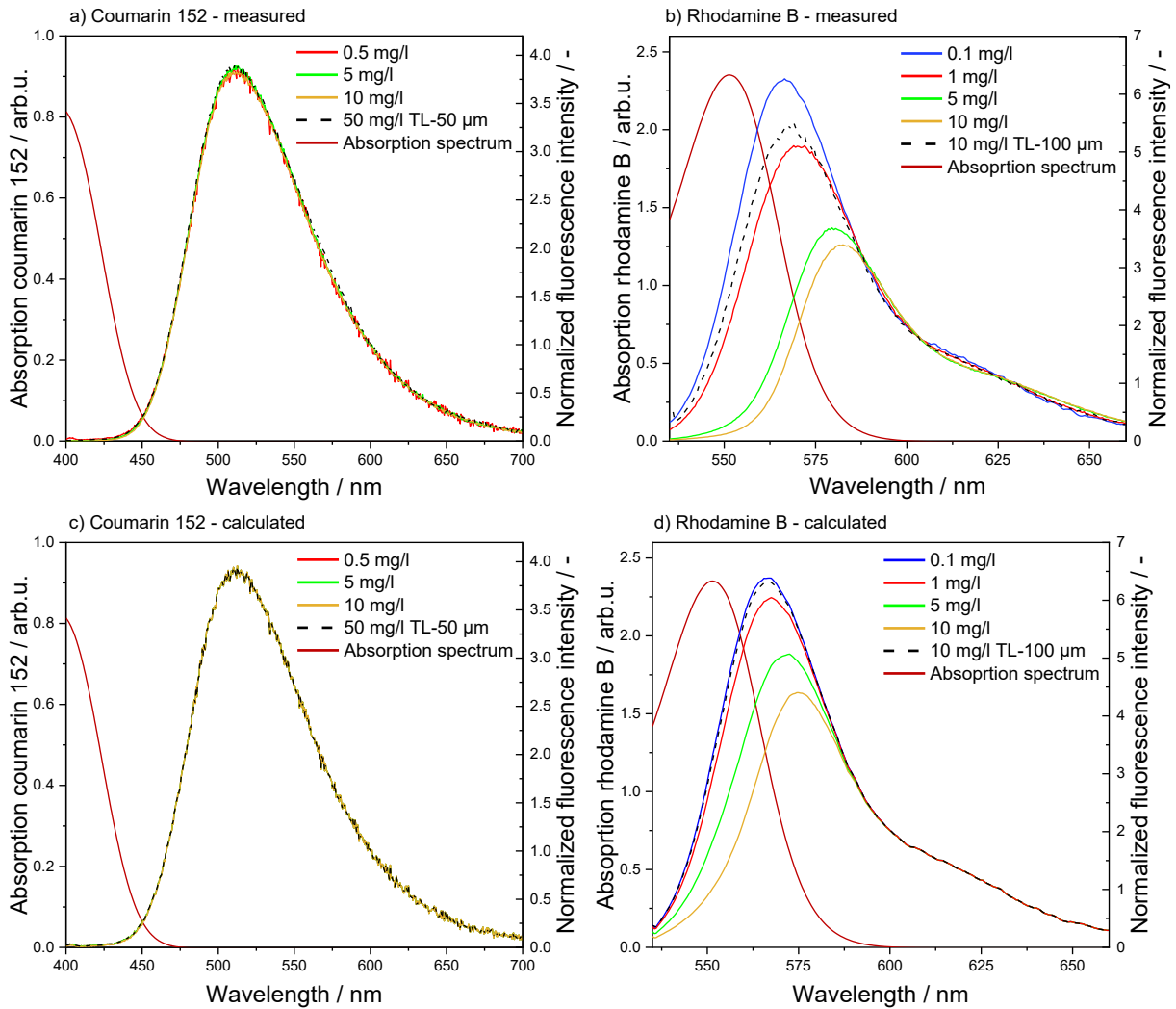


Figure 76: Top: Measured fluorescence spectra of coumarin 152 (a) and rhodamine B (b) for samples at various concentrations and re-absorption path lengths (5 mm within a $10 \times 10 \text{ mm}^2$ cuvette (solid lines), or a thin layer cuvette (50 μm (a, c), or 100 μm (b, d), (dashed lines)) at 303 K: The spectra are normalized at 600 nm (a, c) and at 630 nm (b, d), respectively. Bottom: Calculated fluorescence spectra of coumarin 152 (c) and rhodamine B (d) using a simple re-absorption model (see text)

Even for small optical path lengths like 100 μm , a reduction of the detected fluorescence intensity and a red shift of the spectra of rhodamine B can be observed whereas for coumarin 152 this is not measurable. It can be concluded that for the two-color LIF thermometry method with considerable absorption path lengths or comparatively high tracer concentration changes, coumarin 152 with its large Stokes shift significantly reduces the measurement error caused by re-absorption effects.

The measured results agree reasonably well with a simple model calculation of fluorescence spectra affected by re-absorption. This is illustrated by the lower row of graphs in Figure 76, which shows spectra scaled according to the re-absorption effects at the same concentrations and absorption path lengths as given in the experiments. The calculations were done under the simplifying assumptions that the fluorescence signal linearly scales with dye concentration (ignoring quenching effects) and that the excitation light intensity at the probe volume is the same for all concentrations. The fluorescence spectra generated in solutions with higher tracer concentrations were calculated from the measured low-concentration spectra using the Beer-Lambert law

$$I_{\text{fluo}} = I_{\text{fluo},0} \exp(-\varepsilon_{\lambda} c l_{\text{abs}}) \quad (7.7)$$

with the detected fluorescence intensity I_{fluo} , the initial fluorescence intensity $I_{\text{fluo},0}$, the molar attenuation coefficient ε_{λ} , the dye concentration c and the assumed absorption path length l_{abs} , through the tracer-doped liquid towards the detector. The molar attenuation coefficient ε_{λ} was measured for coumarin 152 at 396 nm with 2.1×10^4 l/(mol cm) and for rhodamine B at 552 nm with 11.2×10^4 l/(mol cm) which is very close to the values given by Brackmann [396]. The results of this simple model are presented in the lower row of Figure 76 (for coumarin 152 (c) and rhodamine B (d)). It can be observed that for rhodamine B the measured peak reduction and the resulting apparent peak shift in the measured fluorescence spectra is larger than suggested by the calculated results, whereas for coumarin 152 the spectra are virtually unaffected by re-absorption effects.

Overall, since this simplified model confirms the trends observed in the experiments in the investigated concentration range, the calculations prove that the change of the fluorescence spectra is mainly driven by re-absorption, and not caused by tracer–tracer interactions. Due to the increased re-absorption of fluorescence radiation in the blue wing of the rhodamine B spectra, there is an apparent shift in the normalized fluorescence peak to longer wavelengths, which will predominantly affect the “blue” fluorescence channel – and thus the fluorescence ratio used for the two-color thermometry. The results also suggest that, because this effect is negligible for coumarin 152, it makes this tracer a promising candidate for temperature measurements in spatially extended evaporating sprays with variation in concentration (cf. section 8.1.4) or in tracer-doped fluids in large-scale containers with significant re-absorption path lengths.

7.3.4.2 Fluorescence signal re-absorption in evaporating ethanol droplets: Temperature measurement error

To assess the impact of fluorescence signal re-absorption for 2cLIF temperature measurements for applications in, e.g., spray flames, the measurement error was calculated caused by re-absorption in spherical evaporating ethanol droplets of different initial diameter and tracer concentration. The calculations are an extension of our model calculations presented in the previous section 7.3.4.1 and are based on the Lambert-Beer law as given in equation (7.7). For the initial fluorescence intensity and the determination of the molar attenuation coefficients, measured spectra were used, which were verified by data given by Brackmann [396]. Neglecting reflections within the droplet, the average fluorescence signal path length through the liquid was assumed as the droplet radius. Considering a tracer-doped ethanol droplet in a spray flame: With progressing evaporation, its radius decreases and hence the tracer concentration increases. Originating from the fact that the concentration increases significantly stronger than the radius of the droplet decreases, the fluorescence signal re-absorption increases with progressing droplet evaporation (cf. equation (7.7)). This would cause an increasingly lower detected fluorescence intensity in chosen 2cLIF color bands located in the spectral range of the overlap region of absorption and fluorescence spectrum (see, e.g., Figure 65 for the case of rhodamine B). With progressing droplet evaporation this consequently leads to color band intensity ratios different from the ones derived from spectra measured for more dilute solutions, and hence to increased temperature measurement errors.

To achieve a sufficient signal-to-noise ratio in measurements, the tracer concentration needs to be adjusted according to its fluorescence quantum yield. For the present estimation of

temperature error this was not taken into consideration; the temperature dependence of the fluorescence quantum yield and possible detection band widths (trade-off with good temperature sensitivity) were also not included. Furthermore, reflections within the droplet and additional droplets within the signal path between the considered droplet and the detector were not taken into account. The calculation results of rhodamine B (large spectral overlap) and coumarin 152 (small spectral overlap) are presented in Figure 77. The measurement error caused by fluorescence signal re-absorption is plotted against the droplet diameter. Various application-related initial droplet diameters (15–100 μm) [397] and tracer concentrations (1–20 mg/l) were considered. Once the laser dye reaches its maximum solubility, it precipitates as a solid and is anticipated to decompose in the flame without generating additional fluorescence. The maximum solubility of the laser dye is a limit for the measurement error. Since the maximum solubility of the laser dyes investigated in this study is unknown to us, as an indication, dye concentrations >50 g/l are plotted as dashed lines in Figure 77 and Figure 78.

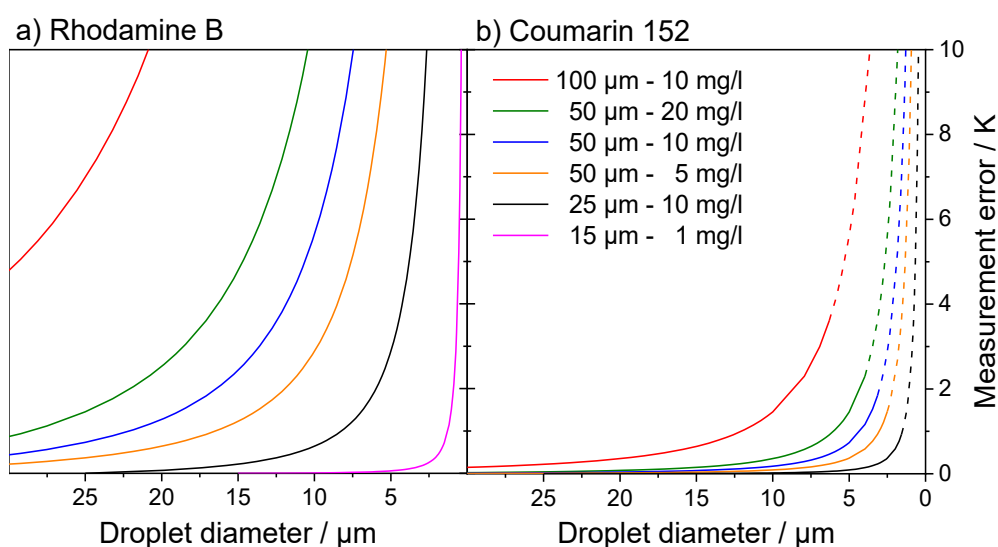


Figure 77: Measurement error caused by fluorescence re-absorption vs. droplet diameter; given in the legend are the initial droplet diameter and the initial tracer concentration, a) rhodamine B and b) coumarin 152 dissolved in ethanol. Assumed detection bandwidths: 10 nm, dashed lines: Tracer concentration exceeding 50 g/l.

It can be seen from the diagrams that for fixed starting parameters of droplet size and tracer concentration, the ratio-based temperature error increases exponentially with decreasing droplet diameter. Larger initial droplet diameters and higher initial tracer concentrations cause larger measurement errors during the droplet evaporation process. The impact of fluorescence signal re-absorption on the measurement accuracy is significantly larger for rhodamine B in comparison to coumarin 152 originating from the larger spectral overlap of absorption and fluorescence spectra, which includes regions where the optimized color detection channels are located. Three-color ratio techniques [376] have been developed to circumvent this diagnostic deficiency, but are experimentally more involved. In order to minimize the measurement error caused by fluorescence signal re-absorption within evaporating droplets in general a low tracer concentration (e.g., achievable with tracers having high fluorescence quantum yields) and tracers with small spectral overlaps are beneficial.

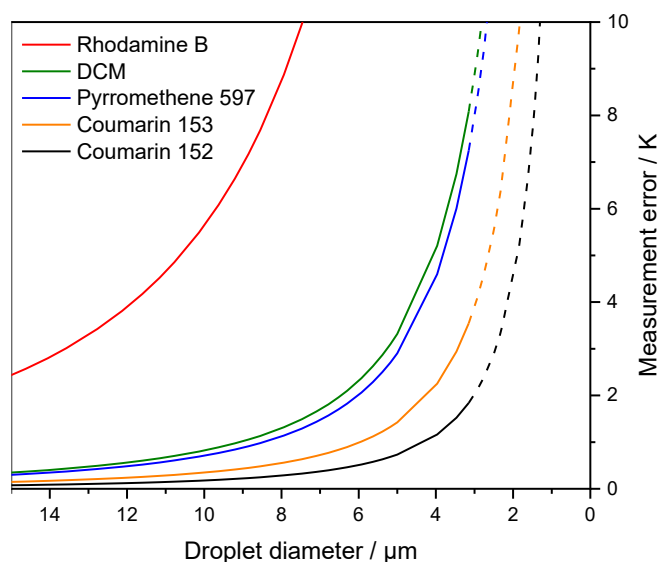


Figure 78: Measurement error caused by fluorescence signal re-absorption vs. droplet diameter, initial droplet diameter: 50 μm , initial tracer concentration: 10 mg/l, chosen tracers dissolved in ethanol. Optimized detection bandwidth: 10 nm, dashed lines: Tracer concentration exceeding 50 g/l.

Figure 78 shows the developing temperature error for the tracers investigated in this work for fixed initial droplet conditions, where the tracers are dissolved with a concentration of 10 mg/l in an ethanol droplet with a diameter of 50 μm . It can be seen that the coumarin tracers exhibit the smallest measurement error due to re-absorption and rhodamine B the highest. Among the tracers excitable at 532 nm pyrromethene 597 shows the smallest error.

7.3.5 Spectral influence of solvent composition

In this chapter, the effect on the fluorescence spectra is investigated when chosen tracers are dissolved in a solvent mixture composed of two components of varying amount typically present in spray-based nanoparticle synthesis flames, where 2cLIF liquid-phase temperature measurements may be applied. Related research to this topic was published by [378, 393, 398]. Changes in spectral signature with varying solvent-mixture composition which interfere with spectral shifts caused by temperature changes induce measurement errors to 2cLIF thermometry. Thus, the lowest possible spectral variation of tracer fluorescence spectra with solvent compositions is desired for 2cLIF thermometry.

Figure 79 shows the normalized fluorescence spectra of coumarin 152, rhodamine B and pyrromethene 597 (columns) dissolved in solvent mixtures of EHA/ethanol, HMDSO/ethanol, H₂O/ethanol (rows). The shown spectra were all recorded with 355 nm excitation. To verify for possible impacts due to another excitation wavelength, the fluorescence spectra of rhodamine B and pyrromethene 597 were also recorded with 532 nm excitation (not shown) without any noticeable spectral difference as a result of the different excitation wavelength. The black arrows in Figure 79 indicate the direction of the spectral shift with increasing solvent fraction of EHA, HMDSO and H₂O. A general statement to the spectral shift direction linked to the solvent or the laser dye cannot be made.

Further fluorescence spectra of laser dyes (coumarin 153, coumarin 47, DCM, pyrromethene 567, stilbene 3 and PTP) in various mixing ratios of EHA/ethanol are presented in the appendix in section 12.6.3. Among these tracers, DCM features the strongest spectral shift while pyrromethene 567 shows the smallest.

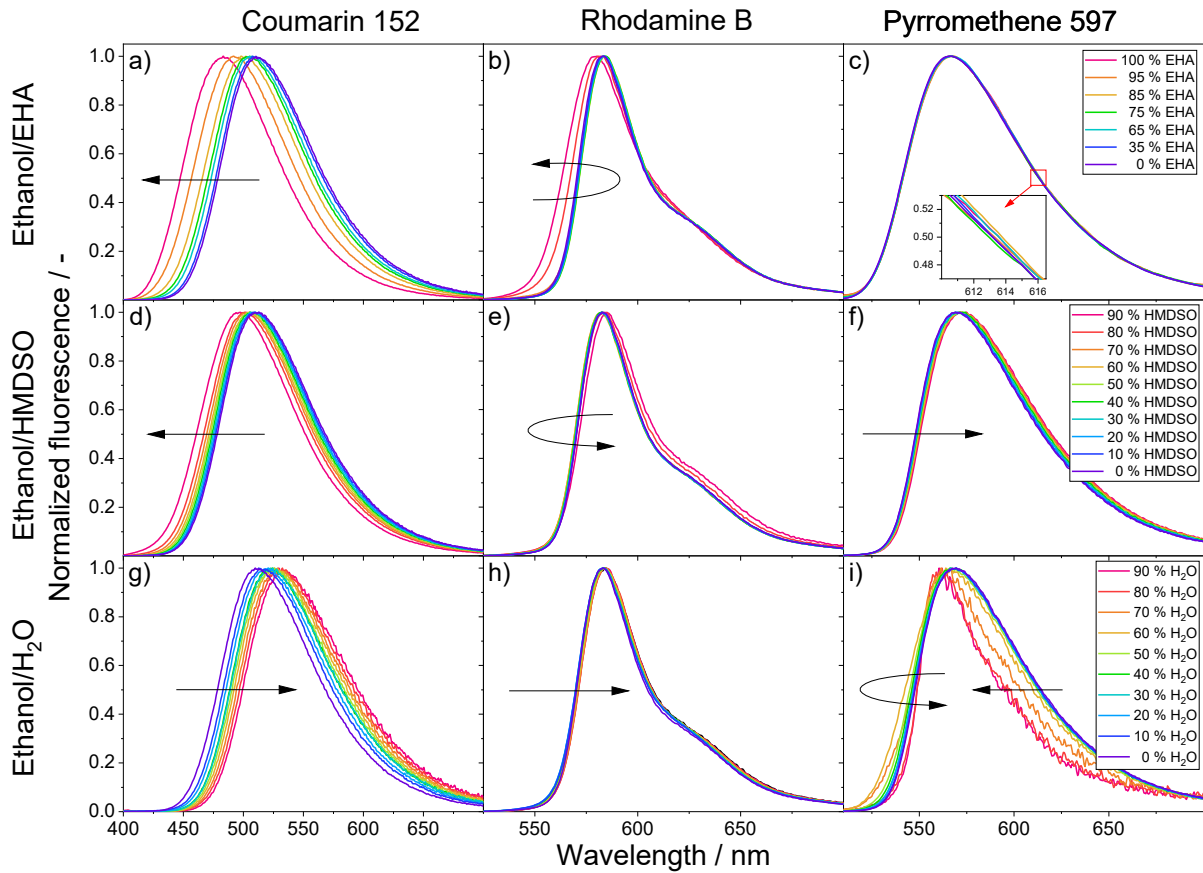


Figure 79: Normalized fluorescence spectra of 10 mg/l coumarin 152, rhodamine B and pyromethene 597 dissolved in different solvent mixtures at various volume fractions; excitation wavelength: 355 nm, temperature: 298 K. The arrows indicate the spectral shift with increasing solvent fraction of EHA, HMDSO, and H₂O.

7.3.5.1 Solvent mixture: EHA/ethanol

The mixture of 65 vol.% EHA and 35 vol.% ethanol is commonly used as a solvent for metal-nitrate precursors in spray-flame based nanoparticle synthesis [154, 156]. To measure the liquid-phase temperature of this evaporating fuel composition, a tracer is desired, whose fluorescence spectrum is not affected by preferential evaporation processes inside this two-component mixture. Since the vapor pressure of ethanol is significantly higher than that of EHA (EHA: <1 Pa, ethanol: 5.9 kPa at 20 °C), a strong increase in volume fraction of EHA is expected during evaporation. Figure 79a–c shows the fluorescence spectra of coumarin 152, rhodamine B and pyromethene 597 dissolved in mixtures of various EHA/ethanol fractions. As can be seen from the diagrams, a change in solvent composition of EHA/ethanol causes a strong blueshift for coumarin 152 (Figure 79a) with increasing fractions of EHA whereas pyromethene 597 (Figure 79c) is not detectably affected (see inset). The fluorescence spectra of rhodamine B (Figure 79b) show a slight redshift up to a volume fraction of 60 % EHA, which turns with higher EHA fractions into a strong blueshift. From these results it can be concluded, that coumarin 152 and rhodamine B are no suitable temperature tracers for this two-component solvent since the described spectral shift is clearly predominant compared to the spectral shift caused by temperature changes. In contrast, pyromethene 597 is well-suited for this application case due to its independence of the fuel composition. Similar results were reported by Deprédurand et al. [393], who did a spectroscopic study on pyromethene 597-8C9 in multi-component fuels and successfully performed droplet-temperature measurements of ethanol/3-

pentanone mixtures in a heated-air environment. Unfortunately, this tracer exhibits a comparatively low temperature sensitivity (cf. chapter 7.3.3.2) and is more affected by fluorescence signal re-absorption than the coumarin tracers.

7.3.5.2 Solvent mixture: HMDSO/ethanol

For the spray-flame synthesis of silica nanoparticles, one common precursor is HMDSO (hexamethyldisiloxane) dissolved in ethanol which provides the liquid mixture in the spray combustion process [28]. Because of the slightly different vapor pressures (HMDSO: 44 hPa, ethanol: 59 hPa at 20 °C) a variation of the fractional composition during the combustion process cannot be excluded. A comparison of the resulting fluorescence spectra of coumarin 152, rhodamine B and pyromethene 597 in HMDSO/ethanol is shown in Figure 79d–f. With an increasing amount of HMDSO the fluorescence spectra show either a blueshift (coumarin 152), a redshift (pyromethene 597), or a mix of both (rhodamine B). In consequence of partial evaporation of one of the components during the heat-up phase of the solution in a spray flame, the spectral shift with solvent composition will affect the accuracy of the 2cLIF temperature measurements. For the here considered example of coumarin 152, a change in the solvent fraction from 90 % ethanol and 10 % HMDSO to 50 % ethanol and 50 % HMDSO would cause a ratio change by a factor of 1.8 (using the optimized color band positions for the first mentioned case). This would correspond to a temperature bias of 43.7 K.

7.3.5.3 Solvent mixture: H₂O/ethanol

The solvent mixture of ethanol and water is relevant in the context of spray flame based nanoparticle synthesis because dissolved metal nonahydrates (e.g., iron(III) nitrate nonahydrate) release water when mixed with a fuel, e.g., ethanol. Due to a difference in vapor pressure (H₂O: 23.4 hPa, ethanol: 59 hPa at 20 °C) a change of solvent fraction towards a higher water content is expected. In contrast to the strong blueshift of coumarin 152 in the other solvent mixtures presented in Figure 79a,d, the spectra in H₂O/ethanol show a strong redshift (Figure 79g). The fluorescence spectra of rhodamine B (Figure 79h) shift slightly to longer wavelength with increasing water fraction. Pyromethene 597 (Figure 79i) exhibit a declining fluorescence-signal intensity with increasing water fractions. A general spectral response which is associated with a respective solvent due to the changing solvent mixture cannot be determined.

7.4 Discussion

The present work shows that the best suitable tracer for 2cLIF thermometry in liquids depends on the specific application. For measurements with single-component liquids, all investigated tracers can be used (with a ranking in temperature sensitivity of selected tracers of coumarin dyes, DCM, rhodamine B, and pyromethene 597). They exhibit different temperature sensitivities depending on the solvent. In general, coumarin 152 exhibits the highest temperature sensitivity, rhodamine B only features a high temperature sensitivity when using a narrow blue color band, and pyromethene 597 shows the lowest temperature sensitivity compared to the tracers presented in this work. Another issue for tracer suitability is the need for large absorption cross-sections at available laser excitation wavelengths to provide sufficient fluorescence signal with a low desired concentration. With a view to the desired temperature measurements, rhodamine B, pyromethene 597, and DCM have the disadvantage that their fluorescence quantum yield strongly decreases with rising temperatures (Figure 65, Figure 68, and Figure A35), which will necessitate higher tracer concentrations for measurements at higher

temperatures. In contrast, the fluorescence quantum yield of the coumarin dyes (Figure 62 and Figure A32) tend to rise with temperature, although from a lower level compared with rhodamine B (Table A4).

The extent of fluorescence signal re-absorption is another factor that can affect the tracer performance for 2cLIF thermometry. Choosing tracers with a small overlap between absorption and fluorescence spectra reduces errors resulting from variations in tracer concentration and/or from variations in path length through tracer-doped liquid. We have shown in this work that the investigated coumarin tracers exhibit very low re-absorption while rhodamine B is strongly affected due to the large overlap of its absorption and fluorescence spectra. To reduce signal re-absorption, a preferably low tracer concentration is essential, which favors tracers with high fluorescence quantum yield.

In systems where the solvent consists of more than one component with different evaporation characteristics, a tracer needs to be preferably unaffected by changes in the solvent composition. For the specific cases aimed for spray-flame synthesis of oxide nanoparticles, the results show that for the EHA/ethanol solvent mixture, coumarin 152 is not suitable since the spectral shift caused by a change in composition dominates over that caused by the temperature variation. In this respect, pyromethene 597 turned out to be much less affected by a compositional change and might be well-suited for this thermometry method, although, its comparatively low temperature sensitivity and sizeable signal re-absorption limits its applicability. It is therefore obvious, that a global estimation of tracer performance is essential when choosing a suitable tracer for the 2cLIF thermometry method, taking into account all mentioned aspects under the specific limitations of the application case, before a meaningful temperature measurement can be performed.

Excitation at different Nd:YAG laser harmonics did not show any spectral impact on the fluorescence spectra of the fluorescent tracers investigated in this study. Merely due to a different absorption cross-section at the respective excitation wavelengths, a change in the fluorescence intensity was observed. The comparison of measured laser-dye fluorescence spectra in various solvents shows that there is no general impact on the spectral shift direction or magnitude which can be linked to the solvent (Figure 71). Also, for the laser dyes dissolved in various compositions of dual-component solvents, a statement on the general shift direction or impact on the spectra cannot be made (Figure 79 and Figure A38).

The spectral shift of organic dyes with changing solvent compositions enables the possibility of concentration measurements of two-component solvents based on the spectral signature using the two-color LIF approach. For this application a strong, preferably constant spectral shift of the fluorescence spectra with the mixing ratio is desired. On the other hand, spectral changes as a result of temperature changes should be as low as possible. One possible application of this approach is the spatially and temporally resolved investigation of mixing processes of two liquids with the determination of local liquid compositions. For this application case with long fluorescence signal path lengths, low fluorescence signal re-absorption is prerequisite.

7.5 Conclusions

The absorption and fluorescence spectra of various tracers (most notably: Coumarin 152, coumarin 153, DCM, pyrromethene 597 and rhodamine B) were investigated for the impact of changes in temperature, concentration, excitation wavelength, type and solvent composition. The tracers were selected for their high fluorescence quantum yield after excitation by harmonics of Nd:YAG lasers (266, 355, 532 nm) that would be able to generate signal strong enough for single-shot measurements in liquids. The applicability of the laser dyes as tracer for liquid phase two-color laser-induced fluorescence (2cLIF) temperature measurements was assessed. The focus was on temperature sensitivity and the effect of fluorescence signal re-absorption and changes of solvent composition on the measurement accuracy. The results show that temperature sensitivity and signal re-absorption effects strongly depend on the tracer and solvent. The influence of varying solvent composition can lead to spectral changes and hence to significantly decreasing measurement accuracies. On the other hand – provided that the temperature stays constant – the spectral changes due to different solvent compositions provide the potential for solvent composition measurements.

Among the investigated tracers, coumarin 152 was found to be best suitable as tracer for 2cLIF in the examined single-component liquids related to temperature imaging in spray flames. For the two-component solvent EHA/ethanol, pyrromethene 597 turned out to be best suitable because its fluorescence spectra are independent towards composition changes. Coumarin 152 can be dissolved in all examined solvents (in water poor solubility) and exhibits the highest temperature sensitivity for all considered solvents. With respect to the transmissivity of the used solvents it is excitable by Nd:YAG lasers at 266 or 355 nm and just like the other tracers proved stable against temperature up to at least 393 K. Compared to the other tracers, the detectable fluorescence spectra of coumarin 152 are significantly less affected by concentration changes or fluorescence path length variations in the liquid phase (lowest fluorescence signal re-absorption due to a large Stokes shift). This leads to a significantly higher measurement accuracy for our desired application in spray flames.

8 Liquid-phase temperature imaging in the SpraySyn flames with two-color tracer LIF

Some sections of the following chapter are reprints or else contain contents from the listed publications:

M.M. Prenting, M.I. Bin Dzulfida, T. Dreier, C. Schulz, Characterization of tracers for two-color laser-induced fluorescence liquid-phase temperature imaging in sprays, *Exp. Fluids* 61 (2020) 77.

<https://doi.org/10.1007/s00348-020-2909-9>

© Springer-Verlag GmbH Germany, part of Springer Nature 2020. Reprinted with permission.

M.M. Prenting, S.-J. Baik, T. Dreier, T. Endres, A. Kempf, C. Schulz, Liquid-phase temperature in the SpraySyn flame measured by two-color laser-induced fluorescence thermometry and simulated by LES, *Proc. Combust. Inst.* 39 (2023) 2621-2630.

<https://doi.org/10.1016/j.proci.2022.07.131>

© 2022 The Combustion Institute. Published by Elsevier Inc. Reprinted with permission.

My contributions to the publications were the design and setup of the experiment, execution of the measurements supported by students under my supervision, analysis and interpretation of the data, conception and writing of the manuscripts supported by the coauthors who especially contributed to structuring and wording. All presented LES simulations in this chapter were contributed by Seung-Jin Baik.

The aim of the work presented in this chapter is to apply averaged and instantaneous two-color laser-induced fluorescence thermometry to the liquid phase of the SpraySyn flames (section 3.1 and 3.2).

In the context of improvement of combustion processes, it is desired to validate and support kinetics and fluid-dynamics simulations and to gain insight into particle formation processes. An extended database is being collected for various operating conditions and various measurement and simulation approaches [56]. The SpraySyn burner was already investigated for droplet size and velocity [397], the gaseous velocity field [186], synthesized nanoparticle characteristics [143], and gas-phase temperature [210]. The liquid-phase temperature of the SpraySyn flames is of particular interest for understanding involved transport phenomena and fluid mechanics during liquid disintegration, and when modeling evaporation processes [154, 399], and particle formation in the liquid phase [143, 154], and when investigating droplet breakup, evaporation, superheating [400], droplet explosion [126, 401, 402] and droplet puffing [194] that are known to strongly influence the resulting quality of nanoparticles [154]. Therefore, *in situ* measurements of the liquid-phase temperature in sprays – if possible, with high temporal and spatial resolution – are highly desired. Various approaches for non-intrusive liquid-phase temperature measurements have already been reported, such as rainbow refractometry [403-405], infrared emission [406], or Raman scattering [407]. Two-color tracer LIF (2cLIF) thermometry has been applied to probing the temperature of single droplets [365, 408] and temperature maps of sprays [281, 368]. Ulrich et al. [409, 410] investigated the combination of two laser dyes in single ethanol droplets to increase the temperature sensitivity of two-color LIF thermometry.

8.1 Averaged liquid-phase temperature maps

In this work, two-color laser-induced fluorescence (2cLIF) thermometry based on the fluorescence tracer coumarin 152 dissolved in ethanol is applied to provide temporally averaged but spatially resolved liquid-phase temperature maps of the SpraySyn1 flame. It was decided to derive temperature from temporally averaged LIF signals for each color channel, enabling implementation of 2cLIF through sequential measurements with a single camera. In contrast to

instantaneous single-pulse measurements with two cameras, this approach is less affected by artifacts caused by noise in low-intensity regions, e.g., representing weak signal from small droplets. While in single-shot measurements such artifacts must be suppressed by signal thresholding, this is not required for averaged LIF images. Signal from small droplets is thus considered in the evaluation due to the acquisition of sufficient signal relative to the background through excitation with a sequence of laser shots. Because of the improved signal-to-noise ratio, the signal intensity ratio and thus the temperature can be calculated with a significantly lower error. In the single-shot approach in contrast, the signal of small droplets is very low towards the background causing large errors (section 8.2.4). The single-shot approach can also be affected by imperfect spatial mapping of the highly structured images, a requirement that is relaxed in the smoother signal distributions in averaged images. The resulting potential bias resulting from averaging the LIF signal before calculating temperature from the signal ratio is quantified in this work based on simulation data (section 8.1.2.3).

8.1.1 Two-color LIF thermometry with coumarin 152

The measurement technique of two-color laser-induced fluorescence is based on the temperature-sensitive fluorescence of a tracer added to the liquid under investigation and excited by laser light at a fixed wavelength within its absorption spectrum. The temperature dependence of the resulting fluorescence is exploited by detecting two spectral bands, where the fluorescence intensity ($I_1(T)$, $I_2(T)$) changes with temperature as differently as possible to each other to obtain the highest temperature sensitivity from the signal ratio. Sufficient fluorescence signal intensities in the color channels are necessary to maximize the signal-to-noise ratio. From the signal-intensity ratio of the two fluorescence bands ($R_{\text{LIF}}(T)$), the local liquid-phase temperature can be derived:

$$R_{\text{LIF}}(T) = \frac{I_1(T)}{I_2(T)} = \frac{\eta_1}{\eta_2} \exp((\beta_1 - \beta_2)/T) \quad (8.1)$$

More details of the theoretical background of the two-color LIF technique are provided in section 7.2.5. Detailed information about 2cLIF thermometry utilizing laser dyes is presented in Refs. [365, 368, 393, 411].

As a result of the study on suitable fluorescence tracers for two-color LIF (for more details refer to chapter 7), coumarin 152 turned out to be the most appropriate tracer for the measurement application in the SpraySyn flame operated with ethanol. Coumarin 152 was dissolved in the fuel ethanol at a concentration of 10 mg/l. The corresponding absorption and fluorescence spectra at various temperatures are given in Figure 80. The transmission spectra of the chosen optical filters are shown as colored areas and were measured with the UV/VIS absorption spectrometer described in section 7.2.2. The β factor is plotted as black symbols and was calculated from the spectra at 303 and 343 K. The laser excitation at 266 nm is indicated by a purple line.

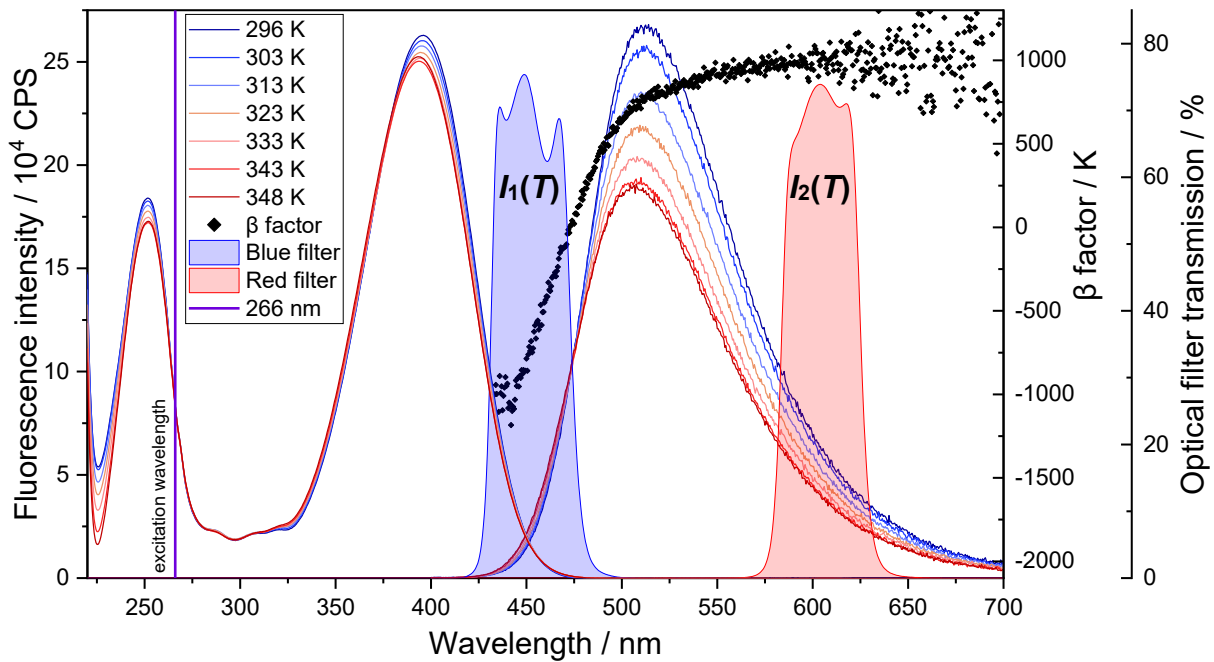


Figure 80: Temperature-dependent absorption (left) and fluorescence (right) spectra of coumarin 152 in ethanol (10 mg/l, 3.9×10^{-5} mol/l). The vertical line indicates the Nd:YAG excitation wavelength of 266 nm and the black symbols show the β factor calculated for a temperature difference of 40 K (between spectra taken at 303 and 343 K). Colored areas indicate the optical transmission of the utilized optical filters.

Among the Nd:YAG laser harmonics, coumarin 152 can be excited at 266 or 355 nm and its fluorescence spectra show a maximum at around 510 nm at room temperature. The fluorescence spectra range from 430–750 nm. At the peak wavelength, the absolute fluorescence intensity decreases from 296 to 348 K by about 29 %. At wavelengths shorter than 475 nm, the fluorescence intensity increases with temperature whereas at wavelengths larger than 475 nm the intensity decreases. This is reflected in β changing from negative to positive values, which results in a difference of the temperature sensitivity of about 2000 K between the spectral ranges at 445 and 640 nm. The normalized fluorescence spectra (appendix Figure A39) exhibit a significant blue shift with temperature up to 0.15 nm/K in the temperature range investigated. The absorption cross-section does not change significantly with temperature, and is almost equal to each other at the two standard Nd:YAG laser excitation wavelengths of 266 and 355 nm; at the excitation wavelength of 266 nm used in this work the absorption cross-section varies by 0.9 % (0.017 %/K) in the considered temperature range.

8.1.2 Experimental setup for 2cLIF temperature imaging

The two-color LIF temperature imaging experiments were conducted in an ethanol spray flame generated by the SpraySyn1 burner (section 3.1) designed for the synthesis of oxide nanoparticles [174]. In this burner, the spray is generated in a two-fluid nozzle where the liquid exits a small capillary (inner/outer diameter: 0.4/0.7 mm) and is atomized by a co-annular (internal diameter 1.5 mm) high speed (approx. 130 m/s at the standard operating condition) dispersion gas flow of oxygen. The spray nozzle is surrounded by a premixed methane/oxygen pilot flame stabilized on a sintered bronze matrix (outer diameter 15 mm). This flame is shielded against laboratory air by a nitrogen flow through a co-annular 70 mm diameter sintered bronze matrix.

For the temperature imaging measurements, the beam of a frequency-quadrupled Nd:YAG laser (B.M. Industries, Serie 5000, 266 nm) was formed into a vertical light sheet with a

cylindrical telescope (LaVision) resulting in low fluence ($F = \sim 1.25 \text{ mJ/cm}^2$) excitation. The energy of each laser pulse was recorded with a reference photodiode (LaVision, Energy Monitor V9) for laser-energy correction during postprocessing. Fluorescence within an area of $31 \times 43 \text{ mm}^2$ was imaged from the spray flame (section 3.1) or the calibration cell (section 7.2.1) with an achromatic lens (Nikon, Nikkor UV, $f = 105 \text{ mm}$, $f/4.5$) onto an intensified CCD camera (LaVision, Nano-Star) with a spatial dispersion of 14.8 pixel/mm ($67.6 \text{ }\mu\text{m/pixel}$). The deviation from linearity is specified by the manufacturer to less than 1 % up to its maximum allowable number of counts per pixel. Furthermore, the intensifier was operated in the linear regime in medium range gain regions exposing the CCD to not more than 80 % of its maximum counts.

Two interference filters (ThorLabs) were chosen according to the selected fluorescence detection bands of coumarin 152 (section 7.3.3.1) with center wavelengths of 452 and 605 nm (FWHM: 40 nm each). The filter transmission curves for the blue and red color channels are shown in Figure 80. The optical filters were placed sequentially in front of the lens, and a series of LIF-signal images was acquired for averaging and further post processing. Because the spray is sparse, a large number of individual experiments were averaged (21,000 LIF images and 4,200 background images (without laser excitation) in sequences of 3,000 LIF images and 600 background images each) to generate a continuous intensity distribution for each color channel. The experimental setup is shown in Figure 81.

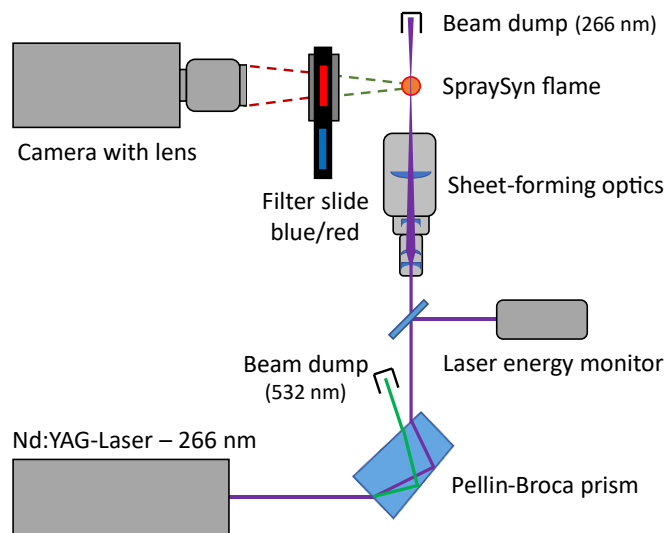


Figure 81: Top view of the 2cLIF thermometry setup in the SpraySyn flame.

The ethanol fuel was doped with the laser dye coumarin 152 (10 mg/l , $3.89 \times 10^{-5} \text{ mol/l}$) as the fluorescence tracer, which has several advantages for applications in spray flames. In our previous study (chapter 7), the tracer coumarin 152 (dissolved in ethanol) showed the highest temperature sensitivity and no measurable fluorescence signal re-absorption. The dye does not co-evaporate with the solvent and is expected to burn without further fluorescence once the solvent is evaporated. Chaze et al. [369] did a detailed analysis regarding the effect of saturation of the molecular transition excited in the dye molecules on the temperature sensitivity of the tracer. According to their results, our experiments were conducted in the linear LIF regime since for the laser dyes they investigated (including rhodamine B, which has a higher absorption cross-section than coumarin 152) the laser intensity limiting the linear range was about $1.2 \times 10^6 \text{ W/cm}^2$, which is one order of magnitude above the intensity we used for our measurements with coumarin 152. With tracer concentrations c_m in the 10^{-5} mol/l range in our

experiments, self-quenching is not important, because according to the relation derived in Ref. [365] (section 2.3.2), the threshold value of $c_m < 0.01 C^*$ (with a critical concentration C^* for self-quenching of approx. 0.6 mol/l for rhodamine B) is not violated.

8.1.2.1 Calibration of LIF measurement setup

For the calibration of the two-color LIF-measurement setup depicted in Figure 81, the same temperature-controlled UV-transmitting quartz cuvette utilized in the spectroscopic measurements (section 7.2.1) was placed in the laser sheet at the position of the spray flame and heated to the desired temperature. The imaging setup with its wavelength-dependent sensitivities was calibrated with homogeneous ethanol/coumarin 152 solutions for the desired range of temperatures and various concentrations in the temperature-stabilized quartz cuvette. The two-color LIF ratios were determined for temperatures between 296 and 348 K by taking $5 \times 300 = 1,500$ fluorescence images of the cuvette through the chosen filters. In the following Matlab evaluation code the fluorescence images were background and laser-pulse-energy corrected to compensate background light and laser intensity fluctuation. In the next step, the corrected fluorescence intensity from a region of interest was averaged and the ratios for each camera pixel were calculated from the respective LIF signals at various temperatures. The resulting intensity ratios correspond to unique temperature values and are plotted versus temperature for three solute concentrations in the diagram in Figure 82.

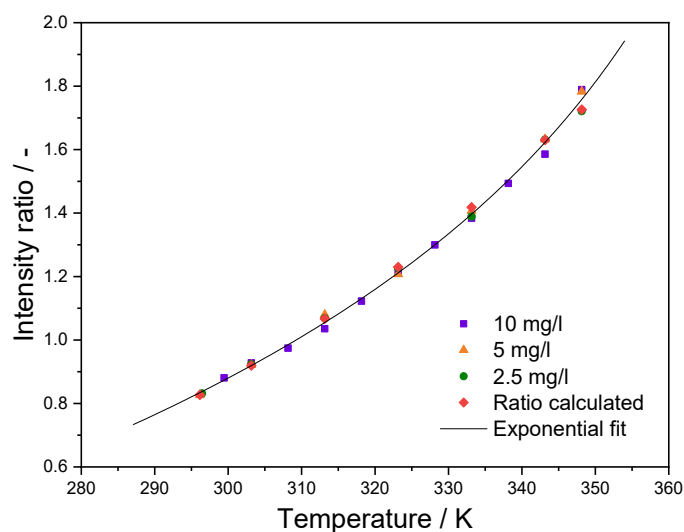


Figure 82: Two-color LIF intensity ratios (symbols) as a function of temperature, measured for coumarin 152 solutions (2.5, 5, 10 mg/l in ethanol). An exponential fit is plotted as solid line. Intensity ratios calculated from the measured spectra (5 mg/l solution) are shown as red diamonds.

The temperature dependence of the two-color intensity ratio follows the expected behavior based on the measured fluorescence spectra (Figure 82). Due to the large Stokes shift for coumarin 152, the signal-ratio-temperature function (or alternatively termed calibration function) does not change within the tracer concentration range investigated here. A least-squares data fit with an exponential function ($R^2 = 0.99786$) results in

$$T(R_{\text{LIF}}) = 383.39184 - 197.74433 \exp(-0.981 R_{\text{LIF}}) \quad (8.2)$$

To compare the calibration results to the optimal signal-ratio-temperature function derived from the measured fluorescence spectra, the calculated ratios are normalized to the fit function at 303 K and plotted in Figure 82. The accordance of the calibrated to the calculated signal-

ratio-temperature function is very high. In the following the determined signal-ratio-temperature function is used to convert measured ratios to their corresponding temperature.

8.1.2.2 Data evaluation and postprocessing

To maximize the signal-to-noise ratio and to generate consistent averaged LIF-signal images from the sparse and highly intermittent spray, 21,000 LIF images and 4,200 background images were recorded per color channel and operating condition. By using a Matlab script [232], background-subtracted LIF images were corrected for fluctuations in laser energy using data from the reference photodiode before averaging. The averaged LIF-signal images are depicted in Figure 83 for the red (a) and blue (b) channel with an exponential color scale. In the last step, both LIF signal maps are divided pixel by pixel to obtain the ratio map that was finally converted by the determined signal-ratio-temperature function (Figure 82) to the desired temperature map shown in Figure 83c). For comparison with the visible flame structure within the same field of view, the intensity of the flame luminescence (measured without any optical filters in front of the camera) is shown in Figure 83d) as a false-color image.

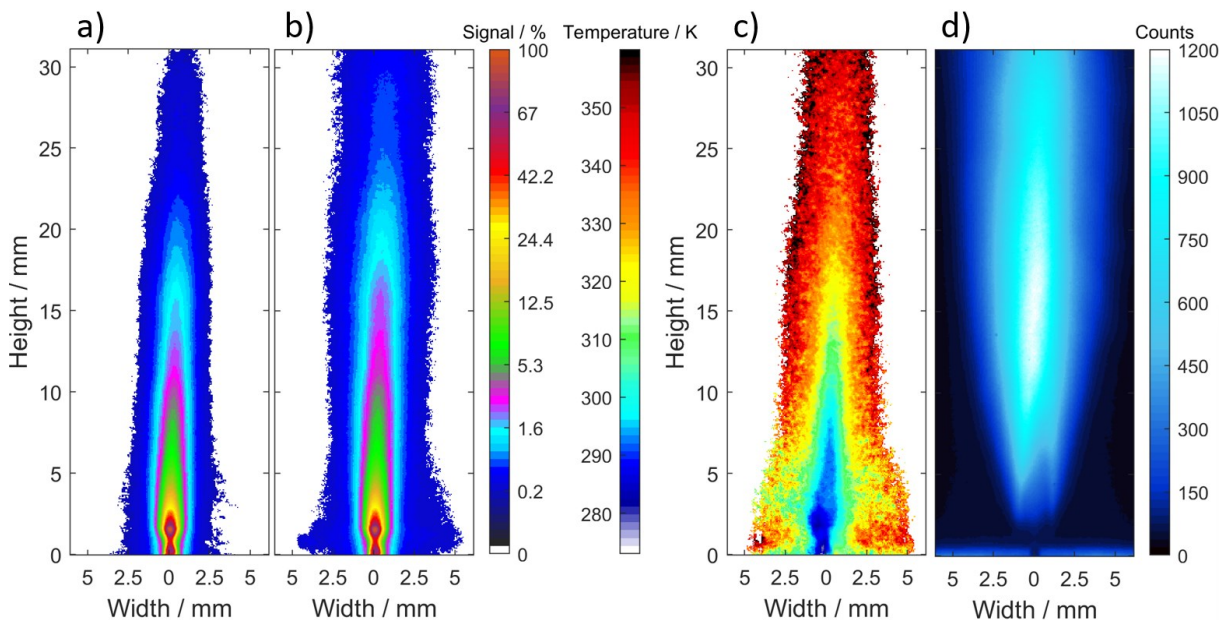


Figure 83: Measurement results from the SpraySyn flame operated with ethanol seeded with coumarin 152 (10 mg/l , $3.89 \times 10^{-5} \text{ mol/l}$). Burner operating conditions: 5 ml/min ethanol, 10 slm O_2 dispersion gas, $2/16 \text{ slm}$ CH_4/O_2 pilot flame, 120 slm N_2 coflow, a) red and b) blue LIF channel (exponential color scale). c) Liquid-phase temperature map d) Flame luminescence intensity map in false colors.

For the depiction of the temperature map, pixels with signal levels in either one of the color channels below an average LIF-signal intensity threshold of 0.5 counts per image were colored white (maximum values of averaged counts per pixel are ranging in the magnitude of 500 counts). It is expected that after droplet evaporation the tracer disintegrates and oxidizes with no significant fluorescence generated from the gas phase.

The SpraySyn flame features a turbulent combustion process for which ‘true’ temperatures would only be obtained with optical diagnostics of instantaneous (i.e., single-pulse) measurement capability. For the current method, this would need simultaneous image acquisition of the two color channels, e.g., by two separate cameras triggered simultaneously. Therefore, with the current measurement strategy, only temporally averaged temperature fields can be obtained. An error propagation analysis was conducted to estimate the uncertainty of the

present approach. The analysis included the magnitude of the camera noise and the fluctuation of the measured ratio to quantify the statistical error (ranging in the magnitude of $\Delta R/R = 0.1\text{--}0.4\%$), the standard error of the fit parameters of Eq. (8.2) calculated by least-square fitting ($\Delta a/a = 1.19\%$, $\Delta b/b = 1.93\%$, $\Delta c/c = 8\%$), and the uncertainty of the thermocouple measurements ($\Delta T = \pm 0.15\text{ K}$). A Matlab routine was created to calculate the uncertainty of the measured temperature for every single pixel resulting in values ranging from 6.5 to 9.5 K depending on the region within the liquid-phase temperature map. The measurement uncertainty in the outer regions of the flame is higher due to the strong intermittency of the signal compared to regions close to the capillary outlet where LIF signal is detected regularly.

Depending on the operating conditions, liquid temperatures down to 283 K were measured in the core region of the SpraySyn flame close to the nozzle outlet of the SpraySyn burner. For validation purposes, the temperature in the spray core of liquid ethanol at the capillary outlet without flame was measured by a thermocouple showing values down to less than 278 K due to ethanol evaporation. Deprédurand et al. [393, 412] measured droplet temperatures of acetone and ethanol/3-pentanone mixtures by two-color LIF in a heated air environment (air temperature ranging from 21 to 370 °C) and observed a similar initial cooling effect accompanied with a decrease in droplet size due to evaporation. These results confirm the plausibility of average droplet temperatures lower than ambient at the nozzle outlet of the SpraySyn flame since in our case an environment of cool dispersion gas is present and thermal fluxes should be lower than in the referenced work where the cooling effect was observed despite a surrounding air temperature of 370 °C. Consequently, the measured temperatures in the SpraySyn flame at the capillary outlet are plausible.

8.1.2.3 Discussion of experimental error

An experimental bias is caused by the determination of an averaged liquid-phase temperature by the intensity-ratio method detailed in section 8.1.2.2. In the experiment, the temperature maps are not recorded instantaneously but are ensemble-averaged from single-shot measurements. The two bandpass-filtered LIF images were recorded sequentially and averaged before the temperature maps were calculated from their pixel-count ratios [188]. Based on the assumption that droplets are present intermittently at different temperatures across most of the imaged region of the spray, using averaged images for the temperature calculation leads to a systematic error because the fluorescence intensity ratio is not a linear function of temperature (Figure 82). This non-linearity causes a bias towards higher temperatures if LIF images are averaged before ratioing.

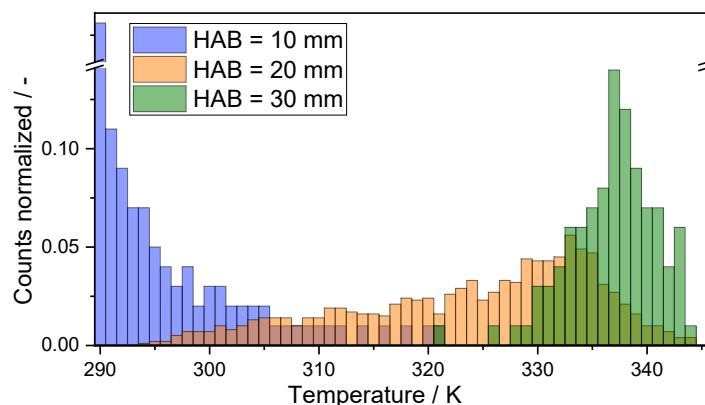


Figure 84: Simulated droplet-temperature distributions (Seung-Jin Baik) at the SpraySyn flame center-line (i.e., $r = 0\text{ mm}$) at various HAB for the standard operating condition.

Table 13: Bias error at various HAB and radial positions as a result of LIF-signal averaging before temperature calculation from pixel-count ratios. In this evaluation the simulated droplet distributions shown in Figure 84 were used.

HAB / mm	10	20	30	10	20	30
Radial pos. / mm	0	0	0	1	1	1
Biased error / K	0.6	0.9	0.2	1.4	0.5	0.1

The magnitude of this bias is assessed in a numerical experiment based on simulated droplet-temperature distributions at the flame centerline and at 1 mm radial offset for various HAB. Figure 84 shows the distributions at the flame centerline which were obtained by sampling droplets located in a cube (1 mm^3) centered on the given coordinate for the simulation time of 22 ms. From these temperature distributions, a resulting averaged LIF signal was calculated from which a temperature could be computed. This temperature differs from the real averaged temperature. The difference between these temperatures is the bias sought. The calculations show that the error increases with broader temperature distributions. Due to the minor nonlinearity of the calibration function, the bias is small (Table 13) and not considered for the further evaluations.

The tracer concentration builds up within the droplets during evaporation keeping the fluorescence signal intensity approximately constant (neglecting quenching effects, see [365, 413, 414]) until the maximum solubility is reached. At this point, the droplet diameter is expected to be so small that according to the D^2 law [266] it disappears very quickly without significant contribution to the average fluorescence signal. Therefore, the detected fluorescence signal per droplet corresponds approximately to its initial droplet diameter. Initial diameters range between 5 and 35 μm , thus a factor of 7 which is significantly smaller than the dynamic range factor of the utilized 12-bit camera ($4096^{1/3} = 16$). Initially large droplets provide stronger signal than small ones. This leads to a volumetric average of the measured temperature.

In droplets containing laser dyes, morphology-dependent resonances (MDRs) can cause droplet lasing [411, 415, 416] resulting in narrower emission spectra with modified temperature dependence [378, 417]. This effect is most relevant in cases with high dye concentration, strong excitation laser fluence [418], and spherical droplets [378, 411, 419]. Perrin et al. observed that MDRs are extremely sensitive to the droplet sphericity [378]. The magnitude of lasing also depends on the droplet size [409, 416, 417, 419]. To suppress lasing in our experiments, a low tracer concentration and low laser intensity ($1.25 \times 10^5 \text{ W/cm}^2$ at 266 nm) was applied. The absence of lasing was checked by inspecting fluorescence spectra of coumarin 152 (10 mg/l) at various laser fluences in a cuvette (MDR-free reference), in the cold ethanol spray, and in different regions of the SpraySyn flame at various operating conditions. The detected fluorescence spectra showed no indications of lasing-induced spectral narrowing or lasing peaks [420-426].

8.1.3 Large-eddy simulation of the SpraySyn flame

The SpraySyn flames were reproduced by large-eddy simulation (LES) performed by Seung-Jin Baik (EMPI Fluid Dynamics, University Duisburg-Essen) using their in-house solver PsiPhi [427, 428], where the gas and liquid phases are modeled by a Eulerian-Lagrangian approach. Inlet turbulence is generated with the method of Klein [429, 430], turbulent viscosity is determined following Nicoud et al. [431]. Gas-phase combustion is described by the premixed

flamelet-generated manifold (PFGM) approach [432] with a reduced reaction mechanism for ethanol by Olm et al. [433]. In contrary to pure gas-phase combustion, in the spray flame the mixture fraction is no longer a conserved scalar because local fuel sources are provided from evaporating liquid. In the present burner, fuel evaporation occurs rapidly due to the high-speed oxygen dispersion flow. Since such fast spray evaporation leads to an earlier mixing of the fuel and oxidizer before reaction [434], a premixed condition can be assumed in the present study. In the PFGM approach in the SpraySyn flame, the chemical source terms of these flamelets are tabulated into a manifold, where the compositions and progress spaces are controlled by two mixture fractions of the burned pilot products ($Z_1 = Y_{CO_2} + Y_{H_2O} + Y_{O_2} + Y_{CO}$) and the unburned evaporated spray ($Z_2 = Y_{Ethanol}$), and the progress variable ($Y_P = Y_{CO} + Y_{CO_2}$). Moreover, B_h represents the Spalding number for heat transfer, and B_m represents the Spalding number for mass transfer. In the present study, the liquid droplets are represented by Lagrangian particles, which are two-way coupled with the carrier gas through momentum exchange and evaporation and are described from a set of differential equations of the droplet location $x_{d,i}$, velocity $u_{d,i}$, mass m_d , and temperature T_d [428, 435, 436]:

$$\frac{dx_{d,i}}{dt} = u_{d,i} \quad (8.3)$$

$$\frac{du_{d,i}}{dt} = \frac{f_1}{\tau_d} (\tilde{u}_i - u_{d,i}) + \left(1 - \frac{\bar{\rho}}{\rho_d}\right) g_i \quad (8.4)$$

$$\frac{dm_d}{dt} = -\frac{Sh m_d}{3Sc \tau_d} \ln(1 + B_m) \quad (8.5)$$

$$\frac{dT_d}{dt} = \frac{Nu c_p}{3 Pr c_{p,d}} \frac{T - T_d}{\tau_d} \frac{\ln(1 + B_h)}{B_h} + \frac{\dot{m}_d L_d}{m_d c_{p,d}} \quad (8.6)$$

Previous work by Rittler et al. [399, 427] can be consulted for further details on the gaseous and liquid-phase modeling. In the present study, the simulations were performed in a domain of $90 \times 40 \times 40 \text{ mm}^3$ on an equidistant cartesian grid with a 0.5 mm spacing for the simulations, which feature 1.15 million cells. To check for grid independence, finer (0.25 mm spacing) simulation of the SpraySyn flame standard operating condition was performed in the same domain using 9 million cells. Each simulation represents a process time of 0.2 s and requires ~3,500 core hours for the main simulation and ~20,000 core hours for the finer grid, respectively. Since the simulated liquid droplet temperature showed identical results on both grids, we relied on the coarser grid for all other simulations.

The computational domain starts at 3 mm height above burner (HAB), where the primary and secondary fluid breakup processes can be assumed to be complete [397, 428]. Droplet velocities and diameters were measured at this HAB with a fiber-coupled PDA (phase-Doppler anemometry, Dantec Dynamics A/S) in the cold ethanol spray with the sinter matrix supporting the pilot flame and the co-flow removed. This was necessary to not cut one of the laser beams of the crossed two-color PDA sending unit, which would preclude measurements lower than 6 mm HAB. It is assumed that within the initial distance of 3 mm, the flame has no significant influence on the droplet size and velocity and hence the cold spray measurement results are used as input for the spray flame simulations. Nevertheless, minor deviations can originate from this modification. In the simulation, one numerical particle represents one liquid droplet. These droplets are injected into the computational domain, where their initial velocity and diameter are obtained from samples of measured data, which ensures that the measured joint

probability density function (PDF) of particle size and velocity vector is satisfied. The maximum droplet temperature is set as the boiling temperature, and any droplet that has a diameter below 1 μm is treated as fully evaporated.

8.1.4 Results

Temporally averaged liquid-phase temperature maps for five operating conditions (OC) of the SpraySyn flame (version 1, section 3.1) were measured by two-color laser-induced fluorescence based on the tracer coumarin 152. The operating conditions for the spray formation are shown in Table 14 and were modified by varying the ethanol injection rate and the oxygen dispersion gas flow. In the standard operating condition of the SpraySyn burner (OC1), the pilot flame is fed with 16 slm O_2 and 2 slm CH_4 and surrounded by a 120 slm nitrogen sheath-gas flow [174]. Ethanol is injected with 2 ml/min and atomized by a dispersion gas flow of 10 slm. In two other cases (OC2 and 3), the spray was varied by changing the fuel injection rate at constant dispersion gas flow, while for OC4 and 5, the dispersion gas flow was varied at a constant fuel flow.

Table 14: SpraySyn flame operating conditions: Variation of dispersion gas flow and injection rate.

Operating condition	Dispersion gas (O_2) / slm	Injection rate (ethanol) / (ml/min)
OC1	10	2
OC2	10	5
OC3	10	10
OC4	7	5
OC5	15	5

With the main aim to understand, model, and ultimately optimize spray-flame based nanoparticle synthesis processes, the same operating conditions were modeled by large-eddy simulation (LES), where the spray is modeled by a Eulerian–Lagrangian approach based on measured liquid droplet properties (initial liquid-phase temperature, droplet size, and velocity distribution). Droplet size and velocity were measured by phase-Doppler anemometry (PDA) to provide input data for the simulation and to enable a better interpretation of the liquid phase temperature results. Average droplet size and velocity are given in Figure 85. Droplet temperature distributions were provided by the simulation to assess the systematic measurement error caused by LIF-signal averaging (section 8.1.2.3). From various publications it is known that the SpraySyn flame inherently features a minor flame tilt [174, 204]. For the comparison to the simulation a correction for these minor flame tilts was done to ensure comparability to the simulated liquid-phase temperature maps. In the context of liquid mixing with the surrounding gas phase the droplet temperature is affected by heat transfer with the potentially reacting gas and evaporative cooling. The simulation results were found to be in good agreement with the experiment by showing a suitable prediction of the droplet evaporation and heat-up process within the experimentally probed spray region.

8.1.4.1 Droplet size and velocity (PDA)

The PDA results at 3 mm HAB for operating conditions (OC1–5, Table 14) that were used as simulation input are presented in Figure 85. The droplet mean diameter is plotted as data

points connected by solid lines and the downstream droplet velocity as dashed lines. Additionally, the fuel capillary and the dispersion gas outlet are indicated in black close to the abscissa.

At a constant ethanol injection rate and increasing dispersion gas flow (OC4, OC2, OC5), at 3 mm HAB the droplet mean diameter decreases and the droplet velocity increases. With an increasing injection rate at a constant dispersion gas flow (OC1–OC3), generally, the droplet mean diameter increases and the velocity decreases. The droplet velocity depends on the dispersion gas flow and is slightly influenced by the injection rate. The droplets at larger radial positions show lower velocities with respect to the core region, because in the latter the dispersion gas flow continuously accelerates the droplets. From the peaks of the downstream droplet velocity the shear region between dispersion gas and fuel can be identified. At HAB = 3 mm, the velocity corresponds to the position of the capillary and the dispersion gas outlet. The majority of droplets are detected within a radius of 0.75 mm around the flame center line. For OC1, 90 % of the droplets are detected within this region. On the centerline, the droplet count is 10^5 within 10 s for OC1, which is a high count rate for this evaluation and statistical analysis. In the outer regions where the droplets feature a larger diameter, the droplet count rate is significantly lower.

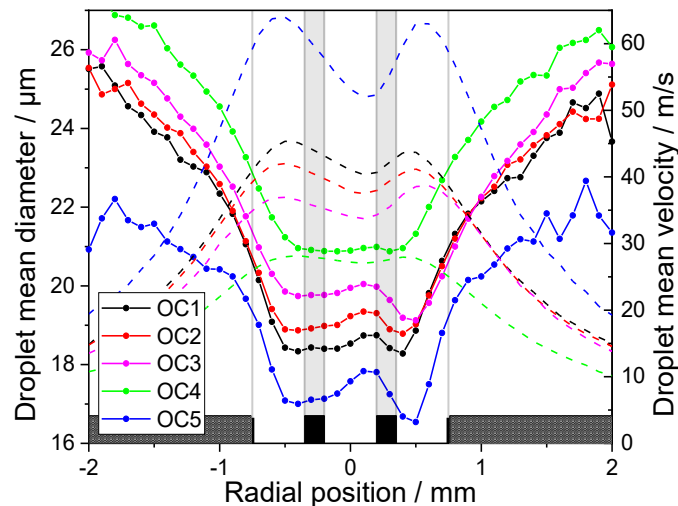


Figure 85: PDA results for operating conditions OC1–5 at 3 mm HAB, droplet mean diameter (solid lines) and downstream droplet mean velocity (dashed lines), burner capillary and dispersion gas outlet indicated in black.

8.1.4.2 Gas-phase temperature, evaporation (LES)

Figure 86 shows simulated instantaneous (left) and mean (right) gas temperature (a), and evaporation rate (b) of ethanol to illustrate the general shape of the SpraySyn flame. Since the computational domain starts 3 mm above the burner, it is assumed that the O_2/CH_4 pilot flame is completely burned at the computational domain inlet, as can be seen in Figure 86a. The surrounding cold sheath-gas flow cools the hot pilot flame and prevents external influences on the nanoparticle synthesis. Simulated gas-phase temperatures have shown good agreement with experimental data in so-far unpublished work. Strong turbulence and mixing are observed in the shear layer between the fast dispersion gas and the surrounding pilot flame, as shown in Figure 86a. Since evaporation occurs mainly near the burner, as shown in Figure 86b, the measurements were focused on the region up to HAB = 30 mm.

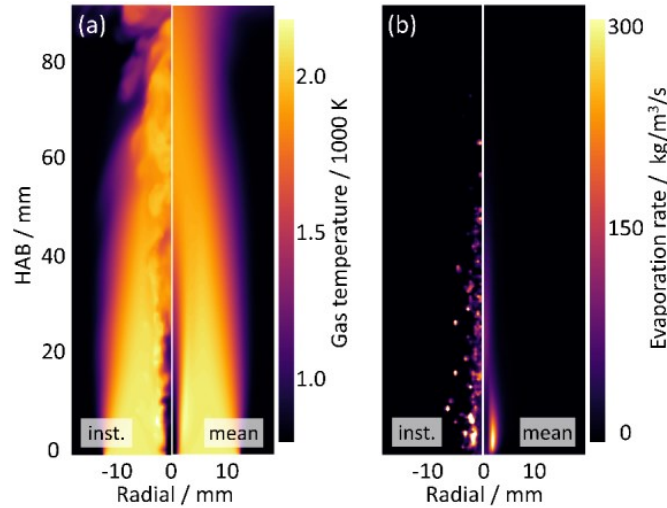


Figure 86: Instantaneous (left) and mean (right) contour plots of a) the gas-phase temperature and b) evaporation rate in a centerline plane of the flame for OC1 from LES. Figure created by Seung-Jin Baik, reprint from Ref. [189].

8.1.4.3 Liquid-phase temperature (2cLIF, LES)

Figure 87 shows the measured (upper row) and simulated (lower row) liquid-phase temperature maps of the five investigated operating conditions (Table 14). The dashed lines at $HAB = 3$ mm indicate the boundary of the simulations. In the experimental maps, pixels with averaged LIF-signal intensities of less than 0.5 counts in at least one of the two LIF channels were masked and colored white [188]. The effect of the dispersion gas flow and the fuel injection rate representing the operating conditions are discussed in the following.

It can be seen from the experimental liquid-phase temperature maps in Figure 87a,c,e, i.e., for varying the fuel flow rate at constant dispersion gas flow, that the temperature in the lower regions of the flame increases with increasing ethanol injection rate. The core temperature (averaged over $30 \times 21 = 630$ pixels, corresponding to a spatial region of interest (ROI) between 3 and 5 mm in HAB and ± 0.7 mm in radial direction resulting in a ROI of 2×1.4 mm²) increases from about (a) 290 K over (c) 293 K to (e) 298 K. A similar observation is made for the temperature maps in Figure 87g,c,i, i.e., for varying the dispersion gas flow at constant fuel injection rate. In this case, the core temperature at $HAB = 3$ –5 mm decreases from (g) 295 K over (c) 293 K to (i) 287 K. From these findings, one can infer that an increase in the ratio between dispersion-gas flow to liquid flow rate (DGL ratio) causes a decrease of the liquid-phase temperature in the respective core region of the spray flame. Figure 85 shows that at higher DGL ratios the spray atomization is more effective [397] with droplet distributions shifted to smaller count mean diameters (CMD) at constant liquid volume and hence larger total droplet surface areas leading to accelerated evaporation. The higher dispersion gas flow velocity also supports evaporation in the shear layer between fuel and oxidizer, leading to faster liquid breakup, smaller droplets, and faster evaporation. On the other hand, stronger evaporative cooling accompanying the larger DGL ratios causes liquid-phase temperatures lower than the ambient temperature of injected ethanol in the regions close to the capillary outlet, as was confirmed by thermocouple measurements in the core of the cold ethanol spray [188]. Since the simulation of the droplet temperature starts at $HAB = 3$ mm, where the droplets are assumed to have been formed, this observation cannot be confirmed by the simulation. Instead, the measured liquid-phase temperatures at this height (dashed line) were taken as initial temperature values for the simulated droplets.

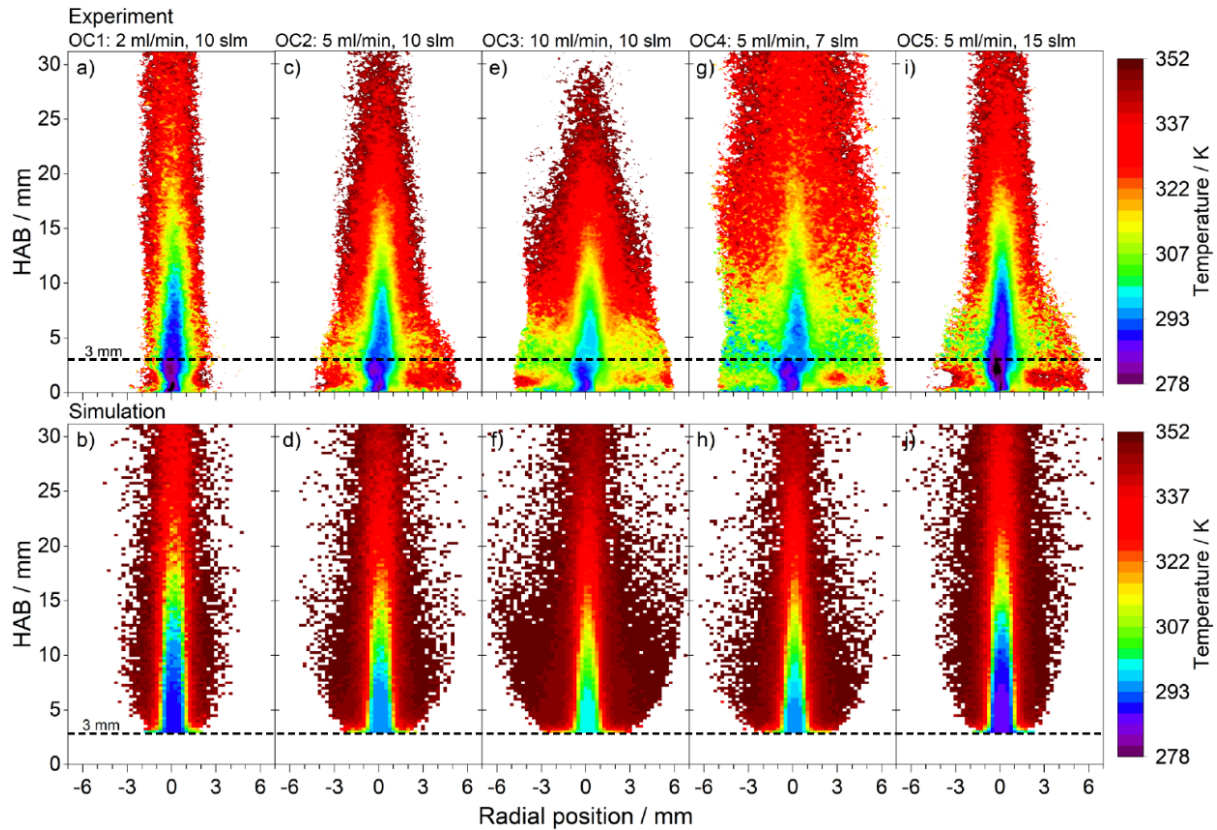


Figure 87: Liquid-phase temperature maps of the ethanol SpraySyn flame at various operating conditions, i.e., where the dispersion-gas flow and the fuel injection rate were varied from the standard OC1. Upper row: Measurement, lower row: Simulation.

With decreasing DGL ratios and hence less effective droplet atomization, the regions where significant data is available are further extended in vertical and radial direction (Figure 87g). Larger droplets survive within the flame over longer distances [397] and provide sufficient LIF signal in the outer regions of the flame. Most notably, the temperature maps with a small DGL ratio in Figure 87e and g feature a broad extension in the lower flame regions, with low temperatures in the range of 300 K. The high temperatures at the lower edge region of the liquid-phase temperature maps are caused by the hot pilot flame with heat release close to the sinter matrix.

Figure 88 shows centerline liquid-phase temperature profiles for OC1–3 (solid lines) and corresponding simulation results (dashed lines). The temperature values from the experiment and the simulation were spatially averaged along the flame centerline within 0.75 mm (experiment: 11 pixels, i.e., 74 μm , simulation: 3 voxels, i.e., 75 μm), and both data sets were slightly smoothed with a five-point moving average. Due to low signal strength in the experiment the profiles of OC2 and OC3 were cut at HAB = 27 mm and 29 mm, respectively.

As can be seen in Figure 88, an increase in injection rate at a constant dispersion gas flow leads to a generally higher temperature level along the flame centerline. The less effective atomization (low DGL ratio) with weaker evaporative cooling leads to elevated temperatures for OC2 and OC3 in comparison with OC1. Additionally, with higher injection rates, more fuel is fed into the flame, providing stronger heat release. The slopes of the profiles are almost equal for the chosen operating conditions. In contrast to these observations, with increasing dispersion gas flow (not shown here) the slope of the vertical temperature profiles increases (linear fit, OC4: 1.64 K/mm, OC2: 2.24 K/mm, OC5 2.33 K/mm).

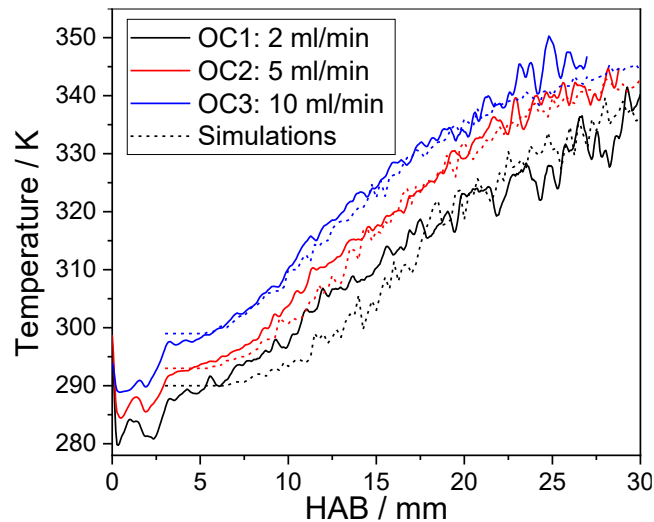


Figure 88: Centerline liquid-phase temperature profiles for OC1–3 (dispersion gas flow: 10 slm, variation of injection rate). Measurement (solid) and simulation (dashed lines).

8.1.4.4 Comparison of experiment and simulation

The dashed lines in Figure 88 show the simulated centerline temperature profiles derived from the liquid-phase temperature maps in Figure 87 (lower row). Overall, the simulations are in good agreement with the measurements. The slope of the simulated and measured centerline temperature profiles changes somewhat in different sections along the flame height. At HAB = 3–10 mm, the slope of the temperature profiles is comparatively low while it increases afterwards and flattens again at higher HAB when approaching the boiling point of ethanol.

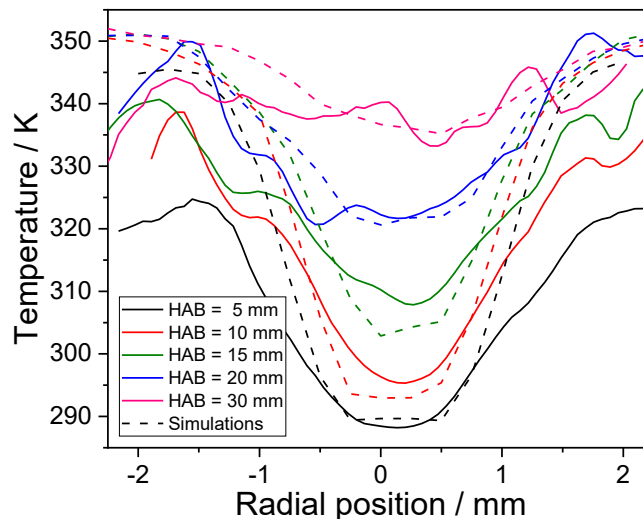


Figure 89: Radial liquid-phase temperature profiles (averaged: 0.75 mm) of experiment (solid lines) and simulation (dashed lines) at various HAB, standard operating condition.

Figure 89 shows radial liquid-phase temperature profiles of the standard operating condition (OC1) for various heights above the burner. The experimental temperatures (solid lines) and simulations (dashed lines) were averaged and smoothed as described for Figure 88. The simulated temperature profiles are overall in good agreement with the experiment. The dip in liquid-phase temperatures in the flame center is well predicted by the simulation. Generally, the measured profiles are broader and the radial temperature gradient, i.e., the droplet heat-up rate, is smaller compared to the simulation, especially at small HAB. It is assumed that heat transfer from the hot pilot-flame environment to the droplets is overpredicted by the simulation,

or the PDA results provide inaccurate droplet-size distributions in the outer flame regions due to low droplet count rates. The flame in the experiment is slightly asymmetric due to imperfections of the nozzle. In the experiment, multiple scattering effects within the dense spray region could result in a spatial broadening of the LIF signal [437]. In general, the same observations regarding the deviation in the radial temperature gradient were made for the other operating conditions not shown here.

Figure 90 shows measured (left image half) and simulated (right) liquid-phase temperature maps for (a) OC1 and (b) OC2 representing the cases of the standard operating condition and an increased liquid injection rate. The other (not shown) SpraySyn flame cases compare similarly (Figure 87). Since the measured temperature maps are asymmetric both sides were averaged to include all information and to enable a more meaningful comparison. As shown in Figure 90, the shape and the magnitude of the simulated liquid-phase temperature are in overall good agreement with the measurements. The figure shows that the temperature increase in vertical and horizontal direction is well predicted by the simulation model (Figure 88 and Figure 89). The simulation provides more reasonable data of the outer regions of the flame where droplet temperatures close to the boiling point exist. In contrast to the simulation, the outer and higher regions of the flame are difficult to resolve in the experiment because the droplet field is already spread out and becomes sparse and hence the signal within the laser sheet becomes weak. These regions were cut out by the LIF-intensity threshold (section 8.1.2.2).

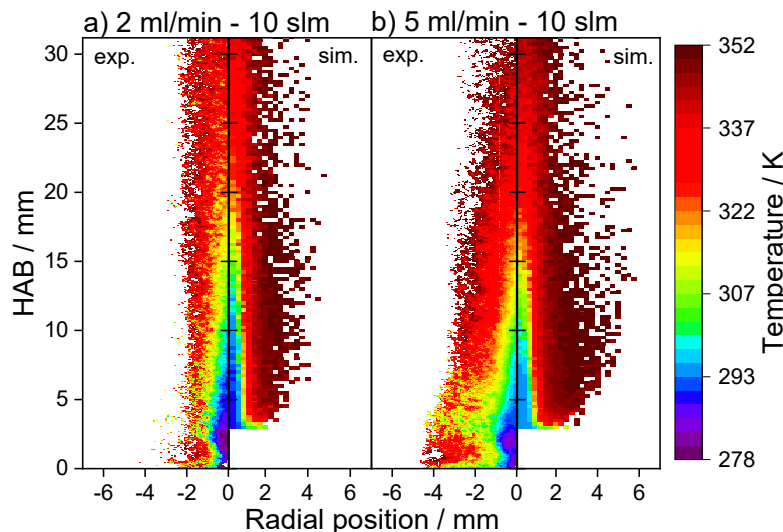


Figure 90: Liquid-phase temperature maps of (a) OC1 and (b) OC2. Left image half: Measurements, right: Simulations.

The strongest deviation between measurement and simulation was observed for OC4 (Figure 87g,h), especially for the lower outer region of the temperature map and the centerline temperature profile, where the simulation predicts a higher slope. One explanation for the disparities is that for the low DGL ratio, atomization of the spray was less efficient, and the PDA was not able to detect the mostly larger and not perfectly spherical droplets. Thus, some parts of the liquid phase (especially larger droplets) are not included in the simulation.

8.1.4.5 Discussion

From the presented results, it can be inferred that one of the main influences affecting the liquid-phase temperature of the SpraySyn flame operated with ethanol is evaporative cooling

in the lower regions of the flame, where spray atomization takes place. The ratio between the dispersion gas flow and the liquid injection rate was found to be crucial for the liquid-phase temperature distribution. Due to better atomization with more evaporative cooling, higher DGL ratios result in lower liquid-phase temperatures down to 278 K in the spray formation zone [188], below the ethanol injection temperature of 295 K.

The simulations show an overall good agreement with the measured liquid-phase temperature in that magnitude and shape of the temperature zones (Figure 87) are well predicted for different SpraySyn flame operating conditions. Temperature gradients in radial and vertical direction show a high correspondence for the investigated operating conditions. Merely for OC4, there are significant deviations between simulation and measurement regarding the vertical temperature profile that is characterized by a low DGL ratio. It is assumed that the PDA measurements were not able to accurately detect larger non-spherical droplets resulting from the less effective atomization. Therefore, a droplet size distribution shifted to smaller diameters was recorded and hence the prediction of a faster temperature increase along the flame center line can be explained. For the same reason, the cool regions in the lower range of OC3 and 4 can be explained. We assume that less efficient atomization causes larger non-spherical droplets that move outwards at low HAB, heat up slowly, and are not included into the simulation and thus causing a deviation between experiment and simulation.

8.1.4.6 Conclusions

Averaged liquid-phase temperature maps were recorded by two-color laser-induced fluorescence in the SpraySyn flame for five operating conditions and were compared to simulation results. The simulation utilized a Euler–Lagrange approach for the gas and spray phases using large-eddy simulation (LES). The simulated ethanol droplets are described by Lagrangian particles and the simulated liquid phase temperatures were found to be in an overall good agreement with the measurements. From the comparison between measurements and simulations, it can be concluded that the model provides a good prediction of the droplet heat-up and evaporation process within the SpraySyn flame. The simulations show that most of the evaporation occurs close to the nozzle outlet [428]. This can be confirmed by the experiment with low liquid-phase temperatures in the spray core near the burner surface indicating fast evaporation in this region due to high gas velocities creating an environment of low gas temperatures in contrast to the outer hot pilot flame. Simulated temperature distributions were used to assess the bias caused by temporal averaging of the experimental data. From the good accordance between experiment and simulation it can be concluded that the available simulation models are suitable for describing liquid temperature and evaporation rates in the SpraySyn flame.

8.2 Instantaneous 2cLIF droplet thermometry in the SpraySyn2 flame

8.2.1 Measurement principle of instantaneous 2cLIF droplet thermometry

In this work, instantaneous 2cLIF thermometry was applied to measure the temperature of the liquid spray in the SpraySyn2 flame (section 3.2). To clarify the distinction between both SpraySyn burner versions the SpraySyn burner version 1 is referenced as SpraySyn1 burner, and version 2 as SpraySyn2 burner. Detailed explanations to the basic principle of two-color tracer-LIF thermometry were given in section 8.1. For the measurement approach with one camera, the color channels are recorded sequentially, so that temporally not correlated LIF-intensity images are obtained for further post-processing. With instantaneous 2cLIF, both color channels are recorded simultaneously and thus the image pairs are temporally correlated. With these image pairs, single-shot ratio maps and thus instantaneous liquid temperature maps can be derived. To perform instantaneous 2cLIF thermometry the measurement setup described in chapter 8.1.2 is extended by a beam splitter and a second camera to enable the simultaneous detection of both color channels. Details to the experimental setup and post-processing are given in chapter 8.2.2.

The advantage of instantaneous 2cLIF is that single-shot temperature maps and thus the temperature of individual temperatures imaged in the spray can be measured. But for single-shot measurements, the signal-to-noise ratio is poorer compared to averaged measurements. For averaged maps more LIF signal is accumulated from many images and the background noise is reduced by averaging. For single-shot measurements, artifacts must be suppressed by signal thresholding, so that only droplets with strong LIF signal are considered for evaluation. When only one camera is used, the color channels are temporally not correlated and the LIF signal from each channel must be averaged before the ratio is calculated. This results in a temperature bias caused by the nonlinearity of the calibration function (sections 8.1.2.1 and 8.2.2.2). By recording both color channels simultaneously, this error is prevented (assuming sufficient signal quality), because each image pair is analyzed individually and only the resulting temperature is averaged in post-processing if desired. The results for temporally-correlated average liquid-temperature maps of the SpraySyn2 flame are presented in chapter 8.2.5.

Recently, Shahbaz et al. [438] performed single-shot 2cLIF thermometry based on the tracer anisole to measure the gas temperature within a combustion engine piston. Due to the high signal level of anisole the quality of single-shot images was improved significantly compared to the previously often used tracer toluene [439].

8.2.2 Experimental setup

In this chapter, the liquid temperature of spray flames and cold sprays generated by the SpraySyn2 burner is investigated. The burner was located in a reactor housing with UV-transmissive quartz windows, which enable the optical access to the flame. The reactor was operated at ambient pressure. Figure 91 shows the experimental setup for instantaneous 2cLIF.

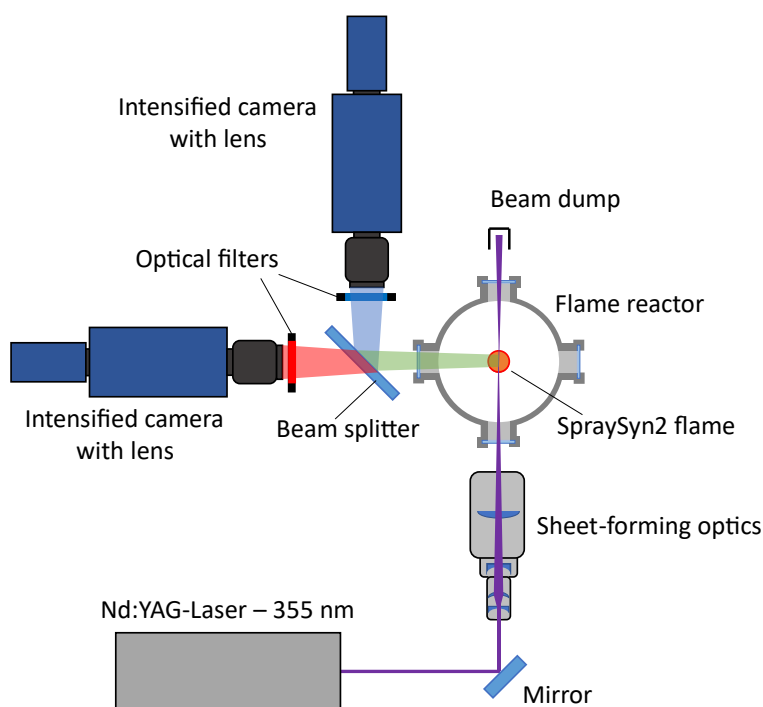


Figure 91: Top view of the experimental setup for instantaneous 2cLIF in the reactor housing of the SpraySyn2 burner.

The instantaneous 2cLIF measurements were based on the fluorescent tracer coumarin 152 (section 7.3.1.1). The used solvent ethanol was seeded with a low dye concentration of 10 mg/l to reduce MDRs with lasing effects (section 8.1.2.3) and fluorescence signal re-absorption (section 7.3.4). Different from the previous chapter, the excitation wavelength was 355 nm, generated by a Nd:YAG laser (InnoLas Laser, SpitLight 1000.1, $f_{\text{Hz}} = 10$ Hz). The laser energy per pulse was 5 mJ at the laser exit. The laser fluence within the laser sheet generated by sheet-forming optics (LaVision, Sheet Optics (divergent), Collimator Optics UV), was 5–10 mJ/cm². The tracer-doped liquid was excited by the laser sheet and the resulting fluorescence light of coumarin 152 (indicated in green) was spectrally divided at ~ 505 nm by a beam splitter (ThorLabs, DMLP505L, longpass dichroic mirror, 505 nm cut-on, $\varnothing = 2$ ") into a transmitted red part and a reflected blue part (Figure 92). In front of each camera lens, optical filters (ThorLabs, bandpass filters, blue: FB450-40, red: FB600-40, $\varnothing = 1$ " , Figure 92) isolated each color band before it was detected by two intensified cameras (LaVision, intensified relay optics (IRO) and Imager M-Lite, resolution: 1936×1216 pixels, pixel size: $3.45 \mu\text{m}^2$) equipped with lenses (Nikon, Nikkor UV, $f = 105$ mm, $f_{\#} = 4.5$). The spatial dispersion of the optical setup was 35 pixel/mm or $28.6 \mu\text{m}/\text{pixel}$. The intensifier gains were set differently to compensate for different wavelength-dependent detection sensitivities of the color channels. The intensifier gate was set to 200 ns to minimize background signal from the flame. Different from the setup shown in section 8.1.2, no laser-energy monitor was needed because the intensity ratios were calculated from images recorded during the same laser pulse. Therefore, the laser energy cancels out.

With this setup, the optical magnification of the detection system was limited by the size of the reactor housing, which prevented to reduce the distance between cameras and flame. An increased optical magnification can be achieved by performing the measurements without reactor housing to reduce the camera distance or by a different optical setup (e.g., telephoto lens or microscope lens with an achromatic tube lens [194]).

8.2.2.1 Beam splitter and optical filters

Figure 92 shows the transmission spectra of the optical filters used as blue and red colored areas, and the reflectance of the dichroic beam splitter in green. The optical filters were the same as utilized in the previous work presented in chapter 8.1.1. Moreover, the absorption and fluorescence spectra of coumarin 152 in ethanol at different temperatures are plotted for comparison to the optical components. The laser excitation wavelength is indicated as purple line at 355 nm. The absorption cross-section is about the same as at 266 nm (4th harmonic of the Nd:YAG laser wavelength), used in the previous work.

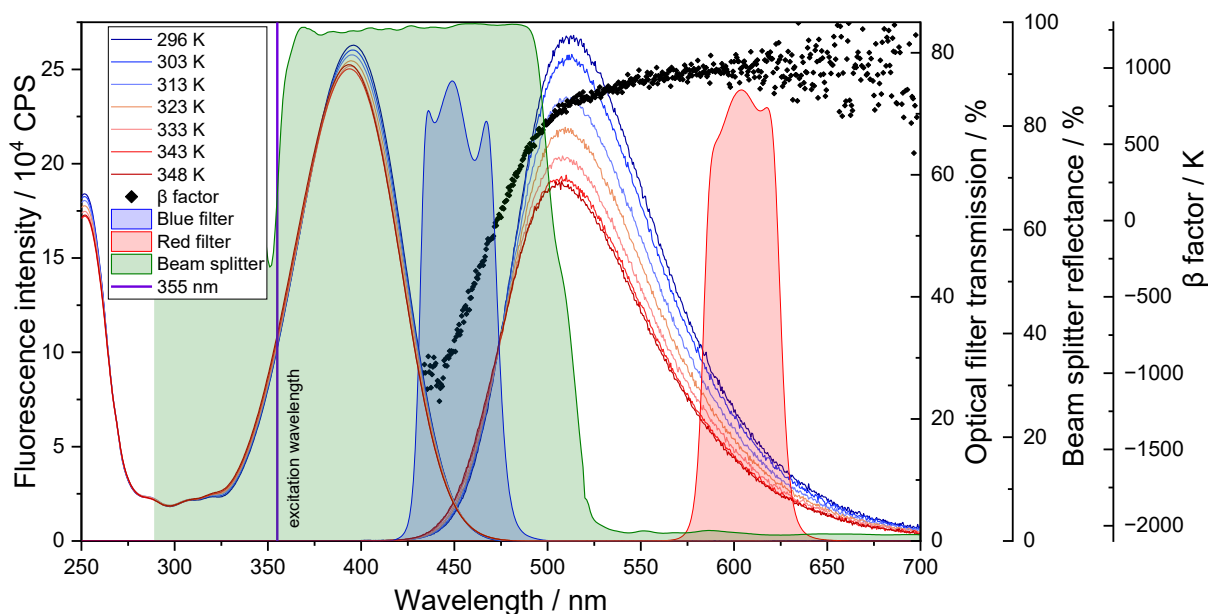


Figure 92: Temperature-dependent absorption (left) and fluorescence (right) spectra of coumarin 152 in ethanol (10 mg/l, 3.9×10^{-5} mol/l). The vertical line indicates the Nd:YAG excitation wavelength of 355 nm and the black symbols show the β factor calculated for a temperature difference of 40 K (between spectra taken at 303 and 343 K). Colored areas indicate the optical transmission of the utilized optical filters and the reflectance of the dichroic beam splitter.

8.2.2.2 Calibration of measurement setup (signal-ratio–temperature function)

For every 2cLIF measurement setup with its specific optical components and also for all different camera and intensifier settings, a signal-ratio–temperature function (or alternatively termed calibration function) needs to be determined. The calibration function is used to convert the measured LIF intensity ratios to temperature values. The procedure to calibrate the function is from the principle the same as described in section 8.1.2.1. In this work, the temperature-controlled measurement cell (section 7.2.1) was used to set the temperature of the cuvette (Hellma, macro cuvette 111-QS, quartz glass, 10×10 mm²) filled with a solution of 10 mg/l coumarin 152 in ethanol. The cell with the cuvette was placed at the same position where the flame is located during the measurements. By controlling the temperature of the cell various temperature stages were targeted and the temperature of the dye solution was kept constant for two minutes to ensure a homogeneous temperature distribution within the cuvette (Figure 94). At each temperature stage, LIF intensity images were recorded simultaneously for both color channels to determine the intensity ratio related to each temperature stage (image mapping was done in advance according to the procedure described in section 8.2.3). Per temperature stage 100 pairs of images were recorded and after background correction the intensity ratio map was calculated for each pair. After averaging the ratio maps a region of interest was

defined to determine the LIF intensity ratio related to the temperature set. The data points are plotted in the diagram shown in Figure 93.

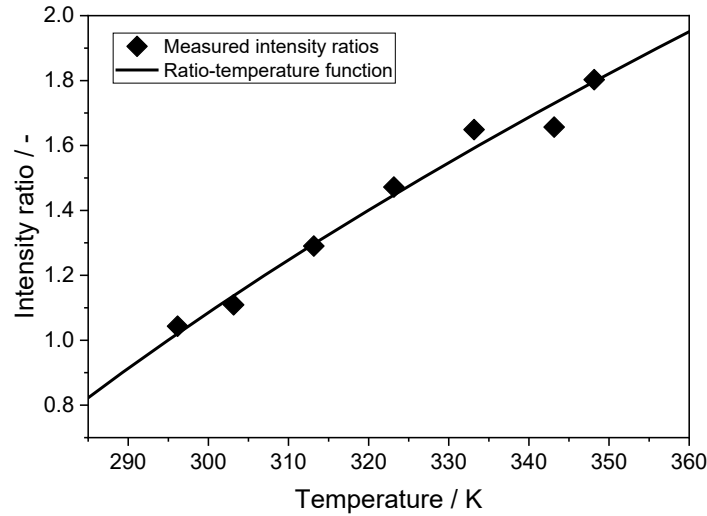


Figure 93: Two-color LIF intensity ratios (symbols) as a function of temperature, measured instantaneously with two cameras for 10 mg/l coumarin 152 in ethanol. A quadratic function fit is plotted as solid line (signal-ratio–temperature function).

The data points were fitted by a quadratic function to determine the signal-ratio–temperature function. The curve is plotted as solid line in Figure 93 and the function is given in Eq. (8.7).

$$T(R_{\text{LIF}}) = 10.77 R_{\text{LIF}}^2 + 36.61 R_{\text{LIF}} + 247.58 \quad (8.7)$$

8.2.3 Measurement procedure

A key point for the successful execution of instantaneous 2cLIF measurements is to align the field of view of the two cameras exactly. The position and angle of the cameras were manually adjusted by multi-axis linear translation stages as precisely as possible to establish the best matching field of view towards a target placed on top of the burner. An image mapping feature integrated in the DaVis software was used to correct minor camera misalignments. With this feature, slightly different view angles and distances between camera and target were compensated. A target (calibration plate) was placed on top of the burner in the plane of the laser sheet and an image was taken by each camera. Based on the pattern of the target a correction file was generated. The SpraySyn2 flame was operated with ethanol as solvent with 10 mg/l coumarin 152. Dye concentration and laser excitation intensity were kept low to reduce MDRs with lasing effects (section 8.1.2.3) and fluorescence signal re-absorption (section 7.3.4). The laser sheet was positioned vertically above the capillary outlet with a width of less than 1 mm. For each operating condition, 800 pairs of LIF intensity images were recorded at 10 Hz. The IRO gain of the red channel was set higher than the blue channel to compensate for its lower wavelength-dependent detection sensitivity (typical gain: 90 vs. 85). Background images were recorded with the flame operated at the respective condition and the laser blocked.

Post processing – Matlab script

Postprocessing and data evaluation was done by custom-made Matlab scripts. One script was used to determine the calibration function specific to the given setup and device settings (as described in section 8.2.2.2). The function was saved to a file. A second script calculated the

instantaneous and average liquid temperature maps based on imported LIF intensity images, background images, and the calibration function. First, the LIF intensity images were background corrected. Next, pixels with intensity values below a certain threshold were cut out. A threshold of 15 counts ($\sim 0.5\%$ of typical peak signal) was chosen to exclude areas with too low LIF signals for further evaluation. Then the ratio maps were formed from the processed intensity image pairs (Figure 95). With the calibration function, the ratio maps were converted to single-shot liquid temperature maps. Average liquid temperature maps (section 8.2.5) were formed by averaging the single-shot temperature maps. A mask was applied to the averaged maps to ensure a suitable data basis for averaging. The mask cut out pixels that in less than 10 % of the images provide above-threshold signal.

8.2.4 Measurement error of single-shot liquid-temperature maps

The single-shot liquid temperature maps determined with the experimental setup and measurement procedure described above feature strong spatial fluctuations in temperature. Even within single droplets or liquid ligaments in the spray breakup zone, temperature fluctuations are seen, which are physically not reasonable. One possible source of error is the noise introduced by the measurement approach. To illustrate this, intensity ratio maps of the cuvette are shown in Figure 94. The cuvette was placed in the temperature-controlled cell (section 7.2.1) and was filled with ethanol doped with 10 mg/l coumarin 152 and excited with a 355 nm laser sheet as described in section 8.2.2. The tracer concentration and the settings of the detection system were the same as used for the spray-flame measurements. On the top left, single-shot and on the top right averaged intensity ratio maps are shown. One temperature level is shown per row. The bottom section shows single-shot images for both color channels, from which the single-shot ratio map for the 70 °C case is created.

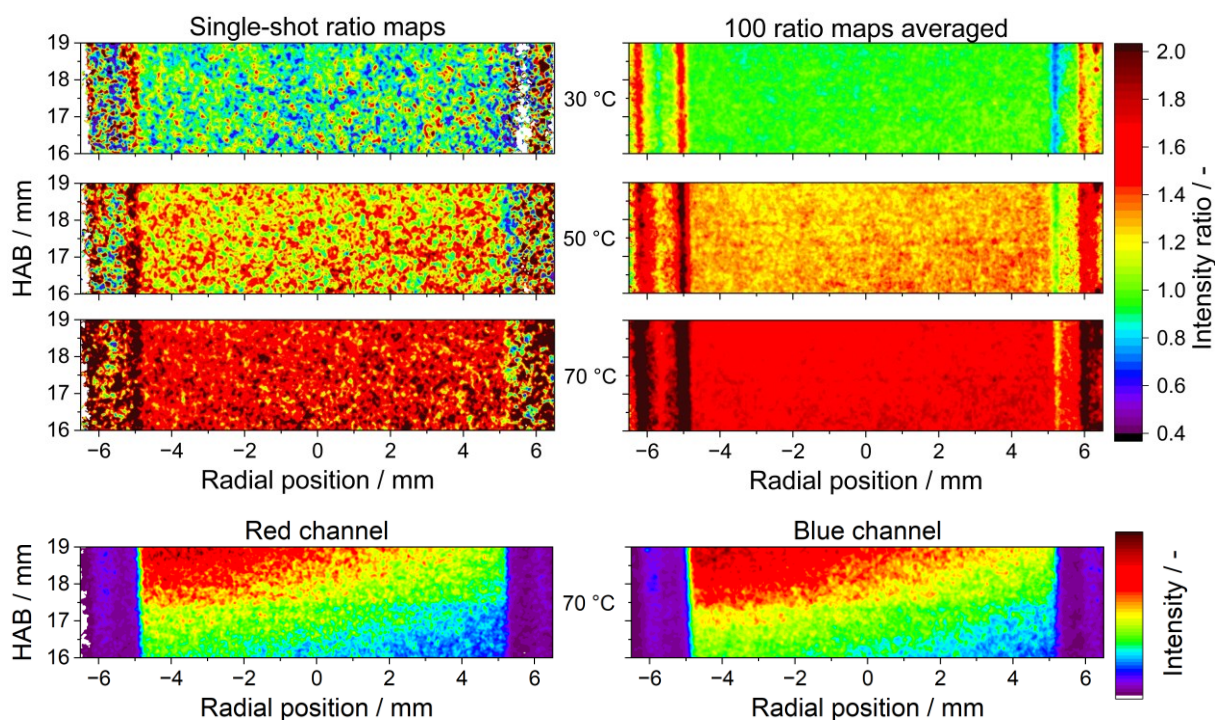


Figure 94: Fluorescence images measured in a quartz cuvette (Hellma 111-QS) with 10 mg/l coumarin 152 in ethanol at various temperatures, top left: Single-shot ratio maps, top right: 100 ratio maps averaged. The vertical lines at the image sides are caused by scattered light from the cuvette walls. Bottom: Single-shot images of both color channels, left: Red channel (CS: 0–1200 counts), right: Blue channel (CS: 0–1750 counts). All images: Full pixel resolution without spatial filtering.

From the left column with single-shot ratio maps one can see that even in a static, continuous and temperature-homogeneous liquid with sufficient signal, strong ratio fluctuations are present when the image is analyzed pixel by pixel. This shows that the photon noise caused by the low dye concentration and low signal intensities strongly amplifies during ratioing. To estimate the noise level, single-shot images of the red and blue color channels are provided in the lower section of Figure 94. Strong intensity variations between closely adjacent pixel ranges are evident, despite the expected homogeneous fluorescence signal in the cuvette. No spatial filtering or software pixel binning was applied. The top right column shows ratio maps averaged over subsequent measurements. The noise of the ratio maps is significantly reduced when the results from 100 image pairs are averaged. For the average liquid temperature maps presented in section 8.2.5, 800 temperature maps were averaged.

Figure 95 shows typical examples of 2cLIF single-shot raw-image ratio maps of the SpraySyn2 flame (left) and the cold ethanol spray (right) generated by the SpraySyn2 burner. The ratios are converted pixel-by-pixel to temperatures based on the calibration function (Figure 93). It is clearly visible that the result is dominated by noise and the color scale in Figure 95 ranging from intensity ratio 0.4 to 2 corresponds to temperatures of approximately 265 to 370 K, partially outside the calibration range. In the lower part of each image the spray nozzle with its capillary is indicated in black. The spatial image section is identical in all cases.

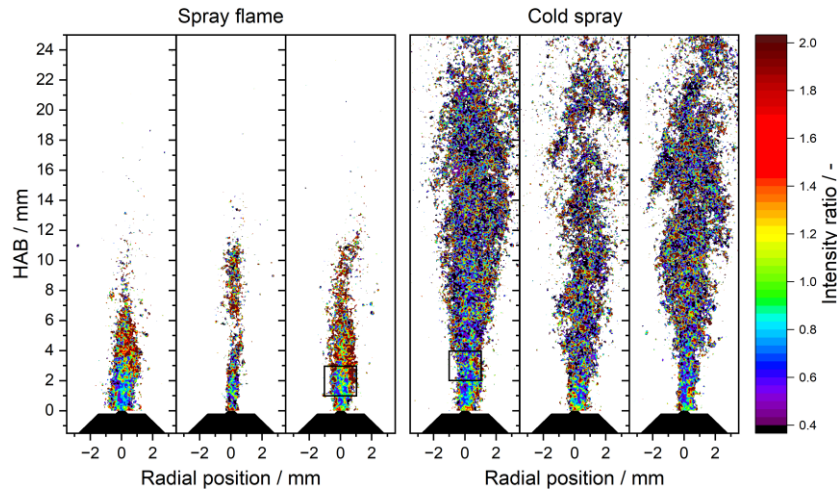


Figure 95: Typical examples for 2cLIF single-shot ratio maps of the SpraySyn2 flame (left) and cold spray (right). Spray conditions: Dispersion gas: 6 slm, liquid flow rate: 4 ml/min ethanol, equal detection and post-processing conditions. Higher intensity ratios correspond to higher temperatures.

The single-shot ratio maps using unfiltered images are affected by strong noise and ratio gradients between local areas are often physically not reasonable. The overall ratio level (\sim temperature level) in turn is reasonable (albeit with large scattering). In the spray flame, the spray break-up zone features rather a low ratio and the outer areas rather higher ratios. Across the whole field of view the cold ethanol spray features a constant lower ratio level. The fluorescence signal of the cold spray is spatially more extended due to the temperature-related lower evaporation rate, so that droplets survive over a longer distance compared to the spray flame.

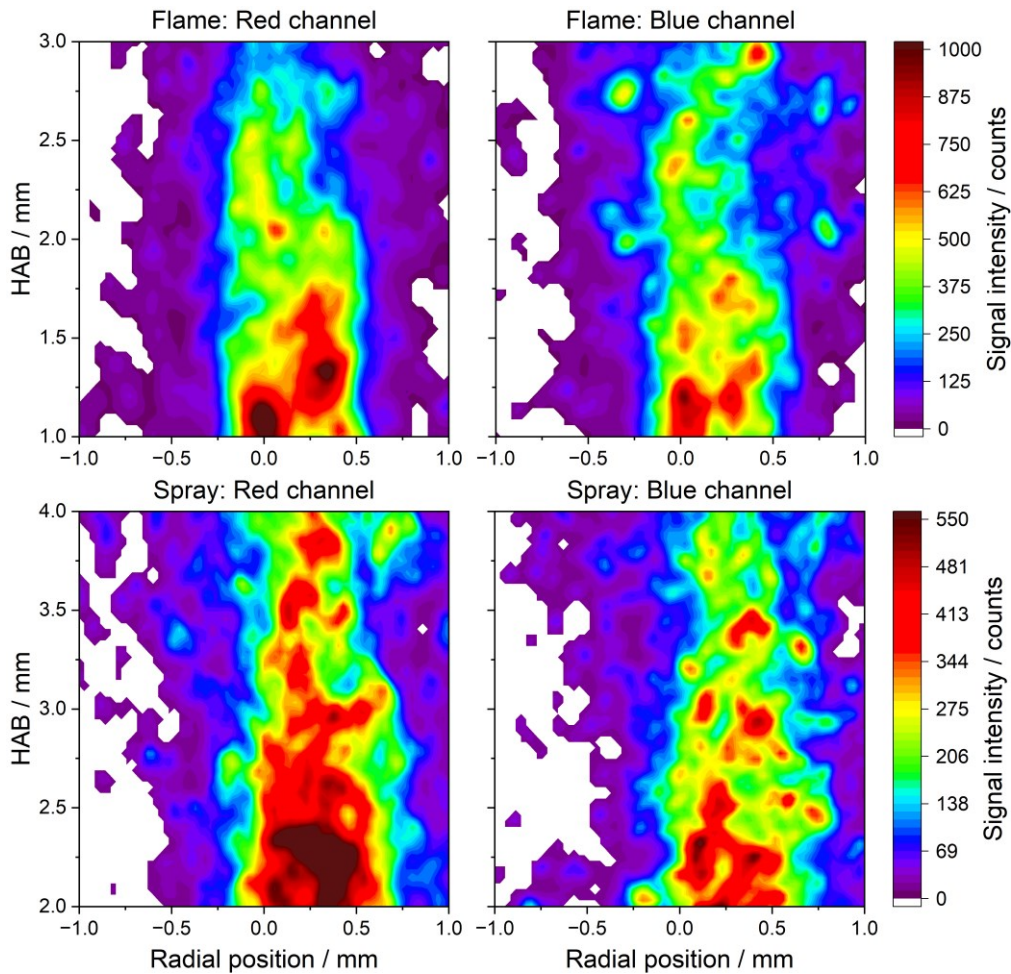


Figure 96: Single-shot images of both color channels which result in the ratio maps shown in Figure 95, enlarged sections of selected areas indicated by black rectangles. Top: Flame, bottom: Cold spray, left: Red channel, right: Blue channel.

To analyze the background for this large scattering, Figure 96 shows selected sections of single-shot images, which are used to generate the intensity-ratio maps depicted in Figure 95 (indicated by black rectangles). The single-shot images of the liquid phase appear blurred, and individual droplets cannot be identified in the spray core. The overall signal intensity distribution roughly corresponds to each other. However, the fine structures differ, possibly due to noise, signal scattering within the spray, and potentially out-of-plane fluorescence from scattered laser light.

To improve the quality of the results, various smoothing filters were applied to the single-shot intensity maps after background correction, effectively reducing the spatial resolution of the analysis. The single-shot images were processed by Gaussian and median filters, as well as by pixel binning at different kernel sizes. The results are provided in section 12.7 in the appendix. The median filter delivered the most promising results, as it preserves the original structure of the intensity images while effectively smoothing. However, significant errors still remain in the single-shot temperature maps, making the results unreasonable in certain areas. The Gaussian filter provides better smoothing and thus ratio calculation but changes the structure of the temperature distribution at larger kernel size in a non-acceptable way.

Even with the various spatial filtering approaches, the single-shot image analysis recorded by the current experimental setup resulted in unreasonable single-shot temperature maps outside

the core area. These problems are associated to the weak signal levels obtained in the attempt to prevent droplet leasing through low dye concentration and excitation fluence resulting in images affected by shot noise. Additionally, multiple light scattering can blur the images and affect local intensity ratios. Scattered laser light can also induce out-of-plane fluorescence. One way to overcome the latter problems is to apply the technique of ‘structured laser illumination planar imaging’ (SLIPI) [437, 440, 441]. Another well-known issue is the occurrence of ‘morphology-dependent resonances’ (MDR) [409, 442, 443] and the resulting lasing effects [378, 415] that can locally lead to non-linear signal response on the laser pulse energy. Various approaches have been suggested to overcome this problem (e.g., the use of a second dye as quencher [411]). As described in section 7.3.4, signal trapping can also be a problem, especially in strongly evaporating sprays when a high dye concentration and a high laser excitation energy exists [444]. A detailed discussion of these topics and improvement suggestions for future work is given in section 8.4.

However, scattering effects and the noise of the recorded single-shot ratio maps can be compensated by multi-shot averaging. But a distinct measurement error should nevertheless still exist. When the single-shot maps are averaged, the noise is reduced significantly and the resulting average liquid-temperature maps become reasonable (section 8.2.5).

8.2.5 Results

Temporally-averaged liquid-temperature maps of the SpraySyn2 flame and cold spray were measured and postprocessed according to section 8.2.2 and section 8.2.3. Table 15 gives an overview of the SpraySyn2 operating conditions investigated in this work. Column 1 defines its identifiers and columns 2–6 provide the flow rates. To investigate the impact of the spray form on the liquid temperature the dispersion gas flow was varied between 4 and 8 slm, and the liquid injection rate between 2 and 6 ml/min. To investigate the impact of the pilot flame on the liquid temperature its heating power was set to standard or 50 % of the standard heating power. OC-D6L2 is the standard operating condition of the SpraySyn2 burner. HAB = 0 mm is defined as the outlet of the burner capillary (section 3.2).

Table 15: SpraySyn2 operating conditions investigated in this chapter: Variation of dispersion gas flow, liquid injection rate and pilot flame power, liquid solvent: Ethanol, identifiers according to scheme: Operating condition – dispersion gas flow (slm) – liquid injection rate (ml/min) – pilot flame heating power (HP = half power).

Operating condition	Dispersion gas	Injection rate ethanol / ml/min	Pilot flame		Sheath gas
	O ₂ / slm		CH ₄ / slm	O ₂ / slm	N ₂ / slm
OC-D4L2	4	2	2	16	120
OC-D6L2	6	2	2	16	120
OC-D8L2	8	2	2	16	120
OC-D4L4	4	4	2	16	120
OC-D6L4	6	4	2	16	120
OC-D8L4	8	4	2	16	120
OC-D6L6	6	6	2	16	120
OC-D6L2-HP	6	2	1	8	120
OC-D6L4-HP	6	4	1	8	120
OC-D6L6-HP	6	6	1	8	120

8.2.5.1 Average liquid temperature maps of the cold spray

Figure 97 shows on the left the average liquid temperature map of a cold ethanol spray generated by the SpraySyn2 burner. The operating condition is equivalent to OC-D6L4 without pilot flame but with a sheath gas flow of 120 slm nitrogen. The cold ethanol spray was measured for reference to check the plausibility of the liquid-temperature results. On the right of the figure centerline temperature profiles are shown. The solid line shows the smoothed temperature profile (Savitzky–Golay filter, 20 data points) while the dashed line indicates the unsmoothed profile from the temperature map on the left.

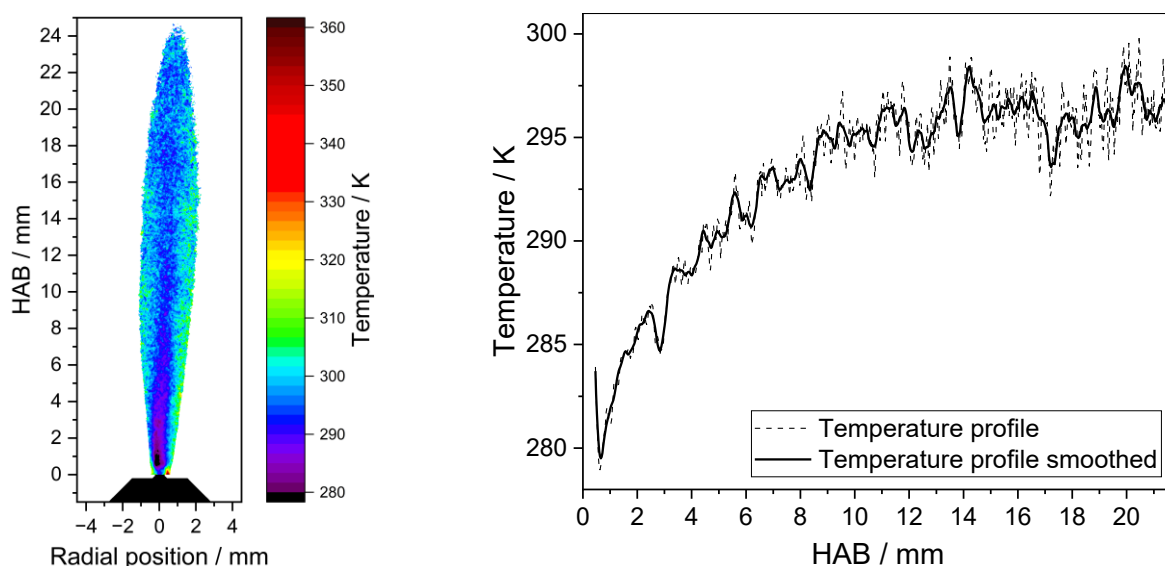


Figure 97: Liquid-phase temperature distribution in a cold ethanol spray generated by the SpraySyn2 burner. Averaged from 800 single 2cLIF temperature measurements. Dispersion gas flow: 6 slm, liquid flow rate: 4 ml/min, left: Temperature map, spray nozzle and capillary are indicated in black, right: Centerline temperature profile from a width of 0.49 mm.

The liquid temperature map on the left is an average of 800 single-shot temperature maps (three of them were shown as typical examples in Figure 95). Ethanol at room temperature (ca. 296 K) was ejected through the capillary. In the lower regions of the spray a low-temperature zone below 290 K can be seen. In the regions above this zone, the liquid-phase temperature is restricted to a narrow range around 300 K. The outer regions tend to feature slightly higher temperatures. The diagram on the right shows the centerline temperature profiles extracted from a radial width of 0.49 mm. The measurement results show that the liquid temperature is decreasing strongly within the first millimeter (down to a minimum temperature of 280 K). This is certainly a result of evaporative cooling of ethanol within the high-speed dispersion gas flow. After the temperature minimum at about HAB = 1 mm the liquid temperature is increasing steadily and approaching room temperature at about 296 K. Overall, the results shown in Figure 97 are reasonable for an ethanol spray and approve the measurement approach.

8.2.5.2 Average liquid temperature maps of the SpraySyn flame

Figure 98 shows average liquid phase temperature maps of various operating conditions of the SpraySyn2 flame. The pilot flame was operated with 2 slm CH₄ and 16 slm O₂ surrounded by a 120 slm N₂ coflow. The ethanol spray was changed by varying the dispersion gas flow rate between 4 and 8 slm and the liquid flow rate between 2 and 6 ml/min. The position and shape of the spray nozzle and capillary is shown in black at the bottom of the temperature

maps to get a better understanding of the size ratio between nozzle and the liquid temperature maps. Identifiers for the operating conditions are shown above the temperature maps (see Table 15 for more details).

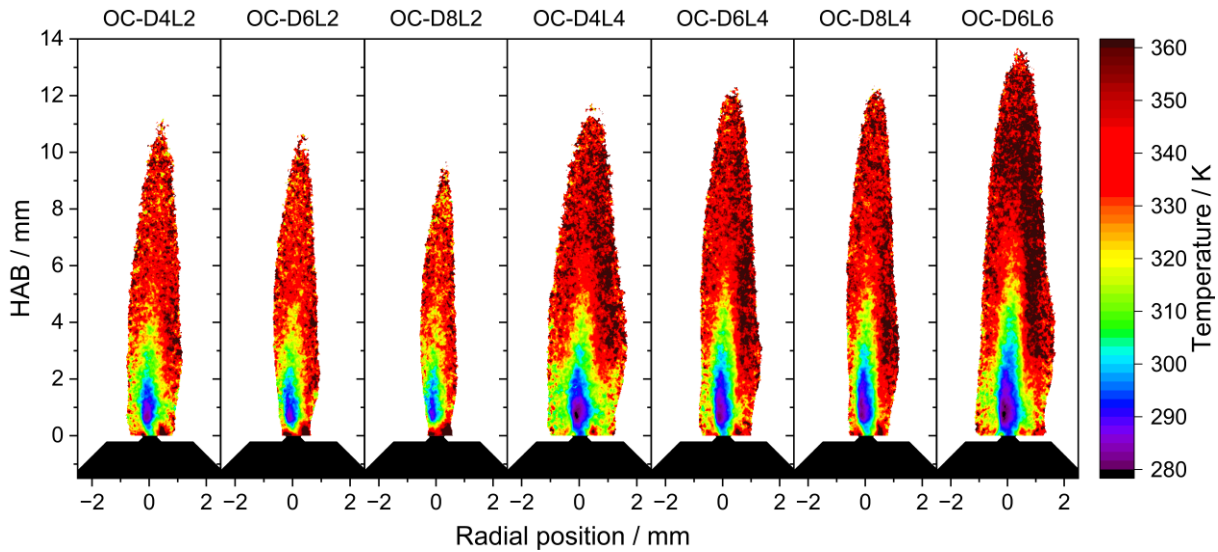


Figure 98: Liquid-phase temperature maps of the SpraySyn2 flame at various operating conditions: Standard pilot flame and sheath gas, identifiers are given on top of each temperature map, liquid: Ethanol, 800 single-shot temperature maps averaged. Spray nozzle and capillary are indicated in black.

The repetition of some of these 2cLIF measurements on different days showed high reproducibility. The range of the liquid temperature and the shape of the maps are reasonable. A cool core in the lower range of the spray flames is observed, as also for the average liquid temperature maps of the SpraySyn1 flame (Figure 87). Towards the outer regions and larger HAB the liquid temperature increases steadily. For a constant liquid flow rate of 2 ml/min the spatial extend where droplets are detected shrinks with an increasing dispersion gas flow. An obvious explanation is a faster evaporation and combustion due to a better atomization. With an increasing dispersion gas flow and a constant liquid flow rate of 4 ml/min the spatial extend gets thinner and higher. This can be explained by more droplets following the faster dispersion gas flow and a lower radial-velocity component. With a constant dispersion gas flow and an increasing liquid flow rate, the temperature maps extend in size because poorer atomization results in larger droplets that survive over longer distances within the flame. Moreover, also the cold zone extends in size and the minimum temperature decreases.

Centerline temperature profiles

Figure 99 shows centerline temperature profiles of liquid temperature maps presented in Figure 98. In the diagram on the left operating conditions with an ethanol injection rate of 2 ml/min and on the right with 4 ml/min are shown. For both diagrams the dispersion gas flow ranges between 4 and 8 slm. The data were slightly smoothed using a Savitzky–Golay filter with a 20-data-point range.

From the diagrams it can be seen that at a constant liquid injection rate (2 or 4 ml/min) the variation in the dispersion gas flow has no significant impact on the general course or slope of the profiles. Only for the liquid injection rate of 2 ml/min (left diagram) in the lower range at about HAB = 1 mm with increasing dispersion gas flow, an increase of the minimum liquid temperature can be seen.

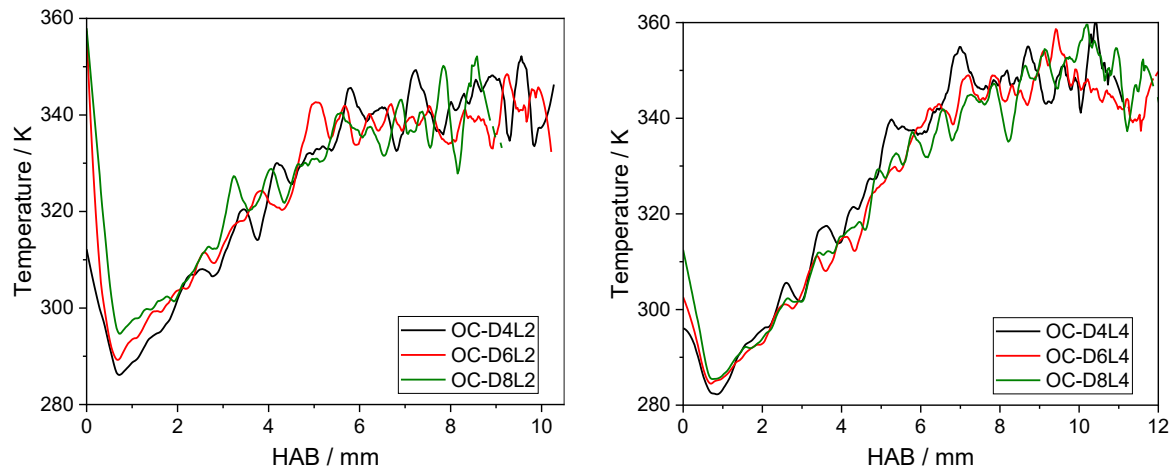


Figure 99: Centerline temperature profiles of average liquid-temperature maps shown in Figure 98, extraction width: 0.26 mm, left: Liquid flow rate of 2 ml/min, right: Liquid flow rate of 4 ml/min.

In comparison to the centerline liquid-temperature profiles of the SpraySyn1 burner (cf. Figure 88) the profiles of the SpraySyn2 flame feature a significantly steeper temperature gradient over HAB (2.25 vs. 9 K/mm). This can be explained by a better atomization of the new two-fluid nozzle (cf. section 3.2) and as a result, a faster droplet combustion. In general, the average liquid temperature maps of the SpraySyn1 burner are spatially more extended than the ones of the SpraySyn2 burner. This finding indicates that the SpraySyn1 burner features a poorer droplet atomization with larger droplets that experience a slower heat-up and thus survive longer distances within the spray flame.

Radial temperature profiles

Figure 100 shows the radial liquid-temperature profiles of OC-D6L4 at different HAB. The radial profiles of the other operating conditions are similar and are shown in the appendix in section 12.8. The data of the radial profiles were slightly smoothed using a Savitzky–Golay filter with a 20-data-point range.

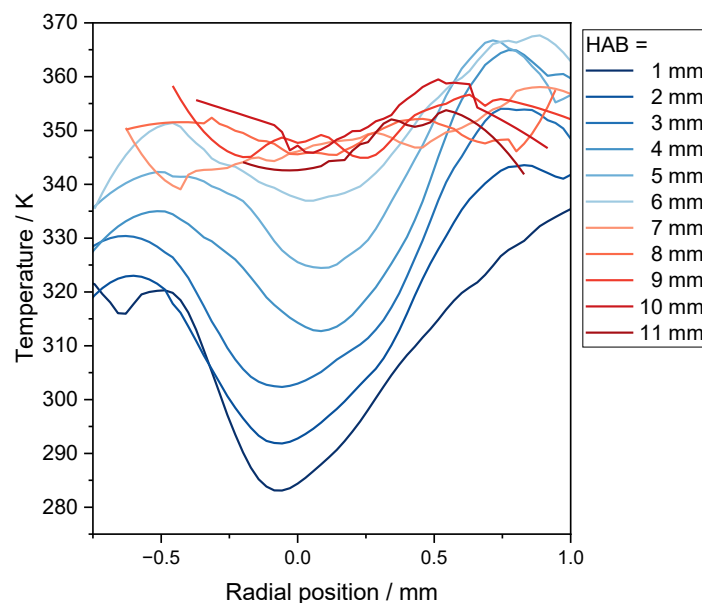


Figure 100: Radial liquid-phase temperature profiles at various heights above burner (HAB), averaged for 800 laser pulses from an extraction width of 0.4 mm, profiles smoothed (Savitzky–Golay filter, 20 data points), dispersion gas flow: 6 slm, liquid flow rate: 4 ml/min ethanol.

In the lower range of the flame (up to $HAB = 6$ mm), the liquid temperature increases from the center to the outer regions of the spray flame. In the higher range of the flame ($HAB > 6$ mm) the liquid temperature is largely constant in radial direction. Up to a height of 6 mm the temperature level on the right is higher than on the left. This can be explained by the fundamental asymmetry of the SpraySyn2 flame, which is mainly caused by manufacturing imperfections of the nozzle.

8.2.5.3 Comparison between standard and half-powered pilot flame

Figure 101 shows a comparison of the impact of the standard (left) and the half-powered pilot flame (right) on the average liquid-temperature maps for three spray conditions. The spray operating conditions were generated by a variation of the liquid flow rate at a constant dispersion gas flow of 6 slm oxygen. To generate the pilot flame with 50 % of the heat energy of the standard operating condition, the methane and oxygen flow rates were halved to 1 slm CH_4 and 8 slm O_2 (Table 15).

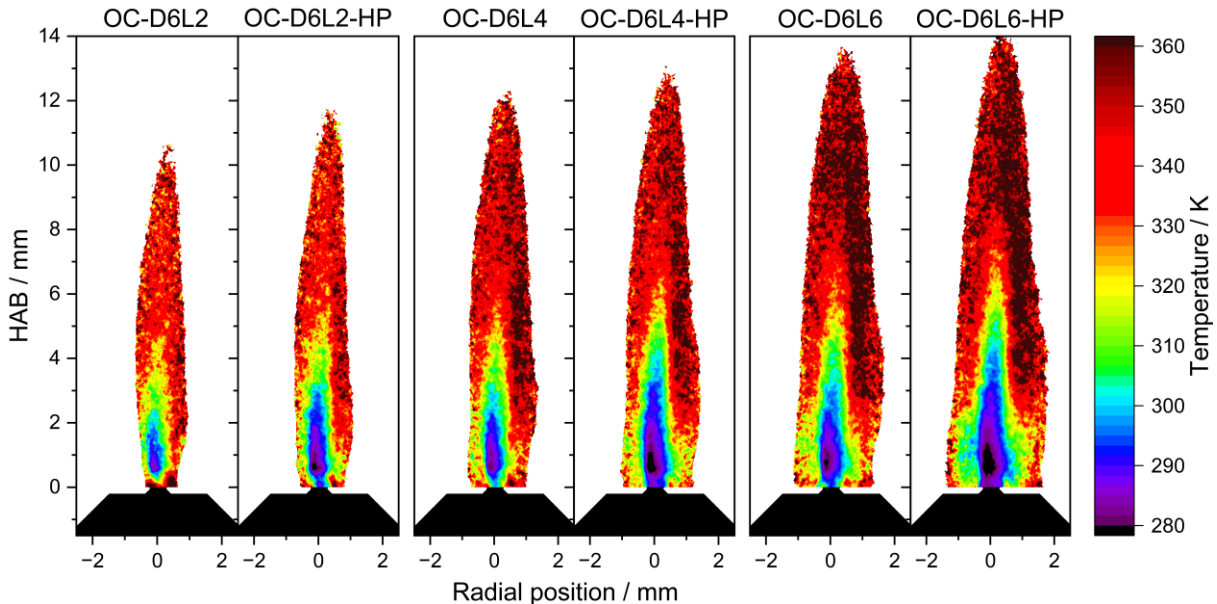


Figure 101: Average liquid-phase temperature maps of the SpraySyn2 flame at various spray operating conditions, identifiers are given on top of each temperature map, liquid: Ethanol, 800 single-shot temperature maps averaged. Spray nozzle and capillary are indicated in black. Variation of liquid flow rates, comparison between standard pilot flame (left) and half-powered pilot flame (right).

The variation in heat release of the pilot flame has essentially the same impact on the three spray operating conditions investigated. The average liquid-temperature maps with the half-powered pilot flame feature a lower temperature and spatially more extended cold zone in the lower range of the spray flames. This is obviously due to the lower heat input from the pilot flame, which results in lower gas temperatures and slower droplet heating. In the higher flame regions, no significant difference of the temperature level is observed as here the heat release is dominated by the burning spray. Moreover, the average liquid-phase temperature maps with the half-powered pilot flame are spatially more extended. This can be explained by a lower droplet heat-up and thus the droplets survive longer distances through the spray flame. Especially in the lower range of the spray flame ($HAB < 2$ mm) the radial extension of the liquid temperature map is larger for the half-powered pilot flame.

Centerline temperature profiles

Figure 102 shows flame-centerline profiles of the average liquid-temperature maps given in Figure 101. The profiles were more strongly smoothed (Savitzky–Golay filter with a 50-data-point range) to reduce the noise. The profiles for operating conditions with the standard pilot flame are plotted as solid lines, the profiles with the half-powered pilot flame as dashed lines.

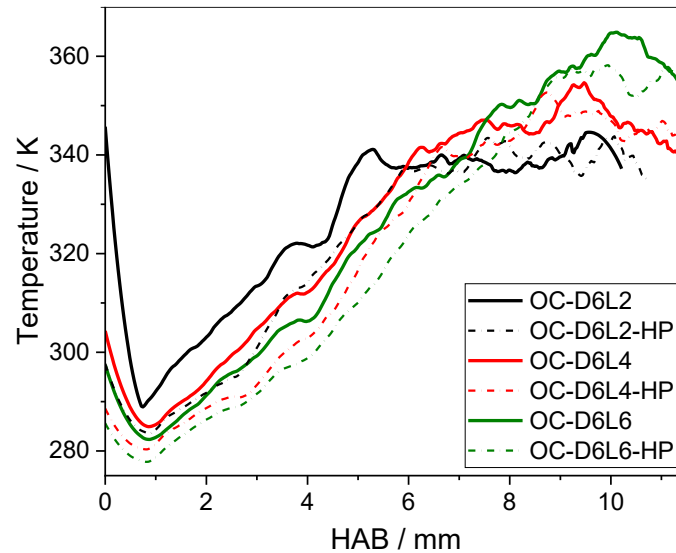


Figure 102: Centerline temperature profiles of averaged liquid-temperature maps shown in Figure 101, extraction width: 0.26 mm, comparison between the standard pilot flame (solid lines) and the half-powered (HP) pilot flame (dashed lines).

The centerline temperature profiles confirm the conclusions stated above. Compared to the standard, the operating conditions with the half-powered pilot flame feature a lower centerline liquid temperature up to about $HAB = 7$ mm. As the HAB increases, the liquid temperature of both pilot-flame operating conditions converges. In the higher flame regions, the temperature level shows no significant difference. For both pilot-flame operating conditions the average liquid temperature in the lower flame regions ($HAB < 7$ mm) decreases with increasing liquid flow rate. The temperature gradient over HAB is approximately the same for all operating conditions shown in Figure 102. Thus, the droplet heating rate is largely the same, but the initial liquid-temperature level at about $HAB = 1$ mm is significantly affected by the variation of the liquid flow rate at a constant dispersion gas flow.

Radial temperature profiles

Figure 103 shows a comparison of the radial liquid-temperature profiles between two operating conditions with different pilot-flame heat inputs (OC-D6L4 vs. OC-D6L4-HP). The operating condition with the standard pilot flame is plotted as solid lines, and with the half-powered pilot flame as dashed lines. To ensure clarity, only the profiles of 4 HAB with an equal distance of 3 mm to each other are shown.

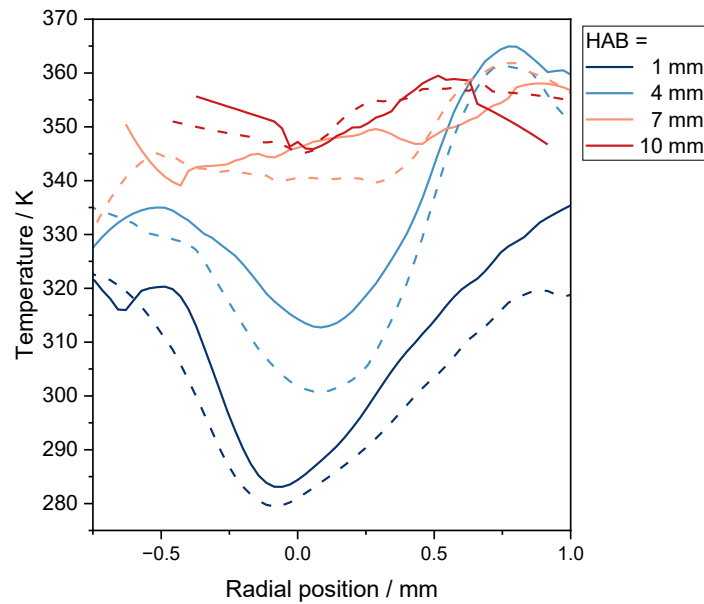


Figure 103: Radial liquid-temperature profiles at chosen HAB for the standard pilot flame (OC-D6L4, solid) vs. half-powered pilot flame (OC-D6L4-HP, dashed), averaged from an extraction width of 0.4 mm. Profiles smoothed (Savitzky–Golay filter, 20 data points), dispersion gas flow: 6 slm, liquid flow rate: 4 ml/min ethanol.

The radial liquid-temperature profiles of both operating conditions investigated feature a similar shape. For the lower flame region (HAB = 1 and 4 mm), the temperature profiles for the flame with the half-power pilot are shifted to lower liquid-phase temperatures. With increasing HAB, the liquid temperatures converge and the profiles (HAB = 7 and 10 mm) end up on the same temperature level. Looking at the profile of HAB = 1 mm, the droplet heating in radial direction appears to be the same for both pilot-flame heating powers.

8.3 Summary and discussion

By using two-color laser-induced fluorescence (2cLIF) thermometry, liquid temperature maps of spray flames generated by the SpraySyn1 (section 8.1) and SpraySyn2 burner (section 8.2) were measured and evaluated.

The average liquid-temperature results of the SpraySyn1 flame show that the dispersion-gas flow rate and the liquid-injection rate affect the liquid-temperature. The ratio between the dispersion gas flow and the liquid injection rate was found to be crucial for the liquid-phase temperature distribution. With an increasing dispersion gas flow the liquid temperature in the lower ranges of the SpraySyn1 flame decreases and with an increasing liquid flow rate the liquid temperature increases. This can be explained by the efficiency of the spray atomization. A higher dispersion gas flow results in a better atomization with smaller droplets, which feature a higher evaporation rate within the faster dispersion gas. These results fit well to gas-phase temperature measurements performed by Karaminejad et al. [51]. They applied multi-line OH-LIF thermometry to various operating conditions of the SpraySyn1 flame. The gas-temperature maps show a decreasing gas temperature with increasing dispersion-gas flows at a constant liquid flow rate of ethanol. Within the spray core of the flames, liquid temperatures below room temperature were measured. This was confirmed by thermocouple measurements in the cold ethanol spray [188]. From these results it can be inferred that evaporative cooling is one

important factor for the liquid temperature in ethanol spray flames. In the spray core it is the main influencing factor for droplet temperature.

The liquid temperature should be substantially different for solvents with other properties. For fuels that feature lower evaporation enthalpies and evaporation rates, evaporative cooling in the spray formation region is expected to be reduced. The cooling effect in the SpraySyn flame should be significantly lower for the mostly used solvent mixture of 65 vol.% 2-ethylhexanoic acid (EHA) and 35 vol.% ethanol [154] because it features a low vapor pressure (EHA: <0.001 kPa, ethanol: 5.9 kPa at 293 K) and a high boiling point (EHA: 501 K, ethanol: 351.5 K) compared to ethanol. Furthermore, fuel properties such as the viscosity affect atomization and consequently influence the droplet size, velocity, and temperature.

The SpraySyn2 burner with the improved two-fluid nozzle (section 3.2) generates an ethanol spray with significantly different droplet properties than the first version. It features a substantially better spray atomization [162], even at lower dispersion gas flow rates (standard operating condition: 6 vs. 10 slm). Despite the lower dispersion gas flow, significantly smaller droplet diameters and higher droplet velocities are achieved (section 5.3 and Ref. [122]). The SpraySyn1 flame features flame instabilities that are manifested by extinguishing and re-ignition of the spray flame [163]. These instabilities were reduced by the new nozzle design [162]. The operating conditions for SpraySyn1 and SpraySyn2 investigated in this work are significantly different in terms of dispersion gas and ethanol mass flows. As a result of these differences, the liquid-phase temperature maps of both burners are not directly comparable.

The average liquid temperature of the SpraySyn2 flame was measured, and ten operating conditions of the SpraySyn2 burner were investigated. The dispersion gas flow, liquid injection rate, and pilot-flame power were varied to analyze their impact on the liquid-phase temperature. The dispersion gas flow rate has no significant impact on the liquid-phase temperature along the centerline of the SpraySyn2 flame. With an increasing ethanol injection rate, the temperature in the lower regions of the flame decreases, whereas the temperature increases stronger with rising HAB. The impact of the pilot flame on the liquid-phase temperature was investigated by halving its heating input. The power of the pilot flame mainly affects the droplet temperatures in the lower regions of the SpraySyn2 flame. The lower heat supply to the spray-generation zone results in slower droplet heating. With greater HAB the impact of the pilot flame decreases and the droplet heating is driven by the burning spray. The heat release originates from the burning ethanol droplets themselves, causing the liquid temperature to converge for both pilot flame operating conditions.

The presented liquid-temperature results measured by 2cLIF thermometry for various operating conditions of the SpraySyn1 and SpraySyn2 flames approve the feasibility of the measurement technique based on the fluorescent tracer coumarin 152. The applicability and effectiveness of the new fluorescent tracer coumarin 152 was demonstrated for the solvent ethanol in the challenging environment of spray flames. More details and the discussion of its advantages compared to other tracers used in the literature are given in section 7. The measured liquid-temperature maps are reasonable. The reproducibility of the results was confirmed by repetition of the measurements. 2cLIF measurements in the cold ethanol spray generated by the SpraySyn2 burner proved to be plausible (section 8.2.5.1). The results show that liquid temperatures lower than ambient are present close to the capillary, which then increase with HAB and converge to ambient temperature. In line with the expectations, the liquid-temperature

maps of all spray flames measured range from slightly below room temperature to approximately the boiling point of ethanol.

To enable single-shot 2cLIF liquid-phase temperature measurements, some open issues need to be addressed, which are listed and discussed in the following section 8.4.

8.4 Outlook and improvement suggestions for future work

For future work, to enable 2cLIF single-shot measurements in sprays the following points should be considered. The most important point is to improve the quality of the single-shot images by reducing erroneous signal caused by, e.g., light scattering and secondary fluorescence in the spray, as well as noise induced by the detection system. The fluorescence-signal detection error amplified by pixel rationing must be significantly lower than the color-channel intensity ratio change caused by temperature variations of the tracer-doped liquid.

An obvious improvement is to use a camera system with generally a low noise level, e.g., by the use of a camera without intensification. The temperature-sensitive color channels in the fluorescence spectrum of coumarin 152 are in the visible light spectrum, which can be detected by common cameras without intensification. It would be beneficial to choose a gated camera to limit the exposure time to the laser pulse length, to reduce interference from background signal due to, e.g., chemiluminescence. High-quality lenses with a low f -number (larger aperture with more light collection) in combination with suitably sized optical filters should be used to increase the detectable fluorescence signal. In case an intensifier is used, the gain can be reduced to a level of operation where the noise introduced by the intensifier is minimized.

Another option to reduce noise from the spray or detection system is to use camera pixel binning. For measurement approaches targeting extended areas, such as instantaneous LIF thermometry in the gas phase, spatial areas can be combined and noise reduced by pixel binning. However, for applications in sprays, this should be done in combination with higher optical magnification to maintain sufficient resolution of single droplets. It may be necessary to limit the field of view to smaller areas of interest in the spray flame. The optical magnification can be realized for example by the use of macro lenses and a shorter distance between spray flame and camera, or microscope lens with an achromatic tube lens [194], or the use of extension tubes to increase the distance between lens and camera sensor [445].

Moreover, cameras with a high dynamic range are an advantage for 2cLIF thermometry. A high dynamic range enables the detection of a broader range of fluorescence signal intensities, thus a wider range of droplet sizes and droplets with an enriched dye concentration due to evaporation (section 8.1.2.3). When the dynamic range of the camera is a limiting factor, the detectable intensity range is constrained, preventing the detection of either low or high fluorescence signal intensities.

Multiple light scattering between the droplets of sprays cause stray light, secondary fluorescence and imaging artifacts [446]. For instantaneous 2cLIF imaging this results in blurry fluorescence images that cause errors in the intensity ratios of the color channels. One way to reduce the multiple light scattering contribution is to apply 'structured laser illumination planar imaging' (SLIPI) [440]. For this technique line patterns are created within the excitation laser sheet, e.g., by placing a transmission grating in the laser light path. Only not scattered light maintains the introduced line pattern while scattered light loses this modulation information. This allows the distinction between not scattered and scattered light to correct the recorded

images by removing the scattered light part. In the initial stage, the degree of scattering in the spray can be assessed by incorporating a grating structure into the laser sheet. Various measures such as varying tracer concentration, adjusting detection settings, and optimizing laser energy can be employed to minimize scattered light as much as possible.

An approach to reduce secondary fluorescence caused by scattered laser light was recently presented by Stiti et al. [447]. They enhanced instantaneous two-color laser-induced fluorescence thermometry in liquids by implementing the two-photon excitation approach earlier introduced by Berrocal et al. [448, 449]. This improvement reduces the excitation of fluorescence-tracer molecules outside the laser-sheet region (e.g., excitation by scattered laser light). This is particularly advantageous for applications in two-phase systems with high refractive indices or significant light scattering, such as sprays.

The detectable fluorescence signal should be maximized without affecting the fluorescence spectrum. Morphology-dependent resonances (MDR) in connection with lasing remain a crucial problem in two-color LIF applications in droplets and sprays. On one hand, higher laser dye concentrations and higher laser excitation energies increase the detectable fluorescence signal, but on the other hand it increases MDR [411] and lasing effects [415] within tracer-doped droplets. Lasing effects are reflected by a narrowing of the fluorescence spectrum or the formation of lasing peaks within the spectrum. These effects can cause large measurement errors when spectrally located within the 2cLIF color channels. These effects tend to occur in droplets when they feature larger diameters and a high roundness [418], a high dye concentration or a high laser excitation intensity is applied (cf. section 8.1.2.3). Especially for instantaneous 2cLIF applications in sprays or droplets this effect becomes relevant in the context of maximizing the signal-to-noise ratio. In contrast to averaged 2cLIF the pixel-intensity ratios and hence the temperature values are derived from only two images recorded during a single laser shot. Consequentially the detectable signal especially from small droplets is a limiting factor. And as indicated above, the detectable signal cannot be arbitrarily increased because lasing effects need to be avoided by using low dye concentrations and low laser excitation intensities. In addition, especially in environments with fast evaporating droplets, low laser dye concentrations should be used, in order to reduce fluorescence signal re-absorption. This problem was discussed in detail in section 7.3.4.

9 Summary and conclusions

The gas-phase synthesis of nanoparticles enables the production of functional materials with a broad range of characteristics and properties, which are of interest for various applications (e.g., in the field of energy technology). The nanoparticle synthesis in spray flames has the advantage that a broad variety of inexpensive precursors can be added to the liquid fuel. This precursor solution is atomized into the spray flame and opens access for all sorts of metal atoms to the gas-phase synthesis. The SpraySyn burner was developed as a standardized burner for the investigation of metal-oxide nanoparticle synthesis in spray flames. The design and the operating conditions were standardized to ensure the reproducible operation in various research laboratories across the globe. A calibration routine was developed to verify the accurate and comparable operation of the SpraySyn burner [174]. After undesired spray-flame instabilities were identified, an improved two-fluid nozzle was developed [163] and a new version of the SpraySyn burner established [162].

The aim of the overarching research project, embedded within the DFG Priority Program SPP1980, is the characterization of the SpraySyn flame and the generation of a comprehensive data base (SpraySyn Database [56]) to support the further development of the process understanding of the gas-phase synthesis of nanoparticles. Within the scope of this project, the burner design and operating conditions shall be further improved. Ultimately, the acquired knowledge is intended to enable the upscaling of the nanoparticle-synthesis process to an industrial production level.

In the context of the work conducted within this subproject, the SpraySyn burners (version 1 and 2) and two pilot-scale spray burners were investigated and measurement data generated for provision to the SpraySyn Database and therefore to the SpraySyn-burner community. Various measurement techniques were applied to the spray flames to generate an extensive data set for the use as input in simulations and to provide information to enable a deeper understanding of the processes relevant for nanoparticle synthesis in spray flames. This data is intended to be the basis for the development of kinetic models, the validation of simulation models, and as boundary conditions for simulations. For various spray flames and operating conditions, spectrally resolved chemiluminescence spectra, droplet velocity and size distributions, gas-phase temperature maps and liquid-phase temperature maps were measured. Moreover, an extensive study on suitable fluorescence tracers for the application of two-color laser-induced fluorescence thermometry in liquids was conducted to enable 2cLIF measurements in the liquid-phase of spray flames. A short summary of the contents of this work with the description of the provided data and the measurement techniques applied to generate this data is given below.

Spectrally resolved Chemiluminescence measurements

Chemiluminescence spectra were measured by a spectrometer setup at different heights above the SpraySyn1 burner for various operating conditions with the precursors iron nitrate nonahydrate and HMDSO. Several species emissions in the SpraySyn1 flame were identified and their spatial distribution analyzed and illustrated in various diagram formats. The chemiluminescence spectra of pure solvents (ethanol, 65EHA35EtOH, 1-butanol, o-xylene) were investigated and the emission of OH^* , CH^* , CO_2^* , C_2^* , and Na^* analyzed. SiO_2 nanoparticles were synthesized from HMDSO in ethanol. Si^* and SiO^* emission was observed in the lower flame regions between 215 to 275 nm. Emission spectra during the synthesis of iron oxide

nanoparticles from iron nitrate nonahydrate were recorded and analyzed. Emission from Fe^* and FeO^* was identified between 340–400 nm and 530–690 nm, respectively.

The chemiluminescence measurements in the SpraySyn1 flame were performed to get deeper knowledge about the presence and location of chemically excited species. The data is intended to help understanding chemical reactions during nanoparticle synthesis in spray flames and can be the basis for the development of reaction mechanisms or the validation of simulation models. This data set was used for the validation of tomographic flame reconstructions [204] and for the identification of flame luminescence in the context of optical measurements in the SpraySyn1 flame [250].

Laser-Doppler and phase-Doppler anemometry

A comprehensive study on droplet velocity and size distributions for various solvents and operating conditions of the SpraySyn2 flame and cold spray is presented and analyzed. The measurements were performed by laser-Doppler and phase-Doppler anemometry with a commercial LDA/PDA system. The spray generated by the SpraySyn2 burner is characterized in all spatial dimensions. Averaged false-color maps of the mean axial droplet velocity, mean radial droplet velocity, mean droplet size and droplet count rate are provided in various spatial planes in vertical and horizontal direction. Moreover, centerline and radial profiles of the same parameters are given.

The results for the SpraySyn2 burner show that the mean axial and radial droplet velocities are significantly driven by the dispersion gas flow rate, while they are less affected by the liquid flow rate or the type of solvent used. The mean droplet size is significantly affected by the chosen solvent and the dispersion gas flow, with comparatively less impact from the liquid flow rate. The chosen solvent has the strongest influence on the droplet count rate, while the dispersion gas and liquid flow rate have rather a minor impact.

These results are of great interest for the understanding of nanoparticle synthesis in spray flames and are especially designed as input for spray flame simulations or its validation. Data of this study and the data presented in section 8.1.4.1 were used as input data for boundary conditions of simulations and for the validation of simulation models by various research groups [179, 181, 183, 189, 269]. Schneider [122] presented a related study for the SpraySyn1 burner measured by the identical LDA/PDA system.

Multi-line NO laser-induced fluorescence thermometry

Gas-temperature maps of two pilot-scale spray flames (Berlin burner and HSW burner) were measured by multi-line NO-LIF thermometry to analyze the impact of the gas temperature on the properties of synthesized iron-oxide nanoparticles. The pilot-scale burners were designed to investigate the process of upscaling nanoparticle production to an industrial level. The pilot-scale Berlin burner was designed to be operated with hydrogen as fuel gas and is equipped with an electrical heat ring to establish continuous auto-ignition of the pilot flame. The HSW burner is an upscaled version of the SpraySyn burner operated with methane and oxygen. The nanoparticles were synthesized from the precursor solutions of iron nitrate nonahydrate dissolved in ethanol or in a mixture by volume of 65 % 2-ethylhexanoic acid and 35 % ethanol. In line with the expectations, the pilot-scale burners show for various operating conditions significant differences in the gas-temperature shape and level. Especially the type of liquid fuel and

the species of pilot and dispersion gas affects the gas temperature. The investigations of the nanoparticle properties conducted by Martin Underberg, showed that higher gas temperatures result in a lower fraction of large particles and thus a higher specific surface area of the particle samples. Furthermore, the size of the particles in the small particle fraction increases. This indicates that higher gas temperatures tend to suppress the liquid-to-particle synthesis pathway and promote the gas-to-particle synthesis pathway [147]. Moreover, gas-phase temperature maps of the pilot-scale HSW burner were used for the validation of three-dimensional RANS-modeling [183].

Two-color laser-induced fluorescence thermometry

The main focus of this work was on two-color laser-induced fluorescence thermometry in the liquid phase of spray flames. The 2cLIF measurements followed a comprehensive study on suitable fluorescent tracers for the single-dye approach, specifically tailored for the application in evaporating droplets within spray flames. This study was necessary, because in the literature there was no reference available for a suitable tracer for this challenging application case. Proposed fluorescent tracers feature disadvantages like, e.g., a low temperature sensitivity or high fluorescence signal re-absorption [376, 450]. As a result of the study, the laser dye coumarin 152 is proposed as a new tracer for 2cLIF thermometry in liquids. Due to its large Stokes shift it features low fluorescence signal re-absorption and therefore is in particular favorable for the application in liquids that face changing tracer concentrations (e.g., evaporating droplets) or when changes in the fluorescence-signal path lengths through the tracer-doped liquid are present (e.g., mixing of liquid flows). Moreover, coumarin 152 is characterized by a high temperature sensitivity, it is soluble in many solvents, and features a high excitation-light absorption at the 3th harmonic (266 nm) and 4th harmonic (355 nm) of Nd:YAG lasers. The ability to pulse Nd:YAG lasers enables single-shot measurements. The applicability of coumarin 152 for 2cLIF thermometry was demonstrated in the challenging application case of spray flames.

The liquid temperature of the SpraySyn1 and SpraySyn2 flames were measured by 2cLIF for various operating conditions. Single-shot measurements in the liquid phase of the SpraySyn2 flame were performed, but it turned out that erroneous signal in the recorded images was too high to obtain reasonable single-shot temperature results. Scattering and secondary fluorescence in the spray and noise from the detection system amplified by color-channel rationing, superimposed the impact of liquid-temperature changes on the color-channel intensity ratios. By averaging the single-shot temperature maps, the noise was significantly reduced and reasonable average liquid-temperature maps were obtained.

The main finding from the comparison between the liquid temperature of both SpraySyn burners is that the liquid-temperature gradient over the measurement position (HAB) is significantly higher for the SpraySyn2 flame compared to the first version. This can be explained by the more efficient atomization resulting in smaller droplets and a faster and more stable combustion of the ethanol droplets [162]. The average liquid-temperature maps of the SpraySyn1 and SpraySyn2 flames show close to the capillary outlet a spray core with liquid temperatures below room temperature, which indicate strong evaporative cooling of ethanol. The average liquid temperature of the ethanol droplets within the flames range between somewhat below room temperature and approximately the boiling point of ethanol, what approves the plausibility of these results. Moreover, 2cLIF temperature measurements in the cold ethanol spray of the SpraySyn2 burner showed reasonable results. To the best of the author's knowledge, there is

no documented application of the 2cLIF technique in sprays or spray flames in the literature that surpasses the results presented in this work. This study represents the most advanced 2cLIF imaging measurements of liquid-phase temperature within the complex environment of spray flames.

10 Outlook and future work

The production of functional materials via the nanoparticle synthesis in spray flames has great potential and offers ample room for further developments. Currently, numerous research groups work on advancing the synthesis process, extending the range of producible materials, and on upscaling of the production output [106]. In this context, the SpraySyn data base [56] for the standardized SpraySyn burners [162, 174] have been established to support the understanding of the nanoparticle synthesis in spray flames.

In future work, the NO-LIF thermometry approach can be applied to pilot-scale spray-flame facilities with iron-oxide nanoparticle synthesis by utilizing an alternative spectral range of the NO excitation spectrum to avoid interference with the Fe-LIF peak [354]. The dye laser output should be improved (by maintenance or a new laser system) to improve the LIF signal and facilitate the use of the bandpass filter to enable the measurement-error analysis based on the relative standard deviation of the NO-LIF signal (section 6.3.2). Moreover, the HSW burner design should be enhanced to enable the alignment of the flame (section 6.4.2). This is especially important in the context of laser sheet-based measurement techniques.

Besides temperature measurements in liquids, the two-color tracer-LIF technique can be used for other application cases such as concentration measurements or measurements of the mixture composition of two liquids. When a constant temperature and laser dye concentration is present, the fluorescence spectrum is primarily affected by the mixture composition (section 7.3.5 and appendix Figure A38). In case temperature variations are present, a tracer that is temperature insensitive can be utilized. Depending on the mixture composition of the solvent the fluorescence spectrum experiences a spectral shift, that can be exploited by the 2cLIF approach. As in the case of 2cLIF thermometry, fluorescence signal trapping needs to be considered (section 7.3.4).

To the author's knowledge, there is no extensive investigation of MDRs, lasing effects and re-absorption within sprays or spray flames available in the literature. Palmer et al. [411] conducted a study on MDRs and lasing effects inside single micro droplets and suppressed the undesired effects by an additional dye for signal quenching [408]. However, this approach results inherently in higher fluorescence signal re-absorption effects (section 7.3.4) and therefore is not applicable in evaporating droplets. For the application in evaporating droplets (laser-dye enrichment), an improvement proposal for this approach would be the application of a quenching species that does not fluoresce and features a more constant absorption spectrum to reduce the impact on the fluorescence signal emitted from the droplets. For future work, a detailed spectral study for the single-dye approach on these effects in sprays and single droplets is of interest to optimize the maximum laser excitation energy and dye concentration that can be applied for various applications (e.g., sprays, spray flames, single droplets). The fluorescence spectra of various laser dyes in systems like sprays should be measured and investigated with regard to the occurrence of spectral narrowing and lasing peaks [420-425]. The knowledge of the thresholds of dye concentration and laser excitation energy would be valuable information for the optimization and customization of 2cLIF setups for desired applications. Parameters to be investigated for its impact on lasing should be the laser-dye concentration, the laser-excitation intensity, the droplet diameter and roundness, the solvent, the type of dye with its fluorescence quantum yield, and the excitation wavelength.

Two-color tracer-LIF thermometry features a high potential for the application in liquids where the accessibility is restricted by the framework conditions, therefore, where common temperature-measurement techniques are not applicable (e.g., turbulent flows or droplets in flames). The 2cLIF technique is a possible option for application cases, where two-dimensional information of temperature is of interest (e.g., temperature maps in turbulent flows, mixing processes). Instantaneous 2cLIF temperature imaging is promising in systems with high temporal dynamics where the temperature could be spatially and visually monitored in real time. It is especially suitable for application cases with rapid events where detailed temperature mapping is of interest. Moreover, the 2cLIF approach is non-intrusive and can be applied to systems without physical interference and can provide information from the inside of fluids. However, numerous unresolved issues remain. There are many possible approaches for further development and optimization of the two-color laser-induced fluorescence thermometry in liquids which should be addressed and solved in future work. The most relevant topics were summarized and discussed in section 8.4.

11 References

- [1] E. Wolf, Einstein's Researches on the Nature of Light, *Optics News* 5 (1979) 24-39.
- [2] G. Schmid, *Nanoparticles: from theory to application*, John Wiley & Sons, 2011.
- [3] S.K. Ghosh, T. Pal, Interparticle coupling effect on the surface plasmon resonance of gold nanoparticles: from theory to applications, *Chemical Reviews* 107 (2007) 4797-4862.
- [4] I. Khan, K. Saeed, I. Khan, *Nanoparticles: Properties, applications and toxicities*, *Arabian Journal of Chemistry* 12 (2019) 908-931.
- [5] P. Throer, *Materials in Today's World*, McGraw-Hill, 1992.
- [6] Y. Lu, L. Wang, D. Chen, G. Wang, Determination of the concentration and the average number of gold atoms in a gold nanoparticle by osmotic pressure, *Langmuir* 28 (2012) 9282-9287.
- [7] T. Mori, T. Hegmann, Determining the composition of gold nanoparticles: a compilation of shapes, sizes, and calculations using geometric considerations, *Journal of Nanoparticle Research* 18 (2016) 295.
- [8] J.C. Slater, Atomic radii in crystals, *The Journal of Chemical Physics* 41 (1964) 3199-3204.
- [9] E. Clementi, D. Raimondi, W.P. Reinhardt, Atomic screening constants from SCF functions. II. Atoms with 37 to 86 electrons, *The Journal of Chemical Physics* 47 (1967) 1300-1307.
- [10] G.A. Somorjai, J.Y. Park, Molecular factors of catalytic selectivity, *Angewandte Chemie International Edition* 47 (2008) 9212-9228.
- [11] X. Zhou, W. Xu, G. Liu, D. Panda, P. Chen, Size-dependent catalytic activity and dynamics of gold nanoparticles at the single-molecule level, *Journal of the American Chemical Society* 132 (2010) 138-146.
- [12] M.J. Hajipour, K.M. Fromm, A.A. Ashkarran, D.J. de Aberasturi, I.R. de Larramendi, T. Rojo, V. Serpooshan, W.J. Parak, M. Mahmoudi, Antibacterial properties of nanoparticles, *Trends in Biotechnology* 30 (2012) 499-511.
- [13] M. Faraday, X. The Bakerian Lecture.—Experimental relations of gold (and other metals) to light, *Philosophical Transactions of the Royal Society of London* (1857) 145-181.
- [14] V. Sharma, K. Park, M. Srinivasarao, Colloidal dispersion of gold nanorods: Historical background, optical properties, seed-mediated synthesis, shape separation and self-assembly, *Materials Science and Engineering: R: Reports* 65 (2009) 1-38.
- [15] G. Zengin, M. Wersäll, S. Nilsson, T.J. Antosiewicz, M. Käll, T. Shegai, Realizing strong light-matter interactions between single-nanoparticle plasmons and molecular excitons at ambient conditions, *Physical Review Letters* 114 (2015) 157401.
- [16] G. Mie, Beiträge zur Optik trüber Medien, speziell kolloidaler Metallösungen, *Annalen der Physik* 330 (1908) 377-445.
- [17] U. Kreibig, M. Vollmer, *Optical properties of metal clusters*, Springer Science & Business Media, 2013.
- [18] G.F. Goya, T. Berquo, F. Fonseca, M. Morales, Static and dynamic magnetic properties of spherical magnetite nanoparticles, *Journal of Applied Physics* 94 (2003) 3520-3528.
- [19] S.H. Jeong, H. Choi, J.Y. Kim, T.W. Lee, Silver-based nanoparticles for surface plasmon resonance in organic optoelectronics, *Particle & Particle Systems Characterization* 32 (2015) 164-175.

- [20] J. Sun, S. Simon, The melting behavior of aluminum nanoparticles, *Thermochimica Acta* 463 (2007) 32-40.
- [21] P. Schlexer, A.B. Andersen, B. Sebok, I. Chorkendorff, J. Schiøtz, T.W. Hansen, Size-dependence of the melting temperature of individual Au nanoparticles, *Particle & Particle Systems Characterization* 36 (2019) 1800480.
- [22] S.H. Lee, B.-H. Jun, Silver nanoparticles: synthesis and application for nanomedicine, *International Journal of Molecular Sciences* 20 (2019) 865.
- [23] C. Burda, X. Chen, R. Narayanan, M.A. El-Sayed, Chemistry and properties of nanocrystals of different shapes, *Chemical Reviews* 105 (2005) 1025-1102.
- [24] V. Arole, S. Munde, Fabrication of nanomaterials by top-down and bottom-up approaches-an overview, *Journal of Materials Science* 1 (2014) 89-93.
- [25] S. Dolgaev, A. Simakin, V. Voronov, G.A. Shafeev, F. Bozon-Verduraz, Nanoparticles produced by laser ablation of solids in liquid environment, *Applied Surface Science* 186 (2002) 546-551.
- [26] M. Niederberger, G. Garnweitner, Organic reaction pathways in the nonaqueous synthesis of metal oxide nanoparticles, *Chemistry—A European Journal* 12 (2006) 7282-7302.
- [27] M. Sokolowski, A. Sokolowska, A. Michalski, B. Gokieli, The “in-flame-reaction” method for Al₂O₃ aerosol formation, *Journal of Aerosol Science* 8 (1977) 219-230.
- [28] L. Mädler, H.K. Kammler, R. Mueller, S.E. Pratsinis, Controlled synthesis of nanostructured particles by flame spray pyrolysis, *Journal of Aerosol Science* 33 (2002) 369-389.
- [29] R. Strobel, L. Mädler, M. Piacentini, M. Maciejewski, A. Baiker, S.E. Pratsinis, Two-nozzle flame synthesis of Pt/Ba/Al₂O₃ for NO_x storage, *Chemistry of Materials* 18 (2006) 2532-2537.
- [30] M. Gockeln, S. Pokhrel, F. Meierhofer, J. Glenneberg, M. Schowalter, A. Rosenauer, U. Fritsching, M. Busse, L. Mädler, R. Kun, Fabrication and performance of Li₄Ti₅O₁₂/C Li-ion battery electrodes using combined double flame spray pyrolysis and pressure-based lamination technique, *Journal of Power Sources* 374 (2018) 97-106.
- [31] E.C. Lovell, H. Großman, J. Horlyck, J. Scott, L. Mädler, R. Amal, Asymmetrical double flame spray pyrolysis-designed SiO₂/Ce_{0.7}Zr_{0.3}O₂ for the dry reforming of methane, *ACS Applied Materials & Interfaces* 11 (2019) 25766-25777.
- [32] E. Pomerantseva, F. Bonaccorso, X. Feng, Y. Cui, Y. Gogotsi, Energy storage: The future enabled by nanomaterials, *Science* 366 (2019) eaan8285.
- [33] A. Tarasov, V. Shvartsman, S. Shoja, D. Lewin, D. Lupascu, H. Wiggers, Spray-flame synthesis of BaTi_{1-x}Zr_xO₃ nanoparticles for energy storage applications, *Ceramics International* 46 (2020) 13915-13924.
- [34] N. Liu, Z. Lu, J. Zhao, M.T. McDowell, H.-W. Lee, W. Zhao, Y. Cui, A pomegranate-inspired nanoscale design for large-volume-change lithium battery anodes, *Nature Nanotechnology* 9 (2014) 187-192.
- [35] J. Lu, Z. Chen, Z. Ma, F. Pan, L.A. Curtiss, K. Amine, The role of nanotechnology in the development of battery materials for electric vehicles, *Nature Nanotechnology* 11 (2016) 1031-1038.
- [36] S.M. Dizaj, F. Lotfipour, M. Barzegar-Jalali, M.H. Zarrintan, K. Adibkia, Antimicrobial activity of the metals and metal oxide nanoparticles, *Materials Science and Engineering: C* 44 (2014) 278-284.
- [37] S. Li, Y. Ren, P. Biswas, S.D. Tse, Flame aerosol synthesis of nanostructured materials and functional devices: Processing, modeling, and diagnostics, *Progress in Energy and Combustion Science* 55 (2016) 1-59.

- [38] W.Y. Teoh, R. Amal, L. Mädler, Flame spray pyrolysis: An enabling technology for nanoparticles design and fabrication, *Nanoscale* 2 (2010) 1324-1347.
- [39] G.A.G. Solero, Synthesis of nanoparticles through flame spray pyrolysis: experimental apparatus and preliminary results, *Nanoscience and Nanotechnology* 7 (2017) 21-25.
- [40] M. Sorvali, M. Nikka, P. Juuti, M. Honkanen, T. Salminen, L. Hyvärinen, J.M. Mäkelä, Controlling the phase of iron oxide nanoparticles fabricated from iron (III) nitrate by liquid flame spray, *International Journal of Ceramic Engineering & Science* 1 (2019) 194-205.
- [41] J. Horlyck, S. Pokhrel, E. Lovell, N.M. Bedford, L. Mädler, R. Amal, J. Scott, Unifying double flame spray pyrolysis with lanthanum doping to restrict cobalt–aluminate formation in Co/Al₂O₃ catalysts for the dry reforming of methane, *Catalysis Science & Technology* 9 (2019) 4970-4980.
- [42] S. Tada, K. Fujiwara, T. Yamamura, M. Nishijima, S. Uchida, R. Kikuchi, Flame spray pyrolysis makes highly loaded Cu nanoparticles on ZrO₂ for CO₂-to-methanol hydrogenation, *Chemical Engineering Journal* 381 (2020) 122750.
- [43] P. Psathas, Y. Georgiou, C. Moularas, G.S. Armatas, Y. Deligiannakis, Controlled-Phase Synthesis of Bi₂Fe₄O₉ & BiFeO₃ by Flame Spray Pyrolysis and their evaluation as non-noble metal catalysts for efficient reduction of 4-nitrophenol, *Powder Technology* 368 (2020) 268-277.
- [44] M.A. Ismail, M.N. Hedhili, D.H. Anjum, V. Singaravelu, S.H. Chung, Synthesis and characterization of iron-doped TiO₂ nanoparticles using ferrocene from flame spray pyrolysis, *Catalysts* 11 (2021) 438.
- [45] Z. Chen, Z. Xu, H. Zhao, Flame spray pyrolysis synthesis and H₂S sensing properties of CuO-doped SnO₂ nanoparticles, *Proceedings of the Combustion Institute* 38 (2021) 6743-6751.
- [46] D. Dasgupta, P. Pal, R. Torelli, S. Som, N. Paulson, J. Libera, M. Stan, Computational fluid dynamics modeling and analysis of silica nanoparticle synthesis in a flame spray pyrolysis reactor, *Combustion and Flame* 236 (2022) 111789.
- [47] K. Wegner, S.E. Pratsinis, Scale-up of nanoparticle synthesis in diffusion flame reactors, *Chemical Engineering Science* 58 (2003) 4581-4589.
- [48] R. Mueller, R. Jossen, S.E. Pratsinis, M. Watson, M.K. Akhtar, Zirconia nanoparticles made in spray flames at high production rates, *Journal of the American Ceramic Society* 87 (2004) 197-202.
- [49] C. Schulz, T. Dreier, M. Fikri, H. Wiggers, Gas-phase synthesis of functional nanomaterials: Challenges to kinetics, diagnostics, and process development, *Proceedings of the Combustion Institute* 37 (2019) 83-108.
- [50] L. Zigan, J. Trost, A. Leipertz, Simultaneous imaging of fuel vapor mass fraction and gas-phase temperature inside gasoline sprays using two-line excitation tracer planar laser-induced fluorescence, *Applied Optics* 55 (2016) 1453-1460.
- [51] S. Karaminejad, A. El Moussawi, T. Dreier, T. Endres, C. Schulz, Multi-line OH-LIF for gas-phase temperature and concentration imaging in the SpraySyn burner, *Applications in Energy and Combustion Science* 16 (2023) 100222.
- [52] N. Jüngst, I. Skenderović, B. Südholt, G. Smallwood, F. Kruis, S. Kaiser, High-speed imaging and statistics of puffing and micro-exploding droplets in spray-flame synthesis, *Applications in Energy and Combustion Science* 15 (2023) 100167.
- [53] L. Zigan, I. Schmitz, A. Flügel, M. Wensing, A. Leipertz, Structure of evaporating single-and multicomponent fuel sprays for 2nd generation gasoline direct injection, *Fuel* 90 (2011) 348-363.

- [54] P. Kranz, D. Fuhrmann, M. Goschütz, S.A. Kaiser, S. Bauke, K. Golibrzuch, H. Wackerbarth, P. Kawelke, J. Luciani, L. Beckmann, In-cylinder LIF imaging, IR-absorption point measurements, and a CFD simulation to evaluate mixture formation in a CNG-fueled engine, *SAE International Journal of Engines* 11 (2018) 1221-1238.
- [55] J. Laichter, S.A. Kaiser, Optical investigation of the influence of in-cylinder flow and mixture inhomogeneity on cyclic variability in a direct-injection spark ignition engine, *Flow, Turbulence and Combustion* 110 (2023) 171-183.
- [56] SpraySyn Database, accessed 3 January 2022, available at <<https://spraysyn.db.cfd.uni-due.de/>>.
- [57] Y. Luo, R. Zhao, J.B. Pendry, van der Waals interactions at the nanoscale: The effects of nonlocality, *Proceedings of the National Academy of Sciences* 111 (2014) 18422-18427.
- [58] S. Tsantilis, S.E. Pratsinis, Soft-and hard-agglomerate aerosols made at high temperatures, *Langmuir* 20 (2004) 5933-5939.
- [59] M. Heurlin, M.H. Magnusson, D. Lindgren, M. Ek, L.R. Wallenberg, K. Deppert, L. Samuelson, Continuous gas-phase synthesis of nanowires with tunable properties, *Nature* 492 (2012) 90-94.
- [60] M. Dresselhaus, Y. Lin, O. Rabin, A. Jorio, A. Souza Filho, M. Pimenta, R. Saito, G. Samsonidze, G. Dresselhaus, Nanowires and nanotubes, *Materials Science and Engineering: C* 23 (2003) 129-140.
- [61] C.E. Ren, M.Q. Zhao, T. Makaryan, J. Halim, M. Boota, S. Kota, B. Anasori, M.W. Barsoum, Y. Gogotsi, Porous two-dimensional transition metal carbide (MXene) flakes for high-performance Li-ion storage, *ChemElectroChem* 3 (2016) 689-693.
- [62] A.C. Anselmo, C.L. Modery-Pawłowski, S. Menegatti, S. Kumar, D.R. Vogus, L.L. Tian, M. Chen, T.M. Squires, A. Sen Gupta, S. Mitragotri, Platelet-like nanoparticles: mimicking shape, flexibility, and surface biology of platelets to target vascular injuries, *ACS Nano* 8 (2014) 11243-11253.
- [63] D. Vollath, F.D. Fischer, D. Holec, Surface energy of nanoparticles—influence of particle size and structure, *Beilstein Journal of Nanotechnology* 9 (2018) 2265-2276.
- [64] K. Nanda, A. Maisels, F. Kruis, H. Fissan, S. Stappert, Higher surface energy of free nanoparticles, *Physical Review Letters* 91 (2003) 106102.
- [65] R. Koirala, S.E. Pratsinis, A. Baiker, Synthesis of catalytic materials in flames: opportunities and challenges, *Chemical Society Reviews* 45 (2016) 3053-3068.
- [66] M.J. Height, S.E. Pratsinis, O. Mekasuwandumrong, P. Praserthdam, Ag-ZnO catalysts for UV-photodegradation of methylene blue, *Applied Catalysis B: Environmental* 63 (2006) 305-312.
- [67] T.A. Dankovich, D.G. Gray, Bactericidal paper impregnated with silver nanoparticles for point-of-use water treatment, *Environmental Science & Technology* 45 (2011) 1992-1998.
- [68] J. Dulińska-Litewka, A. Łazarczyk, P. Hałubiec, O. Szafranski, K. Karnas, A. Krawiec, Superparamagnetic iron oxide nanoparticles—Current and prospective medical applications, *Materials* 12 (2019) 617.
- [69] H. Zhou, I. Honma, H. Komiyama, J. Haus, Controlled synthesis and quantum-size effect in gold-coated nanoparticles, *Physical Review B* 50 (1994) 12052.
- [70] C. Torres-Torres, A. López-Suárez, B. Can-Uc, R. Rangel-Rojo, L. Tamayo-Rivera, A. Oliver, Collective optical Kerr effect exhibited by an integrated configuration of silicon quantum dots and gold nanoparticles embedded in ion-implanted silica, *Nanotechnology* 26 (2015) 295701.

- [71] Y. Volokitin, J.d. Sinzig, L. De Jongh, G. Schmid, M. Vargaftik, I. Moiseevi, Quantum-size effects in the thermodynamic properties of metallic nanoparticles, *Nature* 384 (1996) 621-623.
- [72] A. Gutsch, M. Krämer, G. Michael, H. Mühlenweg, M. Pridöhl, G. Zimmermann, Gas-phase production of nanoparticles, *KONA Powder and Particle Journal* 20 (2002) 24-37.
- [73] M.N. Rittner, T. Abraham, Nanostructured materials: An overview and commercial analysis, *Jom* 50 (1998) 36.
- [74] P. Buffat, J.P. Borel, Size effect on the melting temperature of gold particles, *Physical Review A* 13 (1976) 2287.
- [75] A. Ambrosetti, N. Ferri, R.A. DiStasio Jr, A. Tkatchenko, Wavelike charge density fluctuations and van der Waals interactions at the nanoscale, *Science* 351 (2016) 1171-1176.
- [76] C. Gao, F. Lyu, Y. Yin, Encapsulated metal nanoparticles for catalysis, *Chemical Reviews* 121 (2020) 834-881.
- [77] B.R. Strobel, S.E. Pratsinis, Flame synthesis of supported platinum group metals for catalysis and sensors, *Platinum Metals Review* 53 (2009) 11-20.
- [78] X. Yuan, M. Qing, L. Meng, H. Zhao, One-step synthesis of nanostructured Cu–Mn/TiO₂ via flame spray pyrolysis: Application to catalytic combustion of CO and CH₄, *Energy & Fuels* 34 (2020) 14447-14457.
- [79] V. Mazumder, Y. Lee, S. Sun, Recent development of active nanoparticle catalysts for fuel cell reactions, *Advanced Functional Materials* 20 (2010) 1224-1231.
- [80] A. Münzer, L. Xiao, Y.H. Sehlleier, C. Schulz, H. Wiggers, All gas-phase synthesis of graphene: Characterization and its utilization for silicon-based lithium-ion batteries, *Electrochimica Acta* 272 (2018) 52-59.
- [81] F.-M. Petrat, H. Wiggers, B. Reeken, M. Holzapfel, H. Buqa, P. Novak, Method for producing coated carbon particles and use of the latter in anode materials for lithium-ion batteries, Evonik Degussa GmbH, Essen, Germany, 2014.
- [82] T. Li, W. Yin, S. Gao, Y. Sun, P. Xu, S. Wu, H. Kong, G. Yang, G. Wei, The combination of two-dimensional nanomaterials with metal oxide nanoparticles for gas sensors: a review, *Nanomaterials* 12 (2022) 982.
- [83] A. Dey, Semiconductor metal oxide gas sensors: A review, *Materials Science and Engineering: B* 229 (2018) 206-217.
- [84] F. Qian, S. Gradecak, Y. Li, C.-Y. Wen, C.M. Lieber, Core/multishell nanowire heterostructures as multicolor, high-efficiency light-emitting diodes, *Nano Letters* 5 (2005) 2287-2291.
- [85] M. Gu, Q. Zhang, S. Lamon, Nanomaterials for optical data storage, *Nature Reviews Materials* 1 (2016) 16070.
- [86] S. Gubin, Y.I. Spichkin, G.Y. Yurkov, A. Tishin, Nanomaterial for high-density magnetic data storage, *Russian Journal of Inorganic Chemistry* 47 (2002) S32-S67.
- [87] D. Slavova, Stability and rheological behaviour of oil-in-water emulsions under pressure, Doctoral dissertation, Ruhr-Universität Bochum (2021).
- [88] J. Philip, Magnetic nanofluids (Ferrofluids): Recent advances, applications, challenges, and future directions, *Advances in Colloid and Interface Science* 311 (2023) 102810.
- [89] S. Odenbach, Ferrofluids—magnetically controlled suspensions, *Colloids and Surfaces A: Physicochemical and Engineering Aspects* 217 (2003) 171-178.

- [90] A.Z. Wilczewska, K. Niemirowicz, K.H. Markiewicz, H. Car, Nanoparticles as drug delivery systems, *Pharmacological Reports* 64 (2012) 1020-1037.
- [91] M.J. Mitchell, M.M. Billingsley, R.M. Haley, M.E. Wechsler, N.A. Peppas, R. Langer, Engineering precision nanoparticles for drug delivery, *Nature Reviews Drug Discovery* 20 (2021) 101-124.
- [92] S. Dekkers, P. Krystek, R.J. Peters, D.P. Lankveld, B.G. Bokkers, P.H. van Hoeven-Arentzen, H. Bouwmeester, A.G. Oomen, Presence and risks of nanosilica in food products, *Nanotoxicology* 5 (2011) 393-405.
- [93] S. Nizamuddin, M. Siddiqui, N. Mubarak, H.A. Baloch, E. Abdullah, S.A. Mazari, G. Griffin, M. Srinivasan, A. Tanksale, Iron oxide nanomaterials for the removal of heavy metals and dyes from wastewater, *Nanoscale Materials in Water Purification* (2019) 447-472.
- [94] A. Alonso, J. Moral-Vico, A.A. Markeb, M. Busquets-Fité, D. Komilis, V. Puentes, A. Sánchez, X. Font, Critical review of existing nanomaterial adsorbents to capture carbon dioxide and methane, *Science of The Total Environment* 595 (2017) 51-62.
- [95] X. Wang, T. He, J. Hu, M. Liu, The progress of nanomaterials for carbon dioxide capture via the adsorption process, *Environmental Science: Nano* 8 (2021) 890-912.
- [96] A.G. Tamirat, J. Rick, A.A. Dubale, W.-N. Su, B.-J. Hwang, Using hematite for photoelectrochemical water splitting: a review of current progress and challenges, *Nanoscale Horizons* 1 (2016) 243-267.
- [97] A.K. Gupta, M. Gupta, Synthesis and surface engineering of iron oxide nanoparticles for biomedical applications, *Biomaterials* 26 (2005) 3995-4021.
- [98] M. Bouché, J.C. Hsu, Y.C. Dong, J. Kim, K. Taing, D.P. Cormode, Recent advances in molecular imaging with gold nanoparticles, *Bioconjugate Chemistry* 31 (2019) 303-314.
- [99] L. Galfetti, L. DeLuca, F. Severini, G. Colombo, L. Meda, G. Marra, Pre and post-burning analysis of nano-aluminized solid rocket propellants, *Aerospace Science and Technology* 11 (2007) 26-32.
- [100] J.R. Swider, V.A. Hackley, J. Winter, Characterization of Chinese ink in size and surface, *Journal of Cultural Heritage* 4 (2003) 175-186.
- [101] T. Christiansen, M. Cotte, W. de Nolf, E. Mouro, J. Reyes-Herrera, S. De Meyer, F. Vanmeert, N. Salvadó, V. Gonzalez, P.E. Lindelof, Insights into the composition of ancient Egyptian red and black inks on papyri achieved by synchrotron-based microanalyses, *Proceedings of the National Academy of Sciences* 117 (2020) 27825-27835.
- [102] P. Walter, E. Welcomme, P. Hallégot, N.J. Zaluzec, C. Deeb, J. Castaing, P. Veysseyre, R. Bréniaux, J.-L. Lévêque, G. Tsoucaris, Early use of PbS nanotechnology for an ancient hair dyeing formula, *Nano Letters* 6 (2006) 2215-2219.
- [103] I. Freestone, N. Meeks, M. Sax, C. Higgitt, The Lycurgus cup—a roman nanotechnology, *Gold Bulletin* 40 (2007) 270-277.
- [104] S.E. Pratsinis, Flame aerosol synthesis of ceramic powders, *Progress in Energy and Combustion Science* 24 (1998) 197-219.
- [105] S.E. Pratsinis, History of manufacture of fine particles in high-temperature aerosol reactors, *Aerosol Science and Technology: History and Reviews* (2011) 475-507.
- [106] F. Meierhofer, U. Fritsching, Synthesis of metal oxide nanoparticles in flame sprays: review on process technology, modeling, and diagnostics, *Energy & Fuels* 35 (2021) 5495-5537.
- [107] P. Roth, Particle synthesis in flames, *Proceedings of the Combustion Institute* 31 (2007) 1773-1788.

- [108] N. Salah, S.S. Habib, Z.H. Khan, A. Memic, A. Azam, E. Alarfaj, N. Zahed, S. Al-Hamedi, High-energy ball milling technique for ZnO nanoparticles as antibacterial material, *International Journal of Nanomedicine* 6 (2011) 863-869.
- [109] V. Amendola, M. Meneghetti, Laser ablation synthesis in solution and size manipulation of noble metal nanoparticles, *Physical Chemistry Chemical Physics* 11 (2009) 3805-3821.
- [110] M. Gracia-Pinilla, E. Martínez, G.S. Vidaurri, E. Pérez-Tijerina, Deposition of size-selected Cu nanoparticles by inert gas condensation, *Nanoscale Research Letters* 5 (2010) 180-188.
- [111] D. Bokov, A. Turki Jalil, S. Chupradit, W. Suksatan, M. Javed Ansari, I.H. Shewael, G.H. Valiev, E. Kianfar, Nanomaterial by sol-gel method: synthesis and application, *Advances in Materials Science and Engineering* 2021 (2021) 5102014.
- [112] G.A. Kelesidis, E. Goudeli, S.E. Pratsinis, Flame synthesis of functional nanostructured materials and devices: Surface growth and aggregation, *Proceedings of the Combustion Institute* 36 (2017) 29-50.
- [113] B. Alkan, D. Medina, J. Landers, M. Heidelmann, U. Hagemann, S. Salamon, C. Andronesco, H. Wende, C. Schulz, W. Schuhmann, H. Wiggers, Spray-flame prepared $\text{LaCo}_{1-x}\text{Fe}_x\text{O}_3$ perovskite nanoparticles as active OER catalysts: Influence of Fe content and low-temperature heating, *ChemElectroChem* 7 (2020) 2564-2574.
- [114] H.K. Grossmann, T. Grieb, F. Meierhofer, M. Hodapp, D. Noriler, A. Gröhn, H. Meier, U. Fritsching, K. Wegner, L. Mädler, Nanoscale mixing during double-flame spray synthesis of heterostructured nanoparticles, *Journal of Nanoparticle Research* 17 (2015) 174.
- [115] J. Stahl, J. Ilsemann, S. Pokhrel, M. Schowalter, C. Tessarek, A. Rosenauer, M. Eickhoff, M. Bäumer, L. Mädler, Comparing Co-catalytic Effects of ZrO_x , SmO_x , and Pt on CO_x Methanation over Co-based Catalysts Prepared by Double Flame Spray Pyrolysis, *ChemCatChem* 13 (2021) 2815-2831.
- [116] M. Gäßler, J. Stahl, M. Schowalter, S. Pokhrel, A. Rosenauer, L. Mädler, R. Güttel, The Impact of Support Material of Cobalt-Based Catalysts Prepared by Double Flame Spray Pyrolysis on CO_2 Methanation Dynamics, *ChemCatChem* 14 (2022) e202200286.
- [117] C. Abram, M. Mezhericher, F. Beyrau, H.A. Stone, Y. Ju, Flame synthesis of nanophosphors using sub-micron aerosols, *Proceedings of the Combustion Institute* 37 (2019) 1231-1239.
- [118] M. Aromaa, H. Keskinen, J.M. Mäkelä, The effect of process parameters on the Liquid Flame Spray generated titania nanoparticles, *Biomolecular Engineering* 24 (2007) 543-548.
- [119] C.R. Bickmore, K.F. Waldner, D.R. Treadwell, R.M. Laine, Ultrafine spinel powders by flame spray pyrolysis of a magnesium aluminum double alkoxide, *Journal of the American Ceramic Society* 79 (1996) 1419.
- [120] T. Hirano, D. Tomonaga, T. Ogi, D. Shimokuri, Direct spray combustion in a tubular flame burner toward fine particle synthesis, *Journal of Thermal Science and Technology* 16 (2021) JTST0035.
- [121] C. Liu, S. Li, Y. Zong, Q. Yao, D.T. Stephen, Laser-based investigation of the transition from droplets to nanoparticles in flame-assisted spray synthesis of functional nanoparticles, *Proceedings of the Combustion Institute* 36 (2017) 1109-1117.
- [122] F. Schneider, Optical in situ characterization of lab-scale and pilot-scale burners for nanoparticle synthesis, Doctoral dissertation, Universität Duisburg-Essen (2020).
- [123] M. Sieber, S. Schimek, C.O. Paschereit, Development of a novel hydrogen-based burner concept for pilot-scale spray flame synthesis of nanoparticles, *Applications in Energy and Combustion Science* 15 (2023) 100188.

- [124] K. Takatori, T. Tani, N. Watanabe, N. Kamiya, Preparation and characterization of nano-structured ceramic powders synthesized by emulsion combustion method, *Journal of Nanoparticle Research* 1 (1999) 197-204.
- [125] J. Tikkanen, K. Gross, C. Berndt, V. Pitkänen, J. Keskinen, S. Raghu, M. Rajala, J. Karthikeyan, Characteristics of the liquid flame spray process, *Surface and Coatings Technology* 90 (1997) 210-216.
- [126] C.D. Rosebrock, T. Wriedt, L. Mädler, K. Wegner, The role of microexplosions in flame spray synthesis for homogeneous nanopowders from low-cost metal precursors, *AIChE Journal* 62 (2016) 381-391.
- [127] A. Witte, L. Mädler, Single droplet combustion of iron nitrate-based precursor solutions: Investigation of time-and size scales of isolated burning FSP-droplets, *Applications in Energy and Combustion Science* 14 (2023) 100147.
- [128] C.D. Rosebrock, N. Riefler, T. Wriedt, L. Mädler, S.D. Tse, Disruptive burning of precursor/solvent droplets in flame-spray synthesis of nanoparticles, *AIChE Journal* 59 (2013) 4553-4566.
- [129] R. Volkov, P. Strizhak, Using Planar Laser Induced Fluorescence to explore the mechanism of the explosive disintegration of water emulsion droplets exposed to intense heating, *International Journal of Thermal Sciences* 127 (2018) 126-141.
- [130] A. Witte, S.D. Tse, L. Mädler, Acoustic signatures of single disrupting FSP droplets in a heated oxygen atmosphere, *Journal of Aerosol Science* 179 (2024) 106380.
- [131] M. Stodt, J.D. Groeneveld, L. Maedler, J. Kiefer, U. Fritsching, Microexplosions of multicomponent drops in spray flames, *Combustion and Flame* 240 (2022) 112043.
- [132] Y. Mizutani, M. Muraoka, In situ observation of microexplosion of emulsion droplets in spray flames, *Atomization and Sprays* 11 (2001) 521-532.
- [133] C.K. Law, Recent advances in droplet vaporization and combustion, *Progress in Energy and Combustion Science* 8 (1982) 171-201.
- [134] J. Shinjo, J. Xia, L. Ganippa, A. Megaritis, Physics of puffing and microexplosion of emulsion fuel droplets, *Physics of Fluids* 26 (2014) 103302.
- [135] I. Skenderović, N. Jüngst, S.A. Kaiser, F.E. Kruis, A Population balance method for simulation of particle-induced droplet breakup in spray flame synthesis and suspension spray combustion, *Applications in Energy and Combustion Science* 15 (2023) 100162.
- [136] B. Kunstmann, I. Wlokas, M. Kohns, H. Hasse, Simulation study of superheating in evaporating droplets of (TTIP+ p-xylene) in spray flame synthesis, *Applications in Energy and Combustion Science* 15 (2023) 100156.
- [137] D.V. Antonov, R.M. Fedorenko, L.S. Yanovskiy, P.A. Strizhak, Physical and Mathematical Models of Micro-Explosions: Achievements and Directions of Improvement, *Energies* 16 (2023) 6034.
- [138] H. Li, C.D. Rosebrock, N. Riefler, T. Wriedt, L. Mädler, Experimental investigation on microexplosion of single isolated burning droplets containing titanium tetraisopropoxide for nanoparticle production, *Proceedings of the Combustion Institute* 36 (2017) 1011-1018.
- [139] H. Li, S. Pokhrel, M. Schowalter, A. Rosenauer, J. Kiefer, L. Mädler, The gas-phase formation of tin dioxide nanoparticles in single droplet combustion and flame spray pyrolysis, *Combustion and Flame* 215 (2020) 389-400.
- [140] D. Antonov, R. Fedorenko, P. Strizhak, Z. Nissar, S. Sazhin, Puffing/micro-explosion in composite fuel/water droplets heated in flames, *Combustion and Flame* 233 (2021) 111599.

- [141] S. Pokhrel, L. Mädler, Flame-made particles for sensors, catalysis, and energy storage applications, *Energy & Fuels* 34 (2020) 13209-13224.
- [142] Y. Ren, J. Cai, H. Pitsch, Theoretical single-droplet model for particle formation in flame spray pyrolysis, *Energy & Fuels* 35 (2021) 1750-1759.
- [143] R. Tischendorf, M. Simmler, C. Weinberger, M. Bieber, M. Reddemann, F. Fröde, J. Lindner, H. Pitsch, R. Kneer, M. Tiemann, Examination of the evolution of iron oxide nanoparticles in flame spray pyrolysis by tailored in situ particle sampling techniques, *Journal of Aerosol Science* 154 (2021) 105722.
- [144] R. Jossen, S.E. Pratsinis, W.J. Stark, L. Mädler, Criteria for flame-spray synthesis of hollow, shell-like, or inhomogeneous oxides, *Journal of the American Ceramic Society* 88 (2005) 1388-1393.
- [145] R. Strobel, S.E. Pratsinis, Effect of solvent composition on oxide morphology during flame spray pyrolysis of metal nitrates, *Physical Chemistry Chemical Physics* 13 (2011) 9246-9252.
- [146] S. Angel, J.D. Tapia, J. Gallego, U. Hagemann, H. Wiggers, Spray-Flame Synthesis of $\text{LaMnO}_{3+\delta}$ Nanoparticles for Selective CO Oxidation (SELOX), *Energy & Fuels* 35 (2021) 4367-4376.
- [147] M. Underberg, M.M. Prenting, M. Sieber, S. Schimek, C.O. Paschereit, T. Hülser, T. Endres, C. Schulz, H. Wiggers, S.M. Schnurre, A hydrogen-based burner concept for pilot-scale spray-flame synthesis of nanoparticles: Investigation of flames and iron oxide product materials, *Applications in Energy and Combustion Science* 15 (2023) 100165.
- [148] M. Eslamian, M. Shekarriz, Recent advances in nanoparticle preparation by spray and microemulsion methods, *Recent Patents on Nanotechnology* 3 (2009) 99-115.
- [149] T. Rudin, S.E. Pratsinis, Homogeneous iron phosphate nanoparticles by combustion of sprays, *Industrial & Engineering Chemistry Research* 51 (2012) 7891-7900.
- [150] M.C. Heine, S.E. Pratsinis, Droplet and particle dynamics during flame spray synthesis of nanoparticles, *Industrial & Engineering Chemistry Research* 44 (2005) 6222-6232.
- [151] R. Strobel, S.E. Pratsinis, Direct synthesis of maghemite, magnetite and wustite nanoparticles by flame spray pyrolysis, *Advanced Powder Technology* 20 (2009) 190-194.
- [152] J. Wei, Y. Ren, Y. Zhang, B. Shi, S. Li, Effects of temperature-time history on the flame synthesis of nanoparticles in a swirl-stabilized tubular burner with two feeding modes, *Journal of Aerosol Science* 133 (2019) 72-82.
- [153] S. Hardt, I. Wlokas, C. Schulz, H. Wiggers, Impact of ambient pressure on titania nanoparticle formation during spray-flame synthesis, *Journal of Nanoscience and Nanotechnology* 15 (2015) 9449-9456.
- [154] S. Angel, J. Neises, M. Dreyer, K. Friedel Ortega, M. Behrens, Y. Wang, H. Arandiyán, C. Schulz, H. Wiggers, Spray-flame synthesis of La (Fe, Co) O_3 nano-perovskites from metal nitrates, *AIChE Journal* 66 (2020) e16748.
- [155] J. Wei, S. Li, Y. Ren, Y. Zhang, D.T. Stephen, Investigating the role of solvent formulations in temperature-controlled liquid-fed aerosol flame synthesis of YAG-based nanoparticles, *Proceedings of the Combustion Institute* 37 (2019) 1193-1201.
- [156] M.F.B. Stodt, M. Gonchikzhapov, T. Kasper, U. Fritsching, J. Kiefer, Chemistry of iron nitrate-based precursor solutions for spray-flame synthesis, *Physical Chemistry Chemical Physics* 21 (2019) 24793-24801.
- [157] R. Mueller, R. Jossen, H.K. Kammler, S.E. Pratsinis, M.K. Akhtar, Growth of zirconia particles made by flame spray pyrolysis, *AIChE Journal* 50 (2004) 3085-3094.

- [158] S. Angel, F. Schneider, S. Apazeller, W. Kaziur-Cegla, T.C. Schmidt, C. Schulz, H. Wiggers, Spray-flame synthesis of LaMO_3 (M= Mn, Fe, Co) perovskite nanomaterials: Effect of spray droplet size and esterification on particle size distribution, *Proceedings of the Combustion Institute* 38 (2021) 1279-1287.
- [159] W.Y. Teoh, L. Mädler, D. Beydoun, S.E. Pratsinis, R. Amal, Direct (one-step) synthesis of TiO_2 and Pt/TiO_2 nanoparticles for photocatalytic mineralisation of sucrose, *Chemical Engineering Science* 60 (2005) 5852-5861.
- [160] K. Wegner, S.E. Pratsinis, Nozzle-quenching process for controlled flame synthesis of titania nanoparticles, *AIChE Journal* 49 (2003) 1667-1675.
- [161] J.A. Kemmler, S. Pokhrel, J. Birkenstock, M. Schowalter, A. Rosenauer, N. Bârsan, U. Weimar, L. Mädler, Quenched, nanocrystalline $\text{In}_4\text{Sn}_3\text{O}_{12}$ high temperature phase for gas sensing applications, *Sensors and Actuators B: Chemical* 161 (2012) 740-747.
- [162] S. Karaminejad, S.M. Dupont, M. Bieber, M.A. Reddemann, R. Kneer, T. Dreier, T. Endres, C. Schulz, Characterization of spray parameters and flame stability in two modified nozzle configurations of the SpraySyn burner, *Proceedings of the Combustion Institute* 39 (2023) 2673-2682.
- [163] M. Bieber, M. Al-Khatib, F. Fröde, H. Pitsch, M. Reddemann, H. Schmid, R. Tischendorf, R. Kneer, Influence of angled dispersion gas on coaxial atomization, spray and flame formation in the context of spray-flame synthesis of nanoparticles, *Experiments in Fluids* 62 (2021) 98.
- [164] J. Pan, J.A. Libera, N.H. Paulson, M. Stan, Flame stability analysis of flame spray pyrolysis by artificial intelligence, *The International Journal of Advanced Manufacturing Technology* 114 (2021) 2215-2228.
- [165] H.K. Kammler, L. Mädler, S.E. Pratsinis, Flame synthesis of nanoparticles, *Chemical Engineering & Technology: Industrial Chemistry-Plant Equipment-Process Engineering-Biotechnology* 24 (2001) 583-596.
- [166] R. Mueller, L. Mädler, S.E. Pratsinis, Nanoparticle synthesis at high production rates by flame spray pyrolysis, *Chemical Engineering Science* 58 (2003) 1969-1976.
- [167] R. Jossen, R. Mueller, S.E. Pratsinis, M. Watson, M.K. Akhtar, Morphology and composition of spray-flame-made yttria-stabilized zirconia nanoparticles, *Nanotechnology* 16 (2005) S609.
- [168] A. Heel, P. Holtappels, P. Hug, T. Graule, Flame Spray Synthesis of Nanoscale $\text{La}_{0.6}\text{Sr}_{0.4}\text{Co}_{0.2}\text{Fe}_{0.8}\text{O}_{3-\delta}$ and $\text{Ba}_{0.5}\text{Sr}_{0.5}\text{Co}_{0.8}\text{Fe}_{0.2}\text{O}_{3-\delta}$ as Cathode Materials for Intermediate Temperature Solid Oxide Fuel Cells, *Fuel Cells* 10 (2010) 419-432.
- [169] K. Hembram, D. Sivaprakasam, T. Rao, K. Wegner, Large-scale manufacture of ZnO nanorods by flame spray pyrolysis, *Journal of Nanoparticle Research* 15 (2013) 1461.
- [170] A.J. Gröhn, S.E. Pratsinis, A. Sánchez-Ferrer, R. Mezzenga, K. Wegner, Scale-up of nanoparticle synthesis by flame spray pyrolysis: the high-temperature particle residence time, *Industrial & Engineering Chemistry Research* 53 (2014) 10734-10742.
- [171] M. Estévez, M. Cicuéndez, J. Crespo, J. Serrano-López, M. Colilla, C. Fernández-Acevedo, T. Oroz-Mateo, A. Rada-Leza, B. González, I. Izquierdo-Barba, Large-scale production of superparamagnetic iron oxide nanoparticles by flame spray pyrolysis: In vitro biological evaluation for biomedical applications, *Journal of Colloid and Interface Science* 650 (2023) 560-572.
- [172] K. Wegner, B. Schimmoeller, B. Thiebaut, C. Fernandez, T.N. Rao, Pilot plants for industrial nanoparticle production by flame spray pyrolysis, *KONA Powder and Particle Journal* 29 (2011) 251-265.
- [173] SPP1980, www.uni-due.de/spp1980 funded by the German Research Foundation, DFG.

- [174] F. Schneider, S. Suleiman, J. Menser, E. Borukhovich, I. Wlokas, A. Kempf, H. Wiggers, C. Schulz, SpraySyn—A standardized burner configuration for nanoparticle synthesis in spray flames, *Review of Scientific Instruments* 90 (2019) 085108.
- [175] J. Menser, S. Kluge, H. Wiggers, T. Dreier, C. Schulz, Approach to standardize a spray-flame nanoparticle synthesis burner, *Proceedings of the 7th European Combustion Meeting*, Budapest, Hungary (2015).
- [176] A. Abdelsamie, F.E. Kruis, H. Wiggers, D. Thévenin, Nanoparticle formation and behavior in turbulent spray flames investigated by DNS, *Flow, Turbulence and Combustion* 105 (2020) 497-516.
- [177] A. Abdelsamie, C. Chi, M. Nanjaiah, I. Skenderović, S. Suleiman, D. Thévenin, Direct numerical simulation of turbulent spray combustion in the SpraySyn burner: Impact of injector geometry, *Flow, Turbulence and Combustion* 106 (2021) 453-469.
- [178] J. Sellmann, P. Wollny, S.-J. Baik, S. Suleiman, F. Schneider, C. Schulz, H. Wiggers, I. Wlokas, A. Kempf, LES of nanoparticle synthesis in the spraysyn burner: A comparison against experiments, *Powder Technology* 404 (2022) 117466.
- [179] S.-J. Baik, P. Wollny, M. Nanjaiah, I. Wlokas, A. Kempf, Large eddy simulation of iron (III) oxide nanoparticle synthesis in spray flames, *Applications in Energy and Combustion Science* 15 (2023) 100185.
- [180] A. Abdelsamie, H. Wiggers, F.E. Kruis, D. Thévenin, Direct numerical simulation of SpraySyn burner: Impact of liquid solvent, *International Journal of Spray and Combustion Dynamics* 15 (2023) 237-247.
- [181] J. Kirchmann, A. Kronenburg, M. Prenting, S. Karaminejad, T. Dreier, T. Endres, S. Patil, F. Beyrau, Characterizing the SpraySyn burners with MMC-LES, *Applications in Energy and Combustion Science* 15 (2023) 100182.
- [182] F. Fröde, T. Grenga, S. Dupont, R. Kneer, R. Tischendorf, O. Massopo, H.-J. Schmid, H. Pitsch, Large eddy simulation of iron oxide formation in a laboratory spray flame, *Applications in Energy and Combustion Science* 16 (2023) 100191.
- [183] S. Klukas, M. Giglmaier, M. Underberg, S.M. Schnurre, M.M. Prenting, T. Endres, H. Wiggers, C. Schulz, M. Sieber, S. Schimek, C.O. Paschereit, N.A. Adams, Scale-up analysis of spray flame nanoparticle synthesis by comparison of laboratory and pilot plant-scale burners, *Applications in Energy and Combustion Science* 18 (2024) 100263.
- [184] M. Gonchikzhapov, T. Kasper, Thermal and chemical structure of ethanol and 2-ethylhexanoic acid/ethanol SpraySyn flames, *Applications in Energy and Combustion Science* 15 (2023) 100174.
- [185] M.F. Stodt, C. Liu, S. Li, L. Maedler, U. Fritsching, J. Kiefer, Phase-selective laser-induced breakdown spectroscopy in flame spray pyrolysis for iron oxide nanoparticle synthesis, *Proceedings of the Combustion Institute* 38 (2021) 1711-1718.
- [186] F.J. Martins, J. Kirchmann, A. Kronenburg, F. Beyrau, Experimental investigation of axisymmetric, turbulent, annular jets discharged through the nozzle of the SPP1980 SpraySyn burner under isothermal and reacting conditions, *Experimental Thermal and Fluid Science* 114 (2020) 110052.
- [187] F.J. Martins, A. Kronenburg, F. Beyrau, PIV measurements under reacting and non-reacting conditions at the nozzle outlet of the SPP1980 SpraySyn burner, *13th International Symposium on Particle Image Velocimetry* (2019).
- [188] M.M. Prenting, M.I. Bin Dzulfida, T. Dreier, C. Schulz, Characterization of tracers for two-color laser-induced fluorescence liquid-phase temperature imaging in sprays, *Experiments in Fluids* 61 (2020) 77.

- [189] M.M. Prenting, S.-J. Baik, T. Dreier, T. Endres, A. Kempf, C. Schulz, Liquid-phase temperature in the SpraySyn flame measured by two-color laser-induced fluorescence thermometry and simulated by LES, *Proceedings of the Combustion Institute* 39 (2023) 2621-2630.
- [190] M.F. Stodt, J. Kiefer, U. Fritsching, Ethanol droplet formation, dynamics and combustion mode in the flame of the SpraySyn-nozzle, *Experiments in Fluids* 60 (2019) 125.
- [191] M.F. Stodt, J. Kiefer, U. Fritsching, Drop dynamics in heterogeneous spray flames for nanoparticle synthesis, *Atomization and Sprays* 30 (2020) 779-797.
- [192] S. Aßmann, B. Münsterjohann, F.J. Huber, S. Will, Droplet sizing in spray flame synthesis using wide-angle light scattering (WALS), *Applied Physics B* 126 (2020) 92.
- [193] S. Aßmann, B. Münsterjohann, F.J. Huber, S. Will, In situ determination of droplet and nanoparticle size distributions in spray flame synthesis by wide-angle light scattering (WALS), *Materials* 14 (2021) 6698.
- [194] N. Jüngst, G. Smallwood, S. Kaiser, Visualization and image analysis of droplet puffing and micro-explosion in spray-flame synthesis of iron oxide nanoparticles, *Experiments in Fluids* 63 (2022) 60.
- [195] R. Tischendorf, K. Duschik, S. Dupont, F. Fröde, H. Pitsch, R. Kneer, M. Schaper, H.-J. Schmid, On Formation of Carbonaceous Impurities in Flame Spray Synthesis of Maghemite Nanoparticles, *Aerosol Research Discussions* 2023 (2023) 1-45.
- [196] P. Wollny, S. Angel, H. Wiggers, A.M. Kempf, I. Wlokas, Multiscale simulation of the formation of platinum-particles on alumina nanoparticles in a spray flame experiment, *Fluids* 5 (2020) 201.
- [197] S. Aßmann, F.J. Huber, S. Will, In situ characterization of particle formation in spray flame synthesis using wide-angle light scattering, *Particuology* 86 (2024) 304-312.
- [198] M.Y. Ali, H. Orthner, H. Wiggers, Spray Flame Synthesis (SFS) of Lithium Lanthanum Zirconate (LLZO) Solid Electrolyte, *Materials* 14 (2021) 3472.
- [199] M. Bierwirth, V. Olszok, V.A. Ganesan, J. Poostforooshan, A.P. Weber, Analyse der Partikelbildung aus der Elektrospray-Flammensprühpyrolyse mittels Scanning Mobility Particle Sizer, *Chemie-Ingenieur-Technik* 93 (2021) 1307-1315.
- [200] R. Tischendorf, O. Massopo, O. Prymak, S. Dupont, F. Fröde, H. Pitsch, R. Kneer, H.-J. Schmid, Maghemite Nanoparticles Synthesis via Spray Flame Synthesis and In Situ Particle Characterization by Hole in a Tube Sampling and Scanning Mobility Particle Sizing (HIAT-SMPS), *Applications in Energy and Combustion Science* 17 (2023) 100235.
- [201] M. Simmler, S. Buchheiser, R. Tischendorf, J. Poostforooshan, A.P. Weber, H.-J. Schmid, H. Nirschl, Small angle X-ray scattering of particle growth and structure in spray flame synthesis, *Applications in Energy and Combustion Science* 15 (2023) 100183.
- [202] M. Simmler, M. Meier, L. Rank, G. Buth, A. Plech, H. Nirschl, Beamline setup for in situ measurements of particles in turbulent spray flames using small angle X-ray scattering, *Proceedings of the Combustion Institute* 39 (2023) 949-957.
- [203] S. Suleiman, M. Nanjaiah, I. Skenderovic, T. Rosenberger, F. Kunze, I. Wlokas, F.E. Kruis, H. Wiggers, C. Schulz, Atmospheric-pressure particle mass spectrometer for investigating particle growth in spray flames, *Journal of Aerosol Science* 158 (2021) 105827.
- [204] C.T. Foo, A. Unterberger, F.J.W.A. Martins, M.M. Prenting, C. Schulz, K. Mohri, Investigating spray flames for nanoparticle synthesis via tomographic imaging using multi-simultaneous measurements (TIMes) of emission, *Optics Express* 30 (2022) 15524-15545.
- [205] F.J. Martins, C.T. Foo, A. Unterberger, S. Karaminejad, T. Endres, K. Mohri, Analyzing 3D fields of refractive index, emission and temperature in spray-flame nanoparticle synthesis via

- tomographic imaging using multi-simultaneous measurements (TIMes), *Applications in Energy and Combustion Science* 16 (2023) 100213.
- [206] A. Kumar, J. Kirchmann, F. Beyrau, A. Kronenburg, Jet flapping and its effect on flame oscillations in the SPP1980 SpraySyn burner, *Experimental Thermal and Fluid Science* 142 (2023) 110826.
- [207] H. Li, C.D. Rosebrock, Y. Wu, T. Wriedt, L. Mädler, Single droplet combustion of precursor/solvent solutions for nanoparticle production: Optical diagnostics on single isolated burning droplets with micro-explosions, *Proceedings of the Combustion Institute* 37 (2019) 1203-1211.
- [208] H. Li, Flame spray pyrolysis for synthesizing functional nanoparticles: Fundamental investigations on single and double droplet combustion, Doctoral dissertation, University of Bremen (2021).
- [209] B. Kunstmann, M. Kohns, H. Hasse, Thermophysical Properties of Mixtures of 2-Ethylhexanoic Acid and Ethanol, *Journal of Chemical & Engineering Data* 68 (2023) 330-338.
- [210] M. Gonchikzhapov, T. Kasper, Decomposition Reactions of $\text{Fe}(\text{CO})_5$, $\text{Fe}(\text{C}_5\text{H}_5)_2$, and TTIP as Precursors for the Spray-Flame Synthesis of Nanoparticles in Partial Spray Evaporation at Low Temperatures, *Industrial & Engineering Chemistry Research* 59 (2020) 8551-8561.
- [211] A. Keller, I.u. Wlokas, M. Kohns, H. Hasse, Thermophysical properties of solutions of Iron (III) nitrate-nonahydrate in mixtures of ethanol and water, *Journal of Chemical & Engineering Data* 65 (2020) 3519-3527.
- [212] J. Poostforooshan, S. Belbekhouche, V. Olszok, M.F. Stodt, M. Simmler, M. Bierwirth, H. Nirschl, J. Kiefer, U. Fritsching, A.P. Weber, Synthesis of Pure and Fe-Doped TiO_2 Nanoparticles via Electro-spray-Assisted Flame Spray Pyrolysis for Antimicrobial Applications, *ACS Applied Nano Materials* 6 (2023) 22660-22672.
- [213] S. Mohammadi, J. Poostforooshan, M.F. Stodt, V. Olszok, J. Kiefer, U. Fritsching, A.P. Weber, Tailoring Crystal Structure and Morphology of MnO_x Nanoparticles via Electro-spray-assisted Flame Spray Pyrolysis, *Applications in Energy and Combustion Science* 14 (2023) 100151.
- [214] G. Egels, L.M. Roncery, R. Fussik, W. Theisen, S. Weber, Impact of chemical inhomogeneities on local material properties and hydrogen environment embrittlement in AISI 304L steels, *International Journal of Hydrogen Energy* 43 (2018) 5206-5216.
- [215] S. Hardt, Personal communication: Information and technical drawings of the HSW burner, HSWmaterials, Kamp-Lintfort (2024), 12 January 2024.
- [216] M.A. Alhaleeb, N.E. Machin, A simple method to set the spray properties for flame spray pyrolysis production of nanoparticles, *Heliyon* 6 (2020) e04840.
- [217] A. Gaydon, *The spectroscopy of flames*, Springer science & business media, 2012.
- [218] A. Roda, *Chemiluminescence and bioluminescence: past, present and future*, Royal Society of Chemistry, 2011.
- [219] T. Kathrotia, Reaction kinetics modeling of OH^* , CH^* , and C_2^* chemiluminescence, Doctoral dissertation, University of Heidelberg (2011).
- [220] A. Brockhinke, C. Schulz, Selected papers about chemiluminescence of flames, 107 (2012) 513-514.
- [221] E. Wiedemann, Ueber fluoreszenz und phosphoreszenz I. Abhandlung, *Annalen der Physik* 270 (1888) 446-463.
- [222] T. Kathrotia, U. Riedel, A. Seipel, K. Moshhammer, A. Brockhinke, Experimental and numerical study of chemiluminescent species in low-pressure flames, *Applied Physics B* 107 (2012) 571-584.

- [223] V. Nori, J. Seitzman, Evaluation of chemiluminescence as a combustion diagnostic under varying operating conditions, 46th AIAA Aerospace Sciences Meeting and Exhibit 2008 (2008) 953.
- [224] J. Kojima, Y. Ikeda, T. Nakajima, Basic aspects of OH(A), CH(A), and C₂(d) chemiluminescence in the reaction zone of laminar methane–air premixed flames, *Combustion and Flame* 140 (2005) 34-45.
- [225] S. Carl, M. Van Poppel, J. Peeters, Identification of the CH + O₂ → OH(A) + CO reaction as the source of OH(A–X) chemiluminescence in C₂H₂/O/H/O₂ atomic flames and determination of its absolute rate constant over the range T= 296 to 511 K, *The Journal of Physical Chemistry A* 107 (2003) 11001-11007.
- [226] T. Kathrotia, M. Fikri, M. Bozkurt, M. Hartmann, U. Riedel, C. Schulz, Study of the H+O+M reaction forming OH*: Kinetics of OH* chemiluminescence in hydrogen combustion systems, *Combustion and Flame* 157 (2010) 1261-1273.
- [227] S. Krishnamachari, H. Broida, Effect of Molecular Oxygen on the Emission Spectra of Atomic Oxygen-Acetylene Flames, *The Journal of Chemical Physics* 34 (1961) 1709-1711.
- [228] D. Kilian, S. Engel, B. Borsdorf, Y. Gao, A. Kögler, S. Kobler, T. Seeger, S. Will, A. Leipertz, W. Peukert, Spatially resolved flame zone classification of a flame spray nanoparticle synthesis process by combining different optical techniques, *Journal of Aerosol Science* 69 (2014) 82-97.
- [229] M. Lauer, T. Sattelmayer, On the adequacy of chemiluminescence as a measure for heat release in turbulent flames with mixture gradients, *Journal of Engineering for Gas Turbines and Power* 132 (2010) 061502.
- [230] Y. Hardalupas, M. Orain, Local measurements of the time-dependent heat release rate and equivalence ratio using chemiluminescent emission from a flame, *Combustion and Flame* 139 (2004) 188-207.
- [231] C.S. Panoutsos, Y. Hardalupas, A. Taylor, Numerical evaluation of equivalence ratio measurement using OH* and CH* chemiluminescence in premixed and non-premixed methane–air flames, *Combustion and Flame* 156 (2009) 273-291.
- [232] Matlab (2020), version 7.10.0 (R2019b), The MathWorks, Inc., Natick, Massachusetts, United States.
- [233] A. Brockhinke, J. Krüger, M. Heusing, M. Letzgus, Measurement and simulation of rotationally-resolved chemiluminescence spectra in flames, *Applied Physics B* 107 (2012) 539-549.
- [234] G.P. Smith, J. Luque, C. Park, J.B. Jeffries, D.R. Crosley, Low pressure flame determinations of rate constants for OH(A) and CH(A) chemiluminescence, *Combustion and Flame* 131 (2002) 59-69.
- [235] M.M. Kopp, O. Mathieu, E.L. Petersen, Rate Determination of the CO₂* Chemiluminescence Reaction CO + O + M = CO₂* + M, *International Journal of Chemical Kinetics* 47 (2015) 50-72.
- [236] T. Yi, D.A. Santavicca, Flame spectra of a turbulent liquid-fueled swirl-stabilized lean-direct injection combustor, *Journal of Propulsion and Power* 25 (2009) 1058-1067.
- [237] C.T. Chong, S. Hochgreb, Flame structure, spectroscopy and emissions quantification of rapeseed biodiesel under model gas turbine conditions, *Applied Energy* 185 (2017) 1383-1392.
- [238] W. Swan, XXIX.—On the prismatic spectra of the flames of compounds of carbon and hydrogen, *Earth and Environmental Science Transactions of The Royal Society of Edinburgh* 21 (1857) 411-429.
- [239] J. Kojima, Y. Ikeda, T. Nakajima, Spatially resolved measurement of OH*, CH*, and C₂* chemiluminescence in the reaction zone of laminar methane/air premixed flames, *Proceedings of the Combustion Institute* 28 (2000) 1757-1764.

- [240] W. Meyerriecks, K. Kosanke, Color values and spectra of the principal emitters in colored flames, *Journal of Pyrotechnics* 18 (2003) 710-731.
- [241] N.G. Glumac, Formation and consumption of SiO in powder synthesis flames, *Combustion and Flame* 124 (2001) 702-711.
- [242] A. Burkert, D. Müller, W. Paa, Si and SiO detection in a HMDSO/propane/air flame using spatially resolved optical emission spectroscopy (OES), *Journal of Quantitative Spectroscopy and Radiative Transfer* 114 (2013) 101-108.
- [243] G. Vilmart, N. Dorval, M. Orain, D. Lambert, R. Devillers, Y. Fabignon, B. Attal-Tretout, A. Bresson, Detection of iron atoms by emission spectroscopy and laser-induced fluorescence in solid propellant flames, *Applied Optics* 57 (2018) 3817-3828.
- [244] G.M. Rassweiler, L. Withrow, Emission spectra of engine flames, *Industrial & Engineering Chemistry* 24 (1932) 528-538.
- [245] R. Gattinger, W. Evans, D. Degenstein, E. Llewellyn, A spectral model of the FeO orange bands with a comparison between a laboratory spectrum and a night airglow spectrum observed by OSIRIS on Odin, *Canadian Journal of Physics* 89 (2011) 239-248.
- [246] P. Jenniskens, M. Lacey, B.J. Allan, D.E. Self, J.M. Plane, FeO "orange arc" emission detected in optical spectrum of Leonid persistent train, *Earth Moon Planets* 82 (2000) 429-438.
- [247] R.W.B. Pearse, A.G. Gaydon, R.W.B. Pearse, A.G. Gaydon, The identification of molecular spectra, Chapman and Hall London, 1976.
- [248] R. Dhumwad, N. Narasimham, Rotational analysis of some of the bands of the orange system of FeO, *Proceedings of the Indian Academy of Sciences* 64 (1966) 283-290.
- [249] H. Chagger, D. Hainsworth, P. Patterson, M. Pourkashanian, A. Williams, The formation of SiO₂ from hexamethyldisiloxane combustion in counterflow methane-air flames, *Symposium (International) on Combustion* 26 (1996) 1859-1865.
- [250] N. Jüngst, B.A. Suedholt, G.J. Smallwood, C. Schulz, S.A. Kaiser, Laser-induced emission from iron oxide nanoparticles in spray-flame synthesis: in situ high-speed microscopy, *Applied Physics B* 130 (2024) 63.
- [251] J. Costes, J. Couderc, Study by laser Doppler anemometry of the turbulent flow induced by a Rushton turbine in a stirred tank: Influence of the size of the units—I. Mean flow and turbulence, *Chemical Engineering Science* 43 (1988) 2751-2764.
- [252] W. Kumara, G. Elseth, B. Halvorsen, M. Melaaen, Comparison of Particle Image Velocimetry and Laser Doppler Anemometry measurement methods applied to the oil-water flow in horizontal pipe, *Flow Measurement and Instrumentation* 21 (2010) 105-117.
- [253] R.B. Rask, Laser Doppler anemometer measurements in an internal combustion engine, SAE paper 790094 (1979).
- [254] R. Starke, P. Roth, An experimental investigation of flame behavior during cylindrical vessel explosions, *Combustion and Flame* 66 (1986) 249-259.
- [255] M. Stodt, J. Kiefer, U. Fritsching, Impact of atomization and spray flow conditions on droplet μ -explosions and temporal self-similarity in the FSP process, *Applications in Energy and Combustion Science* 15 (2023) 100170.
- [256] C. Edwards, R. Rudoff, Structure of a swirl-stabilized spray flame by imaging, laser doppler velocimetry, and phase doppler anemometry, *Symposium (International) on Combustion* 23 (1991) 1353-1359.

- [257] W.M. Farmer, Measurement of particle size, number density, and velocity using a laser interferometer, *Applied Optics* 11 (1972) 2603-2612.
- [258] W. Bachalo, M. Houser, Phase/Doppler spray analyzer for simultaneous measurements of drop size and velocity distributions, *Optical Engineering* 23 (1984) 583-590.
- [259] B. Ruck, Laser Doppler Anemometry—a non-intrusive optical measuring technique for fluid velocity, *Particle & Particle Systems Characterization* 4 (1987) 26-37.
- [260] F. Durst, G. Brenn, T. Xu, A review of the development and characteristics of planar phase-Doppler anemometry, *Measurement Science and Technology* 8 (1997) 1203.
- [261] H.-E. Albrecht, N. Damaschke, M. Borys, C. Tropea, *Laser Doppler and phase Doppler measurement techniques*, Springer Science & Business Media, 2013.
- [262] D. Durao, J.H. Whitelaw, The performance of acousto-optic cells for laser-Doppler anemometry, *Journal of Physics E: Scientific Instruments* 8 (1975) 776.
- [263] F. Durst, M. Zaré, Laser Doppler measurements in two-phase flows, *Proceedings of the Laser Doppler anemometry symposium*, Copenhagen, Denmark (1976) 403-429.
- [264] OriginPro, Version 2023. OriginLab Corporation, Northampton, MA, USA.
- [265] J. Grohmann, Experimentelle Untersuchungen zum Einfluss von Kohlenwasserstoffen auf das Verbrennungsverhalten drallstabiler Sprayflammen, Doctoral dissertation, Deutsches Zentrum für Luft- und Raumfahrt, Institut für Verbrennungstechnik (2019).
- [266] G. Godsave, Studies of the combustion of drops in a fuel spray—the burning of single drops of fuel, *Symposium (International) on Combustion* 4 (1953) 818-830.
- [267] C. Spink, I. Wadsö, D. Glick, *Methods of biochemical analysis*, Wiley, New York, 1976.
- [268] R.E. Pennington, K.A. Kobe, The thermodynamic properties of acetone, *Journal of the American Chemical Society* 79 (1957) 300-305.
- [269] N. Jüngst, V. Ersoy, G.J. Smallwood, S.A. Kaiser, Neural networks for classification and segmentation of thermally-induced droplet breakup in spray-flame synthesis, *Journal of Aerosol Science* 176 (2024) 106314.
- [270] R. Strobel, S.E. Pratsinis, Flame aerosol synthesis of smart nanostructured materials, *Journal of Materials Chemistry* 17 (2007) 4743-4756.
- [271] A. Kilian, T. Morse, A novel aerosol combustion process for the high rate formation of nanoscale oxide particles, *Aerosol Science & Technology* 34 (2001) 227-235.
- [272] K. Wegner, S.E. Pratsinis, Gas-phase synthesis of nanoparticles: scale-up and design of flame reactors, *Powder Technology* 150 (2005) 117-122.
- [273] T. Hülser, S.M. Schnurre, H. Wiggers, C. Schulz, Gas-phase synthesis of nanoscale silicon as an economical route towards sustainable energy technology, *KONA Powder and Particle Journal* 29 (2011) 191-207.
- [274] K. Hembram, T. Rao, R. Srinivasa, A. Kulkarni, High performance varistors prepared from doped ZnO nanopowders made by pilot-scale flame spray pyrolyzer: Sintering, microstructure and properties, *Journal of the European Ceramic Society* 35 (2015) 3535-3544.
- [275] S. Kluge, L. Deng, O. Feroughi, F. Schneider, M. Poliak, A. Fomin, V. Tsionsky, S. Cheskis, I. Wlokas, I. Rahinov, Initial reaction steps during flame synthesis of iron-oxide nanoparticles, *CrystEngComm* 17 (2015) 6930-6939.

- [276] T. Dreier, C. Schulz, Laser-based diagnostics in the gas-phase synthesis of inorganic nanoparticles, *Powder Technology* 287 (2016) 226-238.
- [277] M. Yorozu, Y. Okada, A. Endo, Two dimensional rotational temperature measurement by multiline laser induced fluorescence of nitric oxide in combustion flame, *Optical Review* 3 (1996) 293-298.
- [278] W.G. Bessler, C. Schulz, Quantitative multi-line NO-LIF temperature imaging, *Applied Physics B* 78 (2004) 519-533.
- [279] H. Kronemayer, W. Bessler, C. Schulz, Gas-phase temperature imaging in spray systems using multi-line NO-LIF thermometry, *Applied Physics B* 81 (2005) 1071-1074.
- [280] H. Kronemayer, K. Omerbegovic, C. Schulz, Quantification of the evaporative cooling in an ethanol spray created by a gasoline direct-injection system measured by multiline NO-LIF gas-temperature imaging, *Applied Optics* 46 (2007) 8322-8327.
- [281] I. Duwel, H.W. Ge, H. Kronemayer, R. Dibble, E. Gutheil, C. Schulz, J. Wolfrum, Experimental and numerical characterization of a turbulent spray flame, *Proceedings of the Combustion Institute* 31 (2007) 2247-2255.
- [282] A.T. Hartlieb, B. Atakan, K. Kohse-Höinghaus, Effects of a sampling quartz nozzle on the flame structure of a fuel-rich low-pressure propene flame, *Combustion and Flame* 121 (2000) 610-624.
- [283] O.M. Feroughi, L. Deng, S. Kluge, T. Dreier, H. Wiggers, I. Wlokas, C. Schulz, Experimental and numerical study of a HMDSO-seeded premixed laminar low-pressure flame for SiO₂ nanoparticle synthesis, *Proceedings of the Combustion Institute* 36 (2017) 1045-1053.
- [284] R.S. Chrystie, H. Janbazi, T. Dreier, H. Wiggers, I. Wlokas, C. Schulz, Comparative study of flame-based SiO₂ nanoparticle synthesis from TMS and HMDSO: SiO-LIF concentration measurement and detailed simulation, *Proceedings of the Combustion Institute* 37 (2019) 1221-1229.
- [285] M. Tsujishita, A. Hirano, M. Yokoo, T. Sakuraya, Y. Takeshita, Accurate Thermometry Using NO and OH Laser-Induced Fluorescence in an Atmospheric Pressure Flame: Checked by Narrow-Band N₂ Coherent Anti-Stokes Raman Scattering, *JSME International Journal Series B Fluids and Thermal Engineering* 42 (1999) 119-126.
- [286] T. Lee, W.G. Bessler, H. Kronemayer, C. Schulz, J.B. Jeffries, Quantitative temperature measurements in high-pressure flames with multiline NO-LIF thermometry, *Applied Optics* 44 (2005) 6718-6728.
- [287] W. Bessler, C. Schulz, T. Lee, D.-I. Shin, M. Hofmann, J. Jeffries, J. Wolfrum, R. Hanson, Quantitative NO-LIF imaging in high-pressure flames, *Applied Physics B* 75 (2002) 97-102.
- [288] A. Vyrodov, J. Heinze, M. Dillmann, U. Meier, W. Stricker, Laser-induced fluorescence thermometry and concentration measurements on NO_A-X (0-0) transitions in the exhaust gas of high pressure CH₄/air flames, *Applied Physics B* 61 (1995) 409-414.
- [289] M. Hofmann, H. Kronemayer, B. Kock, H. Jander, C. Schulz, Laser-induced incandescence and multi-line NO-LIF thermometry for soot diagnostics at high pressures, *European Combustion Meeting Louvain-la-Neuve, Belgium* (2005).
- [290] H. Kronemayer, P. Ifecho, C. Hecht, T. Dreier, H. Wiggers, C. Schulz, Gas-temperature imaging in a low-pressure flame reactor for nano-particle synthesis with multi-line NO-LIF thermometry, *Applied Physics B* 88 (2007) 373-377.
- [291] R.S. Chrystie, O.M. Feroughi, T. Dreier, C. Schulz, SiO multi-line laser-induced fluorescence for quantitative temperature imaging in flame-synthesis of nanoparticles, *Applied Physics B* 123 (2017) 104.

- [292] O.M. Feroughi, S. Hardt, I. Wlokas, T. Hülser, H. Wiggers, T. Dreier, C. Schulz, Laser-based in situ measurement and simulation of gas-phase temperature and iron atom concentration in a pilot-plant nanoparticle synthesis reactor, *Proceedings of the Combustion Institute* 35 (2015) 2299-2306.
- [293] C. Hecht, A. Abdali, T. Dreier, C. Schulz, Gas-temperature imaging in a microwave-plasma nanoparticle-synthesis reactor using multi-line NO-LIF thermometry, *Zeitschrift für Physikalische Chemie* 225 (2011) 1225-1235.
- [294] N. Petermann, N. Stein, G. Schierning, R. Theissmann, B. Stoib, M.S. Brandt, C. Hecht, C. Schulz, H. Wiggers, Plasma synthesis of nanostructures for improved thermoelectric properties, *Journal of Physics D: Applied Physics* 44 (2011) 174034.
- [295] W.G. Bessler, C. Schulz, V. Sick, J.W. Daily, A versatile modeling tool for nitric oxide LIF spectra, *Proceedings of the Third Joint Meeting of the US Sections of the Combustion Institute* (2003).
- [296] A. El Moussawi, T. Endres, S. Peukert, S. Zabeti, T. Dreier, M. Fikri, C. Schulz, Multi-line SiO fluorescence imaging in the flame synthesis of silica nanoparticles from SiCl₄, *Combustion and Flame* 224 (2021) 260-272.
- [297] K. Levenberg, A method for the solution of certain non-linear problems in least squares, *Quarterly of Applied Mathematics* 2 (1944) 164-168.
- [298] D.W. Marquardt, An algorithm for least-squares estimation of nonlinear parameters, *Journal of the Society for Industrial and Applied Mathematics* 11 (1963) 431-441.
- [299] W.G. Bessler, Quantitative nitric oxide concentration and temperature imaging in flames over a wide pressure range with laser-induced fluorescence, *Doctoral dissertation, Physikalisch-Chemisches Institut* (2003).
- [300] A.C. Eckbreth, *Laser diagnostics for combustion temperature and species*, CRC press, 2022.
- [301] J.W. Daily, Laser induced fluorescence spectroscopy in flames, *Progress in Energy and Combustion Science* 23 (1997) 133-199.
- [302] P. Paul, Calculation of transition frequencies and rotational line strengths in the γ -bands of nitric oxide, *Journal of Quantitative Spectroscopy and Radiative Transfer* 57 (1997) 581-589.
- [303] C. Schulz, *Abbildende laserspektroskopische Verfahren zur Messung von Konzentrationen, Temperaturen und Geschwindigkeiten in Verbrennungsprozessen und chemisch reagierenden Strömungen*, Habilitationsschrift Ruprecht-Karls-Universität Heidelberg (2002).
- [304] C.S. Goldenstein, V.A. Miller, R.K. Hanson, Infrared planar laser-induced fluorescence with a CW quantum-cascade laser for spatially resolved CO₂ and gas properties, *Applied Physics B* 120 (2015) 185-199.
- [305] D.R. Crosley, Laser-induced fluorescence measurement of combustion chemistry intermediates, *High Temperature Materials and Processes* 7 (1986) 41-54.
- [306] M. Kirschner, T. Sander, C. Mundt, Rotational temperature measurement in an arc-heated wind tunnel by laser induced fluorescence of nitric oxide ax (0, 0), *30th AIAA Aerodynamic Measurement Technology and Ground Testing Conference* (2014) 2528.
- [307] E. Malmqvist, M. Jonsson, K. Larsson, M. Aldén, J. Bood, Two-dimensional OH-thermometry in reacting flows using photofragmentation laser-induced fluorescence, *Combustion and Flame* 169 (2016) 297-306.
- [308] Z. Yin, C.D. Carter, W.R. Lempert, Effects of signal corrections on measurements of temperature and OH concentrations using laser-induced fluorescence, *Applied Physics B* 117 (2014) 707-721.

- [309] S. Apazeller, S. Karaminejad, M. Nanjaiah, H. Wiggers, T. Endres, I. Wlokas, C. Schulz, LIF-imaging of temperature and iron-atom concentration in iron nitrate doped low-pressure aerosol flat flames, *Applications in Energy and Combustion Science* 16 (2023) 100199.
- [310] E. Brinkman, G. Raiche, M. Brown, J. Jeffries, Optical diagnostics for temperature measurement in a DC arcjet reactor used for diamond deposition, *Applied Physics B* 64 (1997) 689-697.
- [311] J.B. Bell, M.S. Day, J.F. Grcar, W.G. Bessler, C. Schulz, P. Glarborg, A.D. Jensen, Detailed modeling and laser-induced fluorescence imaging of nitric oxide in a NH₃-seeded non-premixed methane/air flame, *Proceedings of the Combustion Institute* 29 (2002) 2195-2202.
- [312] W.G. Bessler, F. Hildenbrand, C. Schulz, Two-line laser-induced fluorescence imaging of vibrational temperatures in a NO-seeded flame, *Applied Optics* 40 (2001) 748-756.
- [313] M. Tamura, J. Luque, J. Harrington, P. Berg, G. Smith, J. Jeffries, D. Crosley, Laser-induced fluorescence of seeded nitric oxide as a flame thermometer, *Applied Physics B: Lasers & Optics* 66 (1998) 503-510.
- [314] M.P. Lee, B.K. McMillin, R.K. Hanson, Temperature measurements in gases by use of planar laser-induced fluorescence imaging of NO, *Applied Optics* 32 (1993) 5379-5396.
- [315] B. McMillin, J. Seitzman, R.K. Hanson, Comparison of NO and OH planar fluorescence temperature measurements in scramjet model flowfield, *AIAA journal* 32 (1994) 1945-1952.
- [316] S. Kostka, S. Roy, P.J. Lakusta, T.R. Meyer, M.W. Renfro, J.R. Gord, R. Branam, Comparison of line-peak and line-scanning excitation in two-color laser-induced-fluorescence thermometry of OH, *Applied Optics* 48 (2009) 6332-6343.
- [317] J.M. Seitzman, R.K. Hanson, P. DeBarber, C. Hess, Application of quantitative two-line OH planar laser-induced fluorescence for temporally resolved planar thermometry in reacting flows, *Applied Optics* 33 (1994) 4000-4012.
- [318] R. Giezendanner-Thoben, U. Meier, W. Meier, M. Aigner, Phase-locked temperature measurements by two-line OH PLIF thermometry of a self-excited combustion instability in a gas turbine model combustor, *Flow, Turbulence and Combustion* 75 (2005) 317-333.
- [319] R. Devillers, G. Bruneaux, C. Schulz, Development of a two-line OH-laser-induced fluorescence thermometry diagnostics strategy for gas-phase temperature measurements in engines, *Applied Optics* 47 (2008) 5871-5885.
- [320] U. Meier, R. Kienle, I. Plath, K. Kohse-Höinghaus, Two-Dimensional LIF Approaches for the Accurate Determination of Radical Concentrations and Temperature in Combustion, *Berichte der Bunsengesellschaft für physikalische Chemie* 96 (1992) 1401-1410.
- [321] A. Arnold, B. Lange, T. Bouché, T. Heitzmann, G. Schiff, W. Ketterle, P. Monkhouse, J. Wolfram, Absolute Temperature Fields in Flames by 2D-LIF of OH Using Excimer Lasers and CARS Spectroscopy, *Berichte der Bunsengesellschaft für physikalische Chemie* 96 (1992) 1388-1393.
- [322] C. Copeland, J. Friedman, M. Renksizbulut, Planar temperature imaging using thermally assisted laser induced fluorescence of OH in a methane-air flame, *Experimental Thermal and Fluid Science* 31 (2007) 221-236.
- [323] N. Glumac, Y. Chen, G. Skandan, Diagnostics and modeling of nanopowder synthesis in low pressure flames, *Journal of Materials Research* 13 (1998) 2572-2579.
- [324] H. Le, R. Dreyfus, W. Marine, M. Sentis, I. Movtchan, Temperature measurements during laser ablation of Si into He, Ar and O₂, *Applied Surface Science* 96 (1996) 164-169.
- [325] M.S. Smith, L.L. Price, W. Williams, Laser-induced fluorescence diagnostics using a two-line excitation method, *AIAA journal* 31 (1993) 478-482.

- [326] C. Kaminski, J. Engström, M. Aldén, Quasi-instantaneous two-dimensional temperature measurements in a spark ignition engine using 2-line atomic fluorescence, Symposium (International) on Combustion 27 (1998) 85-93.
- [327] J. Engström, J. Nygren, M. Aldén, C. Kaminski, Two-line atomic fluorescence as a temperature probe for highly sooting flames, Optics Letters 25 (2000) 1469-1471.
- [328] J. Nygren, J. Engström, J. Walewski, C. Kaminski, M. Aldén, Applications and evaluation of two-line atomic LIF thermometry in sooting combustion environments, Measurement Science and Technology 12 (2001) 1294.
- [329] P.R. Medwell, Q.N. Chan, P.A. Kalt, Z.T. Alwahabi, B.B. Dally, G.J. Nathan, Development of temperature imaging using two-line atomic fluorescence, Applied Optics 48 (2009) 1237-1248.
- [330] P.R. Medwell, A.R. Masri, P.X. Pham, B.B. Dally, G.J. Nathan, Temperature imaging of turbulent dilute spray flames using two-line atomic fluorescence, Experiments in Fluids 55 (2014) 1840.
- [331] B. Münsterjohann, F.J. Huber, T.C. Klima, S. Holfelder, S.R. Engel, J.D. Miller, T.R. Meyer, S. Will, Potential of two-line atomic fluorescence for temperature imaging in turbulent indium-oxide-producing flames, Journal of Nanoparticle Research 17 (2015) 459.
- [332] T. Fujikawa, K. Fukui, Y. Hattori, K. Akihama, 2-D temperature measurements of unburned gas mixture in an engine by two-line excitation LIF technique, Toyota Central R&D Labs. (2006) 2006-2001-3336.
- [333] T. Ni-Imi, T. Fujimoto, N. Shimizu, Method for planar measurement of temperature in compressible flow using two-line laser-induced iodine fluorescence, Optics Letters 15 (1990) 918-920.
- [334] J.M. Seitzman, G. Kychakoff, R.K. Hanson, Instantaneous temperature field measurements using planar laser-induced fluorescence, Optics Letters 10 (1985) 439-441.
- [335] R.J. Hartfield, S.D. Hollo, J.C. McDaniel, Planar temperature measurement in compressible flows using laser-induced iodine fluorescence, Optics Letters 16 (1991) 106-108.
- [336] M.P. Lee, P.H. Paul, R.K. Hanson, Quantitative imaging of temperature fields in air using planar laser-induced fluorescence of O₂, Optics Letters 12 (1987) 75-77.
- [337] T. Fuyuto, H. Kronemayer, B. Lewerich, W. Koban, K. Akihama, C. Schulz, Laser-based temperature imaging close to surfaces with toluene and NO-LIF, Journal of Physics: Conference Series 45 (2006) 010.
- [338] M. Hofmann, H. Kronemayer, B. Kock, H. Jander, C. Schulz, Soot diagnostics at elevated pressure: Laser-induced incandescence and multi-line NO-LIF thermometry, Proceedings of the 4th Australian Conference on Laser Diagnostics in Fluid Mechanics and Combustion (2005).
- [339] C. Hecht, Laserspektroskopische Charakterisierung von Reaktionsprozessen zur Gasphasensynthese von Nanopartikeln, Cuvillier Verlag, 2011.
- [340] F.J. Duarte, Tunable laser applications, CRC press, 2008.
- [341] W.T. Silfvast, Lasers, Academic Press, New York, 2003.
- [342] NarrowScan Pulsed Dye Laser - Operation and Maintenance Manual, Radiant Dyes Laser Accessories GmbH, Wermelskirch, Germany.
- [343] A. El Moussawi, T. Endres, S. Karaminejad, W. Bessler, J. Menser, T. Dreier, C. Schulz, LIFSim 4.0, a modular laser-induced fluorescence code for concentration and temperature analysis of two-atomic molecules, Applied Physics B (2024) in preparation.
- [344] LIFSim: A versatile modeling tool for NO and O₂ LIF spectra, available at <<http://www.lifsim.com/>>.

- [345] I.E. Gordon, L.S. Rothman, R. Hargreaves, R. Hashemi, E.V. Karlovets, F. Skinner, E.K. Conway, C. Hill, R.V. Kochanov, Y. Tan, The HITRAN2020 molecular spectroscopic database, *Journal of Quantitative Spectroscopy and Radiative Transfer* 277 (2022) 107949.
- [346] O.M. Feroughi, H. Kronmayer, T. Dreier, C. Schulz, Effect of fluctuations on time-averaged multi-line NO-LIF thermometry measurements of the gas-phase temperature, *Applied Physics B* 120 (2015) 429-440.
- [347] H. Kronmayer, Laser-based temperature diagnostics in practical combustion systems, Doctoral dissertation, Heidelberg University (2007).
- [348] P. Walzel, Spraying and atomizing of liquids, *Ullmann's Encyclopedia of Industrial Chemistry* (2000) 1-30.
- [349] M. Nanjaiah, P. Wollny, P. Narasu, S. Apazeller, S. Karaminejad, T. Endres, H. Wiggers, C. Schulz, E. Gutheil, A. Kempf, Simulations of laminar methane flames doped with iron nitrate/1-butanol aerosol in a novel matrix burner, *Applications in Energy and Combustion Science* 15 (2023) 100186.
- [350] C. Schulz, V. Sick, U.E. Meier, J. Heinze, W. Stricker, Quantification of NO A–X (0, 2) laser-induced fluorescence: investigation of calibration and collisional influences in high-pressure flames, *Applied Optics* 38 (1999) 1434-1443.
- [351] C. Schulz, V. Sick, J. Wolfrum, V. Drewes, R. Maly, Quantitative 2D single-shot imaging of NO concentrations and temperatures in a transparent SI engine, *Symposium (International) on Combustion* 26 (1996) 2597-2604.
- [352] C. Schulz, Entwicklung und Anwendung eines laserspektroskopischen Verfahrens zur quantitativen Bestimmung momentaner Stickoxidverteilungen in Verbrennungsmotoren, Dissertation, University of Heidelberg (1997).
- [353] S. Apazeller, M. Gonchikzhapov, M. Nanjaiah, T. Kasper, I. Wlokas, H. Wiggers, C. Schulz, A new dual matrix burner for one-dimensional investigation of aerosol flames, *Proceedings of the Combustion Institute* 39 (2023) 909-918.
- [354] C. Hecht, H. Kronmayer, T. Dreier, H. Wiggers, C. Schulz, Imaging measurements of atomic iron concentration with laser-induced fluorescence in a nanoparticle synthesis flame reactor, *Applied Physics B* 94 (2009) 119-125.
- [355] S. Kluge, Massenspektrometrische Untersuchung der Nanopartikelbildung in vorgemischten Niederdruckflammen, Dissertation, Institut für Verbrennung und Gasdynamik (2017).
- [356] M. Nanjaiah, A. Pilipodi-Best, M.R. Lalanne, P. Fjodorow, C. Schulz, S. Cheskis, A. Kempf, I. Wlokas, I. Rahinov, Experimental and numerical investigation of iron-doped flames: FeO formation and impact on flame temperature, *Proceedings of the Combustion Institute* 38 (2021) 1249-1257.
- [357] M.R. Lalanne, P. Wollny, M. Nanjaiah, J. Menser, C. Schulz, H. Wiggers, S. Cheskis, I. Wlokas, I. Rahinov, Early particle formation and evolution in iron-doped flames, *Combustion and Flame* 244 (2022) 112251.
- [358] P. Wollny, J. Menser, L. Engelmann, J. Sellmann, C. Schulz, H. Wiggers, A. Kempf, I. Wlokas, The role of phase transition by nucleation, condensation, and evaporation for the synthesis of silicon nanoparticles in a microwave plasma reactor—Simulation and experiment, *Chemical Engineering Journal* 453 (2023) 139695.
- [359] D. Antonov, R. Fedorenko, G. Kuznetsov, P. Strizhak, Modeling the micro-explosion of miscible and immiscible liquid droplets, *Acta Astronautica* 171 (2020) 69-82.

- [360] F. Meierhofer, H. Li, M. Gockeln, R. Kun, T. Grieb, A. Rosenauer, U. Fritsching, J. Kiefer, J. Birkenstock, L. Mädler, Screening precursor–solvent combinations for $\text{Li}_4\text{Ti}_5\text{O}_{12}$ energy storage material using flame spray pyrolysis, *ACS Applied Materials & Interfaces* 9 (2017) 37760-37777.
- [361] T.D. Fansler, S.E. Parrish, Spray measurement technology: a review, *Measurement Science and Technology* 26 (2015) 012002.
- [362] C. Schulz, V. Sick, Tracer-LIF diagnostics: quantitative measurement of fuel concentration, temperature and fuel/air ratio in practical combustion systems, *Progress in Energy and Combustion Science* 31 (2005) 75-121.
- [363] D. Greszik, H. Yang, T. Dreier, C. Schulz, Laser-based diagnostics for the measurement of liquid water film thickness, *Applied Optics* 50 (2011) A60-A67.
- [364] A.M. Murray, L.A. Melton, Fluorescence methods for determination of temperature in fuel sprays, *Applied Optics* 24 (1985) 2783-2787.
- [365] P. Lavielle, F. Lemoine, G. Lavergne, M. Lebouché, Evaporating and combusting droplet temperature measurements using two-color laser-induced fluorescence, *Experiments in Fluids* 31 (2001) 45-55.
- [366] M.C.J. Coolen, R.N. Kieft, C.C.M. Rindt, A.A. van Steenhoven, Application of 2-D LIF temperature measurements in water using a Nd : YAG laser, *Experiments in Fluids* 27 (1999) 420-426.
- [367] C.E. Estrada-Pérez, Y.A. Hassan, S. Tan, Experimental characterization of temperature sensitive dyes for laser induced fluorescence thermometry, *Review of Scientific Instruments* 82 (2011) 074901.
- [368] Y.N. Mishra, F. Abou Nada, S. Polster, E. Kristensson, E. Berrocal, Thermometry in aqueous solutions and sprays using two-color LIF and structured illumination, *Optics Express* 24 (2016) 4949-4963.
- [369] W. Chaze, O. Caballina, G. Castanet, F. Lemoine, The saturation of the fluorescence and its consequences for laser-induced fluorescence thermometry in liquid flows, *Experiments in Fluids* 57 (2016) 58.
- [370] M. Koegl, C. Mull, K. Baderschneider, J. Wislicenus, S. Will, L. Zigan, Characterization of Nile Red as a Tracer for Laser-Induced Fluorescence Spectroscopy of Gasoline and Kerosene and Their Mixture with Biofuels, *Sensors* 19 (2019) 2822.
- [371] Y.N. Mishra, A. Yoganantham, M. Koegl, L. Zigan, Investigation of Five Organic Dyes in Ethanol and Butanol for Two-Color Laser-Induced Fluorescence Ratio Thermometry, *Optics* 1 (2020) 1-17.
- [372] M. Koegl, M. Pahlevani, L. Zigan, A Novel Approach for Measurement of Composition and Temperature of N-Decane/Butanol Blends Using Two-Color Laser-Induced Fluorescence of Nile Red, *Sensors* 20 (2020) 5721.
- [373] M. Koegl, C. Mull, Y.N. Mishra, S. Will, L. Zigan, Characterization of fuel/water mixtures and emulsions with ethanol using laser-induced fluorescence, *Applied Optics* 59 (2020) 1136-1144.
- [374] M. Koegl, J. Vogler, L. Zigan, Spectral Investigations of Fluorescence Tracers in Automotive and Aviation Fuels under Cryogenic Conditions, *Sensors* 24 (2024) 724.
- [375] M. Koegl, C. Weiß, L. Zigan, Fluorescence spectroscopy for studying evaporating droplets using the dye eosin-Y, *Sensors* 20 (2020) 5985.
- [376] P. Lavielle, A. Delconte, D. Blondel, M. Lebouché, F. Lemoine, Non-intrusive temperature measurements using three-color laser-induced fluorescence, *Experiments in Fluids* 36 (2004) 706-716.

- [377] P. Dunand, G. Castanet, F. Lemoine, A two-color planar LIF technique to map the temperature of droplets impinging onto a heated wall, *Experiments in Fluids* 52 (2012) 843-856.
- [378] L. Perrin, G. Castanet, F. Lemoine, Characterization of the evaporation of interacting droplets using combined optical techniques, *Experiments in Fluids* 56 (2015) 29.
- [379] M. Koegl, N. Mil 'to, L. Zigan, Simultaneous film temperature and film thickness measurements for jet impingement applications using two-color laser-induced fluorescence, *Experiments in Fluids* 65 (2024) 41.
- [380] H. Briesen, A. Fuhrmann, S.E. Pratsinis, The effect of precursor in flame synthesis of SiO₂, *Chemical Engineering Science* 53 (1998) 4105-4112.
- [381] M.S. Dobbins, R.E. McLay, Method of making fused silica by decomposing siloxanes, U.S. Patent 5,043,002, 1991.
- [382] M. Bruchhausen, F. Guillard, F. Lemoine, Instantaneous measurement of two-dimensional temperature distributions by means of two-color planar laser induced fluorescence (PLIF), *Experiments in Fluids* 38 (2005) 123-131.
- [383] P. Dunand, G. Castanet, M. Gradeck, F. Lemoine, D. Maillet, Heat transfer of droplets impinging onto a wall above the Leidenfrost temperature, *Comptes Rendus. Mécanique* 341 (2013) 75-87.
- [384] Cary 100/300/400/500 Spectrophotometers, UV-VIS-NIR, Varian Analytical Instruments, brochure, 09/2000.
- [385] Fluorolog-3 Operation Manual, Horiba Scientific, rev. G(2 May 2014).
- [386] W.M. Haynes, *Handbook of chemistry and physics: A ready-reference book of chemical and physical data*, CRC press, 2016.
- [387] Sigma-Aldrich – Material Safety Data Sheet, “1-Butanol, CAS-No: 71-36-3, Product number: 281549,” Version 6.3, Revision Date 01/15/2020, Print Date 11/20/2020.
- [388] GESTIS – Substance Database – Institut für Arbeitsschutz der Deutschen Gesetzlichen Unfallversicherung (IFA), 1-Butanol, CAS-No: 71-36-3, Retrieved from <https://gestis.dguv.de/data?name=012650> – accessed: 2021-03-26.
- [389] Sigma-Aldrich – Material Safety Data Sheet, “2-EHA, CAS-No: 149-57-5, Product number: 538701,” Version 6.3, Revision Date 01/20/2020, Print Date 11/20/2020.
- [390] Sigma-Aldrich – Material Safety Data Sheet, “Ethanol, CAS-No: 64-17-5, Product number: V001229,” Version 8.0, Revision Date 04/03/2020, Print Date 03/26/2021.
- [391] Sigma-Aldrich – Material Safety Data Sheet, “o-Xylene, CAS-No: 95-47-6, Product number: 294780,” Version 6.3, Revision Date 01/15/2020, Print Date 11/20/2020.
- [392] Sigma-Aldrich – Material Safety Data Sheet, “Hexamethyldisiloxane, CAS-No: 107-46-0, Product number: 52630,” Version 6.3, Revision Date 14/04/2022, Print Date 22/10/2022.
- [393] V. Deprédurand, P. Miron, A. Labergue, M. Wolff, G. Castanet, F. Lemoine, A temperature-sensitive tracer suitable for two-colour laser-induced fluorescence thermometry applied to evaporating fuel droplets, *Measurement Science and Technology* 19 (2008) 105403-105412.
- [394] P. Lavieille, F. Lemoine, G. Lavergne, J.F. Virepinte, M. Lebouché, Temperature measurements on droplets in monodisperse stream using laser-induced fluorescence, *Experiments in Fluids* 29 (2000) 429-437.
- [395] G. Liu, H. Lu, Laser-induced fluorescence of rhodamine B in ethylene glycol solution, *Procedia Engineering* 102 (2015) 95-105.

- [396] U. Brackmann, *Lambdachrome Laser Dyes*, Lambda Physik AG, Germany, 2000.
- [397] M.F.B. Stodt, J. Kiefer, U. Fritsching, Ethanol droplet formation, dynamics and combustion mode in the flame of the SpraySyn-nozzle, *Experiments in Fluids* 60 (2019) 125.
- [398] C. Maqua, G. Castanet, F. Lemoine, N. Doué, G. Lavergne, Temperature measurements of binary droplets using three-color laser-induced fluorescence, *Experiments in Fluids* 40 (2006) 786.
- [399] A. Rittler, L. Deng, I. Wlokas, A. Kempf, Large eddy simulations of nanoparticle synthesis from flame spray pyrolysis, *Proceedings of the Combustion Institute* 36 (2017) 1077-1087.
- [400] C.T. Avedisian, R.P. Andres, Bubble Nucleation in Superheated Liquid-Liquid Emulsions, *Journal of Colloid and Interface Science* 64 (1978) 438-453.
- [401] C.H. Wang, S.Y. Fu, L.J. Kung, C.K. Law, Combustion and microexplosion of collision-merged methanol/alkane droplets, *Proceedings of the Combustion Institute* 30 (2005) 1965-1972.
- [402] J. Lasheras, A. Fernandez-Pello, F. Dryer, On the disruptive burning of free droplets of alcohol/n-paraffin solutions and emulsions, *Symposium (International) on Combustion* 18 (1981) 293–305.
- [403] J.P. van Beeck, L. Zimmer, M.L. Riethmuller, Global rainbow thermometry for mean temperature and size measurement of spray droplets, *Particle & Particle Systems Characterization* 18 (2001) 196-204.
- [404] Q. Lv, Y. Wu, X. Wu, Surface temperature measurement of cooling and heating droplets by rainbow refractometry, *Applied Optics* 61 (2022) 7455-7462.
- [405] C. Li, W. Peng, T. Li, N. Li, Right partial rainbow refractometry for measuring droplet refractive index and size, *Frontiers in Physics* 11 (2023) 1326332.
- [406] O. Ravel, N. Naudin, O. Adam, J.F. Virepinte, J.A. Farre, G. Lavergne, Infrared temperature measurement of burning droplet, *Combustion Diagnostics* 3108 (1997) 44-53.
- [407] T. Muller, G. Grunefeld, V. Beushausen, High-precision measurement of the temperature of methanol and ethanol droplets using spontaneous Raman scattering, *Applied Physics B* 70 (2000) 155-158.
- [408] J. Palmer, L. Schumacher, M.A. Reddemann, V. Kirsch, R. Kneer, Applicability of pulsed 2cLIF-EET for micro-droplet internal thermometry under evaporation conditions, *Experiments in Fluids* 61 (2020) 99.
- [409] H. Ulrich, S. Sigl, M. Möhnle, E. Berrocal, L. Zigan, Droplet thermometry based on an optimized two dye two-color laser-induced fluorescence concept, *Frontiers in Physics* 11 (2023) 1235847.
- [410] H. Ulrich, L. Zigan, Characterization of a Dye Mixture for Two-Color Laser-Induced-Fluorescence Thermometry in Ethanol, Butanol and Water Droplets and Sprays, *Proceedings of the European Combustion Meeting*, Rouen, France (2023).
- [411] J. Palmer, M.A. Reddemann, V. Kirsch, R. Kneer, Temperature measurements of micro-droplets using pulsed 2-color laser-induced fluorescence with MDR-enhanced energy transfer, *Experiments in Fluids* 57 (2016) 177.
- [412] V. Deprédurand, G. Castanet, F. Lemoine, Heat and mass transfer in evaporating droplets in interaction: Influence of the fuel, *International Journal of Heat and Mass Transfer* 53 (2010) 3495-3502.
- [413] F.L. Arbeloa, P.R. Ojeda, I.L. Arbeloa, Fluorescence self-quenching of the molecular forms of Rhodamine B in aqueous and ethanolic solutions, *Journal of Luminescence* 44 (1989) 105-112.

- [414] J.B. Birks, Fluorescence Quantum Yield Measurements, *Journal of Research of the National Bureau of Standards, Section A: Physics and Chemistry* 80A (1976) 389-399.
- [415] G. Chen, M.M. Mazumder, R.K. Chang, J.C. Swindal, W.P. Acker, Laser diagnostics for droplet characterization: application of morphology dependent resonances, *Progress in Energy and Combustion Science* 22 (1996) 163-188.
- [416] J. Schorr, Entwicklung und Anwendung von Fluoreszenztracer-Verfahren für die lasergestützte, abbildende Spraydiagnostik, Dissertation, University of Heidelberg (2003).
- [417] M. Saito, H. Shimatani, H. Naruhashi, Tunable whispering gallery mode emission from a microdroplet in elastomer, *Optics Express* 16 (2008) 11915-11919.
- [418] A. Serpengüzel, S. Küçükşenel, R.K. Chang, Microdroplet identification and size measurement in sprays with lasing images, *Optics Express* 10 (2002) 1118-1132.
- [419] M. Koegl, H. Dai, M.P. Qomi, F. Bauer, B. Eppinger, L. Zigan, Morphology-dependent resonances in laser-induced fluorescence images of micrometric gasoline/ethanol droplets utilizing the dye Nile red, *Applied Optics* 60 (2021) 5000-5011.
- [420] A.S. Kwok, R.K. Chang, Fluorescence seeding of weaker-gain Raman modes in microdroplets: enhancement of stimulated Raman scattering, *Optics Letters* 17 (1992) 1262-1264.
- [421] M. Tanyeri, R. Perron, I.M. Kennedy, Lasing droplets in a microfabricated channel, *Optics Letters* 32 (2007) 2529-2531.
- [422] M. Essien, R.L. Armstrong, J.B. Gillespie, Lasing emission from an evaporating layered microdroplet, *Optics Letters* 18 (1993) 762-764.
- [423] S.-B. Lee, J.-H. Lee, J.-S. Chang, H.-J. Moon, S.W. Kim, K. An, Observation of scarred modes in asymmetrically deformed microcylinder lasers, *Physical Review Letters* 88 (2002) 033903.
- [424] S.-X. Qian, J.B. Snow, H.-M. Tzeng, R.K. Chang, Lasing droplets: highlighting the liquid-air interface by laser emission, *Science* 231 (1986) 486-488.
- [425] H.-M. Tzeng, K.F. Wall, M. Long, R. Chang, Laser emission from individual droplets at wavelengths corresponding to morphology-dependent resonances, *Optics Letters* 9 (1984) 499-501.
- [426] S.K. Tang, R. Derda, Q. Quan, M. Lončar, G.M. Whitesides, Continuously tunable microdroplet-laser in a microfluidic channel, *Optics Express* 19 (2011) 2204-2215.
- [427] A. Rittler, F. Proch, A.M. Kempf, LES of the Sydney piloted spray flame series with the PFGM/ATF approach and different sub-filter models, *Combustion and Flame* 162 (2015) 1575-1598.
- [428] S.-J. Baik, J. Sellmann, A. Kempf, Large eddy simulations of nanoparticle synthesis in spray flames, *International Conference on Liquid Atomization and Spray Systems (ICLASS)* Edinburgh, United Kingdom (2021).
- [429] O. Colin, F. Ducros, D. Veynante, T. Poinsot, A thickened flame model for large eddy simulations of turbulent premixed combustion, *Physics of Fluids* 12 (2000) 1843-1863.
- [430] A. Kempf, S. Wossocki, M. Pettit, An efficient, parallel low-storage implementation of Klein's turbulence generator for LES and DNS, *Computers & Fluids* 60 (2012) 58-60.
- [431] F. Nicoud, H.B. Toda, O. Cabrit, S. Bose, J. Lee, Using singular values to build a subgrid-scale model for large eddy simulations, *Physics of Fluids* 23 (2011) 085106.
- [432] J. Van Oijen, L. De Goey, Modelling of premixed laminar flames using flamelet-generated manifolds, *Combustion Science and Technology* 161 (2000) 113-137.

- [433] C. Olm, T. Varga, É. Valkó, S. Hartl, C. Hasse, T. Turányi, Development of an ethanol combustion mechanism based on a hierarchical optimization approach, *International Journal of Chemical Kinetics* 48 (2016) 423-441.
- [434] M. Chrigui, A.R. Masri, A. Sadiki, J. Janicka, Large Eddy Simulation of a Polydisperse Ethanol Spray Flame, *Flow, Turbulence and Combustion* 90 (2013) 813-832.
- [435] B. Abramzon, W.A. Sirignano, Droplet Vaporization Model for Spray Combustion Calculations, *International Journal of Heat and Mass Transfer* 32 (1989) 1605-1618.
- [436] R.S. Miller, K. Harstad, J. Bellan, Evaluation of equilibrium and non-equilibrium evaporation models for many-droplet gas-liquid flow simulations, *International Journal of Multiphase Flow* 24 (1998) 1025-1055.
- [437] Y.N. Mishra, E. Kristensson, E. Berrocal, Reliable LIF/Mie droplet sizing in sprays using structured laser illumination planar imaging, *Optics Express* 22 (2014) 4480-4492.
- [438] M.A. Shahbaz, S. Jahangir, S.A. Kaiser, Imaging of flame propagation and temperature distribution in an all-metal gasoline engine with endoscopic access via anisole fluorescence, *Experiments in Fluids* 64 (2023) 196.
- [439] C. Gessenhardt, C. Schulz, S. Kaiser, Endoscopic temperature imaging in a four-cylinder IC engine via two-color toluene fluorescence, *Proceedings of the Combustion Institute* 35 (2015) 3697-3705.
- [440] E. Berrocal, E. Kristensson, M. Richter, M. Linne, M. Alden, Application of structured illumination for multiple scattering suppression in planar laser imaging of dense sprays, *Optics Express* 16 (2008) 17870-17881.
- [441] Y.N. Mishra, E. Kristensson, M. Koegl, J. Jönsson, L. Zigan, E. Berrocal, Comparison between two-phase and one-phase SLIPI for instantaneous imaging of transient sprays, *Experiments in Fluids* 58 (2017) 110.
- [442] F. Lemoine, G. Castanet, Temperature and chemical composition of droplets by optical measurement techniques: a state-of-the-art review, *Experiments in Fluids* 54 (2013) 1572.
- [443] J. Palmer, M.A. Reddemann, V. Kirsch, R. Kneer, Applying 2D-2cLIF-EET thermometry for micro-droplet internal temperature imaging, *Experiments in Fluids* 59 (2018) 51.
- [444] M.M. Prenting, M. Shilikhin, T. Dreier, C. Schulz, T. Endres, Characterization of tracers for two-color laser-induced fluorescence thermometry of liquid-phase temperature in ethanol, 2-ethylhexanoic-acid/ethanol mixtures, 1-butanol, and o-xylene, *Applied Optics* 60 (2021) C98-C113.
- [445] A. Davies, *Close-up and macro photography*, CRC Press, 2012.
- [446] E. Berrocal, Multiple scattering of light in optical diagnostics of dense sprays and other complex turbid media, *Doctoral dissertation*, Cranfield University (2006).
- [447] M. Stiti, V. Kornienko, E. Kristensson, G. Castanet, E. Berrocal, Instantaneous thermometry imaging using two-photon laser-induced fluorescence, *Optics Letters* 49 (2024) 2569-2572.
- [448] E. Berrocal, C. Conrad, J. Püls, C.L. Arnold, M. Wensing, M. Linne, M. Miranda, Two-photon fluorescence laser sheet imaging for high contrast visualization of atomizing sprays, *OSA Continuum* 2 (2019) 983-993.
- [449] H. Ulrich, B. Lehnert, D. Guénot, K. Svendsen, O. Lundh, M. Wensing, E. Berrocal, L. Zigan, Effects of liquid properties on atomization and spray characteristics studied by planar two-photon fluorescence, *Physics of Fluids* 34 (2022) 083305.

- [450] J. Coppeta, C. Rogers, Dual emission laser induced fluorescence for direct planar scalar behavior measurements, *Experiments in Fluids* 25 (1998) 1-15.
- [451] NIST Chemistry WebBook, NIST Standard Reference Database Number 69.
- [452] GESTIS – Substance Database – Institut für Arbeitsschutz der Deutschen Gesetzlichen Unfallversicherung (IFA), retrieved from <https://gestis.dguv.de/> – accessed: 2024-01-03.
- [453] M.M. Prenting, M. Shilikhin, T. Dreier, C. Schulz, T. Endres, Supplementary document for Characterization of tracers for two-color laser-induced fluorescence (2cLIF) thermometry of liquid-phase temperature in ethanol, 2-ethylhexanoic-acid/ethanol mixtures, 1-butanol, and oxylene, *Applied Optics* 60 (2021) C98-C113.
- [454] Sigma-Aldrich – Material Safety Data Sheet, “Coumarin 152, CAS-No: 53518-14-2, Product number: 363325”, Version 3.0, Revision Date 08/28/2009, Print Date 03/27/2011.
- [455] P. Dahiya, M. Kumbhakar, T. Mukherjee, H. Pal, Effect of protic solvents on twisted intramolecular charge transfer state formation in coumarin-152 and coumarin-481 dyes, *Chemical Physics Letters* 414 (2005) 148-154.
- [456] S. Nad, M. Kumbhakar, H. Pal, Photophysical Properties of Coumarin-152 and Coumarin-481 Dyes: Unusual Behavior in Nonpolar and in Higher Polarity Solvents, *The Journal of Physical Chemistry A* 107 (2003) 4808-4816.
- [457] A.N. Fletcher, D.E. Bliss, Laser dye stability. Part 5, *Applied Physics* 16 (1978) 289-295.
- [458] Sigma-Aldrich – Material Safety Data Sheet, “Coumarin 153, CAS-No: 53518-18-6, Product number: 546186,” Version 6.1, Revision Date 01/15/2020, Print Date 11/20/2020.
- [459] C. Würth, M. Grabolle, J. Pauli, M. Spieles, U. Resch-Genger, Relative and absolute determination of fluorescence quantum yields of transparent samples, *Nature Protocols* 8 (2013) 1535-1550.
- [460] K. Rurack, M. Spieles, Fluorescence quantum yields of a series of red and near-infrared dyes emitting at 600–1000 nm, *Analytical Chemistry* 83 (2011) 1232-1242.
- [461] Sigma-Aldrich – Material Safety Data Sheet, “DCM, CAS-No: 51325-91-8, Product number: 410497,” Version 6.3, Revision Date 01/14/2020, Print Date 11/20/2020.
- [462] Sigma-Aldrich – Material Safety Data Sheet, “Pyrromethene 597, CAS-No: 137829-79-9, Product number: 746169,” Version 6.2, Revision Date 06/16/2019, Print Date 03/26/2021.
- [463] J. Bañuelos Prieto, F. López Arbeloa, V. Martínez Martínez, T. Arbeloa López, I. López Arbeloa, Photophysical Properties of the Pyrromethene 597 Dye: Solvent Effect, *The Journal of Physical Chemistry A* 108 (2004) 5503-5508.
- [464] Sigma-Aldrich – Material Safety Data Sheet, “Rhodamine B, CAS-No: 81-88-9, Product Number: R6626,” Version 6.2, Revision Date 01/15/2020, Print Date 11/20/2020.
- [465] R.F. Kubin, A.N. Fletcher, Fluorescence quantum yields of some rhodamine dyes, *Journal of Luminescence* 27 (1982) 455-462.
- [466] M. Galanin, A. Kutyonkov, V. Smorchkov, Y.P. Timofeev, Z. Chizhikova, Measurement of photoluminescence quantum yield of dye solutions by the Vavilov and integrating-sphere methods, *Optics and Spectroscopy* 53 (1982) 405-409.
- [467] Sigma-Aldrich – Material Safety Data Sheet, “Coumarin 47, CAS-No: 91-44-1, Product number: D87759”, Version 6.3, Revision Date 25/03/2022, Print Date 24/10/2022.
- [468] Sigma-Aldrich – Material Safety Data Sheet, “Coumarin 102, CAS-No: 41267-76-9, Product number: 546151”, Version 6.3, Revision Date 21/03/2022, Print Date 24/10/2022.

- [469] Sigma-Aldrich – Material Safety Data Sheet, “Coumarin 120, CAS-No: 26093-31-2, Product number: 257370”, Version 7.5, Revision Date 26/04/2022, Print Date 24/10/2022.
- [470] Sigma-Aldrich – Material Safety Data Sheet, “p-Terphenyl, CAS-No: 92-94-4, Product number: 257389”, Version 6.5, Revision Date 19/02/2021, Print Date 24/10/2022.
- [471] Luxottica Exciton – Material Data Sheet, “Pyridine 1, CAS-No: 87004-02-2, Catalog number: 06980,” Retrieved from <https://www.sirah.com/accessories/dyes/dye-pyridine-1/> – accessed: 2022-10-24.
- [472] M. Shah, K. Thangaraj, M.L. Soong, L.T. Wolford, J.H. Boyer, I.R. Politzer, T.G. Pavlopoulos, Pyrromethene–BF₂ complexes as laser dyes:1., *Heteroatom Chemistry* 1 (1990) 389-399.
- [473] Luxottica Exciton – Material Data Sheet, “Rhodamine 101, CAS-No: 72102-91-1, Catalog number: 06400,” Retrieved from <https://www.sirah.com/accessories/dyes/dye-rhodamine-101/> – accessed: 2022-10-24.
- [474] BLDpharm – Safety Data Sheet, “Stilbene 3, CAS-No: 27344-41-8, Catalog number: BD92014”, Version 6.2, Revision Date 11/01/2019, Print Date 08/02/2022.
- [475] M. Rinke, H. Güsten, Optische Auffheller als Laserfarbstoffe, *Berichte der Bunsengesellschaft für physikalische Chemie* 90 (1986) 439-444.
- [476] M.M. Prenting, M. Shilikhin, T. Dreier, C. Schulz, and T. Endres, Characterization of tracers for two-color laser-induced fluorescence thermometry of liquid-phase temperature in ethanol, 2-ethylhexanoic-acid/ethanol mixtures, 1-butanol, and o-xylene, Zenodo, data set, 5 May 2021, available at <<https://doi.org/10.5281/zenodo.4613143>>.

12 Appendix

12.1 Substances used in this work

Table A1: Chemical and physical properties of the substances used in this work [37, 451-453].

Substance	Formula	CAS number	Molar mass / g/mol	Density / g/cm ³ (20 °C)	Boiling point / °C	Enthalpy of combustion MJ/l	Vapor pressure / hPa (20 °C)	Refractive index
Ethanol	C ₂ H ₆ O	64-17-5	46.07	0.789	78.3	23.4	59	1.36
2-Ethylhexanoic acid	C ₈ H ₁₆ O ₂	149-57-5	144.21	0.903	228	30.6	< 0.01	1.43
1-Butanol	C ₄ H ₁₀ O	71-36-3	74.12	0.81	117.7	29.2	6.7	1.41
o-Xylene	C ₈ H ₁₀	95-47-6	106.17	0.876	143	37.5	7	1.51
iso Propanol	C ₃ H ₈ O	67-63-0	60.1	0.785	82.5	26.2	42.6	1.38
Acetone	C ₃ H ₆ O	67-64-1	58.08	0.785	56.1	24.2	306	1.36
HMDSO	C ₆ H ₁₈ OSi ₂	107-46-0	162.38	0.764	101		44	1.38
Iron nitrate nonahydrate	Fe(NO ₃) ₃ ·(H ₂ O) ₉	7782-61-8	404	1.64	125			
Ammonium nitrate	NH ₄ NO ₃	6484-52-2	80.04	1.73	210			
Oxygen	O ₂	7782-44-7	32	0.00143	-183			1
Methane	CH ₄	74-82-8	16.04	0.00072	-161.5	0.04		1
Nitric oxide	NO	10102-43-9	30.01	0.00125	-152	0.0038		1
Hydrogen	H ₂	1333-74-0	2.02	0.00009	-253	0.013		1
Argon	Ar	7440-37-1	39.95	0.00178	-186			1

12.2 HSW burner

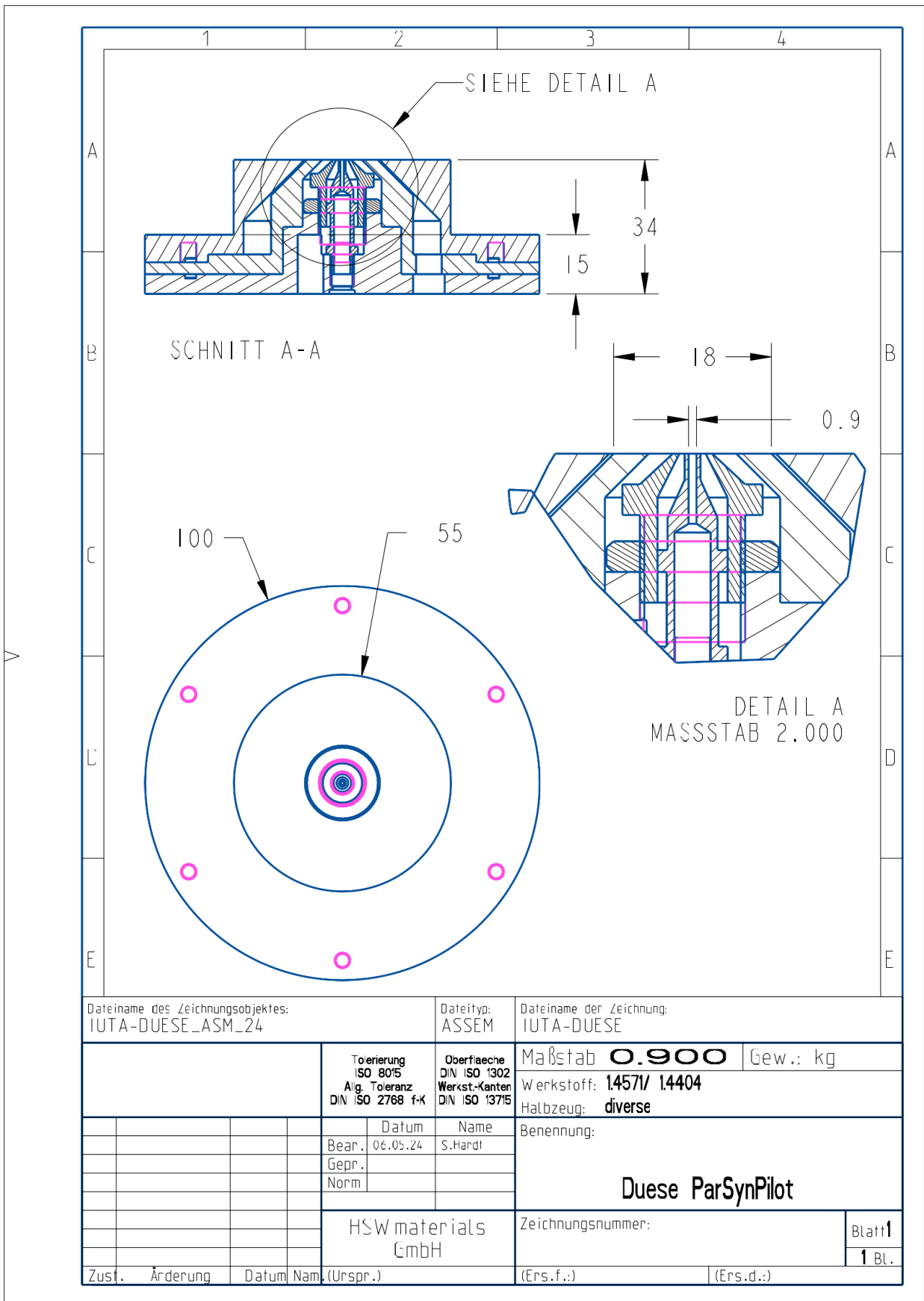


Figure A1: Detailed technical drawings of the HSW burner. Printed with permission of HSWmaterials GmbH (Kamp-Lintfort) [215].

12.3 Spectrally resolved chemiluminescence in the SpraySyn flame

The data presented in this section are chemiluminescence spectra complementing the results discussed in chapter 4. Details regarding the experimental setup can be found in section 4.2.

12.3.1 Liquid fuel: Ethanol

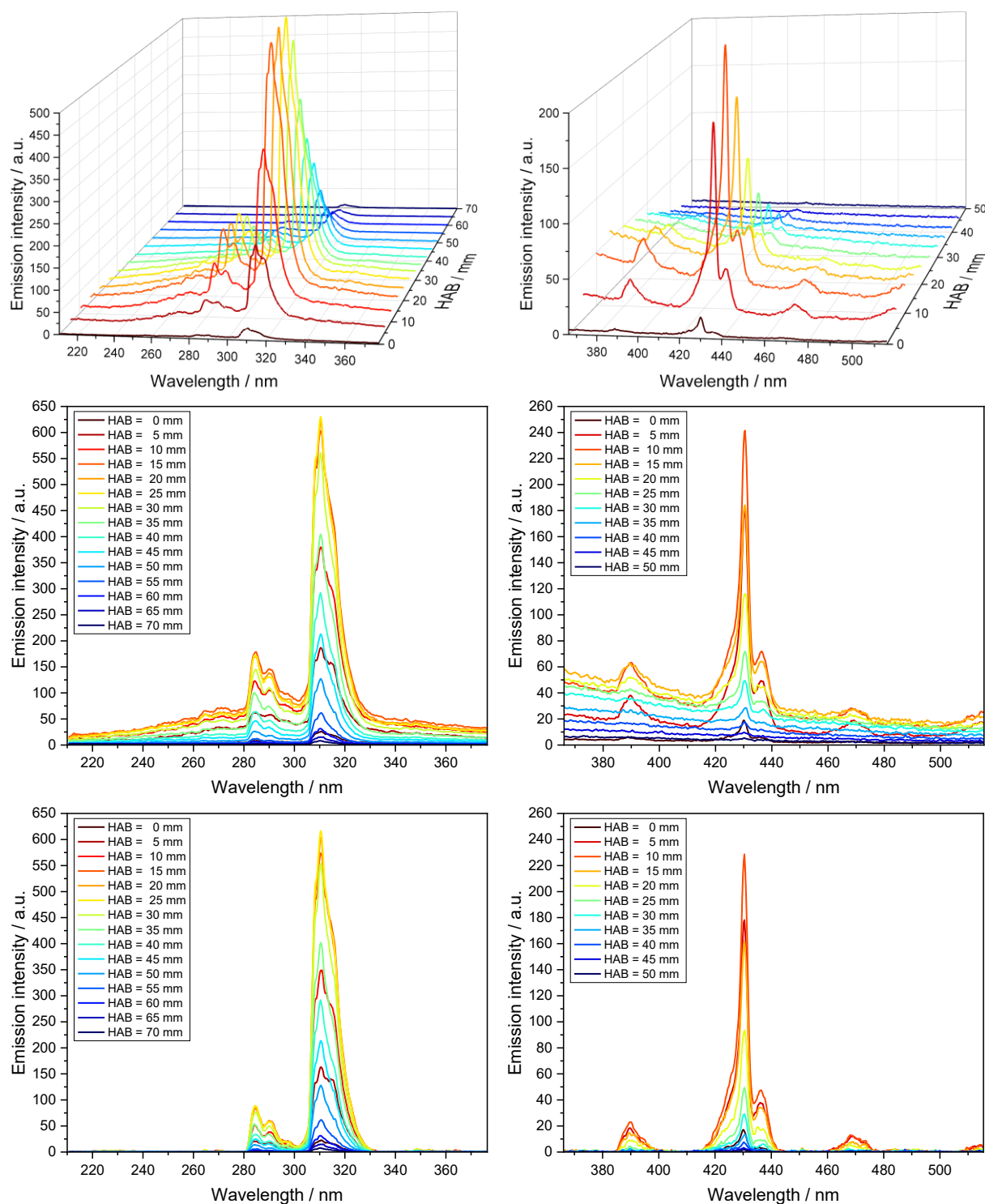


Figure A2: Emission spectra recorded in the SpraySyn flame at the standard operating condition, 2 ml/min ethanol at various HAB, detection-sensitivity corrected, 600 grooves/mm grating, top: Three-dimensional illustration, middle: Uncorrected spectra, bottom: Background corrected.

12.3.2 Liquid fuel: 65EHA35EtOH

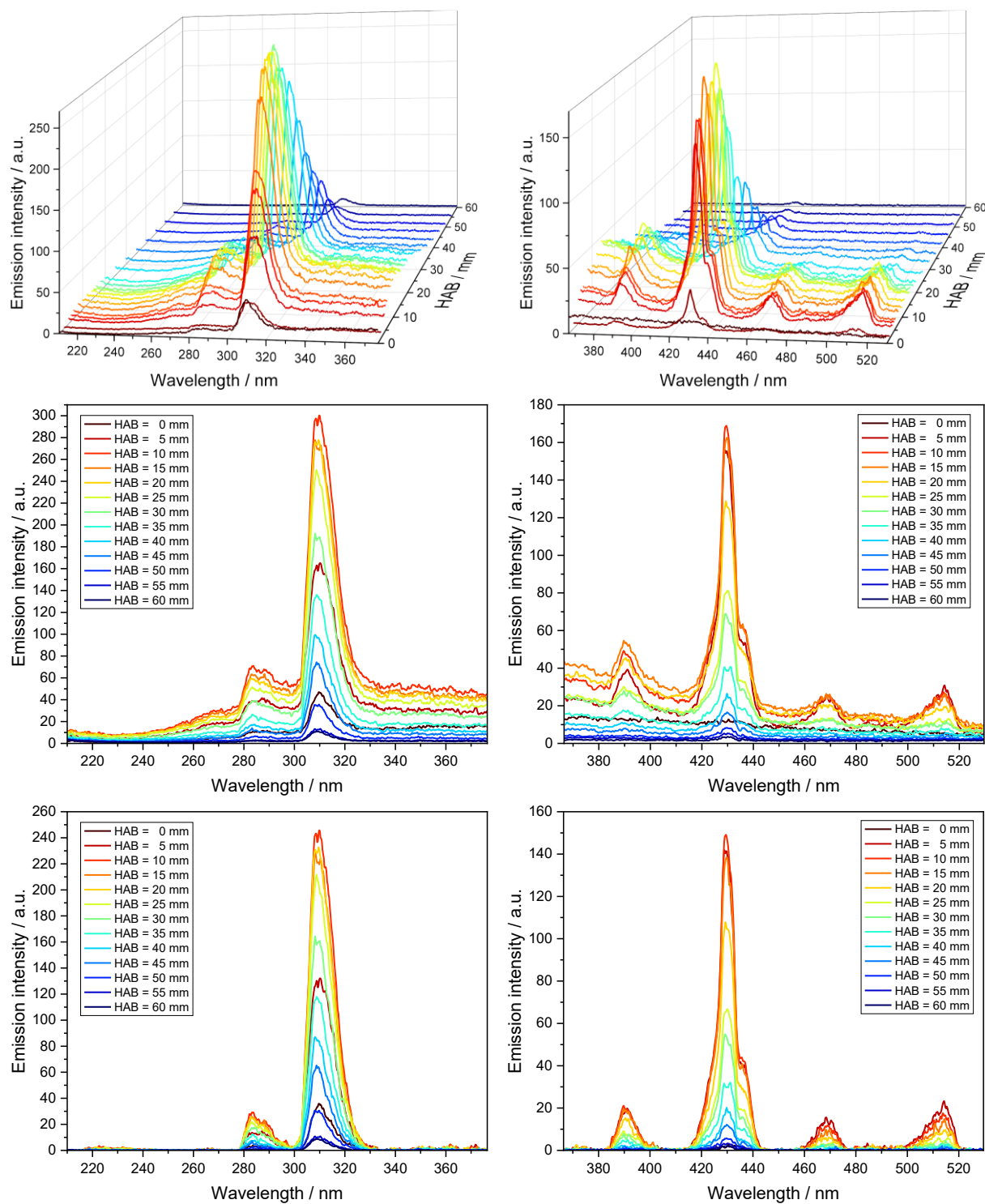


Figure A3: Emission spectra recorded in the SpraySyn flame at the standard operating condition, 2 ml/min 65EHA35EtOH at various HAB, detection-sensitivity corrected, 600 grooves/mm grating, top: Three-dimensional illustration, middle: Uncorrected spectra, bottom: Background corrected.

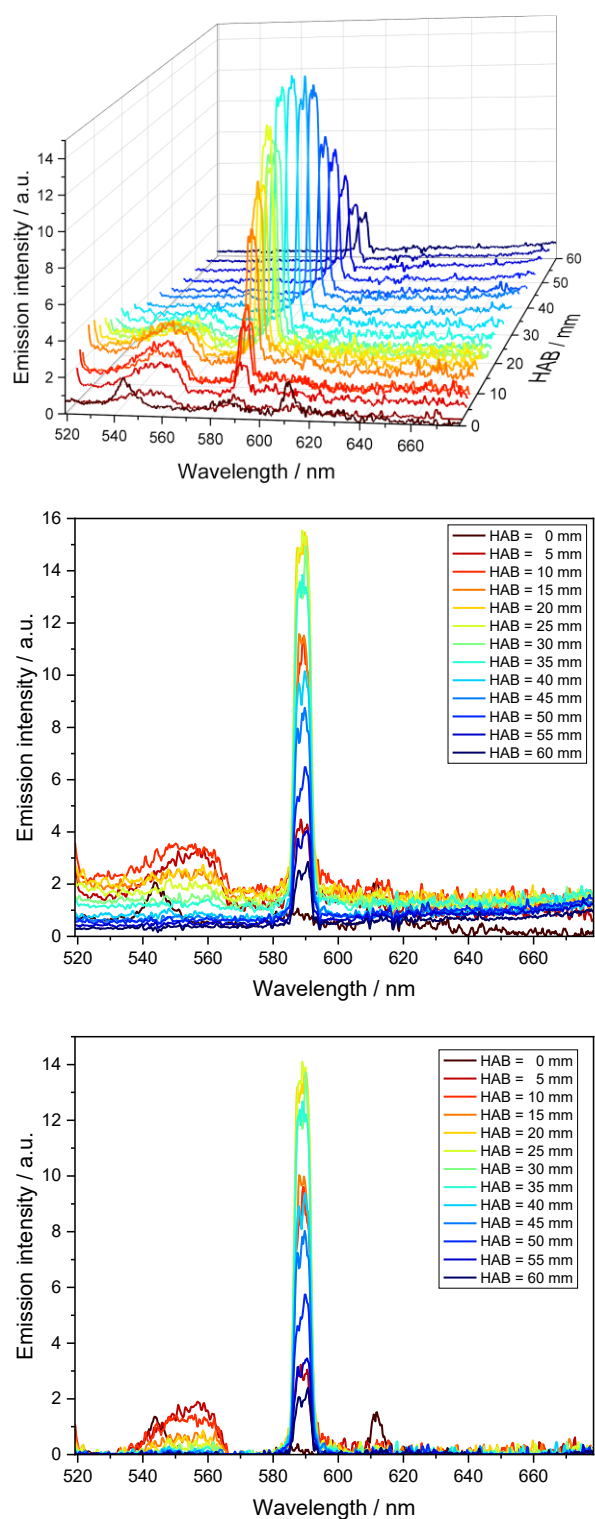


Figure A4: Emission spectra recorded in the SpraySyn flame at the standard operating condition, 2 ml/min 65EHA35EtOH at various HAB, detection-sensitivity corrected, 600 grooves/mm grating, top: Three-dimensional illustration, middle: Uncorrected spectra, bottom: Background corrected.

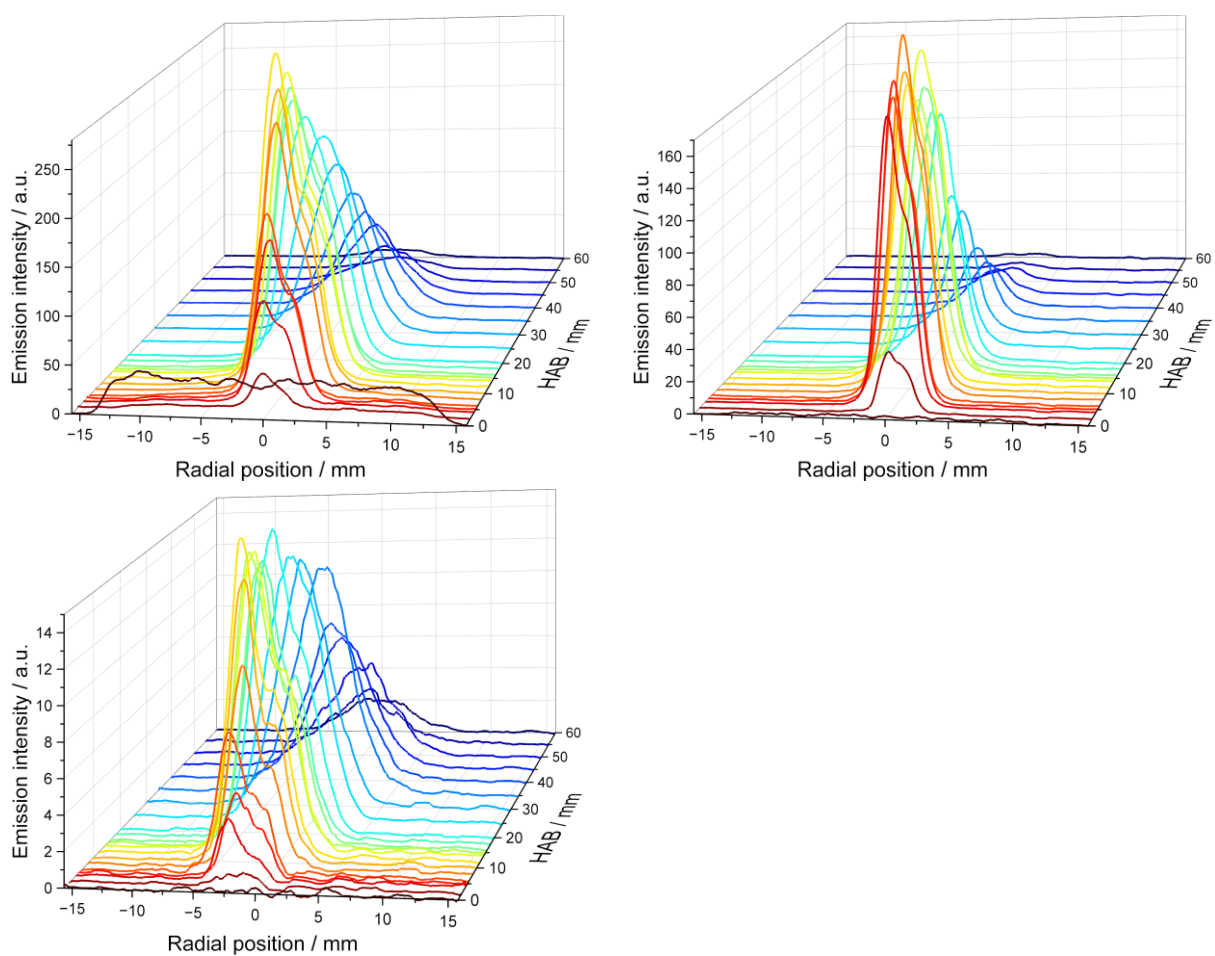


Figure A5: Emission spectra recorded in the SpraySyn flame at the standard operating condition, 2 ml/min 65EHA35EtOH: Smoothed radial emission spectra at chosen peak positions over HAB, top left: OH* emission intensity at 310 nm, top right: CH* emission intensity at 430 nm, bottom: Na* emission intensity at 589 nm.

12.3.3 Liquid fuel: 1-Butanol

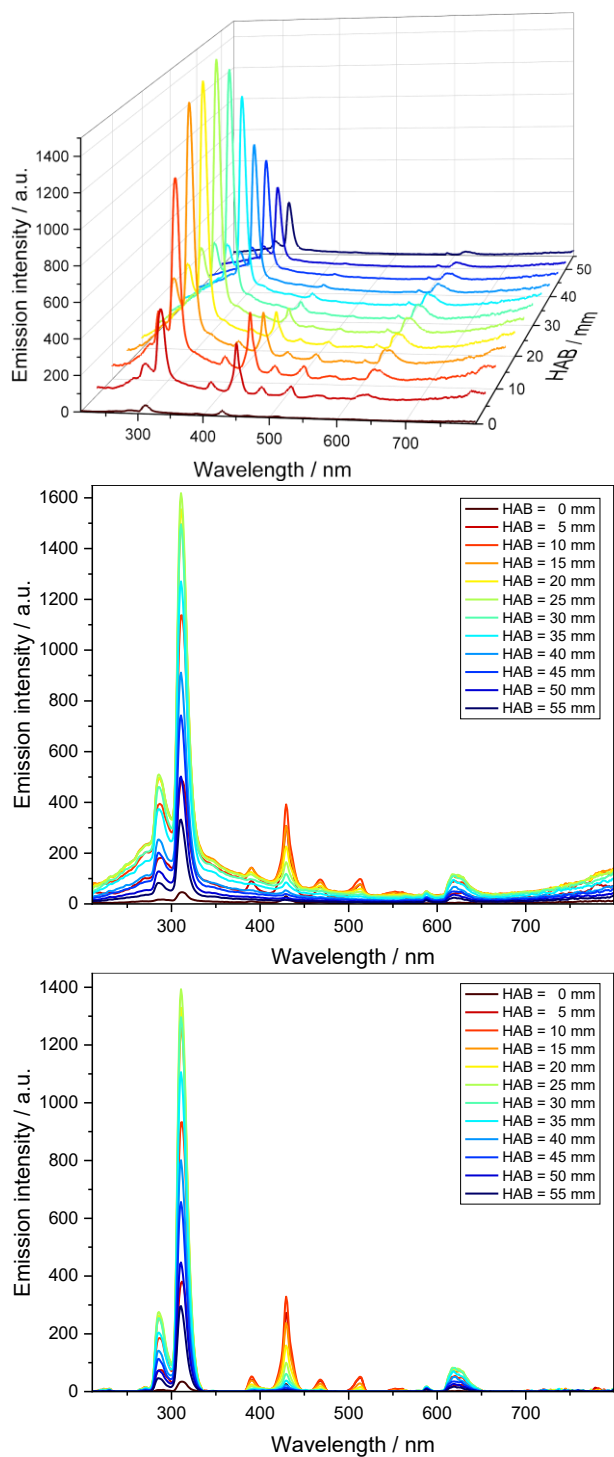


Figure A6: Emission spectra recorded in the SpraySyn flame at the standard operating condition, 2 ml/min 1-butanol at various HAB, detection-sensitivity corrected, 150 grooves/mm grating, top: Three-dimensional illustration, middle: Uncorrected spectra, bottom: Background corrected.

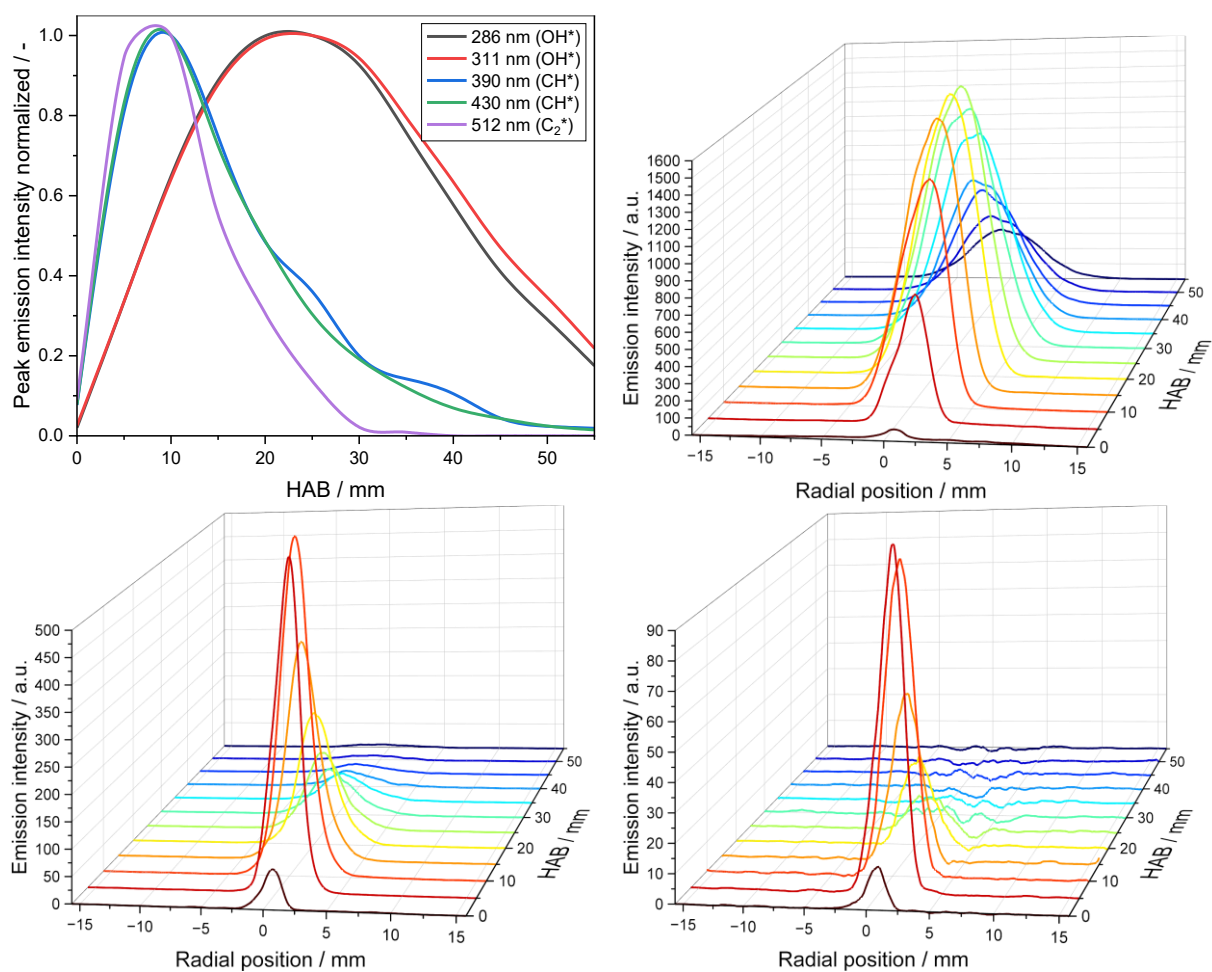
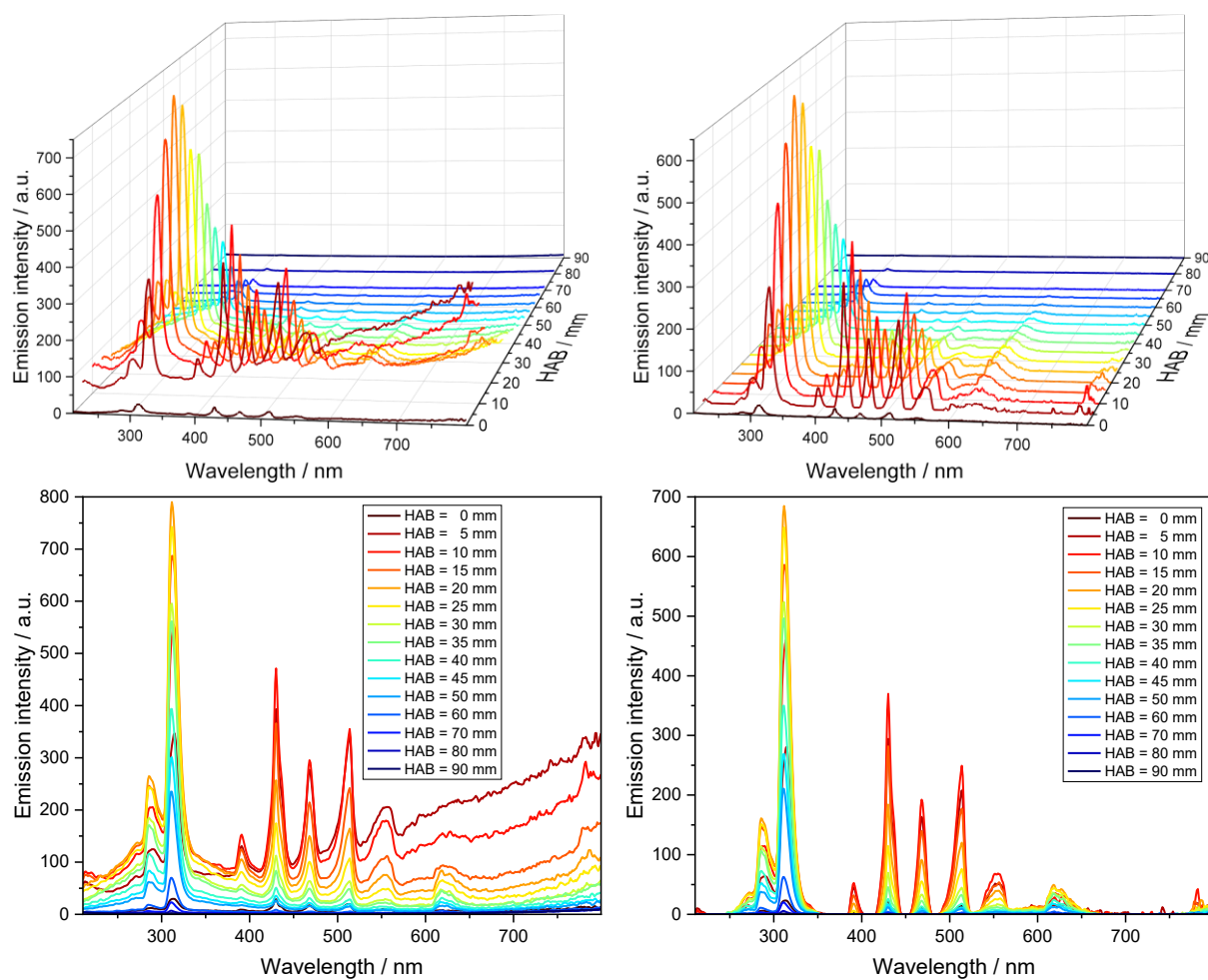


Figure A7: Emission spectra recorded in the SpraySyn flame at the standard operating condition, 2 ml/min 1-butanol, top left: Normalized emission intensity of chosen peaks over HAB extracted from background-corrected spectra (cf. Figure A6), others: Smoothed radial emission spectra at chosen peak positions over HAB, top right: OH* emission intensity at 311 nm, lower left: CH* emission intensity at 430 nm, lower right: C₂* emission intensity at 512 nm.

12.3.4 Liquid fuel: o-Xylene



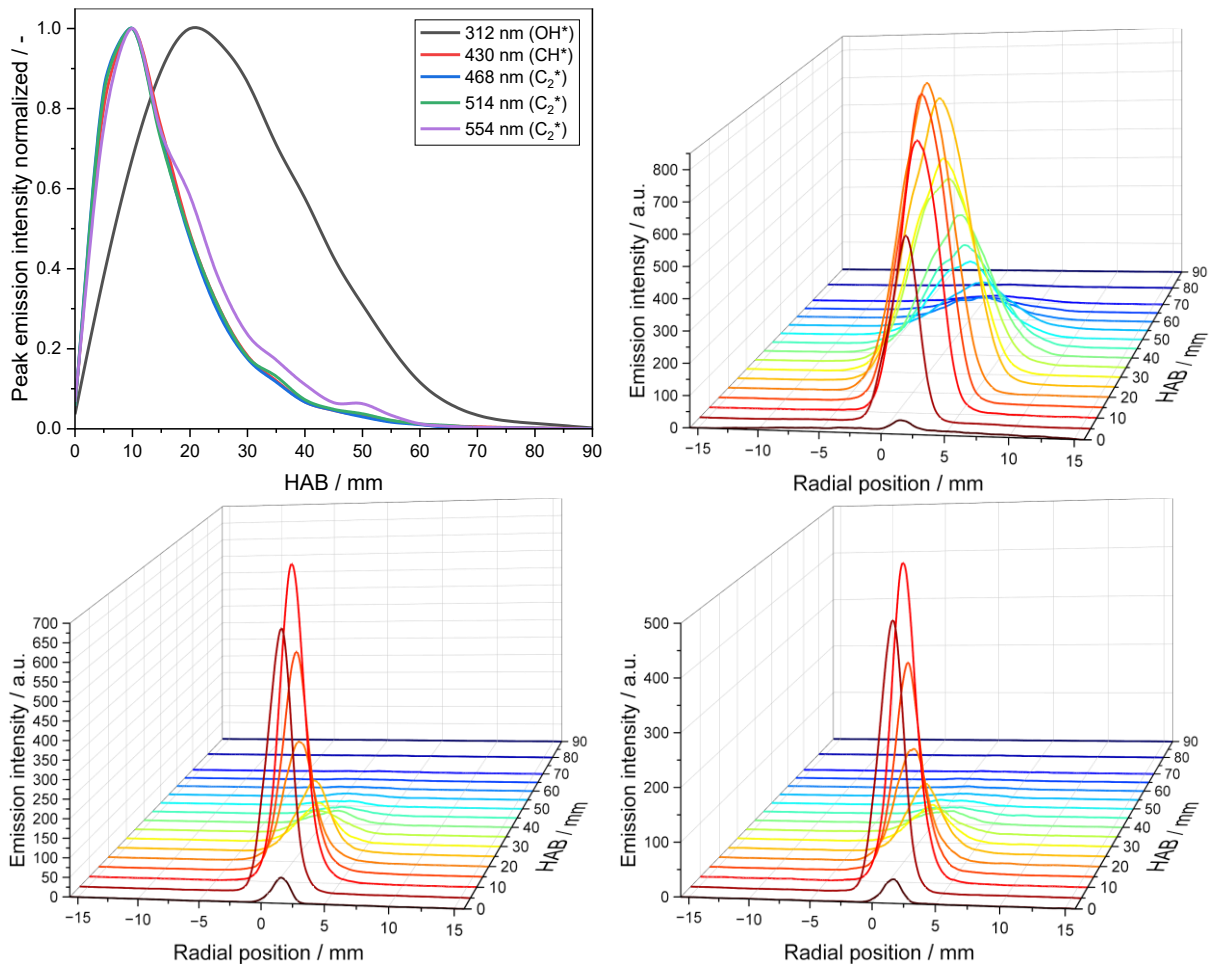


Figure A9: Emission spectra recorded in the SpraySyn flame at the standard operating condition, 2 ml/min *o*-xylene, top left: Normalized emission intensity of chosen peaks over HAB extracted from background-corrected spectra (cf. Figure A8), others: Smoothed radial emission spectra at chosen peak positions over HAB, top right: OH* emission intensity at 312 nm, lower left: CH* emission intensity at 430 nm, lower right: C₂* emission intensity at 514 nm.

12.3.5 Liquid fuel: Iron nitrate nonahydrate in ethanol

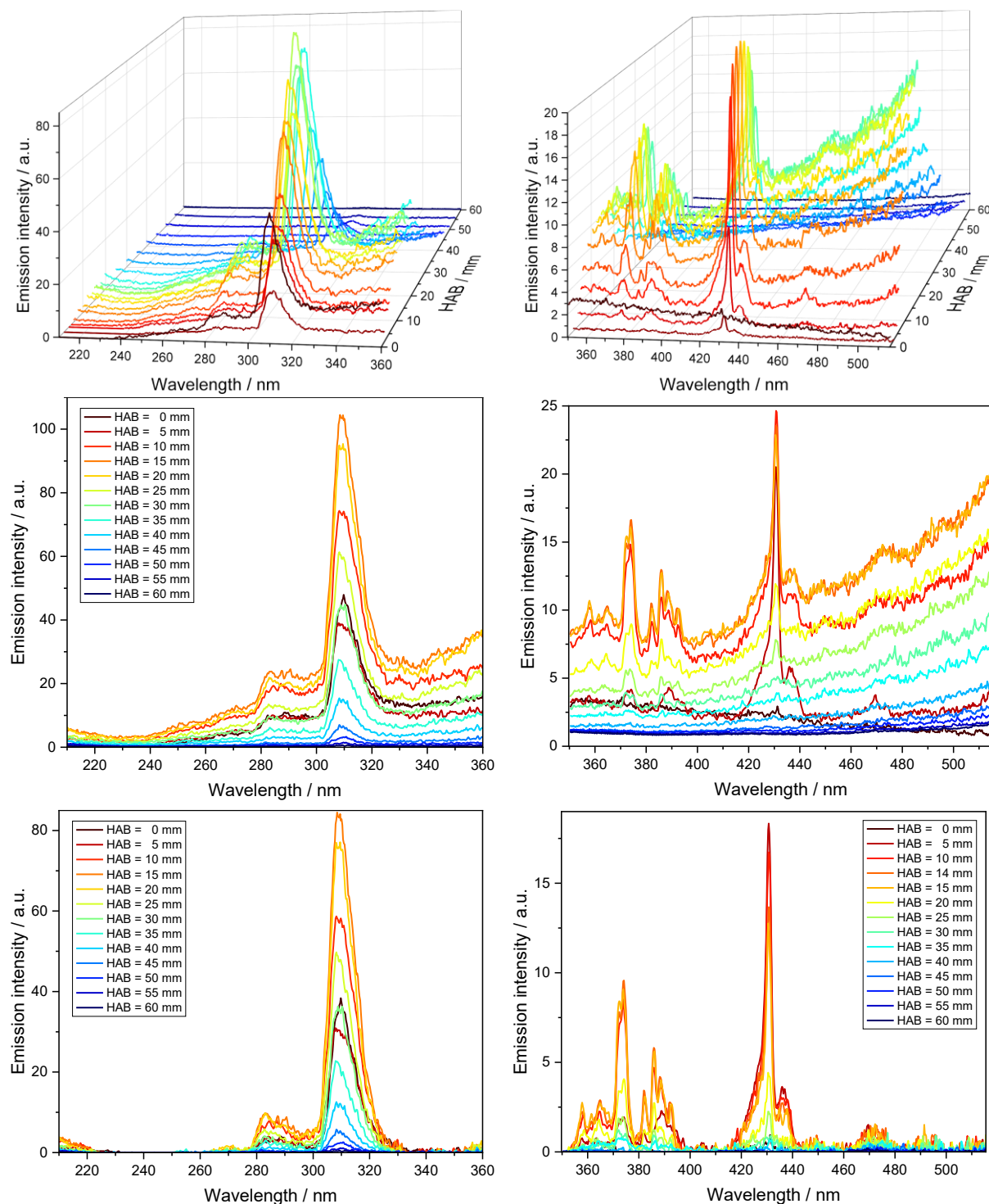


Figure A10: Emission spectra recorded in the SpraySyn flame at the standard operating condition, 2 ml/min iron nitrate nonahydrate (0.05 mol/l) in ethanol at various HAB, detection-sensitivity corrected, 600 grooves/mm grating, spectral region of 210 to 516 nm, top: Three-dimensional illustration, middle: Uncorrected spectra, bottom: Background corrected.

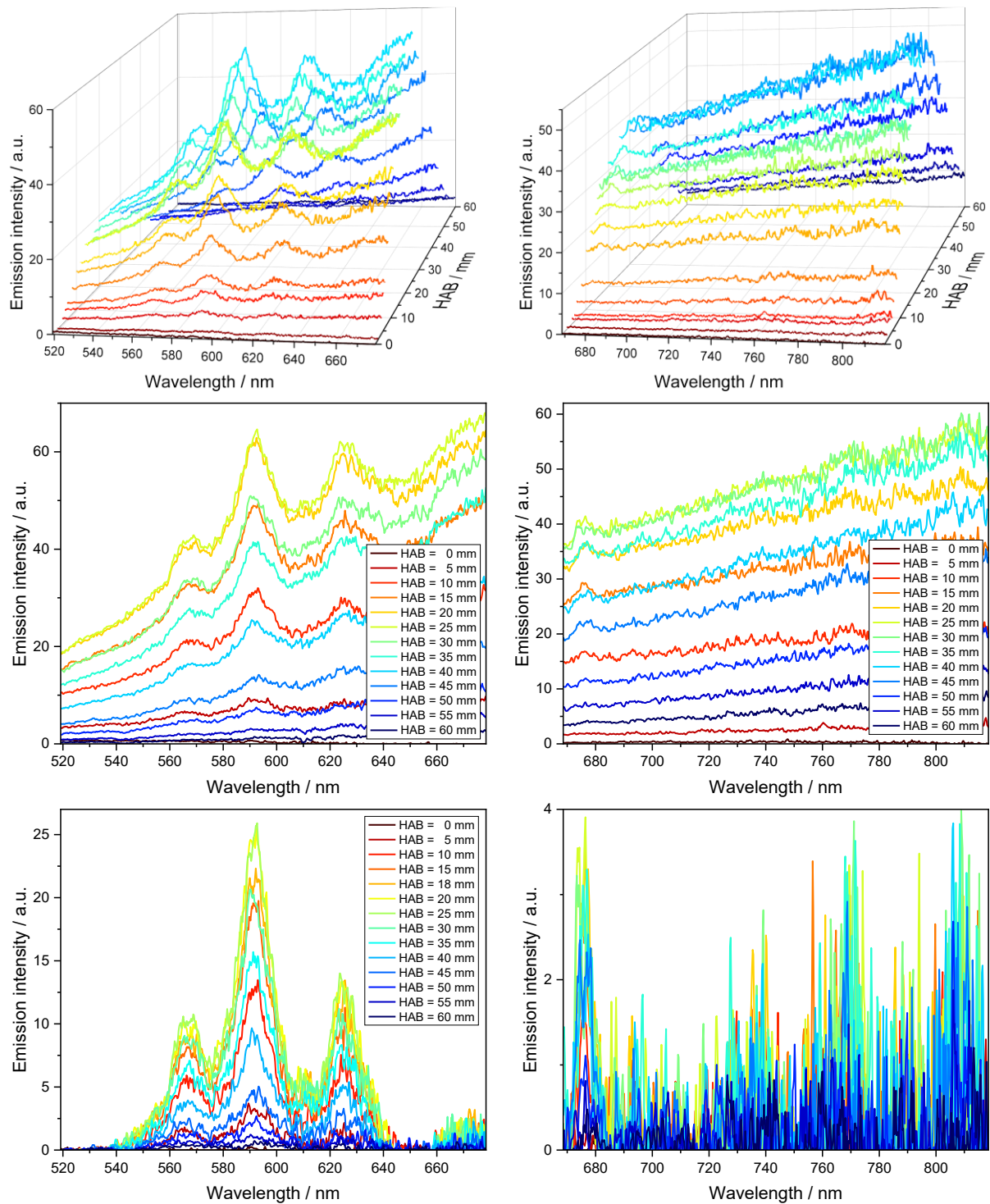


Figure A11: Emission spectra recorded in the SpraySyn flame at the standard operating condition, 2 ml/min iron nitrate nonahydrate (0.05 mol/l) in ethanol at various HAB, detection-sensitivity corrected, 600 grooves/mm grating, spectral region of 519 to 819 nm, top: Three-dimensional illustration, middle: Uncorrected spectra, bottom: Background corrected.

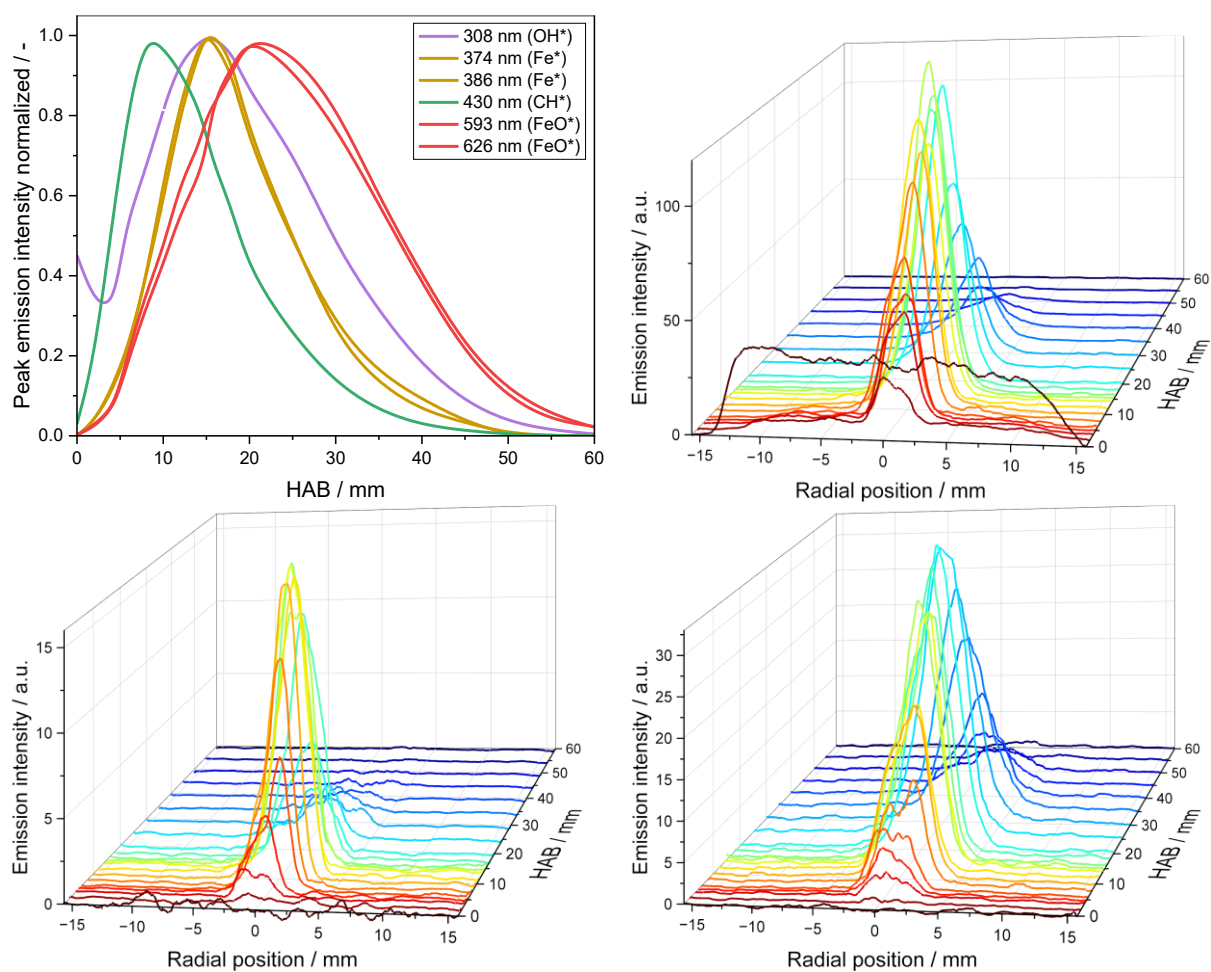


Figure A12: Emission spectra recorded in the SpraySyn flame at the standard operating condition, 2 ml/min iron nitrate nonahydrate (0.05 mol/l) in ethanol, top left: Normalized emission intensity of chosen peaks over HAB extracted from background-corrected spectra (cf. Figure A10 and Figure A11), others: Smoothed radial emission spectra at chosen peak positions over HAB, top right: OH* emission intensity at 308 nm, lower left: Fe* emission intensity at 374 nm, lower right: FeO* emission intensity at 593 nm.

12.4 Droplet velocity and size distributions (PDA)

The data presented in this section are droplet velocity and size distributions complementing the results discussed in chapter 5. Details regarding the experimental setup can be found in section 5.2.

12.4.1 Ethanol

12.4.1.1 Cold spray

Dispersion gas flow rate: 4 slm

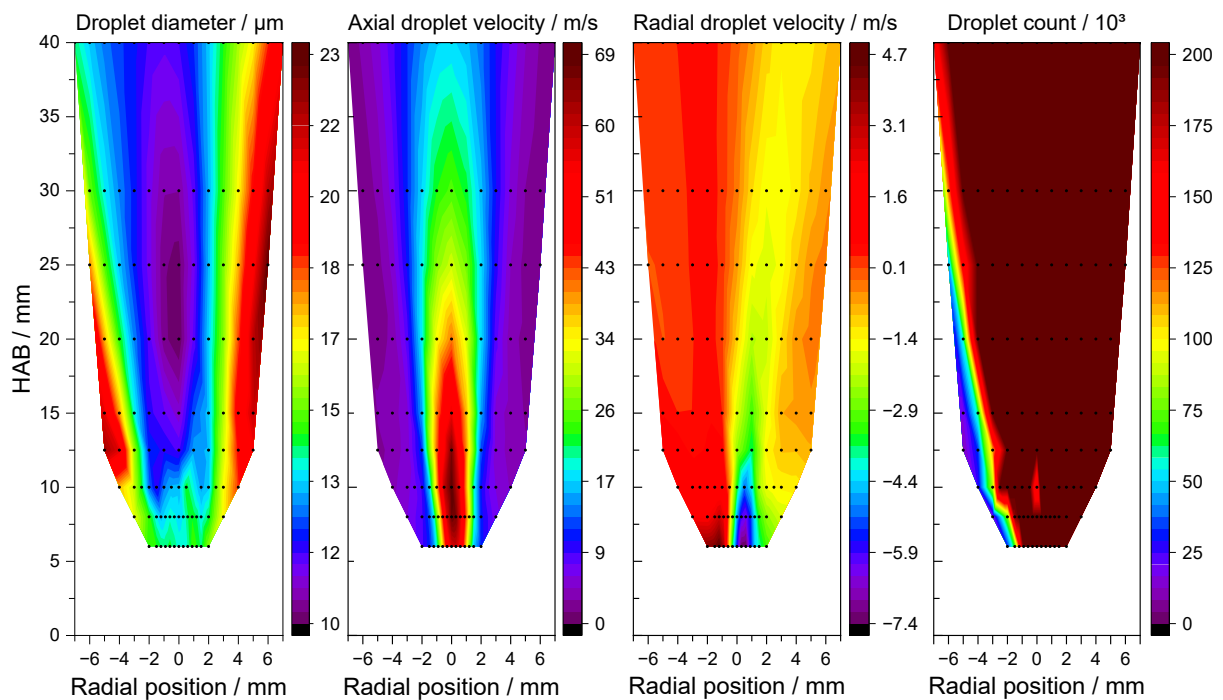


Figure A13: PDA results for the SpraySyn2 cold spray at the standard operating condition, 2 ml/min ethanol, 4 slm dispersion gas flow, vertical cross-sections of (from left to right): Mean droplet diameter, mean axial droplet velocity, mean radial droplet velocity, droplet counts.

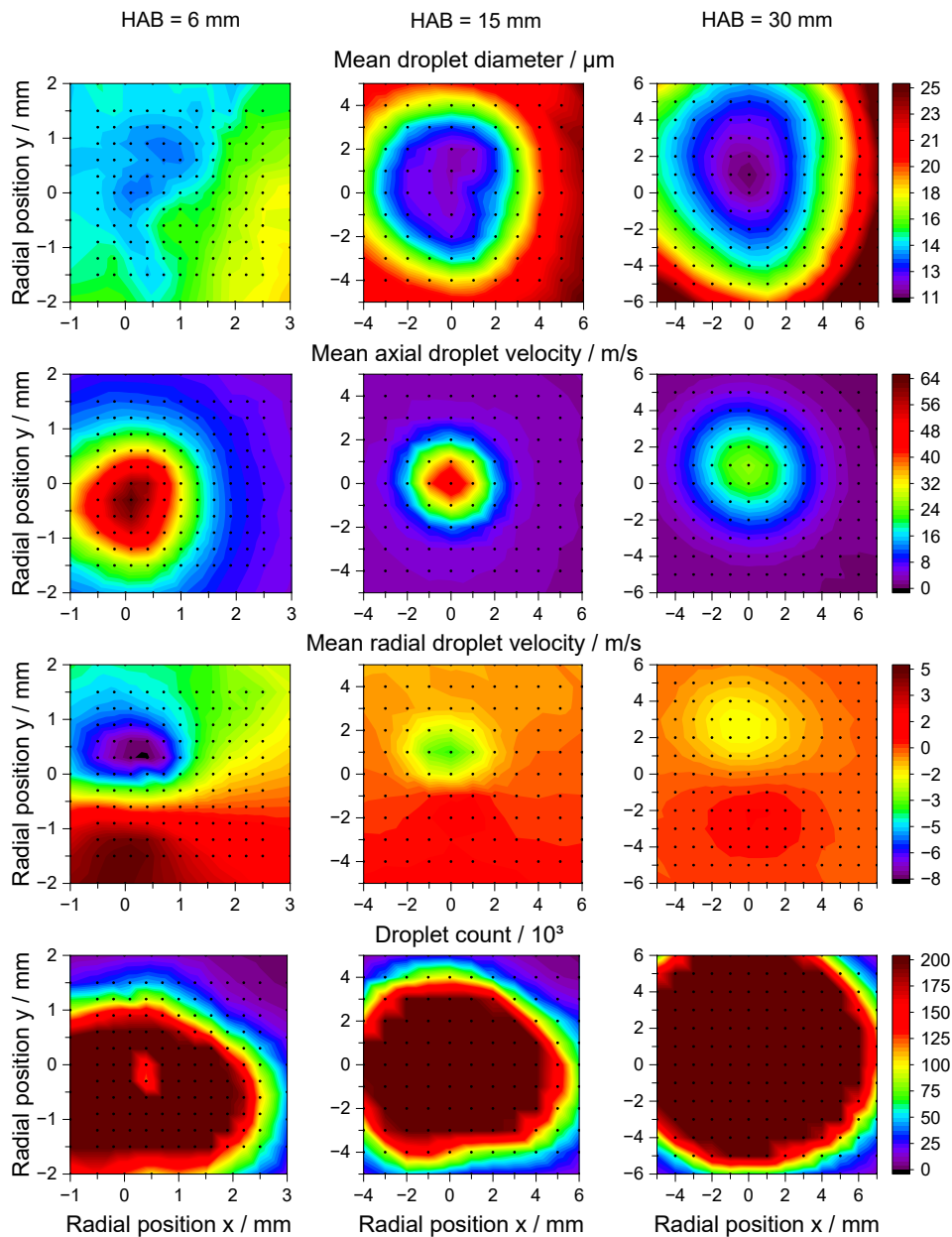


Figure A14: PDA results for the SpraySyn2 cold spray at the standard operating condition, 2 ml/min ethanol, 4 slm dispersion gas flow, horizontal cross-sections of (from top to bottom): Mean droplet diameter, mean axial droplet velocity, mean radial droplet velocity, droplet counts. The HAB from left to right is: 6, 15, and 30 mm. Note the differently scaled spatial axes within each row and the shift of the zero-point by 1 mm relative to the center of the x axis.

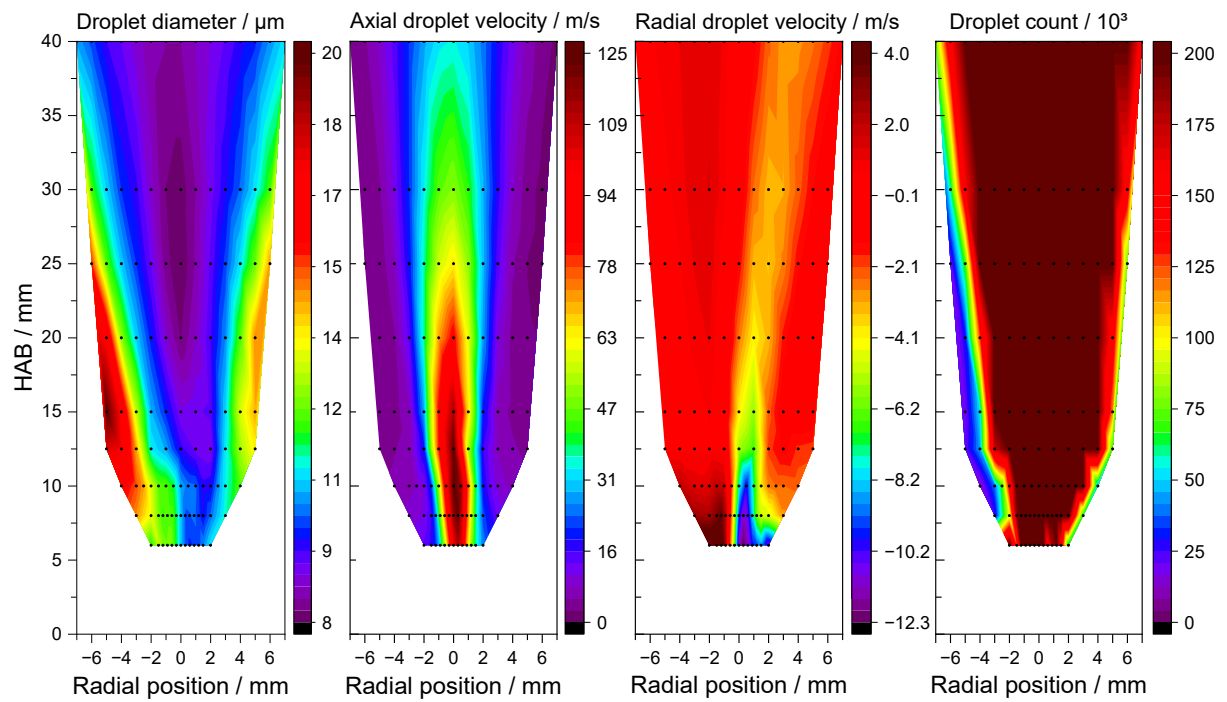
Dispersion gas flow rate: 8 slm

Figure A15: PDA results for the SpraySyn2 cold spray at the standard operating condition, 2 ml/min ethanol, 8 slm dispersion gas flow, vertical cross-sections of (from left to right): Mean droplet diameter, mean axial droplet velocity, mean radial droplet velocity, droplet counts.

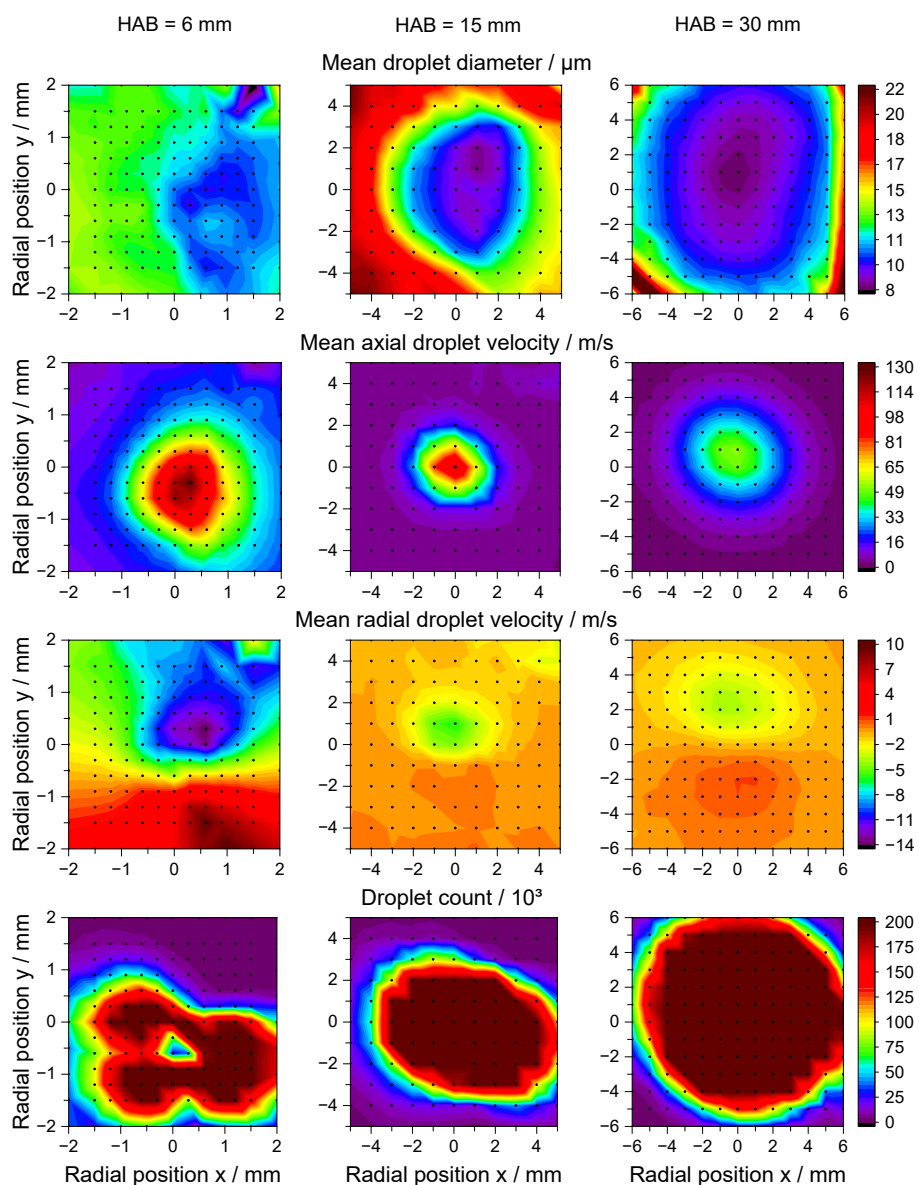


Figure A16: PDA results for the SpraySyn2 cold spray at the standard operating condition, 2 ml/min ethanol, 8 slm dispersion gas flow, horizontal cross-sections of (from top to bottom): Mean droplet diameter, mean axial droplet velocity, mean radial droplet velocity, droplet counts. The HAB from left to right is: 6, 15, and 30 mm. Note the differently scaled spatial axes within each row.

12.4.1.2 Flame

Dispersion gas flow: 4 slm

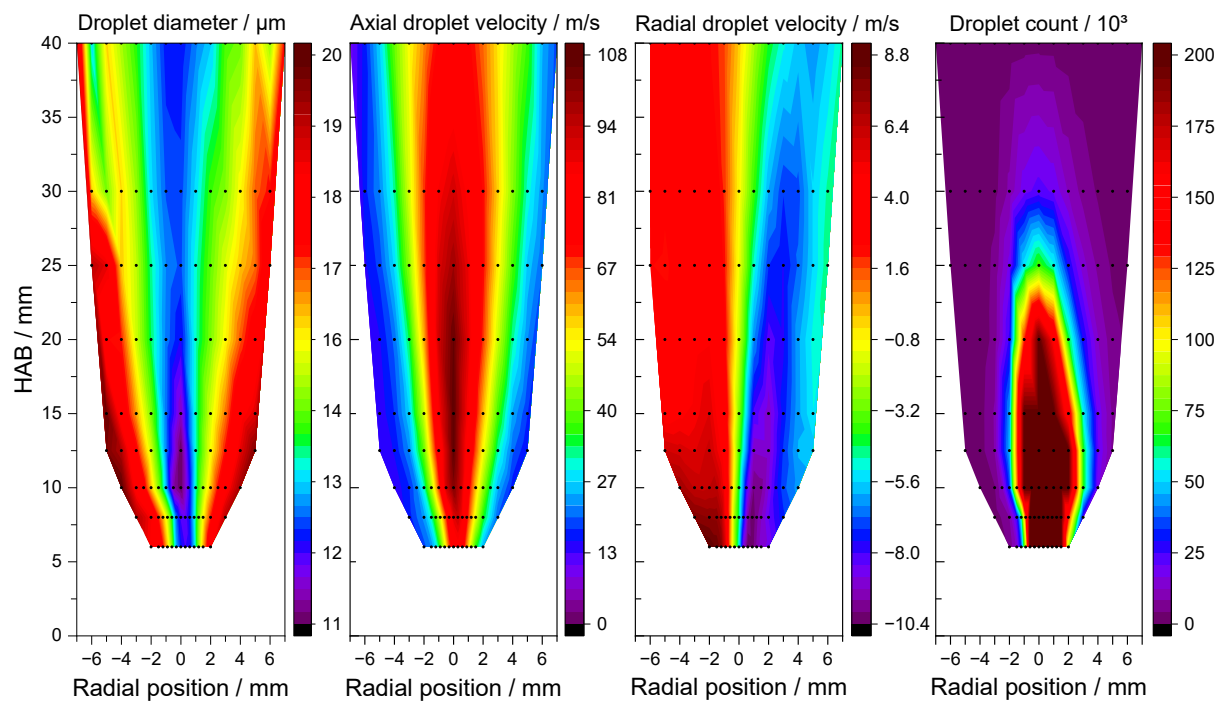


Figure A17: PDA results for the SpraySyn2 flame at the standard operating condition, 2 ml/min ethanol, 4 slm dispersion gas flow, vertical cross-sections of (from left to right): Mean droplet diameter, mean axial droplet velocity, mean radial droplet velocity, droplet counts.

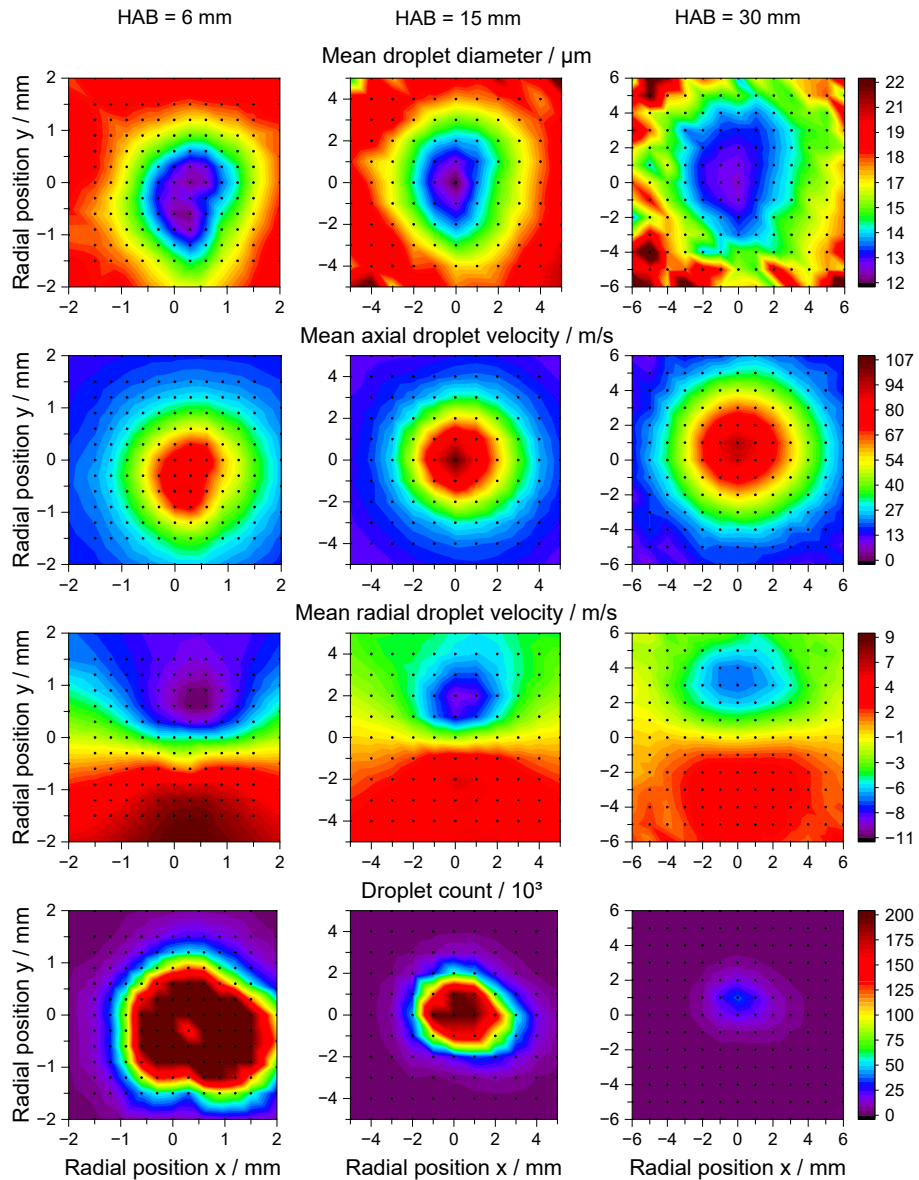


Figure A18: PDA results for the SpraySyn2 flame at the standard operating condition, 2 ml/min ethanol, 4 slm dispersion gas flow, horizontal cross-sections of (from top to bottom): Mean droplet diameter, mean axial droplet velocity, mean radial droplet velocity, droplet counts. The HAB from left to right is: 6, 15, and 30 mm. Note the differently scaled spatial axes within each row.

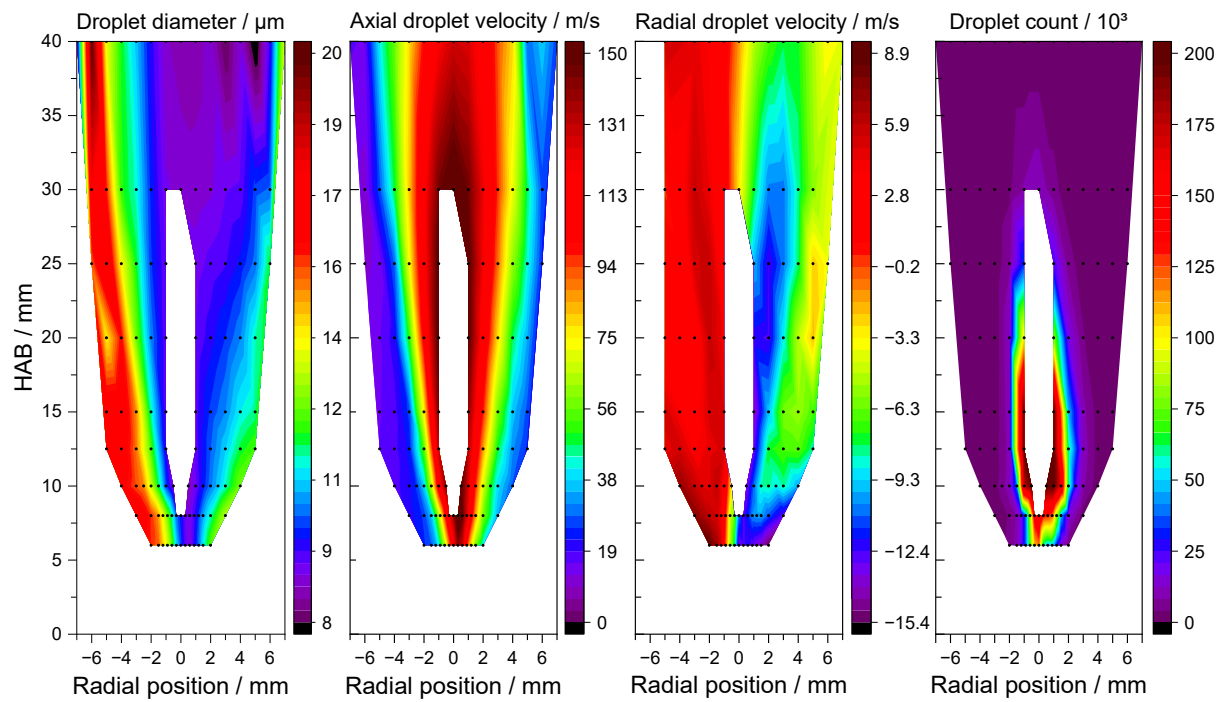
Dispersion gas flow: 8 slm

Figure A19: PDA results for the SpraySyn2 flame at the standard operating condition, 2 ml/min ethanol, 8 slm dispersion gas flow, vertical cross-sections of (from left to right): Mean droplet diameter, mean axial droplet velocity, mean radial droplet velocity, droplet counts.

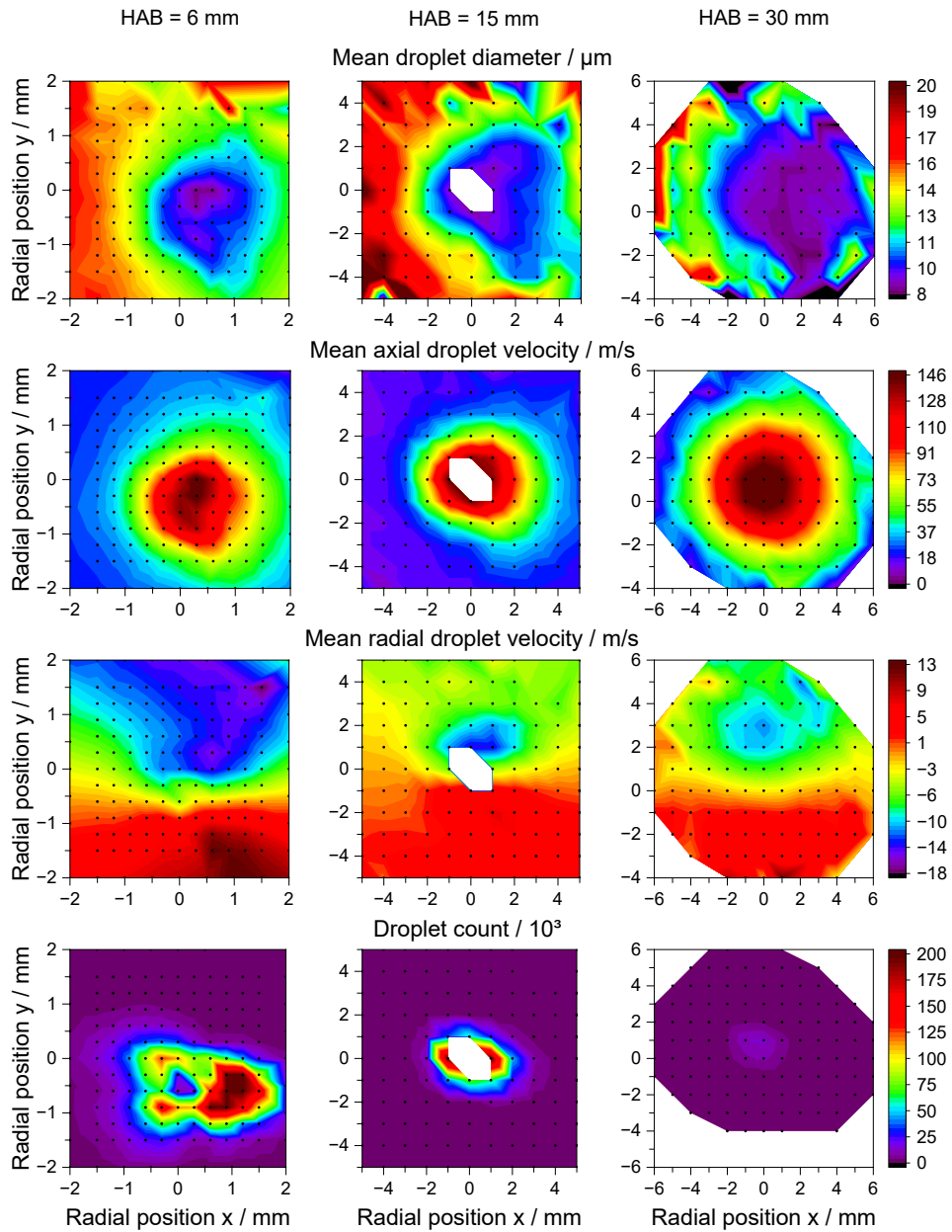


Figure A20: PDA results for the SpraySyn2 flame at the standard operating condition, 2 ml/min ethanol, 8 slm dispersion gas flow, horizontal cross-sections of (from top to bottom): Mean droplet diameter, mean axial droplet velocity, mean radial droplet velocity, droplet counts. The HAB from left to right is: 6, 15, and 30 mm. Note the differently scaled spatial axes within each row.

12.4.2 1-Butanol

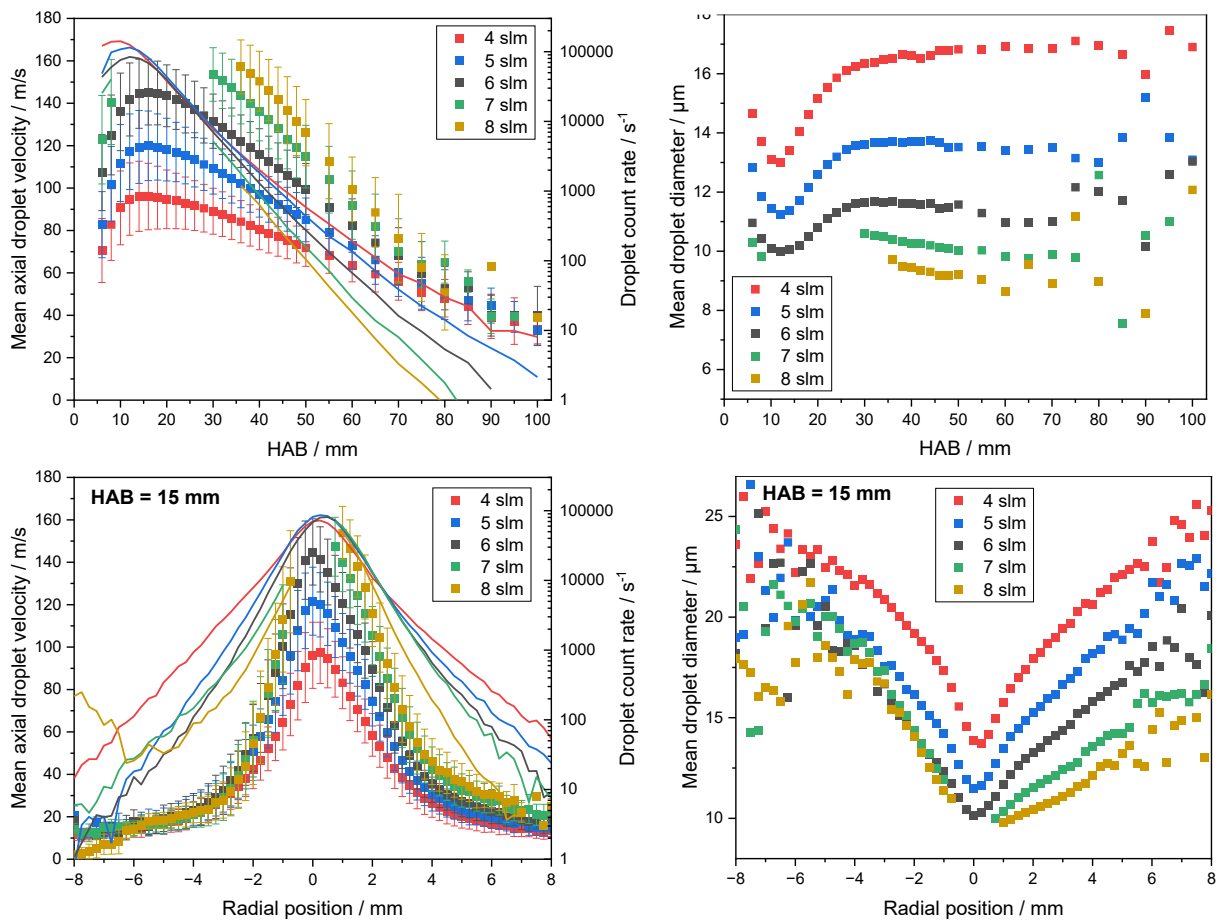


Figure A21: PDA results for the SpraySyn2 flames at standard operating condition, various dispersion gas flow rates, 2 ml/min 1-butanol, top: Centerline profiles over HAB, bottom: Radial profiles through the flame center at HAB = 15 mm. Left: Mean axial droplet velocity (symbols) and droplet count rate (solid lines), right: Mean droplet diameter.

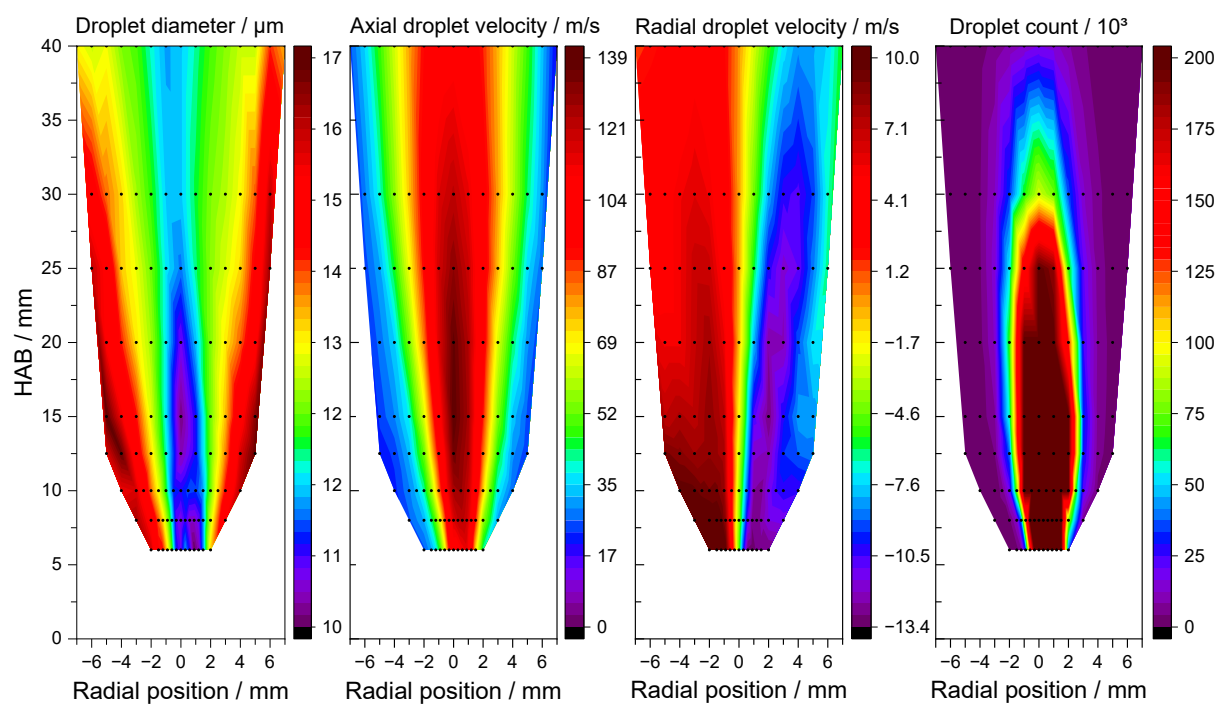


Figure A22: PDA results for the SpraySyn2 flame at the standard operating condition, 2 ml/min 1-butanol, 6 slm dispersion gas flow, vertical cross-sections of (from left to right): Mean droplet diameter, mean axial droplet velocity, mean radial droplet velocity, droplet counts.

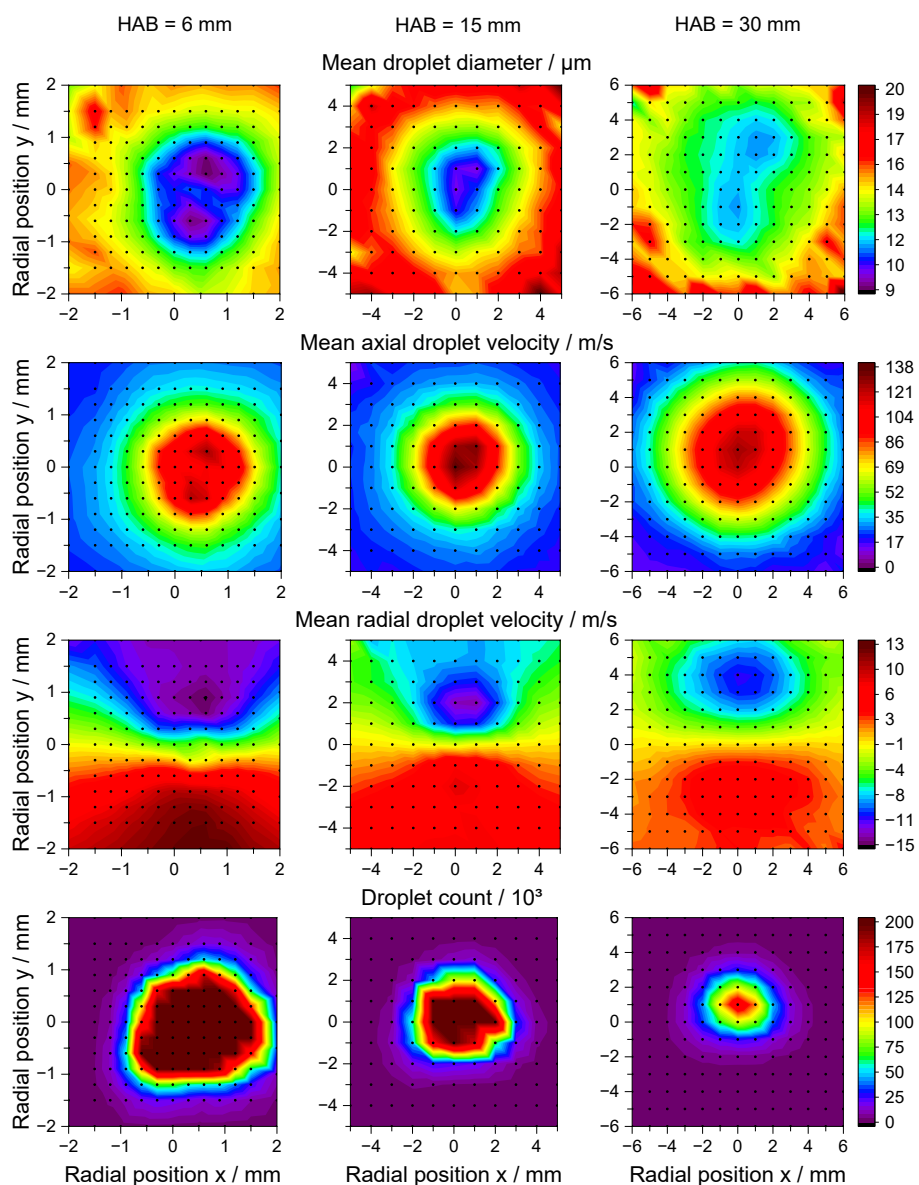


Figure A23: PDA results for the SpraySyn2 flame at the standard operating condition, 2 ml/min 1-butanol, 6 slm dispersion gas flow, horizontal cross-sections of (from top to bottom): Mean droplet diameter, mean axial droplet velocity, mean radial droplet velocity, droplet counts. The HAB from left to right is: 6, 15, and 30 mm. Note the differently scaled spatial axes within each row.

12.4.3 o-Xylene

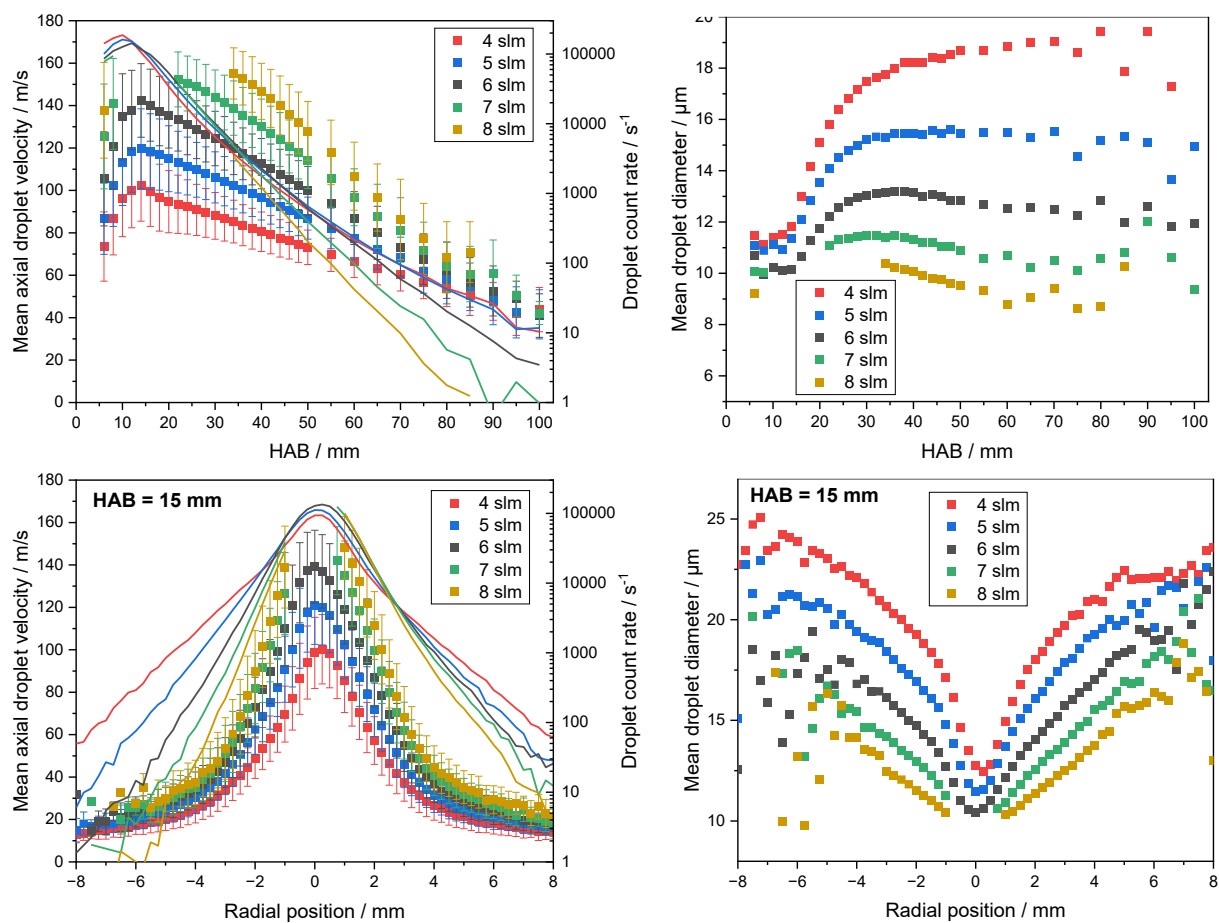


Figure A24: PDA results for the SpraySyn2 flames at standard operating condition, various dispersion gas flow rates, 2 ml/min o-xylene, top: Centerline profiles over HAB, bottom: Radial profiles through the flame center at HAB = 15 mm. Left: Mean axial droplet velocity (symbols) and droplet count rate (solid lines), right: Mean droplet diameter.

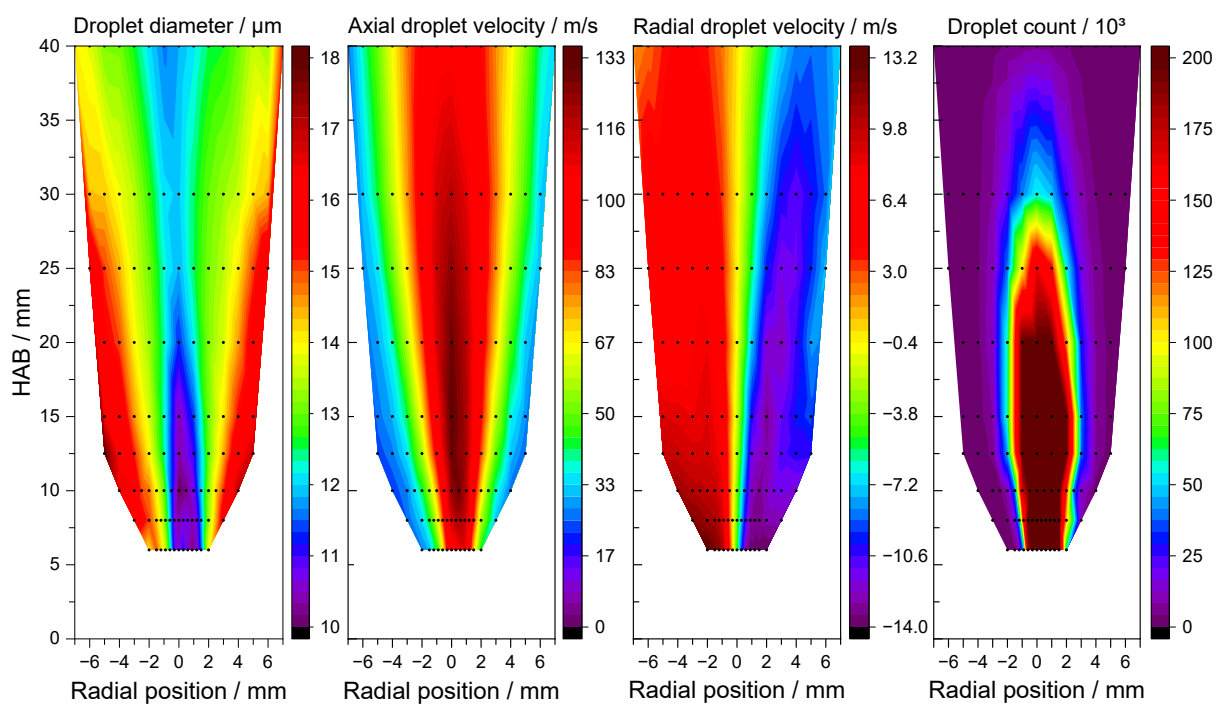


Figure A25: PDA results for the SpraySyn2 flame at the standard operating condition, 2 ml/min o-xylene, 6 slm dispersion gas flow, vertical cross-sections of (from left to right): Mean droplet diameter, mean axial droplet velocity, mean radial droplet velocity, droplet counts.

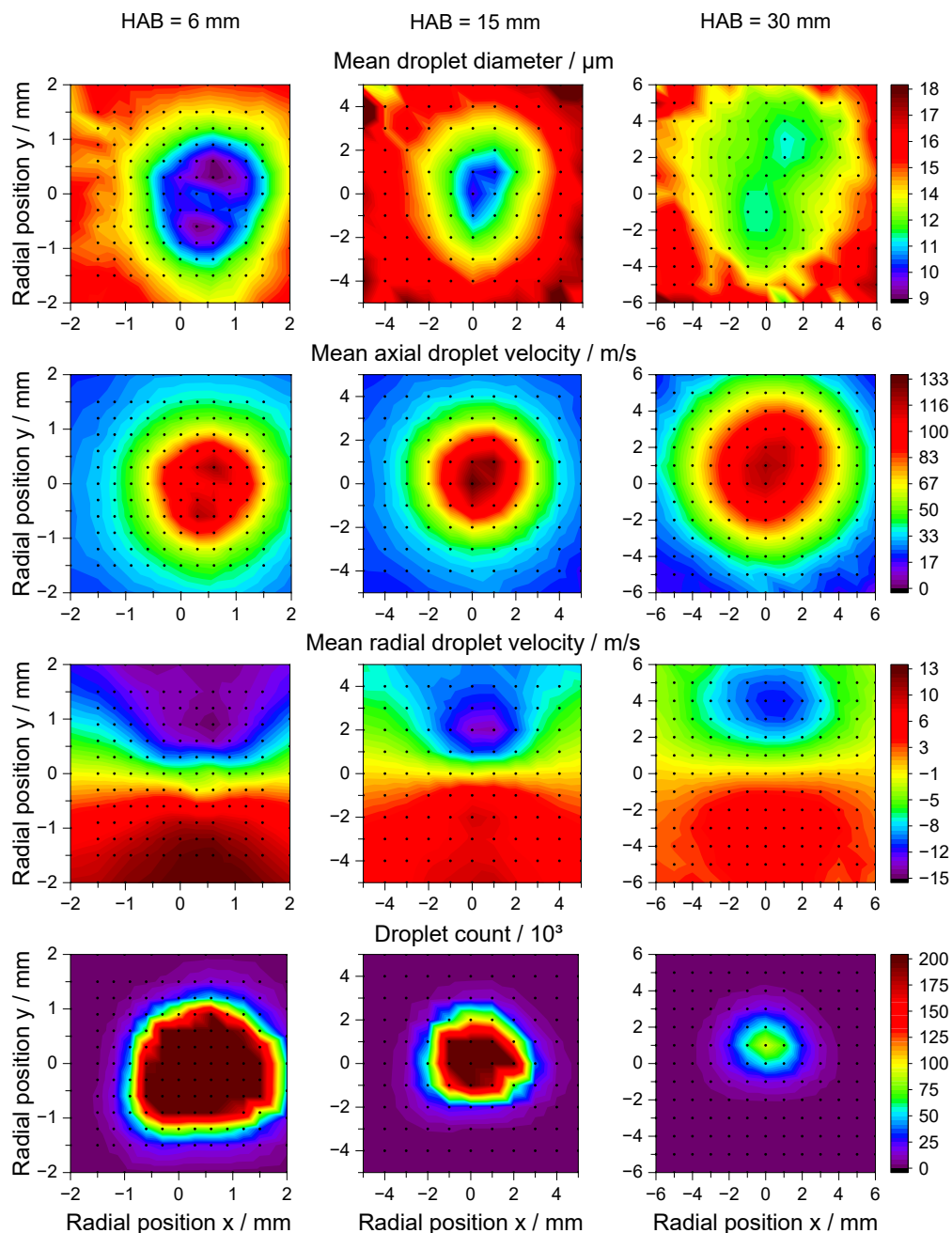


Figure A26: PDA results for the SpraySyn2 flame at the standard operating condition, 2 ml/min o-xylene, 6 slm dispersion gas flow, horizontal cross-sections of (from top to bottom): Mean droplet diameter, mean axial droplet velocity, mean radial droplet velocity, droplet counts. The HAB from left to right is: 6 mm, 15 mm, and 30 mm. Note the differently scaled spatial axes within each row.

12.4.4 Isopropyl alcohol

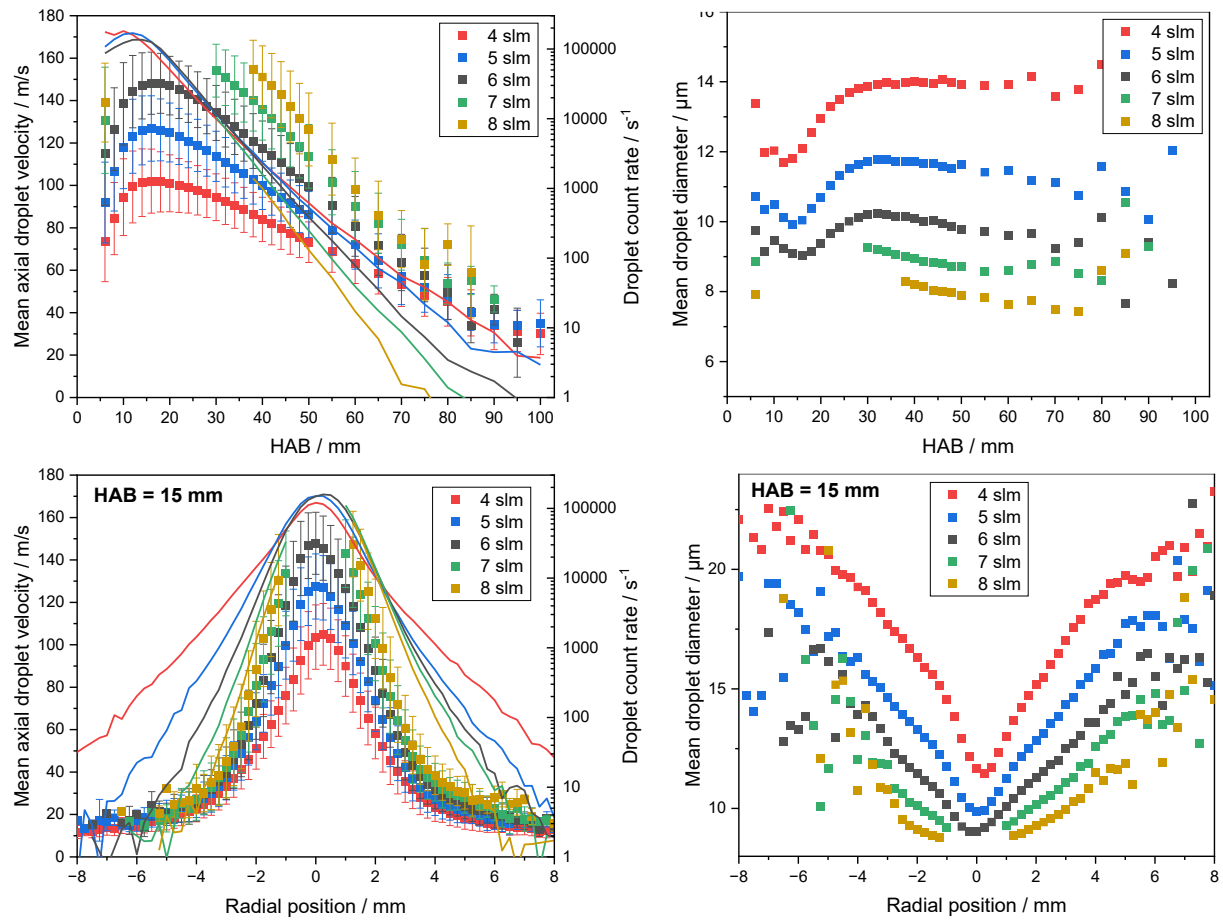


Figure A27: PDA results for the SpraySyn2 flames at standard operating condition, various dispersion gas flow rates, 2 ml/min isopropyl alcohol, top: Centerline profiles over HAB, bottom: Radial profiles through the flame center at HAB = 15 mm. Left: Mean axial droplet velocity (symbols) and droplet count rate (solid lines), right: Mean droplet diameter.

12.4.5 Acetone

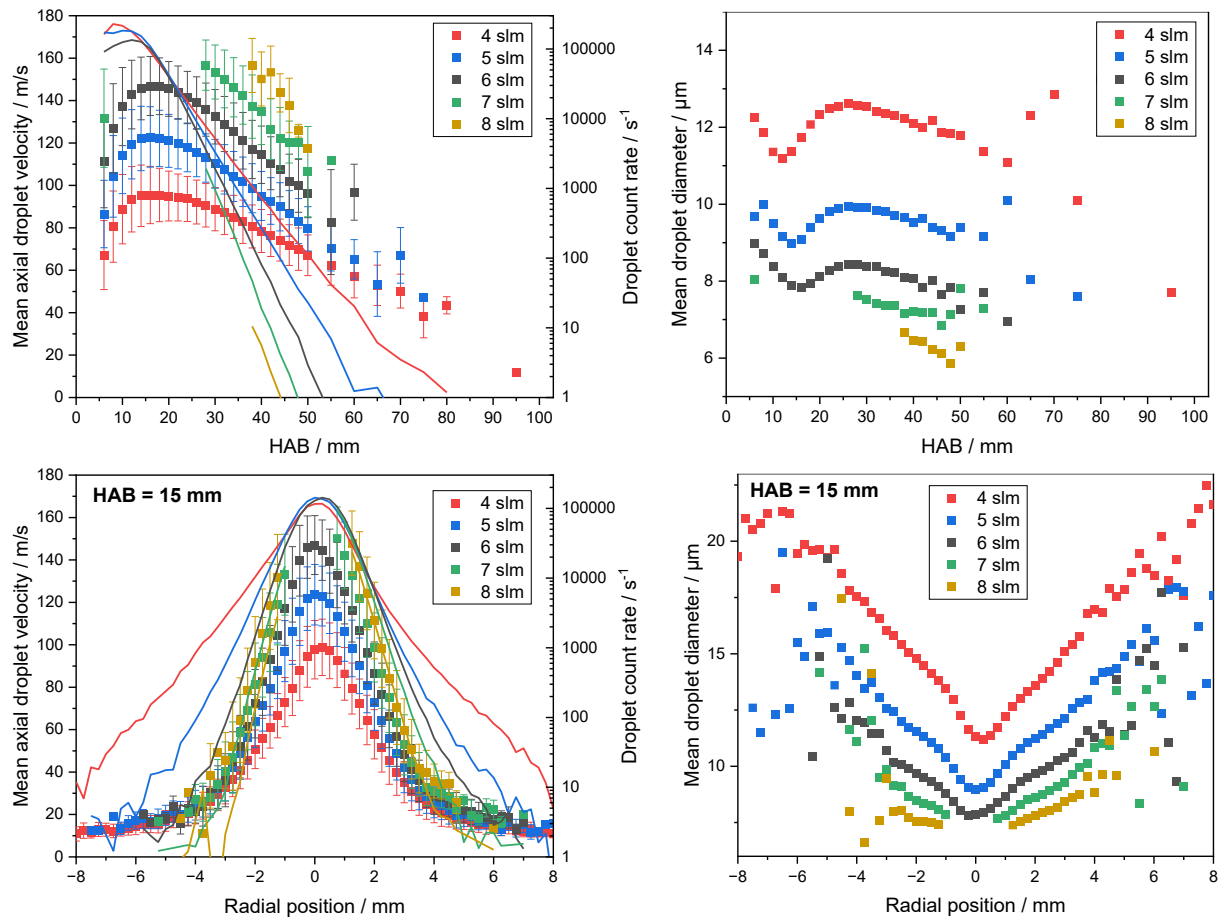


Figure A28: PDA results for the SpraySyn2 flames at standard operating condition, various dispersion gas flow rates, 2 ml/min acetone, top: Centerline profiles over HAB, bottom: Radial profiles through the flame center at HAB = 15 mm. Left: Mean axial droplet velocity (symbols) and droplet count rate (solid lines), right: Mean droplet diameter.

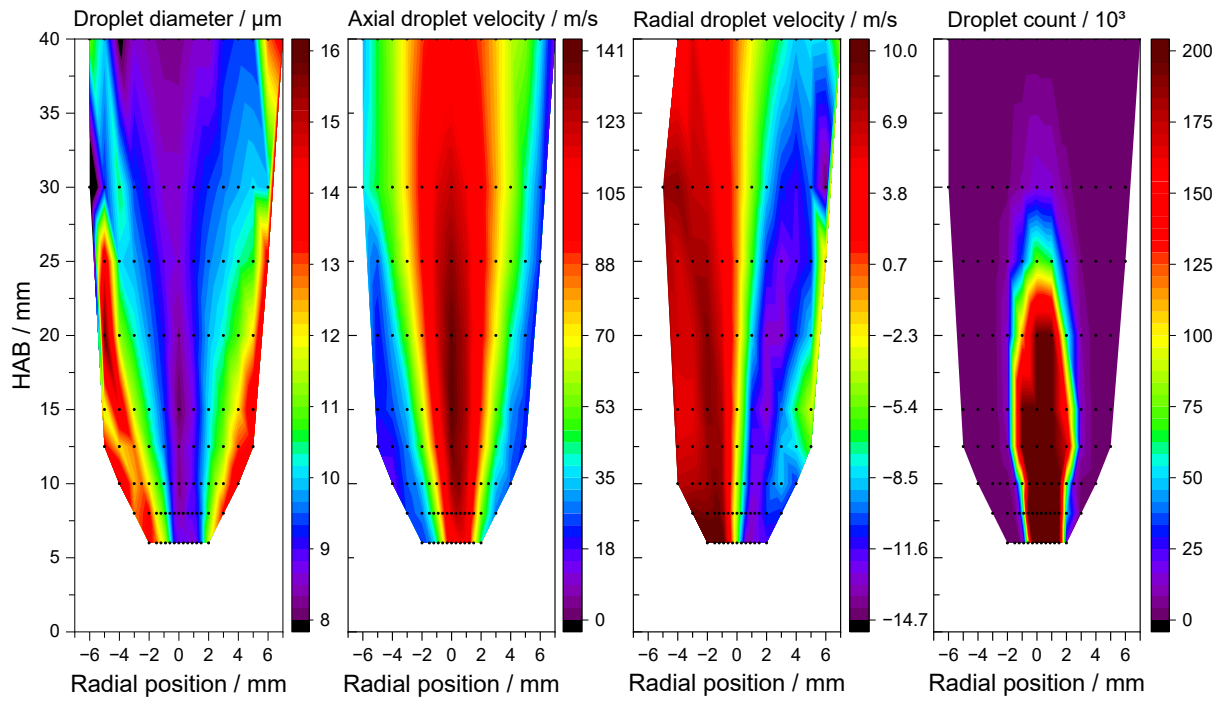


Figure A29: PDA results for the SpraySyn2 flame at the standard operating condition, 2 ml/min acetone, 6 slm dispersion gas flow, vertical cross-sections of (from left to right): Mean droplet diameter, mean axial droplet velocity, mean radial droplet velocity, droplet counts.

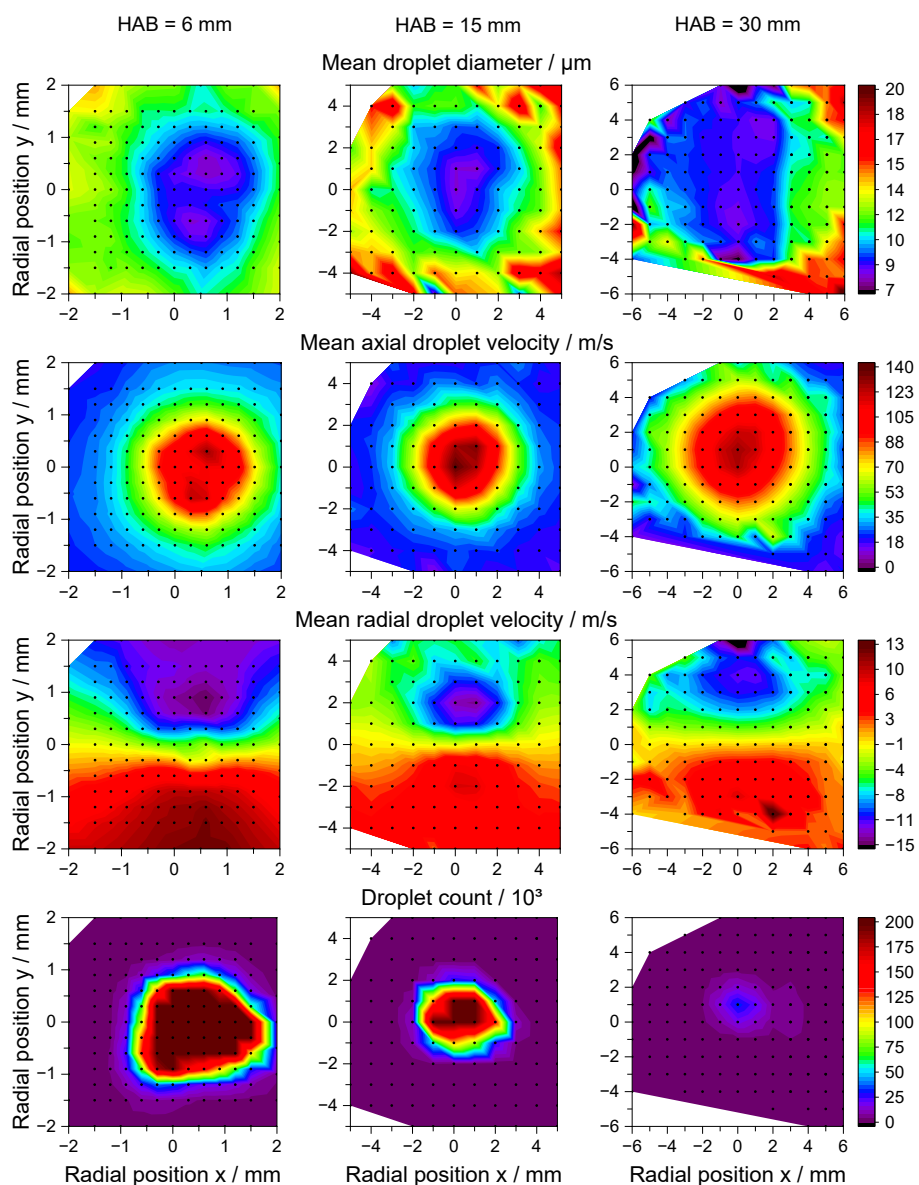


Figure A30: PDA results for the SpraySyn2 flame at the standard operating condition, 2 ml/min acetone, 6 slm dispersion gas flow, horizontal cross-sections of (from top to bottom): Mean droplet diameter, mean axial droplet velocity, mean radial droplet velocity, droplet counts. The HAB from left to right is: 6, 15, and 30 mm. Note the differently scaled spatial axes within each row.

12.4.6 Deionized water

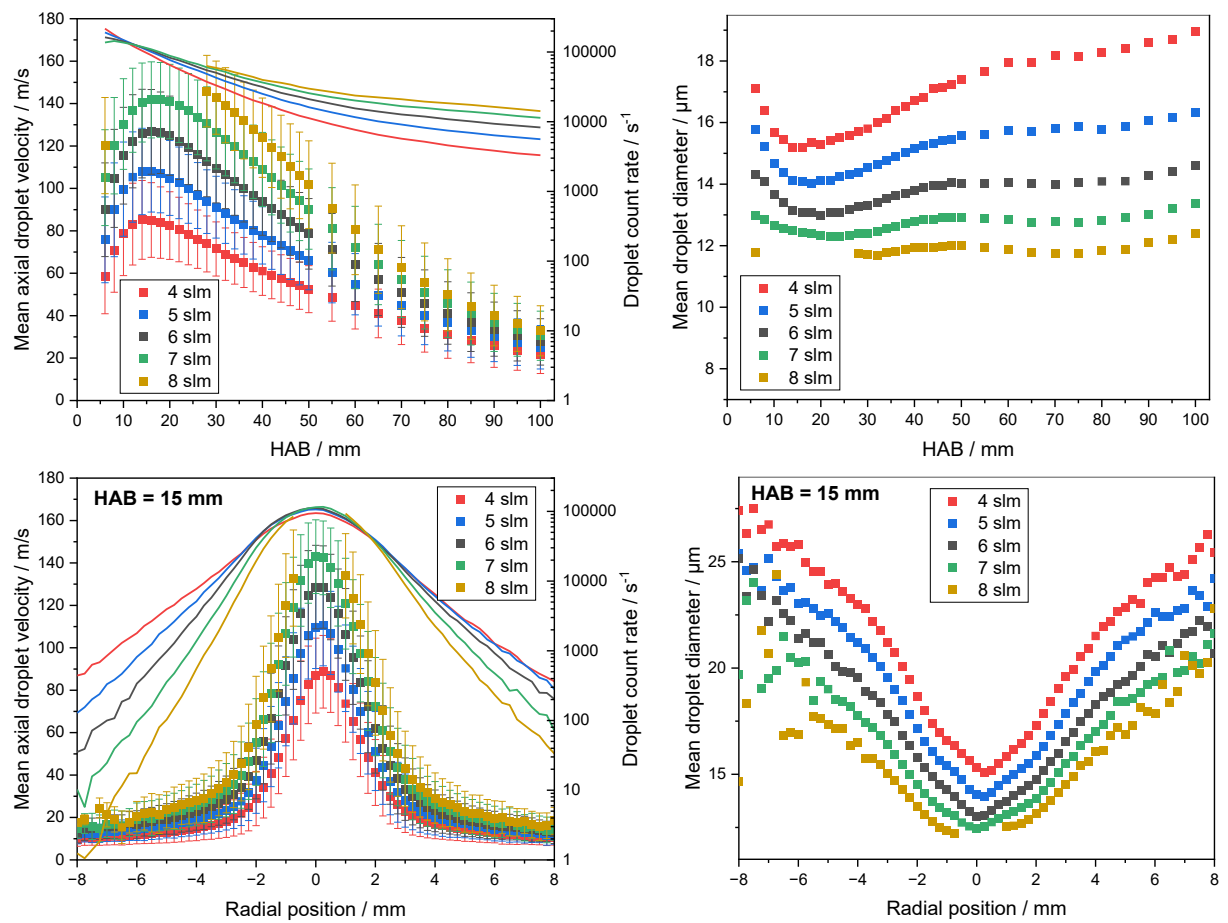


Figure A31: PDA results for the SpraySyn2 flames at standard operating condition, various dispersion gas flow rates, 2 ml/min deionized water, top: Centerline profiles over HAB, bottom: Radial profiles through the flame center at HAB = 15 mm. Left: Mean axial droplet velocity (symbols) and droplet count rate (solid lines), right: Mean droplet diameter.

12.5 Multi-line NO-LIF (IUTA)

12.5.1 Table of devices and components used

Table A2: Devices and components used for the multi-line NO-LIF measurement setup (cf. chapter 6).

Device	Manufacturer	Details and serial number
Nd:YAG laser	Continuum Electro-Optics Inc.	Powerlite Precision II Scientific, 10 Hz, 532 nm and 355 nm, Model PL8010, serial: 6800, Date: 12/08
Dye laser	Radiant Dyes Laser Accessories GmbH	NarrowScan D-R, serial: 1334 03/10
Laser energy monitor	LaVision	Serial: VZ09-0530
Sheet-forming optics	LaVision	Beam steering sheet, Collimator UV, serial: VZ09-0537
Optical longpass filter	Optics workshop UDE	Cut-on wavelength: ~ 230 nm @ 20°
Optical bandpass filter	Laser Optik	Dielectric-reflection bandpass filter with 4 mirrors, transmission: ~ 230 – 255 nm
UV camera lens	LaVision	$f = 85$ mm, $f_\# = 2.8$, serial: VZ20-0620
IRO	LaVision	Intensified relay optics, serial: VC09-0228
CCD camera	LaVision	LaVision Imager Intense, serial: VC09-0231
Pulse generator	Stanford Research Systems	Four Channel Digital Pulse/Delay generator DG535, serial: 18452
Signal interrupter	Custom-made (EMPI)	Equivalent to an AND gate for signals
PC	EMPI	Standard with Windows 7
Dye laser software	Radiant Dyes Laser Accessories GmbH	NarrowScan Laser control, version: Rev. ATMega 3.9 2014
Oscilloscope	Le Croy	Waverunner LT 342, $f_{\text{Hz}} = 500$ MHz, DSO
Laser energy meter	Coherent	FieldMaxII-TOP Laser Power and Energy Meter, equipped with the energy head: EnergyMax 1110743, J-25MB-LE, 25 μJ – 50 mJ

12.5.2 Details of the Berlin burner operating conditions

Table A3: Details of volume and mass flows for the operating conditions of the Berlin burner (BB), pre-heater: 227 °C, heat ring: 700 °C, tracer gas: 10 % NO in argon, calculated NO concentration within pilot and dispersion gas, unit slm is based on reference condition at a temperature of 0 °C. The dispersion gas mass flow includes, in addition to the oxidizer, 0.55 kg/h of tracer gas mixture or argon.

	Berlin burner									
	Ethanol						Pilot CH ₄		H ₂ O	+ AN
	Pilot H ₂			Pilot CH ₄			Pilot H ₂			
	Air2	Air3	Air4	Ox2	Ox3	Ox4	Air3	Ox3	H0.2	H0.2
Sheath gas / m ³ /h	1200	1200	1200	1200	1200	1200	1200	1200	1200	1200
Sheath O ₂ / slm	3235	3235	3235	3235	3235	3235	3235	3235	3235	3235
Sheath N ₂ / slm	12084	12084	12084	12084	12084	12084	12084	12084	12084	12084
Pilot H ₂ / slm	108	108	108	108	108	108	0	0	108	108
Pilot CH ₄ / slm	0	0	0	0	0	0	39.1	39.1	0	0
Pilot air / kg/h	100	100	100	100	100	100	60	60	100	100
Pilot O ₂ / slm	270	270	270	270	270	270	162	162	270	270
Pilot N ₂ / slm	1007	1007	1007	1007	1007	1007	604	604	1007	1007
Disp air/Ar / kg/h	2	3	4	0	0	0	3	0	0	0
Disp O ₂ /Ar / kg/h	0	0	0	2	3	4	0	3	0	0
Disp H ₂ /Ar / kg/h	0	0	0	0	0	0	0	0	0.22	0.22
Disp N ₂ / slm	15.1	25.1	35.4	0	0	0	25	0	0	0
Disp O ₂ / slm	4	6.7	9.5	17.5	29	40.9	6.7	29	0	0
Disp H ₂ / slm	0	0	0	0	0	0	0	0	40	40
Disp Ar / slm	4.5	4.5	4.5	4.5	4.5	4.5	4.5	4.5	4.5	4.5
Disp NO / slm	0.5	0.5	0.5	0.5	0.5	0.5	0.5	0.5	0.5	0.5
Spray EtOH / l/h	3.8	3.8	3.8	3.8	3.8	3.8	3.8	3.8	3.8	3.8
Spray H ₂ O / l/h	0	0	0	0	0	0	0	0	3	3
Spray AN / g/h	0	0	0	0	0	0	0	0	0	0.33
Pilot+Disp NO / ppm	355	352	348	355	352	349	594	596	350	350
Gesamt NO / ppm	29.8	29.8	29.8	29.8	29.8	29.8	30.9	30.9	29.7	29.7
Equivalence ratio ϕ / -	0.46	0.46	0.46	0.44	0.43	0.41	0.90	0.79	0.28	0.28

12.6 Absorption and fluorescence spectra of chosen tracers

Some sections of the following chapter are reprints or else contain contents from the listed publications:

M.M. Prenting, M.I. Bin Dzulfida, T. Dreier, C. Schulz, Characterization of tracers for two-color laser-induced fluorescence liquid-phase temperature imaging in sprays, *Exp. Fluids* 61 (2020) 77. <https://doi.org/10.1007/s00348-020-2909-9>

© Springer-Verlag GmbH Germany, part of Springer Nature 2020. Reprinted with permission.

M.M. Prenting, M. Shilikhin, T. Dreier, C. Schulz, T. Endres, Characterization of tracers for two-color laser-induced fluorescence thermometry of liquid-phase temperature in ethanol, 2-ethylhexanoic-acid/ethanol mixtures, 1-butanol, and o-xylene, *Appl. Opt.* 60 (2021) C98–C113. <https://doi.org/10.1364/AO.419684> and supplementary document [453]

© 2021 Optical Society of America. Reprinted with permission.

My contributions to the publications were the design and setup of the experiment, execution of the measurements supported by students under my supervision, analysis and interpretation of the data, conception and writing of the manuscripts supported by the coauthors who especially contributed to structuring and wording.

12.6.1 Physical and chemical properties of relevant laser dyes

Table A4: Photo-physical and thermo-physical properties of the investigated laser dyes, fluorescence quantum yield (FQY): Most recent literature, solvent ethanol.

Tracer	Formula	Molar mass / (g/mol)	Melting point / °C	FQY in ethanol ϕ_f / -
Coumarin 152 [454]	$C_{12}H_{10}F_3NO_2$	257.21	147–149	0.16 [455]
				0.19 [456]
				0.21 [457]
Coumarin 153 [458]	$C_{16}H_{14}F_3NO_2$	309.28	164–168	0.53 [459]
				0.54 [460]
DCM [461]	$C_{19}H_{17}N_3O$	303.37	215–220	0.44 [460]
Pyromethene 597 [462]	$C_{22}H_{33}BF_2N_2$	374.32	256–261	0.43 [463]
				0.65 [465]
Rhodamine B [464]	$C_{28}H_{31}ClN_2O_3$	479.02	199–201	0.7 [413]
				0.73 [466]
Coumarin 47 [467]	$C_{14}H_{17}NO_2$	231.29	72–75	0.67 [457]
Coumarin 102 [468]	$C_{16}H_{17}NO_2$	255.31	152–156	0.93 [457]
				0.764 [460]
Coumarin 120 [469]	$C_{10}H_9NO_2$	175.18	223–226	0.72 [457]
PTP [470]	$C_{18}H_{14}$	230.3	212–213	
Pyridine 1 [471]	$C_{19}H_{23}N_2 \cdot ClO_4$	378.85		
Pyromethene 567 [472]	$C_{18}H_{25}BF_2N_2$	318.22	208–209	0.83
Rhodamine 101 [473]	$C_{32}H_{31}N_2O_3 \cdot ClO_4$	591.05		0.913 [460]
Stilbene 3 [474]	$C_{28}H_{22}(NaO_3S)_2$	562.56	>320	0.76 [475]

12.6.2 Analysis regarding 2cLIF thermometry

12.6.2.1 Coumarin 153

Temperature dependence of absorption and fluorescence spectra

In Figure A32 the absorption and fluorescence spectra of coumarin 153 dissolved in 65EHA35EtOH and excited at 355 nm are shown up to the temperature of 373 K.

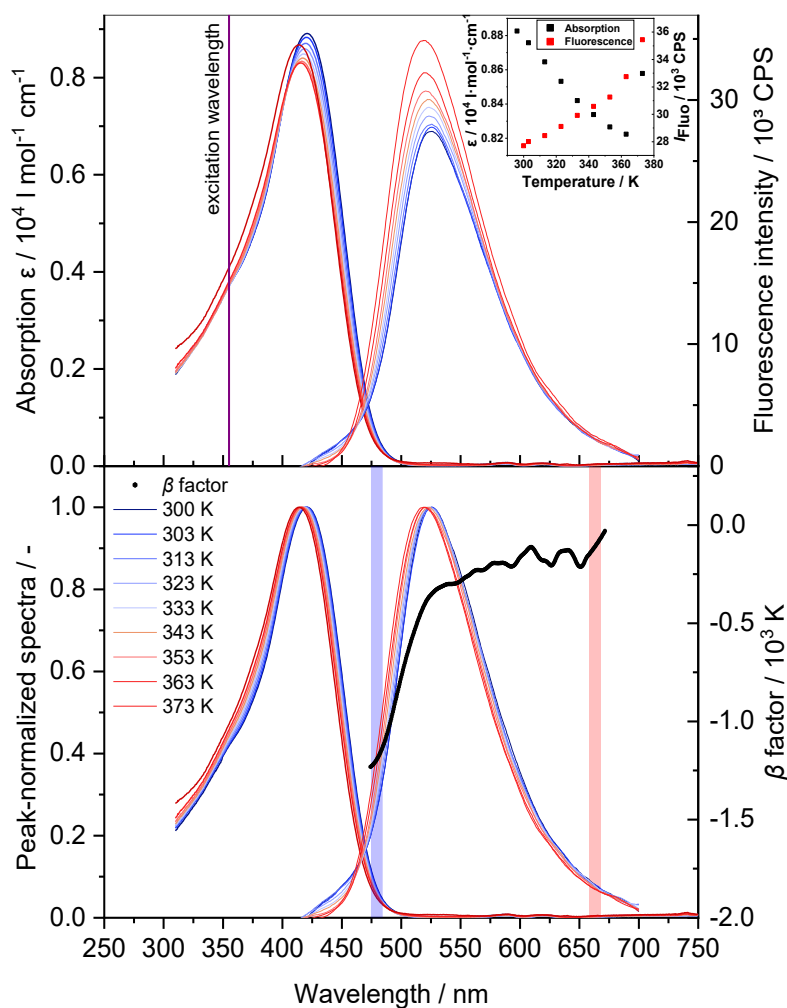


Figure A32: Temperature-dependent absorption (up to 373 K) and LIF spectra (up to 373 K) of 1 mg/l coumarin 153 in 65EHA35EtOH, excitation at 355 nm indicated as purple line. Top: Absolute values and inset illustrating the peak intensities vs. temperature, bottom: Peak-normalized values, optimized 10-nm wide 2cLIF detection bands (blue and red bars) and β factor for the spectra at 303 and 373 K.

As for coumarin 152, it can be observed that coumarin 153 in 65EHA35EtOH has a large Stokes shift resulting in a corresponding small overlap of absorption and fluorescence spectra. In contrast to coumarin 152 the absolute fluorescence intensity of coumarin 153 increases with increasing temperature (see inset in Figure A32) while the temperature-dependent absorption spectra behave very similar to the ones of coumarin 152. The absorption decreases with temperature up to 363 K, from where it starts to strongly increase again. Absorption and fluorescence spectra exhibit a significant blueshift and a low spectral broadening (Table A5). The β factors start to rise from -1250 K at 470 nm to about -200 K in the range between 580–660 nm.

Impact of concentration: Signal re-absorption

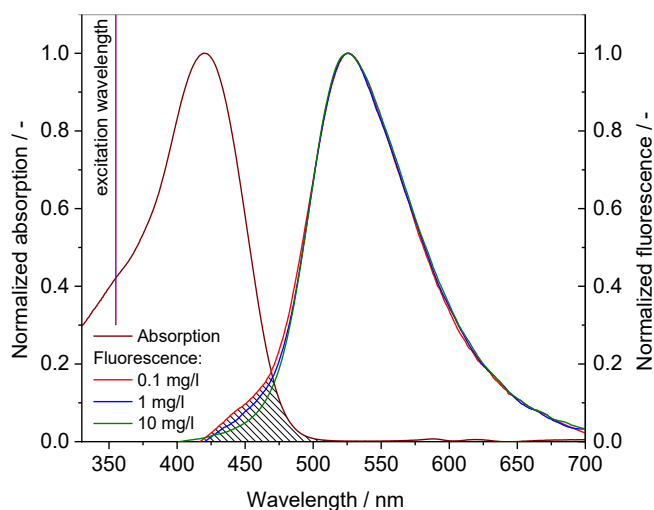


Figure A33: Peak-normalized absorption and fluorescence spectra of coumarin 153 dissolved in 65EHA35EtOH at various concentrations. Excitation wavelength: 355 nm indicated as purple line, temperature: 303 K. The dashed area shows the overlap O (unit: nm) between normalized absorption and emission for the 0.1 mg/l case.

The concentration dependence of the fluorescence spectra of coumarin 153 dissolved in 65EHA35EtOH are presented in Figure A32. It can be seen that the spectral overlap ($O = 6.03$ nm) causes a slight spectral change of the shape in the range of the overlap. In regions where no overlap exists, no difference in the shape or position of the spectra is observable.

Impact of various solvents

Figure A34 shows the absorption and fluorescence spectra of coumarin 153 dissolved in *o*-xylene, 65EHA35EtOH and ethanol. As for coumarin 152, the spectra are significantly affected by the kind of solvent, e.g., a significant blueshift of the spectrum is observed for coumarin 153 dissolved in *o*-xylene.

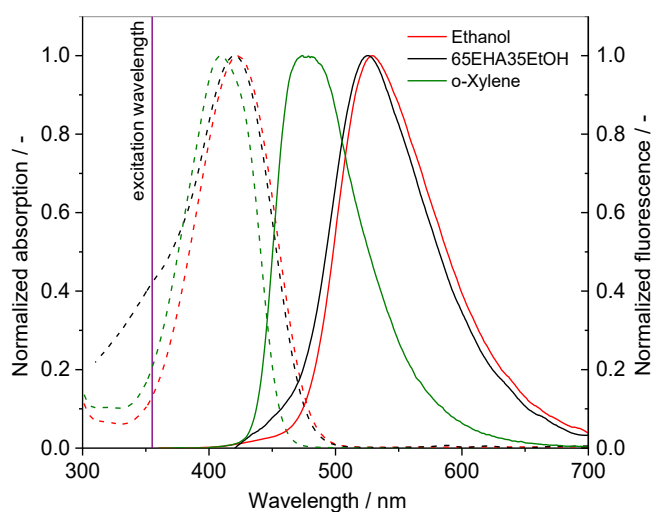


Figure A34: Peak-normalized absorption (dashed lines) and fluorescence (solid lines) spectra of 1 mg/l coumarin 153 dissolved in various solvents, excitation: 355 nm indicated as purple line, temperature: 303 K.

The FWHM of the fluorescence of coumarin 153 in o-xylene is with 76.5 nm much smaller than for the other two solvents presented in Table A5. The absolute fluorescence intensity increases in ethanol with 0.52 %/K significantly stronger than in the other solvents. The blueshift of coumarin 153 is smaller in comparison to coumarin 152 and in o-xylene almost no spectral broadening is observable.

Table A5: Characterization of the fluorescence spectra of 1 mg/l coumarin 153 dissolved in various solvents, excitation at 355 nm. The parameters are extracted from smoothed fluorescence spectra.

	65EHA35EtOH	Ethanol	o-Xylene
Peak position / nm (303 K)	524.5	529.5	477.5
Peak intensity change / %/K (303 to 343 K)	0.21	0.52	0.07
FWHM / nm (303 K)	91.7	90.5	76.5
Blueshift at HM / nm/K (303 to 343 K)	0.12	0.13	0.1
Spectral broadening / nm/K (303 to 343 K)	0.03	0.05	0.01

12.6.2.2 DCM

Temperature dependence of absorption and fluorescence spectra

The absorption and fluorescence spectra of DCM dissolved in 65EHA35EtOH at different temperatures are depicted in Figure A35. DCM dissolved in pure ethanol and 65EHA35EtOH can be excited in the UV at 355 nm as well as in the visible at 532 nm, whereas it is only excitable at 355 nm when dissolved in o-xylene because the absorption spectra are strongly shifted to shorter wavelengths (Figure A37).

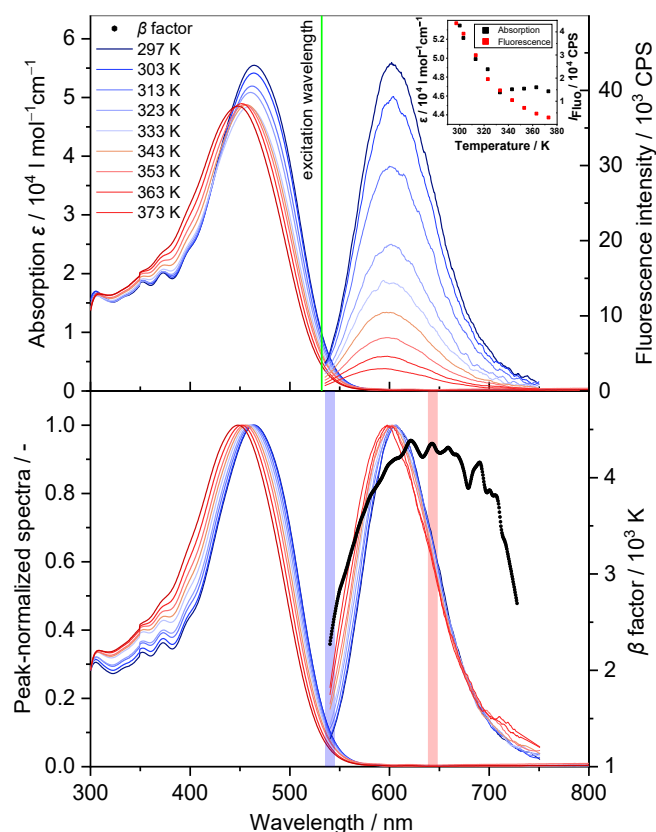


Figure A35: Temperature-dependent absorption (up to 373 K) and fluorescence spectra (up to 373 K) of 1 mg/l DCM in 65EHA35EtOH, excitation at 532 nm indicated as green line. Top: Absolute values and inset illustrating the peak intensities vs. temperature, bottom: Peak-normalized values, optimized 10-nm wide 2cLIF detection bands (blue and red bars) and β factors for the spectra at 303 and 373 K.

For a tracer excitable at 532 nm, DCM shows a comparatively large Stokes shift. As depicted in the inset of Figure A35 the fluorescence intensity decreases strongly with increasing temperature, while the absorption spectra decrease from room temperature to 333 K and then stay almost constant. The normalized spectra show a distinct blueshift, which is stronger for the absorption than for the fluorescence spectra. In comparison to the other investigated tracers, DCM exhibits a notably stronger blueshift of the absorption spectra. As a result of the strong decrease in fluorescence intensity with increasing temperature the β factor features comparatively high values (between 2000 and 4500 K). The lower β factor are located to shorter wavelengths while the highest can be found around 630 nm.

Impact of tracer concentration: Signal re-absorption

Figure A36 shows the fluorescence spectra of DCM at 303 K for various concentrations. Since the spectral overlap between absorption and fluorescence spectra is not reaching out to the fluorescence peak the fluorescence spectra were normalized at their respective peak positions.

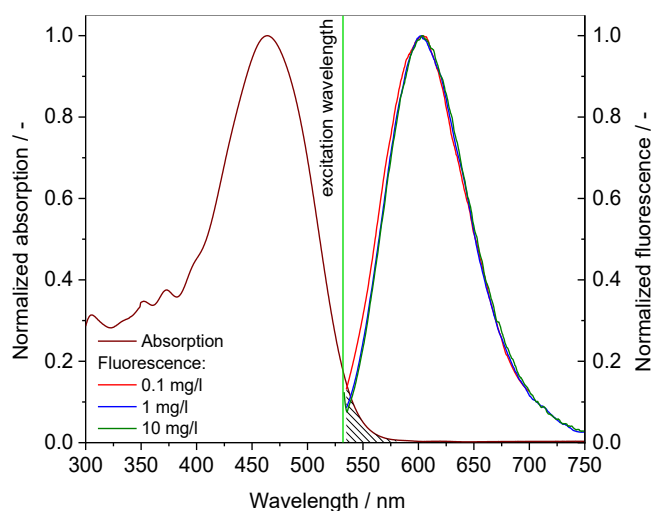


Figure A36: Peak-normalized absorption and fluorescence spectra of DCM dissolved in 65EHA35EtOH at various concentrations. Excitation wavelength: 532 nm indicated as green line, temperature: 303 K. The dashed area shows the overlap O (unit: nm) between normalized absorption and emission for the 0.1 mg/l case.

It can be seen from the diagram that the variation of concentration only slightly affects the fluorescence spectra in the region of the spectral overlap, which is the smallest of the investigated tracers excitable at 532 nm. The same behavior is observed for the other investigated solvents – refer to appendix section 12.6.4.4. For the same reason as for Pyrromethene 597 (cf. 7.3.1.3) only the overlap area up to the intersection of absorption and fluorescence spectrum can be calculated ($O_{\text{intersec.}} = 1.86 \text{ nm}$) resulting in an estimation of $O = 3.72 \text{ nm}$.

Impact of various solvents

The absorption and fluorescence spectra of DCM dissolved in ethanol, 65EHA35EtOH and o-xylene are presented in Figure A37. Two excitation wavelengths are indicated because DCM dissolved in o-xylene can only be excited at 355 nm among the harmonics of the Nd:YAG laser.

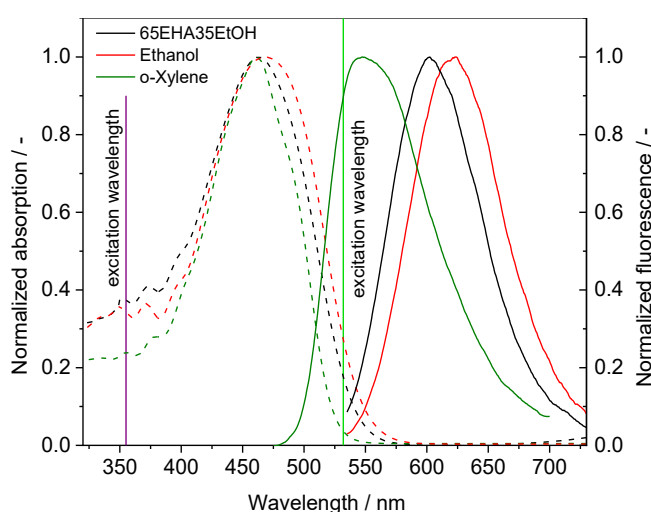


Figure A37: Peak-normalized absorption (dashed lines) and fluorescence (solid lines) spectra of 1 mg/l DCM dissolved in various solvents, excitation for 65EHA35EtOH and ethanol: 532 nm indicated as green line, excitation for o-xylene: 355 nm indicated as purple line, temperature: 303 K.

Also for this tracer, the fluorescence spectrum is strongly affected by the solvent (the shift of the fluorescence color with different solvents is visible by the naked eye). The trends in spectral shift of the absorption spectra with solvent are the same as for the fluorescence spectra.

Table A6: Characterization of the fluorescence spectra of 1 mg/l DCM dissolved in various solvents, excitation at 532 nm, for o-xylene excitation at 355 nm. The parameters are extracted from smoothed fluorescence spectra.

	65EHA35EtOH	Ethanol	o-Xylene
Peak position / nm (303 K)	603.5	622	548.5
Peak intensity change / %/K (303 to 343 K)	-1.83	-1.38	-1.77
FWHM / nm (303 K)	87.9	89.6	96.1
Blueshift at HM / nm/K (303 to 343 K)	0.18	0.16	0.14
Spectral broadening / nm/K (303 to 343 K)	0.13	0.11	0.18

Among the investigated solvents, the decrease of the fluorescence peak intensity of DCM with temperature is the smallest in ethanol. In o-xylene DCM has a significantly larger FWHM than the others, exhibits the largest spectral broadening and has the smallest blueshift.

12.6.3 Spectral influence of the solvent ratio of EHA/ethanol

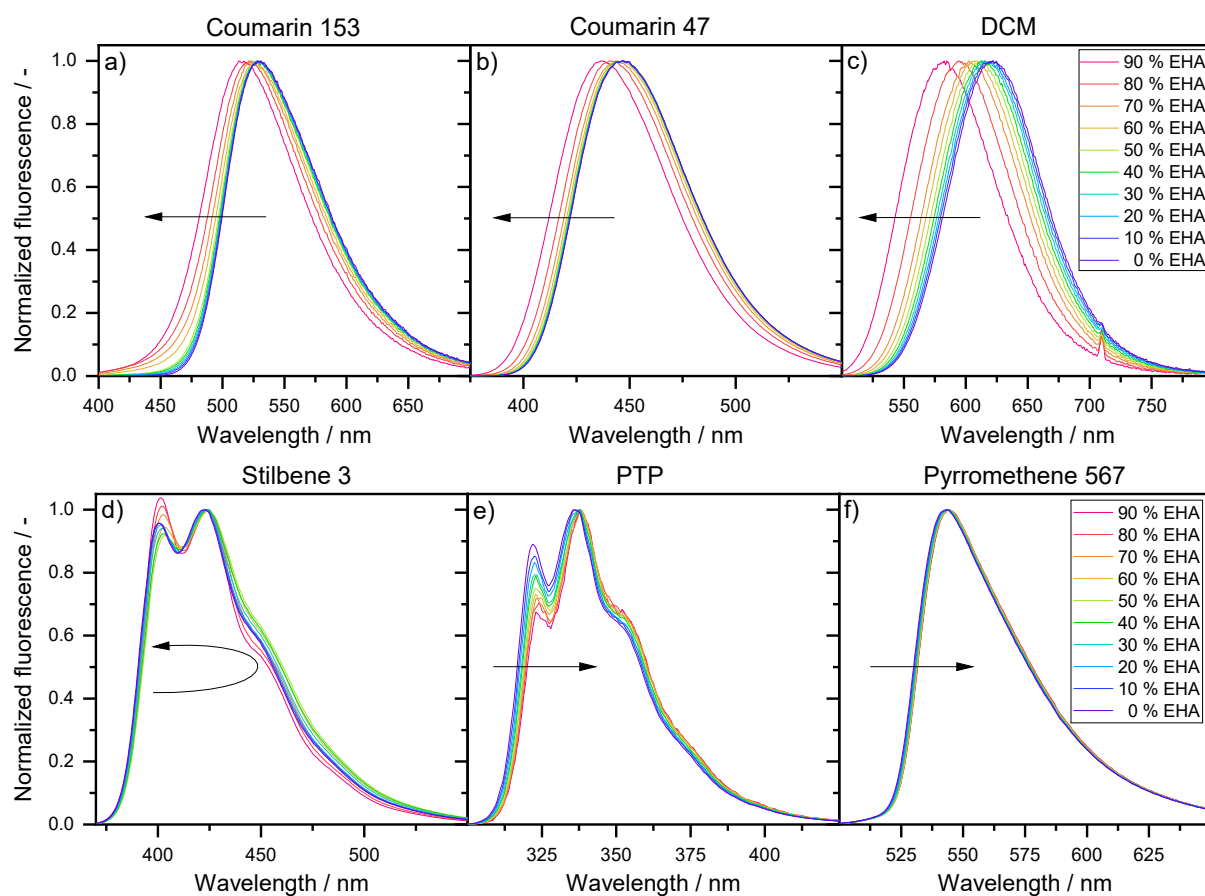


Figure A38: Normalized fluorescence spectra of different tracers (concentration: 10 mg/l) dissolved in EHA/ethanol mixtures at various fractions, displayed are the fractions by volume, excitation wavelength: 355 nm (except for PTP: 266 nm), temperature: 298 K, the arrows indicate the spectral shift with increasing solvent fraction of EHA.

12.6.4 Temperature and concentration dependent spectra in various solvents

12.6.4.1 Coumarin 152

Solvent: Ethanol

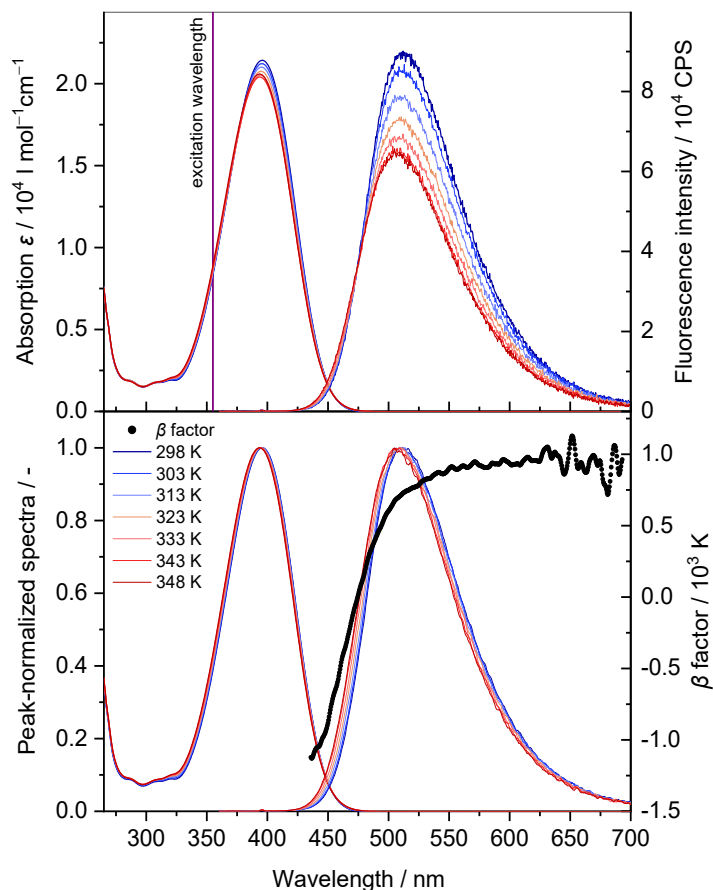


Figure A39: Temperature dependent absorption (up to 348 K) and fluorescence spectra (up to 348 K) of coumarin 152 in ethanol, 1 mg/l, excitation at 355 nm indicated as purple line, upper diagram: Absolute values, lower diagram: Peak-normalized values and β factor for the spectra at 303 and 343 K.

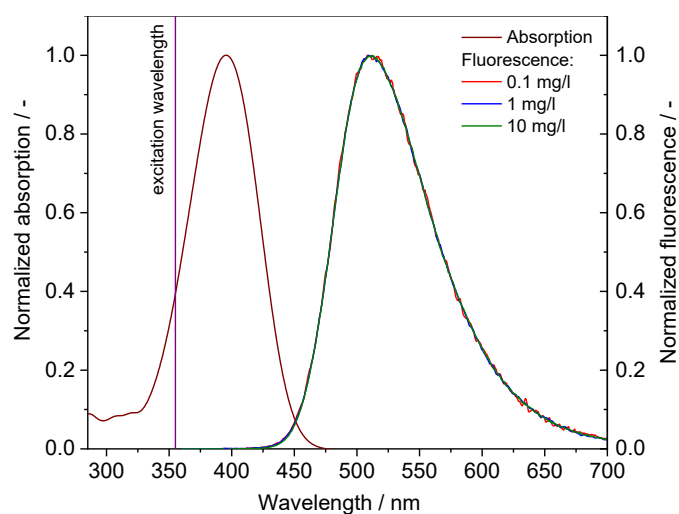


Figure A40: Peak-normalized absorption and fluorescence spectra of coumarin 152 dissolved in ethanol at various concentrations, excitation wavelength: 355 nm indicated as purple line, temperature: 303 K.

Solvent: 1-Butanol

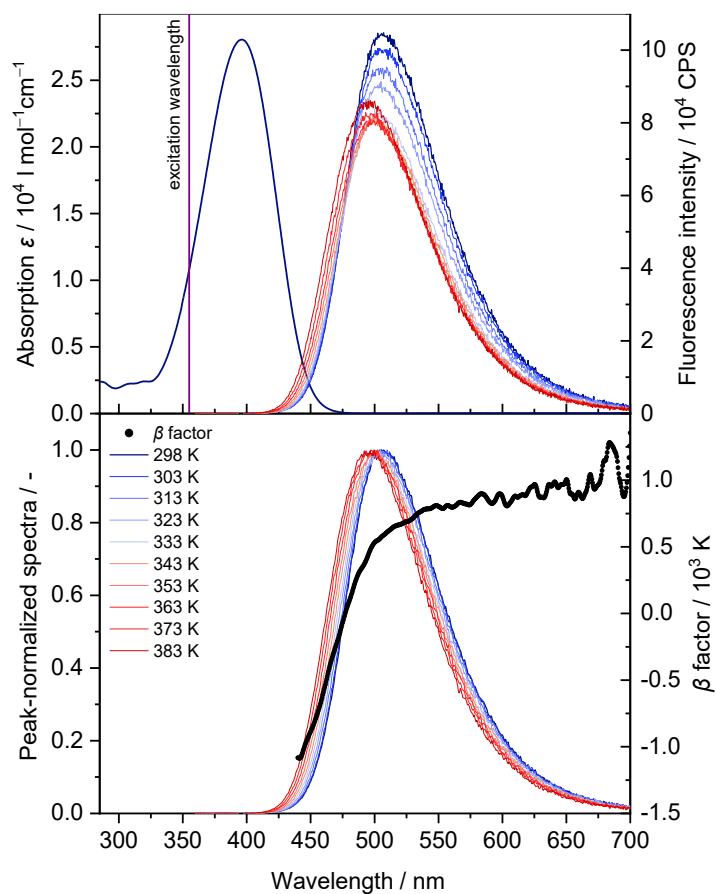


Figure A41: Temperature dependent absorption (298 K) and fluorescence spectra (up to 383 K) of coumarin 152 in 1-butanol, 1 mg/l, excitation at 355 nm indicated as purple line, upper diagram: Absolute values, lower diagram: Peak-normalized values and β factor for the spectra at 303 and 373 K.

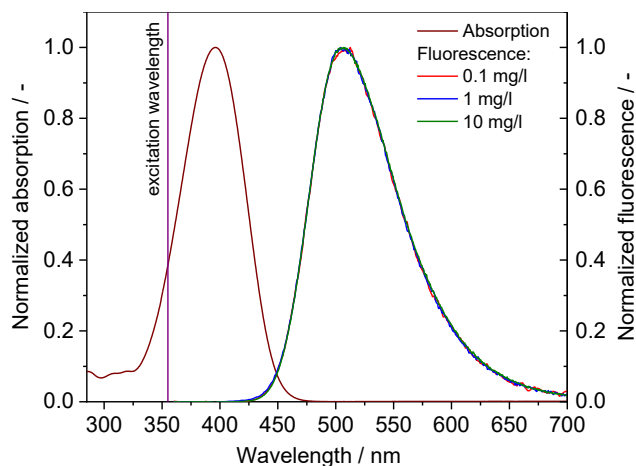


Figure A42: Peak-normalized absorption and fluorescence spectra of coumarin 152 dissolved in 1-butanol at various concentrations, excitation wavelength: 355 nm indicated as purple line, temperature: 303 K.

Solvent: o-Xylene

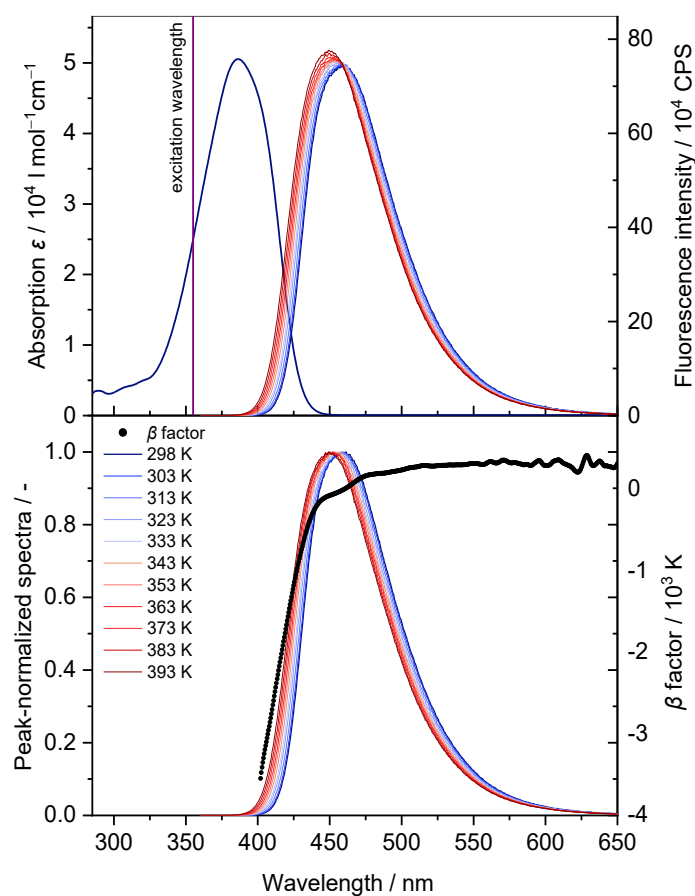


Figure A43: Temperature dependent absorption (298 K) and fluorescence spectra (up to 393 K) of coumarin 152 in o-xylene, 1 mg/l, excitation at 355 nm indicated as purple line, upper diagram: Absolute values, lower diagram: Peak-normalized values and β factor for the spectra at 303 and 373 K.

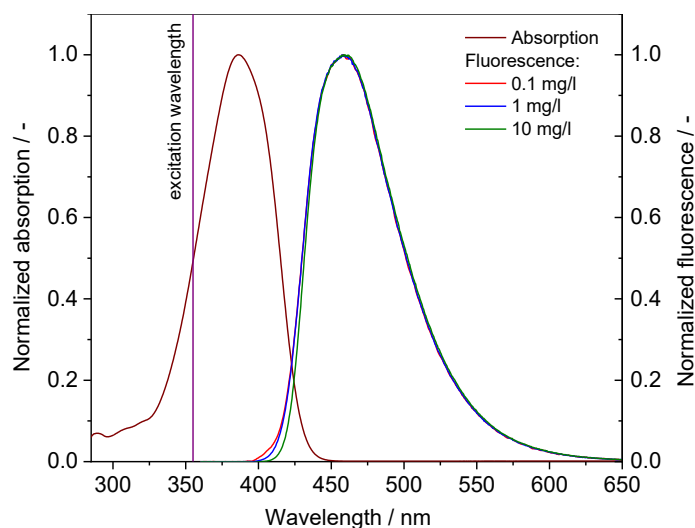


Figure A44: Peak-normalized absorption and fluorescence spectra of coumarin 152 dissolved in o-xylene at various concentrations, excitation wavelength: 355 nm indicated as purple line, temperature: 303 K.

12.6.4.2 Coumarin 153

Solvent: Ethanol

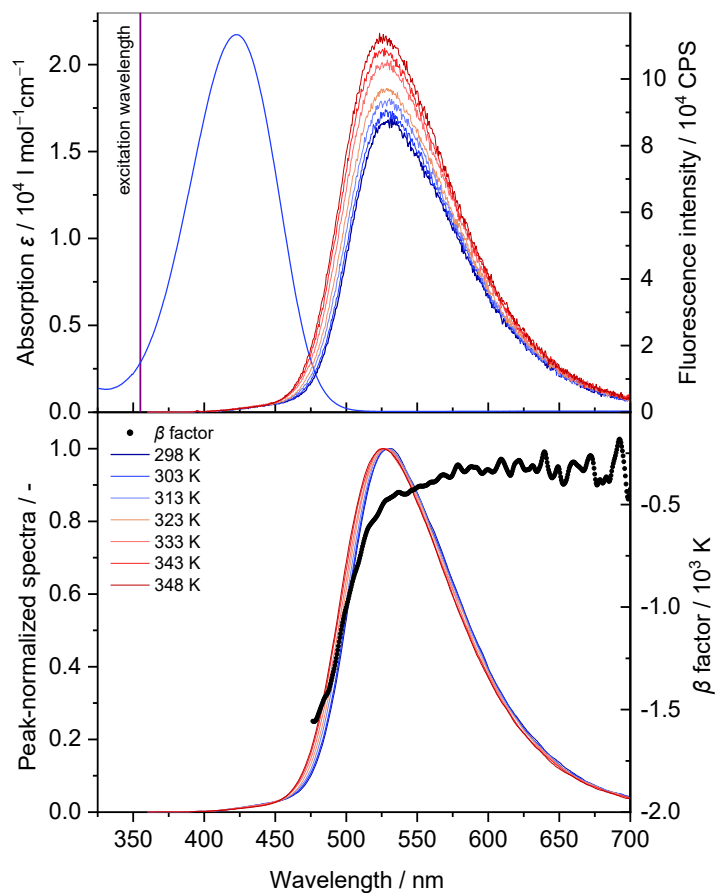


Figure A45: Temperature dependent absorption (298 K) and fluorescence spectra (up to 348 K) of coumarin 153 in ethanol, 1 mg/l, excitation at 355 nm indicated as purple line, upper diagram: Absolute values, lower diagram: Peak-normalized values and β factor for the spectra at 303 and 343 K.

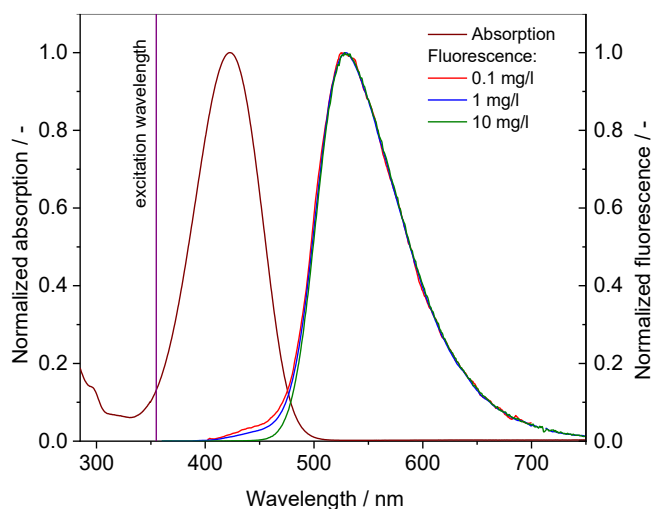


Figure A46: Peak-normalized absorption and fluorescence spectra of coumarin 153 dissolved in ethanol at various concentrations, excitation wavelength: 355 nm indicated as purple line, temperature: 303 K.

Solvent: o-Xylene

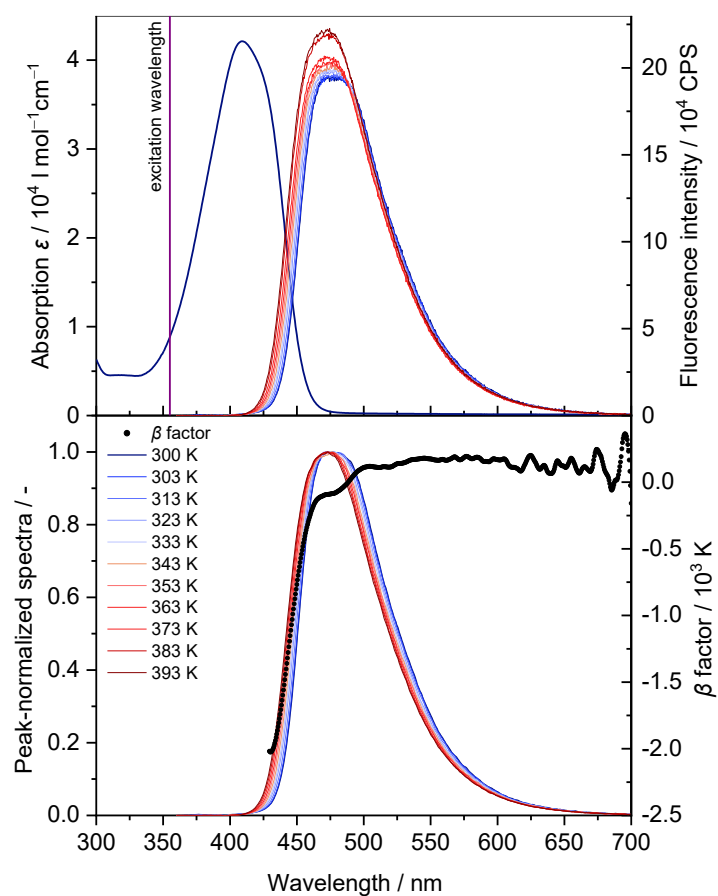


Figure A47: Temperature dependent absorption (300 K) and fluorescence spectra (up to 393 K) of coumarin 153 in o-xylene, 1 mg/l, excitation at 355 nm indicated as purple line, upper diagram: Absolute values, lower diagram: Peak-normalized values and β factor for the spectra at 303 and 373 K.

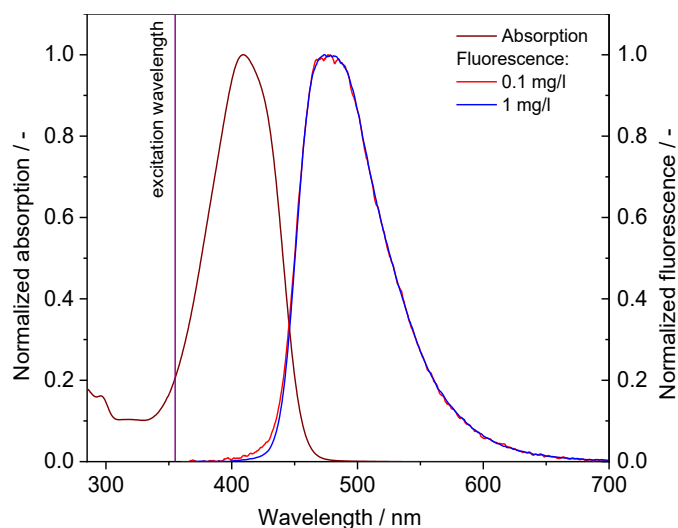


Figure A48: Peak-normalized absorption and fluorescence spectra of coumarin 153 dissolved in o-xylene at various concentrations, excitation wavelength: 355 nm indicated as purple line, temperature: 303 K.

12.6.4.3 Rhodamine B

Solvent: Ethanol

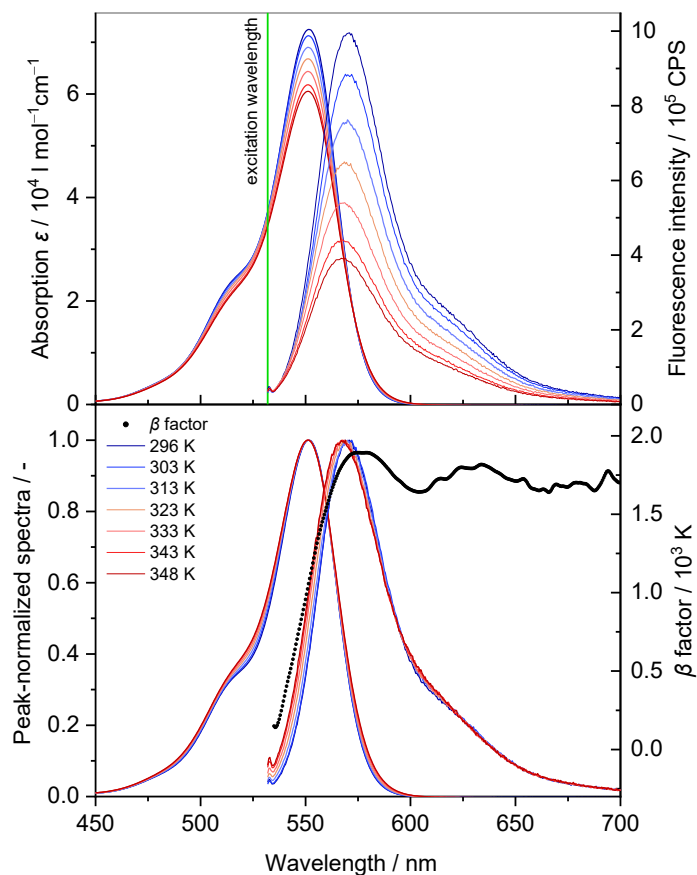


Figure A49: Temperature dependent absorption (up to 348 K) and fluorescence spectra (up to 348 K) of rhodamine B in ethanol, 1 mg/l, excitation at 532 nm indicated as green line, upper diagram: Absolute values, lower diagram: Peak-normalized values and β factor for the spectra at 303 and 343 K.

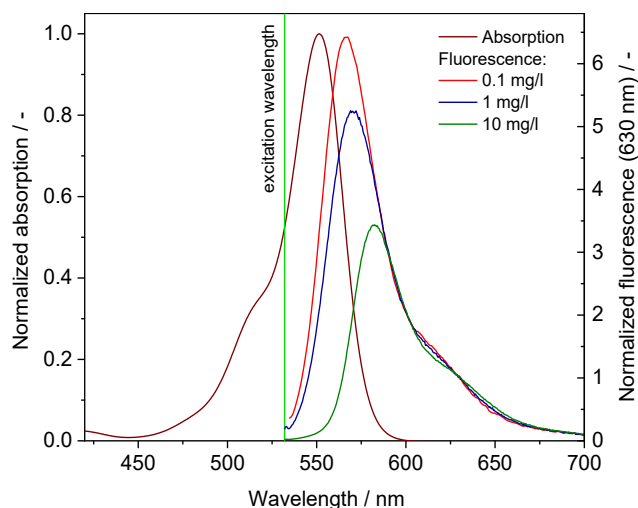


Figure A50: Peak-normalized absorption spectrum and at 630 nm normalized fluorescence spectra of rhodamine B dissolved in ethanol at various concentrations, excitation wavelength: 532 nm indicated as green line, temperature: 303 K.

Solvent: 1-Butanol

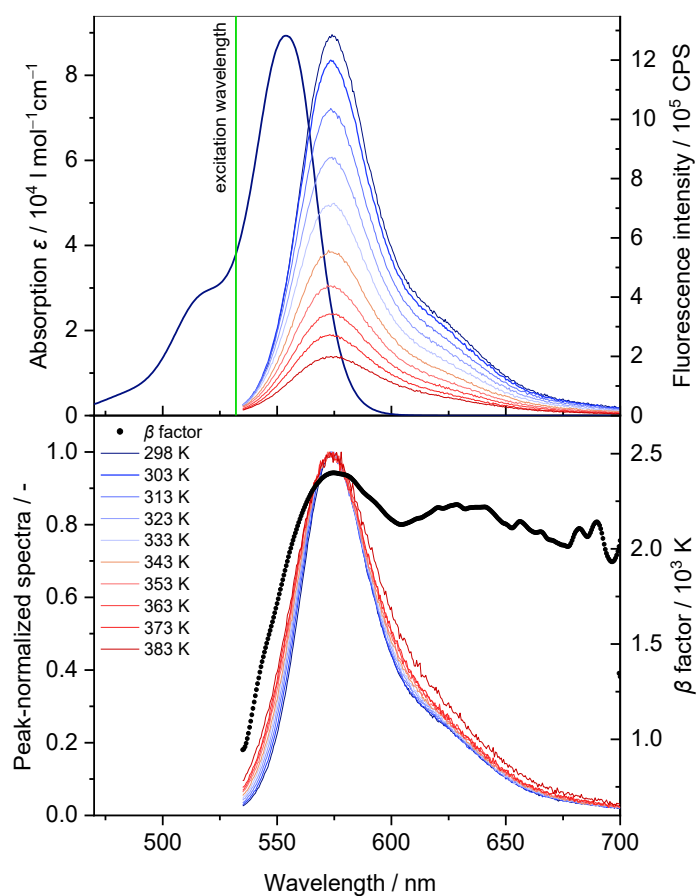


Figure A51: Temperature dependent absorption (298 K) and fluorescence spectra (up to 383 K) of rhodamine B in 1-butanol, 1 mg/l, excitation at 532 nm indicated as green line, upper diagram: Absolute values, lower diagram: Peak-normalized values and β factor for the spectra at 303 and 373 K.

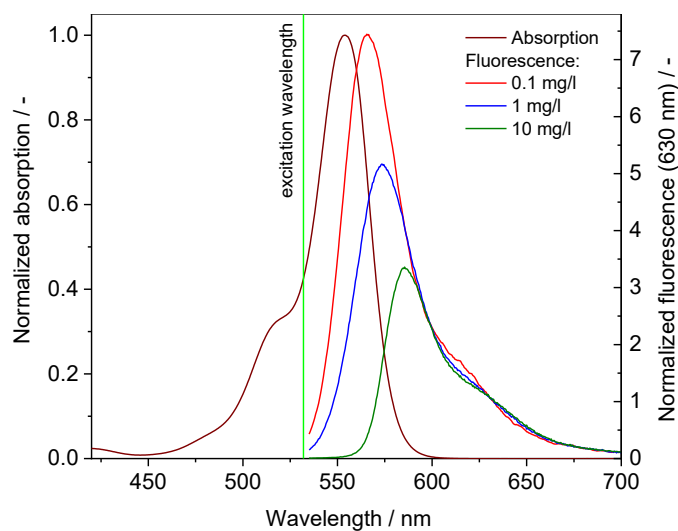


Figure A52: Peak-normalized absorption spectrum and at 630 nm normalized fluorescence spectra of rhodamine B dissolved in 1-butanol at various concentrations, excitation wavelength: 532 nm indicated as green line, temperature: 303 K.

12.6.4.4 DCM

Solvent: Ethanol

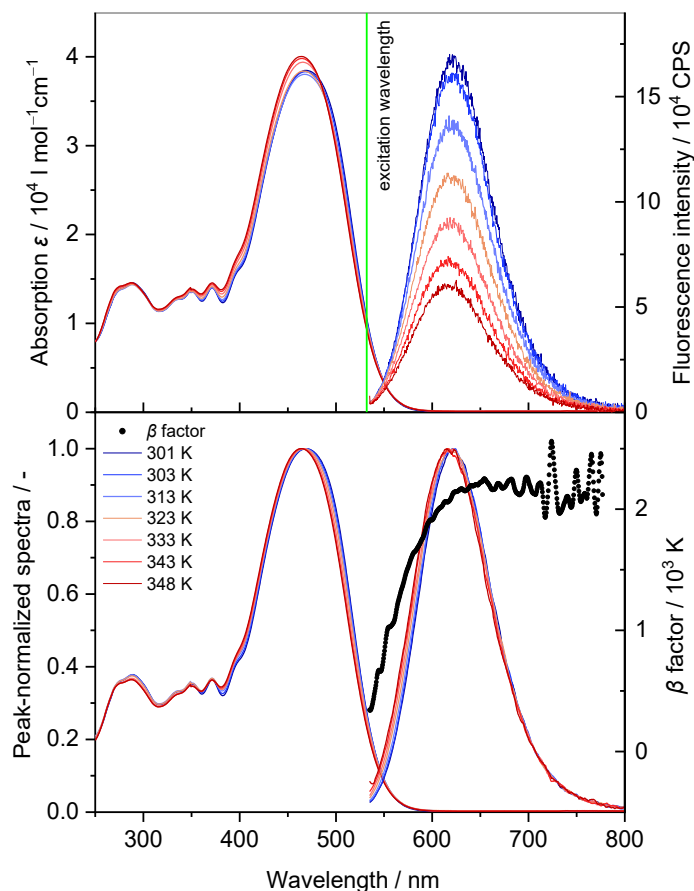


Figure A53: Temperature dependent absorption (up to 348 K) and fluorescence spectra (up to 348 K) of DCM in ethanol, 1 mg/l, excitation at 532 nm indicated as green line, upper diagram: Absolute values, lower diagram: Peak-normalized values and β factor for the spectra at 303 and 343 K.

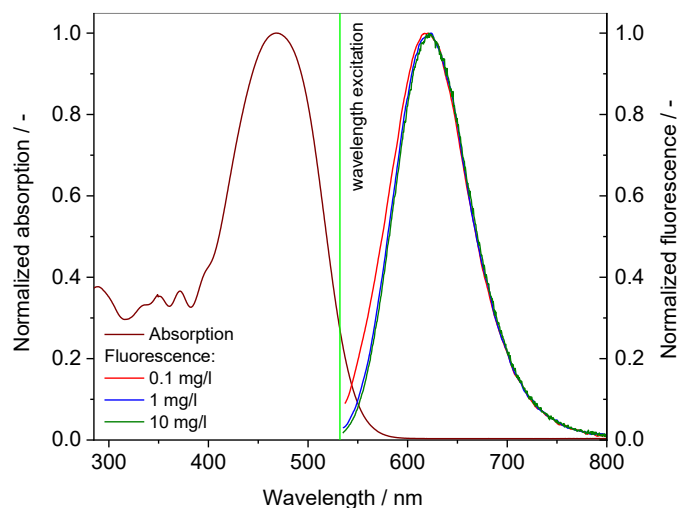


Figure A54: Peak-normalized absorption and fluorescence spectra of DCM dissolved in ethanol at various concentrations, excitation wavelength: 532 nm indicated as green line, temperature: 303 K.

Solvent: o-Xylene

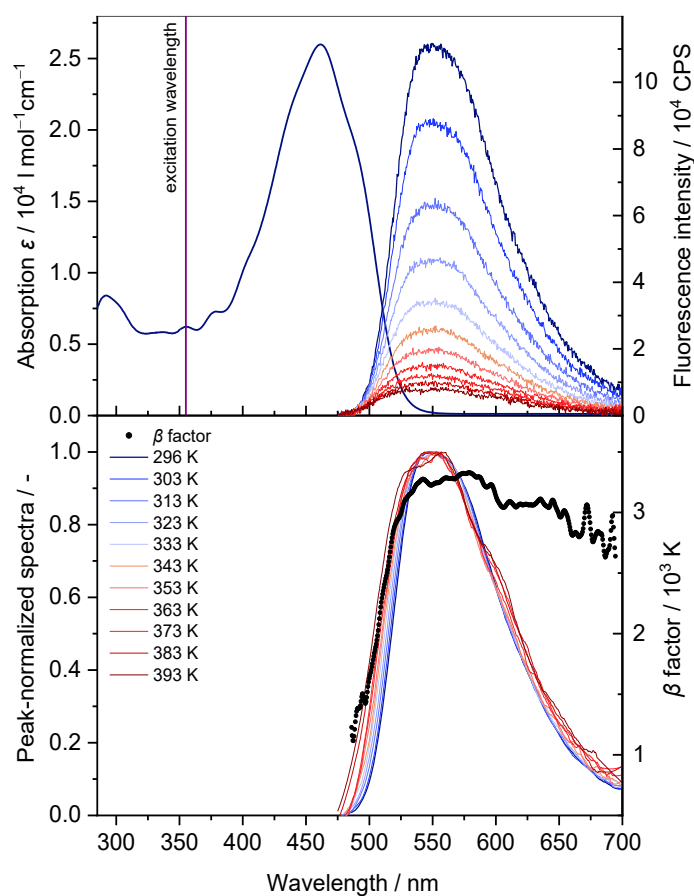


Figure A55: Temperature dependent absorption (296 K) and fluorescence spectra (up to 393 K) of DCM in o-xylene, 1 mg/l, excitation at 355 nm indicated as purple line, upper diagram: Absolute values, lower diagram: Peak-normalized values and β factor for the spectra at 303 and 373 K.

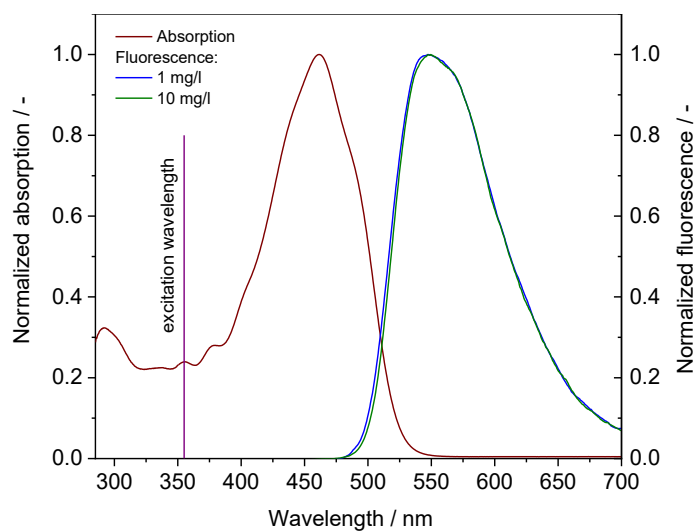


Figure A56: Peak-normalized absorption and fluorescence spectra of DCM dissolved in o-xylene at various concentrations (0.1 mg/l not shown due to low signal-to-noise ratio), excitation wavelength: 355 nm indicated as purple line, temperature: 303 K.

12.6.4.5 Pyrrromethene 597

Solvent: Ethanol

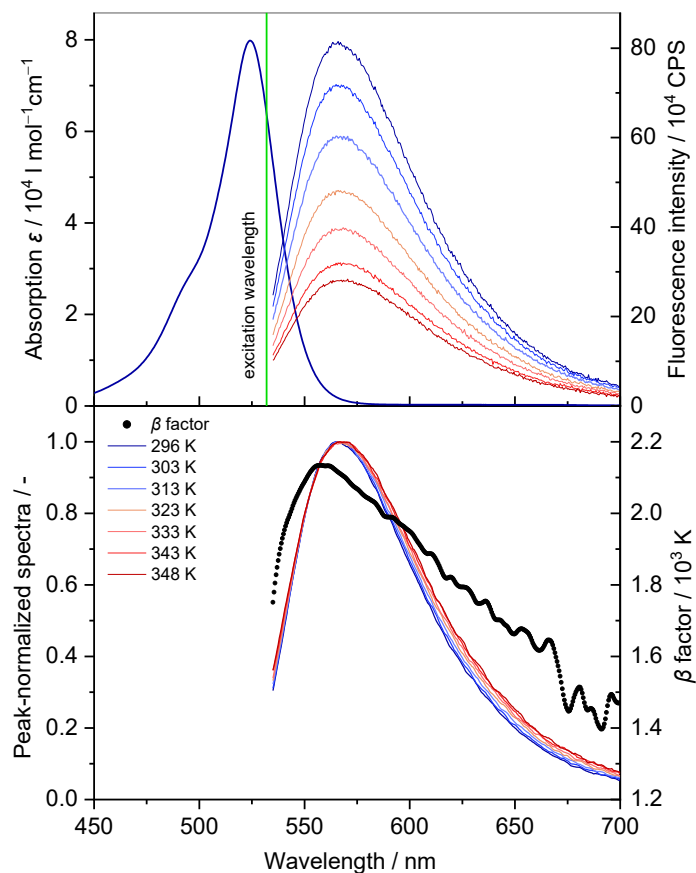


Figure A57: Temperature dependent absorption (296 K) and fluorescence spectra (up to 348 K) of pyrrromethene 597 in ethanol, 1 mg/l, excitation at 532 nm indicated as green line, upper diagram: Absolute values, lower diagram: Peak-normalized values and β factor for the spectra at 303 and 343 K.

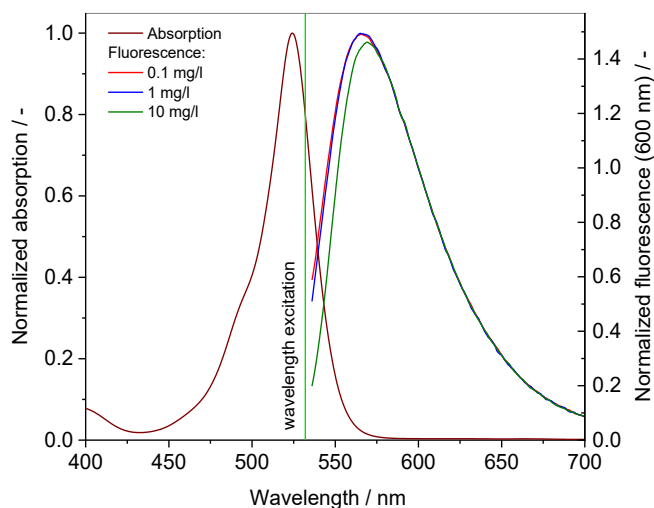


Figure A58: Peak-normalized absorption and at 600 nm normalized fluorescence spectra of pyrrromethene 597 dissolved in ethanol at various concentrations, excitation wavelength: 532 nm indicated as green line, temperature: 303 K.

Solvent: o-Xylene

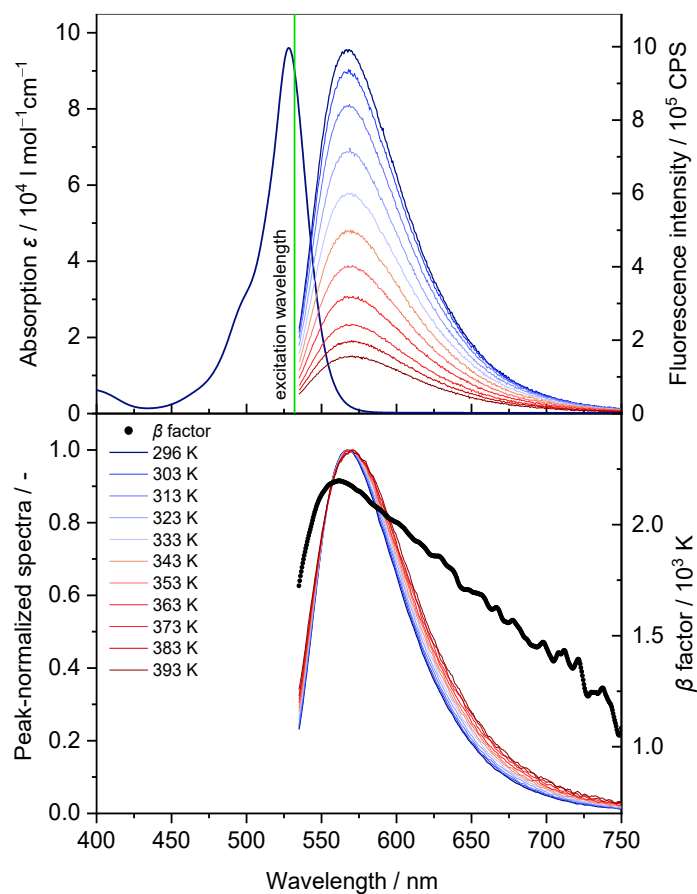


Figure A59: Temperature dependent absorption (296 K) and fluorescence spectra (up to 393 K) of pyrromethene 597 in o-xylene, 1 mg/l, excitation at 532 nm indicated as green line, upper diagram: Absolute values, lower diagram: Peak-normalized values and β factor for the spectra at 303 and 373 K.

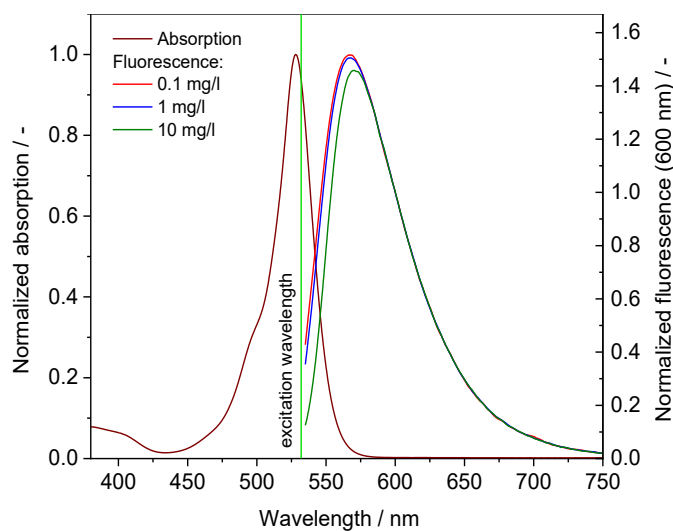


Figure A60: Peak-normalized absorption and at 600 nm normalized fluorescence spectra of pyrromethene 597 dissolved in o-xylene at various concentrations, excitation wavelength: 532 nm indicated as green line, temperature: 303 K.

12.7 Application of smoothing filters to single-shot images (inst. 2cLIF)

This section is connected to section 8.2.4 and presents the results of applying different smoothing filters to single-shot intensity maps (2cLIF color channels) to enhance fluorescence signal quality and improve the single-shot liquid temperature maps.

12.7.1 Single-shot intensity maps

Figure A61 shows single-shot intensity maps of the blue and red color channels smoothed by different filters (Gaussian, median, binning).

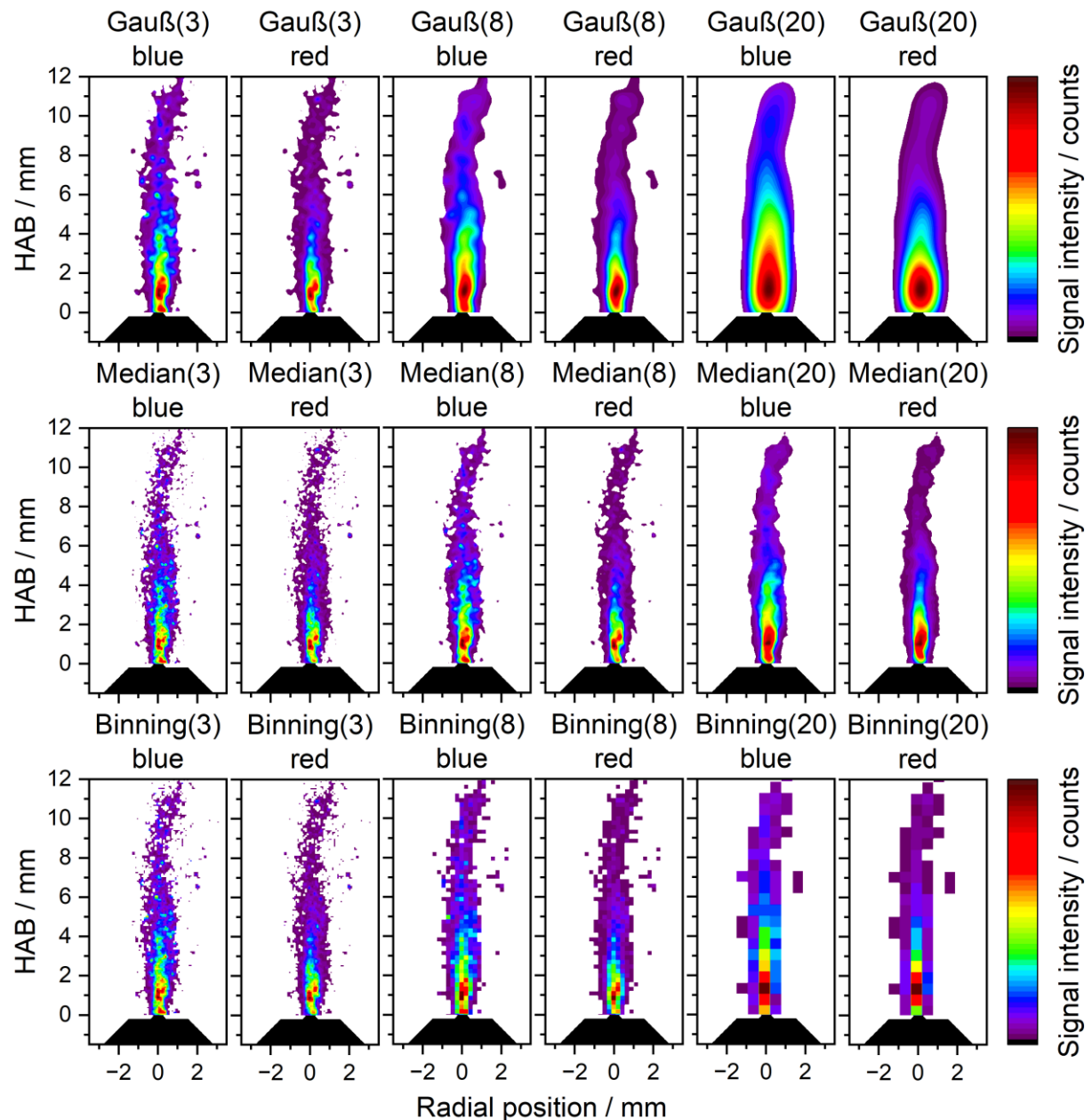


Figure A61: Single-shot intensity maps (same case as shown in Figure 95 and Figure 96) processed with smoothing filters, top row: Gaussian filter, middle row: Median filter, bottom row: Binning filter. The degree of smoothing is indicated in brackets in the headlines. The intensity maps are arranged in pairs, respectively, left: Blue color channel, right: Red color channel. Each intensity map has an individual color scale ranging from its minimum to maximum values. Pixels with values less than 15 counts in either of the two channels after filtering were masked in white.

The numbers in brackets in the headlines of the Gaussian-filtered intensity maps (top row) represent the standard deviation σ_{SD} of the Gaussian distribution used for filtering. The numbers in brackets in the headlines of the median- and binning-filtered intensity maps (middle and bottom rows) represent the kernel size (side length in pixels of the square data window) used for filter application.

12.7.2 Single-shot ratio maps

Figure A62 shows single-shot ratio maps derived from the spatial filter-smoothed single-shot intensity maps, as partially shown in Figure A61.

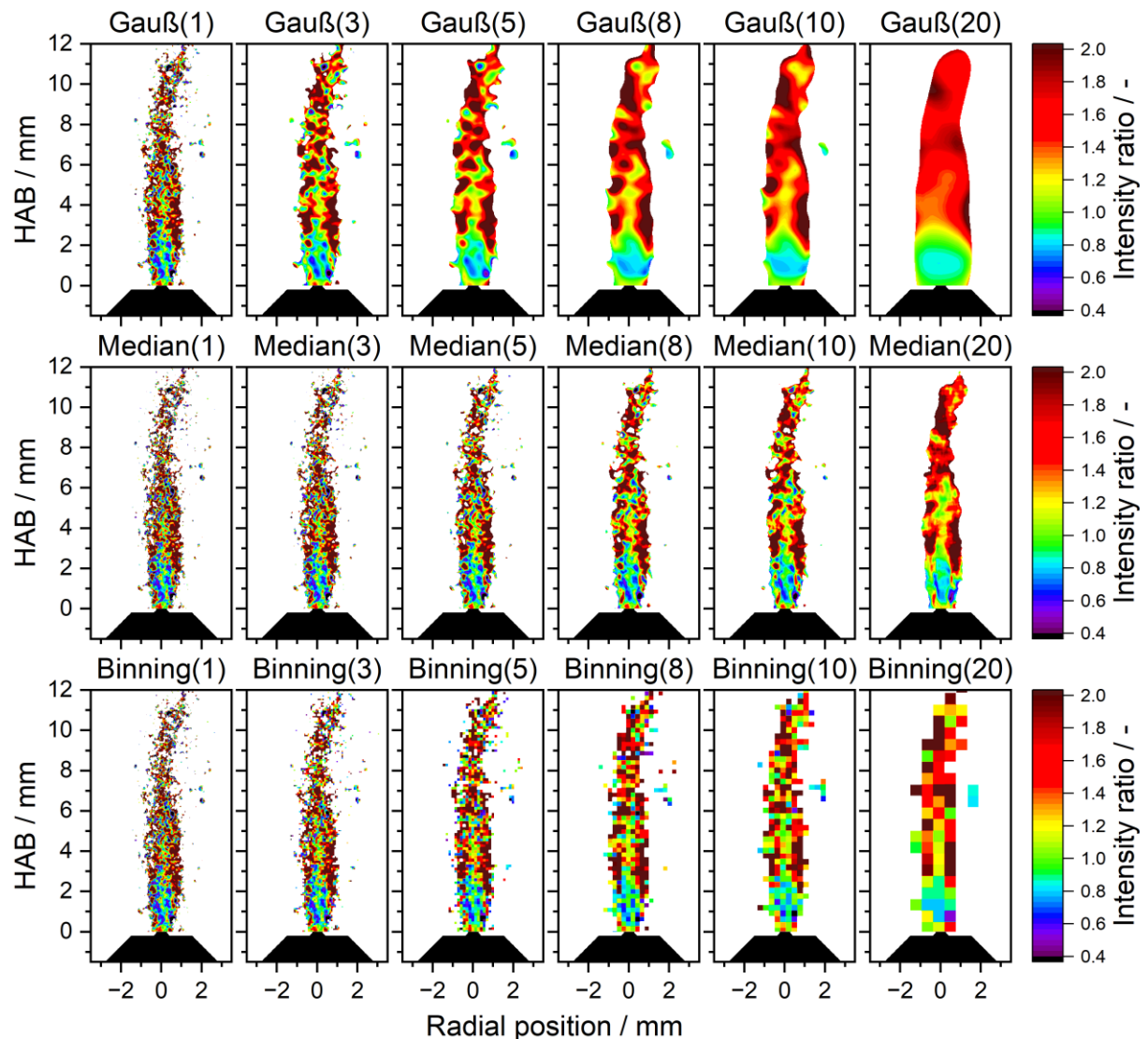


Figure A62: Single-shot ratio maps derived from both color channels processed with smoothing filters at various degrees of filtering as described in section 12.7.1. Top row: Gaussian filter, middle row: Median filter, bottom row: Binning filter.

12.7.3 Average liquid-temperature maps

Figure A63 shows average liquid-temperature maps derived from 200 single-shot ratio maps, as shown in Figure A62.

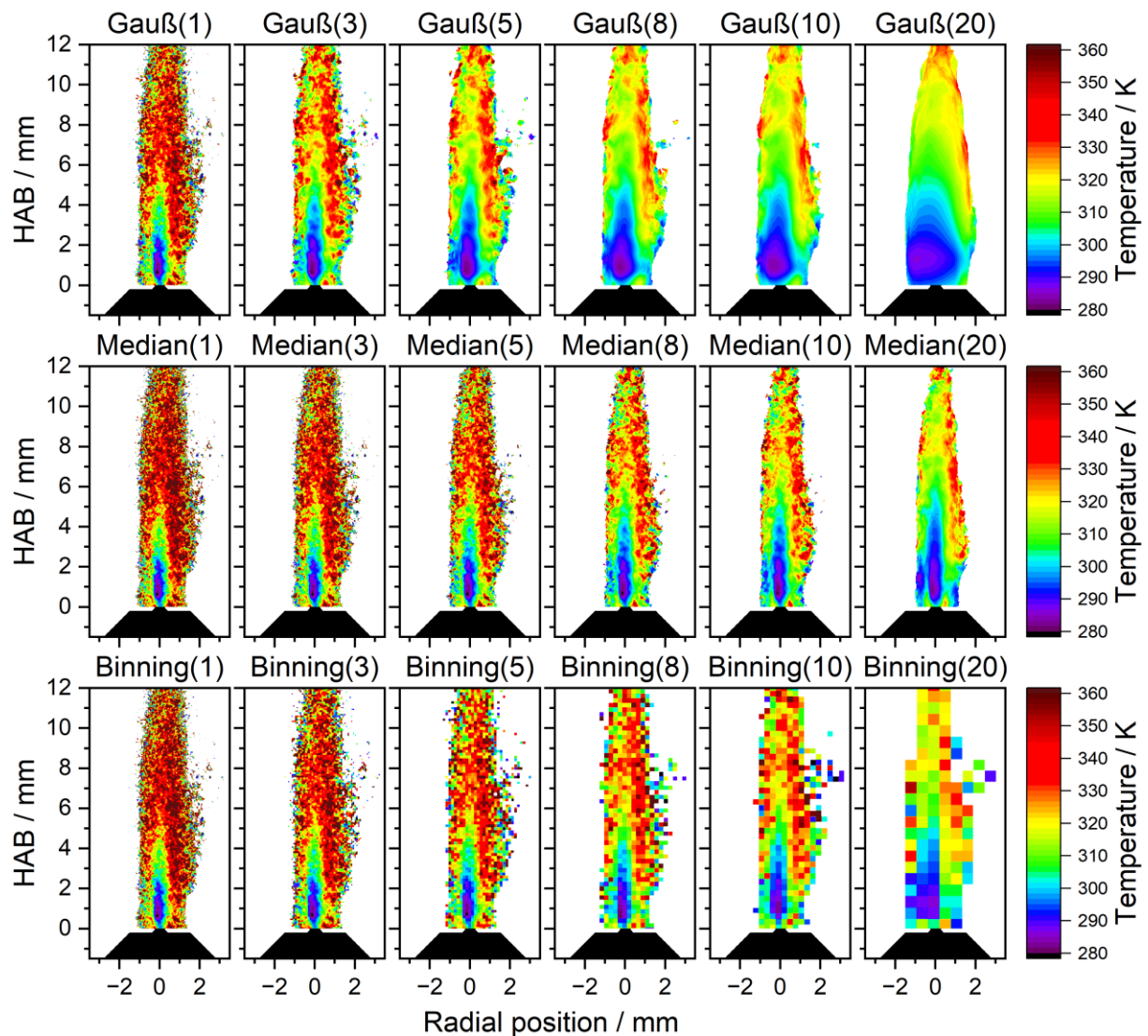


Figure A63: Average liquid-temperature maps derived from 200 single-shot ratio maps as shown in section 12.7.2. The underlying single-shot intensity maps were processed using smoothing filters (degree of smoothing given in brackets), top row: Gaussian filter, middle row: Median filter, bottom row: Pixel binning.

12.8 SpraySyn2 flame: Radial average liquid-temperature profiles

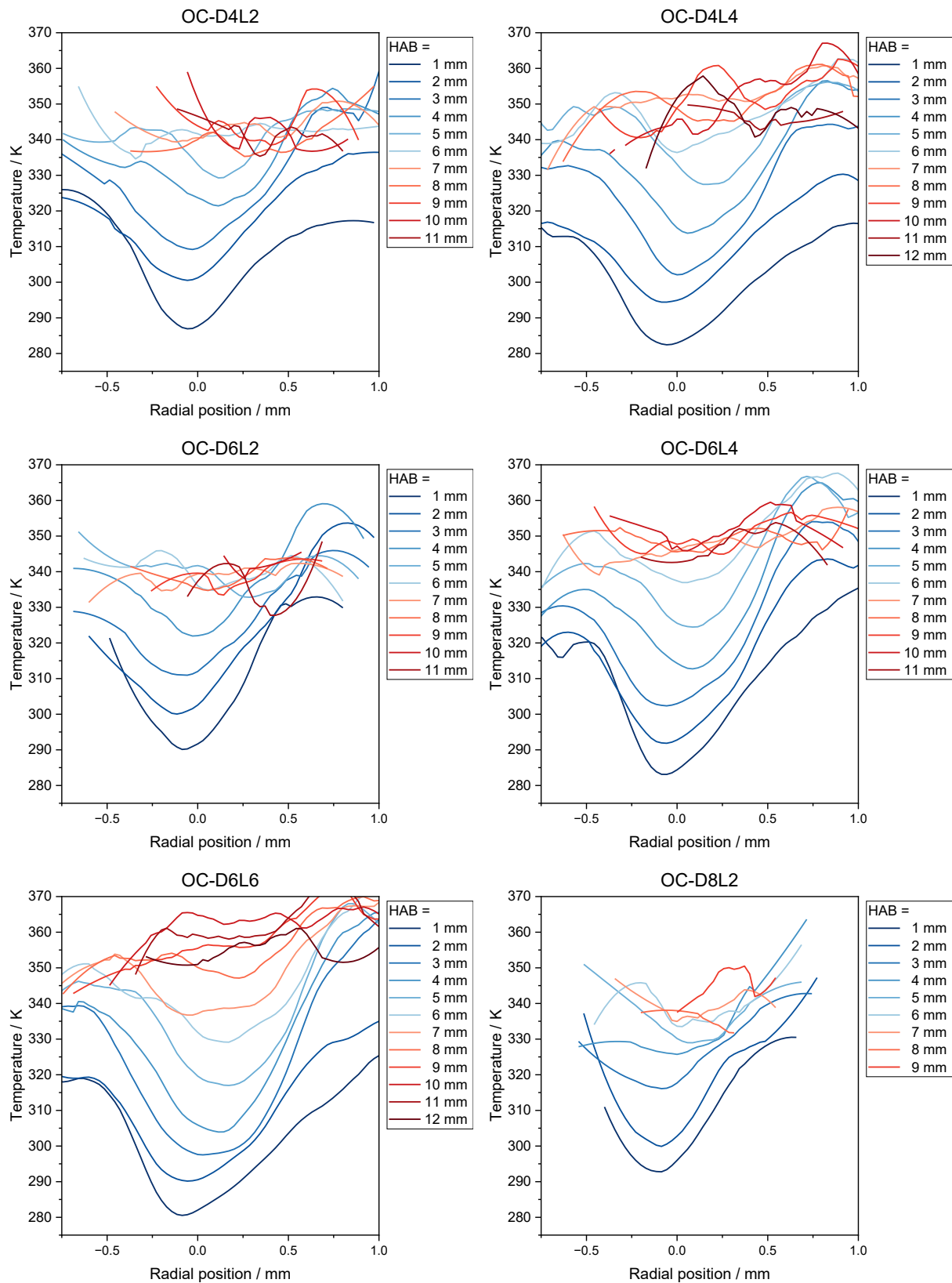


Figure A64: Radial liquid-phase temperature profiles at various height above burner from an extraction width of 0.4 mm, SpraySyn2 flame, identifiers for the operating conditions are given on top of each temperature map.

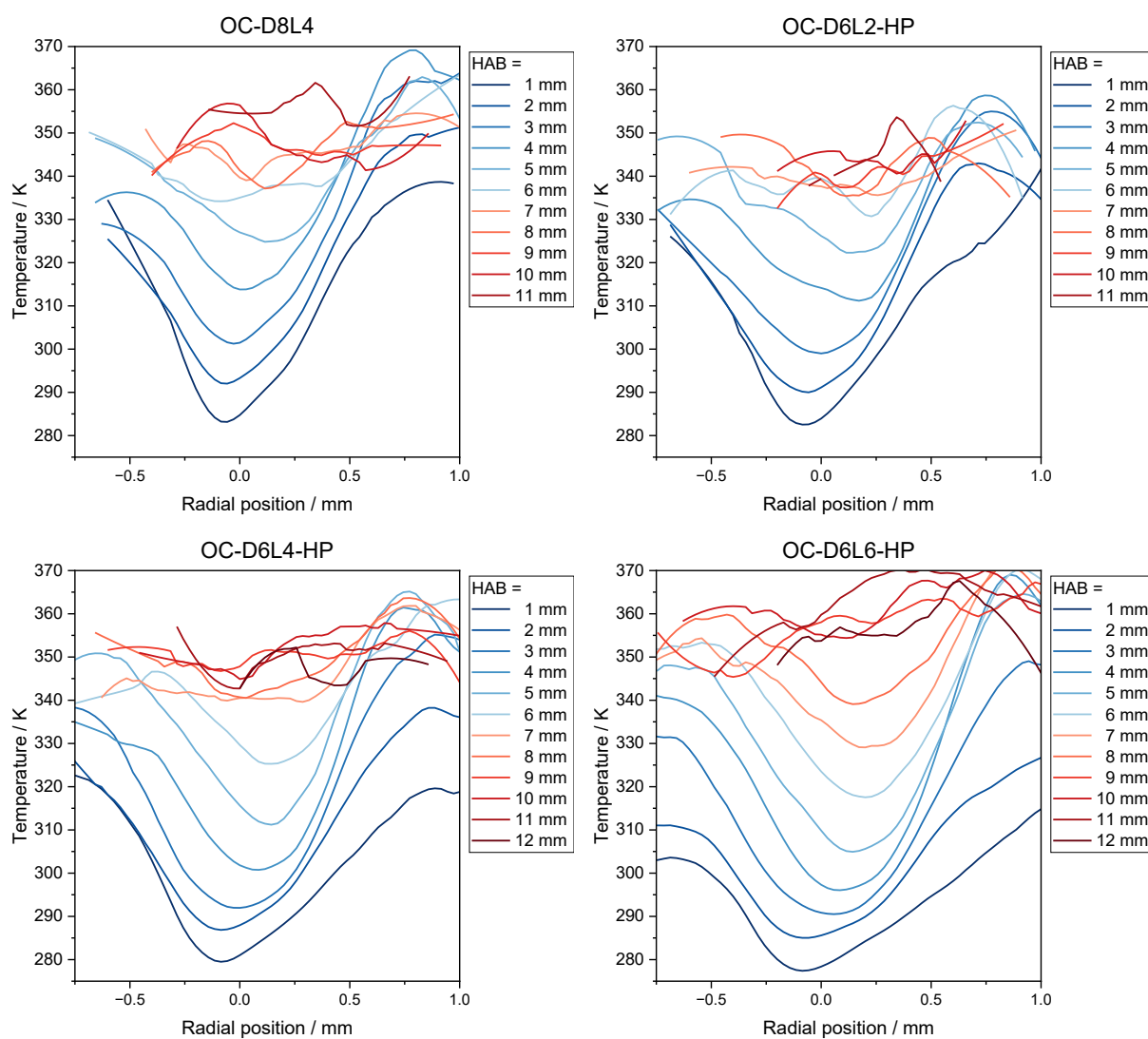


Figure A65: Radial liquid-phase temperature profiles at various height above burner from an extraction width of 0.4 mm, SpraySyn2 flame, identifiers for the operating conditions are given on top of each temperature map.

Archiving and Reuse of Research Data

All research data collected and used in this dissertation have been archived. The data have been partially made publicly accessible in the research data repository SpraySyn Database [56], available at <<https://spraysyn.db.cfd.uni-due.de/>> under the Meta IDs 168, 171, 183, and in the EU Open Research Repository Zenodo [476] available at <<https://doi.org/10.5281/zenodo.4613143>>. Additionally, the data have been fully stored in the research data archive of the Institute for Energy and Materials Processes (EMPI) for reuse. The archived data include raw measurement data with metadata, used programs and evaluation routines, lab books, and descriptions of the experiments and conditions.

Own Publications

Peer-reviewed journal articles

M.M. Prenting, M.I. Bin Dzulfida, T. Dreier, C. Schulz, Characterization of tracers for two-color laser-induced fluorescence liquid-phase temperature imaging in sprays, *Exp. Fluids* 61 (2020) 77. <https://doi.org/10.1007/s00348-020-2909-9>

M.M. Prenting, M. Shilikhin, T. Dreier, C. Schulz, T. Endres, Characterization of tracers for two-color laser-induced fluorescence thermometry of liquid-phase temperature in ethanol, 2-ethylhexanoic-acid/ethanol mixtures, 1-butanol, and o-xylene, *Appl. Opt.* 60 (2021) C98–C113. <https://doi.org/10.1364/AO.419684>

C.T. Foo, A. Unterberger, F.J.W.A. Martins, **M.M. Prenting**, C. Schulz, K. Mohri, Investigating spray flames for nanoparticle synthesis via tomographic imaging using multi-simultaneous measurements (TIMes) of emission, *Opt. Expr.* 30 (2022) 15524-15545. <https://doi.org/10.1364/OE.449269>

M.M. Prenting, S.-J. Baik, T. Dreier, T. Endres, A. Kempf, C. Schulz, Liquid-phase temperature in the SpraySyn flame measured by two-color laser-induced fluorescence thermometry and simulated by LES, *Proc. Combust. Inst.* 39 (2023) 2621-2630. <https://doi.org/10.1016/j.proci.2022.07.131>

M. Underberg, **M.M. Prenting**, M. Sieber, S. Schimek, C.O. Paschereit, T. Hülser, T. Endres, C. Schulz, H. Wiggers, S.M. Schnurre, A hydrogen-based burner concept for pilot-scale spray-flame synthesis of nanoparticles: Investigation of flames and iron oxide product materials, *Appl. Energ. Combust. Sci.* 15 (2023) 100165. <https://doi.org/10.1016/j.jaecs.2023.100165>

J. Kirchmann, A. Kronenburg, **M.M. Prenting**, S. Karaminejad, T. Dreier, T. Endres, S. Patil, F. Beyrau, Characterizing the SpraySyn burners with MMC-LES, *Appl. Energ. Combust. Sci.* 15 (2023) 100182. <https://doi.org/10.1016/j.jaecs.2023.100182>

S. Klukas, M. Giglmaier, M. Underberg, S.M. Schnurre, **M.M. Prenting**, T. Endres, H. Wiggers, C. Schulz, M. Sieber, S. Schimek, C.O. Paschereit, N.A. Adams, Scale-up analysis of spray flame nanoparticle synthesis by comparison of laboratory and pilot plant-scale burners, *Appl. Energ. Combust. Sci.* 18 (2024) 100263. <https://doi.org/10.1016/j.jaecs.2024.100263>

Conference proceedings

F. Schneider, S. Suleiman, **M.M. Prenting**, I. Wlokas, T. Dreier, H. Wiggers, C. Schulz, The SpraySyn standard burner enabling coordinated research on materials synthesis in spray flames, 29. Deutscher Flammentag (2019), Bochum, Germany.

M.M. Prenting, T. Dreier, C. Schulz, Characterization of tracers for two-color laser-induced fluorescence liquid-phase temperature imaging in sprays, *Optical Sensors and Sensing Congress*, Optica Publishing Group (2020), pp. LTh5F.2. <https://doi.org/10.1364/LACSEA.2020.LTh5F.2>

M.M. Prenting, M. Underberg, T. Dreier, T. Endres, S.M. Schnurre, C. Schulz, Multi-line NO-LIF gas-temperature imaging in a pilot-scale spray flame for nanoparticle synthesis. 11th European Combustion Meeting (2023), Rouen, France. <https://ecm2023.sciencesconf.org/>

Conference presentations

F. Schneider, S. Suleiman, **M.M. Prenting**, T. Dreier, C. Schulz, The SpraySyn burner: A new standard burner for coordinated studies on materials synthesis in spray flames, 37th International Symposium on Combustion (2018), Dublin, Ireland.

M.M. Prenting, T. Dreier, C. Schulz, Characterization of tracers for two-color laser-induced fluorescence liquid-phase temperature imaging in sprays, Laser Applications to Chemical, Security and Environmental Analysis, LACSEA (2020), Vancouver, Canada.

M.M. Prenting, S.-J. Baik, T. Dreier, T. Endres, C. Schulz, Two-color laser-induced fluorescence liquid-phase temperature imaging in spray flames for nanoparticle synthesis, Gordon Research Conference on Laser Diagnostics in Energy and Combustion Science (2021), GRC Connects event.

M.M. Prenting, S.-J. Baik, T. Dreier, T. Endres, A. Kempf, C. Schulz, Liquid-phase temperature in the SpraySyn flame measured by two-color laser-induced fluorescence thermometry and simulated by LES, 39th International Symposium on Combustion (2022), Vancouver, Canada.

M. Underberg, **M.M. Prenting**, M. Sieber, T. Endres, T. Hülser, S. Schnurre, Scale-up: spray-flame synthesis of nanoparticles on a pilot scale, 5th International Symposium Gas-Phase Synthesis of Functional Nanomaterials (2022), Mülheim an der Ruhr, Germany.

S.-J. Baik, F. Fröde, J. Kirchmann, S. Klukas, S. Karaminejad, **M.M. Prenting**, M. Gonchikzhapov, M. Stodt, T. Endres, T. Kasper, J. Kiefer, H. Pitsch, A. Kronenburg, N.A. Adams, A. Kempf, SpraySyn: a flame simulation comparison, 5th International Symposium Gas-Phase Synthesis of Functional Nanomaterials (2022), Mülheim an der Ruhr, Germany.

M. Underberg, **M.M. Prenting**, M. Sieber, T. Hülser, S. Schnurre, Prozessskalierung: Sprühflammsynthese von Nanopartikeln im Pilotmaßstab, Jahrestreffen der DECHEMA-Fachgemeinschaft "Prozess-, Apparate- und Anlagentechnik" (2022), Frankfurt am Main, Germany.

M.M. Prenting, M. Underberg, T. Dreier, T. Endres, S. Schnurre, C. Schulz, Multi-line NO-LIF gas-temperature imaging in a pilot-scale spray flame for nanoparticle synthesis, Gordon Research Conference on Laser Diagnostics in Energy and Combustion Science (2023), poster, Newry, Maine, United States.

Student supervision

M.I. Bin Dzulfida: Measurement of the fluorescence spectra of various aromatics respectively dyes in solvents for the implementation as tracer for the imaging laser-induced fluorescence (LIF) diagnostics. Bachelor thesis (2019).

R. Wong: Fluorescence spectra of laser dyes in 1-butanol and 2-ethylhexane-acid/ethanol mixture applicable as tracers for 2-color laser-induced fluorescence thermometry imaging. Bachelor thesis (2019).

S.K. Tan: Measurement of the fluorescence spectra of dyes in various solvents for the implementation as tracer for the imaging laser-induced fluorescence (LIF) diagnostics. Bachelor thesis (2020).

Y. Mu: Measurement of the absorption and fluorescence spectra of dyes dissolved in ethanol for the implementation as tracer for imaging laser-induced fluorescence (LIF) diagnostics. Bachelor thesis (2020).

Danksagung

Die Verfassung dieser Dissertation erfolgte im Rahmen meiner Tätigkeit als wissenschaftlicher Mitarbeiter am Lehrstuhl für Reaktive Fluide des Instituts für Energie- und Material-Prozesse (vormals: Institut für Verbrennung und Gasdynamik) der Universität Duisburg-Essen. Ich möchte hiermit Allen danken, die direkt oder indirekt zur erfolgreichen Erstellung dieser Forschungsarbeit beigetragen haben.

Insbesondere danken möchte ich Prof. Dr. Christof Schulz, Prof. Dr. Thomas Dreier und Dr. Torsten Endres für die Vergabe der Doktorandenstelle mit diesem anspruchsvollen und vielseitigen Forschungsthema. Durch euch wurde ich in die wissenschaftliche Gemeinschaft eingeführt und konnte mich für meine neuen Aufgaben in der notwendigen Weise fachlich wie auch persönlich weiterentwickeln. Mithilfe eurer umfassenden Unterstützung und der hervorragenden Laborausstattung, konnte ich meine Forschungsarbeit bestmöglich durchführen und zu einem erfolgreichen Abschluss bringen. Hervorheben möchte ich an dieser Stelle die außergewöhnlich gute Arbeitsatmosphäre, die unter eurer Leitung am Lehrstuhl ermöglicht wird.

Des Weiteren möchte ich Herrn Prof. Dr. Lars Zigan für die erkenntnisreichen fachlichen Diskussionen auf gemeinsamen Konferenzen und die bereitwillige Übernahme des Zweitgutachtens herzlich danken.

Ich danke Dr. Ralf Starke und Prof. Dr. Sebastian Kaiser für die jahrelange erfolgreiche Zusammenarbeit in der universitären Lehre für das Fach Wärmekraft- und Arbeitsmaschinen.

Darüber hinaus gilt mein besonderer Dank den festen Mitarbeitern, die das Fundament des Lehrstuhls bilden. Ohne euch würde es weder in der Verwaltung noch im Labor so reibungslos laufen, und der wissenschaftliche Fortschritt wäre deutlich eingeschränkt. Dafür danke ich Dr. Erdal Akyildiz, Jörg Albrecht, Beate Endres, Barbara Graf, Dieter Hermanns, Ludger Jerig, Dr. Jan Menser, Birgit Nelius, Barbara Nota, Dr. Hans Orthner, Uwe Rettig, Sebastian Rosendahl, Sonay Saritas und Natascha Schlösser.

Besonderer Dank gilt meinem Bürokollegen vom ersten bis zum letzten Tag Marc Lubnow, sowie meinen engsten fachlichen Arbeitskollegen Dr. Seung-Jin Baik, Sadrollah Karaminejad, Dr. Florian Schneider und Martin Underberg. Ich danke allen Kollegen des Lehrstuhls, insbesondere den Kollegen aus meiner Arbeitsgruppe der Angewandten Spektroskopie und den Kollegen anderer Arbeitsgruppen mit denen ich zusammenarbeiten durfte: Dr. Steven Angel, Sascha Apazeller, Muhammad Asif, Thomas Baranowski, Mehrdad Bathaei, Dr. Matthias Beuting, Felix Luc Ebertz, Laura Engelbracht-Kloß, Dr. Peter Fjodorow, Cheau Tyan Foo, Paolo Fortugno, Dr. Simon Görs, Dr. Sebastian Hardt, Dr. Niklas Jüngst, Dr. Stefan Kilian, Dr. Patrick Kranz, Stefan Kuns, Dr. Judith Laichter, Dr. Guannan Liu, Dr. Hecong Liu, Dr. Claudia Lopez-Camara, Moritz Loewenich, Dr. Raphael Mansmann, Abbas El Moussawi, Dr. Stanislav Musikhin, André Müller, Dr. Adrian Münzer, Dr. Philipp Niegemann, Stephen Robinson-Enebeli, Lin Shi, Dr. Samer Suleiman, Benjamin Südholt und Dr. Alexander Tarasov.

Ferner danke ich allen wissenschaftlichen Mitarbeitern meines DFG-Projektes „Nanopartikel-synthese in Sprayflammen“ für die jahrelange erfolgreiche Zusammenarbeit und die unvergesslich gute Zeit bei den zahlreichen Projekttreffen und Summerschools: Dr. Abouelmagd Abdelsamie, Simon Aßmann, Dr. Malte Bieber, Dr. Efim Borukhovich, Sophie Dupont, Fabian Fröde, Varun Aiyar Ganesan, Dr. Marcus Giglmaier, Dr. Munko Gonchikzhapov, Dr. Yasin Karakaya, Dr. Jonas Kirchmann, Sebastian Klukas, Abhijeet Kumar, Babette Kunstmann, Peter Lang, Dr. Haipeng Li, Dr. Fabio Martins, Orlando Massopo, Shahram Mohammadi, Bettina

Münsterjohann, Dr. Monika Nanjaiah, Praveen Narasu, Dr. Shirin Patil, Dr. Jalal Poostforooshan, Anthony Premkumar, Dr. Johannes Sellmann, Dr. Moritz Sieber, Mira Simmler, Ivan Skenderović, Dr. Malte Stodt, Ricardo Tischendorf, Arne Witte, Guohui Yang und Zhaoping Ying. Darüber hinaus gilt mein Dank Steffi Nickol und Dr. Sebastian Peukert für die Organisation und Koordination des Forschungsprojektes und der Deutschen Forschungsgesellschaft für die Finanzierung meiner Forschungsarbeit.

Ich möchte meiner studentischen Hilfskraft Maksim Shilikhin und meinen Bacheloranden Muhammad Imran Bin Dzulfida, Raymond Chung Seng Wong, Sze Keng Tan und Yubin Mu besonders für ihre Mitarbeit und Unterstützung bei zahlreichen Laborarbeiten und Messungen danken.

Abseits des Fachlichen, gilt mein größter Dank meiner gesamten Familie ohne die, die Erstellung dieser Dissertation nicht möglich gewesen wäre. Besonders danke ich meinen Eltern Adele und Michael Prenting. Ihr habt mir meinen Bildungsweg in jeder Hinsicht ermöglicht, mich motiviert, und mir stets zur Seite gestanden. Ich danke meinem Bruder Julian Prenting für seine breite Unterstützung und motivierenden Worte. Meinen besonders großen Dank möchte ich meiner Ehefrau Felicitas Prenting zum Ausdruck bringen. Vielen Dank für deine Geduld, das Rückenfreihalten im Alltag und deine unerschütterliche Unterstützung.